Universitat
de les Illes Balears

DOCTORAL THESIS
2017

Doctoral Programme of Statistical and Nonlinear Physics

DINÁMICA DE ESTRUCTURAS LOCALIZADAS DISIPATIVAS EN CAVIDADES ÓPTICAS NO LINEALES FORZADAS/ DYNAMICS OF DISSIPATIVE LOCALIZED STRUCTURES IN DRIVEN NONLINEAR OPTICAL CAVITIES

Pedro Parra-Rivas

Doctoral Supervisors:

Dr. Damià Gomila
Prof. Dr. Jan Danckaert
Prof. Dr. Lendert Gelens

Doctor by the Vrije Universiteit Brussel and the Universitat de les Illes Balears

Dynamics of Dissipative Localized Structures in Driven Nonlinear Optical Cavities

Ph. D. thesis by Pedro Parra-Rivas

Faculty of Sciences
Vrije Universiteit Brussel
Pleinlaan 2
B-1050 Brussels, Belgium

Thesis submitted in partial fulfillment of the requirements for the academic degree "Doctor of Phylosophy in Sciences"
Supervisors: Dr. Damià Gomila, Prof. Dr. Jan Danckaert, Prof. Dr. Lendert Gelens

ad astra per ardua

Acknowledgments

When I was a child, and people asked me what I wanted to do once I had grown up, I used to say: A scientist! Well, now I think I am a scientist, and I am very proud of it. Trying to explain nature in all its complexity, and trying to do it rationally, is something to be proud of. For this reason, I would like to thank all the people who helped me to achieve this goal.

First I would like to express my sincere gratitude to my scientific family, for their support and help during this journey. Specially, I am very grateful to my supervisors Jan Danckaert, Damia Gomila, and Lendert Gelens. Thank you, Jan, for giving me the opportunity to embark on my Ph.D. in your research group at the VUB. The nice atmosphere you have created in the group will not be forgotten.

Damia, thanks to you I started this journey already five years ago at IFISC in Palma. With you I took my very first steps in research and I learnt, and I am still learning, a lot. Thank you for being ready to talk every time that I need you. Thank you Lendert, for holding me by the hand since I arrived in Brussels. Your incondicional help, and good advice have been, and still are, something that I could never thank you enough. To both of you, thank you a lot for the motivation, scientific guidance and support, which were essential to get my research on the right track.

Pere, thank you very much for your help during my PhD. I enjoyed a lot the discussions in you company and I learnt a lot from them.

Edgar, thank you for giving me the opportunity to work together with you in Berkeley, it was an honor. From you, I learnt a great deal about nonlinear

dynamics and bifurcation theory, that I will apply during all my research carrier. I enjoyed a lot my stay in California. I hope I could visit you again.

I would also like to thank Manuel Matías, Francois Leo, and Stephane Coen, for interesting discussions and fruitful collaborations, that I would like to maintain in the future.

So to all of you I only have to say that, if I have arrived at this point it is by standing on the shoulders of giants.

I am honored that Prof. Alex Sevrin, Prof. Guy van der Sande, Prof. Pere Colet, Prof. Alan Champneys, Prof. Giovanna Tissoni, Prof. Marc Haelterman, to be part of the jury of my Ph.D. in Brussels, and Prof. Edgar Knobloch, Prof. Alan Champneys, and Dr. Francois Leo, to be part of the jury in Palma.

A special word of thanks goes out to all the colleagues (most of them friends) that I met during these year in Palma and Brussels. I truly enjoyed my time in both places, and I will never forget the nice moments that we spent together.

But not everything in life is science, and within these past years I had the luck of meeting great people that colored my life making it wonderful. Because of that, this thesis is also dedicated to all my friends, which they know who they are, and to the special persons that I met along this period. You have filled my life with the most important thing that any human being can reach: happiness. Thank you for being there.

Y agradezco por encima de todo a mi familia, el pilar mas robusto de mi vida, por apoyarme y animarme en todas las decisiones que he tomado, y por darme en todo momentos su cariño y amor incondicional. Siempre estais conmigo.

Pedro Parra-Rivas
Brussels, Belgium
January 2017

Summary

In this thesis, we study emergent structures in spatially extended systems. We restrict our attention to systems that are internally dissipative and externally driven, also referred to as systems out of thermodynamical equilibrium. We investigate a particular type of emergent structures, called localized structures (LSs). As their name indicates, LSs are confined in time and/or space. LSs can develop instabilities that make them move, deform or oscillate. Oscillations can also lie at the origin of a dynamical, neuron-like phenomenon called "excitability".

Although LSs, and their various instabilities, can be observed in a wide range of physical systems, we focus on the field of optics, where LSs can be observed in nonlinear optical cavities. In this context, LSs are also called cavity solitons. To study this type of cavities we use the Lugiato-Lefever (LL) model, a partial differential equation first proposed in 1987 to describe transversal electric field in a passive optical cavity filled with a nonlinear medium. In the last decade this model has sparked new interest as it was found to also describe the formation and dynamics of Kerr frequency combs in microresonators. A frequency comb consists in a broad optical spectrum of sharp comb lines with an equidistant frequency spacing that can be used to perform ultra-precise measurements of optical frequencies, and has numerous other applications in spectroscopy, optical clocks and waveform synthesis. The interesting and essential point here is that such coherent frequency combs correspond to the frequency spectrum of cavity solitons and patterns circulating inside the cavity. Therefore, by studying LSs in the LL model we obtain crucial information about the dynamics and stability of Kerr frequency combs.

In the first chapters of the thesis we provide a detailed study of LSs in the LL model in its two main regimes of operation, namely the region with anomalous group velocity dispersion (GVD) and the one with normal GVD. For anomalous GVD, we focus on patterned solutions and bright solitons and characterize their bifurcation structure and instabilities leading to oscillations in time and/or space. In contrast, in the normal GVD regime, we show that the main LSs are dark solitons, which have a very different origin and bifurcation structure, but undergo similar instabilities. Next, we focus on how higher order dispersion effects modify the soliton dynamics in both regimes, showing that a various LSs can be stabilized by the higher order dispersion. Another question that we address is how bound states of solitons can form, where interaction between solitons is largely determined by the oscillatory tails in the soliton's profile. Finally, we focus on how defects and advection can modify the dynamics of LSs, showing the combination of defects and advection can induce excitability.

Resumen

En esta tesis estudiamos estructuras emergentes en sistemas extendidos. Restringimos nuestra atención a sistemas con disipación interna, es decir, con pérdidas, y que son forzados externamente, también conocidos como sistemas fuera del equilibrio termodinámico. Investigamos un tipo particular de estructuras emergentes denominadas estructuras localizadas (LSs es su acrónimo en inglés). Como su nombre indica, estas estructuras están confinadas espacial y/o temporalmente. Las LSs pueden desarrollar inestabilidades que induzcan movimiento, deformación, u oscilaciones en las mismas. Las oscilaciones pueden ser el origen en un fenómeno típicamente asociado a la dinámica de neuronas denominado "excitabilidad".

Aunque las LSs, y sus diferentes inestabilidades, pueden observarse en un gran número de sistemas físicos, en esta tesis nos concentraremos en el dominio de la óptica, donde las LSs aparecen en cavidades ópticas no lineales. En este contexto, las LSs son también denominadas solitones de cavidad. Para estudiar este tipo de cavidades utilizamos el modelo de Lugiato-Lefever (LL), una ecuación en derivadas parciales propuesto por primera vez en 1987 para describir la componente transversal del campo eléctrico en una cavidad óptica pasiva con un medio no lineal. En la última década este modelo ha despertado nuevo interés al descubrirse que también puede describir la formación y dinámica de peines de frecuencia tipo Kerr en microcavidades. Un peine de frecuencia consiste en un espectro óptico extenso formado por líneas de frecuencia equiespaciadas que puede ser utilizado para realizar medidas de frecuencias ópticas ultra precisas, las cuales tienen un gran número de aplicaciones en espectroscopía, relojes óp-

ticos y síntesis de formas de onda. El punto más interesante y esencial es que estos peines de frecuencia coherentes corresponden al espectro de frecuencias de solitons de cavidad y patrones circulando en el interior de la cavidad. Por tanto, estudiando las LSs en el modelo de LL se obtiene información crucial sobre la dinámica y estabilidad de estos peines de frecuencia.

En los primeros capítulos de la tesis presentamos un detallado estudio de las LSs en el modelo de LL en sus dos principales regímenes de operación: dispersión anómala de la velocidad de grupo de las ondas (GVD, según su acrónimo en inglés) y GVD normal. Para el caso de GVD anómalo, nos concentramos en el estudio de soluciones tipo patrón y soluciones tipo solitón "brillante", y caracterizamos su estructura de bifurcación y las inestabilidades que dan origen a oscilaciones espaciales y/o temporales. Por el contrario, en el régimen de GVD normal, mostramos que las LSs principales son solitones "oscuros", los cuales tienen un origen y una estructura de bifurcación diferente, aunque las inestabilidades son similares. A continuación nos centramos en investigar como efectos dispersivos a órdenes superiores modifican la dinámica de los solitones en ambos regímenes, mostrando que varias LSs pueden ser estabilizadas por los mismos. Otra cuestión que abordamos es como pueden formarse estados ligados de solitones, donde la interacción entre solitones es determinada por las colas oscilantes presentes en el perfil del solitón. Para finalizar, estudiamos como defectos y advección pueden modificar la dinámica de las LSs, demostrando que la combinación de ambos elementos puede inducir comportamientos complejos y excitabilidad.

Samenvatting

In deze thesis bestuderen we spontaan opkomende structuren in ruimtelijk uitgestrekte systemen. We beperken onze aandacht tot systemen die intern dissipatief zijn en extern aangedreven. Zulke systemen zijn niet in thermodynamisch evenwicht. We onderzoeken een bepaalde soort van deze spontane structuren, genaamd gelokaliseerde structuren (LS). Zoals de naam reeds aangeeft, zijn LS begrensd in de tijd en/of ruimte. LS kunnen destabiliseren zodat ze bewegen, vervormen, of oscilleren. Zulke oscillaties kunnen aan de basis liggen van een dynamisch, neuron-achtig fenomeen, genaamd "exciteerbaarheid"

Ook al kunnen LS geobserveerd worden in een brede waaier van fysische systemen, werken we in het domein van de optica, waar LS kunnen waargenomen worden in niet-lineaire optische caviteiten. In deze context worden LS ook caviteitssolitonen genoemd. Om dit type van optische caviteiten te bestuderen, gebruiken we het Lugiato-Lefever (LL) model, een partiële differentiaalvergelijking die het eerst werd voorgesteld in 1987 om het transversale elektrische veld in passieve optische caviteiten met een niet-lineair medium te beschrijven. Gedurende de laatste jaren heeft dit model opnieuw interesse opgewekt wanneer er werd gevonden dat dezelfde vergelijking kan gebruikt worden om de vorming en dynamiek van Kerr frequentiekammen in microresonatoren te beschrijven. Een frequentiekam bestaat uit een breed optisch spectrum van scherpe lijnen met een gelijke frequentiespreiding, en kan gebruikt worden om heel precieze metingen van optische frequentie uit te voeren, en wordt ook gebruikt in tal van andere toepassingen in spectroscopie, optische klokken, en het maken van golfvormen. Het interessante en essentiele punt is hier dat zulke coherente frequentiekammen

overeenstemmen met het frequentiespectrum van caviteitssolitonen en andere patronen die circuleren in de caviteit. M.a.w., door het bestuderen van LS in het LL model kunnen we cruciale informatie bekomen over de dynamiek en stabiliteit van Kerr frequentiekammen.

In de eerste hoofdstukken van de thesis bestuderen we in detail LS in het LL model in de twee grote werkingsregimes, namelijk het regime met abnormale groepssnelheidsdispersie (GSD), en één met normale GSD. Voor abnormale GSD concentreren we ons op patronen en heldere solitonen, and karakteriseren we hun bifurcatiestructuur en instabiliteiten die leiden tot oscillaties in de tijd en/of ruimte. In tegenstelling, in het normale GSD regime, tonen we dat de voornaamste LS donkere solitonen zijn, dewelke een erg verschillende oorsprong en bifurcatiestructuur hebben, maar toch gelijkaardige instabiliteit ondergaan. Daarna bestuderen we hoe hogere order dispersie de solitondynamiek kan veranderen in beide regimes. We tonen dat verschillende LS gestabiliseerd worden door zulke hogere order dispersie. Een andere vraag die we aanpakken is hoe gebonden toestanden van verschillende solitonen kunnen vormen, waar de interactie tussen deze verschillende LS grotendeels bepaald wordt door de oscillerende staarten in het profiel van een enkel soliton. Tenslotte bestuderen we hoe defecten en advectie de dynamiek van LS veranderen, en we tonen dat de combinatie van beide zaken kan leiden tot exciteerbaarheid.

Resum

En aquesta tesi estudiem estructures emergents en sistemes estesos. Restringim la nostra atenció a sistemes amb dissipació interna, és a dir, amb pèrdues, i que són forçats externament, també coneguts com a sistemes fora de l'equilibri termodinàmic. Investigam un tipus particular d'estructures emergents denominades estructures localitzades (LSs és el seu acrònim en anglès). Com el seu nom indica, aquestes estructures estan confinades espacial i/o temporalment. Les LSs poden desenvolupar inestabilitats que indueixen moviment, deformació, o oscil·lacions en les mateixes. Les oscil·lacions poden ser l'origen d'un fenomen típicament associat a la dinámica de neurones denominat "excitabilitat".

Tot i que les LSs, i les seves diferents inestabilitats, poden observar-se en un gran número de sistemes físics, en aquesta tesi ens concentrarem en el domini de la òptica, on les LSs apareixen en cavitats òptiques no lineals. En aquest context, les LSs són també denominades solitons de cavitat. Per estudiar aquest tipus de cavitats utilitzem el model de Lugiato-Lefever (LL), una equació en derivades parcials proposada per primera vegada al 1987 per descriure la component transversal del camp elèctric en una cavitat òptica passiva amb un mitjà no lineal. A l'última dècada aquest model ha despertat un nou interès en descobrir-se que també pot descriure la formació i dinàmica de "pintes de freqüència" tipus Kerr en microcavitats. Una "pinta de freqüència" consisteix en un espectre òptic extens format per línies de freqüència equiespaiades que poden ser utilitzades per a realitzar mesures de freqüències òptiques ultra precises, les quals tenen un gran número d'aplicacions en espectroscòpia, rellotges òptics i síntesi de formes d'ona. El punt més interessant i essencial és que aquestes "pintes de freqüència"

coherents corresponen a l'espectre de freqüències de solitons de cavitat i patrons circulant a l'interior d'una cavitat. Per tant, estudiant les LSs en el model de LL s'obté informació crucial sobre la dinàmica i estabilitat d'aquests "pintes de freqüència".

En els primers capítols de la tesi presentem un detallat estudi de les LSs en el model de LL en els seus dos principals règims d'operació: dispersió anòmala de la velocitat de grup de les ones (GVD, segons el seu acrònim en anglès) i GVD normal. Per al cas de GVD anòmala, ens concentrem en l'estudi de solucions tipus patró i solucions tipus solitó "brillant", i caracteritzem les seves estructures de bifurcació i les inestabilitats que donen origen a oscil·lacions espacials i/o temporals. Per contra, al règim de GVD normal, mostrem que les LSs principals són solitons "foscos", els quals tenen un origen i una estructura de bifurcació diferent, encara que les inestabilitats són similars. Tot seguit ens centrem en investigar com efectes dispersius a ordres superiors modifiquen la dinàmica dels solitons en ambdós règims, mostrant que diverses LSs poden ser estabilitzades pels mateixos. Una altra qüestió que abordem és com es poden formar estats lligats de solitons, on la interacció entre solitons és determinada per les cues oscil·lants presents en el perfil del solitó. Per acabar, estudiem com defectes i advecció poden modificar la dinàmica de les LSs, demostrant que la combinació dels dos elements pot induir comportaments complexos i excitabilitat.

List of abbreviations

BD	Beliakov-Devaney (transition)
C	Cusp (local bifurcation)
CE	Canard explosion
CM	Coupled mode (equations)
CS	Cavity soliton
CW	Continuous wave
DC	Double-center (global bifurcation)
DS	Dissipative soliton
DW	Dispersive wave
EC	Eckhaus (instability)
FC	Frequency comb
FC	Fold of cycles
FCGL	Forced complex Ginzburg-Landau (equation)
FOD	Fourth order dispersion
FW	Finite-wavelength (instability)
FWH	Finite-wavelength-Hopf (instability)
GG	Gravilov-Guckenheimer (local bifurcation)
GL	Ginzburg-Landau (equation)
GVD	Group velocity dispersion
H	Hopf (local bifurcation)
HH	Hamiltonian-Hopf (local bifurcation)
HOD	Heigh order dispersion
HSS	Homogeneous steady state
KdV	Korteweg de Vries (equation)
KFC	Kerr frequency comb

LL	Lugiato-Lefever (equation)
LS	Localized structure
LW	Long-wavelength (instability)
MF	Mean field
MI	Modulational instability
NLS	Nonlinear Schrodinger (equation)
ODE	Ordinary differential equation
OPO	Optical parametric oscillator
P	Pitchfork (local bifurcation)
P or $\mathcal{P}$	Pattern (solution)
PD	Period doubling (bifurcation)
PDE	Partial differential equation
QZ	Quadruple-zero (local bifurcation)
rhs	right hand side
RTB	Reversible Takens-Bodganov (bifurcation)
RTBH	Reversible Takens-Bodganov-Hopf (bifurcation)
S	Saddle
SC	Saddle-center (global bifurcation)
SF	Saddle-focus
SH	Swift-Hohenberg (equation)
SL	Saddle-Loop (global bifurcation)
SN	Saddle-node (local bifurcation)
SNIC	Saddle-node on the invariant circle (bifurcation)
SO	Spatial oscillation
$SR_{1:2}$	Spatial resonance at 1:2 with $O(2)$ symmetry
SVE	Slowly varying envelope
SW	Switching wave
T	Transcritical (local bifurcation)
TB	Takens-Bodganov (bifurcation)
TOD	Third order dispersion
VCSEL	Vertical Cavity Surface Emitting Laser
WGM	Whispering gallery mode
WI	Wave instability

Table of contents

Chapter 1

Introduction

In this thesis we focus on emergent structures in spatially extended systems. *Emergence* is a particular property of complex systems [1], and consists in the appearance of a behavior that cannot be anticipated from the behavior of one of the constituents of the system alone. In particular in complex systems, this behavior appears through what is known as *self-organization*[2]. This type of behavior is related to *nonlinearity*, in the sense that the superposition principle can not been applied. A rich variety of real-life physical problems, which are still poorly understood, are of a nonlinear nature. Examples include turbulence, weather forecasting, granular flows, detonations and flame propagation, fracture dynamics, and a wealth of new biological and chemical phenomena which are being discovered.

Here we restrict our attention to emergent structures in *spatially extended systems* out of the thermodynamical equilibrium, i.e. systems that are internally dissipative and externally driven. These systems are also called *dissipative systems*. From a thermodynamical point of view a dissipative system is an open system in which there is an exchange of matter and energy with the surrounding medium. In this context emergent structures are patterns that appear spontaneously due to the interaction of each part with its immediate surrounding in space. They will not arise if the various parts are just coexisting, but it is essential that there is spatial interaction. Spontaneous pattern formation can arise in

[1] A complex system can be defined as large aggregations of many smaller interacting parts and that secludes the last one from systems that are merely complicated.

[2] There is no external entity engineering the appearance of emergent features, but these appear spontaneously.

Figure 1.1: Examples of emergent structures in nature. From left to right and from top to bottom: spots in guepard coat [4]; spirals in plants [5]; spiral Galaxy N51 (European Space Agency) [6]; stripes on the coat of the zebras [7]; Belousov-Zhabotinsky reaction [8]; ripple patterns in a sand dune (Royce Blair) [9]; Giant's Causeway in Northern Ireland [10]; frog eggs [11]; and a vortex in the turbines at the Barrage de la Rance electric power generating station in France create a whirlpool in the Rance River. (Photo by James A. Sugar) [12]

hydrodynamical systems, as the Rayleigh-Bénard convection in a layer of viscous fluid heated from below or Faraday surface wave on the surface of a vertically shaken liquid; granular media where one can find also Faraday's waves and oscillons, oscillatory chemical reactions, like for example the Belousov-Zhabotinsky reaction, biological and ecology systems, and nonlinear optics [1–3]. In Figure 1.1 we can see different emergent structures that can be easily found in nature, such as for example, spots in a leopard coat, spirals in plants and in galaxies, stripes on the coat of the zebras, chemical reactions, ripple patterns in a sand dune, hexagon patterns in the basalt columns of the Giant's Causeway in Northern Ireland or frog eggs, and a vortex in a turbine in an electric power generating station. Despite the different natural context, the previous structures share

morphological similarities, which show us that they are not dependent on the details of the systems but they can be understood from the underlying symmetries [3]. This is an interesting and particular feature of the emergent structures in spatially extended systems called *universality*.

Because of this universality, it is possible, combining methods of nonlinear dynamics and bifurcation theory [3], to derive generic models such as *amplitude equations* or *phase equations* describing the dynamical behavior of those structures close to bifurcation points or far from them respectively [1–3].

A special type of these emergent structures are spatially *localized structures* (LSs), which can be seen as one state "embedded" in a background of a different state. In non-equilibrium systems they are also referred to as *dissipative localized structures*.

In this thesis, using principles from dynamical systems and bifurcation theory, we will study these last type of structures in a particular class of dissipative systems: *driven nonlinear optical cavities*.

1.1 Dissipative localized structures

The term *dissipative structure* was proposed in 1967 by the Belgian chemist Ilya Prigogine to describe the spontaneous appearance of ordered structures in the nonlinear domain, far from equilibrium [21]. A dissipative structure is characterized by the spontaneous appearance of symmetry breaking (anisotropy) and the formation of complex, sometimes chaotic, structures. When these dissipative structures are spatially localized, so a single peak, they are also called *dissipative solitons* (DSs) [22–26]. Then along this thesis we will use LSs to refer to any localized dissipative structure, and DSs or simply soliton to those structures formed by a single localized element as a single peak.

DSs are different from the well known *conservative solitons* arising in Hamiltonian systems (see Figure 1.2). In the last case they are formed due to the balance between two opposite effects: spatial coupling (diffusion, diffraction or dispersion) and nonlinearity, and they form usually a one-parameter family of solutions [27]. These solitons are characterized by the fact that they remain unchanged during interactions, apart from a phase shift. Moreover, they arise in *integrable systems*, i.e. described by partial differential equations (PDEs) for which a closed exact analytical solution can be found by means of inverse scat-

[3] A summary of the main concepts in dynamical systems and bifurcation theory is presented in Appendix A. The analytical and numerical methods used in this thesis are found in Appendix B.

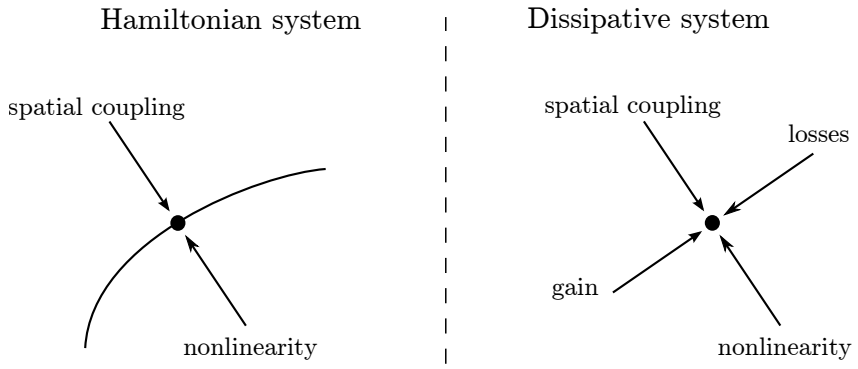

Figure 1.2: Qualitative difference in the formation of soliton solutions in Hamiltonian and dissipative systems. This Figure is inspired in Figure 1 of Ref.[27]. While the formation of a conservative soliton requires a single balance between spatial coupling and nonlinearity, the formation of a DS needs a double balance: spatial coupling/nonlinearity and losses/gain.

tering methods [28, 29]. Some examples of equations supporting these kind of states are: the nonlinear Schrodinger (NLS) equation, the Korteweg de Vries (KdV) equation or the sine-Gordon equation [30].

In contrast, in dissipative systems, the losses must be compensated by including gain in the system, so the formation of DSs requires a double balance between nonlinearity and spatial coupling, and driving and dissipation. This situation is illustrated in Figure 1.2. These structures can display a variety of dynamical regimes such as periodic oscillations [13, 32, 33, 107], chaos [33, 34], or excitability [35, 36]. DSs are unique once the system parameters are fixed, and they can coexist with other DSs in the same region of parameters, and therefore they exhibit multistability. DSs or LSs are common and have been shown to arise in a wide variety of physical systems such as chemical reactions [32, 37, 38], neural systems [39, 40], granular media [13, 41], binary fluid convection [42, 43], ferrofluid driven by an homogeneous magnetic field [15], vegetation patterns [44, 45] and nonlinear optics [18, 46–52]. In particular when they appear in optical cavities they are commonly refereed to as *cavity solitons* (CSs).

Figure 1.3 shows observations of LSs or DSs in nature or in experimental setups in six different systems. We discuss them shortly from left to right and from top to bottom. The first one shows a localized oscillation in a layer of sand, normally called *oscillon*, which alternately takes the shape of a peak and crater

Figure 1.3: Examples of DSs in nature. From left to right and top to bottom we have: An oscillon in a vibrated layer of sand [13]; the fairy circles of Namibia desert (photo by Stephan Getzin and Thorsten Wiegand) [14]; isolated peaks on the surface of a ferrofluid driven by a homogeneous magnetic field [15]; spatially localized patterns in a Faraday waves experiment on the surface of a vertically vibrated container of fluid using a container that is very thin in one direction [16]; A Morning Glory cloud formation between Burketown and Normanton [17], Australia; spatial CS in an active (amplifier) semiconductor system in a cavity [18]

as the sand is vibrated vertically [13]. The second photo shows the presence of localized circular patches, called *Fairy circles*, in the Namibia desert. They consist in land barren of plants, varying between 2 and 15 meters in diameter, often encircled by a ring of stimulated growth of grass. The third image depicts the formation of isolated or clusters of peaks formed in the surface of ferrofluid when a spatially homogeneous, time-independent, vertical magnetic field is applied [15]. The fourth picture shows a spatially localized pattern generated on the surface of a vertically vibrated container of fluid when one of its dimensions is very thin in comparison with the other one [16]. The fifth photo shows a *Morning Glory* cloud formation, a rare meteorological phenomenon consisting of a low-level atmospheric solitary wave and associated cloud, occasionally observed in different locations around the world. The wave often occurs as an amplitude-ordered series of waves forming bands of roll clouds. Finally the last picture represents CSs in an active (amplifier) semiconductor system in a Fabry-Perot

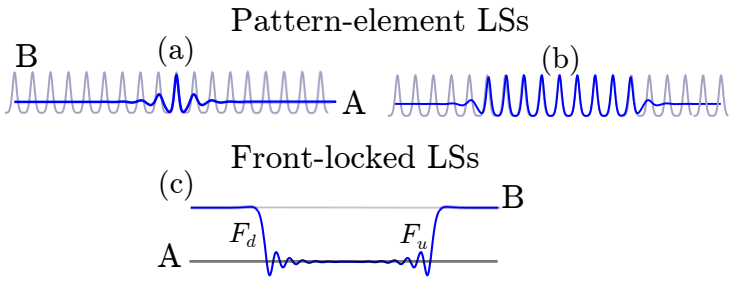

Figure 1.4: Sketch of two different scenarios for LSs formation. (a),(b) Pattern element: a connection between the low intensity homogeneous solution A and the periodic pattern B. (c) The fronts F_d and F_u connecting the low A and high B intensity homogeneous solutions form a stable connection.

cavity [18].

The existence of LSs is directly related to the presence of bistability between two states, let us say A and B in the system under consideration. A LS is then interpreted as a pair of bound fronts between both states. These two fronts typically interact with each other through the interior of the LS. Let us briefly discus the three main mechanism, related with the nature of states A and B i.e. if they are homogeneous or pattern solutions.

1. LSs can form when A is a homogeneous state and B is a pattern. In systems where a homogeneous stable solution is destabilized in a modulational (or Turing) instability, patterns can be created subcritically. In many cases, a a piece of a pattern (one or more peaks) embedded in the homogeneous background can be stable, creating LSs or solitons. Here we refer to them as a *pattern element*-LSs. We illustrate these type of LSs in Figures 1.4(a) and (b).

2. LSs can form when A and B are two different homogeneous solutions or domains, both of them stable. Bistable systems leading to the coexistence of two equivalent homogeneous solutions represent a second large group of systems that possibly allow the formation of LSs. The regions occupied by different homogeneous states are also called domains, and the fronts between the different domains are called domain walls. The formation and stability properties of this kind of LSs is thus intimately related to the general problem of front propagation or domain wall motion. Here we

refer to them as a *locked fronts*-LSs. Figures 1.4(c) and (d) illustrate the formation of this type of structure.

3. Bistability between two different patterns A and B. In some cases a portion of one pattern embedded in another pattern can be stable as well. We will not consider this case in this thesis.

In two extended dimensions the curvature of the fronts connecting two homogeneous states can also generate the formations of LSs as shown in Refs. [19, 20].

1.2 Optical cavities and the Lugiato-Lefever model

In an optical cavity or resonator light can be confined within continuous reflection in the material. When these cavities exhibits a nonlinear *Kerr effect*[4] and are externally driven by a homogeneous beam of light, the dynamics of the the electromagnetic wave $\mathcal{E}$ in the cavity can be described by the Lugiato-Lefever (LL) model.

The Kerr effect consist in that the optical response of these materials is characterized by a polarization with the nonlinear susceptibility $\chi^{(3)}$ term, $P = \varepsilon_0 \chi^{(3)} |\mathcal{E}|^2 \mathcal{E}$. Therefore, the refractive index n of the medium depends linearly on the local light intensity $I = |\mathcal{E}|^2$ as

$$n(\omega) = n_0(\omega) + n_2 I. \tag{1.1}$$

The LL model was originally derived in 1987 to describe a ring cavity (or a Fabry-Perot resonator) with a transverse spatial extension, partially filled with a nonlinear Kerr medium and driven with an homogeneous beam of light [72]. Figure 1.5 shows an example of such a cavity. In these cavities localized bright light spots embedded in a background of a homogeneous light distribution were found to exist at the output of the resonator [18]. These light spots are also known as *spatial* CSs. Here the spatial coupling is introduced by the diffraction in the system. Later, in 1992 this model was also used in single-mode fiber cavities [74]. In this case, the spatial coordinate in the LL equation for a spatially extended cavity with diffraction is replaced by a time coordinate to model chromatic dispersion of light in the longitudinal (temporal) direction. The LSs found here are localized in time, and hence refereed as *temporal* CS. In the following one will refer to these cavities as *temporal cavities.*

[4] Within all this thesis we will consider that this effect is instantaneous.

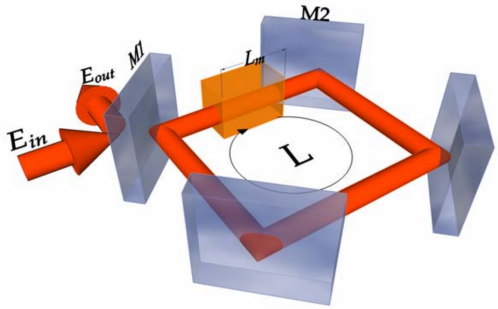

Figure 1.5: Example of a spatial nonlinear optical cavity. Ring-cavity resonator partially filled with a nonlinear medium, typically a gas, is depicted. The presence of the mirrors introduces losses in the system that must be balance by injecting a driving field E_{in}. This Figure has been taken from Ref. [73] with the permission of the authors.

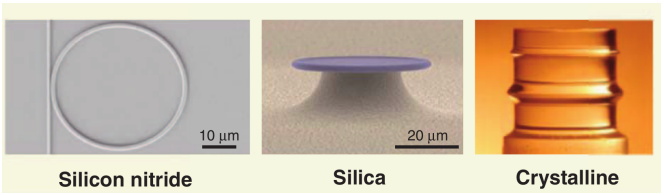

Figure 1.6: Examples of microcavities where FCs have been generated (from left to right): chip-based silicon nitride (SiN) ring resonators and waveguides, ultrahigh Q toroidal microresonators on a silicon chip, and ultrahigh Q millimeter-scale crystalline resonators. This Figure has been adapted from Figure 3 in Ref. [77]. See references therein.

Microresonators, as those shown in Figure 1.6, consist in another type of temporal cavities that can be also described by the LL equation. When dealing with this last type of cavities, two approaches are widely used in literature to describe the intra-cavity optical field evolution. One is using time as evolution variable and relies on the approximation of the modal dispersion through the expansion of the frequency into series in the modal number (propagation constant) [75], and the other one is using the distance along the cavity length as an evolution variable and thus is based on the expansion of the modal number as a function of the frequency [76]. This last approach will be the one adopted within this thesis. The study of microresonator has overcome recently a lot of interest due to the potential application for the generation of frequency combs (FCs) in a high finesse cavity [77].

The goal of this section is to describe the functioning of temporal cavities. Fiber cavities and mircroresonators, in contrast to spatial ones which have two transverse dimensions, are guided-wave cavities, and therefore can be described by the one-dimensional LL equation which will be derived here following Ref. [74]. In order to do that we first show how a pulse of light propagates in a Kerr type of nonlinear wave-guided material. After that, we present the description of a temporal cavity and its feedback mechanism. Later on, we analyze the behavior of the cavity step by step when adding the effects of absorption, nonlinearity and chromatic dispersion one by one. And finally, we will show that, high finesse cavities are described by the mean-field LL equation. Within this section we follow closely Refs. [74],[78],[79] and [80].

1.2.1 Propagation of a pulse within a Kerr nonlinear medium

In this thesis we will focus on guide-wave cavities like those shown in Figure 1.6 that are made of a material with a Kerr type of nonlinearity. Therefore, before describing the cavity it is necessary to understand how light behaves within such type of material.

Here we will derive a nonlinear Schrodinger equation describing the propagation of an electric field $\mathcal{E}(x,y,z,t)$ through a guiding structure that limits the power to the $(x,y)-$plane. If one assumes that the field is quasi-monochromatic, propagating towards z with a phase constant β_0, and angular frequency ω_0, and that maintains its linear polarization along the material, it can be written as:

$$\mathcal{E}(x,y,z,t) = E(z,t)f(x,y)e^{i(\beta_0 z-\omega_0 t)}, \tag{1.2}$$

where E is the envelope, the exponent is the *carrier wave* and $f(x,y)$ represents the shape of the field on the $(x,y)-$plane (transverse direction), and it does not change during propagation because we assumed that the field is guided. Equation (1.2) corresponds to a *wave-packet* centered at the carrier frequency ω_0 whose Fourier transform reads

$$\mathcal{E}(x,y,z,\omega-\omega_0) = \int_{\mathbb{R}} \mathcal{E}(x,y,z,t)e^{-i(\omega-\omega_0)t}dt = \tilde{E}(\omega,z)f(x,y)e^{i\beta_0 z}. \tag{1.3}$$

Inserting (**??**) into the Maxwell equations one obtains the Helmholtz equation in the frequency domain

$$\nabla^2\mathcal{E} + \tilde{n}^2(\omega)k_0^2\mathcal{E} = 0, \tag{1.4}$$

with

$$\tilde{n}(\omega) = n(\omega) + i\frac{\alpha_i}{2k_0}, \tag{1.5}$$

being the the complex refractive index, k_0 the wavenumber associated to the carrier wave, and α_i the linear losses, or absorption, in the material.

The propagation constant can be written as:

$$\tilde{n}(\omega)k_0 = \beta(\omega) = \beta_{\text{lin}}(\omega) + \beta_{\text{nonlin}} + \beta_{\text{losses}}, \tag{1.6}$$

with $\beta_{\text{lin}}(\omega)$ being the linear contribution depending on ω, $\beta_{\text{nonlin}} = k_0 n_2 |E|^2$ the nonlinear contribution, and $\beta_{\text{losses}} = i\alpha_i/2$ the losses, that we consider non depending on ω.

Due to the quasi-monochromaticity of the optical field, $\beta_{\text{lin}}(\omega)$ can be expanded in a Taylor series about the carrier frequency ω_0:

$$\beta_{\text{lin}}(\omega) = \sum_{j=0}^{\infty} \frac{\beta_j}{j!}(\omega - \omega_0)^j \tag{1.7}$$

with the dispersion coefficient

$$\beta_j = \frac{d^j \beta_{\text{lin}}}{d\omega^j}|_{\omega-\omega_0}. \tag{1.8}$$

In general one truncates the series at up to second order in j

$$\beta_{\text{lin}}(\omega) = \beta_0 + \beta_1(\omega - \omega_0) + \frac{1}{2}\beta_2(\omega - \omega_0)^2 + \mathcal{O}(3), \tag{1.9}$$

where β_1^{-1} is the group velocity of light in the material i.e. the speed of the pulse envelope, and β_2 is the second order *group velocity dispersion* (GVD) *coefficient.*

With this, one can write,

$$\beta(\omega) = \beta_0 + \sum_{j\geq 1}^{\infty} \frac{\beta_j}{j!}(\omega - \omega_0)^j + \beta_{\text{nonlin}} + \beta_{\text{losses}} = \beta_0 + \Delta\beta(\omega), \tag{1.10}$$

and assume that $\Delta\beta$ is a small perturbation i.e. $|\beta_0| \gg |\Delta\beta(\omega)|$, which is equivalent to consider that the nonlinearity is a small perturbation.

Inserting Eq.(1.2) in Eq.(1.4), and considering the *slowly varying envelope* (SVE) approximation i.e. $|\partial_z^2 \tilde{E}| \ll |\beta_0 \partial_z \tilde{E}|$[5], we get that the field envelope is described by

$$i\frac{\partial \tilde{E}}{\partial z} + \Delta\beta(\omega)\tilde{E} = 0. \tag{1.11}$$

[5] $\tilde{E}(\omega, z)$ varies slowly with z and therefore one can neglect high-order derivatives.

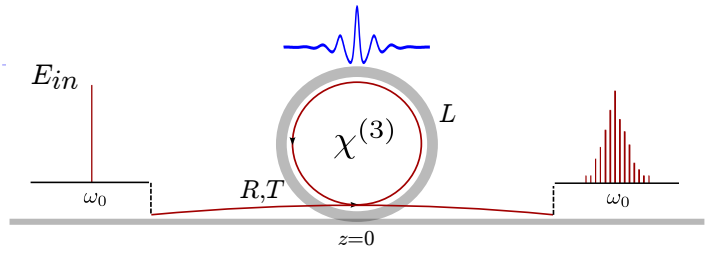

Figure 1.7: Nonlinear temporal optical cavities with Kerr-type of nonlinearity. It can be either a all-fiber ring cavity or a ring-microcavity. Here L is the length of the cavity, R and T are the reflexion and transmission coefficients of the coupler respectively and the injected field is a CW with envelope E_{in}.

Taking the inverse Fourier transform one finally get that

$$\frac{\partial E}{\partial z} = -\frac{\alpha_i}{2}E - i\frac{\beta_2}{2}\frac{\partial^2 E}{\partial \tau^2} + \underbrace{i\sum_{j\geq 3}\frac{\beta_j}{j!}\left(i\frac{\partial}{\partial \tau}\right)^j E}_{\text{HOD}} + i\gamma|E|^2 E, \tag{1.12}$$

where $\tau = t - \beta_1 z$ describes the electromagnetic field envelope in the reference frame moving at the group velocity β_1^{-1}.

The Eq.(1.12) is a (generalized) NLS equation that governs the propagation of an optical signal through one round-trip of an optical cavity with losses and Kerr nonlinearity. Here $\gamma = n_2\omega_0/ca_{\text{eff}}$ is the nonlinearity coefficient due to the Kerr effect in the resonator, with a_{eff} the effective modal area of the resonator mode $f(x, y)$.

Regarding the linear part contribution β_{lin} to the propagation constant, β_2 vanishes at a given wavelength, depending on each material, that is called the *zero dispersion wavelength* λ_{zd}. For wavelengths λ_0 such that $\lambda_0 < \lambda_{zd}$, $\beta_2 > 0$ and the material is said to exhibit *normal dispersion*. In contrast, the opposite occurs in the *anomalous dispersion* regime in which $\beta_2 < 0$. Around λ_{zd} high-order dispersion (HOD) effects, as for instance the third order dispersion (TOD) β_3 must be taking into account. In general we will consider the HOD effects are not present and then $\beta_j = 0$, for $j \geq 0$

1.2.2 Temporal cavity description

Figure 1.7 shows an example of a temporal cavity (guided wave cavity) that can be either a microresonator or a fiber cavity. Light is injected in the cavity by

means of the input coupler. It propagates along the cavity where it suffers the effects of the chromatic dispersion and the Kerr nonlinearity of the material, as described by Eq.(1.12). At each round-trip in the cavity the light wave undergoes losses due to coupler and the material absorption, and at each pass, the external pump or driving field is added coherently to the intra-cavity field. This coherent superposition constitutes the feedback mechanism of the cavity, that can be mathematically expressed by the map

$$E_{m+1}(0,\tau) = \sqrt{T}E_{in} + \sqrt{R}E_m(L,\tau)e^{i\phi_0}, \tag{1.13}$$

where $E_{m+1}(0,\tau)$ is the envelope of the intra cavity field at the beginning of the $(m+1)_{th}$ round trip and $E_{m+1}(L,\tau)$ is the field at the end of the m_{th} round-trip. Here L is the round-trip length of the cavity, and $t_R = \beta_1 L$ is the cavity round-trip time i.e. the time necessary for the intra-cavity field to complete one cavity round-trip. E_{in} is the envelope of the driving field injected into the cavity at the coupler, which a priory, can have any temporal structure, although here we will consider that it consists in a continuous wave (CW), unless otherwise stated. T and R are the intensity transmission and reflection coefficients of the couplers, satisfying $R+T = 1$. Finally, ϕ_0 is the *linear cavity round-trip phase shift*, i.e. the linear phase acquired by the intra-cavity field after propagation over one cavity round-trip, which for a monochromatic pump, is given by $\phi_0 = \beta_0 L = \omega_0 nL/c$, where n is the linear index of the material. This parameter controls the way the intra-cavity and driving field interfere in the coupler, and is one of the main parameters of the cavity dynamics. This phase contribution must be included in Eq.(1.13) because Eq.(1.12) is an envelope equation that therefore does not take into account the carrier of the light pulses. The Eq.(1.12) combined with boundary conditions Eq.(1.13) form an infinite-dimensional map that describes completely the dynamics of the cavity. This map is known as *Ikeda* map [81].

1.2.3 The linear cavity resonances

We begin our study of the temporal cavity by neglecting chromatic dispersion, nonlinearity, as well as absorption in the material. In this configuration, the only physical effect in presence is the cavity feedback, and we simply have $E_m(L) = E_m(0)$. Therefore the cavity boundary conditions reduce to a simple two-dimensional map whose fixed points provides the Airy function of optical resonators

$$E_m(0) = \frac{\sqrt{T}E_{in}}{1 - R\mathrm{e}^{i\phi_0}}, \tag{1.14}$$

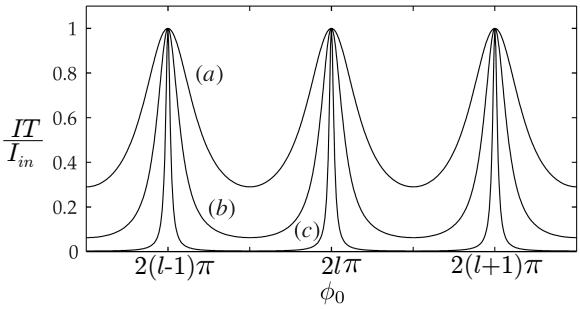

Figure 1.8: Resonances of the linear cavity with T equals to 0.7 in (a), 0.4 in (b), and 0.1 in (c). The cavity finesse $\mathfrak{F}$ is respectively ~ 4.5, ~ 8, and ~ 30. This Figure has been adapted from Figure 2.2 in Ref. [78].

which in terms of beams intensities $I = |E_m|^2$ and $I_{in} = |E_{in}|^2$ becomes

$$\frac{I}{I_{in}} = \frac{1}{T(1 + F\sin^2(\phi_0/2))}, \tag{1.15}$$

with $F = 4R/(1-R)^2$. This last equation exhibit resonances at $\phi_0 = 2\pi l$ with $l \in \mathbb{N}$, where the intra-cavity field intensity exhibits its maximum value $I_{max} = I_{in}/T$. This intensity is greater than the one of the injected beam and therefore the cavity behaves as an energy accumulator.

When ϕ_0 is a multiple of 2π, the intra-cavity field is in phase with the incident driving field at the coupler, and therefore both waves interfere constructively and energy is accumulated inside the cavity. This quantity can be controlled for example by changing the frequency of the injected driving field $f = \omega_0/2\pi$ according to the proportionality relation between ϕ_0 and ω_0, namely $\Delta\phi_0 = 2\pi$ for $\Delta f = c/(nL)$. Then the position and width of the resonances can be characterized either in terms of phase or in terms of driving field frequency.

Figure 1.8 shows the Airy function (1.15) for several values of the transmitted coefficient of the coupler T, that is, the cavity losses. One can see that the resonance peaks get thinner when the cavity losses are decreased. This sharpness is characterized by the cavity finesse parameter $\mathfrak{F}$ which is a dimensionless number equal to the ratio of the separation between two resonances at the full width at half-maximum of the resonance peaks, which in our case reduces to

$$\mathfrak{F} \simeq \frac{\pi}{T}. \tag{1.16}$$

Another parameter which characterizes the way a resonator confines energy is

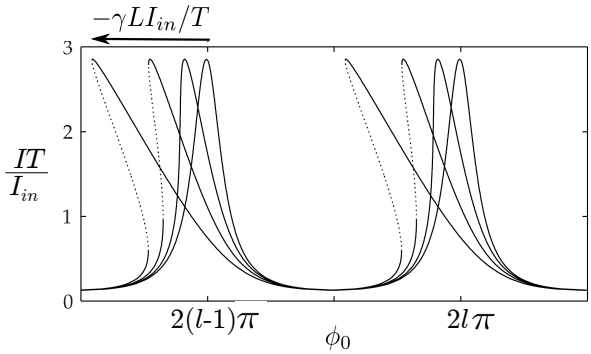

Figure 1.9: Resonances of the nonlinear cavity with $T = 0.35$ ($\mathfrak{F} \simeq 9$) and $\gamma L I_{in} = 0.01, 0.2, 0.5, 1$. Dotted lines indicate unstable states. This Figure has been adapted from Figure 2.3 in Ref. [78].

the quality factor, $Q-$factor, typically used in the context of an herzian resonator (RLC circuit, RF oscillator, maser, laser, etc). The energetic definition of the $Q-$factor reads

$$Q = 2\pi \frac{E_{\text{stored}}}{E_{\text{dissipated}}}, \tag{1.17}$$

where E_{stored} is the energy stored by the resonator, and $E_{\text{dissipated}}$ is the energy dissipated during a cavity round-trip time t_R. With this definition, the finesse of the cavity is exactly equivalent to quality factor $Q-$factor. Indeed, $Q = 2\pi I/(2TI) = \pi/T = \mathfrak{F}$.

The separation between two adjacent resonances is given by the *free spectral range* (FSR) equal to $c/(nL)$, and the spectral width of the resonances is determined by

$$\Delta\phi_0 \simeq \frac{FSR}{\mathfrak{F}}. \tag{1.18}$$

1.2.4 Influence of the Kerr nonlinearity

It is easy to take into account the effect of the Kerr nonlinearity on the response of the cavity (we still neglect the chromatic dispersion and the absorption of the material). The Kerr nonlinearity enters into play through an additional intensity-dependent phase shift $\gamma L|E_m|^2$ acquired by the intra-cavity field over the cavity length L. This phenomenon is known as *self-phase modulation* (SFM) and it is a direct consequence of Eq.(1.1). Therefore, due to the SFM the cavity round-trip phase shift becomes $\phi = \phi_0 + \phi_{\text{NL}}$ with $\phi_{\text{NL}} = \gamma L I$, which once

substituted in Eq.(1.15) gives the transcendent equation describing the nonlinear resonances of the cavity

$$\frac{I}{I_{in}} = \frac{1}{T\left(1 + F\sin^2\left(\frac{\phi_0 + \gamma L I}{2}\right)\right)}. \tag{1.19}$$

Due to the presence of the intensity in the phase term of the previous equation, the resonance peaks will be displaced proportionally to the input intensity. This displacement occurs only at the peaks, and for the other points of the resonances the displacement is proportional to the intra-cavity intensity, which is lower than I_{in}/T. In the wings of the resonances, the intra-cavity intensity is low and the displacement is negligible. From here one can understand that the nonlinear resonances are peaks that are tilted proportionally to the input power. When the maximum phase displacement $-\gamma L I_{in}/T$ becomes larger than the resonance width $\Delta\phi = 2\pi/\mathfrak{F}$, the response function becomes multi-valued and exhibit bistability. Therefore, a nonlinear cavity is a bistable system like many others with positive feedback [82, 83]. Optical bistability can not be derived analytically form Eq.(1.19) because it is transcendent, and it will be discussed in Chapter 2.

1.2.5 Influence of the chromatic dispersion

So far we have focused on the basic characteristics of a ring cavity resulting when considering losses and nonlinearity, but neglecting the contribution of chromatic dispersion. This last ingredient introduces spatial coupling between different points in space allowing the emergence of complex behavior non appearing previously. To consider the effect of chromatic dispersion, we need to deal with the infinite-dimensional Ikeda map made up of the nonlinear Schrodinger equation (1.12) and the boundary conditions (1.13).

In the context of high-$\mathfrak{F}$ cavities the Ikeda map can be reduced, under certain approximations, to a mean-field model which is formally equivalent to the Lugiato-Lefever equation derived in the context of spatial systems [72]. Our aim here is to show step by step how to perform such simplification, and for that we will follow closely Ref. [74].

In the limit of high finesse $\mathfrak{F} \gg 1$, or equivalently for $T \ll 1$ (low losses), one can apply an approximation based on the fact that the intra-cavity field envelope varies slightly round-trip after round-trip due to the small cavity losses. In this situation, the resonances are narrow, and therefore the intra-cavity field is non zero only when the round-trip phase is close to a multiple of 2π. In this context one defines the *cavity detuning* as a small quantity of the first order

$\delta_0 = 2\pi l - \phi_0 \ll 1$, where l designates the nearest resonance of the cavity. As it was done for the resonances, this parameter can be quantified also in terms of the frequency of the driving field. In the same way the nonlinear phase shift ϕ_{NL} must also be limited to a quantity of the first order so as to stay in the vicinity of the resonance peak at high pump power.

With all the previous approximations, one can consider that

$$\sqrt{1-T}e^{-i\delta_0} = \left(1 - \frac{T}{2} + \cdots\right)\left(1 - i\delta_0 - \frac{\delta_0^2}{2} + \cdots\right) \approx 1 - \frac{T}{2} - i\delta_0, \quad (1.20)$$

and hence, the boundary condition equation (1.13) can be written as

$$E_{m+1}(0,\tau) = \sqrt{T}E_{in} + \left(1 - \frac{T}{2} - i\delta_0\right)E_m(L,\tau). \quad (1.21)$$

Together with the mean field approximation it is also necessary to assume that the dispersion length $L_D \equiv \Delta\tau^2/|\beta_2|$, with $\Delta\tau^2$ the initial pulse width, is larger than the cavity length L i.e. $L_D \gg L$.

Under these conditions, the solution of Eq.(1.12) is approximated as

$$E_m(L,\tau) - E_m(0,\tau) = -\frac{\alpha_i L}{2}E_m(0,\tau) + i\sum_{j\geq 2}\frac{\beta_j L}{j!}\left(i\frac{\partial}{\partial\tau}\right)^j E_m(0,\tau) + i\gamma L|E_m(0,\tau)|^2 E_m(0,\tau), \quad (1.22)$$

where the terms on the right hand side are all assumed to be small quantities.

By inserting $E_m(L,\tau)$, calculated from Eq.(1.22), into the Eq.(1.21), and while keeping only first order terms, one obtains an equation describing the electric field at $z = 0$, namely

$$E_{m+1}(0,\tau) = \sqrt{T}E_{in} + E_m(0,\tau) - \left(\frac{\alpha_i L + T}{2} + i\delta_0\right)E_m(0,\tau) i\sum_{j\geq 2}\frac{\beta_j L}{j!}\left(i\frac{\partial}{\partial\tau}\right)^j E_m(0,\tau) + i\gamma L|E_m(0,\tau)|^2 E_m(0,\tau). \quad (1.23)$$

Finally introducing *slow variable* t through the relation

$$E(t = mt_R, \tau) = E_m(z = 0, \tau), \quad (1.24)$$

and thinking on t as a continuous variable one can write

$$\frac{\partial E(t = mt_R, \tau)}{\partial t} \approx \frac{E_{m+1}(z = 0, \tau) - E_m(z = 0, \tau)}{t_R}. \tag{1.25}$$

Using this last equation one can write Eq.(1.23) as the generalized-LL equation [74, 76],

$$t_R \frac{\partial E}{\partial t} = -(\alpha + i\delta_0)E + i \sum_{j \geq 2} \frac{\beta_j L}{j!} \left(i \frac{\partial}{\partial \tau} \right)^j E + i\gamma L |E|^2 E + \sqrt{T} E_{in}, \tag{1.26}$$

with $E \equiv E(t, \tau)$. Here τ is the *fast time* describing the temporal structure of the nonlinear waves while the *slow time* t corresponds to the evolution time scale over many round-trips. We should note that τ is only defined on a finite interval with the duration of the round-trip time, t_R, and that t only has a rigorous meaning whenever it is an integer multiple of t_R. The evolution of the field on the physical axis, and at a fixed position, can then be found by assembling snapshots of the field $E(t, \tau)$ at intervals that are separated by t_R.

Although the approximations applied in the derivation of the mean field model (1.28) may appear rather restrictive, comparison with the Ikeda map defined by Eqs. (1.12) and (1.13), agrees for a large number of practical situations. However, at large cavity detunings the cavity could switch to the so-called "period-2" regime for which the LL model no longer holds. In this regime a mean field model has been also developed [84].

Within this thesis we will work with the adimensional version of Eq.(1.26), that following the normalization used in Ref. [85] reads:

$$\begin{aligned}
A(x, t') &\equiv E(t, \tau) \sqrt{\gamma L / \alpha} \\
t' &\equiv \alpha t / t_R \\
x &\equiv \tau \sqrt{2\alpha / (L|\beta_2|)} \\
\rho &\equiv E_{in} \sqrt{\gamma L T / \alpha^3} \\
\theta &\equiv \delta_0 / \alpha \\
d_j &\equiv \frac{\beta_j L}{j! \alpha} \left(\frac{2\alpha}{|\beta_2| L} \right)^{j/2}
\end{aligned} \tag{1.27}$$

can be written as,

$$\partial A_t = -(1+i\theta)A + i\nu\partial_x^2 A + i\sum_{j\geq 3} d_j\,(i\partial_x)^j\,A + i|A|^2A + \rho, \tag{1.28}$$

where we have dropped ($'$). Here θ and ρ are the normalized frequency detuning of the cavity and the amplitude of the driven field, $\nu = \pm 1$ with $(+)$ for anomalous GVD regime and $(-)$ for the normal one, and d_j are the HOD normalized coefficients. The equation is set to the self-focusing regime. In following and unless stated otherwise we will focus on the study of the LL equation considering dispersion effects up to second-order.

1.2.6 Comparison between temporal and spatial cavities

The LL equation was originally obtained through a mean-field approximation, describing the dynamics of the slowly varying amplitude of the electromagnetic field $\mathcal{E}(x,y,t)$ in the paraxial limit, inside a ring-cavity [72] like the one shown in Figure 1.5, filled with a Kerr nonlinear medium and driven by an external field E_{in} to balance the losses generated by the mirrors, where (x,y) are the spatial coordinates transverse to the propagation direction. In this type of system the LL equation, once normalized reads,

$$\partial_t A = -(1+i\theta)A + i\alpha\nabla_\perp^2 A + i\beta|A|^2A + \rho, \tag{1.29}$$

with $A(x,y,t)$ the scaled slowly varying amplitude of the field. The first term in the rhs of Eq.(1.29) corresponds to the losses, ρ the input field used as a reference frequency, θ the frequency detuning, $\beta = \pm 1$ determining whether the nonlinearity is of the focusing $(+)$ or defocussing $(-)$ type, $\nabla_\perp^2 \equiv \partial_x^2 + \partial_y^2$ the transverse Laplacian modeling diffraction and α its strength. Comparing Eq.(1.28) with $d_j = 0$ for $j \geq 3$ and Eq.(1.29) one can see that there is an immediate correspondence between *temporal* phenomena arising in the *longitudinal* profiles of pulses circulating in a fiber cavity under the influence of chromatic dispersion and *spatial* phenomena arising in the transverse profile of s *CW beam* propagating in a self-defocussing $n_2 < 0$ (self-focusing, $n_2 > 0$) Kerr cavity under the influence of diffraction

1.3 Temporal structures and frequency combs in microresonators

In the recent years, the LL equation has gained a renewed interest as it has been re-derived to describe the formation and dynamics of Kerr frequency combs

(KFC) in high$-Q$ microresonators [77, 86, 87]. A frequency comb consists in a broad optical spectrum of sharp spectral lines with an equidistant frequency spacing [88] that can be used to perform ultraprecise measurements of optical frequencies, and which have numerous others applications to spectroscopy, optical clocks and waveform synthesis [89, 90]. In the type of Kerr cavities that we study, combs are formed due to a parametric frequency conversion via a *four wave mixing* process. Although these effects are well known in nonlinear optics, such processes have been demonstrated only recently in microresonators [77]. The advantage of mircroresonators, together with the small size, is that the threshold for the initiation of parametric oscillations can be strongly reduced (because the threshold scales with the inverse $Q-$factor squared,) implying that high-Q can give a dramatic reduction in required optical power.

The interesting and essential point here is that these FCs correspond to the frequency spectrum, i.e. the Fourier transform, of temporal structures (CSs and patterns) circulating inside the cavity. Therefore, studying these structures one can obtain information about the dynamics and stability of the combs [91, 92].

Together with the LL equation which focuses on a time domain picture, one can also study the FCs by using the coupled mode (CM) equations [93]. These equations consist in a system of ODEs describing each l component (mode) of the FC i.e. they describe the dynamics of each of the coefficients of the Fourier expansion of the temporal structure. The CM equations can be derived from the LL equation (1.28) by assuming the simple modal expansion

$$E(t,\tau) = \sum_{l}^{N} \mathcal{A}_l(t) e^{i\Omega_l \tau}, \tag{1.30}$$

and projecting (1.28) onto each l component, where N is the number of modes considered and Ω_l its frequency.

Instead of using the two time scale approach, usually adopted in the context of nonlinear fiber ring cavities, it is possible to use the equivalent LL equation written in terms of time and the azimuthal angle φ, which follows the viewpoint of cavity nonlinear optics [75]. This angle is related with the fast time τ by the relation $\varphi = 2\pi\tau/t_R$.

Although both the CM equations and the LL equation are equivalent when describing the formation of FCs. Despite of that, the CM equations approach is not computationally efficient when considering a large number of modes, as the time of computations is $\propto N^3$. In contrast, the LL model approach allows the description of the temporal dynamics using a PDE, that is faster to simulate

and easier for analytical investigations. This computational efficiency can be achieved using the split-step numerical integration algorithm with fast Fourier transforms. Moreover stationary combs (i.e. stationary CSs) can be calculated by using a multidimensional Newton-Raphson solver, providing results in a matter of seconds. The Newton method also provides information about dynamical instabilities of Kerr combs through an eigenvalue analysis of the Jacobian of the system, which is obtained at no extra cost.

The bulk of KFC studies so far deals with microresonators exhibiting anomalous second-order GVD at the pump wavelength. However, due to the difficulty in obtaining anomalous GVD in some spectral ranges, generation of KFCs from normal GVD microresonators is now also being sought and has recently been achieved experimentally by several groups [94–96]. In the next sub-sections we discuss the duality between temporal structures and their corresponding FCs. In the rest of the thesis, when studying the LL equation describing these cavities, we will focus on just in the temporal structures, and we refer to this Section to remind the reader of their close relation with FCs. The results shown here have been published in Refs.[92, 97, 98].

1.3.1 Temporal structures and frequency combs in the anomalous regime

In the regime of anomalous GVD, the typical temporal structures that form are patterns and temporal bright solitons, which can be considered as a pattern element. Some of these structures and their corresponding KFCs are shown in Figure 1.10. The LSs shown in panel (i) corresponds to a time-localized pulse circulating in the cavity, and in the same way such a light pulse corresponds to a stable smooth frequency comb in the corresponding frequency domain, as shown in the panel on the right hand side. The distance between all frequency modes is given by the free-spectral range FSR $= 1/L$, where L is the cavity length, while the exact shape of the frequency comb envelope is determined by the Fourier transform of the profile of the LS itself. This equivalence has also been studied in Refs.[75, 76]. A solution with five peaks is plotted in Figure 1.10(ii), with its corresponding frequency comb. It can be seen that the effect of adding extra peaks is to introduce an extra modulation of the frequency comb. The multiple peaks of LSs can only coexist at well-defined separation distances d between them, determined by the typical wavelength of the oscillatory tails of the individual peaks [100]. This separation distance d therefore also determines the modulation distance $1/d$ observed in the frequency comb. The modulation depth becomes more pronounced as more and more peaks are added to the solution. An example of a patterned solution with 19 peaks is shown in Figure 1.10(iii). All

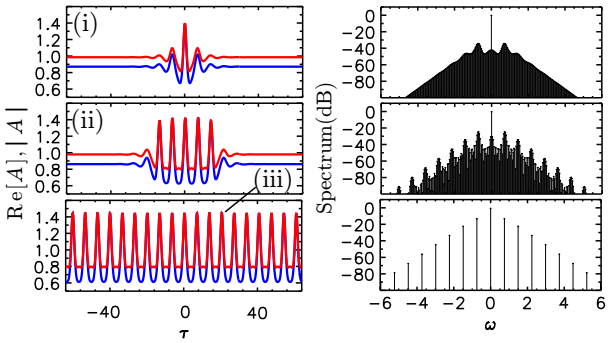

Figure 1.10: Temporal profiles [left; Re(E) in blue, $|E|$ in red] and spectral intensities (right, in dB) of symmetric bright solitons in the anomalous GVD regime. Here $\theta = 1.5$ and $\rho = 1.11445$.

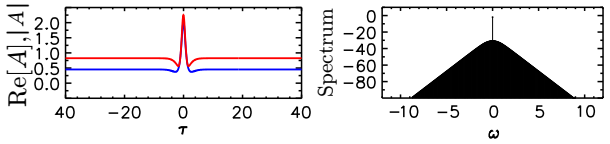

Figure 1.11: Single LS and its KFC for $\theta = 2.2$, $\rho = 1.5$.

frequency modes present in the corresponding frequency comb are now separated by $1/d$ (or equivalently 19 FSR units). Although we have used the same distance d to denote the separation between various peaks in the pattern, we remark that this should not necessarily be the case, as this might vary a bit depending on the exact cavity length. We note also that CSs with $L/d-1$ peaks can be interpreted as one missing cell, or hole, in a periodic pattern.

In Figure 1.11 a single soliton for $\theta = 2.2$ and its corresponding FC are plotted. Comparing this state with the one shown in panel (i) of Figure 1.10 one can appreciate that, when increasing the value of the detuning, oscillatory tails of the solitons are damped and that the LSs becomes sharper. These changes in the temporal structure can also be observed in the their corresponding FC. CSs are the preferred solution for FCs because, in comparison with pattern ones, they are stable over a wider parameter range and they lead broader spectral bandwidth [101]. In other parameter regions, mainly at higher values of the detuning, temporal instabilities such as oscillations and chaos have been found

[33, 92]. Oscillatory solitons or breathers were experimentally first observed in all-fiber ring cavities [33]. Recently breathers have been also observed in microresonators [102]. In this case the FCs oscillate in time with the same period as its corresponding breather soliton.

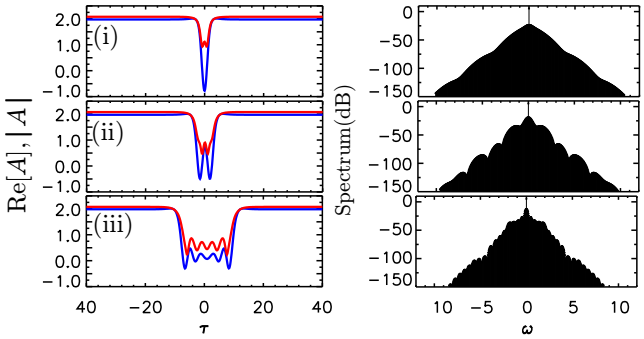

Figure 1.12: Temporal profiles [left; Re(A) in blue, $|A|$ in red] and spectral intensities (right, in dB) of symmetric dark solitons in the normal regime. Here $\theta = 4$.

1.3.2 Temporal structures and frequency combs in the normal regime

In the last years, due to the difficulty in obtaining anomalous GVD in some spectral ranges, generation of KFCs from normal GVD microresonators is now also being sought and has recently been achieved experimentally by several groups [94–96]. In this regime, the typical temporal structures arising are dark solitons, formed by the locking of two fronts or *switching waves* between the stable HSS solutions of the LL model. Some examples of this type of LSs are shown in Figure 1.12. Panel (i) shows the profile of a dark soliton with a single spatial oscillation and on the right its corresponding FC. Panels (ii)-(iii) correspond to dark solitons with two and five spatial oscillations. Looking at the frequency spectrum of these structures one can see how the FCs acquires extra modulations depending on the number of spatial oscillations present in the temporal profile. For a particular region in parameter space there is multistability between a large number of these dark states, and as in the anomalous regime, for large values of detuning, oscillatory and chaotic dynamics exist [97, 98].

1.4 Variational formulation for the Lugiato-Lefever equation

In this section we make overview of the variational formulation for dissipative systems [103–106] in the context of the Lugiato-Lefever (LL) equation that is, by nature, dissipative.

1.4.1 Main definitions for Lagrangian and Hamiltonian formalism

For a dissipative system, the action functional is defined by

$$\mathcal{S} \equiv \int_{\mathbb{R}} e^{2t} L[A, \bar{A}]dt = \int_{\mathbb{R}} e^{2t} \int_{\mathbb{R}} \mathcal{L}[A, \bar{A}]dxdt, \tag{1.31}$$

where $\mathcal{L}$ is the Lagrangian density,

$$L = \int_{\mathbb{R}} \mathcal{L}[A, \bar{A}]dx, \tag{1.32}$$

is the Lagrangian and e^{2t} is the factor modeling the losses.

For the LL equation the Lagrangian density was proposed in Ref.[107] and is given by

$$\mathcal{L} = \frac{i}{2}\left(\bar{A}\partial_t A - A\partial_t \bar{A}\right) - \partial_x A \partial_x \bar{A} - i\rho\left(\bar{A} - A\right) - \theta A\bar{A} + \frac{1}{2}\bar{A}^2 A^2, \tag{1.33}$$

where

$$\mathcal{K} = \frac{i}{2}\left(\bar{A}\partial_t A - A\partial_t \bar{A}\right) \tag{1.34}$$

is its kinetic term.

The canonical momentum related with that Lagrangian are

$$\pi(x,t) = \frac{\delta L}{\delta \partial_t A} = i\bar{A}/2, \qquad \bar{\pi}(x,t) = \frac{\delta L}{\delta \partial_t \bar{A}} = -iA/2, \tag{1.35}$$

where $\dfrac{\delta}{\delta A}$ is the functional derivative.[6]

[6] We define the functional derivative in the following way: let us consider the integral functional

$$\mathcal{F}[u(x)] = \int_{\mathbb{R}} F[u(x)]dx,$$

The Hamiltonian density of this system is given by the Legendre transform:

$$\mathcal{H} = \pi\partial_t A + \bar{\pi}\partial_t \bar{A} - \mathcal{L}, \tag{1.36}$$

and therefore

$$\mathcal{H} = \partial_x A \partial_x \bar{A} + i\rho\left(\bar{A} - A\right) + \theta A\bar{A} - \frac{1}{2}\bar{A}^2 A^2. \tag{1.37}$$

From here we can define the interaction Hamiltonian density by

$$\mathcal{H}_{\mathcal{I}} = -\frac{1}{2}A^2\bar{A}^2, \tag{1.38}$$

that couples non linearly the field A with $\bar{A}$.

The corresponding Hamiltonian function is given by

$$H = \int_{\mathbb{R}} \mathcal{H}[A, \bar{A}]dx. \tag{1.39}$$

From calculus of variations we can get the LL equation by just calculating the critical points (extremals) of the action functional $\mathcal{S}$ with respect *first order variation* of the field A or $\bar{A}$, that is, solving the equation:

$$\delta_A \mathcal{S}(\tilde{A}) \equiv \frac{d}{d\epsilon}\Big|_{\epsilon=0}\mathcal{S}(A + \epsilon\tilde{A}) = 0, \tag{1.40}$$

where $\tilde{A}$ is the variation of A and ϵ a small parameter $0 < \epsilon \ll 1$.

1.4.2 Euler-Lagrange equation

In the Lagrangian formalism the LL equation corresponds to the Euler-Lagrange equation derived from (1.40).

$$\delta_A \mathcal{S}(\tilde{A}) = \frac{d}{d\epsilon}\Big|_{\epsilon=0}\mathcal{S}(A + \epsilon\tilde{A}) = \frac{d}{d\epsilon}\Big|_{\epsilon=0}\int_{\mathbb{R}} dt \int_{\mathbb{R}} dx \mathrm{e}^{2t}\mathcal{L}(A + \epsilon\tilde{A}) = 0. \tag{1.41}$$

---

the first order variation or variational derivative of $\mathcal{F}$ is defined, as

$$d_u\mathcal{F}(\tilde{u}) = \frac{d}{d\epsilon}\Big|_{\epsilon=0}\mathcal{F}(u + \epsilon\tilde{u}),$$

where $\epsilon\tilde{u}$ is the first order variation of u. From there we call functional derivative of $\mathcal{F}$ to $\delta_u\mathcal{F}$ defined by the relation:

$$\frac{d}{d\epsilon}\Big|_{\epsilon=0}\mathcal{F}(u + \epsilon\tilde{u}) = \int_{\mathbb{R}} \frac{\delta\mathcal{F}}{\delta u}\tilde{u}dx.$$

In terms of ϵ we can expand the Lagrangian as

$$\mathcal{L} = \epsilon^0 \mathcal{L}^0 + \epsilon^1 \mathcal{L}^1 + \epsilon^2 \mathcal{L}^2 + \mathcal{O}(\epsilon^3), \tag{1.42}$$

After inserting Eq.(1.42) into Eq.(1.41), taking derivative respect to ϵ and evaluating at $\epsilon = 0$ we obtain that

$$\begin{aligned}
\delta_A \mathcal{S}(\tilde{A}) = \int_{\mathbb{R}} \mathrm{e}^{2t} dt \int_{\mathbb{R}} dx \mathcal{L}^1(A, \tilde{A}) = \\
\int_{\mathbb{R}} dt \int_{\mathbb{R}} \mathrm{e}^{2t} \left[\frac{i}{2} \bar{A} \partial_t \tilde{A} - \frac{i}{2} \tilde{A} \partial_t \bar{A} - \nu \partial_x \tilde{A} \partial_x \bar{A} + i\rho \tilde{A} - \theta \tilde{A} \bar{A} + |A|^2 A \tilde{A} \right] = \\
\int_{\mathbb{R}} \mathrm{e}^{2t} dt \int_{\mathbb{R}} dx \left[-i\bar{A} - i\partial_t \bar{A} + \nu \partial_x^2 \bar{A} + i\rho - \theta \bar{A} + |A|^2 \bar{A} \right] \tilde{A} + \\
\int_{\mathbb{R}} \mathrm{e}^{2t} dt \nu \underbrace{\int_{\mathbb{R}} \partial_x \left[\tilde{A} \partial_x \bar{A} \right] dx}_{=0} - \int_{\mathbb{R}} dx \underbrace{\int_{\mathbb{R}} \partial_t \left[\mathrm{e}^{2t} \bar{A} \tilde{A} \right] dt}_{=0}.
\end{aligned} \tag{1.43}$$

The last two terms represent the boundary terms of the problem and are both zero at the boundaries. To obtain those term we have integrated by parts in (1.43).[7]

If A is a extremal of the action (1.31) then $\delta_A \mathcal{S}(\tilde{A}) = 0$ and therefore the *Euler-Lagrange* equation corresponding to the Lagrangian (1.33) reads:

$$-i\bar{A} - i\partial_t \bar{A} + \nu \partial_x^2 \bar{A} + i\rho - \theta \bar{A} + |A|^2 \bar{A} = 0. \tag{1.46}$$

Multiplying by i and taking the complex conjugate of Eq.(1.46) one obtain the LL equation.

1.4.3 Hamiltonian equations

In the Hamiltonian formalism the action reads,

$$\mathcal{S}[A, \bar{A}, \pi, \bar{\pi}] = \int_{\mathbb{R}} \mathrm{e}^{2t} dt \int_{\mathbb{R}} dx \left[\pi \partial_t A + \bar{\pi} \partial_t \bar{A} - \mathcal{H} \right]. \tag{1.47}$$

[7] We have used the identities:

$$\partial_x \tilde{A} \partial_x \bar{A} = \partial_x \left[\bar{A} \partial_x \tilde{A} \right] - \tilde{A} \partial_x^2 \bar{A}, \tag{1.44}$$

and

$$\mathrm{e}^{2t} \bar{A} \partial_t \tilde{A} = \partial_t \left[\mathrm{e}^{2t} \bar{A} \tilde{A} \right] - 2\mathrm{e}^{2t} \bar{A} \tilde{A} - \mathrm{e}^{2t} \partial_t \bar{A} \tilde{A}. \tag{1.45}$$

The *loses* term $-i\bar{A}$ comes from the second term in the rhs of the equality (1.45) and therefore from the exponent e^{2t}.

Setting the variational derivative of (1.47) respect to A and π to zero, one obtains the *Hamiltonian equations* for the LL model:

$$\partial_t A = \frac{\delta H}{\delta \pi} \qquad \partial_t \pi = -\frac{\delta H}{\delta A} - 2\pi. \tag{1.48}$$

From Eqs. (1.48) one can derive the fundamental property of dissipative systems: *the Hamiltonian is not a conserved quantity and decreases in time.*

To see this we need just to derive H respect to t and use Eqs. (1.48):

$$\partial_t H = \frac{\delta H}{\delta A}\frac{\partial A}{\partial t} + \frac{\delta H}{\delta \pi}\frac{\partial \pi}{\partial t}, \tag{1.49}$$

and inserting Eqs. (1.48) one obtain

$$\partial_t H = -2\pi \frac{\delta H}{\delta \pi} < 0. \tag{1.50}$$

1.5 Other generic models for dissipative localized structures

In this Section, we will shortly present two important model equations admitting DS solutions that will be used in subsequent Chapters: the Swift-Hohenberg (SH) equation and the Ginzburg-Landau (GL) equation. Both the SH equation and the GL equation are generic amplitude equations that describe the universal behavior near a bifurcation point.

1.5.1 The Swift-Hohenberg equation

The real Swift-Hohenberg equation has proved to be an invaluable model equation for systems undergoing a bifurcation to time-independent structured states with a finite wavenumber at onset [53]. The equation was originally suggested as a model of infinite Prandtl number convection [54] but finds application in its simplest form in the theory of buckling [55], phase transitions [56] and nonlinear optics [57, 58]. The equation is particularly useful for understanding DSs that are commonly found in systems exhibiting bistability between two states, one of which is homogeneous in space (the trivial state) and the other heterogeneous or structured [53]. In this case the equation for a real field u in one spatial dimension x takes the following form,

$$\partial_t u = -\left(\partial_x^2 + k_0^2\right)^2 u + ru + f[u] \ , \tag{1.51}$$

where $f[u]$ denotes the nonlinear terms. Among the most common cases are, $f = f_{23} \equiv au^2 - gu^3$ [59], $f = f_{35} \equiv au^3 - gu^5$ [60], with $g > 0$ to avoid divergences. The case $f = f_2 \equiv au^2$ was also studied in Ref. [61].

Of particular interest for our purposes is that the SH equation is variational (for periodic boundary conditions), or in other words the dynamics follows a gradient [62]. This implies that the rhs of Eq.(1.51) can be written as the (functional) derivative of a certain functional, namely

$$\frac{\partial u}{\partial t} = \frac{\delta \mathcal{F}_{\rm SH}}{\delta u}, \tag{1.52}$$

with

$$\mathcal{F}_{\rm SH} = \int_0^L dx \left(-\frac{1}{2} r u^2 + \frac{1}{2} \left(\left(\partial_x^2 + k_0^2 \right) u \right)^2 + V[u] \right), \tag{1.53}$$

with the previous cases $V = V_{23} \equiv -\frac{1}{3}au^3 + \frac{1}{4}gu^4$ and $V = V_{35} \equiv -\frac{1}{4}au^4 + \frac{1}{5}gu^5$, such that $f = \delta_u V$. The dynamics in the SH equation are such that $\mathcal{F}_{\rm SH}$ decreases in time until it reaches a local minimum, i.e. a steady state that minimizes $\mathcal{F}_{\rm SH}$. As a consequence, the SH equation cannot exhibit dynamical regimes different from stationary states (i.e. this excludes oscillations and chaos).

1.5.2 The Ginzburg-Landau equation

The Ginzburg-Landau-type of equations are *amplitude equations* that arise as universal model equations near a bifurcation point [1, 63], and their form depends only on the nature of the bifurcation, but not on other details of the system. This type of equations owe their name to a similar equation appearing in the Ginzburg-Landau theory of superconductivity, although in the last case it does not deal with dynamics [64]. Nevertheless, apart from providing a theory for superconductivity, a large number of pattern forming systems can be described using these type of equations. They describe slow modulations in space and time of a simple basic pattern that can be determined from the linear stability analysis of the equation governing the system.

In this thesis we focus on the real GL equation of the form

$$\partial_t u = \mu u + \partial_x^2 u + f[u], \tag{1.54}$$

with u being a real scalar field, μ the gain parameter with and $f[u]$ the nonlinearity.

If $f[u] = f_3 \equiv -u^3$, Eq.(1.54) is commonly called cubic real GL equation [1], which can be considered as a prototypical model describing a spatially extended system with two equivalent steady state solutions $\pm\sqrt{\mu}$. This equation arises naturally near any supercritical pitchfork bifurcation when the system is translationally invariant and spatially reversible i.e. invariant under transformations

$(x \to -x)$, such as for example as for example in Rayleigh-Bénard convection and Taylor-Couette flow [65].

When $f[u] = f_5[u] \equiv u^3 - u^5$, Eq.(1.54) is called quintic real GL equation and it arises near any stationary subcritical bifurcation [1], with the homogeneous steady state solutions $u = 0$ and the bifurcating states,

$$u = \pm\sqrt{\frac{1}{2} - \sqrt{\mu + \frac{1}{4}}} \ , \ \pm\sqrt{\frac{1}{2} + \sqrt{\mu + \frac{1}{4}}}. \tag{1.55}$$

Both cubic and quintic real GL equations have a Lyapunov functional,

$$\mathcal{F}_{\rm GL}[u] = \int \left(\frac{1}{2} \left(\partial_x u\right)^2 + V[u] \right), \tag{1.56}$$

with $V[u] = V_3[u] \equiv -\mu u^2/2 - u^4/4$ and $V[u] = V_5[u] \equiv -\mu u^2/2 + u^4/4 - u^6/6$ being the potential. Therefore, Eq.(1.54) can be written as

$$\frac{\partial u}{\partial t} = \frac{\delta \mathcal{F}_{\rm GL}}{\delta u}, \tag{1.57}$$

The homogeneous steady state (HSS) solutitons minimizes $\mathcal{F}_{\rm GL}$ and therefore also $V[u]$.

When the instability leads to traveling waves, that is, the pattern emerging is time-dependent, the resulting amplitude equation generalizes to the complex GL equation, that with the cubic nonlinearity reads

$$\partial_t A = \mu A + (1 + i\alpha)\partial_x^2 A - (1 + i\beta)|A|^2 A, \tag{1.58}$$

where A is complex scalar field, μ measures the distance from the oscillatory instability threshold, and α and β represents the linear and nonlinear dispersion. This equation, arises for example, in Rayleigh-Bénard convection, hydrothermal waves, and various optical systems, such as lasers, parametric amplifiers, Fabry-Perot cavities filled with nonlinear material, and optical transmission lines [1, 63, 65].

Finally we also mention the forced complex GL (FCGL) equation,

$$\partial_t A = (\mu + i\theta)A + (1 + i\alpha)\partial_x^2 A - (1 + i\beta)|A|^2 A + \rho \bar{A}^{n-1}, \tag{1.59}$$

which is the amplitude equation describing the dynamics of an extended system near the bifurcation to spatially homogeneous oscillations with natural frequency ω in the presence of spatially homogeneous forcing with frequency Ω. In

Eq.(1.59) μ represents the distance from onset of the oscillatory instability, θ is the detuning from the unforced frequency, and α, β and $\rho > 0$ represent dispersion, nonlinear frequency correction and forcing amplitude, respectively. We distinguish two regimes, $\mu < 0$ in which spatially homogeneous oscillations decay in the absence of forcing and $\mu > 0$ in which they grow. We refer to the former as the damped regime and the latter as the self-exciting regime [66]. Particularly interesting is the behavior near strong resonances of the form $\Omega : \omega = n : 1$, where $n = 1, 2$.

In the case $n = 2$ (2:1 resonance), the system is forced at twice the natural frequency [67] and Eq.(1.59) has been used to describe a light sensitive form of the Belousov-Zhabotinsky reaction [68], and finds applications in the optical vectorial Kerr resonator [69, 70] and the degenerate Optical Parametric Oscillator (OPO) [70, 71].

The case $n = 1$, provides a universal description (or normal form) of 1:1 resonantly forced Hopf bifurcations in spatially extended systems. In particular the LL equation [72] is a specific case of Eq.(1.59) in the damped regime ($\mu = -1$) when the coefficients in the dispersion and nonlinearity terms are purely imaginary, with $\alpha = \nu$ and $\beta = 1$.

1.6 An overview of methods

The models that we study in this thesis, such as the LL equation, the SH equation and the GL equation, are evolution equations of the form

$$\partial_t u(x,t) = F[u(x,t), \partial_x^j u; \mu], \tag{1.60}$$

with $x \in \mathbb{R}$, $t \in \mathbb{R}^+$, u a scalar field, real or complex, belonging to an infinite dimensional functional space[8], and F a nonlinear functional acting on that space. This type of equations can be understood as a dynamical system defined in a infinite dimensional phase space. Thus, one can study such type of systems using techniques from dynamical system theory (see Appendix A).

The nonlinear functional is usually defined by

$$F[u(x,t), \partial_x^j u; \mu] \equiv a_0(\mu)u(x,t) + \sum_{j\geq 1} a_j(\mu)\partial_x^j u(x,t) + \mathcal{N}[u(x,t); \mu], \tag{1.61}$$

where we have separated the linear part from the nonlinear one $\mathcal{N}[u(x,t);\mu]$. Here the coefficients a_0 and a_j do not dependent on the variables x and t but do depend on the set of parameters $\mu \equiv (\mu_1, ..., \mu_p) \in \mathbb{R}^p$.

[8] Within the thesis we normally use u for a real scalar field and A for a complex one

The equations here considered are all invariant under *translations* $x \to x + a$, where $a \in \mathbb{R}$, and *reversible* in space [9] (see Section A.4). Because of the reversibility the solutions of these equations are symmetric respect the transformation $x \to -x$ (they are left/right symmetric).

The presence of the set of parameters μ in the equation makes possible that when modifying one of them, qualitative changes in the solution of Eq.(1.60) can occur. This may involve, the creation or destruction of solutions, change in their stability or in their behaviour, as or for example a stationary state that leads to a oscillatory one, among others. The point at which this type of transitions occur is called *bifurcation*, and is related with the breaking of a given symmetry of system. The bifurcations are called *global* when they depend on the nonlocal behaviour of solutions. In contrast, *local bifurcations* can be analyzed entirely in terms of the local behavior of the solutions near a steady state or periodic orbit. In this case, the center manifold reduction and normal form theory can be applied for their study. In Section A.6 we present a detailed review of these techniques and the main bifurcations appearing within this thesis.

The type of equations described here are non integrable, and direct numerical integration is needed. Thinking in Eq.(1.60) as being equivalent to finite sets of coupled ordinary differential equations (ODEs) brings powerful mathematical concepts to help on the analysis of their solutions. The most efficient algorithms to numerically solve this type of equations on a periodic domain are known as *spectral methods*. To apply such methods, we perform a spatial Fourier transform on the Eq.(1.60) and convert it into a system of ODEs. This ODE system can then be split into a linear part and a nonlinear part, the latter of which can be evaluated by first transforming the current solution to physical space, computing the nonlinear terms at the mesh points, and then transforming back to Fourier space. A detailed review of this method is presented in Section B.2. This will be the main tool when dealing with non stationary solutions, such as oscillatory or chaotic states. However these numerical simulations are very time consuming and, by themselves, do not allow for a complete understanding of the dynamics of a system.

In this work we are particularly interested in stationary dissipative structures described by solutions u_s of Eq.(1.60) satisfying $\partial_t u = 0$ i.e. solutions of the ODE

$$F[u_s(x), \partial_x^j u; \mu] = 0. \tag{1.62}$$

If u_s is homogeneous i.e. does not depend on x, Eq.(1.62) sometimes can be

[9] The LL has this property when odd high-order dispersion terms are excluded from Eq.(1.28). Otherwise the $x-$reversibility is broken.

solve analytically. However, in general when spatial dependence is present, a Newton-Raphson method can be used to find numerically stationary solutions with arbitrary precision (see Section B.3), and continuation techniques to track them as the parameters are varied (see Section B.4). In this way one can build the *bifurcation diagrams* which help to understand the bifurcation structure and the organization of the different solutions of the system.

To determine the stability of these solution one can proceed in the same way that for finite dimensional dynamical systems (see Appendix A), and study the linearization of Eq.(1.60) around those states, which is equivalent to characterize the dynamics of Eq.(1.60) arbitrary close to $u_s(x)$, and therefore of the form $u(x,t) = u_s(x) + \epsilon\xi(x,t)$. After introducing this anzats in Eq.(1.60) one arrives to a linear PDE for $\xi(x,t)$ whose solution is given by

$$\xi(x,t) = \sum_{i=1}^{\infty} A_i(\mu)\psi_i(x)\mathrm{e}^{i\lambda_i(\mu)t}, \tag{1.63}$$

where A_i are the amplitudes of the eigenmodes ψ, and λ its associated and eigenvalues obtained by solving linear eigenvalue problem

$$L[u_s(x);\mu]\psi(x) = \lambda(\mu)\psi(x), \tag{1.64}$$

where L is the linearized operator associated to F. The eigenvalues comprise the spectrum of the linear operator $L[u_s(x);\mu]$ and this spectrum consists of two sets depending on the symmetry of the eigenmodes, namely *amplitude* modes when they are even functions (symmetric), and *phase* modes when they are odd (anty-symmetric). In translationally invariant systems, like those studied here, there is always one neutrally stable (i.e. with eigenvalue $\lambda = 0$) phase mode, the *Goldstone* mode $\mathcal{G}$, which can be identified as the first derivative of u_s with respect to the spatial coordinate x, i.e. $\mathcal{G}(x) \equiv \partial_x u_s(x)$.

For the numerical solutions u_s obtained with the Newton-Raphson method, Eq.(1.64) can also being solved numerically. In this framework the linear operator $L[u_s(x);\mu]$ corresponds to the Jacobian matrix associated with the finite set of coupled ODEs describing Eq.(1.62). Thus, the eigenvalues of this Jacobian determine the stability of the solutions against perturbations that lie on the same phase subspace. The extension of the stability analysis to arbitrary perturbations in the whole infinite phase space is not a trivial point. Finite wavelength instabilities of patterns are examples of bifurcations that occur in directions of the phase space not parallel to the subspace where the solution belongs to (see Section 3.4).

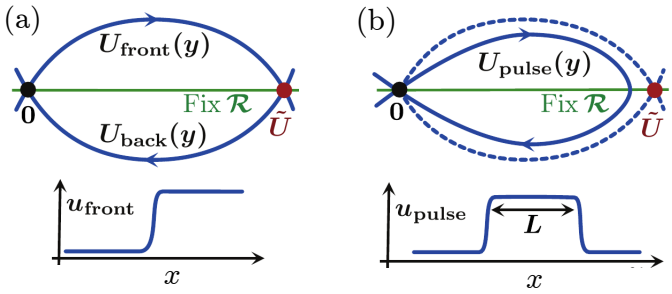

Figure 1.13: Correspondence between LSs and orbits in spatial dynamics. In (a) we show a front connecting states 0 and $\tilde{U}$ (bottom) and its corresponding heteroclinic orbit (top). If another front connects back $\tilde{U}$ with 0, and both states have the same energy, a heteroclic cycle is formed. This cycle corresponds to two fronts connected back-to-back with the HSS 0. Even when the energies are different homoclinic orbits can bifurcate from the previous heteroclinic cycle. This is the situation shown in (b) and these homoclinic orbits correspond to the pulse shown in the bottom panel. This Figure has been adapted from Figure 3 of Ref. [109].

Another approach, that will be used within this manuscript, consists in deriving a set of equations for the spatial evolution (*spatial dynamics*) of the solutions of Eq.(1.62). These equations form a special kind of dynamical system in which space plays the role usually played by time. Then, defining a set of intermediate variables $y_0 = u$, and $y_i = d_x^i u$, for $i = 1, ..., n-1$, where n is such that the higher order spatial derivative in F is of order n, one obtains the following $n-$dimensional *spatial* dynamical system

$$\begin{aligned} &d_x y_0 = y_1 \\ &d_x y_i = y_{i+1}, \qquad i = 1, n-1 \\ &F(y_1, y_2, y_3, ..., y_{n-2}, d_x y_{n-1}; \mu) = 0. \end{aligned} \tag{1.65}$$

The last equation is an implicit equation for $d_x y_{n-1}$. In all the cases studied within this thesis the higher order derivative in F appears in a additive way, and therefore the last equation can be written in a explicit form.

In this framework several correspondences between the stationary solutions of Eq.(1.62) and solutions of this particular dynamical system can be established. For example, the fixed point of the dynamical system (1.65) corresponds to solutions of Eq.(1.62) which do not have any dependence on x, namely the HSS solutions, and a pattern with a wavelength λ_P to a periodic orbit with spatial period λ_P. In the same fashion, a front or domain wall connecting two different states, let us say 0 and $\tilde{U}$, corresponds to a *heteroclinic orbit* like the one shown in Figure 1.13(a), and a LS byasymptotic to the same HSS soltuion, in this case

0, when $x \to \pm\infty$ can be understood as a *homoclinic orbit* to such fixed point as depicted in Figure 1.13(b)[10].

This approach allows to use the theory homoclinic and heteroclinic orbits to study the formation of LSs (see these definitions in Section A.5). Analyzing the linearization of the dynamical system about a given HSS solution one will first identify the bifurcations that such point undergoes, and second, apply the well known results of normal form theory (see Section A.6) to predict for which values of the control parameter LSs or patterns can arise.

Arbitrary close to such bifurcations a weakly nonlinear analytical approximation for the stationary solutions of Eq.(1.62) can be found by using perturbation theory (see Section B.1). Performing an asymptotic expansion of the stationary solution in the form

$$u = u_0\epsilon^0 + u_1\epsilon^1 + u_2\epsilon^2 + \cdots, \tag{1.66}$$

with $0 < \epsilon \ll 1$, related with the onset of the bifurcation, and solving Eq.(1.62) order by order in ϵ one obtains, truncating at first order, the desired solution. Here, the coefficients u_i at each order in ϵ can be functions of multiple spatial scales $x, X_1, X_2 \cdots$. This analytical approximation can be used as an initial guess in a continuation algorithm in such a way that one can track those states to values of the parameters far from the bifurcations.

1.7 A brief summary of the various chapters

1. In **Chapter 2**, we analyze the necessary conditions for the existence of LSs or DSs biasymptotic to the HSS solution in the LL equation. The stationary LL equation is recast to a four-dimensional reversible dynamical system. In this context LSs correspond to reversible homoclinic orbits to a fixed point, i.e. the HSS solution. In this framework we perform a linear stability analysis of that fixed point and we classify the different bifurcations that it undergoes as a function of the parameters of the system. The normal form theory shows that, in the neighborhood of some of these bifurcations LSs exist. We discus in detail the anomalous and normal GVD regimes, establishing a solid base on which we will build in the following chapters.

2. In **Chapter 3**, we study the pattern solutions in the anomalous GVD regime. To start we perform a linear stability analysis of the HSSs. After

[10] This type of homoclinic orbit bifurcates from a heteroclinic cycle, connecting first 0 with $\tilde{U}$, and then back $\tilde{U}$ with 0. For more information see definitions in Section A.5.

that we apply asymptotic perturbation methods to calculate a first order approximation for the pattern solution, only valid in the neighborhood of a modulation instability. This solution is the starting point to build up the complete skeleton for the different patterns coexisting in the model. We show that for certain values of detuning, patterns of a given wavelength are connected with patterns with half of that frequency. The connection takes place through a secondary bifurcation of one of the patterns. Moreover there are many other such bifurcations where the pattern becomes unstable to different wavelengths or where they start to oscillate.

3. In **Chapter 4**, we expand previous studies on the bifurcation structure and stability of bright soliton solutions in the anomalous regime. We show that there are two regimes depending on the frequency detuning parameter for which the origin and bifurcation structure of such states differ. We apply asymptotic techniques to obtain approximated solutions for those LSs in both regimes. For low values of detuning ($\theta < 2$), LSs can be formed due to the bistability between the background field and a pattern state within a range of parameters around the Maxwell point of the system known as pinning region. Those states are organized in a snakes-and-ladders structure. For high values of detuning ($\theta > 2$), we find that the bifurcation structure of the LSs differs from the one in previous situation. In this regime, LSs undergo oscillatory instabilities that make solitons oscillates in amplitude with a single period. Varying the control parameters we find that those oscillations undergo period doubling bifurcations starting a route to temporal chaos. Moreover the system also presents spatiotemporal chaos.

4. In **Chapter 5**, we study the LL equation in the normal GVD regime. In this regime the bistability of two homogeneous states allows the formation of fronts connecting them. In a region close to the Maxwell point, two fronts with different polarities lock and form a dark LS. The asymptotic analysis performed here is the same as the one done in the anomalous regime for $\theta > 2$. In this case, dark solitons are organized in a structure known as *collapsed snaking*. This implies the presence of a region in parameter space with a finite multiplicity of dark solitons. For high values of detuning dark solitons undergo oscillatory instabilities where they start to oscillate in amplitude. The oscillatory states do also undergo a period doubling bifurcation and start a route to temporal chaos. We characterize in parameter space how the bifurcation structure is modified as a function of the parameters of the system.

5. In **Chapter 6**, we focus on how high-order dispersion effects, in particular third order effects, modify the bifurcation structure and stability of the LSs for both the anomalous and normal dispersion regimes. In both regimes a common feature of including third order dispersion is that the LSs, now asymmetric, drift with a constant velocity that depends on the control parameters. We study how the bifurcation structure in both the anomalous and normal GVD regimes is modified when considering this term. The drift is also responsible for the suppression of the oscillatory and chaotic dynamics, and for the stabilization of both bright and dark solitons in the anomalous and normal regimes, respectively. In the last one, we also find that third-order dispersion allows the formation of bright solitons due to the modification of the tails of the fronts.

6. In **Chapter 7**, we investigate the formation of bound states of bright solitons in the anomalous GVD regime. Due to the presence of oscillatory tails, solitons can lock at different separation distances, which are determined by the wavelength of the tails. We derive effective potentials describing the interaction and we relate their shape and periodicity with the spatial eigenvalues of the system. In this way we can predict, given an initial separation, all the stable and unstable separation distances allowed for the bound states. We study the bifurcation structure for these new states and discuss their existence as function of the control parameters. After that we apply the same techniques to the study of the formation of bound states in the presence of higher order dispersion effects, in particular third and fourth order dispersion effects. In these two cases we also study how a noisy background can effect the stability of the new structures, and we calculate the basins of attraction of the system.

7. In **Chapter 8**, we study how the presence of inhomogeneities (or defects) and drift modify the dynamics of LSs in the LL equation. Without loss of generality we focus on the dynamics of a single bright soliton in the anomalous regime, although the results can be extrapolated to the case of dark solitons or even for configurations of several LSs. We show that the competition between the defect, which pins the LSs, and the drift which pulls it out leads to very rich dynamics such as oscillations and excitability. In order to better understand the system we calculate the bifurcation diagrams and identify the bifurcation involved in the appearance of previous dynamics. We perform this analysis considering both absorbing and periodic boundary conditions.

8. In **Chapter 9**, we analyze in detail the mechanism introduced in **Chapter**

9 in a simpler model, the Swift-Hohenberg equation. We show that the appearance of excitability (Type I and Type II) and oscillatory regimes (localized small oscillations and train of solitons) for solitons when defects and drift are present is generic and not just a feature of the LL model. We find that all the dynamics of the system unfold from two codimension-two Takens-Bodganov bifurcations that organize the complete scenario. The study presented in this Chapter is mainly focused on the case where the defect is injected (as in Chapter 8). However, we also show that the same type of dynamics appears when it is added to the gain. In this last case the scenario is much more complex than in the previous one.

9. In **Chapter 10**, we introduce a new mechanism leading to excitability based on just two ingredients: bistability between two HSSs solutions and spatial coupling. We show the existence of a threshold such that, while sitting on one homogeneous state, sub-threshold perturbations decay fast whereas super-threshold perturbations induce a long excursion mediated by the emergence of a structure formed by two back-to-back fronts that join the two homogeneous states. Furthermore, while in typical excitability the trajectory follows the remnants of a limit cycle, here reinjection is provided by front interaction, so that fronts slowly approach each other until eventually annihilating. This front-mediated mechanism shows that excitability can exist in extended systems with no oscillatory regimes. We perform this analysis when the HSSs are equivalent, as is the case in the prototypical GL equation with cubic nonlinearity, and when they are not equivalent as in the real quintic GL equation. We also find that this last situation also exists in the LL equation in the normal dispersion regime.

10. In **Chapter 11**, we briefly revisit the obtained results withing the previous Chapters.

References

[1] M. Cross and P. Hohenberg, *Pattern-formation outside of equilibrium,* Rev. Mod. Phys. **65**, 851-1112, 1993.

[2] J. Murray, *Mathematical Biology,* Springer, New York, 1989.

[3] R. Hoyle, *Pattern Formation: an introduction to methods,* Cambridge University Press, 2006.

[4] http://art-educ4kids.weebly.com/hands-collage.html

[5] https://www.flickr.com/photos/59307966@N03/galleries/72157626013131544/

[6] https://www.wired.com/2011/02/turing-patterns/

[7] http://www.demilked.com/landscape-form-visualization-nature-sound-waves-anna-marinenko/

[8] https://www.flickr.com/photos/zeroglab/galleries/72157627715548745

[9] http://www.noupe.com/inspiration/photography/nature-s-pattern-photography-35-outstanding-photos.html

[10] https://www.pinterest.com/pin/7599893093979808/

[11] https://en.wikipedia.org/wiki/Frog

[12] https://emorfes.com/2012/02/01/photography-water-patterns-in-nature/

[13] P. B. Umbanhowar, F. Melo, and H. L. Swinney, *Localized excitations in a vertically vibrated granular layer,* Nature **382**, 793 (1996).

[14] https://en.wikipedia.org/wiki/Fairy circle (arid grass formation).

[15] R. Richter and I. V. Barashenkov, *Two-dimensional solitons on the surface of magnetic fluids,* Phys. Rev. Lett. **94**, 184503, 2005.

[16] https://clasberkeley.wordpress.com/2016/02/24/from-plant-ecology-to-nonlinear-optics-and-a-few-places-in-between/

[17] https://en.wikipedia.org/wiki/Morning glory cloud.

[18] S. Barland, J. R. Tredicce, M. Brambilla, L. A. Lugiato, S. Balle, M. Giudici, T. Maggipinto, L. Spinelli, G. Tissoni, T. Knodl, M. Miller, and R. Jager, *Cavity solitons as pixels in semiconductor microcavities,* Nature **419**, 699- 702, 2002.

[19] J.D. Gunton, M. San Miguel and P. Sahni, in *Phase Transitions and Critical Phenomena,* edited by C. Domb and J.L. Lebowitz (Academic Press, Ney York, 1983), Vol. 8, p. 269.

[20] E. Meron,*Pattern formation in excitable media,* Phys. Rep. 218, 1 (1992).

[21] I. Prigogine, *Dissipative Structures in Chemical Systems,* in Stig Claesson (ed.), Fast Reactions and Primary Processes in Chemical Kinetics, New York: Interscience (1967); I. Prigogine, and G. Nicolis, *Self-Organization in Non-Equilibrium Systems,* Wiley (1977). ISBN 0-471-02401-5.

[22] N. Akhmediev and A. Ankiewicz (eds.), *Dissipative Solitons, Lecture Notes in Physics,* Vol. 661 (Springer, New York, 2005); *Disipative Solitons: From Optics to Biology and Medicine, Lecture Notes in Physics,* Vol. 751 (Springer, New York, 2008).

[23] S. Trillo and W. Toruellas, *Spatial Solitons,* vol. 82 of Springer Series in Optical Sciences, Springer-Verlag, Berlin, 2001.

[24] Y. S. Kivshar and G. P. Agrawal, *Optical Solitons: From Fibers to Photonic Crystals,* Academic Press, San Diego, 2003.

[25] N. N. Rosanov, *Spatial Hysteresis and Optical Patterns,* Springer series in synergetics, Springer, Berlin, 2002.

[26] T. Ackemann and W. J. Firth, *Dissipative solitons in pattern-forming nonlinear optical systems: Cavity solitons and feedback solitons,* in Lecture Notes in Physics, Berlin Springer Verlag, 661, 55-100, 2005.

[27] J. M. Soto-Crespo, N. Akhmediev, and G. Town, *Interrelation between various branches of stable solitons in dissipative systems conjecture for stability criterion,* Opt. Commun. **199**, 283 (2001).

[28] P. G. Drazin and R. S. Johnson, *Solitons: an introduction,* Cambridge University Press,

Cambridge 1989.

[29] T. Dauxois, and M. Peyrard, *Physics of solitons*, Cambridge University Press, Cambridge 2006.

[30] M. J. Ablowitz and P. A. Clarkson, *Solitons, nonlinear evolution equations and inverse scattering,* Cambridge University Press, Cambridge, 1991; M. J. Ablowitz, D. J. Kaup, A. C. Newell, and H. Segur, *Method for solving the sine-Gordon equation,* Phys. Rev. Lett. **30**, 1262-1264 (1973).

[31] W. J. Firth, A. Lord, and A. J. Scroggie, *Optical bullet holes,* Phys. Scr. T67, **12** (1996); W. J. Firth, G. K. Harkness, A. Lord, J. McSloy, D. Gomila, and P. Colet, *Dynamical properties of two-dimensional Kerr cavity solitons,* J. Opt. Soc. Am. B **19**, 747 (2002).

[32] V. K. Vanag and I. R. Epstein, *Localized patterns in reaction-diffusion systems,* Chaos **17**, 037110, 2007.

[33] F. Leo, L. Gelens, P. Emplit, M. Haelterman, and S. Coen, *Dynamics of one-dimensional Kerr cavity solitons,* Opt. Express **21**, 9180 (2013).

[34] D. Michaelis, U. Peschel, C. Etrich, and F. Lederer, *Quadratic cavity solitons the up-conversion case,* IEEE J. Quantum Electron. 39, 255 (2003).

[35] P. Parra-Rivas, D. Gomila, M. A. Matías and P. Colet, *Dissipative soliton excitability induced by spatial inhomogeneities and drift,* Phys. Rev. Lett. **110**, 064103 (2013); P. Parra-Rivas, D. Gomila, M. A. Matías, P. Colet, and L. Gelens,*Competition between drift and spatial defects leads to oscillatory and excitable dynamics of dissipative solitons,* Phys. Rev. E. **93**, 012211 (2016).

[36] D. Gomila, M. A. Matias, and P. Colet, *Excitability mediated by localized structures in a dissipative nonlinear optical cavity,* Phys. Rev. Lett. **94**, 063905 (2005); D. Gomila, A. Jacobo, M. A. Matías, and P. Colet, *Phase-space structure of two-dimensional excitable localized structures,* Phys. Rev. E **75**, 026217 (2007); *Effects of a localized beam on the dynamics of excitable cavity solitons,* Phys. Rev. A 75, 053821 (2008).

[37] J. E. Pearson, *Complex patterns in a simple system,* Science **261**, 189-192, 1993.

[38] K. J. Lee, W. D. McCormick, Q. Ouyang, and H. L. Swinney, *Pattern formation by interacting chemical fronts,* Science **261**, 192-194, 1993.

[39] C. R. Laing, W. C. Troy, B. Gutkin, and G. B. Ermentrout, *Multiple bumps in a neuronal model of working memory,* SIAM J. Appl. Math. **63**, 62-97, 2002.

[40] S. Coombes, *Waves, bumps, and patterns in neural field theories,* Biological Cybernetics **93**(2), 91-108, 2005.

[41] O. Lioubashevski, Y. Hamiel, A. Agnon, Z. Reches, and J. Fineberg, Oscillons and propagating solitary waves in a vertically vibrated colloidal suspension, Phys. Rev. Lett. **83**, 3190-3193, 1999.

[42] J. J. Niemela, G. Ahlers, and D. S. Cannell, *Localized traveling-wave states in binary-fluid convection,* Phys. Rev. Lett. **64**, 1395, 1990.

[43] O. Batiste and E. Knobloch, *Simulations of localized states of stationary convection in He-3-He-4 mixtures,* Phys. Rev. Lett. **95**, 244501, 2005.

[44] E. Meron, E. Gilad, J. von Hardenberg, M. Shachak, and Y. Zarmi, *Vegetation patterns along a rainfall gradient,* Chaos, Solitons and Fractals **19**, 367-376, 2004.

[45] O. Lejeune, M. Tlidi, and P. Couteron, *Localized vegetation patches: A self-organized response to resource scarcity,* Phys. Rev. E **66**, 010901, 2002.

[46] A. J. Scroggie, W. J. Firth, G. S. McDonald, M. Tlidi, R. Lefever, and L. A. Lugiato, *Pattern-formation in a passive kerr cavity,* Chaos, Solitons and Fractals **4**, 1323, 1994.

[47] V. B. Taranenko, K. Staliunas, and C. O. Weiss, *Spatial soliton laser: Lo- calized structures in a laser with a saturable absorber in a self-imaging resonator,* Phys. Rev. A **56**, 1582-1591, 1997.

[48] M. Pesch, E. Grosse Westhoff, T. Ackemann, and W. Lange, *Observation of a discrete family of dissipative solitons in a nonlinear optical system,* Phys. Rev. Lett. **95**, 143906, 2005.

[49] M. Tlidi, P. Mandel, and R. Lefever, *Localized structures and localized patterns in optical bistability,* Phys. Rev. Lett. **73**, 640-643, 1994.

[50] U. Bortolozzo, L. Pastur, P. L. Ramazza, M. Tlidi, and G. Kozyreff, *Bistability between different localized structures in nonlinear optics,* Phys. Rev. Lett. **93**, 253901, 2004.

[51] X. Hachair, S. Barland, L. Furfaro, M. Giudici, S. Balle, J. R. Tredicce, M. Brambilla, T. Maggipinto, I. M. Perrini, G. Tissoni, and L. Lugiato, *Cavity solitons in broad-area vertical-cavity surface-emitting lasers below threshold,* Phys. Rev. A **69**, 043817, 2004.

[52] P. Genevet, S. Barland, M. Giudici, and J. Tredicce, Cavity soliton laser based on mutually coupled semiconductor microresonators, Phys. Rev. Lett. **101**, 123905, 2008.

[53] A. R. Champneys, *Homoclinic orbits in reversible systems and their applications in mechanics, fluids and optics,* Physica D **112**, 158-186, 1998.

[54] J. Swift and P. Hohenberg, *Hydrodynamic fluctuations at convective instability,* Phys. Rev. A **15**, 319-328, 1977.

[55] G. W. Hunt, M. A. Peletier, A. R. Champneys, P. D. Woods, M. A. Wadee, C. J. Budd, and G. J. Lord, *Cellular buckling in long structures,* Nonlinear Dynamics **21**, 3-29, 2000.

[56] P. L. Geissler and D. R. Reichman, *Nature of slow dynamics in a minimal model of frustration-limited domains,* Phys. Rev. E **69**, 021501, 2004.

[57] M. Tlidi, P. Mandel, and R. Lefever, *Localized structures and localized patterns in optical bistability,* Phys. Rev. Lett. **73**, 640, 1994.

[58] G. Kozyreff and M. Tlidi, *Nonvariational real Swift-Hohenberg equation for biological, chemical, and optical systems,* Chaos **17**, 037103, 2007.

[59] J. Burke and E. Knobloch, *Localized states in the generalized Swift-Hohenberg equation,* Phys. Rev. E **73**, 056211, 2006.

[60] J. Burke and E. Knobloch, *Snakes and ladders: Localized states in the Swift-Hohenberg equation,* Phys. Lett. A **360**, 681-688, 2007.

[61] B. Buffoni, A. R. Champneys and J. F. Toland, *Bifurcation and coalescence of a plethora of homoclinic orbits for a Hamiltonian system,* J. Dyn. and Diff. Eq., **8**, 2, 1996.

[62] S. H. Strogatz, *Nonlinear Dynamics and Chaos,* 2nd ed. (Westview Press, Boulder, CO, 2014).

[63] I. S. Aranson and L. Kramer, *The world of the complex Ginzburg-Landau equation,* Rev. Mod. Phys. **74**, 99-143, 2002.

[64] V. Ginzburg and L. Landau Zh. Eksp. Teor. Fiz. **20**, 1064, 1950.

[65] W. van Saarloos, *Front propagation into unstable states,* Phys. Rep. **386**, 29-222, 2003.

[66] Y. P. Ma, J. Burke, E. Knobloch, *Defect-mediated snaking: A new growth mechanism for*

localized structures, Physica D **239** (2010) 1867-1883.

[67] P. Coullet, J. Lega, B. Houchmanzadeh, and J. Lajzerowicz, *Breaking chirality in nonequilibrium systems,* Phys. Rev. Lett. **65**, 1352-1355, 1990.

[68] V. Petrov, Q. Ouyang, and H. L. Swinney, *Resonant pattern formation in a chemical system,* Nature **388**, 655-657, 1997.

[69] D. Gomila, P. Colet, G.L. Oppo, and M. San Miguel, *Stable droplets and growth laws close to the modulational instability of a domain wall,* Phys. Rev. Lett. **87**, 194101, 2001.

[70] D. Gomila, P. Colet, M. San Miguel, A. J. Scroggie, and G.L. Oppo, *Stable droplets and dark-ring cavity solitons in nonlinear optical devices,* IEEE J. Quantum. Electron. **39**, 238-244, 2003.

[71] K. Staliunas, *Transverse pattern-formation in optical parametric oscillators,* J. Mod. Opt. **42**, 1261, 1995.

[72] L. A. Lugiato and R. Lefever, *Spatial dissipative structures in passive optical systems,* Phys. Rev. Lett. **58**, 2209-2211, 1987.

[73] A. Jacobo, *Spatial structures and information processing in nonlinear optical cavities,* (2009).

[74] M. Haelterman, S. Trillo, and S. Wabnitz, *Dissipative modulation instability in a nonlinear dispersive ring cavity,* Optics Communications **91**, 401-407 (1992).

[75] Y. K. Chembo and C. Menyuk, *Spatiotemporal Lugiato-Lefever formalism for Kerr-comb generation in whispering-gallery-mode resonators,* Phys. Rev. A **87**, 053852 (2013).

[76] S. Coen, H. G. Randle, T. Sylvestre, and M. Erkintalo, *Modeling of octave-spanning Kerr frequency combs using a generalized mean-field Lugiato-Lefever model,* Opt. Lett. **38**, 37 (2013).

[77] T. J. Kippenberg, R. Holzwarth, and S. A. Diddams, *Microresonator-Based Optical Frequency Combs,* Science **332**, 555 (2011).

[78] S. Coen, *Passive nonlinear optical fiber resonators: Fundametals and applications,* PhD Thesis (2000).

[79] L. Lugiato, F. Prati, M. Brambilla, *Nonlinear optical systems,* Cambridge University Press (2015).

[80] T. Hansson, and S. Wabnitz, *Dynamics of microresonator frequency comb generation: models and stability,* Nanophotonics, **5**, 2 231-243 (2016).

[81] K. Ikeda, *Multiple-valued stationary state and its instability of the transmitted light by a ring cavity system,* Opt. Comm. **30** (1979) 257.

[82] W. Chen and D. L. Mills, *Gap Solitons and the Nonlinear Optical Response of Superlattices,* Phys. Rev. Lett. **58**, 160-163 (1987).

[83] A. E. Kaplan and P. Meystre, *Directionally Asymmetrical Bistability in a Symmetrically Pumped Nonlinear Ring Interferometer,* Opt. Comm. **40**, 229-232 (1982).

[84] M. Haelterman, *Period-doubling bifurcations and modulational instability in the nonlinear ring cavity: an analytical study* Op. Lett. **17**, 792-794 (1992).

[85] F. Leo, S. Coen, P. Kockaert, S-P. Gorza, P. Emplit and M. Haelterman *Temporal cavity solitons in one-dimensional Kerr media as bits in an all-optical buffer,* Nature Photon. **4**, 471-476 (2010).

[86] P. Del'Haye, T. Herr, E. Gavartin, M. L. Gorodetsky, R. Holzwarth, and T. J. Kippenberg, *Octave Spanning Tunable Frequency Comb from a Microresonator,* Phys. Rev. Lett., **107** (6), August 2011.

[87] Yoshitomo Okawachi, Kasturi Saha, Jacob S. Levy, Y. Henry Wen, Michal Lipson, and Alexander L. Gaeta, *Octave-spanning frequency comb generation in a silicon nitride chip,* Opt. lett., **36**(17),3398-3400, 2011.

[88] T. Hansch, *Nobel Lecture: Passion for precision. Reviews of Modern Physics,* **78**(4):1297-1309, November 2006.

[89] Scott B. Papp, Katja Beha, Pascal Del'Haye, Franklyn Quinlan, Hansuek Lee, Kerry J. Vahala, and Scott A. Diddams, *Microresonator frequency comb optical clock,* Optica, 1(1):10, July 2014.

[90] J. D. Jost, T. Herr, C. Lecaplain, V. Brasch, M. H. P. Pfeiffer, and T. J. Kippenberg, *Counting the cycles of light using a selfreferenced optical microresonator,* Optica, **2**(8):706, August 2015.

[91] C. Godey, I. V. Balakireva, A. Coillet, and Y. K. Chembo, *Stability analysis of the spatiotemporal Lugiato-Lefever model for Kerr optical frequency combs in the anomalous and normal dispersion regimes,* Phys. Rev. A **89**, 063814 (2014).

[92] P. Parra-Rivas, D. Gomila, M. A. Matías, S. Coen, and L. Gelens, *Dynamics of localized and patterned structures in the Lugiato-Lefever equation determine the stability and shape of optical frequency combs,* Phys. Rev. A **89**, 043813 (2014).

[93] Y. K. Chembo and Nan Yu, Modal expansion approach to optical-frequency-comb generation with monolithic whispering-gallery-mode resonators, Phys. Rev. A, **82**(3), September 2010.

[94] W. Liang, A. A. Savchenkov, V. S. Ilchenko, D. Eliyahu, D. Seidel, A. B. Matsko, and L. Maleki, *Generation of a coherent near-infrared Kerr frequency comb in a monolithic microresonator with normal GVD,* Opt. Lett. **39**, 2920-2923 (2014).

[95] S.W. Huang, H. Zhou, J. Yang, J. F. McMillan, A. Matsko, M. Yu, D.L. Kwong, L. Maleki, and C. W. Wong, *Mode-locked ultrashort pulse generation from on-chip normal dispersion microresonators,* Phys. Rev. Lett. **114**, 053901 (2015).

[96] X. Xue, Y. Xuan, Y. Liu, P.H. Wang, S. Chen, J. Wang, D. E. Leaird, M. Qi, and A. M. Weiner, *Mode-locked dark pulse Kerr combs in normal-dispersion microresonators,* Nature Photon.**9**, 594-600 (2015).

[97] P. Parra-Rivas, E. Knobloch, D. Gomila, L. Gelens, *Dark solitons in the Lugiato-Lefever equation with normal dispersion,* Physical Review A **93**, 063839 (1-17) (2016).

[98] P. Parra-Rivas, D. Gomila, E. Knobloch, S. Coen, L. Gelens, *Origin and stability of dark pulse Kerr combs in normal dispersion resonators,* Optics Letters **41**, 2402-2405 (2016).

[99] P. Parra-Rivas, D. Gomila, and L. Gelens, *Stable dark and bright soliton Kerr combs can coexist in normal dispersion resonators,* Opt. Lett. (2016).

[100] G. Kozyreff and L. Gelens, *Cavity solitons and localized patterns in a finite-size optical cavity,* Phys. Rev. A **84**, 023819 (2011).

[101] S. Coen and M. Erkintalo, *Universal scaling laws of Kerr frequency combs,* Op. Lett. **38**, 11, 1790-1792 (2013).

[102] B Mengjie Yu, Jae K. Jang, Yoshitomo Okawachi, Austin G. Griffith, Kevin Luke, Steven A. Miller, Xingchen Ji, Michal Lipson , and Alexander L. Gaeta, *Breather Soliton Dynamics*

in Microresonators, (https://arxiv.org/pdf/1609.01760).

[103] M. Goldstein, *Classical mechanics*, Addisson Wesley, 2nd edition, (1981).

[104] C. E. Smith *Lagrangians and Hamiltonians with friction,* J. Phys.: Conference Series, **237**, 012021 (2010).

[105] N. Chen, T. Honein and G. Herrmann, Dissipative systems, conservation laws and symmetries, Int. J. Solids Structures, **33**, 20-22, (1996).

[106] R. de Ritis, G. Marmo and G. Platania, *Inverse problem in classical mechanics: dissipative systems*, In. J. Thor. Phys.,**22**, 10 (1983).

[107] W.J. Firth and A. Lord, J. Mod. Opt. **43**, 1071 (1996).

[108] I. V. Barashenkov, Yu. S. Smirnov, and N. V. Alexeeva ,Phys. Rev. E **57** 2 (1998).

[109] D. Avitabile, D.J.B. Lloyd, J. Burke, E. Knobloch and B. Sandstede. *To snake or not to snake in the planar Swift-ÂηHohenberg equation.* SIAM J. Appl. Dyn. Syst. **9** 704-733 (2010).

Chapter 2

Homoclinic orbits to homogeneous steady state solutions: Localized structures

2.1 Introduction

Within this thesis we focus on the study of localized structures (LSs) arising in temporal cavities both the anomalous and normal GVD regimes. In Chapter 1 we have seen that in one extended dimension there are three main mechanism behind the formation of LSs, and all of them related with the coexistence between two different states. In terms of spatial dynamics one can understand a LSs as a homoclinic orbit to the equilibrium HSSs (see Section 1.6). Figure 2.1 shows an example of a pattern-element LS (a) and its associated homoclinic orbit (b). This particular LS is equivalent to a homoclinic orbit consisting in a trajectory leaving the HSS here 0, rolling several times around the pattern (here the cycle in red), and returning back to the same HSS. Due to this correspondence it is possible, using the theory of dynamical systems, to predict the parameter regions where LSs can be expected, identify the bifurcations undergone by the HSS, from where they arise, and obtain an approximate solution for them in a neighborhood of these points. Hence, the goal of this chapter is to analyze the spatial dynamics of the LL equation. In Section 2.2 we discuss briefly the homogeneous steady state solution of the system. In Section 2.3 we derive the dynamical system associated with the stationary LL equation and we study linearization around the HSSs for both the normal and anomalous dispersion regimes. In this way we classify all

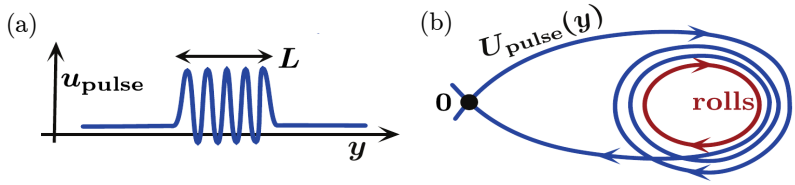

Figure 2.1: Correspondence between a pattern-element LS and homoclinic orbit in the context of spatial dynamics of the LL equation. In (a) a pattern-element type of LS, with a plateau of length L biasymptotic to the HSS 0 is shown. In (b) the associated homoclinic orbit in the spatial dynamics. A trajectory leaves 0 rolls several times the cycle (pattern) and returns back to 0. This Figure has been adapted from Figure 4 of Ref. [1].

the spatial bifurcations that occur in the system, which will be of great interest for the coming sections. To continue, Section 2.4 provides an overview of the normal forms and dynamics of the bifurcations previously identified. In this way we can predict the existence of homoclinic orbits close to those bifurcations and consequently, the appearance of LSs. Finally, in Section 2.5, we study the tails of the LSs using the linearization previously performed. The shape of those tails will be essential for the creation of LSs, both dark and bright solitons, and for the formation of bound states.

2.2 The homogeneous steady state

In the following we will talk mainly about homoclinic orbits to the HSS or continue wave (CW) solution. We will use this mathematical object to study LSs arising in the context of the LL equation, namely

$$\partial_t A = -(1+i\theta)A + i\nu\partial_x^2 A + iA|A|^2 + \rho. \tag{2.1}$$

Before starting with the study of homoclinic orbits i.e. LSs, it is necessary to take a look to the HSSs solution of the system. Any steady state of the LL equation satisfy the ODE,

$$i\nu\frac{d^2A}{dx^2} - (1+i\theta)A + i|A|^2A + \rho = 0, \tag{2.2}$$

or, written in terms of the real variables $U = \mathrm{Re}[A]$ and $V = \mathrm{Im}[A]$,

$$\begin{aligned} -\nu\frac{d^2V}{dx^2} - U + \theta V - V(U^2+V^2) + \rho = 0, \\ \nu\frac{d^2U}{dx^2} - V - \theta U + U(U^2+V^2) = 0. \end{aligned} \tag{2.3}$$

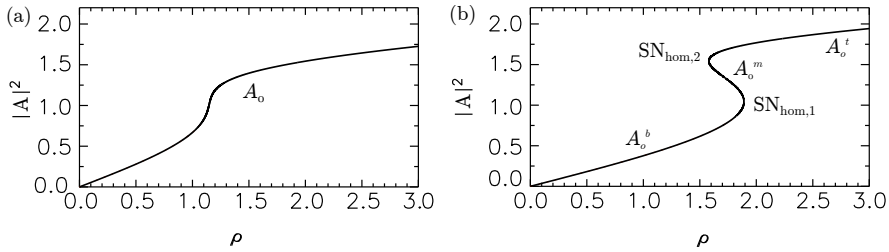

Figure 2.2: Panel (a) shows the HSS in the monostable regime for $\theta = 1.5$ and in panel (b) an example of the HSS solution in the bistable regime ($\theta = 1.8$) is plotted.

The solutions of Eq.(2.2) can be either spatially uniform (HSSs) or spatially nonuniform, consisting either of a periodic pattern, i.e. a spatially periodic state, or spatially localized states, i.e. a LSs, or spatial chaos [2]. The first two types of solution will be the main interest of our work. In this section we focus on the HSSs, $A \equiv A_0$, leaving for subsequent sections the study of the other states. The A_0 states are solution of the classic cubic equation of dispersive optical bistability, namely

$$I_0^3 - 2\theta I_0^2 + (1+\theta^2) I_0 = \rho^2, \tag{2.4}$$

where $I_0 \equiv |A_0|^2$, that in real variables read as

$$\begin{bmatrix} U_0 \\ V_0 \end{bmatrix} = \begin{bmatrix} \dfrac{\rho}{1+(I_0-\theta)^2} \\ \dfrac{(I_0-\theta)\rho}{1+(I_0-\theta)^2} \end{bmatrix}. \tag{2.5}$$

For $\theta < \sqrt{3}$, Eq. (2.4) is single-valued and hence the system is monostable (see Figure 2.2(a)). For $\theta > \sqrt{3}$, Eq. (2.4) is triply-valued as shown in Figure 2.2(b). The transition between the three different solutions occurs via the two saddle-nodes bifurcations $\mathrm{SN}_{hom,1}$ and $\mathrm{SN}_{hom,2}$ located at

$$I_{t,b} \equiv |A_{t,b}|^2 = \frac{2\theta}{3} \pm \frac{1}{3}\sqrt{\theta^2 - 3}. \tag{2.6}$$

These two SNs unfold from a Cusp bifurcation at $\theta = \sqrt{3}$ and will be discussed in the next Chapters.

In the following we denote the bottom solution branch (from $I_0 = 0$ to I_b) by A_0^b, the middle branch between I_b and I_t by A_0^m and the top branch by A_0^t ($I_0 > I_t$).

The linear stability of A_0 is analyzed by considering the effect of finite wavelength perturbations $A = A_0 + \epsilon e^{\Omega t + ikx}$. Linearizing for small ϵ on obtains for Eq.(2.1) the dispersion relation,

$$\Omega(k) = -1 \pm \sqrt{4I_0\theta - 3I_0^2 - \theta^2 + \nu(4I_0 - 2\theta)k^2 - k^4}. \tag{2.7}$$

Since the Eq.(2.1) is symmetric under the transformation $x \to -x$, the dispersion relation fulfills $\Omega(k) = \Omega(-k)$, and as one can see it depends on k only through k^2. The HSS A_0 undergoes an instability if the maximum of Ω becomes positive when varying a system parameter. In coming chapters the linear stability of A_0 is analyzed in the anomalous (Chapter 3) and normal (Chapter 5) GVD regime is analyzed. In the first case, these pattern play an essential role in the formation of bright solitons (see Chapter 4). However, although existing, patterns are not at the origin of the formation of darks solitons in the normal regime.

2.3 Stationary problem as a dynamical system

Within this thesis we will spend quite a few chapters talking about localized stationary states i.e. LSs, solutions of Eq.(2.3). These states are biasymptotic to the HSSs A_0, that is, the field associated with that structure $A(x) \to A_0$, as $x \to \pm\infty$. This type of solution corresponds to homoclinic orbits Γ to A_0 [3–7], that lie in the intersection between the stable and unstable manifolds of A_0, namely $W^s(A_0)$ and $W^u(A_0)$ (see Appendix A).

Due to this correspondence one can apply the theory of homoclinic orbits to obtain some insight about the existence and stability of LSs in our system. In order to do this one first writes the stationary LL equation (2.3) as a dynamical system. We refer to this analysis as *spatial dynamics* of the LL equation. Defining the new system of variables $y_1(x) = U(x)$, $y_2(x) = V(x)$, $y_3(x) = d_x U$ and $y_4(x) = d_x V$, Eq.(2.3) can be recasted as the four dimensional dynamical system given by

$$\begin{aligned} d_x y_1 &= y_3 \\ d_x y_2 &= y_4 \\ d_x y_3 &= \nu\left[y_2 + \theta y_1 - y_1 y_2^2 - y_1^3\right] \\ d_x y_4 &= \nu\left[-y_1 + \theta y_2 - y_2 y_1^2 - y_2^3 + \rho\right]. \end{aligned} \tag{2.8}$$

Taking $y(x) = [y_1(x), y_2(x), y_3(x), y_4(x)]^T$, and the right-hand side of (2.8) as the vector field, $f(x) = [f_1(y), f_2(y), f_3(y), f_4(y)]^T$, the system (2.8) can be written in the compact form:

$$\frac{dy}{dx} = f\left(y(x); \theta, \rho\right). \tag{2.9}$$

In this framework the HSSs A_0 correspond to the fixed point or equilibrium of the system (2.8), namely $y_0 = (y_{0,1}, y_{0,2}, y_{0,3}, y_{0,4}) = (U_0, V_0, 0, 0)$.

This system is invariant under the involution transformation

$$R : (x, y_1, y_2, y_3, y_4) \mapsto (-x, y_1, y_2, -y_3, -y_4), \tag{2.10}$$

and therefore spatially reversible. In this case, the symmetric section is defined by

$$\mathcal{S} \equiv \{(y_1, y_2, y_3, y_4) : y_3 = y_4 = 0\}. \tag{2.11}$$

In the presence of reversibility, Γ is formed by the transverse intersection between $W^u(A_0)$ and the 2-dimensional symmetric section $\mathcal{S}$. If the equilibrium A_0 is hyperbolic, then $W^u(A_0)$ is also two-dimensional and therefore Γ is of codimenison-zero by dimension counting. Because of this, these orbits persist under generic perturbations that preserve reversibility [8]. This will be important when studying homoclinic solutions of truncated normal forms (see Section 2.4), because if this condition is satisfied, any solution of a truncated normal form will be also solution of the complete normal form.

2.3.1 Linearization

Our main interest focus on orbits homoclinic to y_0 (i.e. to the HSS A_0). Therefore, to study this type of orbit, it is first necessary to linearize (2.8) about that point. Separating the field $f(x)$ in its linear and nonlinear components, the system (2.12) can be written as

$$\frac{d}{dx}y(x) = \mathcal{D}f(y_0)y(x) + \mathcal{N}[y(x)] \tag{2.12}$$

where $\mathcal{D}f(y_0)$ is the Jacobian

$$\mathcal{D}f(y_0) = \nu \begin{bmatrix} 0 & 0 & \nu & 0 \\ 0 & 0 & 0 & \nu \\ \theta - y_2^2 - 3y_1^2 & 1 - 2y_1y_2 & 0 & 0 \\ -(1 + 2y_1y_2) & \theta - y_1^2 - 3y_2^2 & 0 & 0 \end{bmatrix}_{y=y_0} \tag{2.13}$$

and with $\mathcal{N}[y(x)]$ representing the nonlinear terms.

The linear dynamics of the system (2.12) about y_0 gives a lot of information about the nature of the equilibrium, changes in the dynamics around those points (when a bifurcation takes place), and the way in which the manifolds $W^u(A_0)$ and $W^s(A_0)$ approach or leave A_0. Thus, one can understand the behavior of

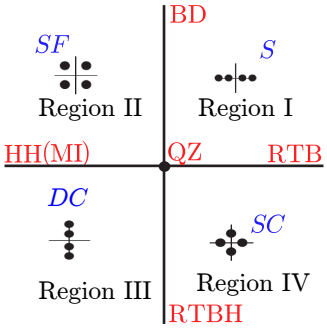

Figure 2.3: Sketch of the possible organization of spatial eigenvalues λ satisfying the biquadratic equation (2.14) for a spatially reversible system. The names corresponding to the different labels are explained in Table 2.1.

homoclinic orbits very close to A_0, and what is the same, predict the shape of the tails of the LSs. The four eigenvalues of $\mathcal{D}f(y_0)$ satisfy the biquadratic equation

$$\lambda^4 + (4I_0 - 2\theta)\nu\lambda^2 + \theta^2 + 3I_0^2 - 4\theta I_0 + 1 = 0. \tag{2.14}$$

This equation is invariant under $\lambda \to -\lambda$ and $\lambda \to \bar{\lambda}$ and leads to eigenvalue configurations symmetric with respect to both axes as depicted in Figure 2.3. The form of this equation is a consequence of spatial reversibility [8–10]. The eigenvalues satisfying Eq. (2.14) are

$$\lambda = \pm\sqrt{(\theta - 2I_0)\nu \pm \sqrt{I_0^2 - 1}}. \tag{2.15}$$

According to the control parameter values one can identify four qualitatively different eigenvalue configurations:

1. the eigenvalues are real: $\lambda_{1,2} = \pm q_1$, $\lambda_{3,4} = \pm q_2$
2. there is a quartet of complex eigenvalues: $\lambda_{1,2,3,4} = \pm q_0 \pm ik_0$
3. the eigenvalues are imaginary: $\lambda_{1,2} = \pm ik_1$, $\lambda_{3,4} = \pm ik_2$
4. two eigenvalues are real and two imaginary: $\lambda_{1,2} = \pm q_0$, $\lambda_{3,4} = \pm ik_0$

A sketch of these possible eigenvalue configurations is shown in Figure 2.3, and their names and codimension are provided in Table 2.1. The crossing from one of the regions to the next one occurs via the following bifurcations or special transitions:

- A Belyakov-Devaney (BD) [4, 5, 8] transition occurs within the transition from region I to region II. Here the spatial eigenvalues are $\lambda_{1,2} = \pm q_0$, $\lambda_{3,4} = \pm q_0$.
- The transition from region II to region III is via a Hamiltonian-Hopf (HH) bifurcation [5, 11], with $\lambda_{1,2} = \pm ik_c$, $\lambda_{3,4} = \pm ik_c$.
- The transition from region I to region IV is via a reversible Takens-Bogdanov (RTB) bifurcation with eigenvalues $\lambda_{1,2} = \pm q_0$, $\lambda_3 = \lambda_4 = 0$ [4, 5].
- The transition from region III to region IV is via a reversible Takens-Bogdanov-Hopf (RTBH) bifurcation with eigenvalues $\lambda_{1,2} = \pm ik_0$, $\lambda_3 = \lambda_4 = 0$ [4, 5].

The unfolding of all these scenarios is related to the quadruple zero (QZ) codimension-two point with $\lambda_1 = \lambda_2 = \lambda_3 = \lambda_4 = 0$ [4, 5, 13]. In regions I and II of Figure 2.3, A_0 is hyperbolic, i.e. $\mathrm{Re}[\lambda] \neq 0$, and therefore homoclinic orbits to A_0 are of codimension zero, so as we said before, if the intersection between the unstable manifold of A_0 and symmetric section $\mathcal{S}$ is transverse then homoclinic orbits must persist under small reversible perturbation.

The configuration of the eigenvalues for the normal and anomalous dispersion regimes are shown in Figures 2.4 and Figures 2.6. Figures 2.5 and 2.7 show the different regions I-IV for each eigenvalue configuration described in Figure 2.3 in the parameter space (ρ, θ) for both regimes.

The condition $I_0 = 1$ defines, in terms of the (θ, ρ), the line

$$\rho = \sqrt{1 + (1 - \theta)^2}. \tag{2.16}$$

For the normal GVD regime this line corresponds to a BD transition when $\theta < 2$ and a HH bifurcation when $\theta > 2$. In contrast, in the anomalous case the HH and BD are exchanged, and now the BD transition occurs for $\theta > 2$ and the HH bifurcation when $\theta < 2$. In the next section we discuss briefly the linear dynamics derived from the normal forms around each of the bifurcation lines RTB, RTBH , HH and BD shown in Figure 2.3, and we see what may be gleaned from those normal forms concerning the existence of homoclinic orbits.

In this particular case one can have two different but similar unfoldings when considering the normal or anomalous GVD regimes.

Cod	$(\lambda_{1,2,3,4})$	Name	Label
Zero	$(\pm q_0 \pm ik_0)$	Saddle-Focus	SF
Zero	$(\pm q_1, \pm q_2)$	Saddle	S
Zero	$(\pm ik_1, \pm ik_2)$	Double-Center	DC
Zero	$(\pm q_0, \pm ik_0)$	Saddle-Center	SC
One	$(\pm q_0, 0, 0)$	Rev.Takens-Bogdanov	RTB
One	$(\pm ik_0, 0, 0)$	Rev.Takens-Bogdanov-Hopf	RTBH
One	$(\pm q_0, \pm q_0)$	Belyakov-Devaney	BD
One	$(\pm ik_c, \pm ik_c)$	Hamiltonian-Hopf	HH(MI)
Two	$(0, 0, 0, 0)$	Quadruple Zero	QZ

Table 2.1: Nomenclature used to refer to different transitions in the spatial eigenspectrum.

2.3.2 Relation between the spatial eigenvalues and the dispersion relation

The spatial stability analysis of the linearized system (2.13) is equivalent to study the linear stability of Eq.(2.1) considering spatial perturbations of the form $A(x) = A_0 + \epsilon e^{\tilde{\lambda} x}$, where in general λ is complex. Since the linearization is around the same state as in the temporal stability analysis and since the perturbations are the same as the ones considered there replacing ik by $\tilde{\lambda}$, the spatial eigenvalues λ satisfy

$$\Omega(-i\lambda) = 0, \tag{2.17}$$

expresion that is equivalent to Eq.(2.14).

This result makes possible to obtain information about the temporal dynamics of the system through the spatial dynamics approach. For example, if the spatial eigenvalue configuration consists on two purely imaginary eigenvalues $\pm ik_1$ and $\pm ik_2$, then, in the framework, $\Omega(k_{1,2}) = 0$ for real k_1 and k_2. As a consequence $\Omega(k)$ must be positive for $k_1 < |k| < k_2$, and therefore A_0 is unstable to perturbations with wavenumber within this range. As one can observe, this situation corresponds to region II of Figure 2.3 where the HSS is a DC.

2.3.3 Spatial eigenvalue configurations in the normal regime

In the normal GVD regime, the configuration of the spatial eigenvalues is the one shown in Figure 2.4. Panel (a) shows the situation for $\theta = 1.4 < \sqrt{3}$ just in the monostable regime. Here the single HSSs state branch is initially a saddle-focus (SF). Increasing ρ the imaginary parts of these complex conjugate eigenvalues

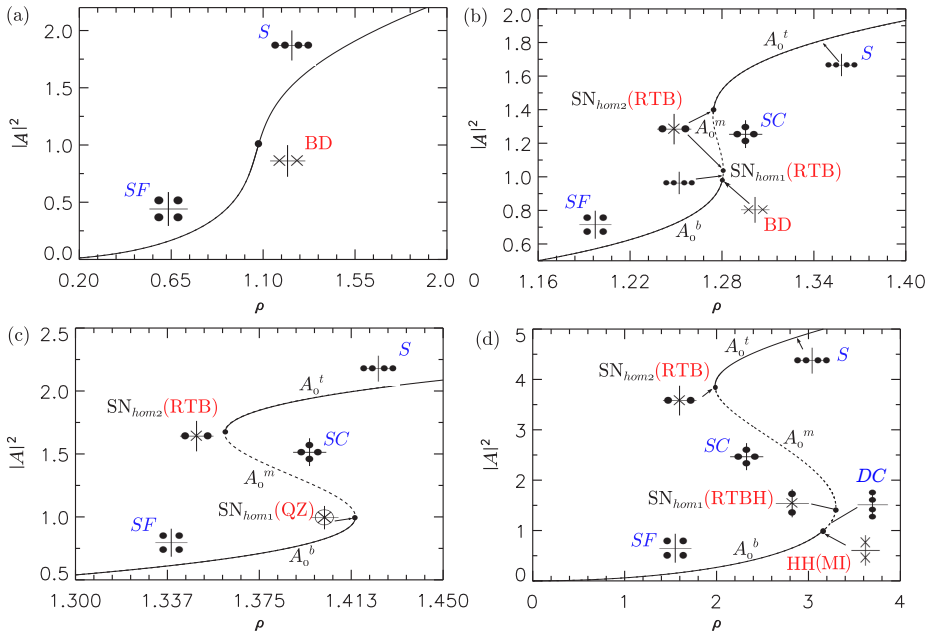

Figure 2.4: Spatial eigenvalues of A_0 for several values of θ. (a) $\theta = 1.4 < \sqrt{3}$; (b) $\sqrt{3} < \theta = 1.8 < 2$; (c) $\theta = 2$; (d) $2 < \theta = 4$. The different labels are explained in Table 2.1. Solid (dashed) lines indicate stability (instability) in time.

approaches $\mathrm{Im}[\lambda] = 0$ until it reaches at the BD transition, and for ρ values on the right of BD A_0 has became a saddle (S). Figure 2.5 shows the projection of the different bifurcation lines for this regime in the $(\theta, \rho)-$parameter space. Increasing further the value of θ we cross the the cusp C shere A_0 becomes trivaluate. This situation corresponds to the diagram shown in panel (b) for $\sqrt{3} < \theta = 1.8 < 2$. For this value both SN$_{hom,1}$ and SN$_{hom,2}$ are RTB bifurcations. A_0^m is a saddle-center (SC) and A_0^t a S for any value $\theta > \sqrt{3}$. When $\theta = 2$, (see panel (c)) all the lines meet at the QZ point at $(\theta, \rho) = (2, \sqrt{2})$, where the BD becomes a HH bifurcation and SN$_{hom,1}$ changes from a RTB to a RTBH bifurcation. When $\theta > 2$, A_0^b is a SF until reaching HH where it becomes a focus that persist until the SN$_{hom,1}$ where it becomes a SC. Figure 2.5 (b) shows a zoom (not in scale) of the panel (a) around QZ where we can appreciate the unfolding of this bifurcation.

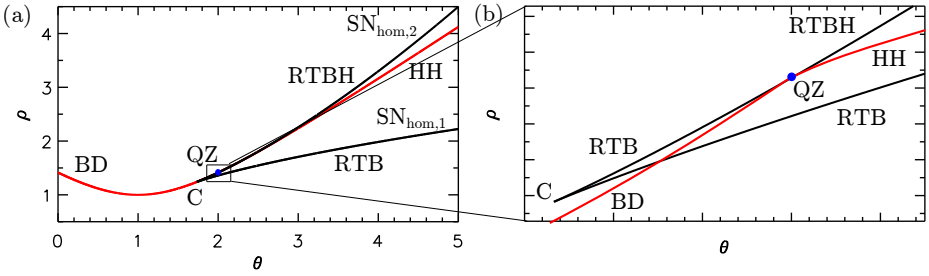

Figure 2.5: In (a) spatial bifurcation lines in the parameter space (θ, ρ) for the normal dispersion regime. In (b) we show a zoom, not at scale, of panel (a) around QZ where one can observe the unfolding of that bifurcation. Here we just show the regions regarding the first branch A_0^b, where the unfolding of the QZ bifurcation takes place.

2.3.4 Spatial eigenvalue configurations in the anomalous regime

The situation regarding the anomalous case is shown in Figure 2.6. The values for the control parameter θ are the same that those in Figure 2.4 although now the eigenvalues configuration is different. In the monostable regime (see panel (a)) A_0, is a SF for $I_0 < 1$ and a DC resonance for $I_0 > 1$. Thus, for $I_0 > 1$ A_0 is unstable to perturbations with a wavenumber within the range $k_1 < |k| < k_2$. At $\theta = \sqrt{3}$, A_0 becomes trivaluate at C, splitting itself in three branches (see panel (b)). Now A_0^t is a DC and A_0^m a SC for any value $\theta > \sqrt{3}$. Here in contrast to the normal regime, SN$_{hom,2}$ is a RTBH bifurcation. Taking a look to the bottom branch and the SN$_{hom,1}$ one can see that there is an inversion in the order of appearance of HH and the BD with respect the normal regime. In this case HH exist for $\theta < 2$ and the BD for $\theta > 2$. At the QZ, as before, these branches meet and the SN$_{hom,1}$ that is a RTBH for $\theta < 2$ becomes a RTB for $\theta > 2$. Figure 2.7 shows the projection of all these lines into the parameter space.

2.4 Unfolding of the quadruple-zero codimension-2 point

As we already said, the HH, RTB, and RTBH bifurcations and the BD transition previously introduced emerge from a codimension-2 bifurcation known as quadruple-zero (QZ) point with spatial eigenvalues $\lambda = 0$ with algebraic multiplicity four and with gometric multiplicity one[1], as depicted in the sketch shown

[1]With *geometric multiplicity* of an eigenvalue λ of a matrix A we refers to the dimension of the subspace spanded by the eigenvector associated with it i.e. the dimension of $\mathrm{Ker}(A - \lambda I)$. In contrast, the *algebraic multiplicity* of λ correspond to the number of times that λ appears

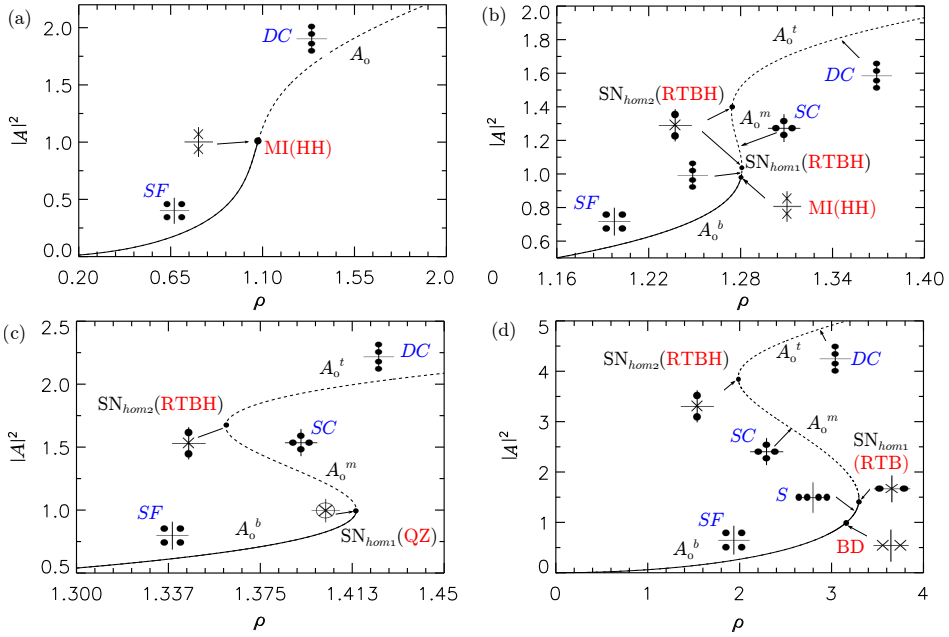

Figure 2.6: HSS together with spatial eigenvalues configuration for several values of θ. (a) $\theta = 1.4 < \sqrt{3}$; (b) $\sqrt{3} < \theta = 1.8 < 2$; (c) $\theta = 2$ and (d) $\theta = 4$. Here RTBH stands for reversible Takens-Bodganov-Hopf, RTB stands for reversible Takens-Bodganov, HH is a Hamiltonian-Hopf, BD a Belniakov-Devaney transition and QZ a quadruple zero codimension-2 point.

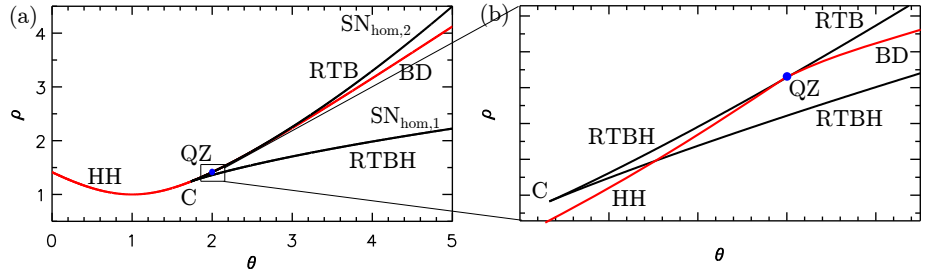

Figure 2.7: Same that in Figure 2.5 but for the anomalous case. The bifurcation lines are now reinvers respect to Figure 2.5.

as a root of the characteristic polynomial of A.

in Figure 2.3. In Ref. [13] G. Iooss derived a normal form for this point in a general fourth-order vector field where the origin is a persistent symmetric fixed point. Despite of that, the study of this bifurcation is widely open. Here we review some aspects about the dynamics of the system around the codimension-one bifurcations and the BD transition shown in Figure 2.3, and to do that we will follow closely Ref.[4] and the references therein. All the normal forms associated with the codimension-one bifurcations HH, RTB and RTBH are integrable, and they all lead to the existence of homoclinic orbits, and therefore to the existence of LSs. Our aim in this section is only didactical and the normal forms presented here have not been derived directly from the dynamical system (2.8), but they refer to a general four dimension reversible vector field. However, this section will be useful to understand, at least qualitatively, the unfoldings shown in Figures 2.5 and 2.7.

2.4.1 Normal form near the reversible Takens-Bodganov bifurcation

In the RTB bifurcation the spatial eigenvalues are $\lambda_{1,2} = \pm q_0$, and $\lambda_3 = \lambda_4 = 0$. The eigendirection associated with $\lambda_{1,2} = \pm q_0$ are unimportant in describing the bifurcating solutions and therefore the center manifold theorem can be applied to reduce (2.8) to a planar system (see Section A.6). Once reduced to the center manifold, the normal form analysis gives the nonlinear oscillator system [14]

$$\begin{cases} w_1'(x) = w_2(x) \\ \\ w_2'(x) = \sum c_j(\mu) w_1^j(x) \end{cases} \tag{2.18}$$

A single parameter μ unfolds the degeneracy with $\mu > 0$ corresponding to the near-zero eigenvalue being real (region 2). Upon truncation to lowest order and after applying a rescaling w_1 and w_2 becomes $\mathcal{O}(\mu)$, and 2.18 becomes

$$\begin{cases} w_1'(x) = w_2(x) \\ \\ w_2'(x) = \pm\mu w_1 - \frac{3}{2} w_1^2, \end{cases} \tag{2.19}$$

which for $\mu > 0$ possesses a single symmetric homoclinic orbit $\Gamma : w_1(x) = \mathrm{sech}^2(x/2)$. This solution profile has monotonic tails and is sometime referred to as the Korteweg-de Vries(KdV)-type soliton.

In presence of an up-down symmetry $w_1 \to -w_1$, the truncated normal form is

$$\begin{cases} w_1'(x) = w_2(x) \\ \\ w_2'(x) = \pm\mu w_1 - \beta w_1^3, \end{cases} \tag{2.20}$$

where $\beta = \pm 1$. If $\beta = -1$, there is a pair of homoclinic orbits $\Gamma_\pm : w_1(x) = \pm\text{sech}(x)$ related by the up-down symmetry for $\mu > 0$. For the other sign there are no homoclinic solutions. For the planar normal forms (2.19) and (2.20) it is possible to prove that the homoclinic orbit persist for $\mu > 0$ against perturbations restoring the original system [14, 15].

Our system does not have up-down symmetry, therefore one does not expect the last type of solutions to occur. On the contrary, as we will see in Chapter 4 and Chapter 5 the LL equation supports KdV-type of solitons in both the anomalous and normal regimes. In the anomalous case these solitons are bumps unfolding from the $\text{SN}_{hom,1}$ for $\theta > 2$. In the normal dispersion case these type of homoclinic orbits arise in both $\text{SN}_{hom,1}$ for $\theta < 2$ and $\text{SN}_{hom,2}$ for any value $\theta > \sqrt{3}$. In the first case they are bumps and in the second one holes. Chapter 4 will be devoted to the understanding of the bifurcation structure and stability of these bump states in the anomalous regime. Chapter 5 will be focused on the study of these structures in the normal regime. In both cases we apply weakly nonlinear analysis around the RTB and we confirm the existence of KdV-type of states.

2.4.2 Normal form near the reversible Takens-Bodganov-Hopf bifurcation

For the RTBH bifurcation the spatial eigenvalues are $\lambda_{1,2} \pm ik_0$, and $\lambda_{3,4} = 0$. The normal form (Ioos-Kirchgaster normal form [14]) about this point is a four dimensional ODE completely integrable in two real variables w_1 and w_2 and a complex one z, that reads

$$\begin{cases} w_1'(x) = w_2(x), \\ w_2'(x) = M(\mu, w_1(x), |z(x)|^2), \\ z'(x) = iz(x)N(\mu, w_1(x), |z(x)|^2), \\ \bar{z}'(x) = -iz(x)N(\mu, w_1(x), |z(x)|^2), \end{cases} \tag{2.21}$$

where M and N are arbitrary order polynomials in their arguments. Truncating this normal form considering

$$M(\mu, u_1, |z|^2) = c_1(\mu)w_1 + c_2(\mu)w_1^2 + d_2(\mu)|z|^2, \tag{2.22}$$

and

$$N(\mu, w_1, |z|^2) = b_0(\mu) + c_1(\mu)w_1, \tag{2.23}$$

one can find two types of homoclinic solutions. The first type is a sech^2 orbit Γ homoclinic to A_0, now a SC in region IV. The problem here is that A_0 is not hyperbolic and therefore, in general, one does not expect these solutions to persist under small reversible perturbation to the truncated normal form. In Hamiltonian systems it was proved that given a primary homoclinic orbit to a SC, symmetric respect the involution, there are, under certain conditions, N-pulses or N-homoclinic orbits occurring at isolated parameter values. The second type of solutions are homoclinic orbits to periodic orbits (known as *generalized solitary waves*) with a sech^2 core and exponentially small tails. The amplitude of the periodic orbit is an exponentially small function of μ and can not be captured by the normal form (2.21) truncated at any order. In our system we have not found, so far, any of these kind of solutions.

2.4.3 Normal form near the Hamiltonian-Hopf bifurcation

At the HH bifurcation (also known as double-Hopf with 1:1 resonance or Turing bifurcation in temporal dynamics), the eigenvalues are $\lambda_{1,2,3,4} = \pm ik_c, \pm ik_c$ and the normal form (known as Iooss-Peroueme [11, 12])[2] is a 4 dimensional completely integrable ODE expressed in terms of two complex variable $z_1(x)$ and $z_2(x)$ that reads

$$\begin{cases} z_1' = ik_c z_1 + z_2 + iz_1 P(\mu, |z_1|^2, i(z_1\bar{z}_2 - \bar{z}_1 z_2)/2), \\ z_2' = ik_c z_2 + iz_2 P(\mu, |z_1|^2, i(z_1\bar{z}_2 - \bar{z}_1 z_2)/2) + z_1 Q(\mu, |z_1|^2, i(z_1\bar{z}_2 - \bar{z}_1 z_2)/2). \end{cases} \tag{2.24}$$

Here P and Q are arbitrary order real polynomials in their arguments and μ is the unfolding parameter, with $\mu < 0$ corresponding to region II where A_0 is a SF, and $\mu > 0$ corresponding to region III, where A_0 is a DC. A truncated normal form can be derived by replacing P and Q by the first-order terms of their Taylor expansions, namely,

$$P(\mu, y_1, y_2) = p_0\mu + p_2 y_1 + p_2 y_2, \tag{2.25}$$

and

$$Q(\mu, y_1, y_2) = q_0\mu + q_1 y_1 + q_2 y_2. \tag{2.26}$$

As Hopf bifurcation the HH can be either supercritical or subcritical. By further reduction to polar coordinates, it is possible to find in the subcritical regime (for $q_2 < 0$) a one-parameter family of homoclinic solutions that bifurcates for $\mu < 0$. These solutions are of the form $\Gamma_\varphi : z_1(x) = A\text{sech}(Bx)\exp(ik_c x + \varphi)$

[2] Although it was originally derived in [12]

for constants A, B and k related with the coefficients of the normal form. This family is parametrized by an arbitrary phase φ. However, terms beyond all algebraic orders (absent in any truncated normal form) select generically two values $\varphi = 0$ and π from the circle $[0, 2\pi)$ [16, 17]. The resulting solution profiles have oscillatory tails and are sometimes referred as nonlinear Schrodinger (NLS)-type solitons or *envelope solitons*. In contrast for the supercritical case the bifurcation of homoclinic orbits to periodic orbits occurs for $\mu > 0$. In the presence of up-down symmetry, there are four possible values $\varphi = 0, \pi/2, \pi$ or $3\pi/2$ selected. In all cases Γ is homoclinic to a SF. Near the codimenison-two transition between the super and subcritical cases, i.e. a degenerate HH point (dHH), there exist homoclinic orbits that wind arbitrary many times around a (reversible) periodic orbit. Those homoclinic orbits are organized into bifurcation curves called *homoclinic snaking* [18]. We will analyze in detail this type of homoclinic orbit and its bifurcation structure in Chapter 4, when studying the LL equation in the anomalous dispersion regime. There, the HH bifurcation exist for $\theta < 2$. The bifurcation structure and stability of patterns unfolding also from HH in the anomalous regime will be studied in Chapter 3.

In the subcritical case, these orbits exist in a region of parameter space where A_0 is a SF, and therefore, hyperbolic. Hence, we should expect that transverse homoclinic solutions to the normal form 2.24 with the truncated terms 2.25 persist against reversible perturbation. Nevertheless, due to the size of the terms ignored in the truncated version (2.25), which are not small compared with the bifurcation solution, the prove is not trivial [11]. It is also possible to prove that given the existence of a primary homoclinic orbit, there are initially many N-pulses homoclinic orbits for each $N > 1$.

2.4.4 Dynamical behavior near the Belyakov-Devaney transition

This line does not correspond to a bifurcation, because the equilibria A_0 remains hyperbolic ($\mathrm{Re}[\lambda] \neq 0$) and only changes between a S (region I) and a SF (region II). This is the reason to refer it as BD transition [8, 19]. Because of this, all finite amplitude homoclinic orbits should persist across the BD transition line. Nonetheless, infinitely many orbits homoclinic to the SF can be created by a dramatic non-local bifurcation at the BD. This bifurcation has been called *broom* bifurcation [20] owing for the infinite number of homoclinic orbits emerging from it. In our context, this phenomenon arises for bright LSs in the anomalous GVD regime when $\theta > 2$. In that scenario $\mathrm{Im}[\lambda] \to 0$, as ρ approaches the BD, and therefore the wavelength of the oscillatory tails of the LSs goes to infinite. Hence, in a infinite domain, two DSs will increase infinitely their separation as

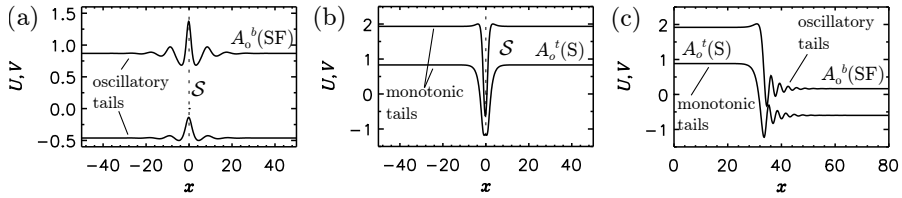

Figure 2.8: Localized states for the LL equation. In (a) a NLS-type of bright solitons arising in the anomalous dispersion regime for $\theta = 1.5$ and $\rho = 1.11445$. In (b) a KdV-type dark type of solitons occurring in the normal dispersion regime for $\theta = 4$ and $\rho = 2.29129$. In (c) a front or SW also in the normal dispersion regime for $\theta = 4$ and $\rho = 2.3252908$. As we can observe structure (a) has oscillatory tails, (b) monotonic and (c) both.

approaching the BD transition. However, in periodic system with period L the maximum separation that they can reach coincides with $L/2$. We will talk more about this in Section 4.4.

2.5 Linearization of the homoclinic orbits around the equilibrium point A_0

In the previous Section we have analyzed the linear dynamics of the system about the different bifurcation points appearing. In the coming chapters we will see that the tails of these LSs are quite relevant to understand the formation of bound states of solitons or soliton molecules (see Chapter 7) and the formation of dark solitons (see Chapter 5). In both cases, the formation of these structures comes from the interaction of single solitons in the first case and fronts with different polarity in the second one.

Regarding the interaction of solitons, it can be attractive or repulsive as function of the separation. Moreover, when the tails have oscillations around A_0, the structures can lock at different distances that differ by the wavelength of the oscillations. In contrast if the tails are monotonic, that locking does not occur and the structures approach or separate infinitely. The nature and shape of the tails around A_0 can be explained by the linearization of the dynamical system (2.8) around A_0. As we have seen before, in principle, in this system one could have homoclinic orbits in four different regions. In this work we just focus in two of them, region II where A_0 is a SF and region I where A_0 is a S. In region III and IV A_0 are DC and SC global bifurcation points. As said before, in region IV LSs are possible although difficult to observe. However in region III, A_0 is a DC and homoclinic orbits to that point cannot exist due to the absence of strong

stable/unstable manifolds. Nonetheless, the dynamics in a neighbourhood of the origin may be quite complex and orbits homoclinic to a periodic orbit or equivalently orbits homoclinic to an equilibrium in a suitable Poincare map are still expected. In Chapter 3 and Chapter 5 we will show that pattern solutions unfold from those global bifurcations in the anomalous dispersion regime.

Figure 2.8 showw three types of localized structures which will be studied along this thesis. In panel (a) a bright soltion occurring in the anomalous dispersion regime is shown. This is an envelope-type of soliton and in spatial dynamics terms, a homoclinic orbit to a SF equilibrium A_0^b. Consequently the tails of this state are oscillatory. Panel (b) shows a dark soliton arising in the normal dispersion regime. This is a KdV-type of soliton and corresponds to an homoclinic orbit to a S equilibrium A_0^t and then their tails are monotonic. Finally in panel (c) a front, domain wall or switching wave (SW) solution connecting the top HSSs A_0^t with the bottom one A_0^b is plotted. In the spatial dynamics terminology this state would correspond to an heteroclinic orbit connecting a S equilibrium with a SF. Therefore its tails are monotonic close to A_0^t and oscillatory close to A_0^b.

The linearization of (2.12) about $A_0 = y_0$ is given by

$$\frac{d}{dx}y(x) = \mathcal{D}f(A_0)y(x) + \mathcal{O}(|y|^2), \tag{2.27}$$

and its solution reads as

$$y(x) = \mathrm{e}^{x\mathcal{D}f(y_0)}y_0, \tag{2.28}$$

where $y_0 = [U_0, V_0, 0, 0]^T$.

Considering the change of variables given by $y(x) = \mathcal{M}^{-1}\tilde{y}(x)$, with $\mathcal{M}$ a given linear transformation (a matrix), solution (2.28) can be written as

$$\tilde{y}(x) = \mathcal{M}\mathrm{e}^{x\mathcal{D}f(y_0)}\mathcal{M}^{-1}\tilde{y}_0 = \mathrm{e}^{x\mathcal{A}}\tilde{y}_0, \tag{2.29}$$

with $\mathcal{A}$ being the linear normal form of $\mathcal{D}f(y_0)$.

The normal form depends on the eigenspectrum of $\mathcal{D}f(y_0)$, and therefore on the nature of the HSSs A_0. In the following we focus in the linearizations around A_0 in the cases where it is a saddle-focus (region I) and a saddle (region II).

2.5.1 Region II: The saddle-focus case

In this region A_0 is a SF i.e. $\lambda_{1,2,3,4} = \pm q_0 \pm ik_0$. With this spectrum it is possible to find a transformation $\mathcal{M}$ (see Ref.[21]) where the normal form reads

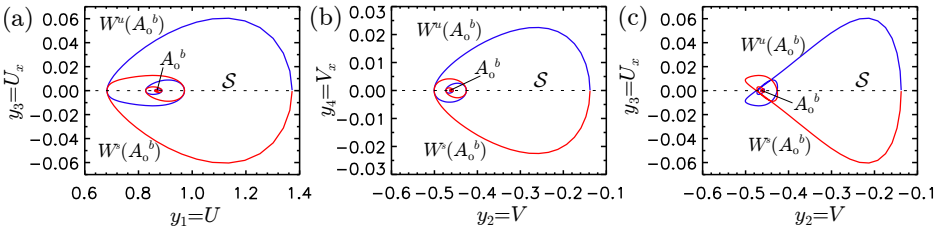

Figure 2.9: Projection of the soliton shown in Figure 2.8(a) into three subspace of the phase space: (y_1, y_3) in (a), (y_2, y_4) in (b) and (y_2, y_3) in (c). The saddle-focus nature of A_0^b is appreciated in the oscillatory way in which $W^u(A_0^b)$ and $W^s(A_0^b)$ leaves and approaches to it. Here $\theta = 1.5$ and $\rho = 1.11445$.

as

$$\mathcal{A} = \begin{bmatrix} q_0 & -k_0 & 0 & 0 \\ k_0 & q_0 & 0 & 0 \\ 0 & 0 & q_0 & -k_0 \\ 0 & 0 & k_0 & q_0 \end{bmatrix}, \tag{2.30}$$

and therefore, the solution of the system around A_0 (in the linear regime) is given by

$$\begin{aligned} \tilde{y_1} &= \mathrm{e}^{q_0 x}\cos(k_0 x)\tilde{y}_{0,1} - \mathrm{e}^{q_0 x}\sin(k_0 x)\tilde{y}_{0,2} \\ \tilde{y_2} &= \mathrm{e}^{q_0 x}\cos(k_0 x)\tilde{y}_{0,1} + \mathrm{e}^{q_0 x}\sin(k_0 x)\tilde{y}_{0,2} \\ \tilde{y_3} &= \mathrm{e}^{-q_0 x}\cos(k_0 x)\tilde{y}_{0,3} - \mathrm{e}^{-q_0 x}\sin(k_0 x)\tilde{y}_{0,3} \\ \tilde{y_4} &= \mathrm{e}^{-q_0 x}\cos(k_0 x)\tilde{y}_{0,3} + \mathrm{e}^{-q_0 x}\sin(k_0 x)\tilde{y}_{0,3} \end{aligned} \tag{2.31}$$

This orbit leaves and approaches A_0 in a oscillating way with frequency equal to k_0 and damped or amplified by q_0. From here one can deduce that, in this regime, the oscillatory tails of LSs, associated with the homoclinic orbit are oscillatory, with a wavelength equal to $2\pi/k_0$, and a decay rate given by q_0. The bright solitons studied in Chapter 4 correspond to this type of homoclinic orbits. Projecting this structure into the phase space $\{(y_1 = U, y_2 = V, y_3 = d_x U, y_4 = d_x V)\}$ one obtains the orbit shown in Figure 2.9, which dynamics around A_0 are described by (2.31). As shown in Figure 2.10, the tails of this soliton are oscillatory, and they can be described by $y_1(x)$ and $y_2(x)$. Both of them are linear combinations of the harmonic functions $\sin(x)$ and $\cos(x)$ and can be simplified to

$$y_{1,2}(x) - y_{0;1,2} = a_{1,2}\mathrm{e}^{q_0 x}\cos(x + \varphi_{1,2}) \tag{2.32}$$

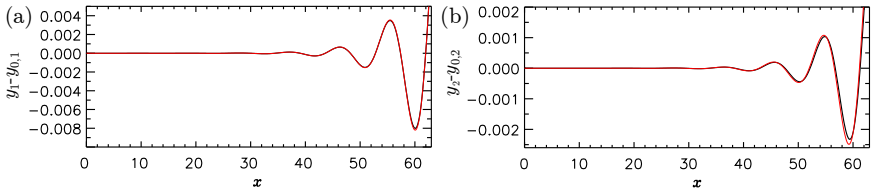

Figure 2.10: Oscillatory tails of the bright soliton shown in Figure 2.8(a) around the saddle-focus point A_0^b. We show both the actual tail of the soltion and its fitting with Eq.(2.32), for the real (panel (a)) and imaginary (panel (b)) parts of the field. The fitting is plotted in red line. The parameters for the fitting are $(a_1, \varphi_1) = (1.4550216 \cdot 10^{-7}, -0.053020265)$ for panel (a) and $(a_2, \varphi_2) = (5.1106923 \cdot 10^{-8}, 2.0644709)$ for panel (b). Here $I_0 = 0.96812475$.

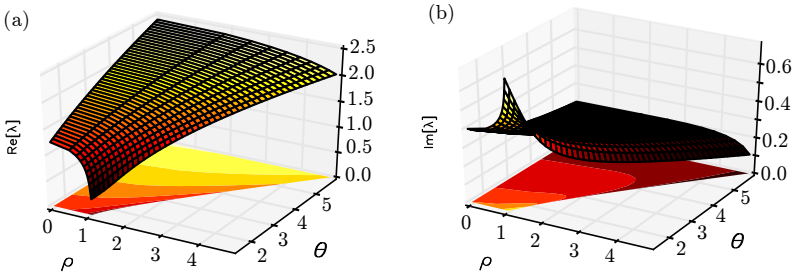

Figure 2.11: Real and imaginary part of the spatial eigenvalue λ in function of θ and ρ in the anomalous dispersion case. In the normal regime the labels Re[λ] and Im[λ] must be interchanged.

being $a_{1,2}$ and $\varphi_{1,2}$ combinations of y_0 elements. Those coefficients can be also calculated by fitting of the actual oscillatory tails shown in Figure 2.10 using as ansatz (2.32). The fitting using Eq.(2.32) is quite good showing the linear analysis done around A_0 can describe the shape of the oscillatory tails.

In the anomalous regime, the real and imaginary parts of λ i.e. q_0 and k_0 are given by

$$q_0 = \frac{1}{\sqrt{2}}\sqrt{\sqrt{\theta^2 - 4\theta I_0 + 3I_0^2 + 1} + \theta - 2I_0} \tag{2.33}$$

and

$$k_0 = \frac{1}{\sqrt{2}}\sqrt{\sqrt{\theta^2 - 4_0 + 3I_0^2 + 1} - (\theta - 2I_0)}. \tag{2.34}$$

In the normal one the real and imaginary parts of λ for the SF A_0^b are reinvers. In Figure 2.11 these parts are plotted in function of θ and ρ.

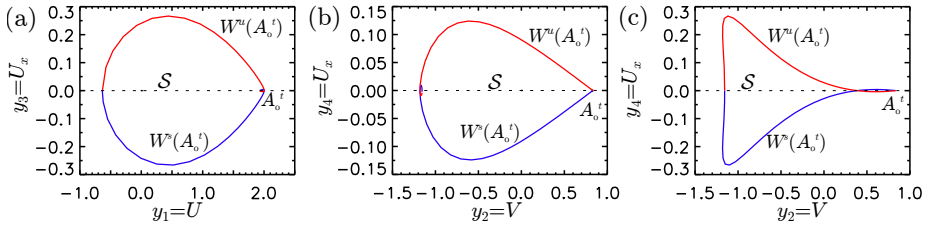

Figure 2.12: Projection of the dark soltion of Figure 2.8(b) into subspaces (y_1, y_3) in (a), (y_2, y_4) in (b) and (y_2, y_3) in (c). As we can see, now the stable and unstable manifolds of A_0^t are monotonic.

In Chapter 7 we will come back to these figures to understand the interaction between bright solitons.

2.5.2 Regime I: The saddle case

In this region A_0 is a S i.e. $\lambda_{1,2} = \pm q_1$ $\lambda_{3,4} = \pm q_2$. In this case the normal form for $\mathcal{D}f(A_0)$ is given by

$$\mathcal{A} = \begin{bmatrix} q_1 & 0 & 0 & 0 \\ 0 & -q_1 & 0 & 0 \\ 0 & 0 & q_2 & 0 \\ 0 & 0 & 0 & -q_2 \end{bmatrix}, \tag{2.35}$$

and therefore,

$$\tilde{y_1} = \mathrm{e}^{q_1 x}\tilde{y}_{0,1} \quad \tilde{y_2} = \mathrm{e}^{-q_1 x}\tilde{y}_{0,1} \quad \tilde{y_3} = \mathrm{e}^{q_2 x}\tilde{y}_{0,3} \quad \tilde{y_4} = \mathrm{e}^{-q_2 x}\tilde{y}_{0,3}. \tag{2.36}$$

Now the orbits leaves and approach A_0 monotonically. In the anomalous regime this region is found for $\theta > 2$, where A_0^b is a saddle between the BD line and the $\mathrm{SN}_{hom,1}$. In the normal dispersion regime this is the configuration for A_0^t for any value of θ, and for A_0^b for $\theta < 2$, between the BD and $SN_{hom,1}$.

Figure 2.12 shows the projection of the KdV-type dark soliton shown in Figure 2.8(b), into three different phase subspaces. Here, $W^u(A_0^t)$ and $W^s(A_0^t)$ leave and approach the equilibrium point monotonically.

2.6 Conclusions

In this chapter we have studied how localized structures or dissipative solitons biasymptotic to the HSSs A_0 can be understood as homoclinic orbits in a suitable

phase space defined by $\{(y_1, y_2, y_3, y_4)\}$. In these variables the stationary LL equation can be recast to a four order dynamical system, that is a system of 4 ODEs where the variable is the space x instead of the time t. A particularity of this equation is that it is reversible i.e. invariant under the transformation $x \to -x$, and therefore the dynamical system is also reversible. Using this feature it is possible to apply existing results of homoclinic orbits in reversible systems to obtain some insight of our case. After linearizing the problem we have classified the different bifurcation points and transitions in both the anomalous and normal GVD regime. In both cases, the different bifurcation lines meet in a codimenison-two point known as a quadruple zero responsible for the linear dynamics of the system. Later we have presented an overview of the linearization and normal forms of the different bifurcation appearing in this case. The theory predicts the existence of homoclinic orbits about some of these points. In particular, in this thesis we will study the bifurcation structure and stability of homoclinic orbits or LSs unfolding from an Hamiltonian-Hopf bifurcation (see Section 4.3) and from a RTB bifurcation (see Section 4.4 and Section 5.3). For these two cases we will confirm the previous results performing a weakly nonlinear analysis in a neighborhood of those points. The linearization of those orbits around A_0 give the shape of the LSs' tails very close to the HSSs. The understanding of how those shapes are modified through the different dynamical transitions in parameter space will allow us to predict the formation of bound states of LSs or the creation of dark soltions.

References

[1] D. Avitabile, D.J.B. Lloyd, J. Burke, E. Knobloch and B. Sandstede. *To snake or not to snake in the planar Swift-ÂηHohenberg equation.* SIAM J. Appl. Dyn. Syst. **9** 704-733 (2010).

[2] P. Coullet, C. Elphick, and D. Repaux, *Nature of spatial chaos*, Phys. Rev. Lett. **58**, 431 (1987).

[3] D. Gomila, A.J. Scroggie, and W.J. Firth, *Bifurcation structure for dissipative solitons,* Phys. D (Amsterdam) **227**, 70 (2007).

[4] A.R. Champneys, *Homoclinic orbits in reversible systems and their applications in mechanics, fluids and optics,* Phys. D (Amsterdam) **112**, 158 (1998).

[5] M. Haragus and G. Iooss, *Local Bifurcations, Center Manifolds, and Normal Forms in Infinite-Dimensional Dynamical Systems* (Springer, Berlin, 2011).

[6] P. Colet, M.A. Matías, L. Gelens, and D. Gomila, *Formation of localized structures in bistable systems through nonlocalspatial coupling. I. General framework,* Phys. Rev. E **89**, 012914 (2014); L. Gelens, M.A. Matías, D. Gomila, T. Dorissen, and P. Colet, *Formation of localized structures in bistable systems through nonlocal spatial coupling. II. The nonlocal Ginzburg Landau Equation,* Phys. Rev. E **89**, 012915 (2014).

[7] J. Burke, A. Yochelis, and E. Knobloch, *Spatially localized oscillating states in periodically forced dissipative systems,* SIAM J. Appl. Dyn. Syst. **7**, 651 (2008).

[8] R. L. Devaney, *Reversible diffeomorphism and flows,* Trans. Amer. Math. Soc., **218**, 89-113, (1976).

[9] A.J. Homburg and B. Sandstede, in *Handbook of Dynamical Systems*, edited by B. Hasselblatt, H. Broer, and F. Takens (North Holland, Amsterdam, The Netherlands, 2010), Chap. 8, 379-524.

[10] E. Knobloch, *Spatial Localization in Dissipative Systems,* Annu. Rev. Cond. Matter Phys. **6**, 325 (2015).

[11] G. Iooss and M.C. Pérouème, *Perturbed Homoclinic Solutions in Reversible 1:1 Resonance Vector Fields,* J. Diff. Eqs., **102**, 62 (1993).

[12] C. Elphick, E. Tirapegui, M. Brachet, P. Coullet, and G. Iooss, *A simple global characterization for normal forms of singular vector fields,* Physica D, 29, 95-127, (1987).

[13] G. Iooss, *A codimension-2 bifurcation for reversible systems,* Field Institute communications, **4**, 201-217, (1995).

[14] G. Iooss and K. Kirchgassner, *Water waves for small surface tension: An approach via normal form,* Proc. Roy. Soc. Edin. A, **112**, 267-200, (1992).

[15] K. Kirchgassner, *Nonlinearly resonant surface waves and homoclinic bifurcation,* Adv. Appl. Mech., **26**, 135-181, (1988).

[16] S. J Chapman and G Kozyreff, *Exponential asymptotics of localized patterns and snaking bifurcation diagrams,* Phys. D, **238,** 319-354 (2009).

[17] G. Kozyreff and S. J. Chapman, *Asymptotics of large bound states of localized structures,* Phys. Rev. Lett., **97**, (2006), 044502.I.

[18] P. D. Woods and A. R. Champneys, *Heteroclinic tangles and homoclinic snaking in the unfolding of a degenerate reversible Hamiltonian-Hopf bifurcation,* Physica D, **129**, 147-170, (1999).

[19] L. A. Belyakov, *Bifurcation of systems with homoclinic curve of a saddle-focus with saddle quantity zero,* Mat. Zam., **36**, 838-843, (1984).

[20] L. A. Belyakov and L. P. Shil'nikov, *Homoclinic curves and complex solitary waves,* Selecta Mathematic Sovietica, 9:219-228, (1990).

[21] P. Glendinning, *Stability, instability and chaos: An introduction to the theory of nonlinear differential equations*, (Cambridge University Press, USA 1994)

Chapter 3

Pattern states in the anomalous group velocity dispersion regime

3.1 Introduction

Modulated states, spatially periodic or pattern solutions have been studied the years since the Lugiato-Lefever (LL) model was proposed in 1987 [1] in both temporal and spatial systems [2–7].

In the LL model, patterns arise through a Turing instability, also known as modulational instability (MI) in the context of optics [8–11]. In this type of instability the homogeneous steady state (HSS) solution initially becomes unstable to perturbations with a given wavelength, leading in this way, to the formation of an ordered modulated structure: a *pattern*. An example of this mechanisms is shown in Figure 3.1, where a initial noisy backgroud develops after a certain time of evolution, a periodic state with a fixed wavelegth. In both, one and two extended dimensions, the pattern can be supercritical or subcritical depending on the values of the detuning parameter [1, 5]. In particular, in the subcritical regime, the bistability between the HSS solution and the stable pattern allows the formation of localized states (LSs) by the locking of two fronts with different polarities connecting the HSS with the pattern and vice versa [12–15]. These types of LSs are studied in Chapter 4.

The different patterns arising in this model undergo secondary bifurcations that make them unstable to patterns with different wavelengths (Eckhaus bifurcation), oscillate in time and in space (wave instabilities), or unstable to finite

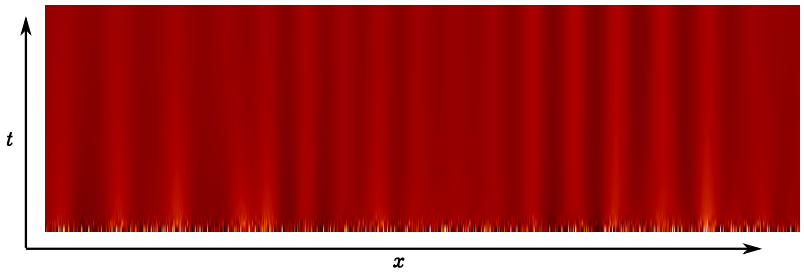

Figure 3.1: First stage of the temporal evolution of an initial condition consisting on the backgroud HSS solution plus white noise. After certain amount of time the noise backgroud develops a periodic ordered structure: a pattern. The range of x is $[-L/2, L/2]$ and the range of t is $[0, 40]$. Here $I_0 = I_c$, $\theta = 1.5$ and $L = 160$.

wavelength perturbation leading to patterns with half the wavelength (finite wave intability).

In this Chapter we focus in the patterns arising in the LL model in the anomalous GVD, and we present a detailed analysis of their bifurcation structure.

The chapter is organized as follows, in Section 3.2 we analyze the linear stability of the homogeneous solutions against non-uniform perturbations obtaining the threshold for the formation of patterns via a MI. Later, in Section 3.3 we apply weakly nonlinear analysis to calculate the pattern solution around the MI, from where they unfold. In Section 3.4, starting from this perturbative solution, we apply numerical continuation techniques to calculate the solution branches for patterns as function of ρ, the driving field amplitude, for a fixed value of the frequency detuning ($\theta = 1.5$). After, in Section 3.5 we extend this analysis to any value of detuning $\theta < 2$, and we map the different types of patterns and their bifurcations to the parameter space (θ, ρ). In Section 3.6 we identify the secondary bifurcations that occur for patterns, in particular to the P_{2k} branch, pattern branch with wavevector $2k$, where k is the pattern emerged close to threshold. In this section we show that this pattern undergoes Eckhaus (EC), finite wavelength (FW) and FW Hopf or wave instabilities. Finally, in Section 3.8 we discuss briefly the case for $\theta > 2$ where LSs can be understood as a single peak pattern.

3.2 Temporal stability analysis and unfolding of patterns

In this section we analyze the linear stability of the HSSs solutions in the anomalous case in detail. The study of how patterns appear in the LL model has been

widely studied since it was proposed in 1987 [1–3, 5]. Here we will follow the steps done in these pioneering works and we will analyze how the MIs change when modifying the detuning θ.

The LL equation in the anomalous regime is given by

$$\partial_t A = -(1+i\theta)A + i\partial_x^2 A + iA|A|^2 + \rho, \tag{3.1}$$

and in terms of the real variables $U = \mathrm{Re}[A]$ and $V = \mathrm{Im}[A]$ is written as

$$\begin{aligned} \partial_t U &= -\partial_x^2 V - U + \theta V - V(U^2+V^2) + \rho, \\ \partial_t V &= \partial_x^2 U - V - \theta U + U(U^2+V^2). \end{aligned} \tag{3.2}$$

To start we first study the linear stability analysis of HSSs (U_0, V_0) to small perturbations of the form

$$\begin{bmatrix} U \\ V \end{bmatrix} = \begin{bmatrix} U_0 \\ V_0 \end{bmatrix} + \epsilon \begin{bmatrix} u_1(x,t) \\ v_1(x,t) \end{bmatrix} + \mathcal{O}(\epsilon^2), \tag{3.3}$$

We consider that any pattern solution of Eq.(3.1) can be described by the ansatz

$$\begin{bmatrix} u_1 \\ v_1 \end{bmatrix} = \begin{bmatrix} a_k \\ b_k \end{bmatrix} e^{ikx+\Omega t} + c.c., \tag{3.4}$$

with a_k, b_k the real amplitudes associated to the mode with wavenumber k.

Inserting this ansatz in Eq.(3.2) the problem at first order in ϵ, reduces to study a linear eigenvalue problem,

$$L(A_0) \begin{bmatrix} u_1 \\ v_1 \end{bmatrix} = \Omega \begin{bmatrix} u_1 \\ v_1 \end{bmatrix}, \tag{3.5}$$

with

$$L[A_0] \equiv \begin{bmatrix} -(1+2U_0V_0) & \theta - U_0^2 - 3V_0^2 - \partial_x^2 \\ -(\theta - V_0^2 - 3U_0^2 - \partial_x^2) & -1 + 2U_0 - V_0 \end{bmatrix} \tag{3.6}$$

being the linear operator associated to the right-hand side of Eq.(3.2) evaluated at A_0, and u_1, v_1 the eigenvectors associated with the eigenvalue Ω.

If any of the eigenvalues positive the HSS will be unstable. Furthermore, the eigenvector associated to this positive eigenvalue indicates the spatial profile of the growing perturbation and therefore the shape of the pattern.

This problem can be solved analytically and we find that the growth rate Ω is given by

$$\Omega(k) = -1 \pm \sqrt{4I_0\theta - 3I_0^2 - \theta^2 + (4I_0 - 2\theta)k^2 - k^4}. \tag{3.7}$$

In the linear approximation, the superposition principle applies and therefore, any pattern solution of the problem can be written as the linear combination,

$$\begin{bmatrix} u_1 \\ v_1 \end{bmatrix}_{(x,t)} = \sum_k \begin{bmatrix} a_k \\ b_k \end{bmatrix} e^{ikx+\Omega t} + c.c., \tag{3.8}$$

Depending on the sign of Ω for a given wavenumber k, the different eigenmodes will grow, if $\Omega(k) > 0$, or decay if $\Omega(k) < 0$, and therefore the HSSs will be stable or unstable against perturbations like those given by Eq.(3.4). In Figure 3.2 we show the growth rate $\Omega(k)$ for $\theta = 1.5$ and for $I_0 = 0.9, 1.0$ and $I_0 = 1.1$. The growth rate corresponding to $I_0 = 0.9$ is negative for any value of k and therefore, perturbations (3.4) will decay for any value of k. When $I_0 = 1.1$, there is an interval of wavenumbers $[k^-, k^+]$, where $\Omega(k) > 0$, and therefore any mode with $k \in [k^-, k^+]$ will grow. Within this set of modes the most unstable mode, labeled by k_u, will be the dominant. Therefore it will grow faster than any other mode forming a pattern state characterized by k_u. The transition between those two situations, happens at a critical value of k_c and defines a bifurcation known as, Turing [8–11] or modulational instability (MI).

The condition $\Omega(k) = 0$, gives the equation

$$k^4 - (4I_0 - 2\theta)k^2 + 3I_0^2 + \theta^2 - 4I_0\theta - 1 = 0, \tag{3.9}$$

and determines the points of intersection between the the growth rate curve and the horizontal axis that we have labeled as k^- and k^+. On the contrary, $\Omega'(k_u) = \frac{d\Omega}{dk}|_{k_u} = 0$, corresponds to the equation

$$k\left(k^2 - (2I_0 - \theta)\right) = 0 \Leftrightarrow k = \sqrt{2I_0 - \theta}, \tag{3.10}$$

whose solution gives the value of k with maximal growth rate, or equivalently, the most unstable mode. In the following we will write $k_u = \sqrt{2I_0 - \theta}$.

The MI occurs when the maximum of Ω is tangent to the horizontal axes, and therefore when both conditions are satisfied simultaneously, namely

$$\Omega(k_c) = 0, \tag{3.11}$$

$$\frac{d\Omega(k)}{dk}|_{k_c} = 0, \tag{3.12}$$

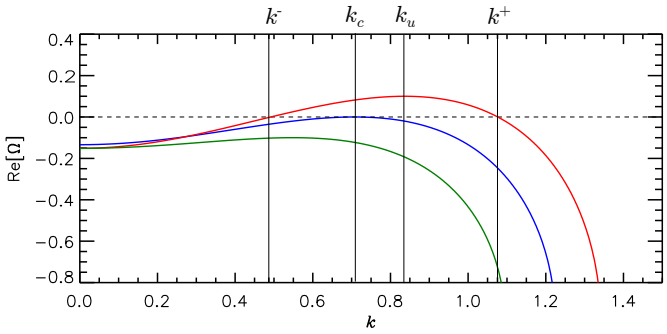

Figure 3.2: Growth rate Ω as a function of the wavenumber k for $\theta = 1.5$ and three different values of I_0, namely $I_0 = 0.9$ (gree), $I_0 = 1$ (blue) and $I_0 = 1.1$ (red).

with k_c being the critical wavenumber. This occurs at the critical wavenumber $k_c = \sqrt{2-\theta}$ and $I_0 = I_c = 1$. The condition $I_0 = 1$ defines a line in the parameter space (ρ, θ) given by

$$\rho_c = \sqrt{1 + (1-\theta)^2}. \tag{3.13}$$

The critical wavenumber k_c is only defined when $\theta < 2$ (in the other case it would be imaginary), and therefore MI only happens for $\theta < 2$. MI corresponds in terms of spatial dynamics to a Hamiltonian-Hopf (HH) bifurcation [16, 17] from which the the pattern with k_c is born. When $\theta > 2$, ρ_c becomes a Belyakov-Devaney (BD) transition [18], and therefore no pattern bifurcates from ρ_c anymore. The point $\theta = 2$ where this transition occurs correspond to a quadruple zero (QZ) from which both MI and BD lines unfold [19]. Throughout this thesis we will use either MI or HH.

The situation is more complex than it appears because together with the critical pattern unfolding from ρ_c when $\theta < 2$, there is a continuous family of patterns with $k \in [k^-, k^+]$ unfolding from the HSS solution for $I_0 > I_c$. The bifurcating point of those patterns corresponds to resonances (non-hyperbolic points) that can be either a saddle-center SC or a double-center (DC) (see Section 2.3). In this chapter, we will just focus on the study of the bifurcation structure and stability of the pattern unfolding from MI, and therefore we will restrict ourselves to $\theta < 2$. The case for $\theta > 2$ will be briefly discussed in Section 3.8. Knowing the range of wavelengths $[k^-, k^+]$, for different values of the control parameters would be useful to estimate the regions of stability of the HSSs solutions against perturbation (3.4). For a fixed value of θ, the set of points k^- and k^+ determine a curve known as *marginal* or *neutral instability curve*. As we know, those points

satisfy Eq.(3.9) that can be also written as

$$I_0^{\pm}(k,\theta) = \frac{2}{3}(\theta + k^2) \pm \frac{1}{3}\sqrt{\theta^2 + k^4 + 2\theta k^2 - 3}, \tag{3.14}$$

Marginal instability curves are shown in the left side of Figure 3.3 for different values of θ. In the right side the HSSs at the same detuning values are plotted. The solid (dashed) lines represent the HSSs solutions that are stable (unstable) against perturbations of the form (3.4). For a fixed value of θ, marginal instability curves, show the values of I_0 for which the HSS is stable or unstable. For a given mode k', the HSS solution is unstable for $I_0^-(k',\theta) < I_0 < I_0^+(k',\theta)$ and stable otherwise. For uniform perturbations i.e. perturbations with $k = 0$, we find that in the monostable regime the HSSs A_0 solutions are always stable. For a given wavenumber k a pattern with that wavenumber emerges from $I_0^{\pm}(k,\theta)$. These precise points are marked for k_c and its harmonics in Figures 3.3 as $\mathrm{MI}_k^{\pm}$.

In terms of spatial dynamics, $\mathrm{MI}_{k_c}^-$ is always is a HH bifurcation. In contrast $\mathrm{MI}_{k_c}^+$,$\mathrm{MI}_{2k_c}^{\pm}$ and $\mathrm{MI}_{4k_c}^{\pm}$ are resonances that can be either a saddle-center or a double-center depending on the control parameters of the system. The spatial eigenvalues of those points are shown in Figure 3.4 for $\theta = 1.1$.

Let us take a look at Figure 3.3. For $\theta = 1.1$, a pattern with wavenumber k_c bifurcates from the modulational instability $\mathrm{MI}_{k_c}^-$ at I_c and for large values of I_0 reconnects with the HSSs at the double-center global bifurcation labeled by $\mathrm{MI}_{k_c}^+$. In the same fashion, a pattern with $2k_c$ arises initially from the double-center labeled as $\mathrm{MI}_{2k_c}^-$ and reconnects at the double-center $\mathrm{MI}_{2k_c}^+$. For the pattern with $4k_c$ the situation is similar.

For $\theta = 1.5$ (see panel (b)) the situation is similar to the previous one despite of the fact that now, the different instability points for k_c and their harmonics come closer and that the tongue of unstable modes shifts to lower values of k. The approaching of the instabilities can be easily observed in Figure 3.5(a) where we plot the instability lines in function in the parameter space (θ, I_0). Together with those lines we have also added the saddle-nodes of the HSS solution, namely $\mathrm{SN}_{hom,1}$ and SN_{hom_2}.

In most of the chapters of this thesis we work in terms of the driving amplitude ρ. Therefore we also show in Figure 3.5(b), the same lines but in terms of (θ, ρ). Figure 3.5(c) is a zoom of Figure 3.5(b). For $\theta < \sqrt{3}$, A_0 is always stable against uniform perturbations $k = 0$. In contrast, when $\theta > \sqrt{3}$, i.e. when the HSSs becomes trivaluate, the HSS is unstable for uniform perturbations between $I_0^-(k,\theta)$ and $I_0^+(k,\theta)$. So, for $\sqrt{3} < \theta < 2$, A_0^b and A_0^t branches are stable against $k = 0$ perturbations and A_0^m unstable, and this is the reason why

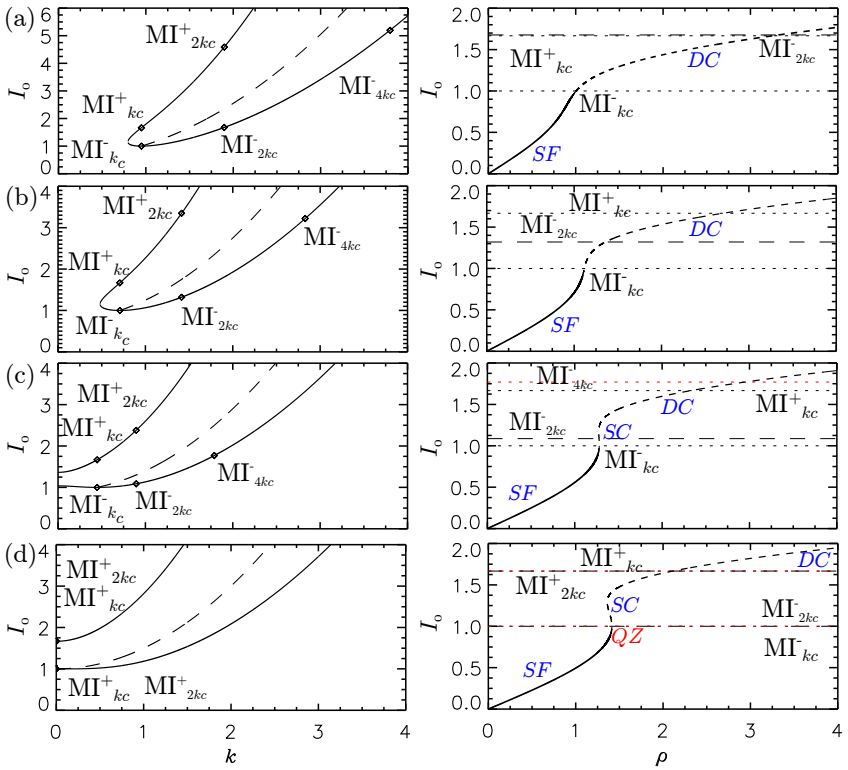

Figure 3.3: On the left marginal instability curves for $\theta = 1.1$ (a), $\theta = 1.5$ (b), $\theta = 1.8$ (c) and $\theta = 2.0$ (d). On the right the HSSs solutions corresponding to the same values of θ. Solid (dashed) lines represent when the HSSs is stable (unstable) against perturbations like (3.4). The different $\mathrm{MI}^{\pm}_{k}$ instabilities are indicated with points and between brackets. The dashed line in the marginal instability curves represents the most unstable mode k_u for value of θ.

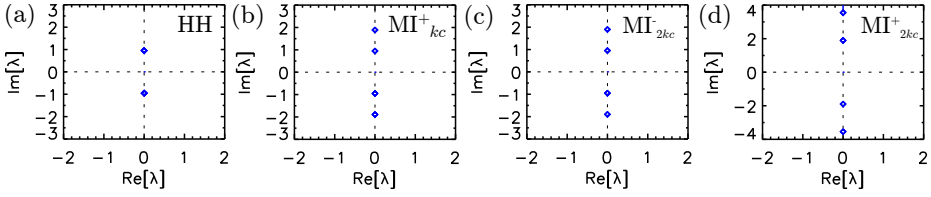

Figure 3.4: Spatial eigenvalues associated with the $\mathrm{MI}^{\pm}_{k_c}$ and $\mathrm{MI}^{\pm}_{2k_c}$ for $\theta = 1.1$ (see Figure 3.3(a)). Panel (a) is a Hamiltonian-Hopf bifurcation. Panels (b)-(d) are *DC* resonances.

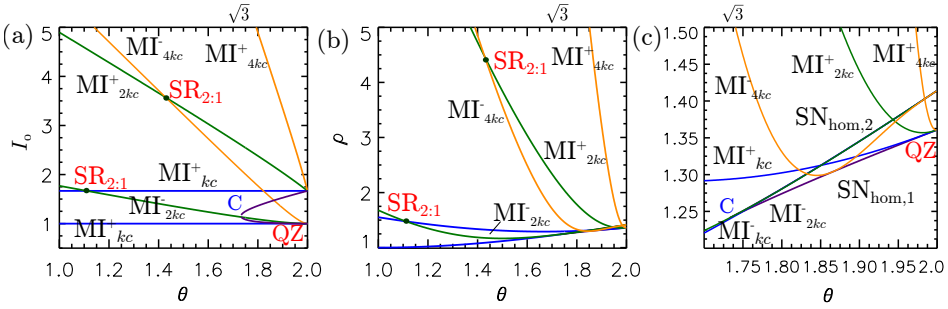

Figure 3.5: In (a) the instabilities lines $\mathrm{MI}^{\pm}_{k_c}$ and the saddle-nodes of the HSSs solution are plotted in parameter space (θ, I_0). In (b) we plot the same lines but now considering (θ, ρ). (c) represent a zoom of (b) around the C bifurcation of the HSSs solutions. Labels $\mathrm{SR}^1_{1:2}$ and $\mathrm{SR}^2_{1:2}$ stand for the spatial resonance at $1:2$ with $O(2)$ symmetry that occur when $\mathrm{MI}^+_{k_c}$ and $\mathrm{MI}^-_{2k_c}$ (both *DC* resonances meet). QZ stands for quadruple zero codimension-2 bifurcation point.

this regime is known as the bistable regime. This situation correspond to panel (c) of Figure 3.3 for $\theta = 1.8$, where the tongue starts now at $k = 0$.

Finally, increasing even more θ, $\mathrm{MI}^{\pm}_k$ points approach each other until all collapse at $k = 0$ for $\theta = 2$ (see panel (d)). This situation corresponds to the codimension-two point QZ (see panels (b) and (c) of Figure 3.5) and at this point the MI disappears.

To summarize, there are two distinct regions in parameter space where patterns have a different nature:

1. For $\theta < 2$ the HSS loses first its stability at the $\mathrm{MI}^-_{k_c}$ instability (spatial HH bifurcation) at $I_0 = I_c = 1$ to a pattern with wavenumber $k_c = \sqrt{2-\theta}$. These patterns bifurcate supercritically if $\theta < 41/30$ and subcritically for $\theta > 41/30$ (see Ref.[5]) and reconnects with HSS at $\mathrm{MI}^+_{k_c}$ (a double-center) (see Figures 3.3). For values of the intensity above $I_0 = I_c$, there is a one parameter family of patterns, defined by the wavenumber k, and each pattern bifurcates from the HSS at MI^-_k and reconnecting with the HSS at MI^+_k.

2. For $\theta > 2$ the HH bifurcation at $I_0 = I_c$ becomes a BD transition. Now the instability takes place for values $I_0 > I_c$, and always with critical wavenumber $k_c = 0$.

As mentioned before, in this chapter we will focus in the first case: the region $\theta < 2$. In the next chapter we will then study what happens with pattern solutions and localized states for $\theta > 2$. There we will see how, in periodic systems, a localized state can be understood as a large wavelength pattern with $k \sim 0$.

3.3 Weakly nonlinear analysis around HH

The LL equation is non integrable, however it is possible to obtain approximative analytical solutions in the neighborhood of certain bifurcation points. In this section we compute weakly nonlinear patterns using multiple scale perturbation theory near the HH bifurcation corresponding to $\mathrm{MI}^-_{k_c}$ in the temporal dynamics. These calculations are detailed in Appendix C. Along this Section we use the HH notation instead of $\mathrm{MI}^-_{k_c}$ for refering this bifurcation. First, we fix the value of θ and suppose that patterns at $\rho \approx \rho_c$, where $\rho = \rho_c$ corresponds to the HH bifurcation,

$$\rho_c = \sqrt{1 + (1-\theta)^2}, \tag{3.15}$$

are captured by the ansatz

$$\begin{bmatrix} U \\ V \end{bmatrix} = \begin{bmatrix} U \\ V \end{bmatrix}^* + \begin{bmatrix} u \\ v \end{bmatrix}, \tag{3.16}$$

where U^* and V^* represent the HSS A_0^b and u and v capture the spatial dependence. We next introduce appropriate asymptotic expansions for each variable in terms of a small parameter ϵ defined through the relation $\rho = \rho_c + \epsilon^2\delta$. Then, the asymptotic expansion for each variable can be written in the form

$$\begin{bmatrix} U \\ V \end{bmatrix}^* = \begin{bmatrix} U_c \\ V_c \end{bmatrix} + \epsilon^2 \begin{bmatrix} U_2 \\ V_2 \end{bmatrix} + ... \tag{3.17}$$

$$\begin{bmatrix} u \\ v \end{bmatrix} = \epsilon \begin{bmatrix} u_1 \\ v_1 \end{bmatrix} + \epsilon^2 \begin{bmatrix} u_2 \\ v_2 \end{bmatrix} + \epsilon^3 \begin{bmatrix} u_3 \\ v_3 \end{bmatrix} + ... \tag{3.18}$$

The scaled variable is $X = \epsilon x$ and we will consider all the variables to be functions of x and X, i.e. $u_i = u_i(x, X(x))$ and $v_i = v_i(x, X(x))$. Then the differential operator on any of those fields will be

$$\partial_x^2 u_i(x, X(x)) = \partial_x^2 u_i + 2\epsilon \partial_x \partial_X u_i + \epsilon^2 \partial_X^2 u_i. \tag{3.19}$$

Inserting the ansatz given by Eq.(C.2) in Eq.(3.2) we can calculate the different variable solving the system order by order in ϵ.

At order $\mathcal{O}(\epsilon^0)$ we find that,

$$\begin{bmatrix} U_c \\ V_c \end{bmatrix} = \begin{bmatrix} \dfrac{\rho_c}{1+(I_c-\theta)^2} \\ \dfrac{(I_c-\theta)\rho_c}{1+(I_c-\theta)^2} \end{bmatrix} \tag{3.20}$$

At order $\mathcal{O}(\epsilon^1)$, we need to solve the equation

$$L \begin{bmatrix} u_1 \\ v_1 \end{bmatrix} = \begin{bmatrix} 0 \\ 0 \end{bmatrix} \tag{3.21}$$

with $L = L[A_0]$ the linear operator defined by Eq.(3.5). In order to do that we consider the ansatz

$$\begin{bmatrix} u_1 \\ v_1 \end{bmatrix} = \begin{bmatrix} a \\ b \end{bmatrix} \left(\phi(X)e^{ik_c x} + \bar{\phi}(X)e^{-ik_c x}\right), \tag{3.22}$$

with $a, b \in \mathbb{R}$ and $\phi \in C^r(\mathbb{R}, \mathbb{C})$. The solvability condition for this equation with the previous ansatz gives us that the value of k_c is

$$k_c = \pm\sqrt{(2I_c - \theta) \pm \sqrt{I_c^2 - 1}}. \tag{3.23}$$

We have to mention that (3.23) is solution of the Eq.(3.9) that was obtained in the linear stability analysis in Section 3.2 and that I_c was also calculated there. However in the present calculation the value I_c will be determined at next order in the calculation. With the previous condition satisfied, we find

$$\begin{bmatrix} a \\ b \end{bmatrix} = \begin{bmatrix} \dfrac{\theta - 2V_c^2 - I_c + k_c^2}{1 + 2U_c V_c} \\ 1 \end{bmatrix}. \tag{3.24}$$

At $\mathcal{O}(\epsilon^2)$, we obtain from the solvability condition related with the HSS contribution that

$$\begin{bmatrix} U_2 \\ V_2 \end{bmatrix} = \delta d_c \begin{bmatrix} 1 - 2U_c V_c \\ 2U_c^2 + I_c - \theta \end{bmatrix} = \delta \begin{bmatrix} \tilde{U}_2 \\ \tilde{V}_2 \end{bmatrix}, \tag{3.25}$$

with

$$d_c = 1 + \theta^2 + 3I_c^2 - 4\theta I_c. \tag{3.26}$$

And from the solvability condition of the equation regarding the spatial dependence, another constraint for k_c, namely

$$k_c^2 = 2I_c - \theta \tag{3.27}$$

Equation (3.23) together with Eq.(3.27) give us the condition

$$I_c = 1, \tag{3.28}$$

as we already showed in Section 3.2.

Finally at $\mathcal{O}(\epsilon^3)$, the solvability condition for the equation at this order give us the amplitude equation or normal form for the functions $\phi(X)$, namely

$$\alpha_1 \frac{d^2\phi(X)}{dX^2} + \delta\alpha_2\phi(X) + \alpha_3|\phi(X)|^2\phi(X) = 0, \tag{3.29}$$

where α_i, $i = 1, 2, 3$ are functions of the control parameters (see Appendix C).

To solve Eq.(3.29) we consider the ansatz $\phi(X) = Ae^{i\varphi}$, with $A \in \mathbb{R}^+$. With this ansatz two kind of solutions can be found depending on the fact that A depends on X or does not.

If $A \neq A(X)$, then Eq.(3.29) becomes

$$\delta\alpha_2 A + \alpha_3 A^3 = 0, \tag{3.30}$$

with solutions $A_0 = 0$ and $A_\pm = \pm\sqrt{-\delta\alpha_2/\alpha_3}$. Then the solution is $\phi = \sqrt{-\dfrac{\delta\alpha_2}{\alpha_3}}e^{i\varphi}$, with φ arbitrary (due to the translational invariance). Consequently at leading order in ϵ we find that from HH a spatially periodic solution (pattern) of the form:

$$\begin{bmatrix} U \\ V \end{bmatrix} = \begin{bmatrix} U_c \\ V_c \end{bmatrix} + \begin{bmatrix} \tilde{U}_2 \\ \tilde{V}_2 \end{bmatrix} (\rho - \rho_c) + 2 \begin{bmatrix} a \\ 1 \end{bmatrix} \sqrt{-\frac{\alpha_2}{\alpha_3}(\rho - \rho_c)}\cos\left(k_c x + \varphi\right), \tag{3.31}$$

arises. Moreover, we have that if $\alpha_2/\alpha_3 > 0$, the pattern bifurcates subcritically toward $\rho < \rho_c$ and when $\alpha_2/\alpha_3 < 0$ it does supercriticaly towards $\rho > \rho_c$. The transition between supercritical and subcritical takes place at the value of θ where α_2/α_3 goes from negative to positive. This occurs for $\theta = 41/30$ as was already calculated in Ref.[5] (first page). These perturbative solutions are only valid in the neighborhood of HH. Nevertheless applying continuation methods we can track these solutions for parameter values far from HH, and therefore we can calculate the bifurcation diagrams of these states. The understanding of the bifurcation structure and instabilities of patterns (3.31) unfolding from HH is the goal of the coming section.

The case $A = A(X)$ has a LSs solutions of sech type that unfold together with the previous patterns from HH [15, 16]. We will study these LSs in Section 4.4.

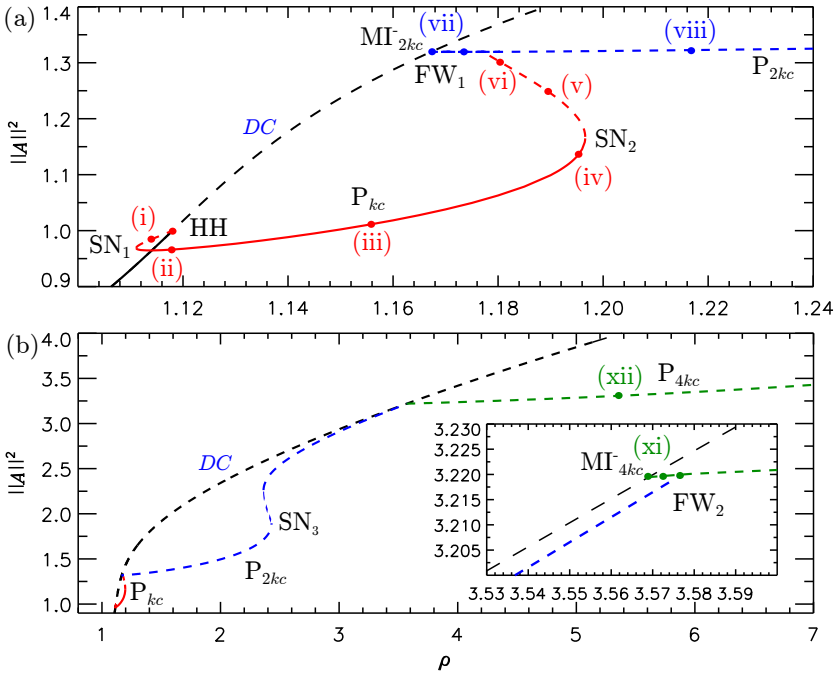

Figure 3.6: Bifurcation diagram of patterns with wavenumbers k_c, $2k_c$, and $4k_c$ for $\theta = 1.5$. Panel (a) show the bifurcations of P_{k_c} and how it connects with P_{2k_c} at FW_1. Panel (b) shows a broader region of the bifurcation diagram. Here the pattern P_{2k_c} connects with the pattern P_{4k_c} at FW_2. A zoom of that connection is shown in the inset.

3.4 Bifurcation structure of patterns

In Section 3.3, we have calculated a perturbative solution for the pattern unfolding from the HH. This solution is only valid in the neighborhood of the HH point, and we wonder how those patterns looks like far from that point and moreover how their bifurcation structure is. These questions are addressed in this section.

First we analyze the bifurcation structure for the critical pattern for a fixed value of the detuning. This pattern is connected with other patterns whose wavevectors are even harmonics of the critical one, i.e. the pattern with λ_c is connected to a pattern with $\lambda_c/2$, the latter with one with $\lambda_c/4$ and so on. Later we will show that for any pattern unfolding for $I_0 > I_c$ (from resonances) the scenario is analogous.

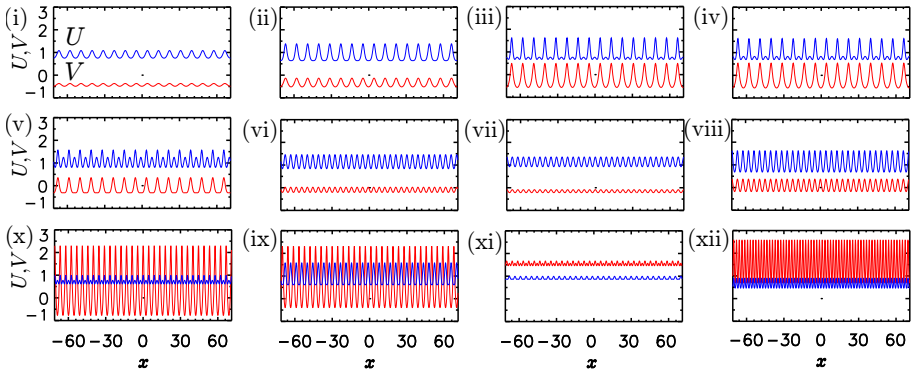

Figure 3.7: Profiles of patterns corresponding to the bifurcation diagrams shown in Figure 3.6. Panels (i)-(vi) correspond to P_{k_c}. Panels (vii)-(x) to P_{2k_c} and (xi)-(xii) to P_{4k_c}.

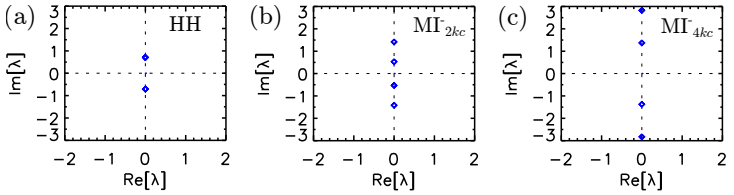

Figure 3.8: Spatial eigenvalues associated with the $\mathrm{MI}^-_{k_c}$, $\mathrm{MI}^-_{2k_c}$ and $\mathrm{MI}^-_{4k_c}$ for $\theta = 1.5$ (see Figure 3.6). Panel (a) is a Hamiltonian-Hopf bifurcation. Panels (b) and (c) are *DC* resonances.

In order to proceed we fix throughout this section $\theta = 1.5$ and a domain size $L = 16\lambda_c$, just a multiple of the critical wavelength λ_c. In Figure 3.6 we can see the bifurcation diagram for the pattern state unfolding from the HH bifurcation with the critical wavelength $\lambda_c = 2\pi/k_c$. As bifurcation measure we choose the L^2-norm,

$$||A||^2 = \frac{1}{L}\int_{-L/2}^{L/2} |A(x)|^2 dx. \tag{3.32}$$

In the following we will label those patterns as P_{k_c}. For this value of detuning, a small amplitude pattern P_{k_c} (see Figure 3.7(i)), bifurcates subcritically from HH at $I_0 = I_c$. Decreasing the value of ρ the pattern increases its amplitude until reaching the saddle-node SN_1 (see Figures 3.6(a)) where it becomes stable. The pattern is the one shown in panel (ii) of Figure 3.7. Profles (ii)-(iv) of the same figure show how the pattern increases its amplitude for larger values of ρ

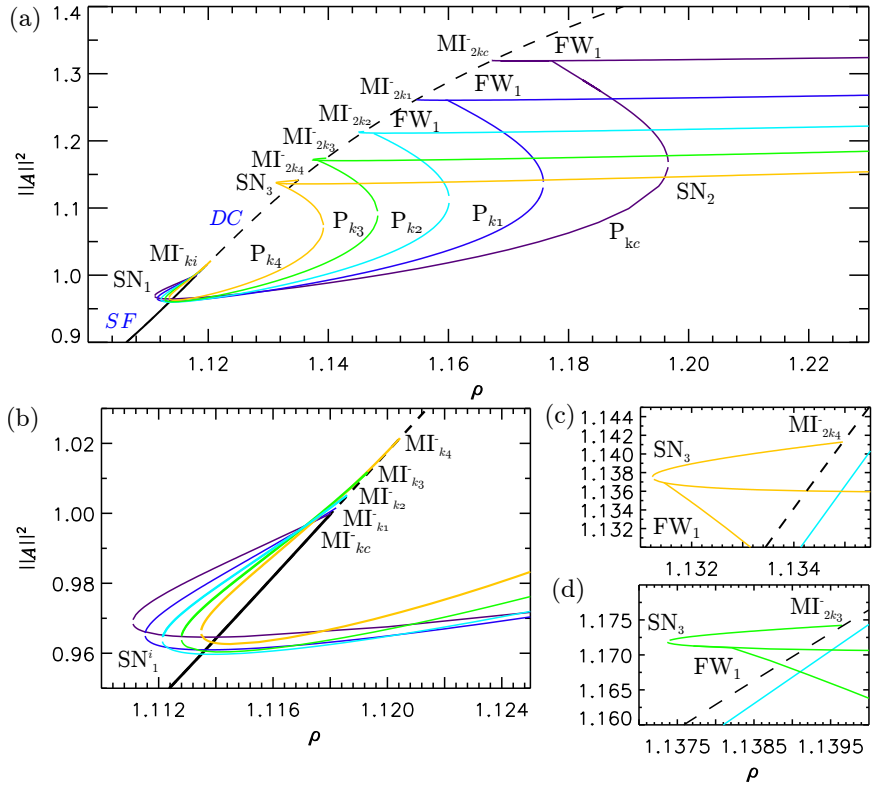

Figure 3.9: In (a) bifurcation diagram for patterns with different wavenumbers unfolding from HHSs at MI^-_k points and MI^-_{2k}. The wavenumbers are $k_c = 8.88$, $k_1 = 9.38577$, $k_2 = 9.88577$, $k_3 = 10.3858$ and $k_4 = 10.8858$. In (b) a zoom of the panel (a) around the $\mathrm{MI}^-_{k_i}$ unfoldings. Panel (c) and panel (d) show the unfolding of P_{2k_3} and $\mathrm{P}2k_4$ from $\mathrm{MI}^-_{2k_3}$ and $\mathrm{MI}^-_{2k_4}$ respectively. FW_1 stands for finite wave instability, *DC* is a double-center and *SF* is a saddle focus.

until reaching SN_2 where it becomes again unstable. Once the fold is passed and ρ is decreased, spatial oscillations (SOs) start to appear in between peaks as we can appreciate looking at the real part of profile (v). These SOs correspond to the growth of the second harmonic $2k_c$ of the pattern wavenumber. These peaks grow in amplitude (see panel (vi)) until P_{k_c} merges with the pattern P_{2k_c} which has a wavenumber $2k_c$. This merging occurs at a finite wavelength FW_1 instability of P_{2k_c} at a double of its wavelength.

This new pattern unfold from $\mathrm{MI}^{-}_{2k_c}$, that corresponds to a double-center DC as we can see by looking at its spatial eigenvalues shown in Figure 3.8. Initially this pattern arises supercritically and unstable (see panel (vii)) but its amplitude grows increasing ρ (see panel (viii)) until reaching SN_3 where it folds back.

Continuing after the fold, several SNs come up in pattern branches P_{2k_c} and as before, SOs in between peaks grow before that the pattern coalesces at point FW_2 with another branch, denoted by P_{4k_c} with characteristic wavenumber $4k_c$. This new pattern bifurcates again supercritically, unstable and with small amplitude (see panel (xi)of Figure 3.7) from the HSS at $\mathrm{MI}^{-}_{4k_c}$, that is also a DC in spatial dynamics (see Figure 3.4 (c)). Increasing ρ the same behavior as in the previous cases is found (see panel (xii) of Figure 3.7).

As we already mention, for $I_0 > I_c$, patterns with different wavelength also unfold from the HSSs at global bifurcations that we label as $\mathrm{MI}^{\pm}_{k}$. Therefore, on top of the bifurcation diagram shown in Figure 3.6, we also have to consider an infinite number of similar bifurcation structures for each of these patterns. In Figures 3.9(a) we show bifurcation diagrams corresponding to different wavenumbers for $\theta = 1.5$. For each pattern we have chosen the domain size L to be equal to just one pattern wavelength, $L = \lambda$. Here we just plot branches for five different wavenumbers, k_c and k_i with $i = 1, ..., 4$ for increasing values of k. The broader diagram corresponds to k_c, already shown in Figure 3.6. As the wavenumber is increasing, we can observe two main different features happening. First, the bifurcation structure is preserve and patterns P_k are also connected with their even harmonics P_{2k} via FW instabilies. Second all the P_k patterns unfold subcritically from their respectives MI^{-}_{k} bifurcations (see Figure 3.9(b)). On the contrary, as we can see in Figure 3.9(a) and 3.9(c)-(d), P_{2k} patterns unfold supercritically from $\mathrm{MI}^{-}_{2k_c}$ and $\mathrm{MI}^{-}_{2k_1}$, but subcritically from $\mathrm{MI}^{-}_{2k_2}$, $\mathrm{MI}^{-}_{2k_3}$ and $\mathrm{MI}^{-}_{2k_4}$. Third, the bifurcation structure although preserved, shrinks increasing the wavenumber.

In the next section we will analyze the modification of the bifurcation structure for patterns as function of θ and we will map those changes into the (θ, ρ)-parameter space.

3.5 Patterns in the (ρ, θ) plane

In the previous Section we have studied the bifurcation scenario for a particular value of detuning, $\theta = 1.5$, where the pattern is known to be subcritical. In this section we analyze how the bifurcation structure is modified when changing the value of θ. In order to do that we will just focus in the pattern with critical

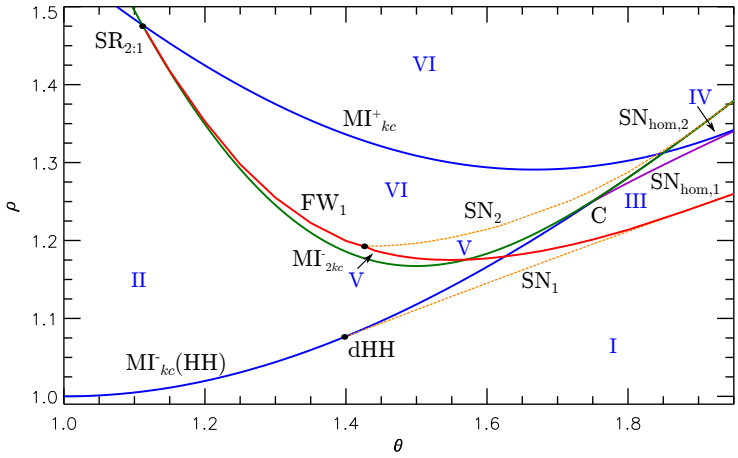

Figure 3.10: Parameter space (ρ, θ). $SR_{2:1}$ is a condimension-two point where $MI^{-}_{k_c}$ and $MI^{2}_{2k_c}$ (both *DCs*) meet. From this point a FW_1 instability line (red) is born. For clarity we also exclude the line corresponding to SN_3. Different cuts of this space for a fixed value of θ are shown in Figures 3.11 and 3.12.

wavenumber P_{k_c}. To have a complete understanding of the dynamics of the pattern we project the bifurcation points calculated for each value of θ in the parameter space (ρ, θ) shown in Figures 3.10.

For low values of θ the situation is like the one depicted in the diagram of Figures 3.11(a) for $\theta = 1.1 < 41/30$. As we can see, the pattern P_{k_c} (red lines) bifurcates supercritically from the HH bifurcation at $I_0 = I_c$ and returns back to the HSS at $MI^{+}_{k_c}$ (a *DC* bifurcation point). Meanwhile P_{2k_c} (blue lines) bifurcates from $MI^{-}_{2k_c}$ (another *DC* point) and extends to higher values of ρ until connecting again with the HSS at $MI^{+}_{2k_c}$.

Increasing a little bit θ, $MI^{+}_{k_c}$ and $MI^{-}_{2k_c}$ encounter each other in a 2:1 spatial resonance with $O(2)$ symmetry ($SR_{2:1}$) [20–22], a codimension-two bifurcation point of the HSS which organize the bifurcation scenario in the $(\rho, \theta)-$parameter space. This point can be calculated analytically by the condition $I_0^{+}(k_c, \theta) = I_0^{-}(2k_c, \theta)$, standing for the collision between $MI^{+}_{k_c}$ and $MI^{-}_{2k_c}$ in the parameter space (θ, ρ).

Increasing further the value of θ we cross the point $SR_{2:1}$ (see Figures 3.10) and a bifurcation line FW_1 emerges from that point. All along this line P_{k_c} and P_{2k_c} patterns connect. This situation can be observed, for instance, at $\theta = 1.2$

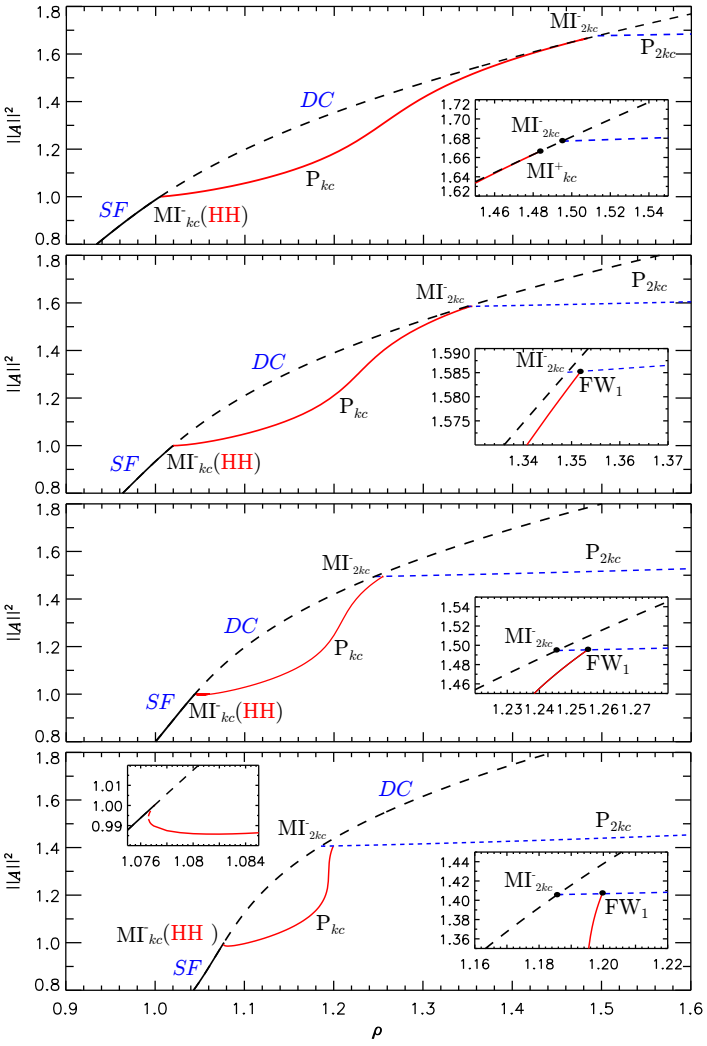

Figure 3.11: Bifurcation diagrams corresponding to $\theta = 1.1$ (a), $\theta = 1.2$ (b), $\theta = 1.3$ (c) and $\theta = 1.4$ (d). As before, the red lines correspond to P_{k_0} and the blue lines to P_{2k_0}. Panel (a) and (b) show the situation before and after crossing $SR_{2:1}$. FW_1 stands for finite wave instability. Panel (b) and (c) show the changing from of pattern P_{k_c} from supercritical to subcritical at the degenerate HH at $\theta = 41/30$. The subpanels show a zoom around the FW_1 instability.

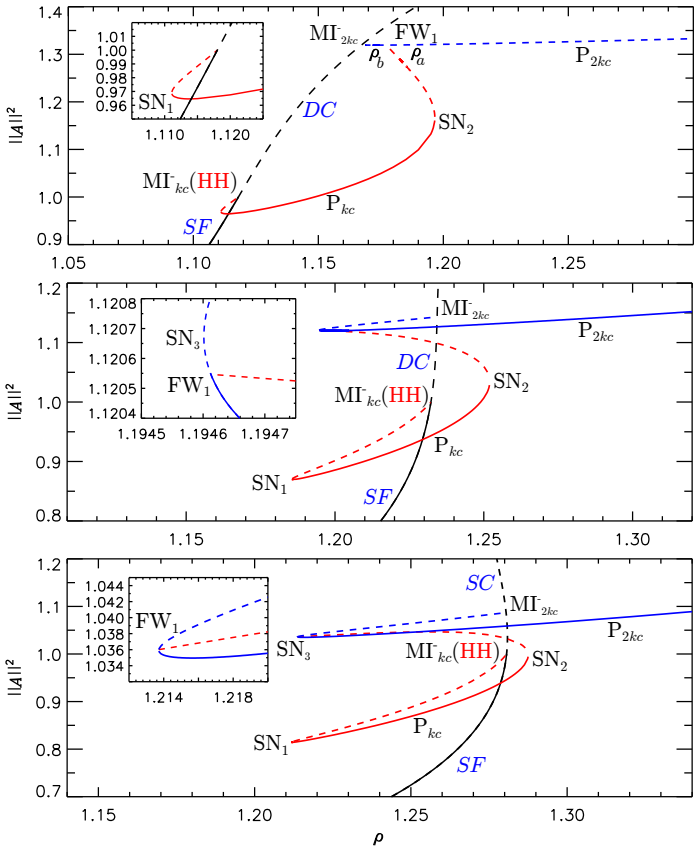

Figure 3.12: Bifurcation diagrams corresponding to $\theta = 1.5$ in (a), $\theta = 1.72$ in (b) and $\theta = 1.8$ in (c). In the subpanels we zoom in some parts of the diagrams. For $\theta = 1.5$ (panel (a)), P_{2k_c} bifurcates supercritically from HSSs at $MI^{-}_{2k_c}$. On the contrary for $\theta = 1.72$, the P_{2k_c} unfolding is subcritical. In panels (b) and (c) we can observe how the FW_1 instability moves forward SN_3.

and $\theta = 1.3$ in Figures 3.11(b)-(c), where both patterns emerge supercritically from the HSSs. At $\theta = 41/30$, the pattern P_{k_c} undergoes a degenerate HH (dHH) where it becomes subcritical for $\theta > 41/30$. This new regime is shown in Figures 3.11(d) for $\theta = 1.4$. Here patterns bifurcate initially unstable from HH and become stable at the saddle-node SN_1 (orange dashed line in Figures 3.10).

This branch of solutions (P_{k_c}) extends until FW_1, where it connects with P_{2k_c}. In this regime A_0 and P_{k_c}, both stable, coexist and therefore LSs arise in terms of a homoclinic snaking structure [14, 15], that will be analyzed in the next Chapter.

At $\theta = 1.5$ (see Figures 3.12(a)) the most relevant change in the bifurcation structure is that P_{k_c} bifurcates subcritically from FW_1, i.e. initially the pattern emerges unstable from FW_1 and gain stability at SN_2 (also in orange dashed line in Figures 3.10). The transition between super and subcritical happens in a degenerate FW_1 bifurcation. The pattern P_{k_c} is stable between SN_1 and SN_2 and unstable between FW_1 and SN_2. The stability of the branch P_{2k_c} is more complex and involves the appearance of Hopf and Eckhaus bifurcations.

For $\theta = 1.72$ (see Figures 3.12(b)) P_{2k_c} becomes also subcritical in another degenerate $MI^-_{2k_c}$ point. Due to this, a new saddle-node bifurcation SN_3 appears (not shown in Figures 3.10). In this saddle-node the pattern, that initially emerges unstable from HSS, becomes stable. In the subpanels of Figures 3.12(b) and (c) we can see a zoom of the region around FW_1 for $\theta = 1.72$ and $\theta = 1.8$ respectively. In the top panel of (b) we see that the unstable pattern P_{k_c} meets P_{2k_c} at FW_1. Increasing θ, the FW_1 point approaches more and more SN_3 until, eventually, they meet in a new degenerate point. This is for example the situation shown in the bottom panel corresponding to $\theta = 1.8$.

We distinguish four main dynamical regions, labeled I-VI in the phase diagram in Figure 3.10, in terms of the existence of HSSs and patterns:

- Region I: The HSS solution A_0 is stable. This region spans the parameter space $\rho < \rho_c$.
- Region II: The pattern P_{k_c} is stable and A_0 unstable. This region spans the parameter space ρ inbetween ρ_c and $MI^+_{k_c}$ for $\theta < \theta_{SR_{2:1}}$ and ρ in between $MI^-_{k_c}$ and $MI^-_{2k_c}$ for $\theta > \theta_{SR_{2:1}}$.
- Region III: Bistability between P_{k_c} and the HSS A_0. This region spans for $\theta > 41/30$ and for $\rho_{SN_1} < \rho < \rho_c$.
- Region IV: Bistability region for the HSSs. For $\theta > \sqrt{3}$, A_0^b and A_0^t coexist in region $\rho_t < \rho < \rho_b$[1]. .
- Region V: Coexistence between P_{2k_c} unfolding from $MI^-_{2k_c}$ and P_{k_c} unfolding from $MI^-_{k_c}$(HH).

[1] ρ_b and ρ_t represent the possition of the $SN_{hom,1}$ and $SN_{hom,2}$ respectively

- Region VI: Coexistence between the P_{2k_c} unfolding from $MI^{-}_{2k_c}$ and the unstable A_0.

In the parameter space shown in Figures 3.10 we only focus on the region around the FW_1 point, and therefore on the bifurcations related only with P_{k_c} and P_{2k_c}. However we find that a similar configuration takes place between the patterns P_{2k_c} and P_{4k_c}, P_{4k_c} and P_{8k_c} and so on. These lines and their intersections were already shown in Figures 3.5(b) and (c). As we can observe in those figures, there is a sequence of $SR_{1:2}$ bifurcation points occurring.

On top all this picture, for the critical pattern and their even harmonics, we also have that a similar organization of patterns occurs for a dense family of patterns for each wavenumber $k \in \mathbb{R}^+$, which implies that the scenario is quite complex.

3.6 Secondary bifurcations of patterns

In this Section we analyze numerically the stability of the pattern solutions $A_p = (U_p, V_p)$ against perturbations with wavenumber q i.e. perturbations of the type $\sim e^{iqx}$. In this way we can find and characterize all the secondary bifurcations that the pattern undergoes for different values of ρ and θ.

First of all, we present the technique that has been used in this analysis. After that, we show the results regarding the stability of P_{2k_c} for a fixed value of detuning, in particular $\theta = 1.5$. We demostrate that P_{2k_c} undergoes three types of instabilities, *Eckhaus* (EC) instabilities, *finite wavelength* (FW) instabilities and *finite wavelength Hopf* (FWH) instabilities. This last type of instability is responsible for the oscillation of the pattern in time and space and is also known as *wave instability* (WI) [11, 23–26].

3.6.1 Linear instability of patterns

This method is a generalization of the technique described in [27]. First we linearize Eq. (3.1) around a stationary pattern $A_p = (U_p, V_p)$ and we calculate the eigenspectrum of the linearized operator, for different values of the wavenumber q. In other words, we have to solve the eigenvalue problem

$$L[A_p]\psi = \lambda\psi, \tag{3.33}$$

where now we consider the linear operator $L[A_p] = L^{\mathbb{C}}[A_p, \bar{A}_p]$ written in function of complex variables, namely

$$L^{\mathbb{C}}[A_p, \bar{A}_p] \equiv \begin{bmatrix} -(1+i\theta) + 2i|A_p|^2 + i\partial_x^2 & iA_p^2 \\ -i\bar{A}_p^2 & -(1-i\theta) - 2i|A_p|^2 - \partial_x^2 \end{bmatrix}, \tag{3.34}$$

and ψ the eigenmodes associated with the eigenvalue λ. If any of the eigenvalues is positive the pattern will be unstable. Furthermore, the eigenvector associated to this positive eigenvalue indicates the spatial profile of the growing perturbation.

Due to the periodicity of $L[A_p]$, we can apply the Bloch theorem and write the eigenmodes as a superposition of Bloch waves,

$$\psi(x,q) = \begin{bmatrix} e^{iqx} f(x,q) \\ e^{-iqx} f^*(x,-q) \end{bmatrix}, \tag{3.35}$$

where

$$f(x+\lambda_p, q) = f(x,q), \tag{3.36}$$

with λ_p the wavelength of A_p. Both f and A_p can be written as the Fourier expansion:

$$f(x,q) = \sum_{m=0}^{N-1} f_m(q) e^{ik_m x}, \tag{3.37}$$

and

$$A_p(x) = \sum_{m=0}^{N-1} a_m e^{ik_m x}, \tag{3.38}$$

with $k_m = 2\pi m/\lambda_p$ and N the number of Fourier modes considered in the analysis.

Inserting Eq.(3.37) and Eq.(3.38) in Eq.(3.34) we get the discretized problem

$$L(a_m, q)\Sigma_n(q) = \lambda_n(q)\Sigma_n(q), \tag{3.39}$$

with $\Sigma_n \equiv (f_0(q), \cdots, f_{N-1}, \bar{f}_0(q), \cdots, \bar{f}_{N-1})$ and $\lambda_n(q)$ the eigenmode and eigenvalue associated with the matrix $L(a_m, q)$. For more details see Refs.[27–29].

Then, the stability of the of $A_p(x)$ reduces to find the $2N$ eigenvalues $\lambda_n(q)$ of the matrix $L(a_m, q)$ for each value of q. The eigenvalues for a given q determine the stability of the pattern against perturbations containing any set of wavenumbers

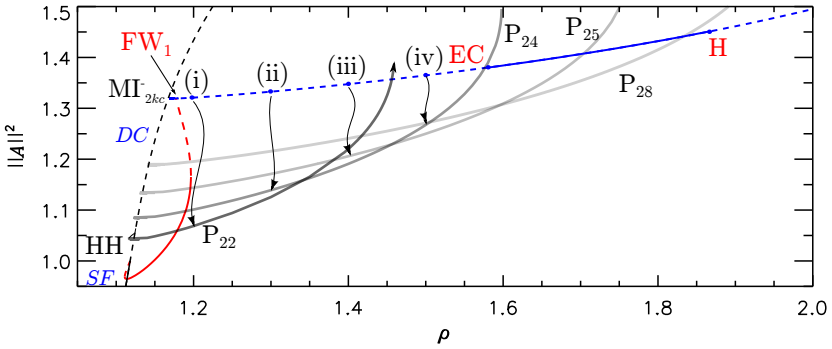

Figure 3.13: Bifurcation diagram for $\theta = 1.5$. In red the pattern branch P_{k_c} unfolding from HH. In blue the branch of P_{2k_c} that arises from $MI^{-}_{2k_c}$. Labels (i)-(iv) correspond to the unstable patterns analyzed in Figure 3.15. Those patterns with initially 32 rolls evolves to patterns with a different number of rolls depending on the value of ρ. The correspondence is signaled by an arrow and the new pattern branches (in gray) are labeled with P_n, being n the number of rolls of the new state.

$k_m \pm q$. To know the stability of the solutions against any possible perturbation it sufficient to consider only the q values inside the first Brillouin zone. Any perturbation with wavenumber q' outside the Brillouin zone is equivalent to another with $q = q' + k_m$. In solid state physics this representation is described as the *reduced zone scheme* [30].

Using this technique we characterize how the the eigenspectrum of $L(A_p)$ change as a function of q for each set of values (θ, ρ) and therefore we will predict instabilities to patterns of any wavelength. We find that patterns P_{k_c} only changes its stability through saddle-node bifurcations, as we can observe in Figure 3.11 and Figure 3.12.

In Figure 3.13 we show a portion of the bifurcation diagram for $\theta = 1.5$ where we can see the branches corresponding to P_{k_c} (in red) and P_{2k_c} (in blue), and as usual, solid (dashed) lines represent stable (unstable) solutions. Regarding the P_{2k_c} three bifurcation occur along its solution branch. From left to right, the first instability that appears is a FW instability, where P_{2k_c} connects with P_{k_c}. In second place a EC instability occurs, and finally a Hopf bifurcation (H) takes place. The pattern P_{2k_c} is stable between H and EC. For values of ρ on the left of EC patterns are unstable against long-wavelength perturbations ($q \sim 0$), and for this reason this instability is also known as long-wavelength (LW) instability[11, 23].

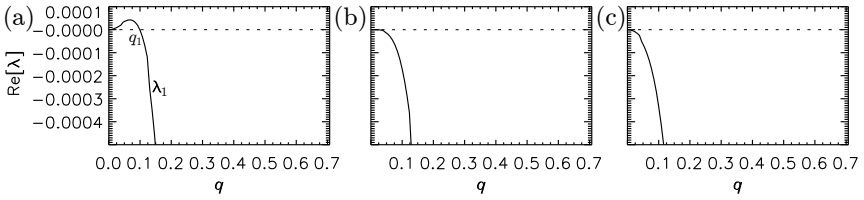

Figure 3.14: Modification of the eigenspectrum around the EC instability. In this figure we plot $\mathrm{Re}[\lambda(q)]$ at $\theta = 1.5$ for different values of ρ. (a) $\rho = 1.57$, (b)$\rho = \rho^{EC} = 1.58$ (c) $\rho = 1.59$. We just show the leading eigenvalue λ_1.

3.6.2 Eckhaus or long-wavelength instability

When a Eckhaus instability takes place, there is one branch of eigenvalues $\lambda_1(q)$ that, for small q, has a parabolic shape centered at $q = 0$, namely $\mathrm{Re}[\lambda_1(q)] \propto |q|^2$. The EC instability is characterized by a change in the convexity of this eigenvalue. This type of change can be observed in Figure 3.14 where we have plotted the eigenvalue of the leading mode of the complete eigenspectrum in function of q for three different values of ρ, namely $\rho = 1.57$, $\rho = 1.58$ and $\rho = 1.59$. The range of q studied belongs to the first Brillouin zone, $[0, k'/2]$ being $k' = 2k_c$. In panel (c) $\rho = 1.59$ and $\mathrm{Re}[\lambda_1(q)]$ is negative. Therefore the pattern P_{2k_c} is always stable no matter the wavelength of the perturbation. In panel (b) ($\rho = 1.58$) the branch of eigenvalues flattens around $\mathrm{Re}[\lambda(q)] = 0$. This value corresponds to the EC or LW instability, and we label it as $\rho^{EC} = 1.58$. Finally in (c), the branch of eigenvalues has change its convexity, and the pattern is unstable to perturbations with $q \in [0, q_1]$. We have found that the pattern P_{2k_c} is EC unstable all the way from EC until MI^{-}_{2k} where it emerges from the HSSs. On top of these instabilities the patterns exhibit a FW instability that will be study in detail in the next section.

Figure 3.15 shows how the the unstable pattern P_{2k_c} behaves depending on its eigenspectrum for different values of ρ between $\mathrm{MI}^{-}_{2k_c}$ and EC. The labels (i)-(iv) correspond to different point along the pattern branch P_{2k_c} plotted in Figure 3.13. The left column of Figure 3.15 shows the real part of the eigenspectrum $\mathrm{Re}[\lambda(q)]$, and the middle column represents a detailed view of the leading eigenvalue $\lambda_1(q)$. The right column shows the temporal evolutions of the initial patterns from (i) to (iv).

For $\rho = 1.5$ (see panel (iv) of Figure 3.15), P_{2k} is unstable to perturbations with q in between 0 and q_1, being the most unstable mode the one corresponding to the maximum of the curve. The evolution of this pattern is shown in the right

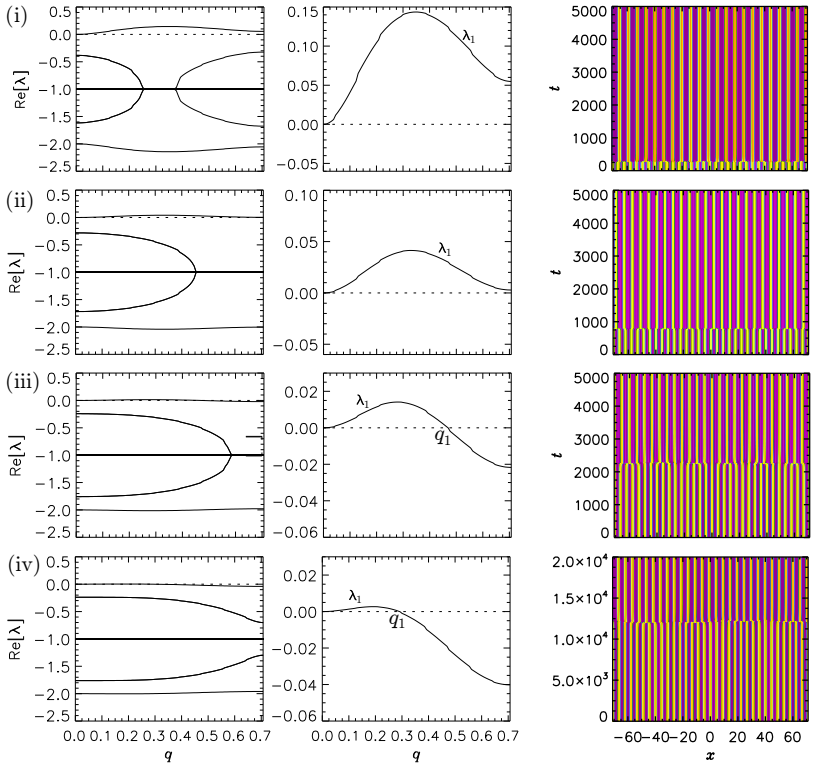

Figure 3.15: Re[$\lambda(q)$] at $\theta = 1.5$ in the region Eckhaus unstable and temporal evolutions of the pattern to patterns of different wavelengths. Those patterns are shown in gray in Figure 3.13. The initially 32 rolls pattern, evolves to P_{28} in (iv) for $\rho = 1.5$, P_{25} in (iii) for $\rho = 1.4$, P_{24} in (ii) for $\rho = 1.3$ and P_{22} in (i) for $\rho = 1.2$.

panel of (iv). In the first stage of the simulation the pattern seems to be stable although, after a large amount of time, the wavelength of the pattern suddenly increases to the wavelegth of the most unstable mode. Thus our pattern that initially had 32 rolls becomes a pattern with 28 rolls that we name as P_{28}. This new pattern can be tracked back and forward on ρ and as result one obtain the solution branch plotted in Figure 3.13.

Decreasing the value of ρ, λ_1 moves upward (see middle panel (iii) Figure 3.15 for $\rho = 1.4$), increasing the region of unstable modes. Reducing even farther the value of ρ, the pattern becomes unstable to any $q \in [0, k'/2]$ (see panel (ii)) for $\rho = 1.3$. As we can also observe, the maximum of λ_1, the most unstable mode,

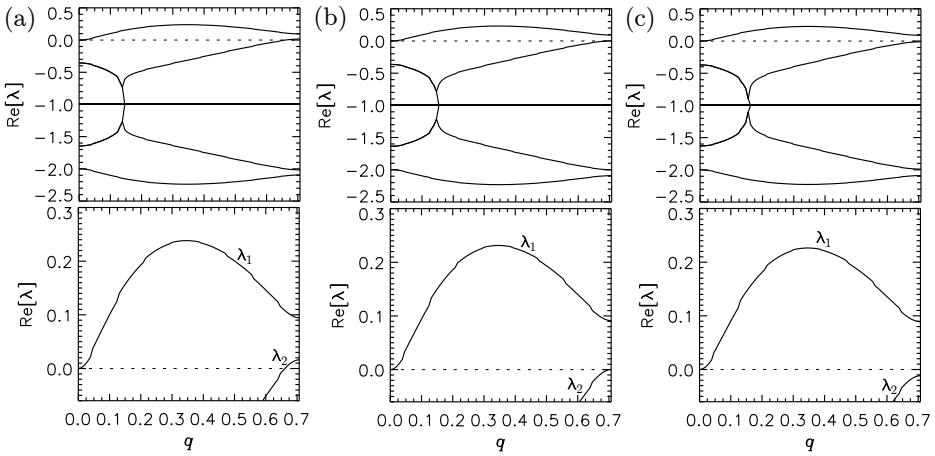

Figure 3.16: Modification of the eigenspectrum around the FW instability. Here we show the eigenspectrum Re[$\lambda(q)$] at $\theta = 1.5$ for different values of ρ. (a) $\rho = 1.176$, (b) $\rho = \rho^{FW} = 1.17715$ (c) $\rho = 1.178$.

becomes larger as decreasing the value of ρ (see middle panels from (iv)-(i)), and therefore the amount of time needed for destabilize the pattern P_{2k} decreases with ρ, as we can observe in the right panels of Figure 3.15.

We can always track the final state of the simulation in ρ and obtain the corresponding solution branches plotted in Figure 3.13. Each new branch is labeled with P_n been n the number of rolls of the final pattern. The correspondence between the pattern branch P_{2k} and the new branches of patterns are indicated by arrows.

3.6.3 Finite wavelength instability

Here we characterize the points that previously we have labeled as FW_i, with $i = 1, 2, ...$ At these points a solution branch corresponding to a pattern with a wavenumber k, lets say P_k connects the branch of a pattern with wavenumber $2k$, i.e. P_{2k}. This instability is a specific type of bifurcation occurring at a finite wavenumber q, and therefore they are called *Finite Wavelength* instabilities.

In our case, it is the pattern P_{2k} with wavenumber $k' = 2k$ the one that undergoes a particular type of FW instability happening at $q = k'/2$. This indeed correspond to a wavenumber $q = k$, and therefore P_{2k} become P_k. This bifurcation is characterized by a branch of eigenvalues $\lambda(q)$ having a parabolic shape cen-

tered at $q = k'/2$ i.e. $\mathrm{Re}[\lambda(q)] \propto |q - k'/2|^2$, that crosses $\mathrm{Re}[\lambda(q)] = 0$ at $q = k'/2$. This transition is shown in Figure 3.16 for the value of detuing $\theta = 1.5$ for three values of ρ around FW_1, namely $\rho_b = 1.176$, $\rho^{FM} = 1.17715$ and $\rho_a = 1.178$, so before the FW_1, at the FW_1 and after. The position of these three values is shown in Figure 3.12(a) and in Figure 3.13. Figure 3.16(a) shows the situation for a value $\rho < \rho^{FW}$. In the bottom panel we see a zoom of the eigenspectrum centered at zero. As we can observe there are two relevant eigenvalues $\lambda_1(q)$ and $\lambda_2(q)$. $\mathrm{Re}[\lambda_1(q)]$ is positive for all the range $q \in [0, k'/2 = k]$ and therefore the pattern P_{2k} is unstable to any perturbation $\sim e^{iqx}$ with $q \in [0, k'/2 = k]$. For all this range, the maximum of $\mathrm{Re}[\lambda_1(q)]$ correspond to the wavenumber of the most unstable mode. The other relevant eigenvalue is λ_2 (see bottom panel). This branch of eigenvalues, as we said before, is centered at $q = k'/2$ and is positive. In panel (b) we show the eigenspectrum at the FW_1 instability occurring at $\rho = \rho^{FW}$. At this value the branch $\lambda_2(q)$ is negative and tangent to $\mathrm{Re}[\lambda(q)] = 0$ at $q = k'/2$. Finally in panel (c) we show the situation at $\rho_a = 1.178$, where the branch $\lambda_2(q)$ is completely negative.

For these values of ρ the pattern is always unstable to any perturbation with $q \in [0, k'/2 = k]$, and therefore we can not observe the FW instability. However, this bifurcation signals the connection of the branches of patterns P_{2k} and P_k. As one can appreciate in Figure 3.10 this instability emanates from a spatial 1:2 resonance with O(2) symmetry $\mathrm{SR}_{1:2}$.

3.6.4 Hopf instability

Here we analyze the last bifurcation that we have found along the branch of patterns P_{2k_c}. As shown in Figure 3.13, the pattern P_{2k_c} is stable between EC and the Hopf (H) bifurcation at $\rho = 1.87$. This bifurcation diagram can be re-plotted in terms of the extrema of $|A|^2$ i.e. $\max(|A|^2)$ and $\min(|A|^2)$ as shown in Figure 3.17. Here as usual solid (dashed) lines represent stable (unstable) stationary states, and the crosses represent simulations. Moreover the Hopf bifurcation is supercritical. In the context of patterns, two types of Hopf bifurcations can occur. The first type corresponds to an amplitude instability occuring at $q = 0$, and it is known as *homogeneous Hopf* bifurcation. In this bifurcation the real part of two complex eigenvalues with $q = 0$, $\lambda_2(0)$ and $\lambda_3(0)$ becomes zero at the critical point, with an imaginary part different from zero. When the real parts becomes positive the pattern start to oscillate uniformly with a period $T = 2/\omega$, with $\omega = \mathrm{Im}(\lambda_2(0)) = \mathrm{Im}(\lambda_3(0))$.

The second type of Hopf bifurcation occurs with $q \neq 0$, and is known as *finite wavelength Hopf* (FWH) or *wave instability* (WI) [11, 23–26]. The pattern that

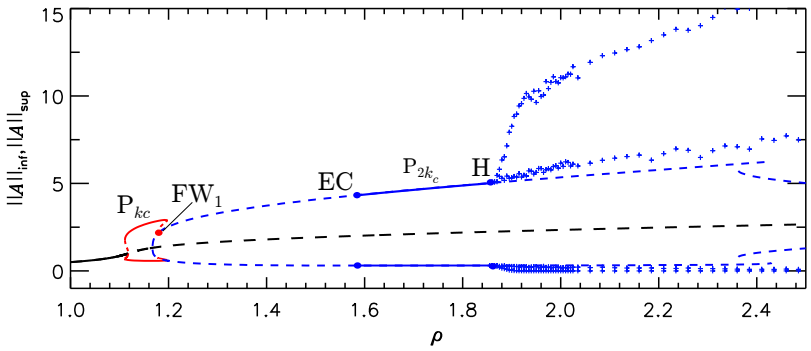

Figure 3.17: Bifurcation diagram for $\theta = 1.5$. Here we plot the extremum of $|A|^2$ i.e. $\max(|A|^2)$ and $\min(|A|^2)$. In blue crosses we represent the oscillatory states. Some of those time evolutions are shown in Figure 3.19.

becomes unstable through this type of bifurcation does not oscillate uniformly, contrary to the previous case, but it oscillates in time and in space. The Hopf indicated in Figure 3.17 is indeed a FWH instability.

The three leading branches of eigenvalues are plotted in the top panels of Figure 3.18 for the values $\rho = 1.84$ in panel (i), $\rho = 1.87$ in panel (ii) and $\rho = 1.9$ in panel (iii). In panel (i) the branches of eigenvalues $\lambda_2(q)$ and $\lambda_3(q)$ are bellow zero and their maximum correspond to $q = k'/2 = k_c$. In the bottom of panel (i) we plot the eigenspectrum of the pattern at $q = k_c$, and as we can observe $\lambda_2(k_c)$ and $\lambda_3(k_c)$ are complex conjugates. When $\rho = 1.87$ (see panel (ii)) the real part of those two complex conjugate eigenvalues becomes zero, and therefore a Hopf bifurcation at $q = k'/2 = k_c$ occurs. Finally panel (iii) the real part of the eigenvalues becomes positive and the pattern start to oscillates, although now not only in time but also in space.

In Figure 3.19 we show the contour plots of this kind of states for three values of ρ. For $\rho = 1.9$ (see panel (i)), the pattern oscillates in time but not uniformly. Thus there are regions where the pattern has different oscillation amplitudes. Increasing a bit more ρ the pattern undergoes some oscillations in space, where some peaks moves from left to right (see panel (iii) for $\rho = 2.11$). Finally for $\rho = 2.41$, the pattern exhibits much complex dynamics where peaks merge and separate. The complete description of the dynamics of these oscillatory states in time and space is beyond the scope of this Chapter and will be studied elsewhere.

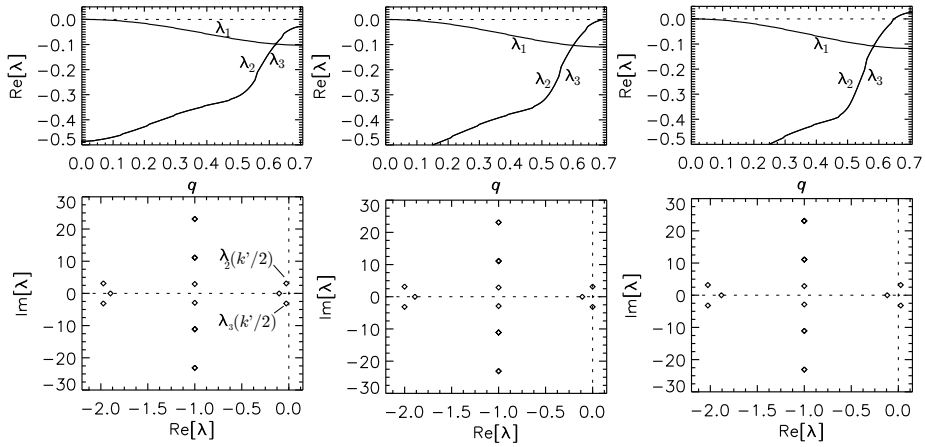

Figure 3.18: Hopf bifurcation at $q = k/2$. Re$[\lambda(q)]$ at $\theta = 1.5$ for different values of ρ. (a) $\rho = 1.84$, (b) $\rho = 1.87$ (c) $\rho = 1.9$. In the bottom panels eigenvalues of the pattern at $q = k/2$.

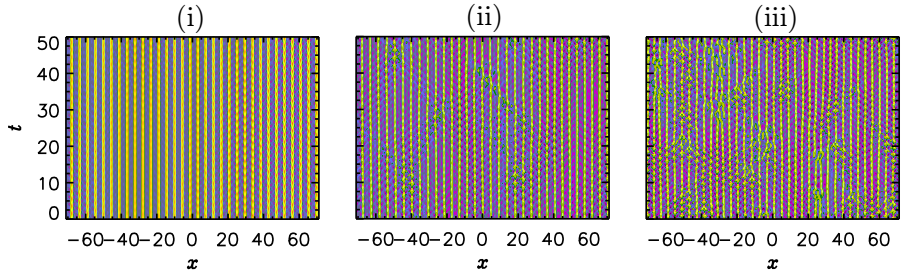

Figure 3.19: Time evolution of the oscillatory patterns for $\theta = 1.5$. In (i) $\rho = 1.9$, (ii) $\rho = 2.11$ and (iii) $\rho = 2.41$. Label correspond to Figure 3.17.

3.7 Discussion

In this Chapter we have focused on the bifurcation structure and stability of patterns for $\theta < 2$. For $\theta > 2$ the HH bifurcation at $I_0 = I_c$ becomes a BD transition, and the first instability takes place for values $I_0 > I_c$, and always with $k_c = 0$. In this case, in addition to the new bifurcating homogeneous solution ($k = 0$), one can consider that above I_c pattern solutions with very large wavelength ($k \sim 0$) exist.

In finite systems with periodic boundary conditions $A(0) = A(L)$, L being the spatial period, the largest possible wavelength corresponds to $\lambda = L$. If the

bifurcation is subcritical, and the pattern is highly nonlinear, this pattern can be interpreted as a single localized structure.

When $k = k_c = 0$, the instabilities $\mathrm{MI}^{\pm}_{k_c=0}$ are given by

$$I_0^{\pm}(k=0) = \frac{2}{3}\theta \pm \frac{1}{3}\sqrt{\theta^2 - 3} \equiv I_{b,t}, \tag{3.40}$$

that in fact represent the positions of $\mathrm{SN}_{hom,1}$ at I_b (with the $-$ sign) and $\mathrm{SN}_{hom,2}$ at I_t (with $+$). The pattern with $k = \Delta k = 2\pi/\lambda = 2\pi/L$ appears at $\mathrm{MI}^{-}_{\Delta k}$, which is closer to $\mathrm{SN}_{hom,1}$ the larger the system is, and disappears at $\mathrm{MI}^{+}_{\Delta k}$ close to $\mathrm{SN}_{hom,2}$.

Due to the accumulation of all the $\mathrm{MI}^{-}_{\Delta k}$, $\mathrm{MI}^{-}_{4\Delta k}$, $\mathrm{MI}^{-}_{4\Delta k}$, ... to $\mathrm{SN}_{hom,1}$ and $\mathrm{MI}^{+}_{\Delta k}$, $\mathrm{MI}^{+}_{2\Delta k}$, $\mathrm{MI}^{+}_{2\Delta k}$, ... to $\mathrm{SN}_{hom,2}$ (see Figure 3.3(d) for $\theta = 2$), this single peak pattern and their harmonics will unfold together.

In terms of spatial dynamics $\mathrm{SN}_{hom,1}$ is indeed a reversible Takens-Bodganov (RTB) bifurcation, and theory predicts that a sech type of LS bifurcates from it. This state, in the context of patterns previously discussed, corresponds to a single peak pattern. In Chapter 4 we will show that this state can be calculated asymptotically in the neighborhood of the RTB point, and that its bifurcation diagram keeps some similarities with the diagram shown in Figure 3.12(c) for $\theta = 1.8$.

As we already mention in Chapter 2, the unfolding of the different type of localized states and pattern is organized through a Quadruple-zero (QZ) point in the spatial dynamics context. Applying weakly nonlinear analysis about the QZ point ($\theta = 2$) we have recently found that the dynamics of the system around that point can be described by a Swift-Hohenberg equation with only quadratic nonlinearity. This type of equation was already studied in the 90's by Buffoni *et al.* [31], and we think that these results can be fundamental to understand the transition between the two previous scenarios.

3.8 Conclusions

In this chapter we have studied the bifurcation structure and stability of patterns arising in the Lugiato-Lefever model in the anomalous GVD dispersion regime. We have restricted to the range of detuning parameter $\theta < 2$, where patterns first unfold from a Hamiltonian-Hopf (HH) bifurcation [16]. The scenario for $\theta > 2$ is more complex and it will be studied in detail in Chapter 4.

Linear perturbation theory predicts that the HSSs becomes modulationally un-

stable at $I_0 = I_c = 1$ to a pattern with a critical wavenumber $k_c = \sqrt{2-\theta}$, namely P_{k_c} [1, 5]. A weakly nonlinear analysis has allowed us to obtain a perturbative solution of this pattern in a neighborhood of the Hamiltonian-Hopf bifurcation. From this calculation one can also predict that P_{k_c} emerges supercritically if $\theta < 41/30$ and subcritically if $\theta > 41/30$, being $\theta = 41/30$ a degenerate Hamiltonian-Hopf bifurcation.

This analytical approximation for the pattern P_{k_c} around HH has been used as initial seed in a numerical continuation algorithm that have allowed us to calculate the bifurcation states for parameter values far from the bifurcation point.

Consequently we can build up the bifurcation structure for patterns as function of ρ for any value of θ. We have found that pattern unfolding from the HH bifurcation reconnects with the HSSs for larger values of I_0 at $\mathrm{MI}^{+}_{k_c}$, and that its even harmonics P_{2k_c} also unfold from the HSSs at the instabilities $\mathrm{MI}^{\pm}_{2k_c}$. Changing the control parameters these two patterns connect in a finite wave (FW) instability. In the same manner, the pattern P_{4k_c} is connected with P_{2k_c} by another FW instability and so on. This behavior occurs not only for the pattern characterized by k_c, but for any pattern unfolding from the HSSs at $I_0 > I_c$. We have characterized the complete parameter space-(θ, ρ) and we have found that the FW instability arises from a spatial resonance at $2:1$ with symmetry $O(2)$ [20–22].

Patterns can experience several dynamical instabilities which infer very rich and complex dynamics. In particular P_{2k_c}, endure Eckhaus instabilies, wave instabilies and finite wavelength instabilities.

In the following Chapters, we will see that pattern are corner stones in the formation of localized states when bistability between the HSSs and the previous ones is achieve [12, 14, 15]. Consequently, this study will be useful for understanding the complete bifurcation scenario regarding localized states.

References

[1] L. A. Lugiato and R. Lefever, *Spatial dissipative structures in passive optical systems,* Phys. Rev. Lett. **58**, 2209-2211 (1987).

[2] W.J. Firth, A.J. Scroggie, G.S. McDonald and L.A. Lugiato, *Hexagonal patterns in optical bistability*, Phys. Rev. A 46, R3609 (1992).

[3] W.J. Firth and G.K. Harkness, *Cavity solitons,* Asian J. Phys. **7,** 665 (1998).

[4] A.J. Scroggie, W.J. Firth, G.S. McDonald, M. Tlidi, R. Lefever and L.A. Lugiato, *Pattern-formation in a passive kerr cavity,* Chaos, Solitons Fractals **4**, 1323 (1994).

[5] M. Tlidi, R. Lefever and P. Mandel, *Pattern selection in optical bistability,* Quantum Semiclass. Opt. **8** 931 (1996).

[6] M. Haelterman, S. Trillo, and S. Wabnitz, *Dissipative modulation instability in a nonlinear dispersive ring cavity,* Opt. Comm. **91**, 401 (1992).

[7] D. Gomila, P. Colet, *Transition from hexagons to optical turbulence* Physical Review A **68**, 011801 (R) (1-4) (2003).

[8] R. Kapral and K. Showalter, *Chemical Waves and Patterns,* Kluwer, Dordrecht, (1995).

[9] A. M. Turing, *The chemical bases of morphogenesys,* Philos. Trans. R. Soc. London, Ser. B 237, **37** (1952).

[10] V. Castets, E. Dulos, J. Boissonade, and P. De Kepper, *Experimental evidence of a sustained standing Turing-type nonequilibrium chemical pattern,* Phys. Rev. Lett. **64**, 2953 (1990).

[11] M. C. Cross and P. C. Hohenberg, *Pattern-formation outside of equilibrium,* Rev. Mod. Phys. 65, 851 1993.

[12] P. Coullet, C. Riera, C. Tresser, *Stable static localized structures in one dimension,* Phys. Rev. Lett. 84 (2000) 3069.

[13] D. Gomila, A.J. Scroggie, and W.J. Firth, *Bifurcation structure for dissipative solitons,* Phys. D (Amsterdam) **227**, 70 (2007).

[14] P.D. Woods, A.R. Champneys,*Heteroclinic tangles and homoclinic snaking in the unfolding of a degenerate reversible Hamiltonian-Hopf bifurcation,* Physica D **129**, 147 (1999).

[15] J. Burke and E. Knobloch, *Localized states in the generalized Swift-Hohenberg equation,* Phys. Rev. E. **73** (2006) 056211.

[16] G. Iooss and M.C. Pérouème,*Perturbed Homoclinic Solutions in Reversible 1:1 Resonance Vector Fields,* J. Diff. Eqs., **102**, 62 (1993).

[17] M. Haragus and G. Iooss, *Local Bifurcations, Center Manifolds, and Normal Forms in Infinite-Dimensional Dynamical Systems* (Springer, Berlin, 2011).

[18] R. Devaney, *Reversible diffeomorphism and flows,* Trans. Am. Math. Soc. **218**, 89 (1976).

[19] A.R. Champneys, *Homoclinic orbits in reversible systems and their applications in mechanics, fluids and optics,* Phys. D (Amsterdam) **112**, 158 (1998).

[20] D. Armbruster, J. Guckenheimer, and P. Holmes, *Heteroclinic cycles and modulated travelling waves in systems with O(2) symmetry,* Physica 29D, 257-282 (1988).

[21] M.R.E. Proctor, and C.A. Jones. *The interaction of two spatially resonant patterns in thermal convection. Part 1. Exact 2:1 resonance,* J. Fluid Mech. Vol. **188**, pp. 301-335 (1988).

[22] J. Porter and E. Knobloch, *New type of complex dynamics in the 1:2 spatial resonance*, Physica D, **159**, 125-154 (2001).

[23] D. Walgraef, *Spatio-Temporal Pattern Formation* ÍŚSpringer-Verlag, Berlin, (1997).

[24] M . Hildebrand, A. S. Mikhailov, and G. Ertl, *Traveling Nanoscale Structures in Reactive Adsorbates with Attractive Lateral Interactions,* Phys. Rev. Lett. **81,** 2602 ÍŚ1998.

[25] A. M. Zhabotinsky, M. Dolnik, and I. R. Epstein, *Pattern formation arising from wave instability in a simple reaction-diffusion system,* J. Chem. Phys. **103,** 10306 1995.

[26] M. Dolnik, A. M. Zhabotinsky, A. B. Rovinsky, and I. R. Epstein, *Standing Waves in*

a Two-Dimensional Reaction-Diffusion Model with the Short-Wave Instability, J. Phys. Chem. A 103, 38 (1999); M. Dolnik, A. B. Rovinsky, A. M. Zhabotinsky, and I. R. Epstein, *Spatio-temporal patterns in a reaction-diffusion system with wave instability,* Chem. Eng. Sci. 55, 223 2000.

[27] G. Harkness, G. L. Oppo, R. Martin, A.J. Scroggie, and W.J. Firth, *Elimination of spatiotemporal disorder by Fourier space techniques,* Phys. Rev. A **58**, 2577 (1998).

[28] D. Gomila, *Dinamics of spatial structures in nonlinear optics*, Ph.D. Thesis (2003).

[29] G. Harkness, W.J. Firth, G. L. Oppo, and J.M. McSloy, *Computationally determined existence and stability of transverse structures. I. Periodic optical patterns,* Phys. Rev. E **66**, 046605 (2002).

[30] N. W. Ashcroft and N. Mermin, *Solid state physics*, Brooks/Cole cengage learning, 1979.

[31] B. Buffoni, A. R. Champneys, and J. F. Toland, *Bifurcation and Coalescence of a Plethora of Homoclinic Orbits for a Hamiltonian System,* Journal of Dynamics and Differential Equations, Vol. **8**, 2, (1996).

[32] B. Ponedel and E. Knobloch, *Forced Snaking: Localized structures in the real Ginzburg-Landau equation with spatially periodic parametric forcing,* EPJ (to be published)

Chapter 4

Bright solitons in the anomalous group velocity regime

4.1 Introduction

In this chapter we study in detail the dynamics, stability and bifurcation structure of bright solitons appearing in the one-dimensional Lugiato-Lefever (LL) equation describing temporal cavities in the anomalous GVD regime. These localized structures (LSs) can be seen as localized spots of higher intensity light embedded in a homogeneous surrounding. This regime has been widely studied in one and two transverse dimensions for $\theta < 2$ [1–3].

As shown in Chapter 3, for $\theta < 2$ a pattern P_{k_c} emerges from the Hamiltonian-Hopf (HH) bifurcation, supercritically if $\theta < 41/30$, and subcritically, if $\theta > 41/30$ [2]. In the subcritical case, the bistability between the pattern and the stable bottom branch of the HSSs (A_0^b) can lead to the formation of bright solitons organized in a bifurcation structure known as *homoclinic snaking* [4, 5]. A very detailed study about the bifurcation structure of those solitons can be found in Ref. [7]. However, for $\theta > 2$, bright solitons bifurcates from the $\mathrm{SN}_{hom,1}$ (a reversible Takens-Bodganov (RTB) bifurcation in spatial dynamics), and they are KdV-type of solitons. In Ref. [9] the authors showed that in this regime bright solitons undergo oscillatory instabilities, temporal chaos and spatio-temporal chaos. Nevertheless a complete understanding of the bifurcation structure and the stability of these states was still lacking. Our main goal along this Chapter is to complete exhaustively previous studies in this regime [11, 12]. As we will see, for $\theta > 2$ bright solitons are organized in a bifurcation structure that has

a different morphology and origin than homoclinic snaking type of bifurcation diagrams, and that we will refer as *foliated snaking* following Ref. [10].

The chapter is organized as follows. In Section 4.2 we summarize the main results regarding the spatial dynamics of the HSS solution in the anomalous GVD regime, identifying the bifurcation from where one could expect the origin of LSs. Later in Section 4.3 we analyze the unfolding of bright solitons from the HH bifurcation for $\theta < 2$. First we perform a perturbative analysis around the HH bifurcation obtaining a first order approximation for a bump solution only valid in the neighborhood of the HH point. After that, using continuation techniques, we build up the bifurcation diagram for those states. In Section 4.4 we study the appearance of bright solitons that unfold from the $\mathrm{SN}_{hom,1}$, a RTB bifurcation in spatial dynamics for $\theta > 2$. Later in Section 4.5 we expose the organization of solitons in the parameter space (θ, ρ) showing the regions of existence of these states. In Section 4.6 we study the oscillatory and chaotic regimes that bright solitons undergo for high values of θ, and finally in Section 4.7 we end the Chapter with some conclusions.

4.2 Overview of spatial dynamics in the anomalous regime

Here we shortly review the spatial dynamics of the LL equation in the anomalous GVD regime, already studied in Chapter 2. The stationary LL equation in this regime, namely:

$$\begin{cases} -V'' - U + \theta V - V(U^2 + V^2) + \rho = 0, \\ \\ U'' - V - \theta U + U(U^2 + V^2) = 0, \end{cases} \tag{4.1}$$

with $'$ standing for the derivative respect to x, can be recast to a four dimensional dynamical system. In this case the spatial eigenvalues i.e. the eigenvalues associated with the dynamical system at the HSS, have the configuration given in Figure 2.6. In Figure 4.1 we have partially reproduced two panels of that diagram representing the two configurations which are relevant in this Chapter. Panel (a) shows the situation for $\theta < 2$, and panel (b) for $\theta > 2$. From Eq. (2.14) with $\nu = 1$ one derives that the condition $I_0 = I_c = 1$ defines the following curve in parameter space:

$$\rho = \rho_c \equiv \sqrt{1 + (1 - \theta)^2}, \tag{4.2}$$

that is a Hamiltonian-Hopf (HH) bifurcation with eigenvalues $\lambda_{1,2} = \pm i k_c$, $\lambda_{3,4} = \pm i k_c$, for $\theta < 2$ and a Beliakov-Devaney (BD) transition with $\lambda_{1,2} = \pm q_0$, $\lambda_{3,4} = \pm q_0$ for $\theta > 2$. Together with these lines, we also have found that

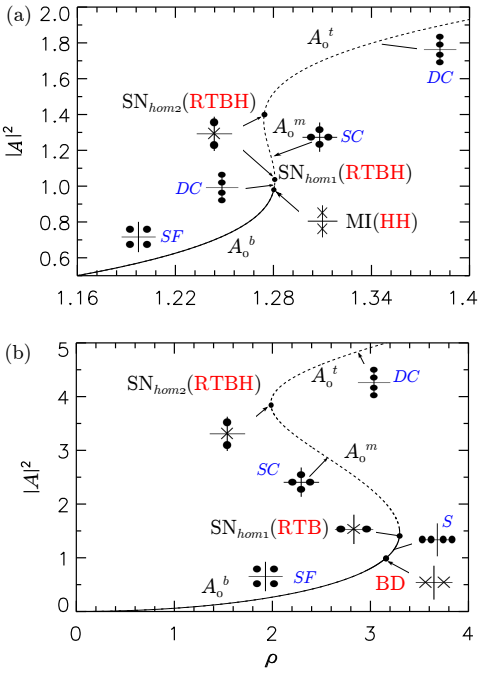

Figure 4.1: Spatial eigenvalues configuration for several values of θ. (a) $\sqrt{3} < \theta = 1.8 < 2$ and (d) $\theta = 4 > 2$

$SN_{hom,1}$ is a Rev.Takens-Bodganov-Hopf (RTBH) bifurcation with $\lambda_{1,2} = \pm ik_0$, $\lambda_3 = \lambda_4 = 0$ for $\theta < 2$ and a Rev.Takens-Bodganov (RTB) bifurcation with $\lambda_{1,2} = \pm q_0$ $\lambda_{3,4} = 0$ for $\theta > 2$. In contrast, $SN_{hom,2}$ is always a RTBH bifurcation for any value of θ. Thus, we expect LSs unfolding from the HH point in the configuration shown in Figure 4.1(a) and from the RTB bifurcation in the configuration of Figure 4.1(b).

For $\theta = 2$ the BD, HH, RTB and RTBH lines meet at the quadruple zero (QZ) point (see Section 2.3).

In Section 4.3 we study the LSs unfolding from the HH point for $\theta < 2$, and in Section 4.4 those unfolding from the $SN_{hom,1}$(RTB) for $\theta > 2$.

4.3 Bifurcation structure and stability of bright solitons for $\theta < 2$

Here we study the existence, stability and bifurcation structure for the LSs unfolding from the HH bifurcation present for $\theta < 2$. In this regime it is well known that there is a large number of states coexisting for the same set of parameters. First we show that the amplitude Eq.(3.29) has two branches of LSs, one with an odd number of peaks and another with an even number, both unfolding from the HH. These kind of states have oscillatory tails and are NSL-type of solitons. Later, using continuation techniques, we continue these states to values of parameters far from the HH point, confirming that the solution branches of these LSs are organized in a *homoclinic snaking* bifurcation structure [4, 7, 8]. After that, we also show that there exist asymmetric states interconnecting these branches of solutions.

4.3.1 Summary of weakly nonlinear analysis around HH for localized states

In Section 3.3, while studying the pattern solution unfolding from the HH, we found that the spatial dependent amplitude $\phi(X)$ of the first order perturbative solution around the HH bifurcation, namely

$$\begin{bmatrix} u_1 \\ v_1 \end{bmatrix} = \begin{bmatrix} a \\ b \end{bmatrix} \left(\phi(X)e^{ik_c x} + \bar{\phi}(X)e^{-ik_c x}\right), \tag{4.3}$$

was solution of the amplitude equation

$$\alpha_1 \frac{d^2\phi(X)}{dX^2} + \delta\alpha_2\phi(X) + \alpha_3|\phi(X)|^2\phi(X) = 0, \tag{4.4}$$

where α_i, $i = 1, 2, 3$ are complex functions of the control parameters (see Appendix C). To solve Eq.(4.4) we consider the ansatz $\phi(X) = Ae^{i\varphi}$, with $A \in \mathbb{R}^+$. With this ansatz two kinds of solutions can be found depending on whether A is a function of X or not. The situation $A \neq A(X)$ gives the pattern type of steady solution of Eq.(4.4). On the contrary, in the subcritical regime i.e $\theta > 41/30$, LSs can also be found if one consider that $A = A(X)$. In this case Eq.(4.4) becomes

$$\frac{d^2A(X)}{dX^2} = \beta_1 A(X) + \beta_2 A^3(X) \tag{4.5}$$

with $\beta_1 = -\delta\alpha_2/\alpha_1$ and $\beta_2 = -\alpha_3/\alpha_1$. This equation has a solution (see Appendix C)

$$\phi(X) = \sqrt{\frac{-2\beta_1}{\beta_2}}\text{sech}\left(\sqrt{\beta_1}(X - X_0)\right)e^{i\varphi} \tag{4.6}$$

and therefore, at leading order, the LS perturbative solution around HH is

$$\begin{bmatrix} U \\ V \end{bmatrix} = \begin{bmatrix} U_c \\ V_c \end{bmatrix} + \begin{bmatrix} \tilde{U}_2 \\ \tilde{V}_2 \end{bmatrix}(\rho - \rho_c) + \begin{bmatrix} u_1 \\ v_1 \end{bmatrix} \tag{4.7}$$

with

$$\begin{bmatrix} u_1 \\ v_1 \end{bmatrix} = 2\begin{bmatrix} a \\ 1 \end{bmatrix}\sqrt{\frac{-2\alpha_2(\rho - \rho_c)}{\alpha_3}}\text{sech}\left(\frac{1}{2}\sqrt{\frac{-\alpha_2(\rho - \rho_c)}{\alpha_1}}x\right)\cos(k_c x + \varphi)$$

(4.8)

The parameters are the same than in Section 3.3 and are given in the Appendix C. This solution is only valid in the neighborhood of HH, therefore just when $\epsilon \propto (\rho - \rho_c) \to 0$. Like the spatially periodic states, this family of localized solutions is parameterized by $\varphi \in S^1$[1], which controls the phase of the pattern within the sech$(\cdot)$ envelope. Within this asymptotic approximation this phase remains arbitrary, and there is no locking between the envelope and the underlying wavetrain at any finite order in ϵ. However, it is known that this is no longer the case once terms beyond all orders are included [17–19]. These terms break the rotational invariance of the envelope equation and result in a weak flow on the circle S^1. This flow in turn selects specific values of the phase: $\varphi = 0$ and $\varphi = \pi$. Moreover these phases are the only two phases that preserve the reversibility symmetry $(x, A) \mapsto (-x, A)$ of Eq.(4.1).

4.3.2 Homoclinic-snaking structure

As we said before the weakly nonlinear LSs solutions, calculated previously, are only valid for $\epsilon \to 0$, and therefore in the neighborhood of the HH bifurcation. Nevertheless, using continuation techniques it is possible to track these states to values of control parameters far from this point. In this way two branches of solutions are found: one branch is associated with $\varphi = 0$ and includes profiles with a local maximum in A at the midpoint, and the other branch is related

[1]The unit circle defined as $S^1 := \{e^{i\varphi} : 0 \leq \varphi < 2\pi\}$

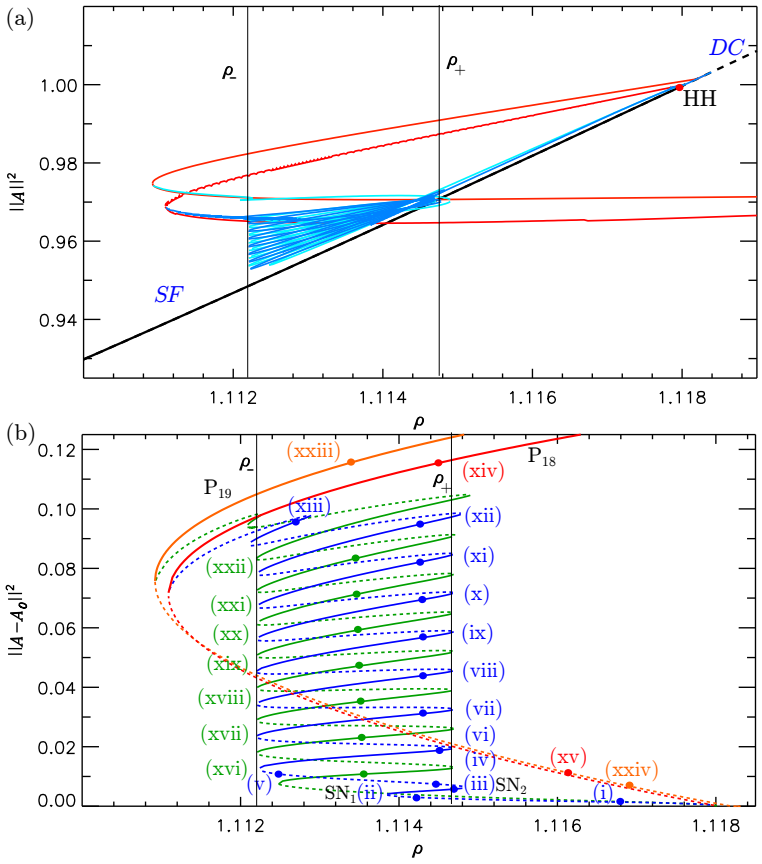

Figure 4.2: Homoclinic snaking bifurcation diagram for $\theta = 1.5$ and $L = 160$. In panels (a) we plot the diagram using $||A||^2$ and in panel (b) we have removed the HSSs A_0. The labels correspond to the profiles shown in Figure 4.3.

with $\varphi = \pi$ and includes profiles with a local minimum in A at the midpoint. We refer to the former branch as L_0 and the latter as L_π.

These two branches of LSs persist to finite amplitude where they undergo homoclinic snaking: sequence of saddle-node bifurcations that cause the branches to intertwine as they oscillate back and forth across a parameter range called the snaking or pinning region [4, 8]. This type of structure is shown in Figure 4.2 for domain size $L = 160$ and for a fixed value of detining $\theta = 1.5$. Here we use

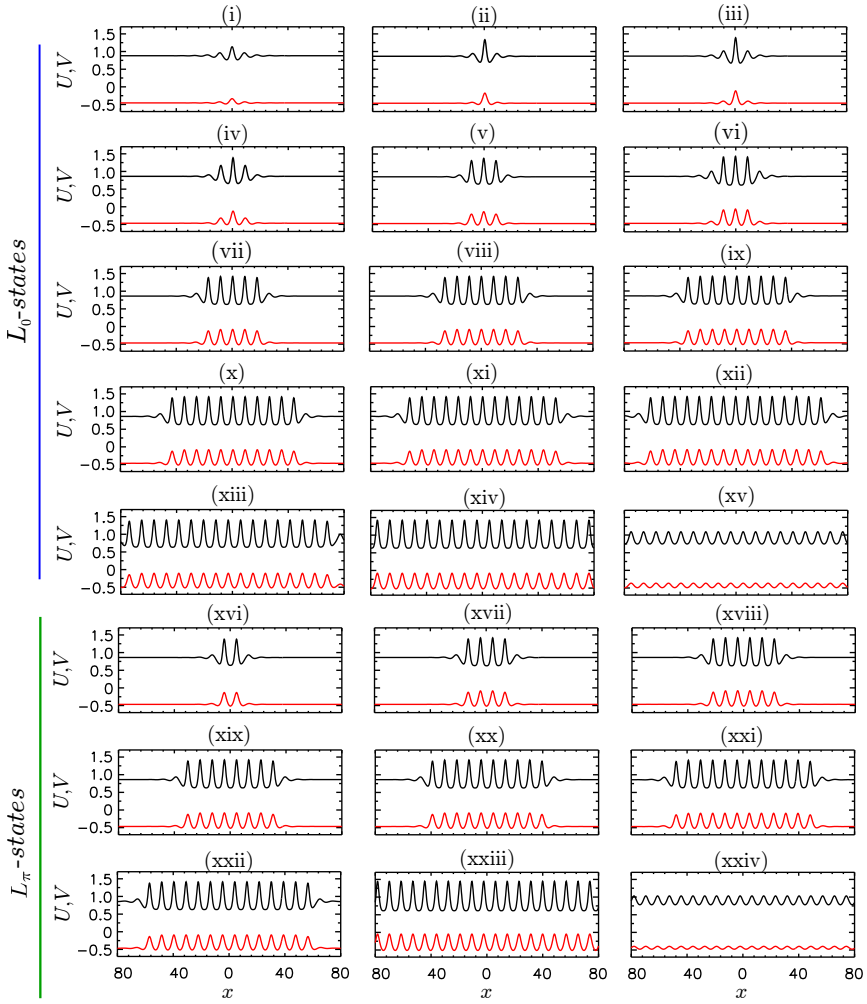

Figure 4.3: Bright solitons profiles for the $\varphi = 0$ (labels (i)-(xv)) and $\varphi = \pi$ (labels (xvi)-(xxiv)) families of solution branches, i.e. states with an odd and even number of peaks respectively, corresponding to labels shown in Figure 4.2.

as bifurcation parameter ρ, although the same type of diagrams appears if ρ is fixed and θ is modified, as shown in Ref. [11].

The diagram obtained corresponds to panel (a) of Figure 4.2. With this quantity

is not so easy to differentiate the different branches of solutions. Because of this in Figure 4.2(b) the same diagram is shown, but removing the background field (HSSs) A_0 from the norm. In this way the unfolding of the different branches is much more clear.

The two branches of symmetric LSs that bifurcate subcritically from HH, enter the snaking or pinning region, in which they undergo repeated saddle-node bifurcations as they snake across the region. These saddle-nodes converge exponentially, rapidly and monotonically to a pair of values ρ_- and ρ_+ (here shown with vertical lines), representing the boundaries of the snaking region.

A sequence of profiles corresponding to L_0 solutions is shown in Figure 4.3, for panels (i)-(xv). Initially these states unfold unstably and with a small amplitude (see profile in panel (i)) from HH. Its amplitude increases as decreasing the value of ρ and entering in the pinning region (profile in panel (ii)). Once reaching SN_1 the state becomes stable and increases its amplitude as increasing ρ. One example of this profile is shown in panel (iii). At SN_2, near ρ_+ the LS becomes again unstable and nucleates a pair of peaks or rolls, one on either side of the central peak (see profile in panel (iv)). As one proceeds up the branch to the next fold on the left ρ_- the new rolls grow to the height of the coexisting periodic state P (see profile (v)) and the branch turns around to repeat the process. In this way as one proceeds up the L_0 branches, the LSs repeatedly add rolls on either side symetrically each back-and-forth oscillation, increasing the width of the state by two wavelengths $2\pi/k_c$ as we can appreciate in panels from (vi) to (xv) of Figure 4.2. The L_π family of solutions shown in panels (xvi)-(xxiv) of Figure 4.3 undergoes the same process.

In an infinite system this process continues indefinitely as both branches approach the periodic state P_{k_c} that arises from the HH bifurcation together with $L_{0,\pi}$. In contrast, in a finite size domain like the one shown in Figure 4.2 ($L = 160$), both families of solutions $L_{0,\pi}$ connect with the pattern at a finite value of the norm. Thus, different configurations can occur. One of these phenomenon is that the $L_{0,\pi}$ states, instead of unfolding from the HH, do it directly from a secondary bifurcation of the pattern. Moreover, if the domain size is also small, the $L_{0,\pi}$ branches can end at different patterns, as it is actually our case, where the L_0 family ends at the pattern P_{18} and L_π in P_{19} with respectively 18 and 19 rolls each.

How the size of the domain affects the structure of the homoclinic snaking is very interesting not only from a theoretical point of view, but also from experimental one. In experiments the size of the optical cavities, either fiber cavities or microresonators, is always finite, and therefore, studing how the existence and

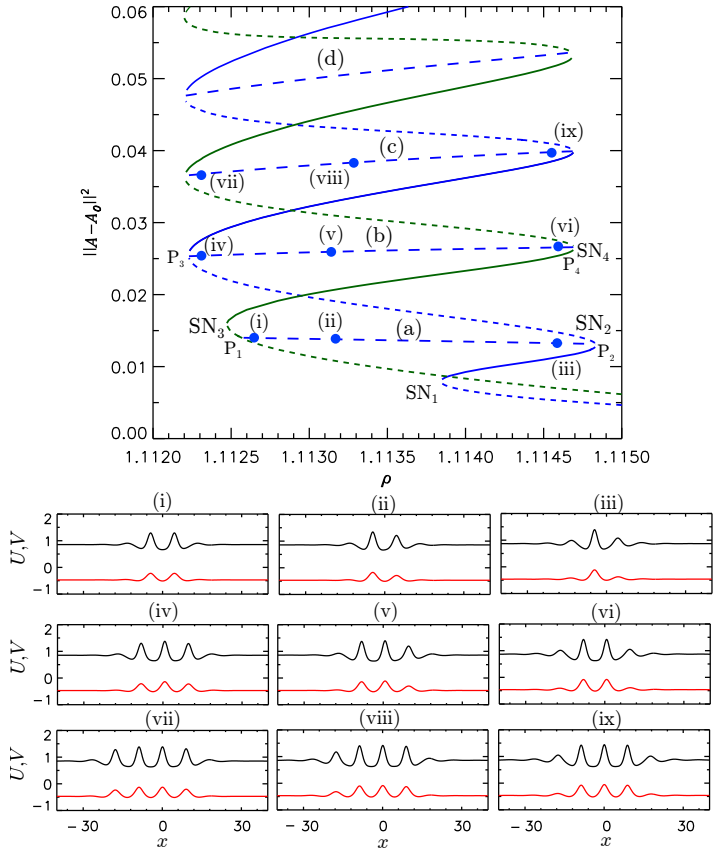

Figure 4.4: Bifurcation diagram showing the snakes-and-ladders structure for $\theta = 1.5$. Together with the $\varphi = 0$ and $\varphi = \pi$ family of solutions branches shown in Figures 4.3 there are extra branches of asymmetric states that connect both types of snaking through a Pitchfork bifurcation P.

stability of LSs is modified with the domain size is of great interest. For the interested reader we recommended Ref. [20], where the authors study this kind of phenomenon in the prototypical Swift-Hohenberg equation.

4.3.3 Snakes-and-ladder structure

Figure 4.4 shows a close-up view of the bifurcation diagram shown in Figure 4.2(b), although here $L = 80$. This diagram also includes a sequence of

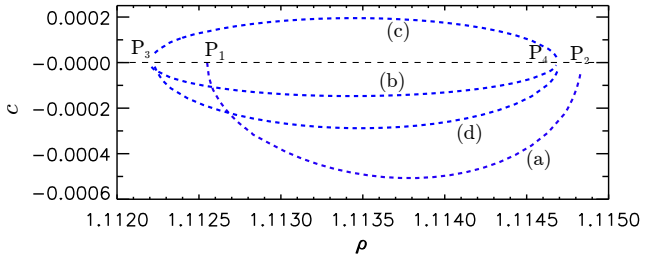

Figure 4.5: Velocity of the rung states as a function of ρ corresponding to the branches (a)-(d) of the snakes-and-ladders diagram shown in Figure 4.4. The velocity become zero at the pitchfork bifurcations P_i, $i = 1, ..., 4$ and is possitive or negative depending on the side at which the extra peak is nucleated.

so-called rung states branches which connect the L_0 and L_π branches of solutions in pitchfork bifurcations located near the saddle-node bifurcations and cross-link the two snaking branches. The profiles on the rung branches are similar to those on the snaking branches, but they are not symmetric with respect to the reflection $x \to -x$. This asymmetry can be observed in the panels (i)-(ix). The LL model does not have a gradient dynamics, and therefore any asymmetric solution, such as the rung states drifts with a constant velocity. These states are stationary solutions of Eq.(3.1) on the moving reference frame obtained through the transformation $x \to x - ct$ i.e. solutions of

$$-c\partial_x A = -(1 + i\theta)A + i\partial_x^2 A + iA|A|^2 + \rho. \tag{4.9}$$

The velocity as a function of ρ for those rung states is plotted in Figure 4.5, and it is calculated as part of the solution of Eq.(4.9), i.e. it is a nonlinear eigenvalue. The rungs are created at pitchfork bifurcations which break the $A(x) \to A(-x)$ symmetry of the $L_{0,\pi}$ states. Consequently each rung in the figure corresponds to two states related by reflection symmetry, and hence, of identical L^2-norm. Profiles from (iii) to (i), on branch (a), show how close to the SN_2 the single peak state belonging to the L_0-branch start to nucleate an extra peak on its right that grows in amplitude as decreasing ρ, until reaching the same height of initial peak at the SN_3 where it connect with $L_\pi-$snaking. The velocity of these states is negative (see Figure 4.5) and becomes zero at the pitchfork bifurcations. The behavior is similar for the states (vi)-(iv) on branch (b). Together to the previous states there are also branches of asymmetric rung states where the nucleated peak occurs on the left of the initial one. An example of such type of states (branch (c)) is shown in panels (vii)-(ix). Here, on the contrary, the velocity is possitive as shown in Figure 4.5.

This type of structure is known as *snake-and-ladders* structure [21]. As we will see in Chapter 6, when the reflection symmetry is broken the pitchfork bifurcations become imperfect and the degeneracy of the rungs states disappears leading to the breaking up of the snaking in a stuck of isolas [22, 23].

4.3.4 Heteroclinic tangles and homoclinic snaking

So far we have discussed the morphology of the homoclinic snaking and the stability of its different states. Behind this structure there is a very rich and complex phenomenon that can be understood in terms of geometrical objects as it was proposed in Refs. [4, 5] in the context of reversible systems. Here, following these works, we discuss briefly this mechanism. It is based on the *heteroclinic tangles* that are formed between the stable and unstable manifolds of the HSS A_0^b, and a family of pattern solutions $\mathcal{P}$. Those heteroclinic tangles are not only behind the formation of LSs, but also explains the way in which those states are organized in terms of an homoclinic snaking structure.

To start let us consider a Poincaré section for the system (2.8) containing the symmetry section $\mathcal{S} \equiv \text{fix}(R)$[2]. This section allows us to display trayectories and to depict the intersections of the stable and unstable manifolds with each other, and with $\mathcal{S}$. Adapted from Ref. [4], Figure 4.6 shows schematically the Poincaré section for different values of one control parameter of the system (here we fix the value of θ and we allow ρ to vary)[3]. In this picture the HSS A_0^b and the periodic orbit (pattern) solution $\mathcal{P}$ have been reduced to two saddle-type equilibrium on the symmetric section $\mathcal{S}$ (see Figure 4.6(a)). The Pincaré section intersects the pattern in two points, one corresponding to its maximum and the other to its minimum, although in Figure 4.6 we only show one of them, let say the one corresponding to the maximum. The intersection with the minimum would occur, in this picture, to the left of the fixed point A_0^b. Figure 4.6 also

[2]As we have seen in Appendix A, the symmetric section is the subspace defined by the points of the phase space which are invariants under the involution R, i.e.

$$\mathcal{S} \equiv \text{fix}(R) = \{x \in \mathbb{R}^n : R(x) = x\}. \tag{4.10}$$

In particular for the LL model the involution is given by (see Section 2.3):

$$R : (x, y_1, y_2, y_3, y_4) \mapsto (-x, y_1, y_2, -y_3, -y_4). \tag{4.11}$$

[3]The system described in Ref. [4] has a gradient dynamics. In contrast, the LL equation does not. Thus the way in which the invariant manifolds intersect in the later case, is not completely the same as the one depicted in Figure 4.6.

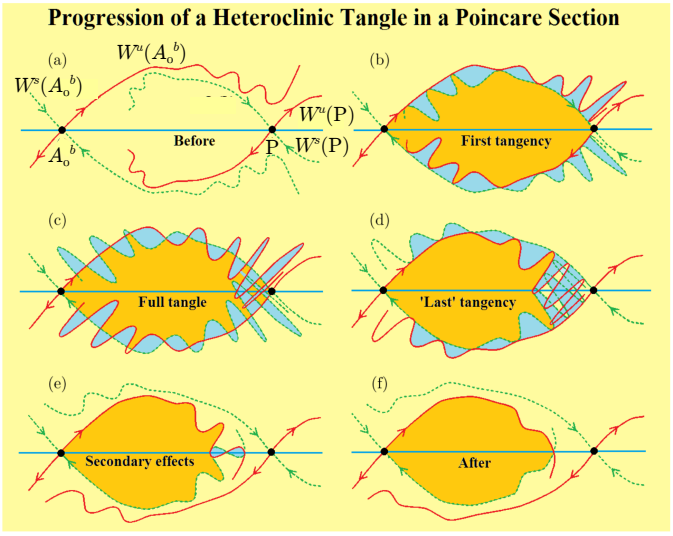

Figure 4.6: Schematic Poincaré section showing the heteroclinic tangle that generates the formation of an standard homoclinic snaking. This has been adapted from Ref. [4]. Panel (a) shows the situation before the heteroclinic tangle. In (b) the first tangency between the stable and unstable manifolds of A_0^b and $\mathcal{P}$ occurs. This is known as outer tangency and correspond to ρ_- in Figure 4.2, where the snaking is created. In panel (c) the full tangle occur and the homoclinic orbits are created. Panel (d) shows the inner tangency at ρ_+. Lately (see panel (f)) the invariant manifolds become disjoint ones more.

shows the tangle between the (two dimensional) unstable and stable manifolds of A_0^b i.e. $W^u(A_0^b)$ and $W^s(A_0^b)$, and (three dimensional) collection of stable and unstable manifolds of the periodic orbit $\mathcal{P}$ i.e. $W^s(\mathcal{P})$ and $W^u(\mathcal{P})$.

On variation of ρ, the manifold $W^u(A_0^b)$ will generically intersect $W^s(\mathcal{P})$ transversally creating an heteroclinic connection between A_0^b and one of the periodic orbits, let say $\mathcal{P}^0$ of $\mathcal{P}$. At this point the homoclinic snaking is created. Just before this intersection, both manifolds are tangent as shown in Figure 4.6(b), and in terms of homoclinic snaking this situation would correspond to one of the limits of the pinning region, for instance ρ_-, known as *outer tangency*.

Increasing a bit further the value of ρ leads to the full heteroclinic tangle shown in Figure 4.6(c) where $W^u(A_0^b)$ intersects $\mathcal{S}$ in the region of the periodic orbit. By reversibility, the intersection of $W^u(A_0^b)$ with $\mathcal{S}$ also implies the intersection of $W^s(A_0^b)$ with $\mathcal{S}$ and therefore the intersection of $W^u(A_0^b)$ with $W^s(A_0^b)$. The

occurrence of these intersections corresponds, therefore, to the formation of homoclinic solutions to A_0^b, but passing close to $\mathcal{P}^0$, i.e. a LS that belongs to the snaking branches L_0 (with a maximum in its center). Each homoclinic solutions has one more oscillation near the periodic orbit $\mathcal{P}$.

The formation of the LSs of the L_π-type, i.e. with a minimum in its center, follows the same porcess around the other intersection of $\mathcal{P}^0$ with $\mathcal{S}$.

In a system with gradient dynamics, as the SH equation, the asymmetric rung states are stationary and are described by the spatial dynamics. They are formed due to non generic intersections occuring outside the symmetric section $\mathcal{S}$. In contrast, in the LL equation, which does not have gradient dynamics, the rung states drift, and they are not solutions of the dynamical system (2.8), and therefore their formation is not described by this mechanism.

Although not shown in Figure 4.6, close to A_0^b homoclinic connections to the periodic solutions can also occur, which would resemble patterns containing holes [5, 6] (see Figure 2 in Ref. [6]).

Varying ρ even further leads, eventually, to the disappearance of the homoclinic connections, and therefore the disappearance of LSs. Figure 4.6(d) represents the *inner tangency* between the manifolds of A_0^b and $\mathcal{P}$ where the homoclinic snaking dissapears at the boundary ρ_+. Finally, increasing further ρ, the invariant manifolds become disjoint again as we can see in Figure 4.6(f). Each tangency point between manifold in Figures 4.6(b) and (d) represent the SNs along the ρ_- and ρ_+ boundaries of the pinning region.

4.4 Bifurcation structure and stability of bright solitons for $\theta > 2$

For $\theta > 2$ the HH bifurcation from where the LSs and patterns used to emerge becomes a BD transition for $\theta > 2$, from where no LSs can unfold. Another important change is that $\mathrm{SN}_{hom,1}$, that for $\theta < 2$ was a RTBH, becomes a RTB that admits KdV-type of soliton solutions. Moreover, in this regime, there are patterns bifurcating from resonances, such as double-center (DC) or saddle-center (SC) points that are relevant in the new organization of the solutions. The bifurcation structure found here is new, although it shares some similarities with the one found in Ref. [10], where the authors study the forced real Ginsburg-Landau equation. In that case, they called it *foliated snaking* and it is the term that we will also use here.

In what follows we first apply perturbative techniques to calculate an approximate solution for the soliton around the RTB point. As we will see, the resulting solution has a $\mathrm{sech}^2(\cdot)$ shape as was already predicted by the normal form theory in Section 2.4. After that we apply continuation techniques to build up the bifurcation diagrams that show the multistability of these type of states.

4.4.1 Weakly nonlinear analysis around RTB

In this section we compute weakly nonlinear LSs using multiple scale perturbation theory near the RTB bifurcation corresponding to $\mathrm{SN}_{hom,1}$. The LSs are solutions of the stationary LL Eq.(4.1). Following Ref. [24], we fix the value of θ and assume that the LSs at $\rho \approx \rho_b$, where $\rho = \rho_b$ corresponds to the $\mathrm{SN}_{hom,1}$ bifurcation, are captured by the ansatz

$$\begin{bmatrix} U \\ V \end{bmatrix} = \begin{bmatrix} U \\ V \end{bmatrix}^* + \begin{bmatrix} u \\ v \end{bmatrix}, \tag{4.12}$$

where U^* and V^* represent the HSS A_0 and u and v capture the spatial dependence. The $\mathrm{SN}_{hom,1}$ occurs at

$$I_b = \frac{1}{3}(2\theta - \sqrt{\theta^2 - 3}), \tag{4.13}$$

or in terms of ρ, at

$$\rho_b = \sqrt{I_b^3 - 2\theta I_b^2 + (1+\theta^2) I_b}. \tag{4.14}$$

The Taylor expansion of ρ about I_b

$$\rho(I_0) = \underbrace{\rho(I_b)}_{\rho_b} + \underbrace{\left(\frac{d\rho}{dI_0}\right)_{I_b}}_{=0}(I_0 - I_b) + \underbrace{\frac{1}{2}\left(\frac{d^2\rho}{dI_0^2}\right)_{I_b}}_{\delta_b}\underbrace{(I_0 - I_b)^2}_{\epsilon^2} + \cdots, \tag{4.15}$$

defines the small parameter ϵ that measures the deviation from the bifurcation point.

Because ρ_b has a maximum at I_b, we have

$$\left(\frac{d\rho}{dI_0}\right)_{I_b} = 0 \tag{4.16}$$

$$\delta_b = \frac{1}{2}\left(\frac{d^2\rho}{dI_0^2}\right)_{I_b} = \frac{\sqrt{\theta^2 - 3}}{2\rho_b} < 0. \tag{4.17}$$

From there the small parameter ϵ in terms of ρ reads,

$$\epsilon = \sqrt{\frac{\rho - \rho_b}{\delta_b}}, \tag{4.18}$$

We next introduce appropriate asymptotic expansions for each variable in function of ϵ as follows:

$$\begin{bmatrix} U \\ V \end{bmatrix}^* = \begin{bmatrix} U_b \\ V_b \end{bmatrix} + \epsilon \begin{bmatrix} U_1 \\ V_1 \end{bmatrix} + \epsilon^2 \begin{bmatrix} U_2 \\ V_2 \end{bmatrix} + ... \tag{4.19}$$

for the HSSs solutions and

$$\begin{bmatrix} u \\ v \end{bmatrix} = \epsilon \begin{bmatrix} u_1 \\ v_1 \end{bmatrix} + \epsilon^2 \begin{bmatrix} u_2 \\ v_2 \end{bmatrix} + ... \tag{4.20}$$

for the space-dependent terms.

We also allow the fields u_1, v_1, u_2 and v_2 to depend on the slow variable $X \equiv \sqrt{\epsilon}x$.

The next step would be to calculate first the HSS terms and next the space-dependent terms. These calculations are detailed in the following subsection and in Appendix D.

Asymptotics for the uniform states

Inserting the ansatz (4.19) in Eq. (4.1), we obtain the correction to the HSS A_0 at any order in ϵ.

At order $\mathcal{O}(\epsilon^0)$ we obtain expressions for U_b and V_b as a function of θ.

$$\begin{bmatrix} U_b \\ V_b \end{bmatrix} = \begin{bmatrix} \dfrac{\rho_b}{1 + (I_0 - \theta)^2} \\ \dfrac{(I_b - \theta)\rho_b}{1 + (I_b - \theta)^2} \end{bmatrix}. \tag{4.21}$$

At order $\mathcal{O}(\epsilon^1)$ we have

$$L \begin{bmatrix} U_1 \\ V_1 \end{bmatrix} = \begin{bmatrix} 0 \\ 0 \end{bmatrix}, \tag{4.22}$$

where

$$L = \begin{bmatrix} 0 & 0 \\ -(\theta - I_b - 2U_b^2) & -2 \end{bmatrix} \tag{4.23}$$

is a singular linear operator. Equation (4.22) has an infinite number of solutions that can be written in the form

$$\begin{bmatrix} U_1 \\ V_1 \end{bmatrix} = \mu \begin{bmatrix} 1 \\ \eta \end{bmatrix}, \tag{4.24}$$

where

$$\eta = -\frac{1}{2}(\theta - I_b - 2U_b^2) \tag{4.25}$$

and μ is obtained by solving the next order system. At $\mathcal{O}(\epsilon^2)$ we obtain the equation

$$L \begin{bmatrix} U_2 \\ V_2 \end{bmatrix} = \begin{bmatrix} 2U_1V_1U_b + (2V_1^2 + I_1)V_b - \delta_b \\ -(2U_1^2 + I_1)U_b - 2V_1U_1V_b \end{bmatrix}, \tag{4.26}$$

where $I_1 \equiv U_1^2 + V_1^2$. Because L is singular, the previous equation has no solution unless a solvability condition is satisfied. This condition is given by

$$\mu = \mu_b \equiv -\sqrt{\frac{\delta_b}{3\eta^2 V_b + 2\eta U_b + V_b}}. \tag{4.27}$$

Asymptotics for the space-dependent states

To calculate the space-dependent component of the weakly nonlinear state, we proceed in the same fashion. We insert the full ansatz for the asymptotic state, namely Eq. (4.12), into the system (4.1) and obtain, at order $\mathcal{O}(\epsilon^1)$,

$$L \begin{bmatrix} u_1 \\ v_1 \end{bmatrix} = \begin{bmatrix} 0 \\ 0 \end{bmatrix}, \tag{4.28}$$

where the first term on the left hand side vanishes. The general solution of this equation is

$$\begin{bmatrix} u_1 \\ v_1 \end{bmatrix} = \begin{bmatrix} U_1 \\ V_1 \end{bmatrix} \psi(X), \tag{4.29}$$

with $\psi(X)$ a function to be determined at the next order.

At order $\mathcal{O}(\epsilon^2)$

$$L \begin{bmatrix} u_2 \\ v_2 \end{bmatrix} = -\mathcal{P}_1 \begin{bmatrix} u_1 \\ v_1 \end{bmatrix} - \mathcal{P}_2 \begin{bmatrix} U_b \\ V_b \end{bmatrix}, \tag{4.30}$$

with the linear operators

$$\mathcal{P}_1 = \begin{bmatrix} -(2U_bV_1 + 2U_1V_b) & -(\nu\partial_X^2 + 6V_bV_1 + 2U_bU_1) \\ \nu\partial_X^2 + 6U_bU_1 + 2V_bV_1 & 2V_bU_1 + 2U_bV_1 \end{bmatrix} \tag{4.31}$$

and

$$\mathcal{P}_2 = \begin{bmatrix} -2v_1u_1 & -(3v_1^2+u_1^2) \\ 3u_1^2+v_1^2 & 2v_1u_1 \end{bmatrix}. \tag{4.32}$$

Because L is singular, Eq. (4.30) has no solution unless another solvability condition is satisfied. In the present case, this condition reads

$$\begin{bmatrix} 1 & 0 \end{bmatrix} \mathcal{P}_1 \begin{bmatrix} u_1 \\ v_1 \end{bmatrix} + \begin{bmatrix} 1 & 0 \end{bmatrix} \mathcal{P}_2 \begin{bmatrix} U_b \\ V_b \end{bmatrix} = 0. \tag{4.33}$$

After some algebra, Eq. (4.33) reduces to an ordinary differential equation for $\psi(X)$,

$$\alpha_1 \frac{d^2\psi(X)}{dX^2} + \alpha_2\psi(X) + \alpha_3\psi^2(X) = 0, \tag{4.34}$$

where

$$\alpha_1 = -\nu V_1, \quad \alpha_2 = -2\delta_b, \quad \alpha_3 = -\delta_b. \tag{4.35}$$

The solution of this equation (see Appendix D) coresponds to,

$$\psi(X) = -3\mathrm{sech}^2\left(\frac{1}{2}\sqrt{-\frac{\alpha_2}{\alpha_1}}(X - X_0)\right), \tag{4.36}$$

representing a hole located at $X = X_0$, hereafter at $X = 0$. Since $X \equiv \sqrt{\epsilon}x$ and $\epsilon \equiv \sqrt{\dfrac{\rho-\rho_b}{\delta_b}}$ the corresponding first order spatial correction is given by

$$\begin{bmatrix} u_1 \\ v_1 \end{bmatrix} = -3\mu_b \begin{bmatrix} 1 \\ \eta \end{bmatrix} \mathrm{sech}^2\left[\frac{1}{2}\sqrt{-\frac{\alpha_2}{\alpha_1}}\left(\frac{\rho-\rho_b}{\delta_b}\right)^{1/4} x\right]. \tag{4.37}$$

Then we have found that the LSs around the $\mathrm{SN}_{hom,1}$, at first order in ϵ can be approximated by

$$\begin{bmatrix} U \\ V \end{bmatrix} = \begin{bmatrix} U_b \\ V_b \end{bmatrix} + \mu_b\sqrt{\frac{\rho-\rho_b}{\delta_b}} \begin{bmatrix} 1 \\ \eta \end{bmatrix} \left[1 - 3\mathrm{sech}^2\left(\frac{1}{2}\sqrt{-\frac{\alpha_2}{\alpha_1}}\left(\frac{\rho-\rho_b}{\delta_b}\right)^{1/4} x\right)\right] \tag{4.38}$$

a bump solution on top the background HSS solution.

4.4.2 Foliated snaking

In this Section we analyze the bifurcation structure associated with the bump solution calculated previously (see Eq. 4.38) in the neighborhood of the $\mathrm{SN}_{hom,1}$

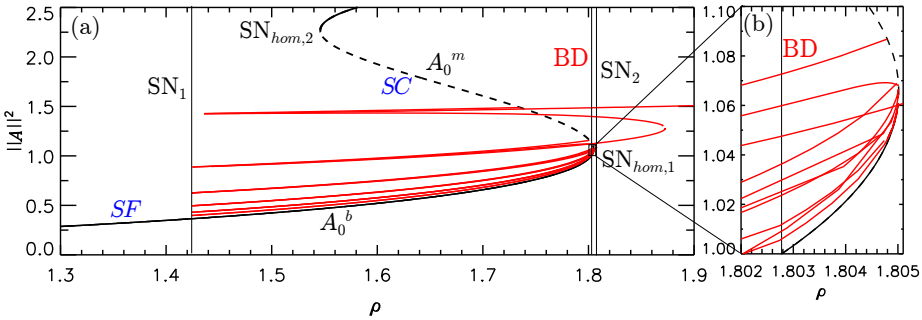

Figure 4.7: (a)Bifurcation diagram showing the L^2-norm, $||A||^2$ in function of ρ for $\theta = 2.5$. In Figure 4.8 we show the same branches when removing the background field A_0.(b) close-up view of panel (a) around the BD point.

(RTB) bifurcation. As we did in other Sections, we take this approximated solution as initial guess in a predictor-corrector algorithm [25] (see Appendix B), that allows us to build up the different solution branches unfolding from the $SN_{hom,1}$ bifurcation. Together to this single bump, there are states with several bumps also unfolding from the $SN_{hom,1}$ bifurcation or nearby as we will confirm.

The bifurcation digram that one obtains has the morphology shown in Figure 4.7(a) where the L^2-norm as function of ρ for a fixed value of detuning $\theta = 2.5$ is plotted. Figure 4.2(b) is a close-up view of panel (a) around the BD point. The unfolding becomes clear if instead of $||A||^2$ we plot $||A-A_0||^2$ as done in Figure 4.8(a). Panel (b) is close-up view of panel (a). One can appreciate that the morphology of this diagram is quite different to the homoclinic snaking one. Here there is a sequence of branches of solutions that unfold from the $SN_{hom,1}$ or nearby and that are interconnected in a similar fashion as patterns were connected in Chapter 3. One can also see that this diagram is very similar, at least in shape, to the one shown in Ref. [10], and therefore we will call it, as therein, *foliated snaking*.

Figure 4.9 shows the different states associated with the branches of Figure 4.8. Initially, the bump unfolding from the $SN_{hom,1}$ bifurcation, i.e. the $SN_{hom,1}$, has the shape shown in panel (i) of Figure 4.9. As the state proceeds up in the branch, that is decreasing ρ, it grows in amplitude (see panel (ii)) until reaching SN_1, where it becomes stable. This state continues growing in amplitude all the way up on the the stable branch until reaching SN_2. At the end of this branch the state has the shape shown in Figure 4.9(iii). In SN_2, the single peak connects with the structure of panel (iv) that is unstable. In this structure, another peak

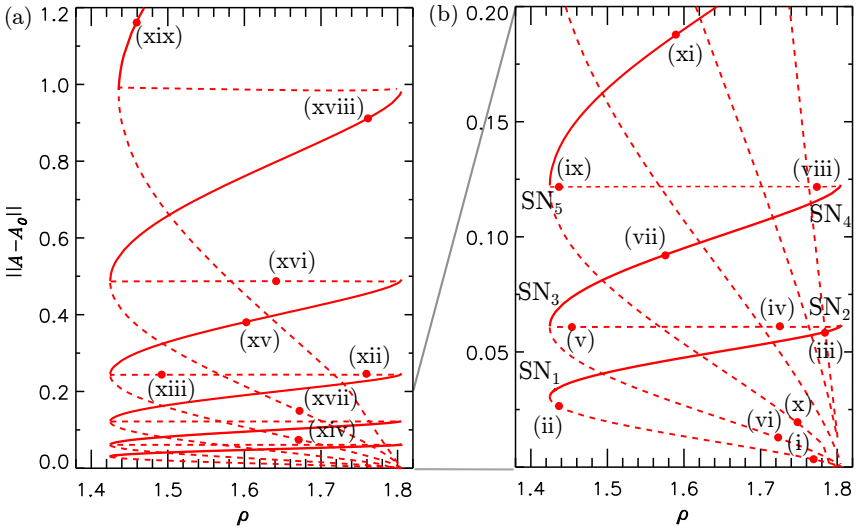

Figure 4.8: Same bifurcation diagram as the one shown in Figure 4.7 when removing the HSS solution A_0. Solid lines represent stable solutions and dashed lines unstable ones. The labels correspond to the profiles in Figure 4.9.

starts to grow at half of the domain size of the previous peak i.e. at $L/2$, and its amplitude grows as moving toward the left of that branch (see panel (v)) until it reaches the amplitude of the former one. This branch connects on the left with two branches close to the SN_3. One of those branches is unstable and goes down as increasing the value of ρ. Along this branch the two-peaks state decreases (see panel (vi)) in amplitude until reaching the $SN_{hom,1}$ form where it rises. The other branch, goes up and its states, like the one of panel (vii), are stable until reaching SN_4. After this fold the state (vii) loses stability and as shown in panel (viii) two new peaks start growing in-between the initial two resulting in a state with four peaks separated by $L/4$ each. Again, moving to the left on this branch, the new peaks grow in amplitude until reaching SN_5 (see panel (ix)) where it connects from below with a branch of unstable states like the one shown in panel (x), and from the top with a high amplitude state like the one shown in panel (xi). The nucleation of new peaks in-between the old ones is repeated each time that crossing the SNs on the right of the diagram, until filling with peaks all the domain. As we mention before, the structure with two peaks bifurcate from the $SN_{hom,1}$ together with the single soliton, however, the structures with more peaks (xi) with 4, (xv) with 8, (xvii) with 16 and (xviii)

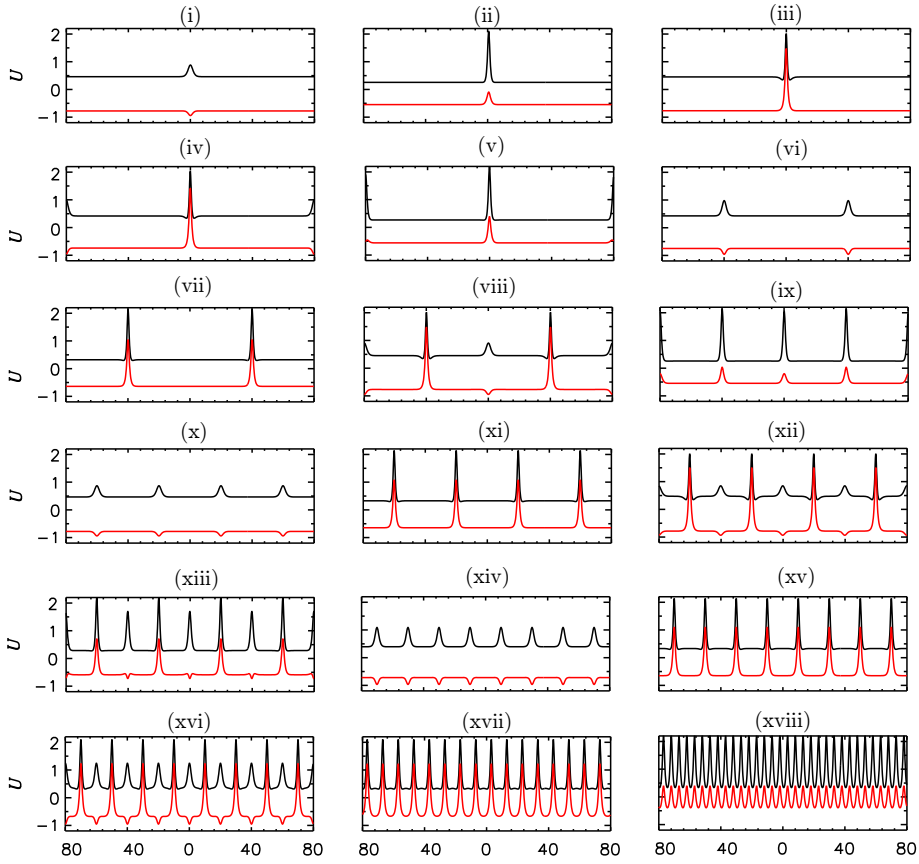

Figure 4.9: Profiles corresponding to the solution branches shown in Figure 4.7 and Figure 4.8.

with 32 behave as patterns and rise from the global bifurcation SC along the A_0^m of the HSSs solution. Initially the points of birth of those states are very close to $\mathrm{SN}_{hom,1}$ but as adding more peaks they moves up in the A_0^m branch. This situation can be observed in the diagram shown in Figure 4.7. This type of nucleation and reconnection of branches resembles the organization of patterns studied in Chapter 3, where it was found that there exist a sequence of FW instabilities reconnecting patterns which wavelengths are half the wavelength of the previous one. We will come back to this point later on this Section.

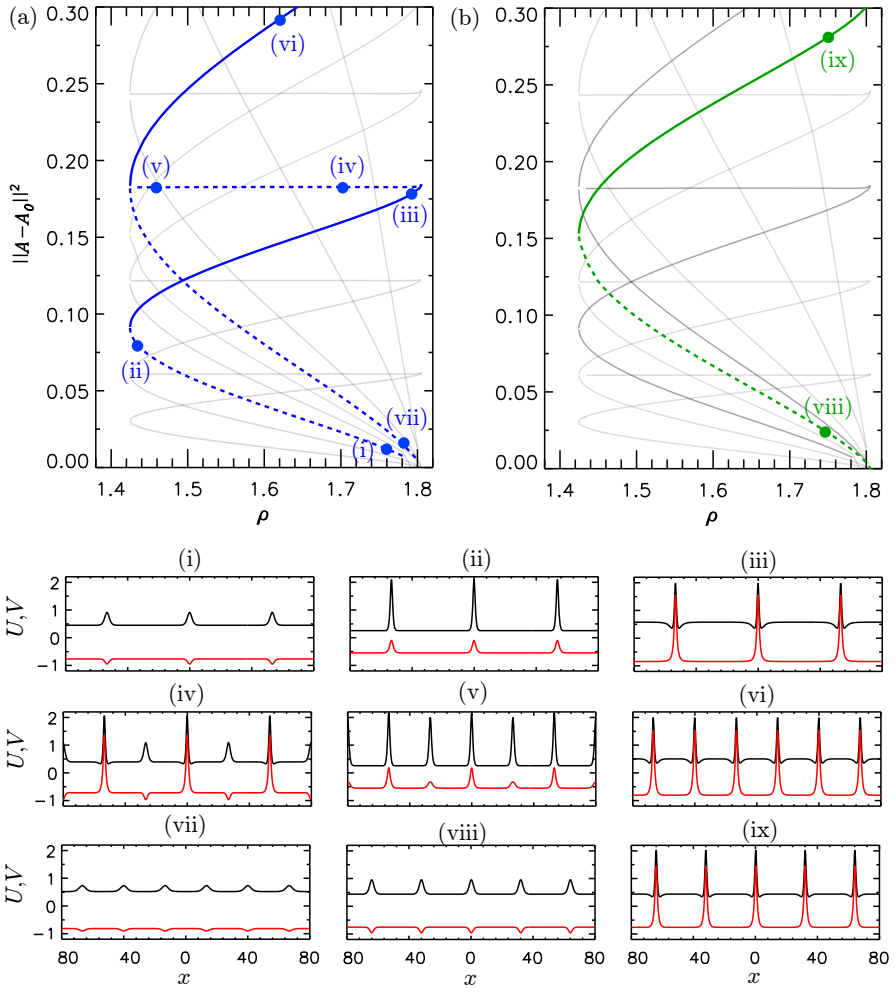

Figure 4.10: In (a) we show in blue the branches the foliated snaking corresponding to states shown in panels (i)-(vi). In (b) the snaking associated with states (vii)-(ix). In both the gray branches represent the foliated snaking calculated previously and shown in Figure 4.2.

Two examples of those snakings are shown in Figure 4.10(a) and (b). In the diagram (a) the branches corresponding to the states shown in subpanels (i)-(vi) are plotted in blue and in gray those of Figure 4.8 for comparison. Here the initial block is a 3 peaks state that undergoes the same type of nucleation that

the one shown before. In panel (b), the branches in green correspond to states (vi)-(viii) where the initial block is a states with 5 peaks. Thus we can deduce that any state with an odd number of equidistant peaks will behave in the same way, and each one ends in a different final pattern.

The *broom* bifurcation

At this point we can make the question of how is this new type of snaking related or connected with the homoclinic snaking studied previously for $\theta < 2$. In order to answer this, one can continue numerically any of the LSs of the homoclinic snaking shown in Figure 4.3 to higher values of θ and see how do they fit with the bifurcation skeleton shown in Figure 4.8.

For example we chose a two peak state for $\theta = 1.5$, like the one on panel (xvi) in Figure 4.3, and we continue it in ρ and θ until reaching $\theta = 2.5$. Once reached this value, we track in ρ the complete branch of solutions and we plot it on the top of the diagram shown in Figure 4.8. The result is shown in panel (a) of Figure 4.11. In red we show the first foliated snaking that we have calculated previously and in blue the two branches corresponding to the two-peaks state connected with the homoclinic snaking. The branches for this state have the same norm that the branches of the two peaks separated by $L/2$. The continuation of the top blue branch close to the SN gave us a lot of difficulties already for parameter values far from saddle-node SN_4. For clarifying this situation we decided, instead of potting the norm, to plot the separation distance between peaks for both the blue branches (I), (II) and the branch (III) corresponding to asymmetric states like those shown in Figure 4.9(v). The result can be seen in Figure 4.11(b) and (c). As we can see in panel (b), the separation distance for the states on the branch (III) remain almost constant with ρ. However, the separation distance of branch (II) increases drastically, when approaching the value of ρ at which the BD occurs, as one can appreciate looking at the panels (i)-(iii). Although it was not possible to continue this branch, the tendency of the branches suggest that it could collide with the branch (III), around the separation $d \approx 80$ at BD. Panel (c) shows a close-up view of the branch (II) and (I).

When approaching the BD transition the real part of the complex spatial eigenvalue of A_0^b, i.e. $k_0 \equiv \mathrm{Im}[\lambda] \to 0$ and therefore, the the wavelength of the oscillatory tails of the soliton profiles goes to infinity. As a result, in an infinite domain, two single-peak LSs will separate infinitely when approching the BD. In contrast, in a periodic domain, the they will separate until reaching $L/2$ at the BD transition, which is the situation that one can observe in Figure 4.11(b) and (c). This phenomenon corresponds to a dramatic non-local bifurcation known

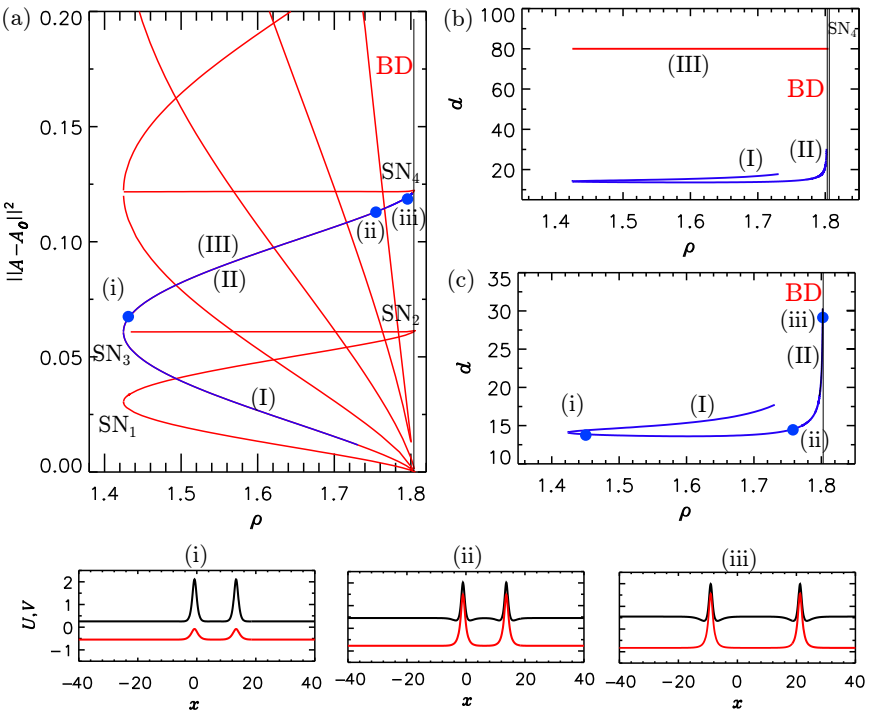

Figure 4.11: Bifurcation using d as bifurcation measure. We can see in panels (b) and (c), that plotting d, branches (II) and (III) in panel (a) are now distinguishable from each other. In (i) $\rho = 1.425$, in (ii) $\rho = 1.763$ and in (iii) $\rho = 1.802$

as *broom* bifurcation, at which an infinite number of homoclinic orbits emerges [27].

In the same way one can track any of the several-peaks solitons from low detuning (see Figure 4.2) to larger values of detuning and obtain the same divergence in the separation between the peaks.

Understanding bright solitons via patterns

We can try to understand the structure of the diagram shown in Figure 4.7 in terms of patterns and their bifurcation structure already found in Chapter 3. For $\theta > 2$ the HH bifurcation at $I_0 = I_c = 1$ becomes a BD transition. Now the first instability takes place for values $I_0 > I_c$, and always with critical wavenumber $k_c = 0$.

Analogously to the previous section, in this case, in addition to the new bifurcating homogeneous solution ($k = 0$), one can consider that above threshold pattern solutions with very large wavelength ($k \sim 0$) exist.

In finite systems with periodic boundary conditions $A(0) = A(L)$, being L the spatial period, the largest possible wavelength corresponds to $\lambda = L$. If the bifurcation is subcritical, and the pattern is highly nonlinear, this pattern can be interpreted as a single localized structure. In the following we choose $L = 160$.

When $k = k_c = 0$, the instabilities $\mathrm{MI}^{\pm}_{k_c=0}$ are given by

$$I_{t,b}(k_c = 0) = \frac{2}{3}\theta \pm \frac{1}{3}\sqrt{\theta^2 - 3}, \tag{4.39}$$

that in fact represents the positions of $\mathrm{SN}_{hom,1}$ (with the $-$ sign) and $\mathrm{SN}_{hom,2}$ (with $+$). The pattern with $k = \Delta k = 2\pi/\lambda = 2\pi/L$ appears at $\mathrm{MI}^{-}_{\Delta k}$, which is closer to $\mathrm{SN}_{hom,1}$ the larger the system is, and disappears at $\mathrm{MI}^{+}_{\Delta k}$ close to $\mathrm{SN}_{hom,2}$. Nevertheless, as discussed above, this pattern seems to reconnects with another pattern with $k = 2\Delta k$ ($\lambda = L/2$) as we can observe in Figure 4.7 and Figure 4.9(iv)-(v). In this case, the branches of LSs corresponding to states (i)-(ii), and (iii) in bifurcation diagram of Figure 4.7 have to be compared with the branches of patterns P_{k_c} (in red) in Figure 3.12(b) and (c). After SN_2, the state shown in Figure 4.9(iv)-(v) appears, and here, another peak separated from the previous one a distance $L/2$ starts to grow. For decreasing ρ, state (v) collides in a FW_1 instability to $\lambda/2$ i.e. $\lambda = L/2$ very close to SN_3, with the branches corresponding to states (vi) and (vii). These last two states in Figure 4.7 would be analogous to P_{2k_c} (in blue) in Figure 3.12. In the same fashion, the branch corresponding to states (vii) has a SN_4 where again two new peaks start to grow all of them separated by $L/4$ (see panel (viii) Figure 4.9). Again we found that decreasing ρ, the branch corresponding to the state (viii) joins branches (ix) and (x), in another FW_2 very close to SN_5. These structures would correspond to a pattern with $\lambda = L/4$. This kind of structure will be repeated continuously and at every FW instability the number of peaks in the structure will be doubled. Note that, as shown in Figure 3.3 and Figure 3.5, points $\mathrm{MI}^{\pm}_{\Delta k}$, $\mathrm{MI}^{\pm}_{2\Delta k}$, $\mathrm{MI}^{\pm}_{4\Delta k}$, for $\theta \geq 2$, would be all very close to $\mathrm{SN}_{hom,1}$ and $\mathrm{SN}_{hom,2}$ if the system is very large. For this reason patterns with $\lambda = L$, $\lambda = L/2$ and $\lambda = L/4$ should all appear and disappear for very similar parameter values.

Accordingly, if in a periodic system of period L, we accept that for $\theta \geq 2$ the one peak localized structure is in fact a pattern with $\lambda = L$, finite-wavelength-like instabilities would connect the pattern with wavenumber Δk with the one with $2\Delta k$, where the latter correspond to two peaks separated a distance $L/2$.

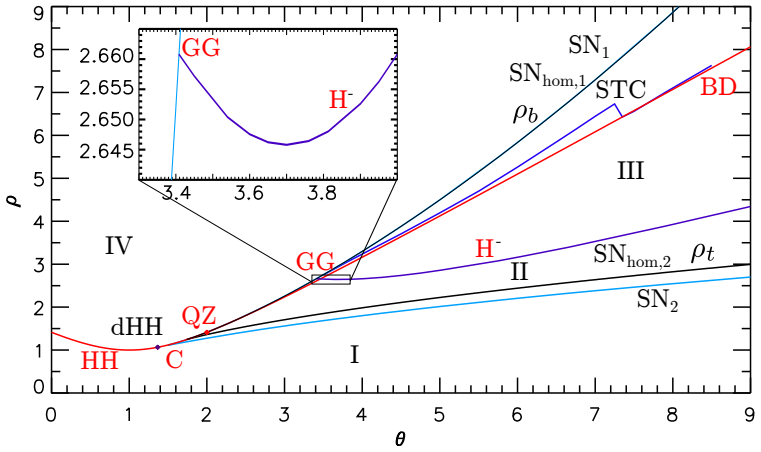

Figure 4.12: Phase space in (θ, ρ)-parameters. The bifurcation lines: $SN_{1,2}$ represent the region of existence of bright solitons; $SN_{hom,1,2}$ are the saddle-node bifurcations of the HSSs solution, also labeled as $\rho_{b,t}$; H^- stands for supercritical Hopf bifurcation that emerges from the GG (Gravilov-Guckenheimer) codimension-two bifurcation; HH is a Hamiltonian-Hopf bifurcation or a MI in temporal dynamics; dHH is a degenerate HH bifurcation occuring at $\theta = 41/30$, where the pattern becomes subcritical; BD represents a Belniakov-Devaney transition; QZ is a quadruple-zero bifurcation; C a cusp bifurcation for the HSSs and STC the onset of the spatio-temporal chaos. The different dynamical regions I-IV are described in Section 4.5. The inset represent a close-up view of the unfolding of the H^- bifurcation from the GG point.

4.5 Bright solitons in the parameter space

Tracking each bifurcation point in the bifurcation diagram as function of θ one obtains the parameter space shown in Figure 4.12. The red solid line defined by Eq.(4.2) corresponds to a HH bifurcation for $\theta < 2$ and a BD transition for $\theta > 2$. Together with this line there are other two bifurcation lines corresponding to the saddle-node bifurcations of the HSSs solution, namely $SN_{hom,1}$ and $SN_{hom,2}$, and those corresponding to the LSs, namely SN_1 and SN_2. As we can appreciate from Figure 4.7, the region of existence of the different branches of solutions can be described by the saddle-nodes of the single soliton state SN_1 and SN_2. Therefore, the area between these two saddle-nodes bifurcation determines the region of multistability of LSs. Looking at Figure 4.12 we see that upon increasing θ the region of existence of these states becomes broader.

We distinguish four main dynamical regions, labeled I-IV in the phase diagram in Figure 4.12, in terms of the existence of HSSs and bright LSs:

- Region I: The only attractor of the system is the stable bottom HSS A_0^b. No bright solitons or top HSS A_0^t exist. This region spans the parameter space $\rho < \rho_c$ for $\theta < \sqrt{3}$ and $\rho < \rho_t$ for $\theta > \sqrt{3}$[4].
- Region II: The HSS solution branches A_0^b, A_0^m and A_0^t coexist, and multistability between bright solitons is found. This region spans the parameter space $\rho_{\mathrm{SN}_2} < \rho < \rho_{\mathrm{SN}_1}$ for $\theta > \sqrt{3}$.
- Region III: Here the bright LSs become unstable through supercritical Hopf bifurcation H^- (see purple line in Figure 4.12), generating a oscillatory regime. This region spans the parameter space $\rho_{\mathrm{H}^-} < \rho < \rho_{\mathrm{STC}}$.
- Region IV: This region spans the parameter space $\rho > \rho_c$ for $\theta < \sqrt{3}$, where A_0 is modulational unstable, and $\rho > \rho_b$ for $\theta > \sqrt{3}$, where the only HSS solution is A_0^t. In this region no bright LSs exist and spatio-temporal chaos develops.

Regions III and IV are the main region of interest in this chapter. In the next section we will show that region III can be further subdivided in subregions reflecting the different dynamics that the bright solitons undergo, such as amplitude oscillations of different periods, temporal chaos and spatio-temporal chaos.

4.6 Oscillatory and chaotic dynamics for bright solitons

So far we have focused on the study of stationary LSs and their bifurcation structure. In this Section we will see that these states can undergo oscillatory instabilities that can make them oscillate in time. The presence of these instabilites modifies the region of existence of stable LSs and generates a very rich dynamical behavior. The oscillatory instability consist in supercritical Hopf H^- bifurcations that lead to stable temporal oscillations resembling breathings of the individual solitons. To characterize these dynamics we combine both time stability analysis and direct integration of the LL equation. We also compute secondary bifurcations of these oscillation clarifying the different oscillatory regimes.

In Figure 4.13 we show the foliated snaking diagram for $\theta = 3.5$. For this value, each branch of stable states becomes oscillatory unstable at a different H^-, bifurcation that occur for very similar values of the driving amplitude around $\rho = 2.6532$. This instability leads to oscillatory states like those shown in Figure 4.14.

[4] ρ_b and ρ_t represent the possition of the $\mathrm{SN}_{hom,1}$ and $\mathrm{SN}_{hom,2}$ respectively

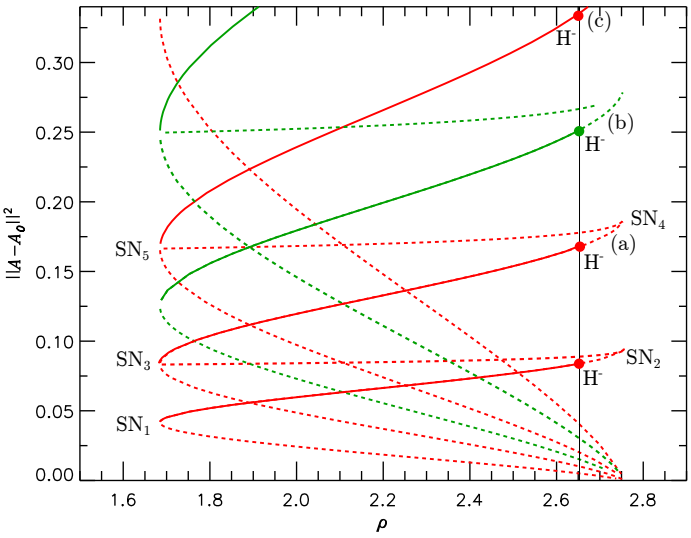

Figure 4.13: Bifurcation diagram for $\theta = 3.5$. The Hopf bifurcations are represented by H in the figure. The labels (a)-(c) correspond to the oscillatory states shown on Figure 4.14 for $\rho = 2.67$.

From bottom to the top in the diagram of Figure 4.13 the first soliton that start to oscillates is the single-peak soliton (not shown here). Going up in the branches of the diagram one sees how the Hopf bifurcations destabilize the states with two, three and four equidistant peaks, resulting in the oscillatory states that one can observe in Figure 4.14. The different peaks of those states oscillates synchronously or not depending on the control parameters. On top of these states there exist a wide variety of oscillatory states coexisting for the same value of the parameters. Three of these possible states are shown in Figure 4.15. The reason of the existence of these states is that when a single soliton oscillates generates spatial oscillations in its tails that allow the pinning of a random number of states due to the the overlapping of the tails of one soliton with those of its mate's core. This behavior was studied in an equivalent model in Ref. [28] and in the Sine-Gordon equation in Ref. [29].

Dynamics of a single-peak localized state

In what follows, instead of focusing in the collective dynamics generated by a number of breathers, we study how these oscillatory instabilities get modified

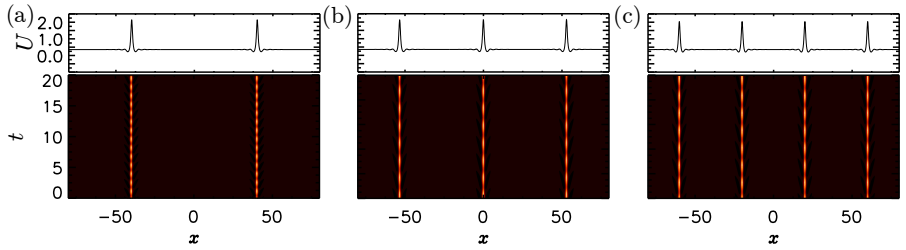

Figure 4.14: Heat maps showing the spatio-temporal evolution of the real part (U) of an oscillatory state for $\theta = 3.5$ and $\rho = 2.67$. The labels correspond to those shown in Figure 4.13.

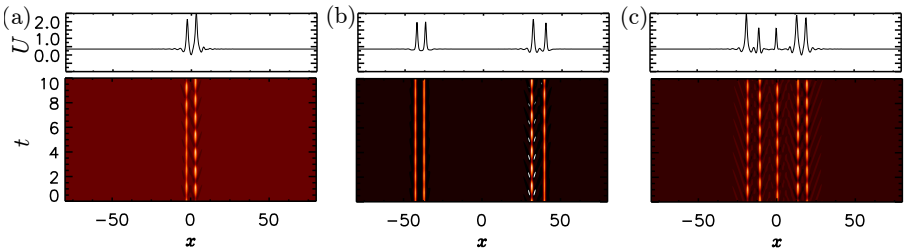

Figure 4.15: There is a large variety of oscillatory states for the same values of parameters. In this figure we show some of those possible states.

when changing the detuning θ for a single soliton. Figure 4.16 shows different slices of the parameter space in Figure 4.12. Here we plot the $||A||_{\text{sup}} \equiv \max(|A|)$ instead of the L^2-norm in order to improve the clarity of the diagrams, and we use crosses to indicate the maximum and minimum of the amplitude of the oscillatory states. The diagram in Figure 4.16(a) corresponds to a value $\theta = 3.5$, just the same value than for the foliated snaking shown in Figure 4.13. For clarity we have just plotted the branches connected with the single peak soliton (in red) and the HSSs (in black). The branch of stable solitons become unstable in the supercritical Hopf bifurcation H^- where an oscillatory state arises. The amplitude of the oscillations of these states increases with ρ, until it becomes unstable to spatio-temporal chaos (STC) when overpassing the $\text{SN}_{hom,1}$. After that point the STC persist for high values of ρ. At $\theta = 5.5$ (see Figure 4.16(b)) the region of existence of the solitons becomes broader, although in most of the region the solitons are unstable due to the presence of the Hopf bifurcation. Now the amplitude of the oscillations that arise in H^- is bigger and the STC occurs before the $\text{SN}_{hom,1}$.

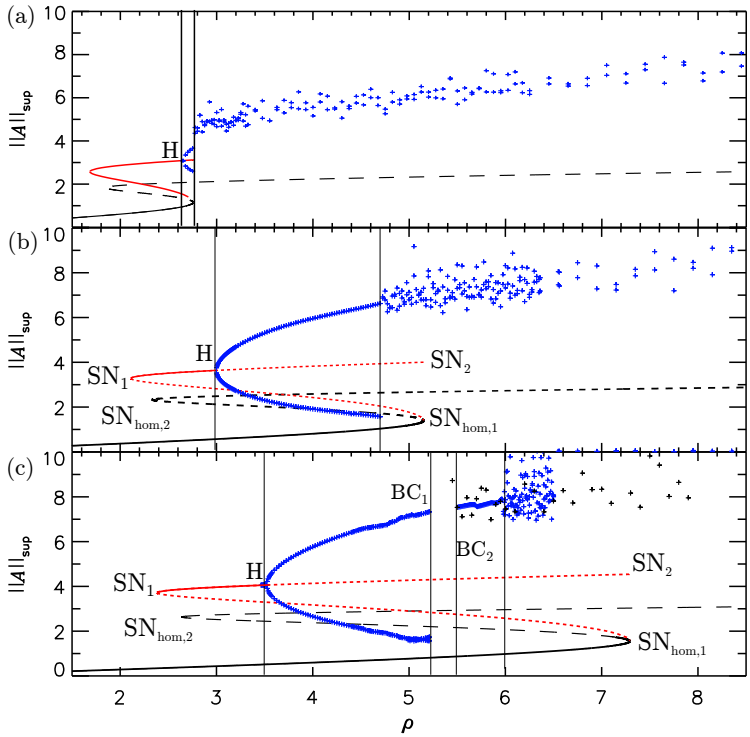

Figure 4.16: Bifurcation diagram showing the $||A||_{\text{inf}}$ and $||A||_{\text{sup}}$ for three different values of detuning, namely $\theta = 3.5$ in (a), $\theta = 5.5$ in (b) and $\theta = 7$ in (c). In black we show the HSS A_0, in red the branches corresponding to the one-peak bright soliton unfolding unstably from RTB bifurcation at $\text{SN}_{hom,1}$. H stands for the Hopf bifurcation where the bright soliton becomes unstable to amplitude oscillations.

Figure 4.16(c) shows the situation for $\theta = 7$. Here the behavior of the oscillatory states changes drastically in comparison to the previous cases. Now, together with the increasing of the amplitude of the oscillations, the cycle undergoes a period-doubling (PD) bifurcation, starting a route to a very complex dynamics passing through a sequence of oscillatory states characterized by period-2, period-4 oscillations, and temporal chaos, with periodic windows of period-5, period-10 oscillations, before disappearing possibly in a homoclinic bifurcation or boundary crisis (BC_1) [30, 31]. Figure 4.17 shows contour plots with the different oscillatory dynamics. Between BC_1 and BC_2, the only attractor of the system is the HSSs branch A_0^b. After BC_2 stable oscillations exist until they

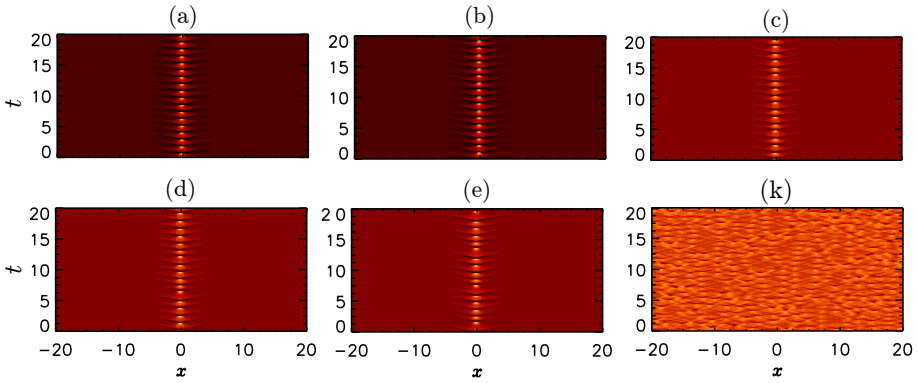

Figure 4.17: Heat maps showing the oscillatory and chaotic dynamics for $\theta = 7$ corresponding to the bifurcation diagram shown in Figure 4.18. These dynamics correspond to period-1 oscillations in (a) for $\rho = 4.525$, period-2 in (b) for $\rho = 4.6$, period-4 in (c) for $\rho = 4.8$, temporal chaos in (d) for $\rho = 4.9$, period-5 oscillations in (e) for $\rho = 5.2$ and spatio-temporal chaos in (k) for $\rho = 6$.

disappear into STC. Let us discuss this process in detail, first starting with the cycle emerging from H^- on the left of the diagram and after studing the cycle that reappears and becomes STC on the right part of the diagram. For that we show in Figure 4.18 a zoom of the diagram in Figure 4.16(c) that capture the change in the dynamics of the oscillatory states. The iformation presented in this figure is complemented by Figures 4.19 and 4.20 showing a series of panels characterizing the dynamics of the cycle at different values of ρ. From left to right we show a time series of the evolution of the maximum of the soliton, the Fourier transform of this time series , and a two-dimensional phase space projection onto $(U(x_0,t), V(x_0,t))$, being x_0 the position of the center of the structure. Panel (a) in Figure 4.19 correspond to the situation at $\rho = 4.525$ in Figure 4.18 labeled with (a). The time trace and the frequency spectrum in Figure 4.19(a) shows a limit cycle with a singel period. In the phase space shown in Figure 4.19 we observe a fixed point A_0^b, a saddle point S corresponding to the unstable soliton, and a periodic orbit corresponding to the cycle. For $\rho = 4.6$ panel (b) shows (corresponding to label (b) in Figure 4.18) the time series and its spectrum which indicates that the cycle has two periods as one can also appreciate looking at the phase space projection. Panel (c) corresponds to the situation shown in Figure 4.18 for $\rho = 4.8$ where the cycle has undergone another period-doubling resulting in a cycle with period-4. Later, for $\rho = 4.9$ the cycle becomes irregular, possibly a chaotic attractor, as we can see in panel (d) of Figure 4.19.

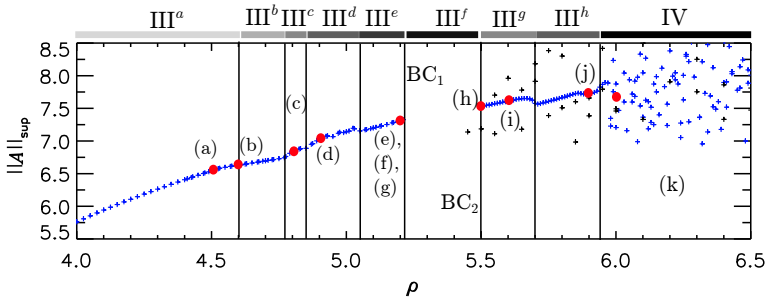

Figure 4.18: Detail of the bifurcation diagram of Figure 4.16(c) for $\theta = 7$. Vertical lines corresponds to the separation between period-1 oscillations in region III^a, period-2 oscillation (region III^b), period-4 oscillations (region III^c), temporal chaos (region III^d), period-5, period-10 oscillations followed by temporal chaos (region III^e), region III^f where only A_0^b is stable, region III^g where we find again temporal chaos, and period-4 oscillations, region III^h with period-2 oscillations and spatio temporal chaos in region IV. The labels from (a) to (k) correspond to dynamics shown in Figures 4.19 and 4.20.

In panel (e) for $\rho = 5.2$ a periodic window of period 5 is shown, and in panel (h) for $\rho = 5.21$ a periodic window of period-10. For $\rho = 5.221$ the cycle becomes again irregular (see panel (g)). Finally increasing a bit further the value of ρ, the irregular cycle collides with the unstable soliton S and disappears via an homoclinic bifurcation or a BC. As we can appreciate in Figure 4.18 the region II in which the only attractor is the HSS dissapears suddenly and a new chaotic attractor appears via another BC. This is the situation shown in Figure 4.20(h) for $\rho = 5.5$ corresponding to the same label in Figure 4.18. For $\rho = 5.6$ (see panel (i)) a cycle of period-4 appears. This cycle comes from a period-doubling of the period 2 cycle shown in panel (j) for $\rho = 5.8$. Increasing further the value of ρ there is a transition to spatio-temporal chaos as one can see in panel (k). At this point we can differentiate eight main dynamical subregions:

- III^a: Oscillatory solitons with a single period.
- III^b: The soliton oscillates with period-2.
- III^c: The soliton oscillates with period-4.
- III^d: Region of temporal chaos with periodic windows of periodicity-5 and 10.
- III^e: Temporal chaos and the soliton oscillates with period-4.

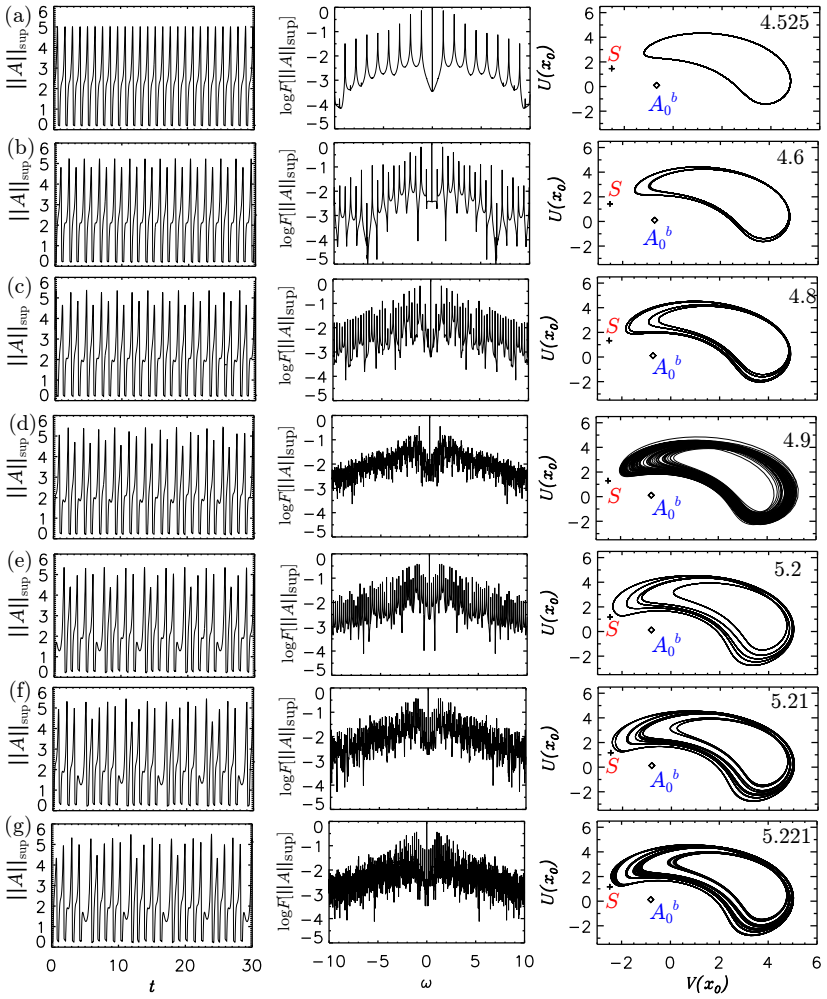

Figure 4.19: Oscillatory and chaotic dynamics for $\theta = 7$ corresponding to the bifurcation diagram shown in Figure 4.18. From left to right: temporal trace of $||A||_{\sup}$, its frequency spectrum that allows us to differentiate between the different types of temporal periodicity, and the two-dimensional phase space considering the projection of the dynamics on the variables $U(x_0)$ and $V(x_0)$, with x_0 representing the position of the center of the peak. The pump values are $\rho = 4.525$ in (a), $\rho = 4.6$ in (b), $\rho = 4.8$ in (c), $\rho = 4.9$ in (d), $\rho = 5.2$ in (e), $\rho = 5.21$ in (d), and $\rho = 5.221$ in (g).

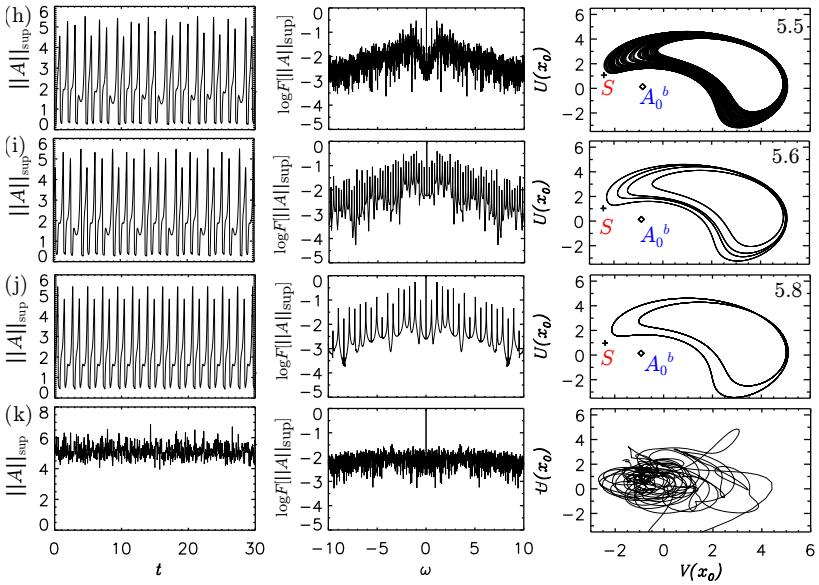

Figure 4.20: Same that in Figure 4.19 but for $\rho = 5.5$ in (h), $\rho = 5.6$ in (i), $\rho = 5.8$ in (j) and $\rho = 6$ in (k) (spatio-temporal chaos).

- III^f: The only attractor of the system is A_0^b.
- III^g: The soliton oscillates with period-2.
- III^h: Region with spatio-temporal chaos.

The scenario can be even more complex for higher values of θ [9]. We have found that the supercritical Hopf H$^-$ is born from a codimension-two bifurcation point called Gravilov-Guckenheimer (GG) or Fold-Hopf bifurcation [32, 33]. At this bifurcation two codimension-one bifurcations, namely the saddle-node SN$_2$ and the Hopf bifurcation H$^-$ occur simultaneously, and the temporal eigenspectrum of the linear operator associated to the LL equation and evaluated in that point has three eigenvalues $\lambda_{a,b} = \pm i\lambda$ and $\lambda_c = 0$. Thus, the Hopf bifurcation line emerges from the GG point, and although the Hopf line looks like it terminates perpendicularly to SN$_2$, the inset in Figure 4.12 shows that in fact it approaches the GG point in a tangential manner, as expected for a GG point. One of the possible unfoldings of this bifurcation shows that complex temporal dynamics as Shilnikov chaos arise from this situation [33]. In future work we will try to

identify the unfolding that we have in our case and therefore determine if the complex temporal dynamics is originated, like the H^-, in the GG bifurcation.

4.7 Conclusions

In this chapter we have studied in detail the bifurcation structure and stability of bright solitons arising in the anomalous GVD regime of the LL equation. In this regime, bright solitons arise from two different bifurcations, namely a Hamiltonian-Hopf (HH) bifurcation, from where a pattern solutions also rises (as studied in Chapter 3), and from the $SN_{hom,1}$, a reversible Takens-Bodganov (RTB) bifurcation The HH bifurcation only exist for $\theta < 2$, and the RTB only for $\theta > 2$. As we saw in Chapter 2, all these bifurcation lines arise from a QZ codimension-two bifurcation point.

For $\theta < 2$, the bright solitons unfolding from HH are of NLS-type. The formation of these structures comes from the intersection of the stable and unstable manifolds of A_0^b (see Section 4.2 and Refs. [4–6]). As predicted from normal form theory there are two families of bright solitons, one with an odd number of peaks, that we have previously refered as L_0, and another with an even number of peaks, L_π organized in two curves that snakes back and forward, forming a bifurcation structure known as homoclinic snaking [4, 7, 8]. Together with that two families of states, there are also rung branches of solutions corresponding to asymmetric states that interconnect both snaked curves. The resulting bifurcation structure is now known as *snakes-and-ladders* structure [21].

For $\theta > 2$, bright solitons unfold from a RTB bifurcation at the $SN_{hom,1}$ and they are of KdV-type of solitons. These solitons are organized in a new type of bifurcation structure that we have called *foliated snaking* following Ref. [10]. The single soliton, after arising from the RTB, grows in amplitude and at a certain point it develops an extra peak separated from the previous one by exactly $L/2$. When tracking this new state back and forward we find that it is also connected with another structure that have four peaks equally separated from each other by $L/4$. This process is repeated and each time a new state appears with twice the number of peaks of the previous state. This type of behavior resembles the process observed for the pattern solution when undergoing finite-wavelength instabilities (FW). Therefore, we think that the origin of this foliated snaking is closely related with the bifurcation structure of patterns.

For hight values of θ solitons become unstable to oscillations via a supercritical Hopf bifurcation. We have found that this Hopf bifurcation emanates from a Gravilov-Guckenheimer bifurcation, a codimension-two point where a saddle-

node and the Hopf collides in parameter space. These oscillatory regimes exist not only for single solitons but also for structures with any number of peaks. The oscillations undergo a series of secondary bifurcations starting a route to temporal chaos. Along these bifurcations the dynamics increase in complexity. Moreover, in the anomalous regime, spatio-temporal chaos is also present.

We expect that these results to be useful for experimentalist in the frequency combs comuninty, specially those working on microresonators.

References

[1] A.J. Scroggie, W.J. Firth, G.S. McDonald, M. Tlidi, R. Lefever and L.A. Lugiato, *Pattern-formation in a passive kerr cavity,* Chaos, Solitons Fractals 4, 1323 (1994).

[2] M. Tlidi, R. Lefever and P. Mandel, *Pattern selection in optical bistability,* Quantum Semiclass. Opt. 8 931 (1996).

[3] M. Haelterman, S. Trillo, and S. Wabnitz,*Dissipative modulation instability in a nonlinear dispersive ring cavity,* Opt. Comm. **91**, 401 (1992).

[4] P. D. Woods and A. R. Champneys, *Heteroclinic tangles and homoclinic snaking in the unfolding of a degenerate reversible Hamiltonian-Hopf bifurcation,* Phys. D, **129** (1999), pp. 147-170.

[5] P. Coullet, C. Riera, C. Tresser, *Stable static localized structures in one dimension,* Phys. Rev. Lett. **84** (2000) 3069.

[6] P. Coullet, C. Riera, *A new approach to data storage using localized structures,* Chaos **14** 1 (2004).

[7] D. Gomila, A.J. Scroggie, and W.J. Firth, *Bifurcation structure for dissipative solitons,* Phys. D (Amsterdam) **227**, 70 (2007).

[8] J Burke and E. Knobloch, *Localized states in the generalized Swift-Hohenberg equation,* Phys. Rev. E, 73 (2006), 056211.

[9] F. Leo, L. Gelens, P. Emplit, M. Haelterman, and S. Coen, *Dynamics of one-dimensional Kerr cavity solitons,* Opt. Express **21**, 9180 (2013).

[10] B. Ponedel and E. Knobloch, *Forced Snaking: Localized structures in the real Ginzburg-Landau equation with spatially periodic parametric forcing,* Euer. Phys. Jur. D (to be published).

[11] P. Parra-Rivas, D. Gomila, M.A. Matías, S. Coen, and L. Gelens, *Dynamics of localized and patterned structures in the Lugiato-Lefever equation determine the stability and shape of optical frequency combs,* Phys. Rev. A **89**, 043813 (2014).

[12] C. Godey, I.V. Balakireva, A. Coillet, and Y.K. Chembo, *Stability analysis of the spatiotemporal Lugiato-Lefever model for Kerr optical frequency combs in the anomalous and normal dispersion regimes,* Phys. Rev. A **89**, 063814 (2014).

[13] G. Iooss and M.C. Pérouème, *Perturbed Homoclinic Solutions in Reversible 1:1 Resonance Vector Fields,* J. Diff. Eqs., **102**, 62 (1993).

[14] R. Devaney, *Reversible diffeomorphism and flows,* Trans. Am. Math. Soc. **218**, 89 (1976).

[15] A.R. Champneys, *Homoclinic orbits in reversible systems and their applications in mechanics, fluids and optics,*Phys. D (Amsterdam) **112**, 158 (1998).

[16] M. Haragus and G. Iooss, *Local Bifurcations, Center Manifolds, and Normal Forms in Infinite-Dimensional Dynamical Systems* (Springer, Berlin, 2011).

[17] S. J Chapman and G Kozyreff, *Exponential asymptotics of localized patterns and snaking bifurcation diagrams,* Phys. D, 238 (2009), pp. 319-354.

[18] G. Kozyreff and S. J. Chapman, *Asymptotics of large bound states of localized structures,* Phys. Rev. Lett., 97 (2006), 044502.I.

[19] Melbourne *Derivation of the time-dependent Ginzburg-Landau equation on the line,* J. Nonlinear Sci., 8:1-15, 1998.

[20] A. Bergeon, J. Burke, E. Knobloch, and I. Mercader, *Eckhaus instability and homoclinic snaking,* Phys. Rev. E **78**, 046201 (2008).

[21] J. Burke and E. Knobloch, *Snakes and Ladders: Localized states in the Swift-Hohenberg equation,* Phys. Lett. A 360, 681 (2007).

[22] J. Burke, S. M. Houghton, and E. Knobloch, *Swift-Hohenberg equation with broken reflection symmetry,* Phys. Rev. E 80, 036202 (2009).

[23] P. Parra-Rivas, D. Gomila, F. Leo, S. Coen and L. Gelens, *Third order chromatic dispersion stabilizes Kerr frequency combs,* Opt. Lett. **39**, 2971 (2014).

[24] J. Burke, A. Yochelis, and E. Knobloch, *Classification of spatially localized oscillations in periodically forced dissipative systems,* SIAM J. Appl. Dyn. Syst. **7**, 651 (2008).

[25] E.L. Allgower and K. Georg, *Numerical Continuation Methods: An Introduction* (Springer, Berlin, 1990).

[26] P. Colet, M.A. Matías, L. Gelens, and D. Gomila, *Formation of localized structures in bistable systems through nonlocal spatial coupling. I. General framework,* Phys. Rev. E **89**, 012914 (2014) ; L. Gelens, M.A. Matías, D. Gomila, T. Dorissen, and P. Colet, *Formation of localized structures in bistable systems through nonlocal spatial coupling. II. The nonlocal Ginzburg-Landau equation,* Phys. Rev. E **89**, 012915 (2014).

[27] L. A. Belyakov and L. P. Shil'nikov, *Homoclinic curves and complex solitary waves,* Selecta Mathematic Sovietica, 9:219-228, (1990).

[28] D. Turaev, A. G. Vladimirov, and S. Zelik, *Long-range interaction and synchronization of oscillating dissipative solitons,* Phys. Rev. Lett. **108**, 263906 (2012).

[29] B. A. Malomed, *Bound states of envelope solitons,* Phys. Rev. E **47** 4 2874-2880 (1993).

[30] R. Hilborn, *Chaos and Nonlinear Dynamics: An introduction for Scientists and Engineers* (Oxford University Press, Oxford, 2000).

[31] C. Grebogi, E. Ott, and J.A. Yorke, *Crises, sudden changes in chaotic attractors, and transient chaos,* Phys. D (Amsterdam) **7**, 181 (1983). C. Grebogi, E. Ott, and J. A. Yorke, *Crises, sudden changes in chaotic attractors, and transient chaos,* Physica D 7, 181-200 (1983).

[32] J. Guckenheimer and P. Holmes, *Nonlinear Oscillations, Dynamical Systems, and Bifurcations of Vector Fields,*(Springer, New York, 1983).

[33] P. Gaspard, *Local birth of homoclinic chaos*, Phys. D (Amsterdam) 62, 94 (1993).

Chapter 5

Dark solitons in the normal group velocity dispersion regime

5.1 Introduction

Dark solitons, localized spots of lower intensity embedded in an homogeneous surrounding, are a particular type of solitons appearing dissipative systems far from thermodynamic equilibrium [1]. In the normal group velocity dispersion (GVD) regime of temporal cavities, these type of localized structures (LSs) have been studied theoretically using the LL model [2–4], and recently found experimentally in microresonators [5]. However, neither a complete understanding of their bifurcation structure, nor a detailed characterization of their dynamics existed. Hence, the goal of this chapter is to present an in-depth analysis of the dynamics, bifurcation structure, and stability of the dark LSs arising in this regime.

The type of dark LSs reported here, does not arise due to the bistability between a HSS solution and a pattern (as it was the case for the bright LSs discussed in Chapter 4), but they are related with the coexistence between two different HSSs, A_0^b and A_0^t, within the same range of parameters. If the two HSS states are stable, fronts connecting them can form. In this context, two fronts with different polarities can be considered: one that connects A_0^t with A_0^b, which will be called F_d, and another, F_u, connecting back A_0^b with A_0^t. In the LL model A_0^b and A_0^t are not equivalent, and therefore F_d and F_u move with constant velocity and in opposite directions. However, at the Maxwell point of the system their velocity becomes zero, and the fronts can lock, forming in this way, a dark LS, i.e.

a *heteroclinic cycle* in the spatial dynamics. Moreover, even when the velocities are no zero (i.e. in a region of parameters around the Maxwell point), LSs can bifurcate from the previous one, and all of them undergo bifurcation structure known as *collapsed snaking* [6].

The organization of this chapter is as follows. In Section 5.2, we give an overview of the spatial dynamics of spatially uniform states similar as studied in Chapter 2. Later, in Section 5.3 we perform an analysis of the bifurcation structure of dark solitons. In Section 5.7 we analyze oscillatory and chaotic dynamics of dark solitons. In Section 5.8 we present a discussion of the different results found here and how these results connect with previous ones. Finally we conclude in Section 5.9 by discussing the generality of the analysis provided in the earlier sections and in particular its relevance to frequency combs in nonlinear optics.

5.2 Overview of the spatially uniform states in the normal regime

In this section we give a summary of the spatially uniform states or HSSs of the LL equation, going from their temporal stability to their spatial dynamics. These results were already presented in more detail in Chapter 2, for both, the anomalous and normal dispersion regimes. In this way this section serve as our starting point for further analysis in the coming sections.

5.2.1 Temporal stability

In the normal dispersion regime, the LL equation is given by

$$\partial_t A = -(1+i\theta)A - i\partial_x^2 A + i|A|^2 A + \rho, \tag{5.1}$$

where we have taken $\nu = -1$.

As we have seen in previous chapters, the HSSs are the same in both regimes, and are solutions of the cubic algebraic equation,

$$I_0^3 - 2\theta I_0^2 + (1+\theta^2)I_0 = \rho^2, \tag{5.2}$$

where $I_0 \equiv |A_0|^2$. Nevertheless, their stability against perturbations $e^{ikx+\Omega t} + c.c.$, differs and it is determined by the dispersion relation

$$\Omega(k) = -1 \pm \sqrt{4I_0\theta - 3I_0^2 - \theta^2 - (4I_0 - 2\theta)k^2 - k^4}. \tag{5.3}$$

In contrast to the anomalous regime, here it follows that in the monostable regime the A_0 solution is always stable while for $\sqrt{3} < \theta < 2$ (see Figure 5.1(a))

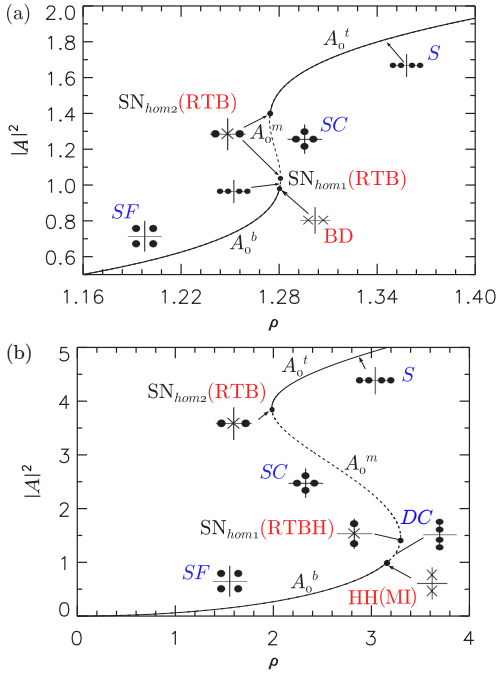

Figure 5.1: In (a) $\sqrt{3} < \theta = 1.8 < 2$ and in (b) $2 < \theta = 4$. The different labels are explained in Table 2.1 in Chapter 2. Solid (dashed) lines indicate stability (instability) in time.

the A_0^b and A_0^t states are stable and A_0^m is unstable. However, when $\theta > 2$ the A_0^b branch becomes unstable at a steady state bifurcation with $k \neq 0$. This Turing or Modulational instability (MI) occurs at $I_0 = I_c = 1$ and generates a stationary periodic wave-train with wave number $k_c = \sqrt{\theta - 2}$; A_0^m remains unstable while A_0^t is always stable. An example of this configuration can be seen in Figure 5.1(b).

5.2.2 Overview of spatial dynamics in the normal regime

Although we have already studied spatial dynamics in Chapter 2, here we revisit such analysis focusing on the LSs arising from the reversible Takens-Bodganov (RTB) point $\lambda_{1,2} = \pm q_0$, $\lambda_{3,4} = 0$ and the HH point with $\lambda_{1,2} = \pm ik_c$ $\lambda_{3,4} = \pm ik_c$. Figure 5.1 summarizes the possible eigenvalue configurations for normal

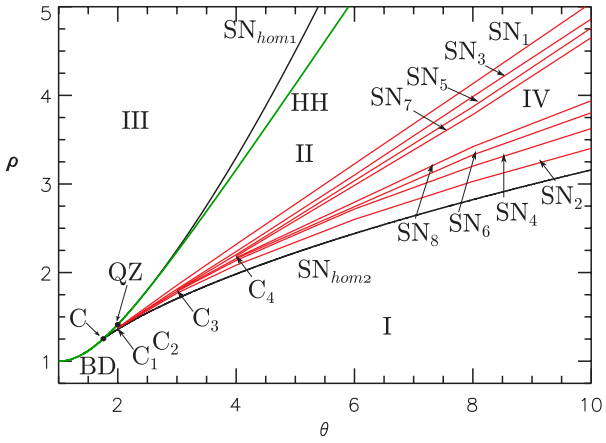

Figure 5.2: The (θ, ρ) parameter space for normal dispersion in the region of existence of dark solitons. The green line corresponds to the HH bifurcation, the black lines to the SN bifurcations of the HSS, and the red lines to the SN bifurcations of the dark DSs. The bifurcation lines and the regions I-IV are discussed in more detail in the text.

dispersion ($\nu = -1$). The transition at $I_0 = I_c$, i.e., along the green curve

$$\rho = \rho_c \equiv \sqrt{1 + (1 - \theta)^2} \tag{5.4}$$

in Figure 5.2, corresponds to a Belyakov-Devaney (BD) transition when $\theta < 2$ and an HH transition when $\theta > 2$. Figures 5.1(a) correspond to the case $\theta < 2$, and we see that the saddle-node bifurcation at $\mathrm{SN}_{\mathrm{hom},1}$ corresponds to a RTB bifurcation. In contrast, for $\theta > 2$ $\mathrm{SN}_{\mathrm{hom},1}$ has become a reversible Takens-Bodganov-Hopf (RTBH) bifurcation (Figure 5.1(b)). For $\theta = 2$ the BD, HH, RTB and RTBH lines meet at the quadruple zero (QZ) point (see Section 2.3). In the parameter space of Figure 5.2 the QZ point corresponds to $(\theta, \rho) = (2, \sqrt{2})$. The other relevant bifurcation lines in this scenario correspond to $\mathrm{SN}_{\mathrm{hom},2}$. This point corresponds to a RTB bifurcation in space regardless of the value of θ. As we will see in next sections, several families of dark solitons emerging from the $\mathrm{SN}_{hom,2}$, a RTB in terms of spatial dynamics, are found doing a weakly nonlinear analysis around that point (see Section 5.3). Later applying continuation techniques we continue these states in both parameters ρ and θ. These results are shown in Section 5.5.

5.3 Weakly nonlinear analysis around $\mathrm{SN}_{hom,2}$

In this section we compute weakly nonlinear DSs using multiple scale perturbation theory near the RTB bifurcation corresponding to $\mathrm{SN}_{hom,2}$. The procedure is the same as applied in the case of the SN_{hom1}, because here the bifurcation is also a RTB. The DSs are solutions of the ordinary differential equation

$$-iA'' - (1+i\theta)A + i|A|^2A + \rho = 0, \tag{5.5}$$

where $A'' \equiv \dfrac{d^2A}{dx^2}$. In terms of the real variables $U = \mathrm{Re}[A]$ and $V = \mathrm{Im}[A]$ Eq. (5.5) is written as,

$$\begin{cases} V'' - U + \theta V - V(U^2+V^2) + \rho = 0, \\ -U'' - V - \theta U + U(U^2+V^2) = 0. \end{cases} \tag{5.6}$$

Here we will make a short summary of the steps followed in this calculation. As we did in Section 4.4, and following [6], we fix the value of θ and suppose that the DSs at $\rho \approx \rho_t$, where $\rho = \rho_t$ corresponds to the $\mathrm{SN}_{hom,2}$ bifurcation, are captured by the ansatz $U = U^* + u$, $V = V^* + v$, where U^* and V^* represent the HSS A_0^t and u and v capture the spatial dependence. We next introduce appropriate asymptotic expansions for each variable in terms of a small parameter ϵ defined as follows. First we consider a Taylor series expansion of ρ around the $\mathrm{SN}_{hom,2}$ at $I_t = \left(2\theta + \sqrt{\theta^2-3}\right)/3$:

$$\rho(I_0) = \underbrace{\rho(I_t)}_{\rho_t} + \underbrace{\left(\frac{d\rho}{dI_0}\right)_{I_t}}_{=0}(I_0 - I_t) + \underbrace{\frac{1}{2}\left(\frac{d^2\rho}{dI_0^2}\right)_{I_t}}_{\delta}\underbrace{(I_0-I_t)^2}_{\epsilon^2} + \cdots \tag{5.7}$$

Because ρ_t has a minimum at I_t, we have

$$\left(\frac{d\rho}{dI_0}\right)_{I_t} = 0$$

$$\delta_t = \frac{1}{2}\left(\frac{d^2\rho}{dI_0^2}\right)_{I_t} = \frac{\sqrt{\theta^2-3}}{2\rho_t} > 0.$$

From there we can define a small parameter ϵ in terms of ρ,

$$\epsilon = \sqrt{\frac{\rho-\rho_t}{\delta_t}}, \tag{5.8}$$

Each variable is written in the form

$$\begin{bmatrix} U^* \\ V^* \end{bmatrix} = \begin{bmatrix} U_t \\ V_t \end{bmatrix} + \epsilon \begin{bmatrix} U_1 \\ V_1 \end{bmatrix} + ... \tag{5.9}$$

and

$$\begin{bmatrix} u \\ v \end{bmatrix} = \epsilon \begin{bmatrix} u_1 \\ v_1 \end{bmatrix} + \epsilon^2 \begin{bmatrix} u_2 \\ v_2 \end{bmatrix} + ... \tag{5.10}$$

and these expressions inserted into Eq. (5.6). Solving order by order in ϵ we find that the leading order asymptotic solution close to the RTB point is given by

$$\begin{bmatrix} U \\ V \end{bmatrix} = \begin{bmatrix} U_t \\ V_t \end{bmatrix} + \epsilon \begin{bmatrix} U_1 + u_1 \\ V_1 + v_1 \end{bmatrix}, \tag{5.11}$$

where U_t and V_t correspond to the HSS at $\rho = \rho_t$, and

$$\begin{bmatrix} u_1 \\ v_1 \end{bmatrix} = \begin{bmatrix} U_1 \\ V_1 \end{bmatrix} \psi(x), \tag{5.12}$$

with

$$\begin{bmatrix} U_1 \\ V_1 \end{bmatrix} = \mu_t \begin{bmatrix} 1 \\ \eta \end{bmatrix} \tag{5.13}$$

and

$$\psi(x) = -3\text{sech}^2 \left[\frac{1}{2} \sqrt{-\frac{\alpha_2}{\alpha_1}} \left(\frac{\rho - \rho_t}{\delta_t} \right)^{1/4} x \right]. \tag{5.14}$$

Here η, μ_t, α_1 and α_2 are parameters defined in the Appendix D, where the details of the calculation can be found. Of course, on a large domain we expect to find states with 2 or more dark solitons as well. When these are well separated these states behave like 1-soliton states and so should bifurcate from the vicinity of $\text{SN}_{hom,2}$ just like the 1-soliton states.

We now discuss the bifurcation structure of dark solitons in two regimes: the bistable region before the QZ point, namely for $\sqrt{3} < \theta < 2$ and the bistable region after QZ, i.e., for $\theta > 2$.

5.4 Bifurcations and stability of dark solitons for $\sqrt{3} < \theta < 2$

In the following we use the L^2 norm, $||A||^2 \equiv \frac{1}{L} \int_0^L |A|^2 \, dx$, to represent the DSs in a bifurcation diagram. Figure 5.3, computed for $\theta = 1.95$, reveals the presence

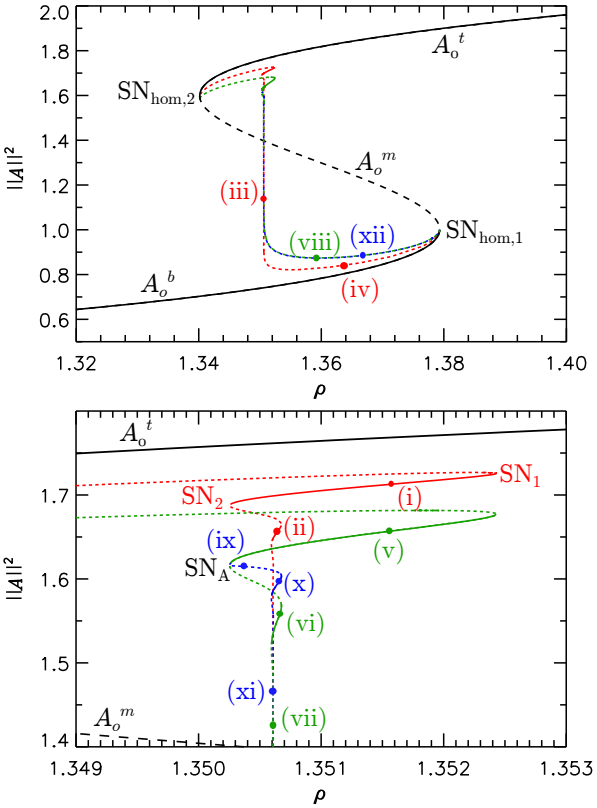

Figure 5.3: (a) Bifurcation diagram at $\theta = 1.95$. (b) Zoom of panel (a) around $SN_{hom,2}$. The homogeneous steady states HSS are shown in black, 1-soliton states in red and 2-soliton states in green. Temporally stable (unstable) DSs are indicated using solid (dashed) lines. Profiles corresponding to the labeled locations are shown in Figure 5.4 and in more detail in Figure 5.5.

of a branch of single dark solitons in the domain (hereafter the 1-soliton state, red curve). This branch bifurcates from HSS very close to $SN_{hom,2}$ as anticipated in the preceding section and undergoes collapsed snaking [6, 8], i.e., it undergoes a series of exponentially decaying oscillations in the vicinity of a critical value of ρ, hereafter $\rho = \rho_M \approx 1.3506074$. During this process the hole corresponding to the dark soliton deepens, forming a pair of fronts F_d connecting A_0^t with A_0^b, and F_u connecting A_0^b with A_0^t. This structure broadens as the A_0^b state expels A_0^t (Figure 5.4, profiles (i)–(iii)), becoming in an infinite system a heteroclinic

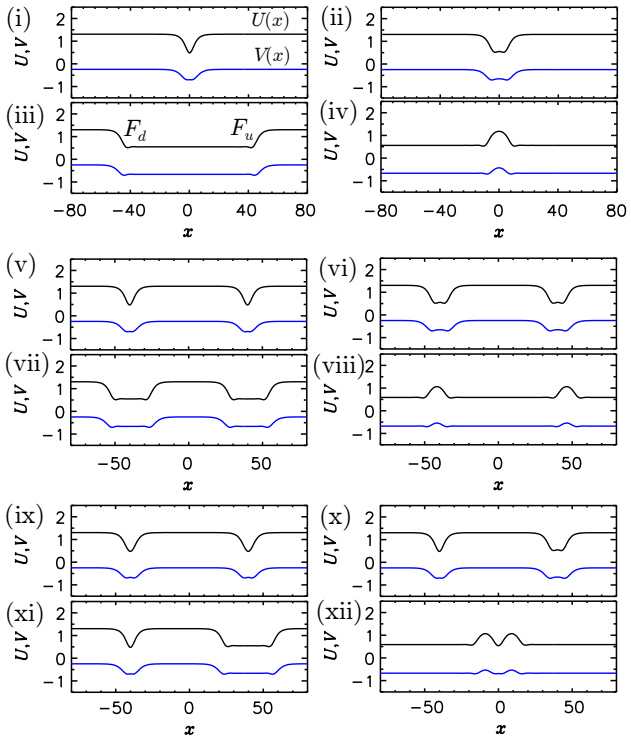

Figure 5.4: Spatial profiles of DSs (dark and bright 1-soliton and 2-soliton states) corresponding to the locations indicated in Figure 5.3(a,b), with $U(x)$ in black and $V(x)$ in blue. Near $\mathrm{SN}_{hom,2}$ the states resemble holes (dark solitons) while near $\mathrm{SN}_{hom,1}$ they resemble localized pulses (bright solitons).

cycle between A_0^t and A_0^b at ρ_M. In gradient systems this point corresponds to the so-called Maxwell point, where both homogeneous solutions have equal energy. In nongradient systems, such as LL equation, such a cycle may still be present, even though an energy cannot be defined, and we retain this terminology to refer to its location, i.e., the parameter value corresponding to the presence a pair of stationary, infinitely separated fronts connecting A_0^t to A_0^b and back again. States A_0^b and A_0^t are not equivalent, and therefore, fronts move with a constant veolcity c_F, which depends on the control parameters of the system i.e. $c_F = c_F(\theta, \rho)$, into the left or right depending on their orientation and the value of ρ. Then we say that the veolcity c_F is positive if a front F_u (resp. F_d) moves from left to right (resp. from right to left) and negative in the other case. In

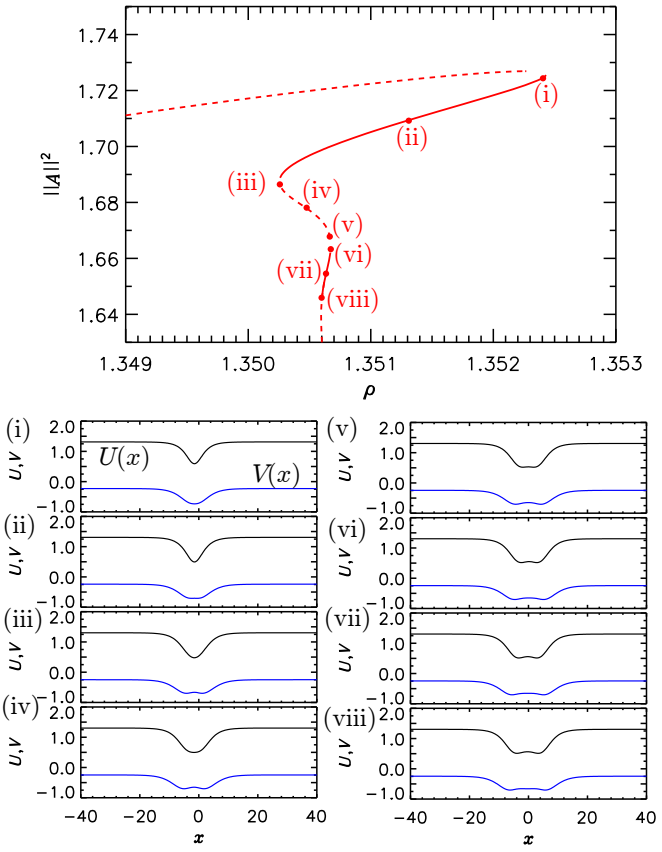

Figure 5.5: Spatial profiles of dark solitons near the upper end of the $\theta = 1.95$ 1-soliton branch at locations indicated in the middle panel, showing that the splitting of the central peak (dip) in $(U(x), V(x))$, shown in black and red, respectively, occurs at different locations along the branch.

this context, the Maxwell point of a nongradient system can be understood as the point where the velocity of fronts is zero.

The successive saddle nodes seen in Figure 5.3 correspond to the appearance of additional oscillations in the tails of the fronts as the local maximum (minimum) at the symmetry point $x = 0$ turns into a local minimum (maximum) and back again, and hence to a gradual increase in the width of the hole. Figure 5.5 shows a detail of this process. The associated hole states are temporally stable between

SN_1 and SN_2, and on all the subsequent branch segments with positive slope [6, 8], shown using solid lines. A profile of a stable localized hole on the SN_1–SN_2 segment is shown in Figure 5.4(i). For the value of θ used in Figure 5.3 the collapse of the saddle nodes to ρ_M is very abrupt because the spatial oscillations in the tail of the front decay very fast. Figure 5.6 shows a clearer example of the behavior in this region, albeit for a larger value of θ.

In finite systems the hole or 1-soliton branch departs from $\rho \approx \rho_M$ when the maximum amplitude starts to decrease below A_0^t and the solution turns into a bright soliton sitting on top of A_0^b (Figure 5.4, profile (iv)). The branch then terminates at $SN_{hom,1}$, where the amplitude of this soliton falls to zero. On an infinite domain the DS branches bifurcating from $SN_{hom,2}$ and $SN_{hom,1}$ remain distinct and do not connect up.

Figure 5.3 also shows the 2-soliton branch (green curve). This branch consists of a pair of equidistant dark solitons within the periodic domain (Figure 5.4, profiles (v)–(viii)). The states on this branch can be viewed as 1-pulse states on the half-domain and it is no surprise therefore that they follow the behavior of the 1-pulse states shown in red. In fact, this is so for all n-soliton branches ($n \geq 3$, not shown), provided the solitons remain sufficiently well separated; finite size effects push the bifurcation to these states farther from the saddle-node at $SN_{hom,2}$ as n increases, with similar behavior near $SN_{hom,1}$.

Of particular interest is the third soliton branch (Figure 5.3(b), blue curve). This branch bifurcates from the vicinity of the first left fold on the 2-soliton branch, labeled SN_A. This branch also undergoes collapsed snaking in the vicinity of ρ_M. The states on this branch start out as a 2-soliton state consisting of a pair of (nearly) identical solitons (Figure 5.4, profile (ix)) but only one of the two solitons broadens near ρ_M (Figure 5.4, profiles (x)–(xi)). The result is the profile (xii) shown in Figure 5.4 after translation by $L/4$. This state is seen to correspond to a single bright soliton, with a dip in the middle; numerical continuation shows that these states terminate on HSS near $SN_{hom,1}$ at the same location as the 1-soliton branch (red curve). This new branch plays a particularly important role for $\theta > 2$, as discussed next.

5.5 Bifurcation and stability for dark solitons for $\theta > 2$

For $\theta > 2$ the saddle node $SN_{hom,1}$ becomes a RTBH point with spatial eigenvalues $\lambda_{1,2} = \pm ik_0$ $\lambda_{3,4} = 0$ and homoclinic orbits are exceptional [6, 9]. However, in this case this point is preceded by a HH bifurcation on A_0^b, which gives rise to a branch of patterns. The pattern bifurcates subcritically (Figure 5.6) but remain

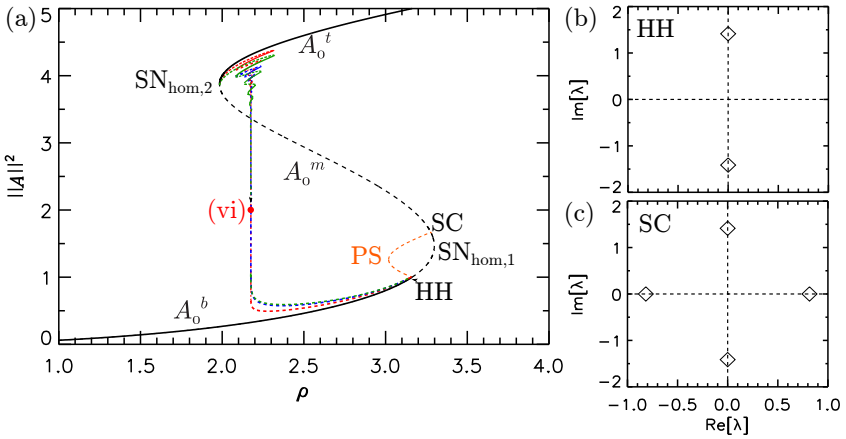

Figure 5.6: (a) Bifurcation diagram for $\theta = 4$ showing collapsed defect-mediated snaking of 1-soliton (red line) and 2-soliton (green line) branches, showing their reconnection with the PS branch (orange line) that bifurcates from HH on A_0^b. Temporally stable (unstable) structures are indicated using solid (dashed) lines. Black lines correspond to HSS. Enlargements of panel (a) can be found in Figs. 5.7 and 5.11. (b) The spatial eigenvalues λ of A_0 at locations HH and SC in (a).

unstable throughout their existence range, despite the presence of a saddle node. This is the case for all values of the detuning θ we explored ($2.3 < \theta < 10$). Thus no bistability between the pattern and A_0^b results and no snaking of bright DSs takes place [10, 11]. Instead the bright solitons bifurcating from HH connect to the dark solitons originating at $\rho = \rho_t$, as we now discuss.

Figure 5.6(a) shows the bifurcation diagram of the 1-soliton states (red branch) for $\theta = 4$ obtained by numerically continuing the analytical prediction obtained in Eq. (5.14) away from $SN_{hom,2}$. Figure 5.7(a) shows a detail of this branch. These states are initially unstable but as ρ increases these unstable 1-soliton states grow in amplitude and acquire stability at saddle node SN_1. The DS profile on this segment of the branch is shown in Figure 5.8(i). This solution loses stability at SN_2 but starts to develop a spatial oscillation (SO) in the center; solutions of this type become stable at SN_3. An example of the resulting stable solution can be found in Figure 5.8(ii). This process repeats in such a way that between successive saddle nodes on the left or right a new spatial oscillation is inserted in the center of the dark soliton profile and the soliton broadens, decreasing its L^2 norm. As a result, as one proceeds down the snaking branch the central peak (dip) repeatedly splits. Details of this process are shown in

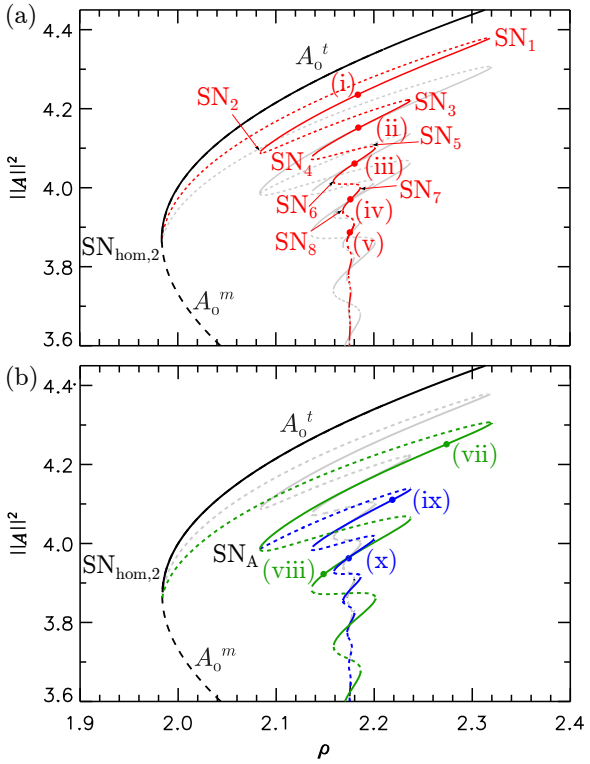

Figure 5.7: Detail of the 1-soliton (panel (a), red line) and 2-soliton (panel (b), green line) branches in the vicinity of $SN_{hom,2}$ for $\theta = 4$. Black lines show the homogeneous states HSS. Panel (b) also shows a family of nonidentical 2-soliton states (blue line) that bifurcate from the saddle node SN_A on the 2-soliton branch and also undergo collapsed defect-mediated snaking. Temporally stable (unstable) structures are indicated using solid (dashed) lines. Profiles corresponding to the labeled locations are shown in Figure 5.8, with details of this process shown in Figure 5.10.

Figure 5.10. Numerically the collapse occurs at $\rho = \rho_M \approx 2.1753479$. The DSs at this location correspond to broad hole-like states of the type shown in Figure 5.8(v). As in Section 5.4 further decrease in the norm signals that the two fronts F_d and F_u connecting states A_0^t and A_0^b at ρ_M are starting to separate (Figure 5.8(vi)). These two fronts are asymmetric i.e. $F_{u,d}(-x) \neq F_{u,d}(x)$, although they are related by a reflection transformation, $F_u(-x) = F_d(x)$. Figure 5.9 shows the front velocity as a function of ρ for $\theta = 4$. The vertical line stands for the Maxwell point of the system ρ_M where $c_F(\rho_M) = 0$,

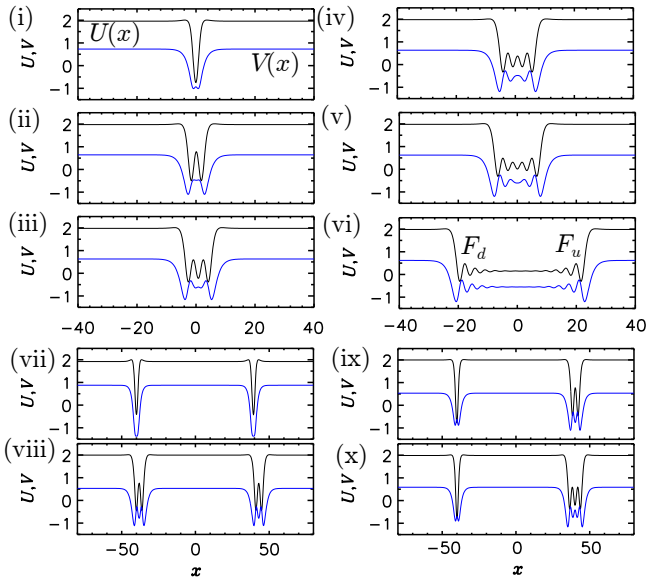

Figure 5.8: Spatial profiles of the solutions represented in Figure 5.6(a) for $\theta = 4$, showing $U(x)$ in black and $V(x)$ in blue. Panels (i)-(vi) correspond to 1-soliton states (red branches in Figs. 5.6(a) and 5.7(a)), panels (vii)-(viii) to 2-soliton states (green branches in Figs. 5.6(a) and 5.7(b)) and panels (ix)-(x) to the branch of nonidentical 2-soliton states (blue branch in Figure 5.7(b)).

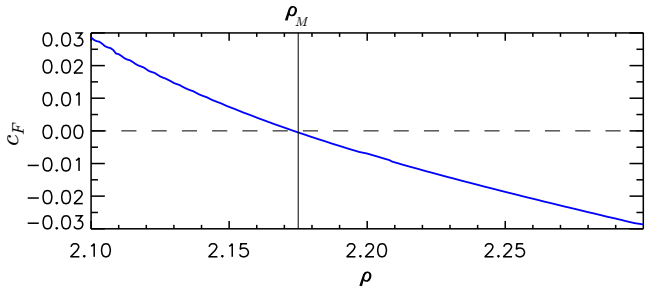

Figure 5.9: Velocity of the front in function of ρ for $\theta = 4$. At the Maxwell point, at $\rho = \rho_M \approx 2.1753479$ the velocity of the fronts is zero.

and the velocity of fronts switches its sign.

The separation of fronts continues, resulting in the bright soliton state shown in

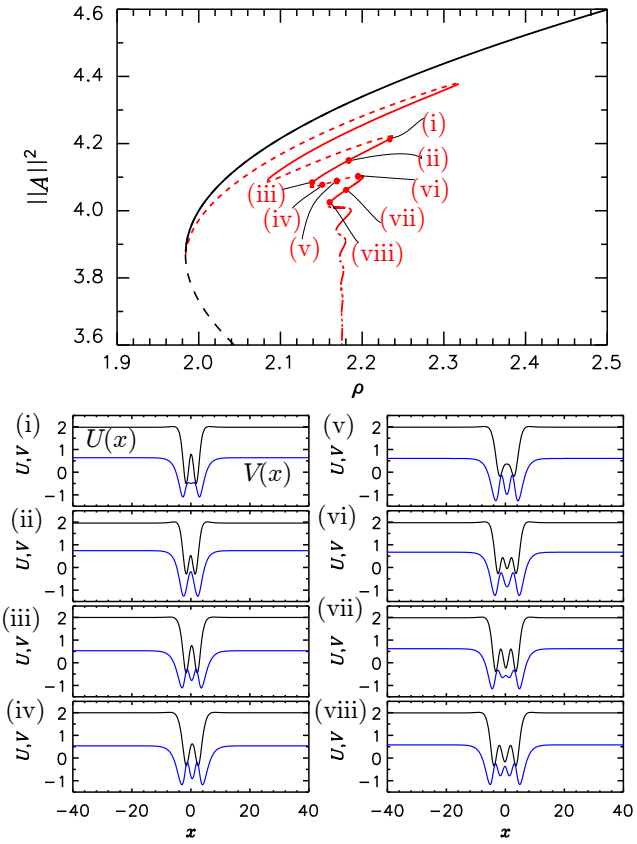

Figure 5.10: Spatial profiles of the dark solitons near the upper end of the $\theta = 4$ 1-soliton branch at locations indicated in the middle panel, showing that the splitting of the central peak (dip) in $(U(x), V(x))$, shown in black and red, respectively, occurs at different locations along the branch.

Figure 5.11(iv); this state is shifted by half the domain width relative to panels (i)-(vi) of Figure 5.8. Thereafter the amplitude of the peak at $x = 0$ starts to decrease and the 1-soliton branch departs from ρ_M, ultimately connecting to the branch of small amplitude PS (Figure 5.11(i)) that bifurcates subcritically from HH (see inset in Figure 5.11, top panel).

Figure 5.6(a) also shows the 2-soliton state (green line) that bifurcates from the vicinity of $\mathrm{SN}_{hom,2}$ for $\theta = 4$ just as in the case $\theta = 1.95$. For $\theta > 2$ this second

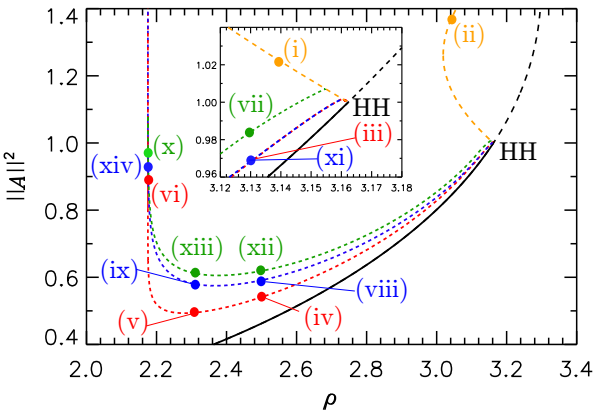

Figure 5.11: Bifurcation diagram for $\theta = 4$ showing the bifurcation of the three families of localized states (bright solitons) from the subcritical PS branch. States with maxima at $x = 0$ (red line) connect with the corresponding branch of dark solitons shown in Figs. 5.6(a) and 5.7(a) while states with minima at $x = 0$ (blue line) connect with the corresponding branch in Figure 5.7(b). The states shown in green consist of two equidistant bright solitons and these connect to the corresponding branch in Figure 5.7(a).

DS family plays a key role since it is responsible for providing the second of the two branches of localized states that are known to be associated with HH. Figures 5.7(b), 5.11 and 5.13 show how this happens. The green branch in Figure 5.7(b) consists of states with identical equidistant solitons; like the 1-soliton states, the 2-soliton states proceed to develop internal oscillations (Figs. 5.8(vii)-(viii)). These undergo a symmetry-breaking pitchfork bifurcation at SN_A giving rise to a branch of nonidentical solitons (in blue). One of these gradually acquires complex internal structure while the other remains unchanged. Figures 5.8(ix)-(x) show this state at the locations shown in Figure 5.7(b), while Figure 5.13(xii) shows a translate of such a 2-soliton state by a quarter of the domain size. Figures 5.13(xii)-(ix) and 5.11(xiv)-(xi) show the subsequent evolution of this 2-soliton state into a single wave packet with a minimum at its center $x = 0$. It is this state that connects to PS at the same location as the corresponding wave packet (red) with a maximum at $x = 0$ that originates in the 1-soliton state near $\mathrm{SN}_{hom,2}$. In contrast, the 2-soliton state that also appears near $\mathrm{SN}_{hom,2}$ (green) terminates in a distinct bifurcation on PS, as also shown in Figure 5.11. All three branches undergo collapsed defect-mediated snaking inbetween. Evidently there are similar branches that bifurcate from other folds on the 2-soliton branch (not shown).

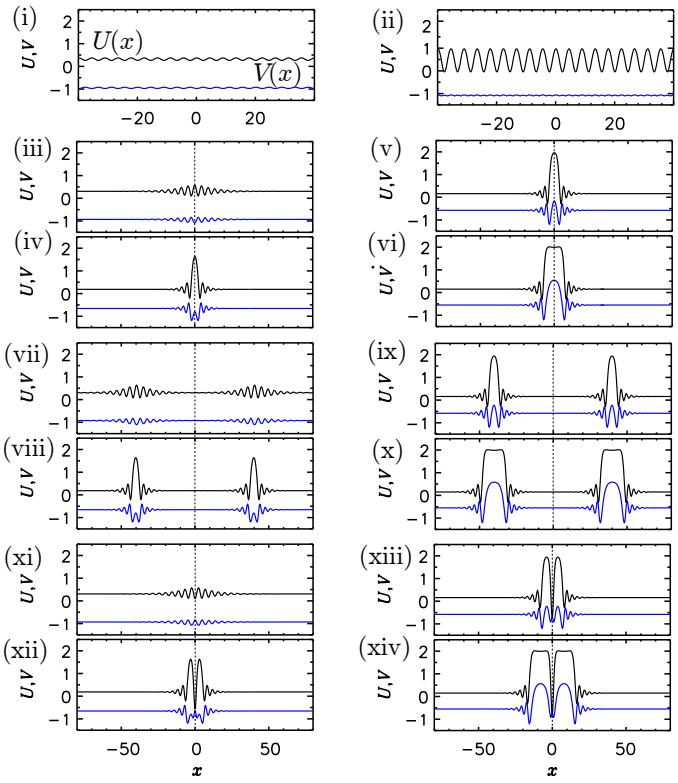

Figure 5.12: Sample of solution profiles corresponding to the locations indicated in Figure 5.11.

We note that as the domain length increases the termination point of the 1-soliton (red line) and the nonidentical 2-soliton branch (blue line) migrates towards HH and in the limit of an infinite domain the bright solitons bifurcate from A_0^b simultaneously with the pattern, exactly as predicted by the normal form for the spatial Hopf bifurcation with 1:1 resonance [12]. We also mention that, in principle, the Maxwell point ρ_M may collide with the saddle node of the pattern branch (see [13] for details). However, we have determined that such a collision does not occur in the LL equation and that the pattern branch remains well-separated from the collapsed snaking branches of dark solitons around ρ_M (at least in the parameter range $2.3 < \theta < 10$).

We turn, finally, to the structure of the spatial eigenvalues shown in Figure 5.6(b,c).

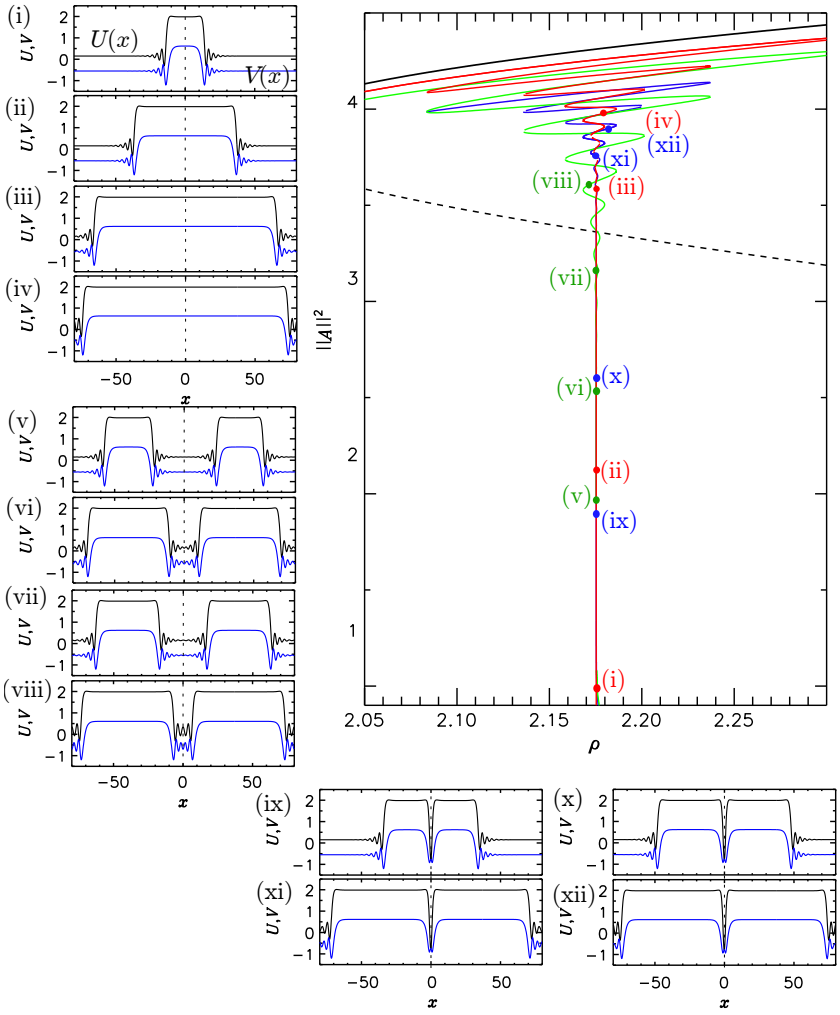

Figure 5.13: Details of the profile transformation at $\theta = 4$ that changes two nonidentical dark solitons (blue branch in Figure 5.7(b)) into a bright soliton with a minimum at its center $x = 0$, allowing it to connect to the PS state at the same location as the 1-soliton state (red branch in Figure 5.7(a)) which evolves into a bright soliton with a maximum at its center $x = 0$. The 2-soliton state consisting of two identical equidistant solitons (green branch in Figure 5.7(b)) also terminates on PS, but at a distinct location.

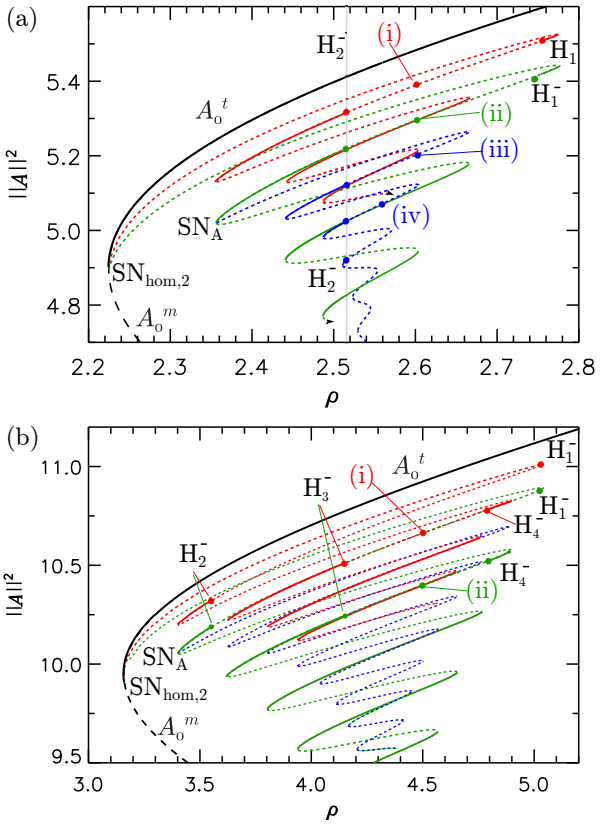

Figure 5.14: Bifurcation diagram for (a) $\theta = 5$ and (b) $\theta = 10$ showing that the DSs are now unstable within intervals between back-to-back Hopf bifurcations. The Hopf bifurcations on the left (H_2^-, panel (a)) for the 2-soliton states (green and blue lines) coincide with that of the 1-soliton states (red line).

Panel (b) confirms that HH corresponds to a Hamiltonian-Hopf bifurcation in space. Panel (c) shows that at the termination point of the pattern branch the HSS state A_0^m has 2 purely real eigenvalues and 2 purely imaginary spatial eigenvalues, indicating that SC corresponds to a global bifurcation in space and not a local bifurcation. Both HH and SC are formed in the process of unfolding the spatially reversible QZ bifurcation that takes place at $SN_{hom,1}$ when $\theta = 2$.

5.6 Soliton location in the (θ, ρ) plane

Tracking each bifurcation point in the bifurcation diagram as a function of θ we obtain the (θ, ρ) parameter plane shown in Figure 5.2. The green solid line represents a BD transition for $\theta < 2$ that turns into a HH bifurcation for $\theta > 2$. The saddle-node bifurcations determine the regions of existence of the different dark solitons shown previously. With increasing θ the region of existence of these states becomes broader (Figure 5.14(a,b)). In contrast, when θ decreases the branches of solutions with several SO progressively shrink, disappearing in a series of cusp bifurcations C_1,...,C_4, as shown in Figure 5.2.

We distinguish four main dynamical regions, labeled I to IV in the phase diagram in Figure 5.2, in terms of the existence of HSS and dark DSs:

- Region I: The bottom HSS A_0^b is stable. No dark DSs or top HSS A_0^t exist. This region spans the parameter space $\rho < \rho_{BD}$ for $\theta < \sqrt{3}$ and $\rho < \rho_{SN_{hom,2}}$ for $\theta > \sqrt{3}$.
- Region II: The bottom HSS A_0^b and top HSS A_0^t coexist and are both stable. No dark DSs are found. This region spans the parameter space $\rho_{SN_1} < \rho < \rho_{SN_{hom,1}}$ for $\theta > \sqrt{3}$.
- Region III: The top HSS A_0^t is stable. No dark DSs or bottom HSS A_0^b exist. This region spans the parameter space $\rho > \rho_{BD}$ for $\theta < \sqrt{3}$ and $\rho > \rho_{SN_{hom,1}}$ for $\theta > \sqrt{3}$.
- Region IV: The bottom HSS A_0^b and top HSS A_0^t are stable and coexist with possibly unstable or stable dark DSs. This region spans the parameter space $\rho_{SN_{hom,2}} < \rho < \rho_{SN_1}$ for $\theta > \sqrt{3}$.

Region IV is the main region of interest in this work. It can be further subdivided to reflect the locations of different types of DSs. In the next Section, we refer to the region between SN_1 and SN_2, i.e., the region of existence of dark solitons with one spatial oscillation (1-SO dark solitons), as subregion IV_1. Similarly, subregion IV_2 corresponds to 2-SO dark solitons between SN_3 and SN_4 and so on. While both HSS are stable in region IV, the stability of dark DSs in the various subregions depends on the parameter values (θ,ρ) as discussed next.

5.7 Oscillatory and chaotic dynamics

We have seen that the range of values of the parameter ρ within which one finds dark solitons increases rapidly with increasing detuning θ although the interval

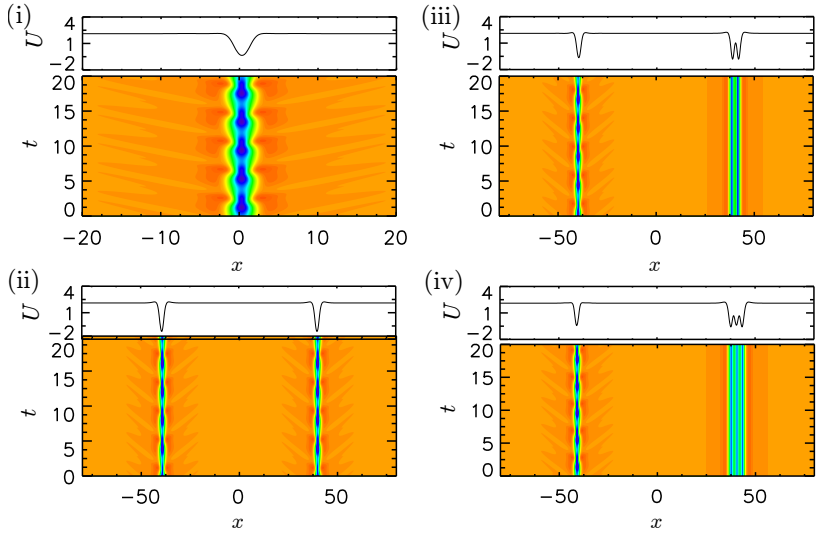

Figure 5.15: (i) Oscillatory 1-soliton state, (ii) oscillatory 2-soliton state, (iii) a bound state of an oscillating and a stationary dark soliton, all computed for $\theta = 5$, $\rho = 2.6$. (iv) A similar state to panel (iii) but for $\theta = 5$, $\rho = 2.56$. The solutions are represented in a space-time plot of $U(x,t)$ with time increasing upwards. The profile at the final instant, $t = 20$, is shown above each space-time plot.

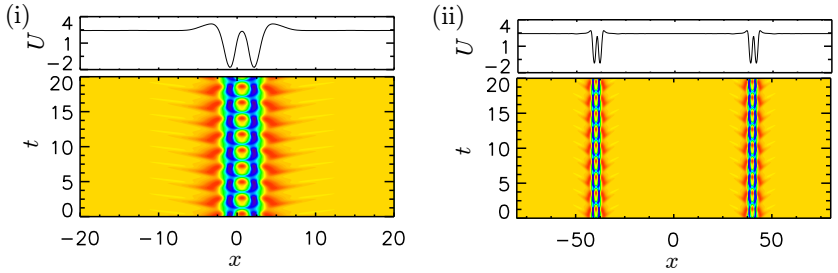

Figure 5.16: (i) Oscillatory 1-soliton state, and (ii) oscillatory 2-soliton state, when $\theta = 10$, $\rho = 4.5$. The solutions are represented in a space-time plot of $U(x,t)$ with time increasing upwards. The profile at the final instant, $t = 20$, is shown above each space-time plot.

with stable stationary dark solitons is reduced by the presence of oscillatory instabilities that set in as θ increases (Figure 5.14). These intervals of instability open up on the stable portions of the collapsed snaking branches, between pairs of supercritical Hopf bifurcations on either side. Consequently these instabili-

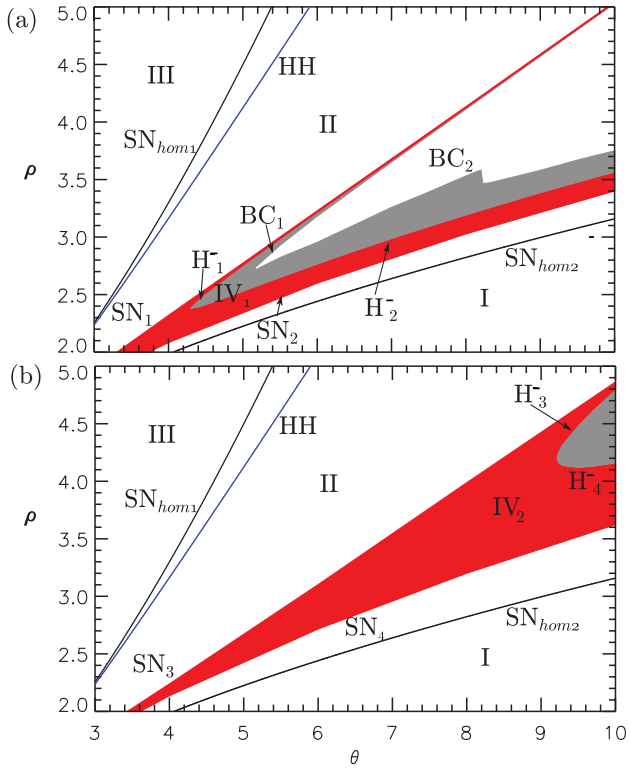

Figure 5.17: (The (θ, ρ) parameter space for normal dispersion ($\nu = -1$) showing the region of existence of (a) the 1-SO dark soliton and (b) the 2-SO dark soliton. The different bifurcations are labeled, with H_j^- indicating a supercritical Hopf bifurcation at location H_j. The red (gray) region corresponds to stable stationary (oscillatory) dark DSs.

ties lead to stable temporal oscillations resembling breathing of the individual solitons. To characterize the resulting dynamics we combine here linear stability analysis in time with direct integration of the LL equation. We also compute secondary bifurcations of time-periodic states and point out that in appropriate regimes the LL equation exhibits dynamics that are very similar to those exhibited by excitable systems.

As already noted, for $\theta = 5$ (Figure 5.14(a)) and $\theta = 10$ (Figure 5.14(b)) the single dark soliton becomes unstable in a supercritical Hopf bifurcation (H_1^-) leading to an oscillatory state. Figure 5.15(i) shows the resulting oscillatory state at

location (i) in Figure 5.14(a). The temporal oscillations disappear upon further decrease in ρ and do so in a reverse supercritical Hopf at H_2^-, thereby restoring the stability of the single dark soliton. For larger values of θ this behavior not only persists but the soliton with 2 spatial oscillations (SO) also exhibits temporal oscillations between two back-to-back Hopf bifurcations (Figure 5.14(b)). An example of such oscillatory 2-SO dark soliton is shown in Figure 5.16(i).

Figure 5.15(ii) shows the corresponding oscillation of the 2-soliton state for $\theta = 5$ at location (ii) in Figure 5.14(a). The solitons oscillate in phase, in a non-sinusoidal manner. Figures 5.15(iii)-(iv) show oscillations of a bound state of two nonidentical dark solitons at locations (iii) and (iv) in Figure 5.14(a). In these states the simple dark soliton on the left oscillates in a periodic fashion while the structured dark soliton on the right remains essentially time-independent. Figure 5.16(ii) shows a periodic oscillation of a 2-soliton state for $\theta = 10$ corresponding to location (ii) in Figure 5.14(b). The individual solitons are structured and oscillate as in panel (i). Once again, both oscillate in phase.

We can complete the parameter space shown in Figure 5.2 by adding the curves corresponding to the oscillatory instabilities at H_1^- and H_2^-. Figure 5.17 shows the parameter space with the curves corresponding to the temporal instabilities of the 1-SO and 2-SO dark solitons included; the saddle nodes of the remaining dark solitons are omitted in order to give a clearer understanding of this behavior. Bifurcation lines separating different dynamical regimes are labeled according to Figure 5.14. With increasing θ the Hopf bifurcation H_1^- of the single dark DS approaches SN_1 and we see that both lines are almost tangent although, for the parameter values presented, they do not meet. The same scenario repeats for the Hopf bifurcation H_3^- of the 2-SO state.

This scenario can be better understood by looking at Figure 5.18 where several slices of Figure 5.17(a) at different values of θ are shown. We choose to plot $||A||_{\text{inf}} := \min(|A|)$ instead of the L^2 norm to improve the clarity of the bifurcation diagram, and denote the maximum and minimum amplitude of the oscillatory DSs using crosses. The diagram in Figure 5.18(a) corresponds to a cut of Figure 5.17 at $\theta = 4.6$. At this θ value the oscillatory state bifurcates from H_1^-, grows in amplitude as ρ decreases, before reconnecting to the stationary DS at H_2^- in a reverse Hopf bifurcation. For larger θ, the amplitude of the limit cycle between H_1^- and H_2^- increases, and at some point the cycle undergoes a period-doubling (PD) bifurcation, starting a route to a chaotic attractor. This happens already at $\theta = 5$ as can be seen in Figure 5.18(b). At $\theta = 5.2$ (Figure 5.18(c)) the chaotic attractor touches the saddle branch S corresponding to unstable dark solitons and disappears through a boundary crisis (BC) [14]. Let us discuss this

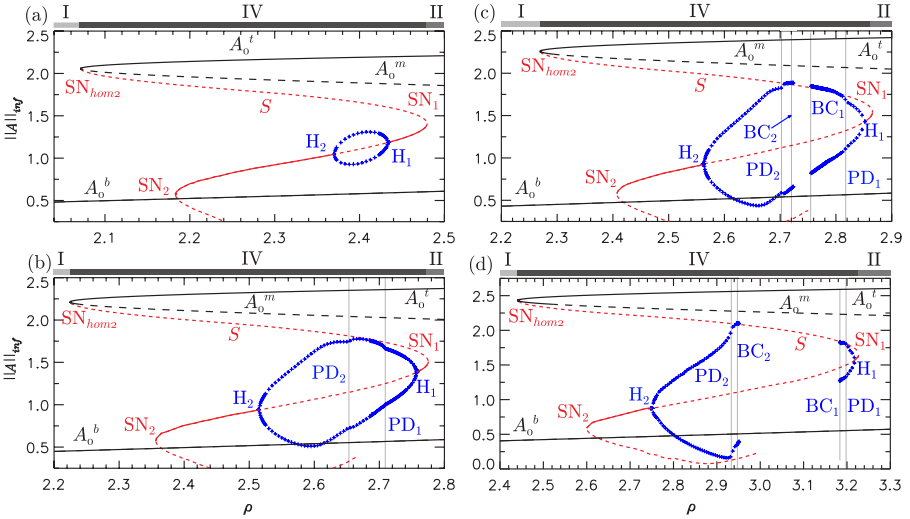

Figure 5.18: Bifurcation diagrams corresponding to different slices of the parameter space in Figure 5.17 plotted using $||A||_{\text{inf}}$ as a measure of the amplitude. Solid (dashed) lines correspond to stable (unstable) structures, and red (black) colors correspond to 1-SO dark DSs (HSS). The blue crosses represent maxima and minima of the amplitude of the oscillatory dark DSs. The gray labeled bars above each panel show the extent of the regions I, II, and IV. (a) $\theta = 4.6$, (b) $\theta = 5$, (c) $\theta = 5.2$, (d) $\theta = 5.5$.

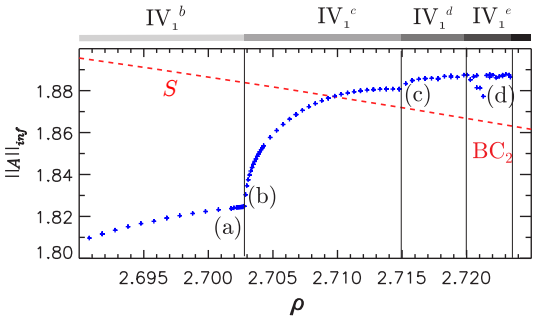

Figure 5.19: Detail of the bifurcation diagram of Figure 5.18(c) for $\theta = 5.2$ close to the BC_1 point. Vertical lines represent the separation between period 1 oscillations in region IV_1^b, period 2 oscillations (region IV_1^c), period 4 oscillations (region IV_1^d) and temporal chaos in IV_1^e. Lines and markers in red (black) correspond to dark DSs (HSS). Labels from (a) to (d) correspond to the dynamics shown in Figure 5.20.

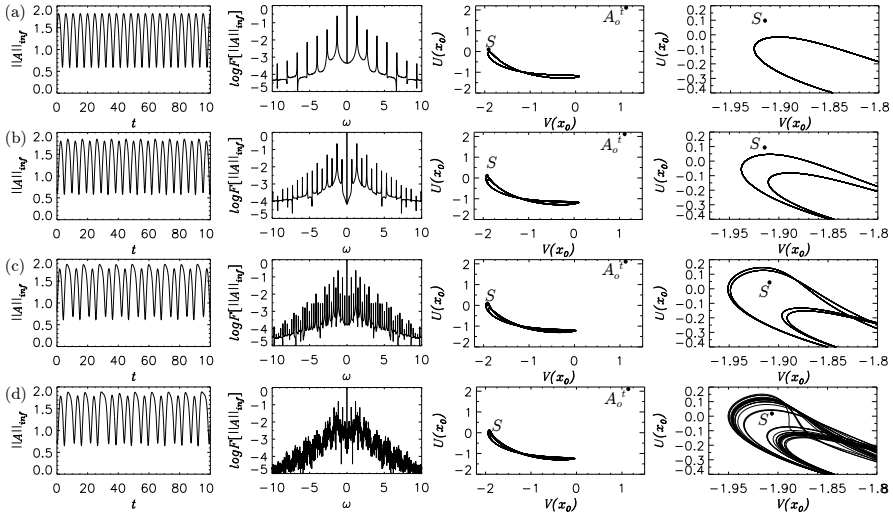

Figure 5.20: Route to temporal chaos for $\theta = 5.2$. Panels (a)–(d) represent the transition from (a) period 1 oscillations to (d) temporal chaos, corresponding to the labels in Figure 5.19. From left to right: temporal trace of $||A||_{\text{inf}}$, its frequency spectrum that allows us to differentiate between the different types of temporal periodicity, a portion of the phase-space containing A_0^t, S and the periodic attractors, and a zoom of the latter where we can appreciate the proximity of S to the cycle. (a) $\rho = 2.70248$ (period 1), (b) $\rho = 2.70358$ (period 2), (c) $\rho = 2.71528$ (period 4), (d) $\rho = 2.72178$ (temporal chaos).

process in detail for the cycle emerging from H_2^- (the case of H_1^- is analogous). In Figure 5.19 we show a zoom of the diagram in Figure 5.18(c) close to BC_2 and in Figure 5.20 a series of panels characterizing the cycle at different values of ρ is shown. From left to right we show a series of time traces corresponding to the temporal evolution of the minima of the soliton, i.e., $||A||_{\text{inf}}$, the Fourier transform of these time traces, a two-dimensional phase space projection onto $(U(x_0,t), V(x_0,t))$, x_0 being the position of the center of the structure, and a zoom of the phase space. Panel (a) in Figure 5.20 corresponds to the situation at $\rho = 2.70248$ in Figure 5.19 labeled with (a). As we can see in the time trace and in the frequency spectrum, the cycle has a single period. In the phase space shown in Figure 5.20 we observe a fixed point corresponding to A_0^t, a saddle point corresponding to the unstable dark soliton denoted by S and a periodic orbit corresponding to the cycle. For this value of ρ the saddle S is far from the cycle. For $\rho = 2.70358$ (panel (b) corresponding to label (b) in Figure 5.19 the time trace and the spectrum reveal that the cycle has period two as can also

be discerned from the phase space projection. In Figure 5.20(c) for $\rho = 2.71528$ the cycle has just suffered another period-doubling resulting a cycle with period four. Finally, Figure 5.20(d) shows the situation for $\rho = 2.72178$, where the cycle has become a chaotic attractor. At this parameter value the system is very close to the boundary crisis BC_2 as can be appreciated from the near tangency between S and the chaotic attractor. Once S touches the attractor, the latter disappears and only A_0^t and A_0^b remain as attractors of the system. The same occurs to the cycles appearing at H_1^-. Using time simulations we were able to estimate the position of the boundary crises BC_1 and BC_2 in parameter space, labeled in Figure 5.17(a). From Figure 5.18(c) to Figure 5.18(d) we can see that at the same time as BC_1 moves toward H_1^-, H_1^- itself approaches SN_1 and therefore that the region of existence of oscillatory DSs shrinks. This behavior can also be seen in Figure 5.17(a).

At this point we can differentiate five main dynamical subregions related to region IV_1, i.e., the 1-SO dark soliton, namely:

- IV_1^a : The 1-SO dark soliton is stable.
- IV_1^b : The soliton oscillates with a single period.
- IV_1^c : The soliton oscillates with period two.
- IV_1^d : The soliton oscillates with period four.
- IV_1^e : Region of temporal chaos bounded by a boundary crisis (BC_2).

The region IV_2 of 2-SO dark solitons has the same sequence of subregions IV_2^a,...,IV_2^e, etc.

Close to BC_2 (respectively, BC_1) the system can exhibit behavior reminiscent of excitability [15]. Here the stable manifold of the saddle soliton S acts as a separatrix or threshold in the sense that perturbations of A_0^t across that threshold do not relax immediately to A_0^t but lead first to a large excursion in phase space before relaxing to A_0^t. In this case the excursion corresponds to what is known as a chaotic transient, where the system exhibits transient behavior reminiscent of the chaotic attractor at lower values of ρ [16, 17]. In Figs. 9.12(a) and (b) we show two examples of this kind of transient dynamics. We choose a value of ρ close to BC_2, namely $\rho = 2.7235$, and modify the parameter ρ for a brief instant using a Gaussian profile of width σ and height h using the instantaneous transformation

$$\rho \mapsto \rho + h(t) \exp\left[-\frac{(x - L/2)^2}{\sigma^2}\right], \tag{5.15}$$

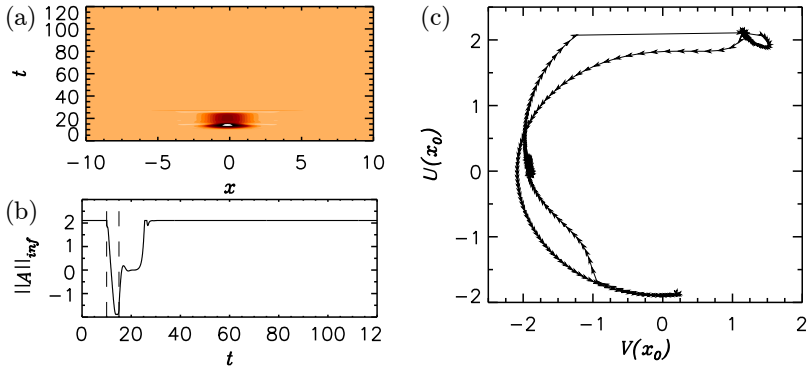

Figure 5.21: Chaotic transient dynamics for $\theta = 5.2$: A chaotic transient is generated when A_0^t is temporally perturbed with a Gaussian perturbation of height $h = -2.55$ (see gray area in time traces); Panel (a) represent space-time plots of the temporal evolution of the field $U(x,t)$, panel (b) shows the time series of the norm $||A||_{\text{inf}}$ and panel (c) is a projection of the phase space.

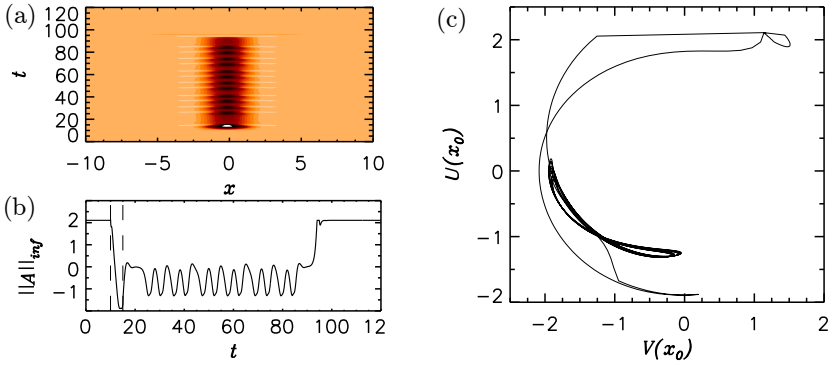

Figure 5.22: Chaotic transient dynamics for $\theta = 5.2$ similar to Figure 9.12 but now for $h = -3.4431$. Supanels (a), (b) and (c) represent the same than in Figure 9.12.

where $\rho = 2.7235$ and $\sigma = 0.781250$ with $h(t) = -2.55$ for $10 \leq t \leq 15$ and $h = 0$ elsewhere [18]. Such a perturbation of A_0^t allows the system to explore the chaotic attractor before returning to the rest state. In Figure 9.12(b) the system explores just one loop of the cycle before returning to the rest state. In usual excitable systems the shape of the large excursion in phase space is a single pulse corresponding to one cycle around a reminiscent periodic orbit, however, in this case several pulses can be observed, corresponding to a piece of the reminiscent

chaotic attractor

5.8 Discussion

In the present chapter we have presented a comprehensive overview of the dynamics of the LL equation in the normal dispersion regime. The bifurcation structure of dark solitons, their stability and the regions of their existence were determined. In this section we will discuss the main results presented along this chapter.

Families of dark solitons

Three families of dark solitons, the 1-soliton and two different types of 2-soliton states, located on three intertwined branches undergoing collapsed snaking in the vicinity of the same Maxwell point, were identified. The 1-soliton states bifurcate from the top left fold of an S-shaped branch of spatially homogeneous states and terminate either on the lower homogeneous steady state (HSS) branch in a Hamiltonian-Hopf (HH) (equivalently, modulational instability) or at the bottom right fold, depending on the detuning parameter θ. On a periodic domain of finite spatial period, these bifurcations are slightly displaced from the folds, and in the case of the HH bifurcation to finite amplitude on the branch of periodic states created in this bifurcation. The 2-soliton states consisting of a pair of identical equidistant solitons in the domain follow a similar branch but branch off the HSS farther from the folds. This is a finite size effect: these states behave like the 1-soliton states on a periodic domain with half the domain length. The third branch consists of a pair of nonidentical solitons and plays a key role: this branch bifurcates from the branch of identical 2-soliton states in a pitchfork bifurcation; as one follows this branch to lower L^2 norm these states undergo a remarkable metamorphosis into a bright soliton with a minimum at its center that allows it to terminate on the periodic states created in the HH bifurcation at the same location as the 1-soliton states, as demanded by theory. The details of this transition are captured in Figs. 5.11 and 5.13. Related behavior likely occurs in the Swift-Hohenberg equation as well (see Figure 19 of [19]). On top of this, solutions with more than 2 peaks and with an arbitrary number of peaks (spatial chaos) may also exist.

Oscillatory instabilities

At yet higher values of the detuning parameter θ we found that the localized states undergo oscillatory instabilities, and at a certain point a period-doubling

bifurcation initiates a period-doubling cascade into chaos. We have used this observation to determine the regions in parameter space where different stationary and dynamical states coexist.

Quadruple zero point

We have shown that the bifurcations that organize the spatial dynamics undergo an important transition at a Quadruple-Zero (QZ) point, which occurs at $(\theta, \rho) = (2, \sqrt{2})$. Here, in the normal dispersion regime, the Belyakov-Devaney (BD) transition turns into an HH bifurcation as the detuning θ increases through $\theta = 2$. For $\theta > 2$ a spatially periodic pattern bifurcates subcritically from the bottom homogeneous state at this HH bifurcation. These periodic solutions were found to be unstable, and hence no stable bright DSs were found. However, the saddle-node bifurcation of the top homogeneous solution remains a reversible Takens-Bogdanov (RTB) bifurcation for all $\theta > \sqrt{3}$. This observation explains the existence of multiple families of dark DSs in this regime, and their organization in the so-called *collapsed snaking* structure [6, 20]. As mentioned, these dark DSs undergo various dynamical instabilities for larger values of the detuning θ.

Normal versus anomalous dispersion

The bifurcation scenario is largely reversed in the case of anomalous dispersion, where the same QZ point plays an equally important role, but now the HH bifurcation turns into a BD bifurcation when $\theta > 2$ [2, 21]. Moreover, the top homogeneous solution is now always unstable and the upper fold never corresponds to a RTB bifurcation. This reverse character of the bifurcation points has important consequences. First, dark DSs no longer exist, although the inclusion of additional, higher order dispersion can stabilize the top homogeneous solution and hence lead to stable dark DSs [22]. Second, for $41/30 < \theta < 2$, a stable periodic solution coexists with the stable bottom homogeneous solution giving rise to bright DSs that are organized in a homoclinic snaking structure [10, 11]. However, as we have seen in Chapter 4, for $\theta > 2$, the homoclinic snaking structure disappears and bright solitons are organized in a foliated snaking type of structure. Finally, despite these differences in the regions of existence of dark and bright DSs in the normal vs. anomalous dispersion regime, the temporal dynamics of the existing solutions are very similar at higher values of the detuning θ. Here, for normal dispersion, we reported the existence of oscillatory and chaotic dynamics of dark DSs as the detuning is increased. The same dynamical instabilities have been observed in the case of anomalous dispersion at high values of θ, but this time for bright DSs [16, 21]. This suggests that the

unfolding of the dynamics can be related to the same type of bifurcation point in both cases.

5.9 Conclusions

The analysis presented in this chapter provides a detailed map of the regions of existence and stability of dark DSs, which could serve as a guide for experimentalists to target particular DS solutions. We have shown that dark DSs exist only in a well-defined zone within the wider region of bistability between two stable homogeneous solutions. Within this zone, dark DSs are organized in a bifurcation structure called a *collapsed snaking* structure. The word "collapsed" refers to the fact that the region of existence of dark DSs shrinks exponentially with increasing number of spatial oscillations (SOs) in the soliton profile (Figure 5.6). The collapse of the snaking structure implies that DSs with many SOs can only be found at the Maxwell point ρ_M, a fact that favors the observation of DSs with a single SO over that of broader DS with many SOs.

Although such a collapsed snaking structure persists for higher values of the detuning θ, we also showed that narrow dark DSs with a low number of SOs destabilize first as θ increases (Figure 5.14) and start to oscillate in time. Therefore, at higher values of θ stable stationary dark DSs found experimentally will most likely have an intermediate number of SOs. Our general analysis of the multistability of dark DSs may also explain the numerical observations in Ref. [2], where it was shown that the pulse profile of dark DSs becomes more distorted as the detuning increases. This may be due to the fact that stable dark DSs with a larger number of SOs are more likely to be found for higher values of the detuning.

As shown in Figure 5.2, in the normal dispersion regime rather large values of the detuning θ and pump power ρ are required to obtain a sufficiently wide region of dark DSs (region IV) to observe such states experimentally. However, in recent years, the FC community has become increasingly successful at reaching the required values of pump power and detuning. As a result, dark DSs with different numbers of spatial oscillations (SOs) in their center (see, e.g., Figure 5.8) have been observed in experiments [5]. In Ref. [5] dark DSs were found using a normalized pump power $\rho \approx 2.5$ and normalized detuning $\theta \approx 5$. Figures 5.17 and 5.18 show that around these parameter values one can indeed find dark DSs with different numbers of SOs that can undergo oscillatory instabilities.

In Chapter 6 we will analyze how dark solitons and their bifurcation structure are modified by considering higher orders of dispersion, in particular we focues

on TOD effects.

References

[1] N. Akhmediev and A. Ankiewicz, eds., *Dissipative Solitons*, Lecture Notes in Physics **661** (Springer, New York, 2005); N. Akhmediev and A. Ankiewicz, eds., *Dissipative Solitons: From Optics to Biology and Medicine*, Lecture Notes in Physics **751** (Springer, New York, 2008).

[2] C. Godey, I.V. Balakireva, A. Coillet, and Y.K. Chembo, *Stability analysis of the spatiotemporal Lugiato-Lefever model for Kerr optical frequency combs in the anomalous and normal dispersion regimes,* Phys. Rev. A **89**, 063814 (2014).

[3] V.E. Lobanov, G. Lihachev, T.J. Kippenberg, and M.L. Gorodetsky, *Frequency combs and platicons in optical microresonators with normal GVD,* Opt. Expr. **23**, 7713-7721 (2015).

[4] P. Parra-Rivas, D. Gomila, E. Knobloch, S. Coen, L. Gelens, *Origin and stability of dark pulse Kerr combs in normal dispersion resonators,* Optics Letters **41**, 2402-2405 (2016)

[5] X. Xue, Y. Xuan, Y. Liu, P.-H. Wang, S. Chen, J. Wang, D.E. Leaird, M. Qi, and A.M. Weiner, *Mode-locked dark pulse Kerr combs in normal-dispersion microresonators,* Nature Photon. **9**, 594 (2015).

[6] Y.P. Ma, J. Burke, and E. Knobloch, *Defect-mediated snaking: A new growth mechanism for localized structures,* Phys. D (Amsterdam) **239**, 1867 (2010).

[7] E. Knobloch, *Spatial Localization in Dissipative Systems,* Annu. Rev. Cond. Matter Phys. **6**, 325 (2015).

[8] J. Knobloch and T. Wagenknecht, *Homoclinic snaking near a heteroclinic cycle in reversible systems,* Phys. D (Amsterdam) **206**, 82 (2005).

[9] K. Kolossovski, A.R. Champneys, A.V. Buryak, and R.A. Sammut, *Multi-pulse embedded solitons as bound states of quasi-solitons,* Phys. D (Amsterdam) **171**, 153 (2002).

[10] A.R. Champneys, *Homoclinic orbits in reversible systems and their applications in mechanics, fluids and optics,* Phys. D (Amsterdam) **112**, 158 (1998).

[11] D. Gomila, A.J. Scroggie, and W.J. Firth, *Bifurcation structure of dissipative solitons*, Phys. D (Amsterdam) **227**, 70 (2007).

[12] G. Iooss and M.C. Pérouème, *Perturbed Homoclinic Solutions in Reversible 1:1 Resonance Vector Fields,* J. Diff. Eqs., **102**, 62 (1993).

[13] A.R. Champneys, E. Knobloch, Y.P. Ma, and T. Wagenknecht, *Homoclinic snakes bounded by a saddle-center periodic orbit,* SIAM J. Appl. Dyn. Syst. **11**, 1583 (2012).

[14] R. Hilborn, *Chaos and Nonlinear Dynamics: An introduction for Scientists and Engineers* (Oxford University Press, Oxford, 2000).

[15] D. Gomila, M. A. Matias, and P. Colet,*Excitability mediated by localized structures in a dissipative nonlinear optical cavity,* Phys. Rev. Lett.**94**, 063905 (2005); D. Gomila, A. Jacobo, M. A. Matías, and P. Colet, *Phase-space structure of two-dimensional excitable localized structures,* Phys. Rev. E **75**, 026217 (2007); *Effects of a localized beam on the dynamics of excitable cavity solitons,* Phys. Rev. A 75, 053821 (2008).

[16] F. Leo, L. Gelens, P. Emplit, M. Haelterman, and S. Coen, *Dynamics of one-dimensional*

Kerr cavity solitons, Opt. Express **21**, 9180 (2013).

[17] C. Grebogi, E. Ott, and J.A. Yorke, *Crises, sudden changes in chaotic attractors, and transient chaos,* Phys. D (Amsterdam) **7**, 181 (1983).

[18] P. Parra-Rivas, D. Gomila, M.A. Matías, and P. Colet, *Dissipative soliton excitability induced by spatial inhomogeneities and drift,* Phys. Rev. Lett. **110**, 064103 (2013); P. Parra-Rivas, D. Gomila, M.A. Matías, P. Colet, and L. Gelens, *Effects of inhomogeneities and drift on the dynamics of temporal solitons in fiber cavities and microresonators,* Opt. Express **22**, 3486 (2014); P. Parra-Rivas, D. Gomila, M.A. Matías, P. Colet, and L. Gelens, *Competition between drift and spatial defects leads to oscillatory and excitable dynamics of dissipative solitons,* Phys. Rev. E **93**, 012211 (2016).

[19] J. Burke and E. Knobloch, *Localized states in the generalized Swift-Hohenberg equation,* Phys. Rev. E **73**, 056211 (2006).

[20] J. Burke, A. Yochelis, and E. Knobloch, *Spatially localized oscillating states in periodically forced dissipative systems,* SIAM J. Appl. Dyn. Syst. **7**, 651 (2008).

[21] P. Parra-Rivas, D. Gomila, M.A. Matías, S. Coen, and L. Gelens, *Dissipative soliton excitability induced by spatial inhomogeneities and drift,* Phys. Rev. A **89**, 043813 (2014).

[22] M. Tlidi and L. Gelens, *High-order dispersion stabilizes dark dissipative solitons in all-fiber cavities,* Opt. Lett. **35**, 306 (2010); M. Tlidi, P. Kockaert, and L. Gelens, Phys. Rev. A **84**, 013807 (2011).

Chapter 6

Third order dispersion effects: stabilization of solitons

6.1 Introduction

Previously in this thesis, we have studied the dynamics, stability and bifurcation structures of LSs in the two main regimes of operation of the temporal cavities described by the LL model, namely the anomalous and normal group velocity dispersion (GVD) regimes. In the anomalous regime (see Chapter 4) the typical LSs are bright solitons, while in the normal one (see Chapter 5) they are dark. We have also shown that these two type of structures have a different origin: while a bright LS arises as a pattern-element, the dark ones are formed due to the locking of two fronts with different polarities. However, in a real experimental setup, high-order chromatic dispersion (HOD) effects must be taken into account. For instance, for certain values of the driving field frequency the GVD coefficient $\beta_2 \approx 0$, and therefore the third order of dispersion (TOD) becomes relevant. Because of that, it is relevant, from a theoretical and experimental point of view, to know how these HOD terms modify the scenario. Hence, in this Chapter we will focus on analyzing how the dynamics, stability, and bifurcation structure of the LSs studied previously get, modified when considering the effect of TOD in the system.

This term breaks the reflection reversibility $x \to -x$, which leads to asymmetries in the temporal and spectral profiles [1–4]. This asymmetry is also responsible for the observed constant-velocity temporal drift. In microresonators, the carrier frequency of the LS is shifted from the pump due to spectral recoil from the

emission of dispersive waves [3–5], and its group-velocity differs slightly from that of the pump. In fiber cavities, a similar change in group-velocity occurs through acoustic effects and leads to long-range LS interaction [6].

Here, we will show that TOD can stabilize solitons in both regimes of operation (anomalous and normal GVD), suppressing oscillatory instabilities [7, 8]. Moreover, in the normal GVD regime we have also found that bright solitons sitting on a low-intensity background A_0^b, which in the absence of higher order terms are found to be unstable, can come into stable existence with TOD due to the appearance of oscillatory tails around the top HSSs solutions A_0^t.

This Chapter is organized as follows: in Section 6.2 we present some features of the influence of TOD terms on the dynamics of solitons in the LL equation. Later, in Section 6.3 we study the spatial dynamics of the system, analyzing the structure of homoclinic orbits to the HSSs when reflection symmetry is broken. In Section 6.4 we present the results of adding TOD to the LL equation in the anomalous regime. Together with the suppression of oscillatory and chaotic dynamics we analyze how the bifurcation structure of solitons is modified. After that, in Section 6.5, we show a similar analysis for the normal dispersion regime, where the dynamics of dark solitons is altered and bright solitons appears. Finally in Section 6.6 we draw some conclusions for this chapter.

6.2 Overview of the Lugiato-Lefever equation with drift instability

Using the normalization of [9], and including dispersion up to third-order, the LL equation reads,

$$\partial_t A = -(1+i\theta)A + i\nu\partial_x^2 A + d_3\partial_x^3 A + iA|A|^2 + \rho \tag{6.1}$$

where, ρ, θ are real control parameters representing the normalized injection and frequency detuning. Parameter d_3 represents the relative strength of the TOD. In Section 1.2 we have seen that d_3 can be calculated from the physical parameters of the system, $d_3 = (1/3)(2\alpha/L)^{1/2}\beta_3/|\beta_2|^{3/2}$ [10], where α is half the percentage of power lost per round-trip, L is the cavity length, and β_2 (β_3) is the second (third) order dispersion coefficient.

In this section we present some results regarding several effects of adding a TOD term in the model. First, TOD breaks the reflection symmetry in Eq.(6.1) such that its structured solutions now have an asymmetric profile. This leads to the advection of the different states with a velocity depending on the control pa-

rameters. The advection leads to convective instabilities in regions of parameter space where there is bistability between two different states.

6.2.1 The breaking of the reflection symmetry induces drift

When $d_3 = 0$, Eq.(6.1) is invariant under the transformation $(x, A) \to (-x, A)$ and one says that the system has reflection symmetry, or that the system is reversible in space ($x-$reversible). In contrast, when $d_3 \neq 0$, the system is no longer $x-$reversible due to the introduction of an odd derivative in the right-hand side of Eq.(6.1). Because of that the solutions of (6.1) are asymmetric with respect to the center of the structure, let us say $x = 0$, and they drift with a constant velocity. Here we will show that, in the linear regime, the breaking of the reflection symmetry induced by the TOD, causes a modification of the profile of the solution with the form of the *Goldstone* mode, which induces on one hand a permanent shift of the solution (i.e. a drift), and on the other hand the asymmetry of such a state.

Any traveling solution of the form $A(x,t) = A(x - ct, t)$ satisfies the equation

$$\partial_t A - c\partial_x A = -(1 + i\theta)A + i\nu\partial_x^2 A + d_3\partial_x^3 A + iA|A|^2 + \rho, \tag{6.2}$$

where the Galilean transformation $x \mapsto x' = x - ct$ has been performed, and where $'$ has been dropped. In particular, here we are interested on steadily drifting LSs, and therefore in states that, on the moving reference frame at velocity c, are stationary (i.e. $\partial_t A = 0$).

Let us assume that, for $d_3 = 0$, the steady state solutions of the LL are given by A_s. Then, if the reflection symmetry is weakly broken ($d_3 \ll 1$), any solution on the moving reference frame can be expanded as an asymptotic series on d_3 as,

$$A(x) = A_s(x) + d_3 A_1(x) + \cdots, \tag{6.3}$$

with A_1 beeing the (first order) modification of the solution due to the influence of the TOD. Introducing the ansatz (6.3) into Eq.(6.13), and scaling the velocity as $c = c_1 d_3 + \cdots$, one gets, at first order in d_3

$$L[A_s]A_1 = -\partial_x^3 A_s - c\partial_x A_s. \tag{6.4}$$

This equation will have a solution if the next solvability condition holds

$$\langle w, -\partial_x^3 A_s - c\partial_x A_s \rangle = 0, \tag{6.5}$$

where w is the eigenfunction of the adjoint operator $L^\dagger$ with eigenvalue zero (i.e. $L^\dagger w = 0$), which has the same spatial symmetry as the Goldstone mode of the

system $\mathcal{G}(x) \equiv \partial_x A_s$, and $\langle \cdot, \cdot \rangle$ denotes the scalar product defined in terms of full spatial integration over the considered domain (see Section B.1).

From Eq.(6.5), one gets that the solutions (6.3) drift with a constant velocity

$$c = -d_3 \frac{\langle w, \partial_x^2 \mathcal{G} \rangle}{\langle w, \mathcal{G} \rangle}, \tag{6.6}$$

proportional to d_3.

Once this condition is satisfied Eq.(6.4) becomes

$$L[A_s]A_1 = 0, \tag{6.7}$$

which has solutions of the form

$$A_1(x) = a\mathcal{G}(x), \tag{6.8}$$

where the coefficient a is determined at higher-orders on d_3. So, at first order in d_3, we can see that the asymmetry in the solution (6.3) is generated by an excitation of the (anty-symmetric) Goldstone mode, driven by the TOD.

6.2.2 Linear stability analysis

In this section we will first apply a linear stability analysis on the HSSs and we derive the dispersion relation of the system. Later we will introduce the concept of convective and absolute instabilities arising when advection is considered in regions of bistability between two states. Assuming perturbation of the HSSs of the form

$$\begin{bmatrix} U \\ V \end{bmatrix} = \begin{bmatrix} U_0 \\ V_0 \end{bmatrix} + \epsilon \begin{bmatrix} a \\ b \end{bmatrix} e^{ikx+\Omega t} + c.c., \tag{6.9}$$

with a and b real numbers, and inserting (6.9) into Eq.(6.1), we obtain that at first order in ϵ the dispersion relation is given by

$$\Omega(k) = \Omega_r + i\Omega_i = -1 \pm \sqrt{a_1 + a_2 k^2 - k^4} - id_3 k^3 \tag{6.10}$$

where we have defined $a_1 = 4I_0\theta - 3I_0^2 - \theta^2$ and $a_2 = \nu(4I_0 - 2\theta)$.

The real part of Eq.(6.10) equal to zero, namely $\Omega_r(k) = 0$, gives us the conditions for HSS to be modulationally unstable to perturbations (6.9), and is not affected by the TOD terms. Therefore, the regions of stability remain the same as in the case when $d_3 = 0$, which we discussed in details in Chapter 3, 4 and 5. A MI occurs at $I_0 = 1$ when $\theta < 2$ in the anomalous case and when $\theta > 2$ in the normal one.

TOD does not change the onset of the MI, but it changes its nature and leads to convective and absolute instabilities by introducing a group velocity. In the dispersion relation (6.10), $\Omega_i \neq 0$, such that the perturbation becomes $e^{\Omega t+ikx} = e^{\Omega_r t+i(kx+\Omega_i t)}$, which has the form of a traveling wave. As a result perturbations to the HSSs drift away. In next section we will introduce briefly the concepts of absolute and convective instabilities.

6.2.3 Convective and absolute instabilities

To explain these two instabilities we need to consider a system with bistability between two different extended states, which we call A and B. These states can be either HSSs solutions or patterned states.

In the absence of drift, we can say that a solution (e.g. A) is stable if, for any perturbation of finite size and amplitude, the system relaxes everywhere back to A. In contrast, A is said to be unstable if this perturbation grows and the system eventually reaches the other state B [12]. In the LL system, the state A is a HSS, while the state B could be either a patterned state or another HSS. Which bistability exists depends on the parameters and dispersion regime (see Chapter 3 and Chapter 5).

When $d_3 \neq 0$, any spatial inhomogeneity of the system drifts. In particular initial localized perturbations (i.e. finite size and amplitude) on state A can evolve in two different ways depending on the balance between the growth of the initial perturbation and the advection. If the advection is faster than the growth of the perturbation the system will return locally to its initial state A, and the system is said to be *convective unstable*. On the contrary, if the growth is faster than the upstream drift, then the system does not relax to A, but state B will instead overtake the whole domain. In this last case we would say that the system is *absolute unstable*.

In the anomalous dispersion case, convective instabilities where studied in the LL model in Ref.[1]. In that work, the authors calculate analytically and numerically the thresholds of both instabilities. The convective threshold is obtained by the condition

$$\Omega_r(k_c) = 0, \tag{6.11}$$

with k_c the most unstable mode. This is the condition needed for the MI to occur. On the contrary, the absolute threshold is reached when

$$\Omega_r(k_s) = 0, \tag{6.12}$$

where k_s is a saddle point satisfying $d\Omega/dk = 0$. A plot of both thresholds can

be seen in Figure 2 of Ref.[1].

As a result, any perturbation above convective threshold $I_0 = 1$ and under the absolute threshold, will develop a pattern that will drift in such a way that locally the system returns to A_0^b. However, any perturbation above the absolute threshold will grow everywhere, and therefore the pattern will occupy the whole domain. As far as we know, convective instabilities have not been yet studied in the normal dispersion regime and it is an interesting topic for a future work.

In Chapter 10, we will use these concepts again when studying the excitability induced by fronts in the real Ginzburg-Landau equation, where the states A and B are HSSs.

6.2.4 Computation of steadily drifting localized states

The weakly nonlinear analytical expresion (6.3) for the asymmetric solution, arising in the presence of TOD, is only valid for $d_3 \ll 1$. However, any steadily drifting solution of Eq.(6.1) can be computed numerically, using a Newton-Raphson algorithm (see Section B.3) to solve the equation,

$$-c\partial_x A = -(1+i\theta)A + i\nu\partial_x^2 A + d_3\partial_x^3 A + iA|A|^2 + \rho. \tag{6.13}$$

To do that, one also needs to calculate the velocity c as part of the solution of Eq.(6.13), which can be done by adding to Eq.(6.13) an extra condition on the form $Q[A(x)] = 0$. This is then equivalent to solve the following nonlinear eigenvalue of the problem,

$$\begin{cases} d_3\dfrac{d^3U}{dx^3} - \nu\dfrac{d^2V}{dx^2} + c\dfrac{dU}{dx} - U + \theta V - V(U^2+V^2) + \rho = 0 \\ \\ d_3\dfrac{d^3V}{dx^3} + \nu\dfrac{d^2U}{dx^2} + c\dfrac{dV}{dx} - V - \theta U + U(U^2+V^2) = 0 \\ \\ Q[A(x)] = 0, \end{cases} \tag{6.14}$$

which has been written considering the real variables U and V.

Without loss of generality we constrain a maximum of the field A to occur at $x = 0$. Such,

$$Q[A(x)]|_{x=x_0} = \frac{d|A|^2}{dx}|_{x_0} = 2\left(U\frac{dU}{dx} + V\frac{dV}{dx}\right)_{x_0}, \tag{6.15}$$

or

$$Q[A(x)]|_{x=x_0} = \frac{dU}{dx}_{x_0}. \tag{6.16}$$

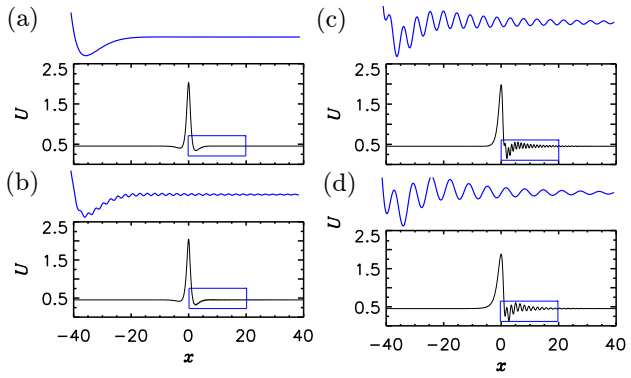

Figure 6.1: Single DSs for $d_3 = 0.07$ in (a), $d_3 = 0.1$ in (b), $d_3 = 0.2$ in (c) and $d_3 = 0.3$ in (d) for $(\theta, \rho) = (2.2, 1.5)$ and $L = 160$. In blue a detail of the oscillatory tails are shown.

One could also use integral phase conditions as done in Refs. [13, 14].

Solving the system (6.14), we can continue any of the LSs of the LL equation from $d_3 = 0$ to any value $d_3 \neq 0$. In Figure 6.1 we can observe some single peak LS of Eq.(6.13) for $(\theta, \rho) = (2.2, 1.5)$ and different values of d_3. The TOD strength for each panel are $d_3 = 0.07, 0.1, 0.2$ and 0.25 from (a) to (d) respectively. As we can observe the field profiles are asymmetric and the tails at one side and the other of the central core are different. Moreover, the asymmetry increases with the strength of TOD. These oscillatory tails can be interpreted as dispersive wave or Cerenkov radiation emitted by the soliton [4, 5, 15].

In what follows we will just focus in the modification of the properties of LSs when including TOD in both the normal and anomalous dispersion regimes.

6.3 Spatial dynamics: homoclinic orbits in non-reversible systems

As we said before, the introduction of an odd derivative breaks the spatial reversibility $(x, A) \mapsto (-x, A)$ of the system, and therefore solutions of Eq.(6.1) are no longer symmetric with respect to the symmetry plane at $x = 0$, i.e. respect to the symmetry section $\mathcal{S} \equiv \text{fix}(R)$ defined in Chapter 2. The stronger the TOD (d_3), the larger the asymmetry and drift velocity of LSs will be.

Nevertheless, despite this symmetry breaking, any LS can still be described as an homoclinic orbit to the HSSs A_0 in the reference frame moving with the LS.

In this section we will mainly focus on the spatial dynamics in the anomalous dispersion regime, although the concepts introduced here can also be applied to the normal dispersion case as we will see in Section 6.6.

The stationary LL equation in the moving reference frame i.e. Eq.(6.13) can also be written as the dynamical system,

$$\begin{aligned} d_x y_i &= y_{i+2}, \qquad i = 1, ..., 4 \\ d_x y_5 &= d_3^{-1}[\nu y_4 - c y_3 + y_1 - \theta y_2 - y_2 y_1^2 - y_2^3 - \rho] \\ d_x y_6 &= d_3^{-1}[-\nu y_3 - c y_4 + y_2 - \theta y_2 - y_1^3 - y_1 y_2^2], \end{aligned} \tag{6.17}$$

considering the 6-dimensional phase space defined by variables $y_1 = U$, $y_2 = V$, $y_3 = d_x U$, $y_4 = d_x V$, $y_5 = d_x^2 U$ and $y_6 = d_x^2 V$. This procedure has been extensively applied in Chapter 2 in the context of the reversible LL Eq.(2.1). Previous work related with the application of this concept in reversible systems can be found in Refs. [16–20]. As we saw in the previous Section the absence of x-reversibility can be easily seen by plotting the profiles of the LSs shown in Figure 6.1, where the fronts leaving and approaching the HSS A_0 are now different.

In terms of the dynamical system defined by (6.17), these fronts can be interpreted as heteroclinic orbits in a six dimensional phase space and a LS as a homoclinic orbit results from the intersection of the unstable and stable manifolds of A_0. In Figure 6.2 we show the projection of the single LS for $d_3 = 0.25$ (see Figure 6.1(d)) into three different subspaces of the phase space. In blue we plot the unstable manifold $W^u(A_0^b))$ that leaves the fixed point A_0 monotonically. In red we show the stable manifold $W^s(A_0^b))$ that approaches A_0 in an oscillatory way characterized by a given frequency and decay rate. In the linear approximation we can characterize these manifolds studying the spatial eigenvalues of the system (6.17). In order to do this we calculate the eigenvalues of the linear operator associated with the dynamical system (6.17) i.e. its Jacobian,

$$\mathcal{D}f(y_0) = d_3^{-1} \left[\begin{array}{cccccc} 0 & 0 & d_3 & 0 & 0 & 0 \\ 0 & 0 & 0 & d_3 & 0 & 0 \\ 0 & 0 & 0 & 0 & d_3 & 0 \\ 0 & 0 & 0 & 0 & 0 & d_3 \\ 1+2y_1y_2 & \theta - y_1^2 - 3y_2^2 & -c & 0 & \nu & 0 \\ \theta - y_2^2 - 3y_1^2 & 1-2y_1y_2 & 0 & -c & -\nu & 0 \end{array} \right]_{y=y_0}, \tag{6.18}$$

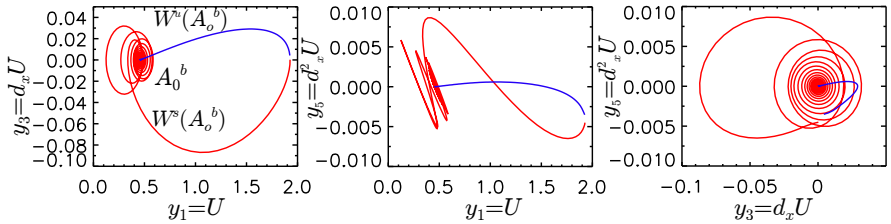

Figure 6.2: Projection of the single LS shown in Figure 6.1(d) into subspaces (y_1, y_3) in (a), (y_1, y_5) in (b), and (y_3, y_5) in (c) of the phase space defined by (6.17). In red (blue) we plot the stable (unstable) manifolds $W^{s,u}(A_0^b))$ of A_0^b.

with $y_0 = [U_0, V_0, 0, 0, 0, 0]$.

We find that the eigenvalues of (6.18) are roots of the characteristic polynomial

$$d_3^2\lambda^6 + (2cd_3 + 1)\lambda^4 - 2d_3\lambda^3 + (a_2 + c^2)\lambda^2 - 2c\lambda + 1 + a_1 = 0. \tag{6.19}$$

[1] If $d_3 = 0$ we recover the characteristic equation for the LL equation, namely Eq.(2.14), where the solutions always come in pairs: each spatial eigenvalue λ is accompanied by its counterpart $-\lambda$. This property is also reflected in the fact that with $d_3 = 0$, Eq.(6.19) is biquadratic in λ and as a result the fronts leaving and approaching A_0 have the same envelope and wavelength. When $d_3 \neq 0$, this is no longer the case and therefore the trajectories leaving and approaching A_0 are different (see the field profiles in Figure 6.1). The eigenvalues of (6.18) can be calculated numerically. In Figure 6.3 we can observe the dependence of $\mathrm{Re}[\lambda]$ and $\mathrm{Im}[\lambda]$ with d_3 for $(\theta, \rho) = (2.2, 1.5)$. Panels (i) and (ii) of Figure 6.3 show the spatial eigenspectrum corresponding to two slices of Figure 6.3 for $d_3 = 0.1$ and $d_3 = 0.25$ respectively. Due to the reversibility symmetry breaking, the spatial eigenvalues do not appear in pairs. From all these eigenvalues, there are two that are dominant in the dynamics.

The frequency and decay rate of the $W^s(A_0^b))$ correspond to the imaginary and real part of the eigenvalue with the smallest, in absolute value, negative real part, namely $\mathrm{Im}[\lambda^-]$ and $\mathrm{Re}[\lambda^-]$. On the contrary $W^u(A_0^b))$ is characterized by the eigenvalue with the smallest positive real part, that is λ^+. λ^+ has no imaginary part which explains the monotonic way in which $W^u(A_0^b))$ approaches A_0^b (see Figure 6.2). Due to this, trajectories leaving A_0^b do so following $e^{i\lambda^+ x}$

[1] Characteristic equation (6.19) can be equivalently obtained by calculating the grow rates of perturbations to the HSSs, i.e. considering the ansatz for trajectories leaving/approaching the HSSs, $U(x) = U_0 + \epsilon u(x)$ and $V(x) = V_0 + \epsilon v(x)$, with ansatzs $u(x) = ae^{\lambda x}$, $v(x) = be^{\lambda x}$, and $\lambda \in \mathbb{C}$. These calculations are shown in the Appendix at the end of this Chapter.

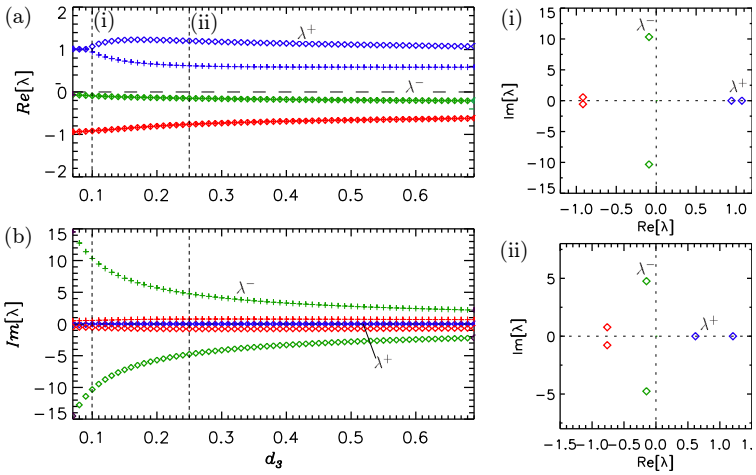

Figure 6.3: Real and imaginary part of the spatial eigenvalues of the HSSs (solutions of Eq.(6.19)) in function of d_3 for $(\theta, \rho) = (2.2, 1.5)$. In (i) $d_3 = 0.1$, (ii) $d_3 = 0.25$ (see panels (a) and (b).

and trajectories approaching A_0 can be described by $e^{i\lambda^- x}$. We verified this for two different values of d_3, namely $d_3 = 0.1$ and $d_3 = 0.25$, where the two oscillatory trajectories approaching A_0^b can be described by the function

$$y_1(x) - y_{0,1} = c_1 e^{\mathrm{Re}[\lambda^-]x} \cos(\mathrm{Im}[\lambda^-]x + \varphi_1). \tag{6.20}$$

This fitting is shown in Figure 6.4. In blue we plot the fronts and in red the fitted approximation using Eq.(6.20). The red dashed line represents the decay of the oscillatory tails determined by the $\mathrm{Re}[\lambda^-]$. For both values of d_3, the fitting is very accurate confirming that the linear theory gives a good approximation of the shape of the tails of the LSs.

An analytical approximation for those eigenvalues can be obtained by solving by Eq.(6.19) only considering the highest order in λ. In this way, we obtain that λ^- can be approximated by the expression

$$\lambda = \lambda^- = \pm i \frac{\sqrt{1 + 2cd_3}}{d_3}. \tag{6.21}$$

This expression shows that the eigenvalue approaches infinity ($\lambda^- \to \infty$) when TOD becomes zero ($d_3 \to 0$), result that can be observed looking at the spectrum of $\mathcal{D}f(y_0)$ for different values of d_3. When $d_3 \to 0$, these two eigenvalues λ^-,

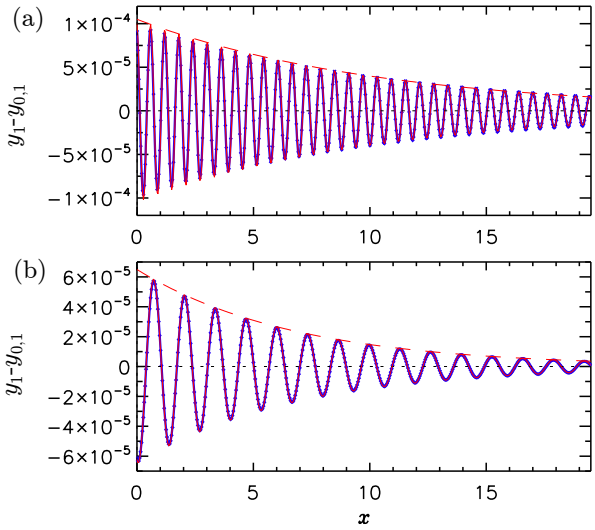

Figure 6.4: Fitting (in red) of the real part of front (in blue) approaching the HSS, A_0^b for parameters $\rho = 1.5$, $\theta = 2.2$ and $L = 160$. In (a) $d_3 = 0.1$ and this value $\mathrm{Re}[\lambda^-] = -0.0902543$, $\mathrm{Im}[\lambda^-] = 10.3256$, $\varphi = 0.3$ and $c_1 = 0.000105$. In (b), $d_3 = 0.25$, $\mathrm{Re}[\lambda^-] = -0.148424$, $\mathrm{Im}[\lambda^-] = 4.75771$, $\varphi = 2.85$ and $c_1 = 0.000065$. The red dashed line correspond to the envelope of the front approximated by $e^{\mathrm{Re}[\lambda^-]}$.

and its complex conjugate, tends to $\pm i\infty$. Figure 6.5 shows how the wavelength $\lambda_{tails} = 2\pi/\mathrm{Im}[\lambda^-]$ of the oscillatory tails changes as function of d_3, where $\mathrm{Im}[\lambda^-]$ has been calculated with approximation given Eq.(6.21) (in red diamonds) and by solving the complete polynomial (6.19) in blue crosses. Indeed, for small values of d_3 the agreement is quite good.

6.4 Bifurcation structure and stability of solitons in the anomalous dispersion regime

In this section we will study how the bifurcation structure of bright solitons and their stability are modified by the effects of the TOD term. As we saw in Chapter 4, in the absence of TOD, the LL equation in anomalous GVD, exhibits a multistability of soliton states with a different number of peaks. For $\theta < 2$, these states are organized in a snake-and-ladders structure [16, 21]. In contrast, as we showed in Section 4.5, when θ become larger than 2, LSs are organized in a foliated snaking type of structure [22].

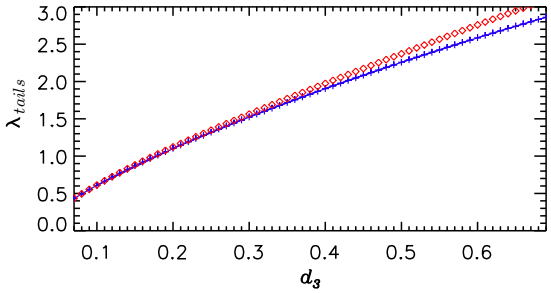

Figure 6.5: Wavelength of the oscillatory tails λ_{tails}. In blue crosses the exact value and in red diamonds the approximated one using expression (6.21).

When TOD is taken into account, these bifurcation structures are modified. In the first case we will show how the branches of solutions of the snakes-and-ladders structure, present for $\theta < 2$, are reorganized in a stack of isolas. In the second case, the scenario is much complex, and the main bifurcation structure is a kind of *mixed snaking*, where the solution branches corresponding to a odd or even numbers of peaks are now interconnected [7].

6.4.1 Dynamics and stability of single bright solitons

In Section 4.6 we have studied the temporal instabilities arising in the anomalous regime for high values of detuning. In this parameter range, a bright soliton can exhibit temporal oscillations, temporal chaos and even spatio-temporal chaos. Here we will analyze how the dynamical regions of single bright solitons are modified when considering TOD effects. As we will see any oscillatory or chaotic regimes can be suppressed by a large enough TOD showing that TOD in microresonators can stabilize Kerr combs [4, 7].

An example of oscillatory and chaotic behavior of an isolated bright soliton in the absence of TOD ($d_3 = 0$) is shown in Figure 6.6(a) and 6.7(a), respectively. Only the pump amplitude differs in these two simulations as indicated in the captions. The pseudocolor plots show the evolution of the temporal intensity profile of the intracavity field. Figures 6.6(b) and 6.7(b) reveal that when the magnitude of TOD is sufficiently large the dynamical instabilities are completely suppressed: the soliton is stable, albeit in a moving reference frame. In order to verify whether the stabilization of the LSs is a general feature in the presence of TOD, we analyzed the stability of solitons in the whole parameter space (θ, ρ) for various values of the TOD. The result of this analysis is shown in

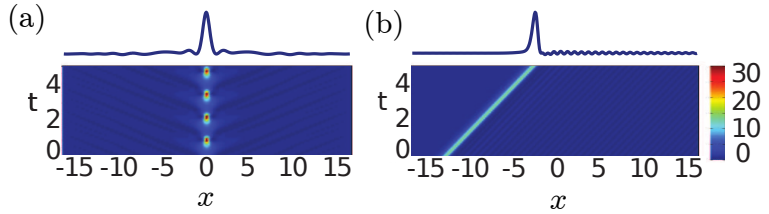

Figure 6.6: Evolution of (a) the temporal intensity profile of an oscillating soliton over successive round trips in the absence of TOD ($d_3 = 0$). (b) With $d_3 = 0.15$, the system is stable. The profiles at time $t = 5$ are shown on top of each graph. $\theta = 6.1$, $\rho = 4$.

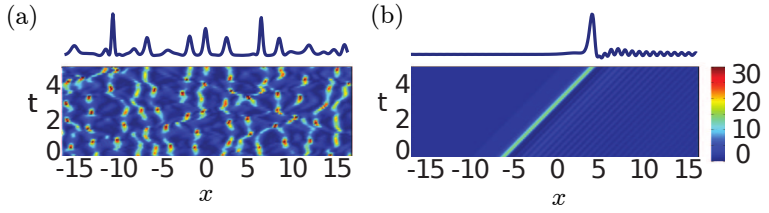

Figure 6.7: Same as Figure 6.6 but for $\rho = 5.5$, for which the solution exhibits spatio-temporal chaos in the absence of TOD.

Figure 6.8. As we already know for $\theta < \sqrt{3}$, only one HSS exists, hence the system is monostable. For $\theta > \sqrt{3}$ three HSS states appear, one of which is a saddle point (unstable), hence this regime is referred as bistable. These homogeneous solutions are connected through the saddle-node bifurcations $\mathrm{SN}_{hom,1,2}$ and $\mathrm{SN}_{hom,2}$ shown in Figure 6.8. We also plot the saddle-node bifurcation SN_1 and SN_2 that determine the region of existence of LSs (see Section 4.6) Figure 6.8(a)-(c) represent the same $(\theta, \rho)-$parameter space for increasing values of d_3.

From Figure 6.8, it is clear that while the region of existence of the HSSs is independent of TOD, the snaking region in which LSs can be found (between the blue lines) shrinks with increasing values of the TOD. To highlight this point, we plot in Figure 6.9 the width of the snaking region, $\Delta\rho = \rho(\mathrm{SN}_2) - \rho(\mathrm{SN}_1)$, versus the TOD strength d_3 for a fixed detuning $\theta = 6.1$. Here it can be seen that the shrinking, while initially rapid, somewhat saturates at higher d_3 such that a region admitting solitons solutions can be found independent of the TOD strength d_3.

Figures 6.8(a)–(c) also illustrate the dependence of various regions of instabilities of a single bright soliton as a function of the TOD strength d_3. We distinguish

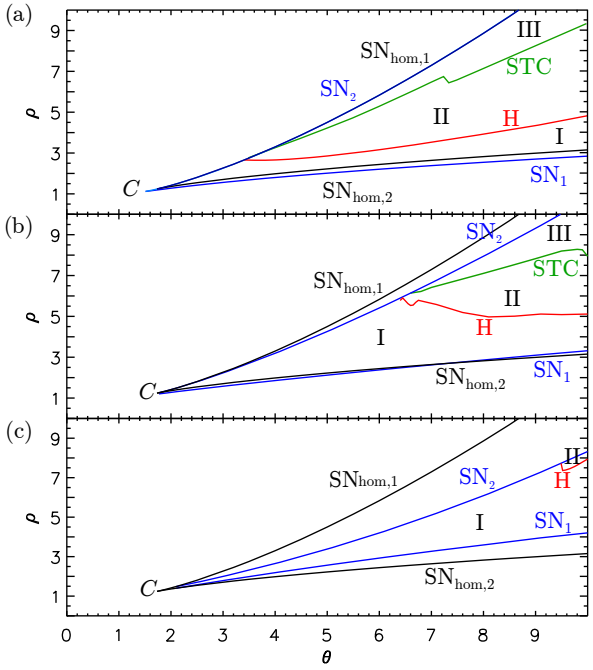

Figure 6.8: Regions of existence of single bright solitons and their instabilities in the (θ,ρ) parameter space for (a) $d_3 = 0$, (b) $d_3 = 0.15$, (c) $d_3 = 0.9$. Region I: stable bright solitons; region II: time-oscillation solutions arising through Hopf bifurcation H (red line); region III: spatio-temporal chaos (STC) emerging in the green line. The blue and black solid lines denote the saddle-node bifurcations of the HSS and single solitons, respectively.

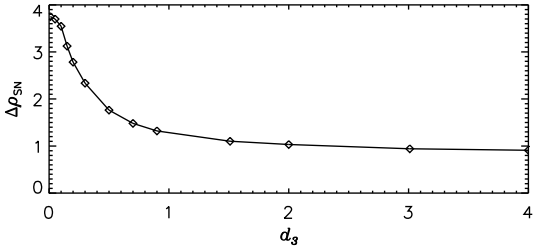

Figure 6.9: Width of the pinning region where bright solitons exist versus d_3 for $\theta = 6.1$.

three main dynamical regions, labeled I to III, in the phase diagrams shown in Figure 6.8, namely:

1. Region I: Single bright solitons are stable.
2. Region II: Single bright solitons are found to exhibit a time-oscillatory behavior (as was illustrated in Figure 6.6(a)).
3. Region III: Temporal evolution of the LSs lead to spatio-temporal chaos.

Oscillatory solutions emerge through a Hopf bifurcation H (thin red line). In Section 4.6, we saw that in the absence of TOD, this Hopf bifurcation unfolds from a Gavrilov-Guckenheimer codimension-2 point [21] and has been experimentally observed using fiber resonators [23]. Above region II, for increasing values of pump power and detuning, we find that the temporal evolution of the LSs evolve to spatio-temporal chaos (as was illustrated in Figure 6.7(a)). Figure 6.8(a)–(c) demonstrate that both the oscillatory (II) and chaotic (III) regions of instabilities shrink and shift to higher values of the detuning θ, confirming that the stabilization of LSs in the presence of TOD, which was exemplified in Figure 6.6 and 6.7, is a general feature.

The dynamical regimes discussed above concerns only single LSs. However, in the absence of TOD, multistability between many different stationary solutions is known to exist [21]. These solutions consist of multiple DSs and can be understood as bound states of single LSs. Therefore, in the next section, we proceed to studying the effect of TOD on the stability and bifurcation structure of multi-peak solutions.

6.4.2 Formation of isolas for $\theta < 2$

The modification of homoclinic snaking when reversibility is broken was first studied in Ref. [24] in the context of a system with gradient dynamics: the Swift-Hohenberg equation. The authors reported that the loss of reversibility symmetry destroys the pitchfork bifurcation responsible for the rung states present near of each saddle-node of the homoclinic snaking. When the pitchfork bifurcation becomes imperfect, the different branches of solutions are reorganized in a different fashion. In the LL equation the snakes-and-ladders bifurcation structure is also present and the breaking of reversibility generates the same kind of structures, as we will see below. In Figure 6.10, we can observe the snakes-and-ladders structure in the context of the LL equation for $\theta = 1.5$. In this diagram we use, similary as in Chapter 4, the L^2-norm

$$||A - A_0||^2 = \frac{1}{L}\int_{L/2}^{L/2} |A(x) - A_0|^2 dx, \tag{6.22}$$

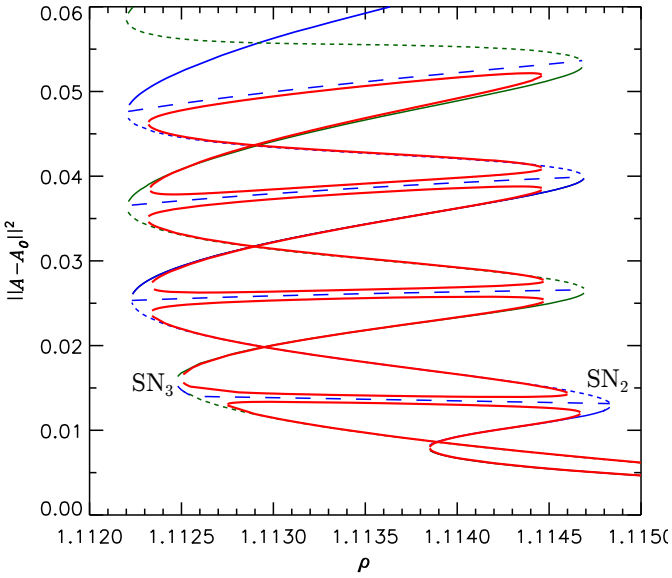

Figure 6.10: The breakup of the snakes-and-ladders structure into a stack of isolas when $d_3 = 0.01$. The underlying snakes-and-ladders structure ($d_3 = 0$) is shown for comparative in blue. Here $\theta = 1.5$.

as bifurcation measure. In blue we plot the homoclinic snaking corresponding to the LSs with an odd number of peaks, that we referred to as L_0 in Section 4.3; the homoclinic snaking corresponding to LSs with an even number of peaks, refereed as L_π are colored in green; the rung states solution branches are plotted in blue dashed lines. Solid and dashed lines represent, as usual, the stable and unstable states respectively. The first of these rung state branches extends from a pitchfork bifurcation in the neighborhood of SN_2 to another pitchfork near SN_3. A sequence of rung states branches connect the rest of the pitchforks of the snaking structure. When $d_3 \neq 0$, the destruction of the pitchfork bifurcations leads to the appearance of a stack of isolas as we can observe in Figure 6.10 for $d_3 = 0.1$. We point out that for a fixed value of the detuning, the isolas shrink with increasing values of d_3, until they eventually disappear in a cascade of cusp (C) or hysteresis bifurcations. This phenomenon can be observed in Figure 6.11 for a single isola and different values of d_3 in the range $0.01 - 0.0788$. For $d_3 = 0.076$ they almost have disappeared. In the same figure we also plot the profiles of LSs on some of these isolas. As we can appreciate, the asymmetry

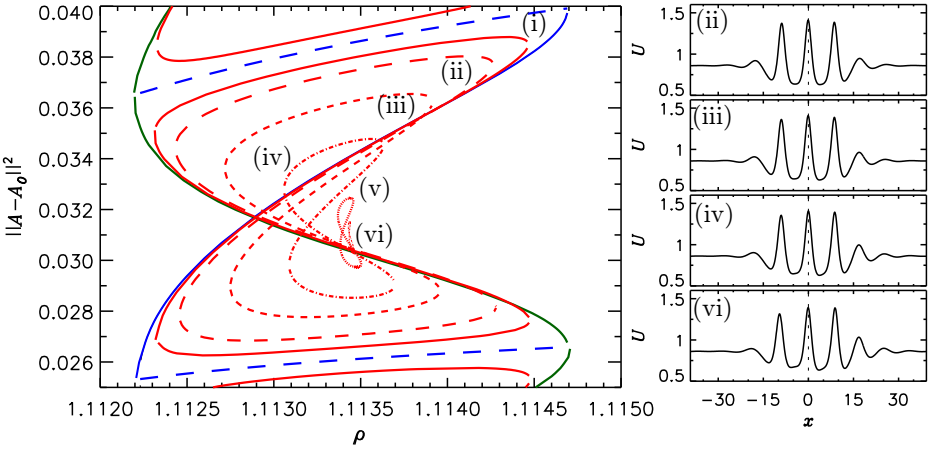

Figure 6.11: Here we show isolas formed within a pair of rings of the snakes-and-ladders structure for $\theta = 1.5$. The strength of the TOD are $d_3 = 0.01, 0.02, 0.04, 0.06, 0.076$ and 0.0788 from (i) to (vi). and 5. The underlying snake-and-ladders structure is indicated by blue lines. As d_3 increases the size of the isola decreases. The isolas are plotted in red. The profiles on the left are three peak soliton corresponding to the stable branch of the isolas labeled with the same roman number. The vertical dashed line represents the reflection symmetry plane when $d_3 = 0$. As we can observe, the asymmetry increases with d_3.

respect to $x = 0$ also increases with d_3.

We have also checked how the drift velocity changes along the isolas for several values of d_3. In Figure 6.12, we plot the isolas shown already in Figure 6.11, but using the drift velocity c instead of the norm $||A - A_0||^2$. The panel on the left, show all the six isolas. From bottom to top the strength of TOD increases, as it does c. The six panels from (i)-(vi) show a zoom of those isolas. As we can observe, in terms of c, the isolas keep their morphology. For every value of d_3, the drift velocity increases and decreases along the isolas' branches.

The shrinking of the pinning region with d_3 is clear in Figure 6.11. The width of the pinning can be predicted analytically as it was shown in Ref.[25]. In this work, the authors derived conditions that allow predicting bifurcation diagrams and drift speeds upon adding perturbative terms to the underlying system. These conditions rely on evaluation of the perturbative terms $g(A, \partial_i^i A)$ (in our case $g = \partial_x^3 A$) along the solutions of the unperturbed system. Moreover, with this method it is only necessary to know half of the localized structure i.e. the two fronts solutions. In future work we plan to apply these methods to the LL equation. In Ref.[24], the authors showed that for some parameter values, in-

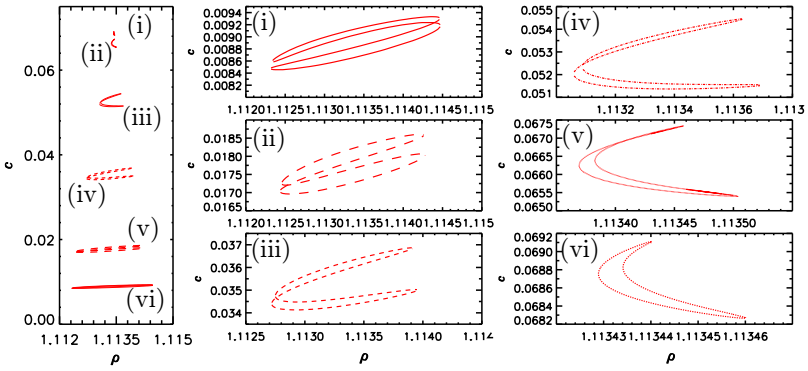

Figure 6.12: On the left we show the modification of the velocity of the LSs along the isolas for the same values of d_3 than in Figure 6.10. On panels from (i)-(vi) we show a zoom of each of the isolas shown in Figure 6.11. As we can see the average velocity along the isolas increases with d_3.

stead of stack of isolas, it was also possible to find a different morphology, as for example a pair of interwined snakes. More recently, analytical work has shown that the bifurcation structure of an homoclinic snaking can be modified in two different ways [25]. This change in the morphology depends on a scalar quantity defined within the evaluation of the perturbation along the unperturbed solution branches. Although we did not observe interwined snakes in the LL equation, theory tell us that it is possible to find a region of parameters where this structure exist.

All these results apply in the case where the underlying bifurcation structure, in the absence of a reflection symmetry perturbation, is a snakes-and-ladders structure. When this is not the case, the resulting bifurcation scenario is more complex as we will see in next section.

6.4.3 Mixed snaking for $\theta > 2$

In Section 4.5 we have studied that, when $\theta > 2$, LSs unfold from the $\mathrm{SN}_{hom,1}$(RTB) bifurcation and they are organized in a foliated snaking type of bifurcation structure. In Figure 6.13 we show how this bifurcation structure changes with increasing values of TOD strength, namely $d_3 = 0.1, 0.15, 0.6$ and 0.9.

For low values of d_3, all the multi-peak LSs are unstable, and as we can see the LSs branches corresponding to even and odd numbers of peaks are merged in a type of *mixed snaking*. In panels (i)-(iv) we observe the profiles of LSs for

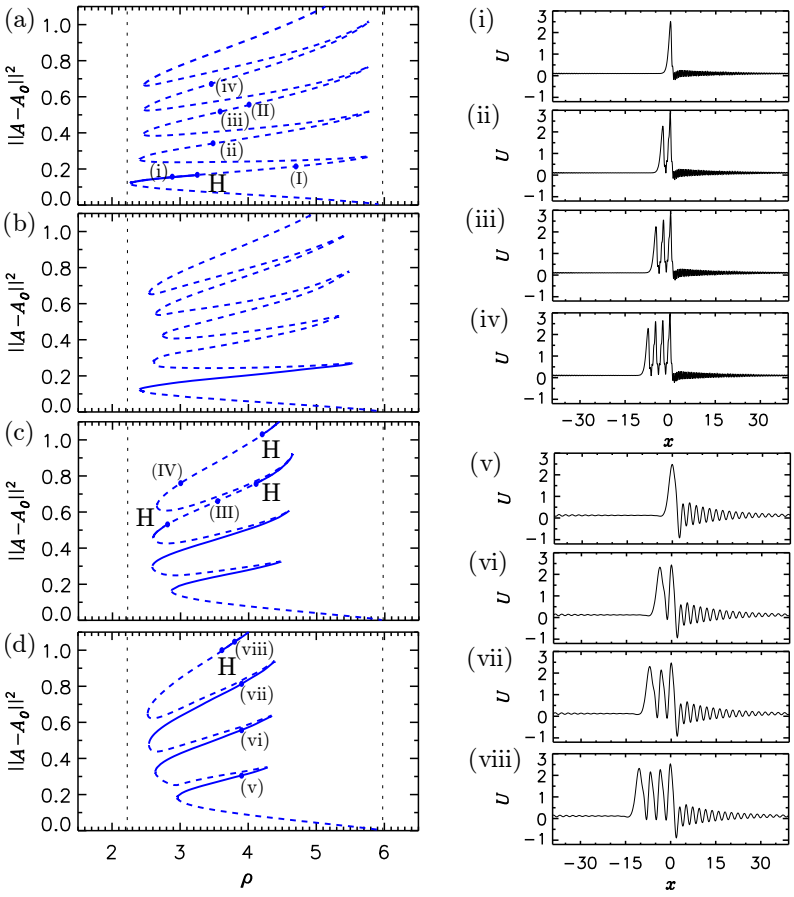

Figure 6.13: Mixed snaking for $\theta = 6.1$ and $d_3 = 0.1, 0.15, 0.6$ and 0.9 from panel (a) to panel (d). On the right we can see localized structures corresponding to single and multipeak states for $d_3 = 0.1$ in panels (i)-(iv) and for $d_3 = 0.9$ in panels (v)-(viii). As we can see, different solution branches are stabilized within Hopf bifurcations H. Vertical dashed lines represent the bistability region when $d_3 = 0$.

$d_3 = 0.1$ corresponding to the bifurcation diagram (a). The structure (i) with one single peak is stable until the Hopf bifurcation H where it starts to breathe at the same time it starts drifting. The oscillation of an initially unstable single pulse can be seen in Figure 6.14(I). Profiles (ii)-(iv) correspond to LSs that are unstable all the way along the solution branches in Figure 6.13(a). The

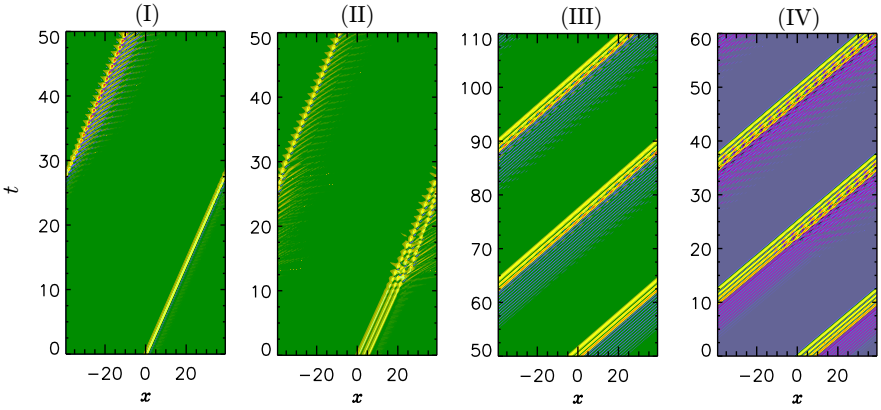

Figure 6.14: Evolution in time of localized states corresponding to diagrams shown in Figure 6.13 for $\theta = 6.1$. In panels (I-II), $d_3 = 0.1$ and in panels (III-IV), $d_3 = 0.6$. The values for parameter ρ are $\rho = 4.6755$ in panel (I), $\rho = 4.08452$ in panel (II), $\rho = 3.55955$ in panel (III) and $\rho = 3.04058$ in panel (IV).

integration of Eq.(6.13) using as initial condition one of these structures (here we chose a 3-peaks state) is shown in Figure 6.14(II). As we can see the different peaks, initially oscillating, start to merge until finally only a single breather soliton persist.

Figure 6.13(b)-(d) show that TOD increasingly stabilizes the multiple peak solutions, starting with the one peak branch in panel (b), and then gradually stabilizing the two-peak one in panel (c), three-peak one in panel (d), etc. This stabilization process seems to involve multiple Hopf bifurcations as most clearly seen in Figure 6.13(c). Panels (v)-(viii) show the real profiles of stable LSs corresponding to diagram (d) of Figure 6.13. In Figure 6.14(III) and (IV) we see the temporal evolution of initially unstable states labeled corresponding to the bifurcation diagram shown in Figure 6.13(d). In this case, each of the peaks of the LS starts to oscillate with a different phase until reaching an stable cycle.

Although difficult to appreciate in panels (i)-(ii) of Figure 6.13, unstable localized states present a single spatial oscillation in-between consecutive peaks, a feature that does not appear in the case of the higher TOD profiles (iv)-(viii). Comparing the bifurcation diagrams in Figure 6.13, we can see that there is a change in the shape and extension of the solution branches between diagram (b) and (c). Because the previous bifurcation diagrams are constructed by continuing a single peak LS, it is possible that we miss additional solution branches

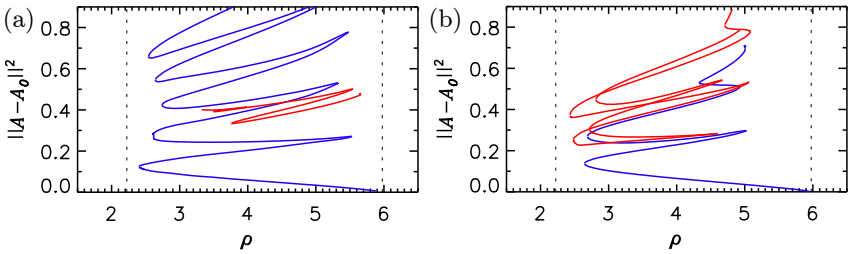

Figure 6.15: Mixed-snaking and isolas for $\theta = 6.1$. In panel (a) ($d_3 = 0.15$) mixed snaking (in blue) connected with the single peak soliton and in red isolas corresponding calculated tracking structures (vii) and (viii) from $d_3 = 0.9$ to $d_3 = 0.15$. In panel (b)($d_3 = 0.29$) the isola grows and the mixed snaking suffers shrinking of the top branches. For higher values of d_3 both structures merge resulting in a bifurcation diagram as the one in panels (c)-(d) of Figure 6.13.

that are disconnected. In order to clarify this we took the LSs (v)-(viii) and we tracked them back to smaller values of d_3. The result is as shown in Figure 6.15. In panel (a) the blue diagram represents the same solution branches plotted in Figure 6.13(b) for $d_3 = 0.15$. The red diagrams comes from tracking (iv)-(viii) from $d_3 = 0.9$ back to $d_3 = 0.15$. When continued both snaking diagrams for higher values of TOD (see Figure 6.15(b) for $d_3 = 0.29$), the region of existence of the multiple peaks branches for the blue structure starts to shrink, and the red snaking branch broaders until reaching a similar width than the blue diagram. Therefore, we expect that for $d_3 > 0.29$ these two snakings will merge resulting in the bifurcation diagram shown in Figure 6.13(c).We finally remark that other solutions (not shown here) such as multiple displaced single LSs connected via their oscillatory tails can also exist, as we will show in Chapter 7.

6.5 Bifurcation structure and stability of solitons in the normal dispersion regime

After studying the influence of TOD in bright solitons in the anomalous GVD regimes, we extended this study to the normal regime and we analyze how breking of the reversibility symmetry affects the stability and bifurcation structure of dark solitons [26, 27]. In Section 5.5 we have seen that in the normal GVD regime, dark solitons exist and that they are organized in a type of bifurcation structure known as *collapsed snaking*. For high values of detuning we also found (see Section 5.7) that those steady states have oscillatory instabilities and they start to breath. For some parameter values these oscillatory states undergo

a period doubling bifurcation starting in this way a route to temporal chaos [26, 27]. In this section we present first how the collapsed snaking is modified when increasing the TOD strength. Secondly, we will show how due to the effect of TOD, bright solitons of different widths occur in a similar way than the dark ones, forming a second collapsed snaking on the bottom of the bifurcation diagram and close to the $\mathrm{SN}_{hom,1}$. Finally we will see that TOD, as occurred in the anomalous regime, also stabilizes the oscillatory regimes of dark solitons, showing that this mechanism of stabilization is generic and not specific to the anomalous regime.

6.5.1 Modification of front solutions

When $d_3 = 0$, dark solitons can be understood as the pinning of two fronts, F_u and F_d, connecting the top and bottom branches of the HSSs, namely A_0^t and A_0^b. As we known (see Section 5.5), the fronts move with a constant velocity c_F (see Figure 5.9) that depends on the control parameters of the system. Around the Maxwell point, there is a pinning region in which both fronts can lock at different separation distances, allowing the multistability of of hole states or dark solitons which are organized within a collapsed snaking bifurcation structure.

When $d_3 \neq 0$, the reflection symmetry is broken, so $F_u(-x) \neq F_d(x)$, and LSs are no longer left/right symmetric. One example of a typical structure in the context is shown in Figure 6.16(a) for $\theta = 4$, $\rho = 2.3251$ and $d_3 = 0.7$. This solution is the result of the locking of the two fronts F_d and F_u shown in Figure 6.16(b) Figure 6.16(c). The front F_d leaves A_0^t monotonically and approaches A_0^b in an oscillatory way, with a characteristic frequency ω_b. On the contrary, F_u leaves A_0^b monotonically and reaches A_0^t in a oscillatory way with a frequency ω_t. In terms of spatial dynamics, taking into account the phase space defined by the dynamical system (6.17) in Section 6.3, the fronts can be understood as heteroclinic connections between the fixed point of the system A_0^b and A_0^t. The analysis of the eigenvalues of the Jacobian (6.18) at each of these points reveals how the stable and unstable manifolds of the system behave in a neighborhood of those equilibriums, and therefore the shape of the monotonic and oscillatory tails of both fronts. In panels (d), (e) and (f) of Figure 6.16 we show the projection of the two fronts into three different subspaces of the phase space $\{(y_1, y_2, y_3, y_4, y_5, y_6)\}$. Red color shows the heteroclinic connection corresponding to F_u, and the blue the one corresponding to F_d. The intersection of these two connections generates the *heteroclinic cycle* (homoclinic orbit) corresponding to the LS shown in Figure 6.16(a). The way in which trajectories wind around A_0^b and A_0^t is described by the angular frequencies $\omega_b = \mathrm{Im}[\lambda^-(A_0^b)] = 1.3905$

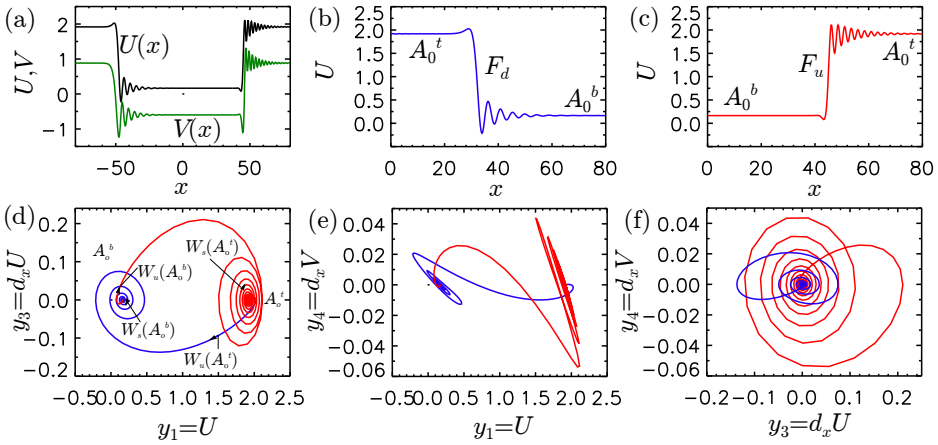

Figure 6.16: In (a) localized state for $\theta = 4$, $\rho = 2.3251$ and $d_3 = 0.7$, formed by the connection of two fronts F_u shown in (b) and F_d shown in (c). In (d), (e) and (f) we show different projections of the localized state shown in (a) into three different subspaces of the phase space defined by the dynamical system (6.17). In red we show the heteroclinic orbit corresponding to the front F_u (see panel (b)). In blue we plot the heteroclinic orbit corresponding to F_d (see panel (c)).

and $\omega_u = \mathrm{Im}[\lambda^-(A_0^t)] = 2.5478$, and by the decay rates $\mathrm{Re}[\lambda^-(A_0^b)] = -0.1528$ and $\mathrm{Re}[\lambda^-(A_0^t)] = -0.13$ respectively.

With $d_3 = 0$, the monotonic behavior of the front near A_0^t prevents the appearance of bright solitons. In contrast, with $d_3 \neq 0$ oscillatory behavior appears around A_0^t at least in one of the fronts, allowing the formation of bright structures. In the next Section we will see how the collapsed snaking for the dark solitons is modified by TOD. Moreover, we will show how bright solutions appear in a similar collapsed bifurcation diagram as it was the case for dark solitons.

In Figure 6.17 we show the spatial eigenvalues around A_0^b (panel (a)) and around A_0^t (panel (c)), where we label the dominant eigenvalues as λ^+ for the repulsive one and λ^- for the attracting one. In red crosses we also show the spatial eigenvalues for the top and bottom branches when $d_3 = 0$. In panel (b) and (d) of the same figure the fitting of the oscillatory tails of fronts F_d and F_u around A_0^b and A_0^t are shown respectively.

The fitting parameters for the real part of the oscillatory tails without the HSS background, are $c_1 = 0.048395184$ and $\varphi_1 = 2.9244074$ for panel (b) and $c_2 = 0.025797178$ and $\varphi_2 = 0.18703286$ for panel (d).

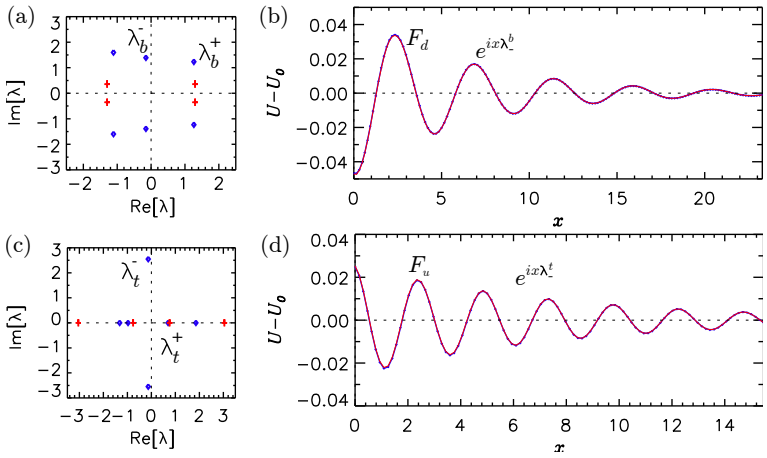

Figure 6.17: Panels (a) and (c) show the spatial eigenvalues for $\theta = 4$ and $d_3 = 0.7$ around A_0^b and A_0^t respectively. In panels (b) and (d) we show the fitting, using spatial eigenvalues λ^- shown in (a) and (c), of the oscillatory tails corresponding to fronts F_d and F_u shown in Figure 6.16. The fitting parameters are are $c_1 = 0.0484$ and $\varphi_1 = 2.9244$ for panel (b) and $c_2 = 0.0258$ and $\varphi_2 = 0.1870$ for panel (d). In red crosses by comparative we add the spatial eigenvalues for $d_3 = 0$.

6.5.2 Collapsed snaking for dark and bright solitons

In previous sections we saw how the TOD modified the shape of solitons and their bifurcation structure in the context of anomalous dispersion, forming either isolas, due to the breaking up of the snake-and-ladders structure for $\theta < 2$, or a mixed snaking type of structure for $\theta > 2$.

Figure 6.18 shows in black the bifurcation structure of dark solitons for $d_3 = 0$ and $\theta = 4$. As also discussed in Chapter 5, dark solitons unfold initially unstable from the $\mathrm{SN}_{hom,2}$, that in terms of spatial dynamics corresponds to RTB bifurcation. These states, after a sequence of saddle-nodes collapses into the Maxwell point of the system at ρ_M along which dark solitons become broader and broader when decreasing their norm $||A||^2$. In finite systems, this branch of solutions departs from $\rho = \rho_M$ when the maximum amplitude starts to decrease below A_0^t and the solution turns into a bright soliton sitting on A_0^b. This unstable soliton decreases their amplitude for increasing values of ρ until reaching the HH point from where all the structure unfolds.

When TOD is taken into account, the modification of the spatial eigenvalues that we studied previously is responsible for the appearance and stabilization

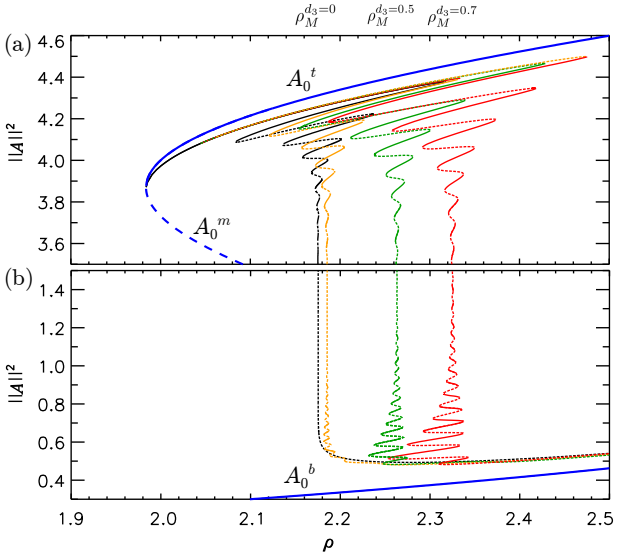

Figure 6.18: Collapsed snaking diagrams for $\theta = 4$ and different values of d_3, namely $d_3 = 0$ in black, $d_3 = 0.3$ in yellow, $d_3 = 0.5$ in green, $d_3 = 0.7$ in red. In (a) collapsed snaking for dark solitons. As we can see, snakings shift for larger values of ρ when increasing d_3 and pinning regions for the different type of structures becomes broader. In (b) collapsed snaking for bright solitons. For $d_3 = 0$ a single branch of states exist. When increasing d_3 new branches of bright solitons start to nucleate through cusp bifurcations. As it was the case for darks solitons, the snaking becomes broader for increasing d_3. Solid lines (dashed) lines represent stable (unstable) solutions.

of structures, in particular bright states, that were not present before. In Figure 6.18 we can see the modification of the collapsed snaking structure for several values of d_3, namely $d_3 = 0, 0.3, 0.5$ and 0.7. Regarding panel (a), we can see how the collapsed snaking becomes broader when increasing TOD strength d_3. Due to this, the regions of existence of the different types of dark solitons increase with d_3 at the same time that the collapsed region is shifted to higher values of ρ. This can be easily seen by looking at Figure 6.18(a) where the Maxwell point is shifted with d_3 in such a way that $\rho_M^{d_3=0} < \rho_M^{d_3=0.3} < \rho_M^{d_3=0.5} < \rho_M^{d_3=0.7}$.

If we now take a look to panel (b) of Figure 6.18 we observe that the vertical snaking branch collapses monotically for $d_3 = 0$. In contrast, when $d_3 \neq 0$, that branch starts to develops oscillations around $\rho_M^{d_3}$ and the amplitude of the oscillations increases with d_3, as one can see in Figure 6.18. This new bifurcation structure explains the existence of stable bright solitons sitting on A_0^b, that for

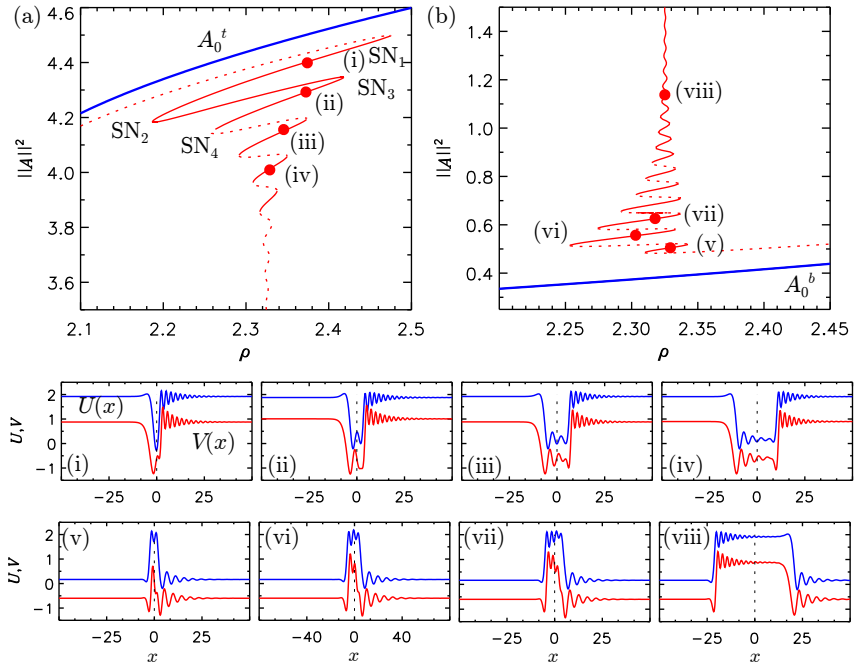

Figure 6.19: Detail of the collapsed snaking for dark (in panel (a)) and bright solitons (panel (b)) shown in Figure 6.18 for $d_3 = 0.7$. Subpanels (i)-(iv) make reference to the dark solitons corresponding to solution branches of panel (a). Subpanels (v)-(viii) correspond to bright solitons branches shown in panel (b).

$d_3 = 0$ were accumulated at ρ_M.

As it was the case for dark solitons, separation between consecutive saddle-nodes increases with d_3, and so does the region of existence of bright solitons. In order to understand the organization of the different states in the new bifurcation structure we plot in Figure 6.19 two portions of the bifurcation diagram for $d_3 = 0.7$ already shown in Figure 6.18. In panel (a) we can see the collapsed snaking related with dark pulses. Dashed lines represent unstable states and solid ones the stable solutions. Profiles of these states corresponding to each branch are shown in Figure 6.19(i)-(iv). At this point we can clearly appreciate the asymmetry generated by TOD. Panel (b) shows the collapsed snaking for bright pulses. These states undergo bifurcations similar to those of the dark ones. As before, two things happen at the saddle-nodes. On one hand the localized structure change from stable to unstable, or vice-versa; on the other

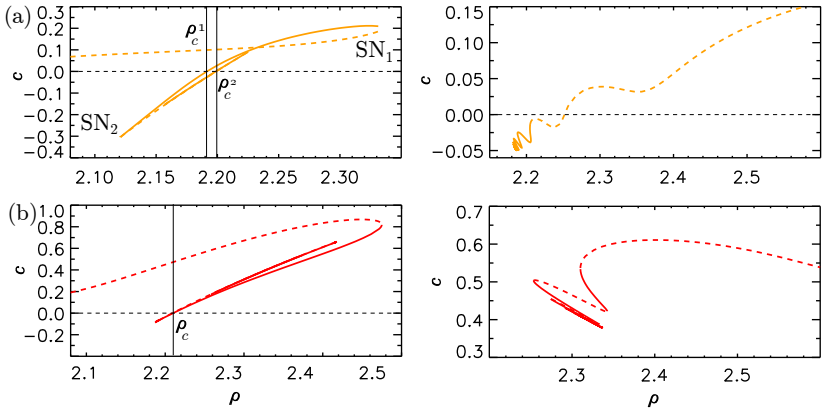

Figure 6.20: Bifurcation diagram showing the velocity c of the dark (left column) and bright solitons (right column) as function of ρ, for different values of d_3. In (a) $d_3 = 0.3$, and in (b) $d_3 = 0.7$. As we can appreciate the velocity change direction when crossing a critical value ρ_c, that depends on d_3.

hand spatial oscillation are also generated on the profiles. Some of these stable bright solitons are shown in Figure 6.19 (v)-(viii).

Increasing even further, the velocity of solitons become always positive. The right column shows the velocities of bright solitons. In this case one can see a change of the direction in the velocity for $d_3 = 0.3$, that for the other values of d_3 is always positive. Another interesting feature of this scenario is related with the drift velocity of the localized states. In Figure 6.20 we show how the velocities of solitons change along the bifurcation diagram shown in Figure 6.18, for both, dark solitons (left column) and bright ones (right column). For $d_3 = 0.3$ (see Figure 6.20(a)), dark solitons unfolding from $\mathrm{SN}_{hom,2}$ drift with constant positive velocity that increases with ρ. In SN_1, where the single dark soliton becomes stable, the velocity starts to decrease, until it becomes negative at ρ_c^1. At SN_2, it starts to increase again, and solutions change velocity at ρ_c^2. This oscillation in the velocity is repeated all along the snaking. Increasing d_3, the situation is similar despite of the fact that the ρ_c^i calues shift and accumulate to the same value, and the interval in which solitons have negative velocity decreases for high values of d_3. This is the situation shown in Figure 6.20(b) for $d_3 = 0.7$.

We have also characterized how the velocity c of the dark solitons depends on other features, as for example their width. Figure 6.21 shows, for $\theta = 4$, how c oscillates as a function of its width at the half minimum Δ for three

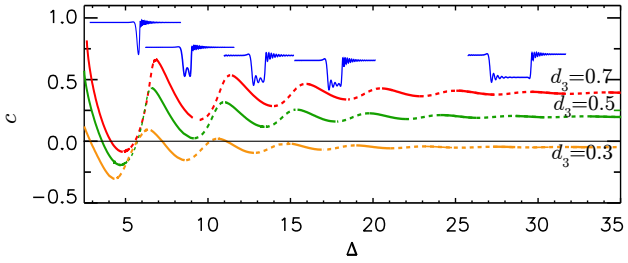

Figure 6.21: Velocity of the dark solitons as a function of the width at half minimum Δ for $\theta = 4$ and $d_3 = 0.3, 0.5, 0.7$. The velocity changes in a damped oscillatory way as a function of Δ. The stable (unstable) dark solitons correspond to the solid (dashed) lines.

different values of TOD ($d_3 = 0.3, 0.5, 0.7$). In both cases, the difference between the minimum and maximum velocity of a soliton decreases as they get wider, approaching a constant value for very wide dark solitons (large Δ). This constant velocity in the limit of very wide structures increases with the TOD.

6.5.3 Stabilization of oscillatory regimes

Here, we show that TOD can suppress oscillatory and chaotic dynamics, similarly as in the anomalous GVD regime. To illustrate this we first show the bifurcation diagram for $\theta = 5$ and $d_3 = 0$ in Figure 6.22(a). Dark solitons are unstable between H_1 and H_2. We choose this value of detuning, in order to avoid the temporal-chaos and the disappearance of this one when reaching the BC of the attractor. In this way we will observe stabilization for the oscillatory states but not of the chaotic ones, although the last ones can also be stabilized by TOD.

When $d_3 \neq 0$, the Hopf bifurcations shift in such way that the region of oscillatory states shrinks. This can be seen in the diagrams (b) and (c) shown in Figure 6.22 for $\theta = 5$ and $d_3 = 0.2, 0.3$ and 0.7 respectively.

While for $d_3 = 0.2$, dark solitons between H_1 and H_2 oscillate and drift, for $d_3 = 0.3$ and 0.7 the oscillatory instabilities have been suppressed and only a drifting soliton remains. The direction in which the soliton drifts is not obvious by looking at its profile and changes with the pump ρ . In Figure 6.22, solid purple (green) lines correspond to dark solitons with positive (negative) velocity, while the solid red lines (for $d_3 = 0$) indicate zero velocity. By increasing the strength of TOD, the parameter range of solitons with negative velocity shrinks. Although in principle bright solitons could also undergo oscillatory instabilities and similar stabilization with increasing TOD, for the parameter range considered in this

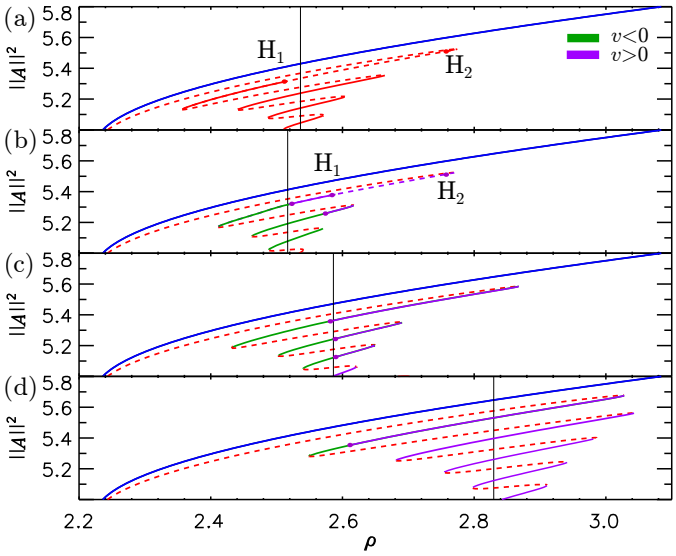

Figure 6.22: Stabilization of dark solitons for $\theta = 5$. In panel (a) $d_3 = 0$, in (b)$d_3 = 0.2$, in (c) $d_3 = 0.3$ and , in (d) $d_3 = 0.7$. The Hopf bifurcation stabilizes the branches of single dark solitons when increasing d_3. $H_{1,2}$ correspond to Hopf bifurcations (black dots). Solid (dashed) lines stand for stable (unstable) states. In solid purple (green) lines we refer to states with positive (negative) velocity. Solid red lines (for $d_3 = 0$) and red dots indicate zero velocity.

work, no such oscillations of bright solitons have been found.

6.6 Conclusions

In summary in this chapter we have shown that the dynamics, stability and bifurcation structure of solitons is largely modified in the presence of TOD in both the anomalous and normal GVD regimes. Third order dispersion tends to suppress dynamical instabilities of the single DSs such as oscillations and chaos. In the anomalous dispersion regime the so-called snaking structure, organizing the single and multiple bright soliton solutions, is altered by TOD. For $\theta < 2$, homoclinic snaking breaks down due to the destruction of the Pitchfork bifurcation responsible for the existence of the rung states, resulting in the formation of a stack of isolas. For $\theta > 2$, another type of snaking structure, where branches of states with an odd and even number of peaks are connected, is created. We refer to this type of structure as *mixed snaking*. Moreover, our analysis has also revealed that despite multi-peak solutions can be stabilized by TOD, such stabi-

lization requires an increasing amount of TOD as the number of peaks increases. In the normal dispersion regime, TOD also alters the bifurcation structure for dark solitons. As we have seen, the Maxwell point, and thus the collapsed snaking, is shifted to larger values of ρ when increasing d_3, and together with this shift, the regions of existence of dark solitons becomes broader. Another interesting feature is that TOD can also favor the formation of bright solitons due to the presence of oscillatory tails around the top branch of HSSs, A_0^t. We find that these structures are also organized in a collapsed snaking structure unfolding from a HH and merge with the collapsed snaking of the dark solitons as the norm increases. Finally, as occurs in the anomalous regime, oscillatory and chaotic regimes for dark solitons are suppressed due to the influence of TOD terms. The stabilization of dark/bright solitons within TOD can be seen as an alternative to the stabilization accounting when non-local terms are present [30].

Appendix

As we said in section 6.3, the spatial eigenvalues can be just obtained inserting $U(x) = U_0 + \epsilon u(x)$ and $V(x) = V_0 + \epsilon v(x)$, with ansatzs $u(x) = ae^{\lambda x}$, $v(x) = be^{\lambda x}$, and $\lambda \in \mathbb{C}$, into Eqs.(6.14). At order 0 in ϵ we just recover the HSSs algebraic equation. At first order in ϵ, we have,

$$\begin{aligned} d_3 u''' - \nu v'' + cu' - u + \theta v - 2V_0 U_0 u - 2V_0^2 v - vI_0 = 0 \\ d_3 v''' + \nu u'' + cv' - v - \theta u + 2V_0 U_0 v + 2U_0^2 u + uI_0 = 0, \end{aligned} \tag{6.23}$$

with $'$ standing for the derivative respect to x. This system of coupled ODEs, when taking into account the ansatzs for $u(x)$ and $v(x)$, have a non trivial solution if and only if, the next determinant satisfy,

$$\begin{vmatrix} d_3\lambda^3 + c\lambda - (1 + 2U_0V_0) & -\nu\lambda^2 + \theta - 3V_0^2 - U_0^2 \\ \nu\lambda^2 - \theta + 3U_0^2 + V_0^2 & d_3\lambda^3 + c\lambda - (1 - 2U_0V_0) \end{vmatrix} = 0. \tag{6.24}$$

And from there, after some algebra, we arrive to Eq.(6.19).

References

[1] A. Mussot, E. Louvergneaux, N. Akhmediev, F. Reynaud, L. Delage, and M. Taki, *Optical fiber systems are convectively unstable,* Phys. Rev. Lett. **101**, 113904 (2008).

[2] F. Leo, A. Mussot, P. Kockaert, Ph. Emplit, M. Haelterman, and M. Taki, *Nonlinear symmetry breaking induced by third-order dispersion in optical fiber cavities,* Phys. Rev. Lett. **110**, 104103 (2013).

[3] J. K. Jang, M. Erkintalo, S. G. Murdoch, and S. Coen, *Observation of dispersive wave emission by temporal cavity solitons,*, Op.Lett. Vol. 39, No. 19 (2014).

[4] C. Milián and D. Skryabin, *Soliton families and resonant radiation in a micro-ring resonator near zero group-velocity dispersion,* Opt. Express **22**, 3732 (2014).

[5] S. Coen, H. G. Randle, T. Sylvestre, and M. Erkintalo,*Modeling of octave-spanning Kerr frequency combs using a generalized mean-field Lugiato-Lefever model,* Opt. Lett. **38**, 37 (2013)

[6] J. K. Jang, M. Erkintalo, S. G. Murdoch, and S. Coen, *Ultraweak long-range interactions of solitons observed over astronomical distances,* Nat. Photonics **7**, 657 (2013).

[7] P. Parra-Rivas, D. Gomila, F. Leo, S. Coen and L. Gelens *Third order chromatic dispersion stabilizes Kerr frequency combs,* Opt. Lett. **39**, 2971-2974 (2014).

[8] P. Parra-Rivas, D. Gomila, and L. Gelens, *Stable dark and bright soliton Kerr combs can coexist in normal dispersion resonators,* submitted to Opt. Lett. (2016).

[9] F. Leo, S. Coen, P. Kockaertl, S.-P. Gorza, Ph. Emplit, and M. Haelterman, *Temporal cavity solitons in one-dimensional Kerr media as bits in an all-optical buffer,* Nat. Photonics **4**, 471 (2010).

[10] Y. Xu and S. Coen, *Experimental observation of the spontaneous breaking of the time-reversal symmetry in a synchronously-pumped passive Kerr resonator,* Op. Lett. **39** 12 (2014).

[11] R. Zambrini, M. San Miguel, C. Durniak, and M. Taki, *Convection induced nonlinear-symmetry-breaking in wave mixing,* Phys. Rev. E **72**, 025603(R) (2005).

[12] J. M. Chomaz, *Absolute and convective instabilities in nonlinear systems,* Phys. Rev. Lett. **69**, 13, (1992).

[13] A. J. Scroggie, D. Gomila, W. J. Firth, G. L. Oppo,*Spontaneous and induced motion of optical patterns,* Applied Physics B **81**, 963-968 (2005).

[14] Y.A. Kuznetsov, *Elements of Applied Bifurcation Theory,* 2nd edn. (Springer, New York 1998).

[15] J. M. Dudley, G. Genty, and S. Coen, *Supercontinuum generation in photonic crystal fiber,* Rev. Mod. Phys. **78**, 1135 (2006).

[16] D. Gomila, A. J. Scroggie, and W. J. Firth, *Bifurcation structure of dissipative solitons,* Phys. D (Amsterdam) 227, **70** (2007).

[17] P. D. Woods and A. R. Champneys, *Heteroclinic tangles and homoclinic snaking in the unfolding of a degenerate reversible Hamiltonian-Hopf bifurcation,* Physica D **129**, 147 (1999).

[18] M. Haragus and G. Iooss, *Local Bifurcations, Center Manifolds, and Normal Forms in Infinite-Dimensional Dynamical Systems,* (Springer, Berlin, 2011).

[19] P. Colet, M. A. Matías, L. Gelens, and D. Gomila, *Formation of localized structures in bistable systems through nonlocalspatial coupling. I. General framework,* Phys. Rev. E **89**, 012914 (2014).

[20] J. Burke, A. Yochelis, and E. Knobloch, *Spatially localized oscillating states in periodically forced dissipative systems,* SIAM J. Appl. Dyn. Syst., **7** (3), 651-711 (2008).

[21] P. Parra-Rivas, D. Gomila, M. A. Matías, S. Coen, and L. Gelens, *Dynamics of localized and patterned structures in the Lugiato-Lefever equation determine the stability and shape of optical frequency combs,* Phys. Rev. A **89**, 043813 (2014).

[22] B. Ponedel and E. Knobloch, *Forced Snaking: Localized structures in the real Ginzburg-*

Landau equation with spatially periodic parametric forcing, EPJ (to be published).

[23] F. Leo, L. Gelens, Ph. Emplit, M. Haelterman, and S. Coen, *Dynamics of one-dimensional Kerr cavity solitons,* Opt. Express **21**, 9180 (2013).

[24] J. Burke, S. M. Houghton, and E. Knobloch *Swift-Hohenberg equation with broken reflection symmetry,* , Phys. Rev. E **80**, 036202 (2009).

[25] E. Makrides and B. Sandstede, *Predicting the bifurcation structure of localized snaking patterns,* Physica D **268**, 59 (2014).

[26] P. Parra-Rivas, E. Knobloch, D. Gomila, L. Gelens, *Dark solitons in the Lugiato-Lefever equation with normal dispersion,* Physical Review A **93**, 063839 (1-17) (2016).

[27] P. Parra-Rivas, D. Gomila, E. Knobloch, S. Coen, L. Gelens, *Origin and stability of dark pulse Kerr combs in normal dispersion resonators,* Optics Letters **41**, 2402-2405 (2016).

[28] N. N. Rozanov, V. E. Semenov, and G. V. Khodova, *Transverse structure of a field in nonlinear bistable interferometers. I. Switching waves and steady-state profiles* , Sov. J. Quantum. Electron. **12**, 193-197 (1982).

[29] S. Coen, M. Tlidi, Ph. Emplit, and M. Haelterman, *Convection versus dispersion in optical bistability,* Phys. Rev. Lett. **83**, 2328-2331 (1999).

[30] M. Tlidi, C. Fernandez-Oto, M. G. Clerc, D. Escaff, and P. Kockaert, *Localized plateau beam resulting from strong nonlocal coupling in a cavity filled by metamaterials and liquid-crystal cells,* Phys. Rev. A **92**, 053838 (2015).

Chapter 7

Interaction of solitons and the formation of bound states

7.1 Introduction

In this chapter we study the formation of *bound states* (BS) or soliton molecules due to the interaction of single-peak solitons in the LL equation. This interaction arises from the overlapping of the tail of one soliton with the other [1]. When the tails have spatial oscillations, locking or pinning between two solitons can occur at fixed distances related with the wavelength of the oscillations, forming a BS. In Chapter 2 and 6 we have analyzed the properties of these tails from the spatial dynamics point of view [2]. Here, following references [1, 3–5], we derive an effective potential of interaction and relate its periodicity to the spatial eigenspectrum of the HSSs A_0.

In [1] an analytical expression for the effective interaction potential in the driven and damped nonlinear Schrodinger (NLS) equation was derived. It was found that equilibrium distances correspond to the maximum and minimum of that potential. The maximum gives the unstable equilibrium separations and the minimum the stable ones. The interaction in the presence of "skew" terms (terms breaking spatial reversibility) has also been studied [3, 4]. It was shown that locking of solitons can be produced via radiative interaction or dispersion wave emission [6, 7]. In this particular case it is the maximum of the potential, and not the minimum, which determines the stable equilibrium separation distances allowed for BSs [3]. This last case is very relevant in the context of our model where dispersion wave emission is present, for example, when including third

order dispersion effects in the system. In the same work, the formation of BSs of breather solitons in the ac-driven Sine-Gordon equation was studied. In [5], the interaction and formation of BSs was analyzed in the same equation as in [1], but in this case the interaction potential was calculated using the complete Hamiltonian, and not just the interaction one, as done in [1, 3, 4]. A comparison between these different procedures showed that the obtained separation distances were equivanlent.

Interaction of solitons in dissipative systems has also been studied using perturbation theory, such as in Ref. [8], for the modified Swift-Hohenberg equation [9]. The formation of LSs via front or domain wall interactions was also analyzed using similar techniques in the context of the Ginzburg-Landau equation [10] and in the degenerate optical parametric oscillator (DOPO) [11].

In summary, the presence of oscillatory tails is essential for the formation of BSs of solitons at discrete separation distances, determined by the spatial oscillations of the tails. When the tails are monotonic, locking at fixed and discrete distances is no longer possible and the two solitons move towards or away from each other.

In this chapter we will apply these methods to the LL equation. This equation is dissipative in nature and it is not integrable. Therefore we can not obtain a closed analytical expression for the interaction potential. Nevertheless we can use the numerical solution for the soliton to calculate such potential and the locking distances.

The chapter is organized as follows. In Section 7.2 we calculate the interaction potential via the complete Hamiltonian and the interaction one. We compare the locking distances obtained with both methods with the exact ones showing good agreement. We find that the periodicity in the potential is given by the wavelength of the oscillatory tails and therefore by the imaginary part of its spatial eigenvalues (see Chapter 2). In Section 7.3 we review some of the different types of bifurcation structures that one can obtain considering two soliton states separated at different distances and the case of several solitons. In Section 7.4 we briefly discuss how the interaction gets modified depending on the control parameters of the system. After that, in Section 7.5 we apply the same method to generalization of the LL equation in two cases, one considering terms conserving the reversibility and another one with terms breaking it, in particular we choose fourth and third order dispersion effects. Finally in Section 7.6 we use simulations in the presence of noise to show how two soliton structures jump between neighbouring stable distances increasing or decreasing their separations. We also calculate the probability for the system to reach a given separation distance.

7.2 Interaction potential

The LL model has a variational formulation in terms of a generalized action functional

$$\mathcal{S} \equiv \int_{\mathbb{R}} e^{2t} L[A, \bar{A}] dt = \int_{\mathbb{R}} e^{2t} \int_{\mathbb{R}} \mathcal{L}[A, \bar{A}] dx dt, \tag{7.1}$$

and the Lagrangian density for the anomalous GVD regime[12]

$$\mathcal{L} = \frac{i}{2}\left(\bar{A}\partial_t A - A\partial_t \bar{A}\right) - \partial_x A \partial_x \bar{A} - i\rho\left(\bar{A} - A\right) - \theta A\bar{A} + \frac{1}{2}\bar{A}^2 A^2. \tag{7.2}$$

In this framework the LL equation corresponds to the Euler-Lagrange equation derived from the least action principle defined by:

$$\delta_A \mathcal{S}(\tilde{A}) \equiv \frac{d}{d\epsilon}\Big|_{\epsilon=0} \mathcal{S}(A + \epsilon\tilde{A}) = 0, \tag{7.3}$$

where $\tilde{A}$ is the variation of A and ϵ a small parameter $0 < \epsilon \ll 1$.

The Hamiltonian density is given by,

$$\mathcal{H} = \partial_x A \partial_x \bar{A} + i\rho\left(\bar{A} - A\right) + \theta A\bar{A} - \frac{1}{2}\bar{A}^2 A^2, \tag{7.4}$$

and the interaction Hamiltonian density by just the term

$$\mathcal{H}_{\mathcal{I}} = -\frac{1}{2} A^2 \bar{A}^2. \tag{7.5}$$

Integrating Eq.(7.2), (7.4) and (7.5) over space we obtain the Lagrangian, Hamiltonian and interaction Hamiltonian functions respectively.

In this section we will calculate the effective potential of interaction using both the full Hamiltonian function coming from (7.4) and the interaction Hamiltonian function coming from (7.5).

To start we check the temporal evolution of two single-peak solitons separated by different distances to obtain some insight about their interaction behavior. In Figure 7.1 we can observe the time evolution of two solitons initially separated by distances $z_0 = 32.8157$ in panel (a) and by $z_0 = 39.0613$ in panel (b). Looking at the right panel in (a) and (b), where we plot the separation z between both peaks, those initial conditions converge to the same attractor i.e. a BS characterized by a separation $z_s \approx 36.2$. Figure 7.1(c) and Figure 7.1(d) show a similar time evolution but now the initial separations are $z_0 = 42.1881$ and $z_0 = 46.8747$ respectively, and as before, they converge to the same stable separation $z_s =$

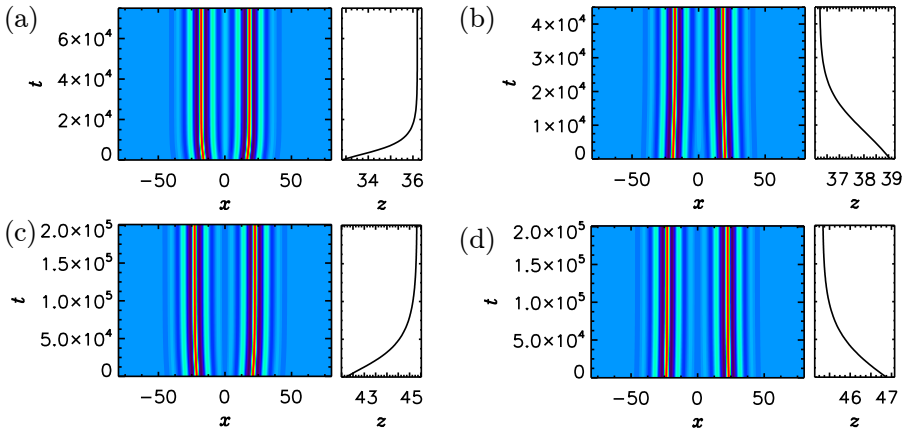

Figure 7.1: Temporal evolution of two solitons with different initial separations for $\theta = 1.5$ and $\rho = 1.11445$. (a) $z_0 = 32.8157$ and $z_f = 36.1968$, (b)$z_0 = 39.0613$ and $z_f = 36.2084$ (c) $z_0 = 42.1881$ and $z_f = 45.3205$ and (d) $z_0 = 46.8747$ and $z_f = 45.3415$. The subpanels on the right of each panel show how the separation distance between the peaks z evolves in time.

45.3. From Figure 7.1 we can therefore conclude two things, first only certain separation distances are allowed for the two-peaks solitons BSs, and second, the interaction between the individual solitons can be repulsive as in panels (a) and (c), or attractive as in panels (b) and (d). The question now is if we can predict these distances and obtain information about the BSs without using time evolution simulations, that need a large amount of time to converge to the stable attractor. In the same way as in Refs.[1, 5], we derive effective interaction potentials, depending on the separation distances z, where the extrema give these stable and unstable separations. The potential is determined by the overlapping integral between the tail of each soliton and its mate's core. Therefore, the interaction depends strongly on the nature of the tails [1, 2, 5]. We will show how the periodicity of the potential is given by THE wavelength of the oscillatory tails, and therefore, as we showed in Chapter 2, it can be determined by the spatial eigenvalues of the HSSs A_0.

In what follows we derive an Euler-Lagrange equation describing the interaction. This equation has the form of a constraint, such that the action functional (7.1) is extremal. Similarly as in Ref.[5], we consider that the BS formed by two solitons that are widely separated can be described by the ansatz

$$A(x, z) = A_-(x) + A_+(x) - A_0, \tag{7.6}$$

where $A_-(x) = A_{sol}(x - z/2)$ represent a one soliton state displaced by a distance $z/2$ to the left of the center of the domain at $x = 0$, and $A_+ = A_{sol}(x + z/2)$ a soliton displaced by a distance $z/2$ to the right, with z being a time dependent free parameter. As we do not have an exact analytical solution, we use the numerical stationary solutions obtained via continuation techniques to calculate the potential. The potential is calculated considering first the full Hamiltonian (7.4) and later the interaction one (7.5). Comparing both approaches with the exact separation, obtained numerically, one can see that the agreement is quite good.

7.2.1 Full Hamiltonian

With the ansatz (7.6) the action functional depends on z i.e. $\mathcal{S} = \mathcal{S}[A(z), \bar{A}(z)]$. The critical points of the action functional, that is, the solution of

$$\delta_z \mathcal{S}(\tilde{z}) = 0, \tag{7.7}$$

correspond to the pinning distance z.

With the state configuration given by Eq.(7.6) the kinetic term in Eq.(7.1) is zero [5] and the variational problem reduces to

$$\delta_z \mathcal{S}(\tilde{z}) = \frac{d}{d\epsilon}\Big|_{\epsilon=0} \int_{\mathbb{R}} e^{2t} H(z + \epsilon\tilde{z}) dt = 0 \tag{7.8}$$

The Taylor expansion of H about z gives

$$\frac{d}{d\epsilon}\Big|_{\epsilon=0} \int_{\mathbb{R}} e^{2t} \left(H(z) + \epsilon \frac{dH}{dz}\tilde{z} + \mathcal{O}(\epsilon^2) \right) =$$

$$= \int_{\mathbb{R}} e^{2t} \frac{dH}{dz}\tilde{z} dt = 0.$$

The last equation holds for any variation $\tilde{z}$ and therefore the Euler-Lagrange equation for this problem is given by

$$\frac{dH}{dz} = 0. \tag{7.9}$$

This equation has the form of a constraint and its zeros correspond to the equilibrium separation distances for the BSs. Then H as a function of z defines an effective potential

$$U_H(z) = H[A(z)] = \int_{\mathbb{R}} \mathcal{H}[A(z)] dx. \tag{7.10}$$

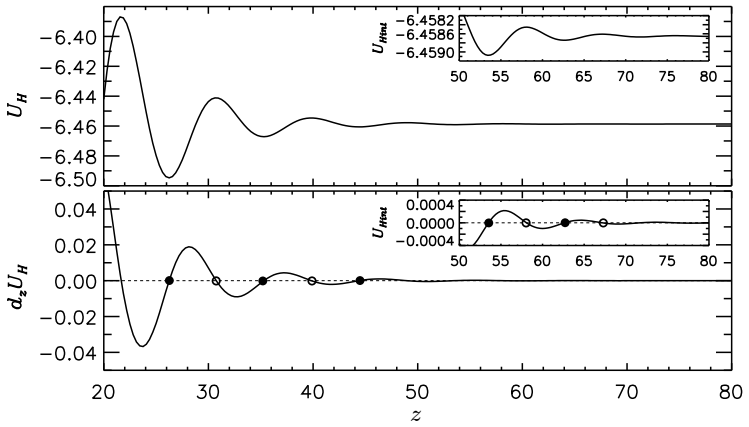

Figure 7.2: (a) Effective potential U_H as function of separation distance between peaks z. In (b) the derivative of U_H with respect to z is shown.

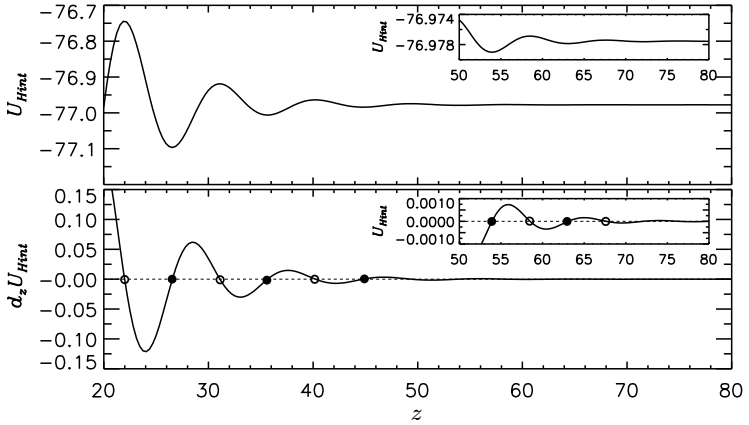

Figure 7.3: In (a) the effective potential U_{H_I} as function of separation distance between peaks, i.e. z. In (b) the derivative of U_{H_I} respect to z.

Taking the numerical solution for a single-peak soliton state for a given set of parameters, (θ, ρ) we evaluate U_H describing the interaction between two of them widely separated. This potential is shown in Figure 7.2 (a) for $(\theta, \rho) = (1.5, 1.11445)$. This potential oscillates in z with a fixed period or wavelength Λ_U and decays for increasing values of z. The subpanel inside panel (a) shows that even at large distances the oscillations are still present. The minimum (maxi-

mum) of the potential correspond to stable (unstable) equilibrium separations and therefore to stable or unstable BSs. The zeros of Eq. (7.9) give the values of the stable and unstable separation distances z_n^s and z_n^u respectively. These points are signaled by $\bullet$ and $\circ$ in Figure 7.2(b) and they have been calculated numerically interpolating the function dH/dz to find zeros. The numerical values for some of those stable points are shown in Table.(7.1). For comparison we have also added the exact separations distances calculated using numerical simulations. Although the agreement is not complete, the difference seems to be of the order of those found in Ref.[5] whith a similar equation.

The periodicity of this potential $\Lambda_U = z_{n+1}^s - z_n^s$, i.e. the different between the position of two consecutive local minimum (or maximum) can be calculated for every set of control parameters. For the present case, $\theta = 1.5$ and $\rho = 1.11445$, and using this method, one finds that $\Lambda_{U_H} \approx 9.11673$.

7.2.2 Interaction Hamiltonian

Another constraint equation similar to Eq.(7.9) can be obtained by minimizing the interaction Hamiltonian

$$H_I = -\frac{1}{2}\int_{\mathbb{R}} A^2\bar{A}^2 dx = -\frac{1}{2}\int_{\mathbb{R}} |A|^4 dx. \tag{7.11}$$

instead of the complete one given by Eq.(7.4). This Hamiltonian defines an effective interaction potential

$$U_{H_I}(z) = H_I[A(z)] = -\frac{1}{2}\int_{\mathbb{R}} |A(x,z)|^4 dx. \tag{7.12}$$

This potential is plotted in Figure 7.3 for the same set of parameters used in Figure 7.2. As in the previous case, the zeros of equation

$$\frac{dH_I}{dz} = 0, \tag{7.13}$$

provide the equilibrium distances, where the minima (maxima) correspond to stable (unstable) solutions. As before Table (7.1) shows the stable equilibrium distances and the periodicity calculated with this method.

In Figure 7.4 four examples of BSs corresponding to some of the separations given in Table 7.1 are shown. The bifurcation structure of some of these states will be explored in Section 7.3. We will show that when the separation distance is large enough ($L/2$ or similar), each single-peak soliton within a BS behaves as

Pinning dist.	U_H	U_{H_I}	Exact
z_1^s	35.297953	35.657525	36.318053
z_2^s	44.392649	44.789084	45.485578
z_3^s	53.511588	53.930950	54.652346
z_5^s	80	80	80
$z_{n+1}^s - z_n^s$	9.11673	9.14159	9.16677
$(z_{n+1}^s - z_n^s)/2\pi$	0.689192	0.687318	0.685378

Table 7.1: Several stable separations z_n^s calculated with different methods. The last column represent the exact numerical values calculated by temporal simulations.

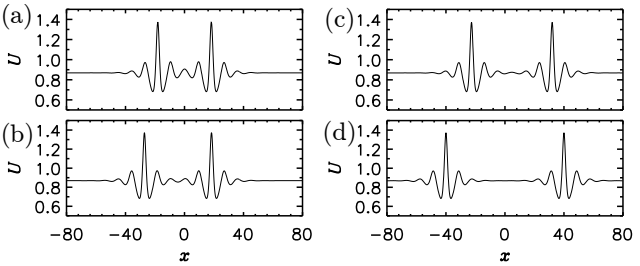

Figure 7.4: Two pulses BSs corresponding to the separation distances: $z_1^s = 36.3180$ in panel (a), $z_2^s = 45.4855$ in panel (b), $z_3^s = 54.6523$ in panel (c) and $z_5^s = 80$ in panel (d) for $\theta = 1.5$ and $\rho = 1.11445$.

an individual soliton and its bifurcation structure shows also homoclinic snaking [13]. In contrast when the solitons are closer the snaking breaks up in a stack of isolas.

7.2.3 Interaction via tails

As previously mentioned, the mechanism behind the interaction is related with the shape of the solitons' tails, and therefore with the presence of spatial oscillations. As shown in Chapter 2 such tails are described by the spatial eigenvalues of the dynamical system (2.8) and they arise when the solitons are asymptotic to a saddle-focus (SF) type of HSSs. In contrast if the HSS is a saddle (S) the tails are monotonic and the pinning does not occur. In the linear regime, the oscillatory tails are approximated by

$$U = U_0 + a_1 \mathrm{e}^{q_0 x} \cos(k_0 x + \varphi_1), \tag{7.14}$$

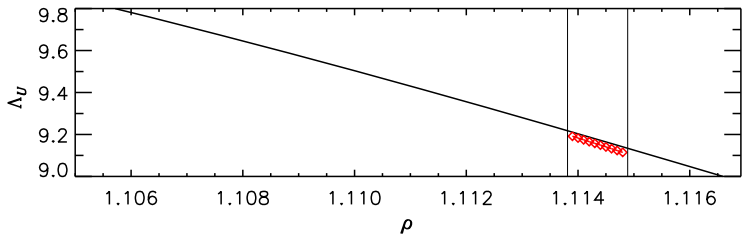

Figure 7.5: Wavelength of the interaction potential. In solid line the value calculated using Eq. (7.15) and in red diamonds the value obtained using the interaction potential in the region of existence of LS.

where a_1 and φ_1 are functions of the control parameters (θ, ρ), and can be estimated by fitting the tails with function (7.14).

For the control parameter values used here the frequency and the decay rate are respectively $k_0 = 0.6853$ and $q_0 = 0.1827$, and the fitted parameters are $(a_1, \varphi_1) = (1.45 \cdot 10^{-7}, -0.053)$. The imaginary part of the tails is described by a function analogous to (7.14). For these parameters A_0 is a SF, and k_0 and q_0 can be determined analytically by Eqs. (2.33) and (2.34). Consequently the wavelength of the oscillatory decaying tails is

$$\lambda_0^{tails} = \frac{2\sqrt{2}\pi}{\sqrt{\sqrt{\theta^2 - 4\theta I_0 + 3I_0^2 + 1} - (\theta - 2I_0)}}. \tag{7.15}$$

This expression is plotted in Figure 7.5 as function of ρ for $\theta = 1.5$. The points on top of this line correspond to the periodicity of the potential calculated, using Eq.(7.3), in the pinning region of the homoclinic snaking. The agreement between λ_0^{tails} and Λ_U is quite good although not perfect possibly because the errors introduced when evaluating the potential and when calculating the equilibrium distances. So the fact that $\Lambda_U \approx \lambda_0^{tails}$ tails reveals the connection between the interaction and the spatial eigenvalues of the HSSs solution. Thus, given a initial stable separation distance z_n^s, one can calculate any other equilibrium position wiht the relation $z_{n+1}^s = z_n^s + \Lambda_U$. Moreover, some properties of the interaction can be understood by analizing the spatial eigenvalues of A_0 .

7.3 Bifurcation structure

We explore the bifurcation structure of some of BSs that can be formed combining one, two, three, ... peaks LSs, as those found in Section 4.4, at different

pinning distances. A detailed study of the bifurcation structure of BSs has been done in Ref.[13] in the context of the Swift-Hohenberg equation. In Section 7.2 we have seen that the equilibrium separations between two soliton states is given by the overlapping of the tail of one soliton with the other, and therefore interaction is intrinsically determined by the spatial eigenvalues of the HSSs. Then, for a fixed set of parameters (ρ, θ), one expects to have as many BSs as combinationS of existing pulses are possible. In an infinite domain, the number of possible states is infinite, however in a finite size system is finite, constrained by the domain size.

7.3.1 Two-pulses bound states

First let us discuss the two-pulses structures. The simplest class of these states consist in two single solitons separated by $L/2$, like the one shown in Figure 7.4(d). These pulses are equidistant from the nearest neighbours on either side, and their behavior is identical to the behavior of single pulses on a periodic domain of size $L/2$. These type of structures are organized in a snaking bifurcation diagram as the one shown in Figure 7.6(a). Modifying ρ back and forward the different branches of the diagram have been calculated. The first stable branch corresponds to a BS in Figure 7.4(d) (here relabeled by (i)). Because both single soliton behave as if they are independent, their modification along the branches is related with the way in which both behave separately. For example, after folding the second saddle-node, each of the 1-peak states of the BS (i) develops extra peaks, one on the left and one on the right of its central peak resulting in a new BS like the one shown in Figure 7.6(a)(ii). This process is repeated and at each saddle-node two extra peaks are added to the previous state in the same fashion than in the homoclinic snaking shown in Figure 4.2 of Section 4.3. The process of adding peaks continues until filling the domain. As a result the snaking is reconnected with a pattern branch (P_{18}) from which it originated. In the same way a BS formed by two 2-peaks pulses separated by $L/2$ like the one shown in Figure 7.6(b)(i) does also exist. In this case the behavior of the even-peaks equidistant BSs is similar to the previous ones. The process of adding two extra peaks happens to each of the base states resulting in the sequence of structure (i)...(iv) plotted in Figure 7.6. In this case the branches also reconnect with the pattern P_{18}.

Together with the stable separation $L/2$, other stable equilibrium separation z_n^s (see Table 7.1) are possible and therefore two pulses symmetric BSs separated by z_n^s, as those shown in Figure 7.4, do also exist. Bound states corresponding to z_2^s and z_3^s (see Figure 7.4(b) and Figure 7.4(c)) share the same bifurcation struc-

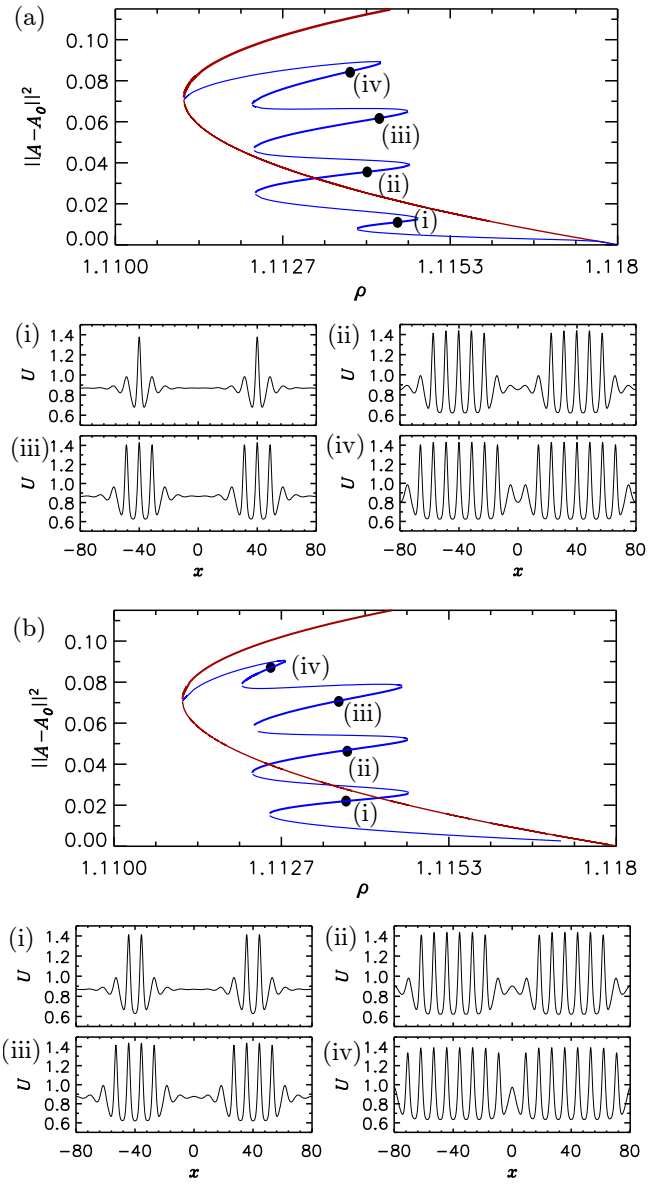

Figure 7.6: (a) Bifurcation diagram of two equidistant single-peak pulses separated by $L/2$ (see structure in subpanel (i)). In Panel (b) the diagram showing the bifurcation structure of a BS composed by two 2-peaks LSs separated by $L/2$ is shown. Parameters: $\theta = 1.5$, $L = 160$.

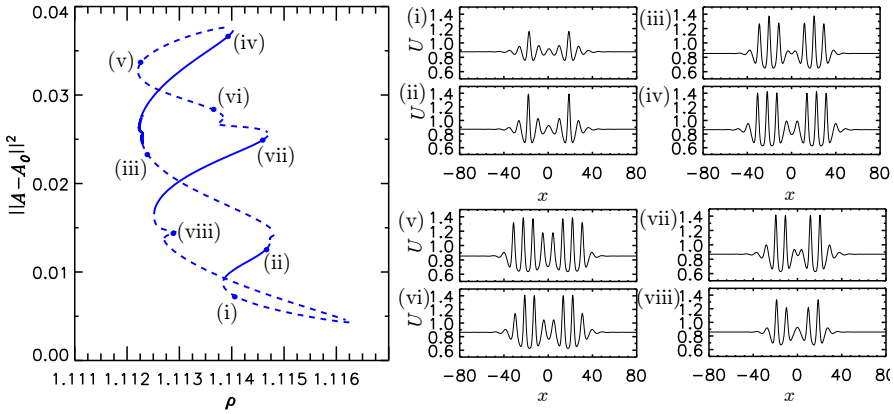

Figure 7.7: Isola formed by two-pulses BSs at pinning distance z_1^s for $\theta = 1.5$, $L = 160$. On the right column the real part of the field for the different positions marked on the diagram.

ture than those separated by $L/2$. This can be understood because at pinning distances z_2^s and z_3^s the solitons are far enough to behave as independent ones. Bound states corresponding to z_1^s (Figure 7.4(a)) are organized into large isolas and do not connect directly with the pattern branches. The type of isolas that are found are like those shown in Figure 7.7. This kind of behavior was reported in Ref.[13] (see Figure 5 in page 7) to be originated by using insufficient accuracy in the continuation algorithm, what generates jumps the soliton between independent isolas, generating in this way a large one. Despite of improving the accuracy in the numerical continuation algorithm it was not possible to find such independent isolas.

In addition to the symmetric two-pulses states, there are many more states which are not related by reflection symmetry i.e. which are asymmetric. As a consequence such states in the LL equation move with a constant velocity. If the separation is $L/2$ these asymmetric states form also snaking type of bifurcation diagrams (see Figure 6 in Ref.[13]). However, when the separation between the DSs is smaller these BSs are also organize in isolas.

7.3.2 Several-pulses bound states

Moreover, together with the two-pulses BSs presented before, there is a wide variety of states built up by any number of pulses randomly separated by the pinning distances z_n^s. Figure 7.8 shows two examples of isolas which occur in

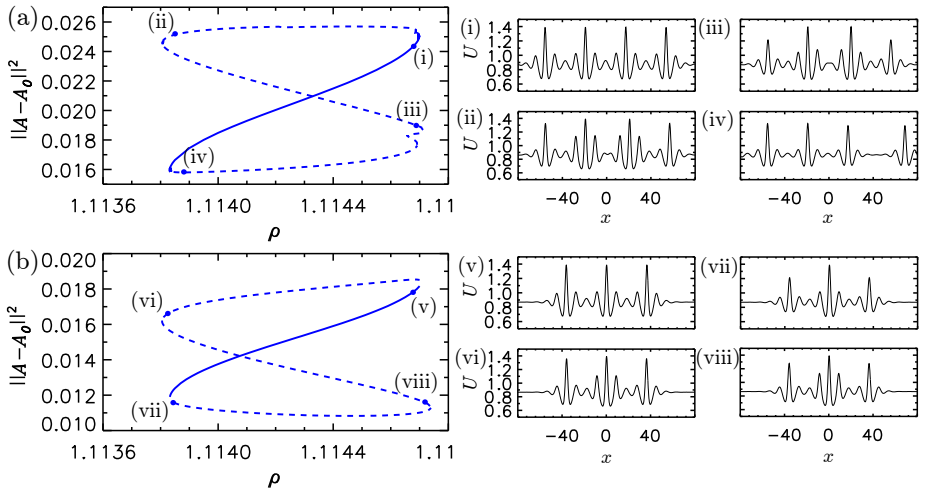

Figure 7.8: In (a) isola corresponding two a 3-pulses BS separated by a distance z_2^s. In (b) isola for a 4-pulses BSs separated also by z_2^s. On the right column we plot the real part of the field on the indicated positions. Parameters $\theta = 1.5$, $L = 160$.

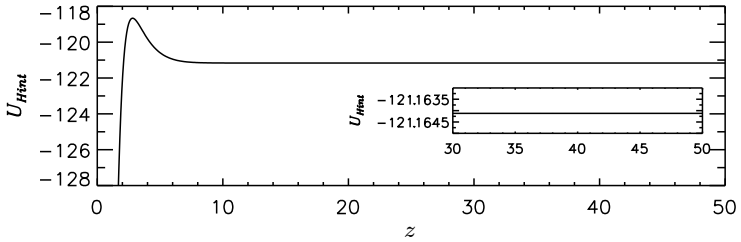

Figure 7.9: Monotonic effective interaction potential U_{H_I} for $\theta = 2.2$ and $\rho = 1.5$.

this case. Panel (a) shows the isola corresponding to a 4-pulse BS whose peaks are separated by a distance z_2^s. Panel (b) shows a similar structure but for a 4-pulse BS where the inter-distance between peaks is also given by z_2^s.

7.4 Dependence of the interaction on parameters

In this section we disccus how the spatial eigenvalues of the HSS A_0, and therefore the interaction between pulses, are modified depending on the control parameters (θ, ρ).

In Chapter 4, it was shown that in the anomalous GVD regime, two situations can been found depending on the value of θ. For $\theta < 2$, the bottom HSS branch A_0^b is stable all the way until the MI(HH) at $I_0 = I_c = 1$, where it becomes modulational unstable. Moreover A_0^b is, from $I_0 = 0$ to $I_0 = I_c$, a SF with spatial eigenvalues $\lambda_{1,2,3,4} = \pm q_0 \pm ik_0$ and therefore a wide variety of BSs exist.

For $\theta > 2$, A_0^b is stable all the way until $\mathrm{SN}_{hom,1}$. Nevertheless, the spatial eigenvalues get modified when crossing the BD line at $I_0 = I_c$, and two subregions must be considered, one below the BD line ($I_0 < I_c$), where A_0^b is a SF, and one above the BD line ($I_0 > I_c$) where A_0^b is a saddle with eigenvalues $\lambda_{1,2} = \pm q_1$ and $\lambda_{3,4} = \pm q_2$. In the first subregion, the LSs have oscillatory tails although they are highly damped (see the plot for q_0 shown in Figure 2.11(a)). Consequently the interaction potential is almost monotonic as shown in Figure 7.9 for $\theta = 2.2$ and $\rho = 1.5$. In the second subregion ($I_0 > I_c$), the tails of LSs are monotonic, and so it is the potential, and consequently no pinning between solitons is possible.

7.5 Interaction with higher order effects

In this section we apply the previous techniques to study the formation of BSs when high order dispersion (HOD) terms are considered in the LL model (see Section 1.2). These terms modify the spatial eigenspectrum of the HSSs A_0, and therefore the tails of the LSs. To illustrate this we fix ($\theta = 2.2, \rho = 1.5$) just in a region where the tails are monotonic and so is the interaction potential (see Figure 7.9). We will show that, for these values, HOD effects produce spatial oscillations on the soliton's tails and as a consequence on the interaction potential, allowing the formation of a wide variety of BSs.

The LL equation in the anomalous regime including HOD terms reads

$$\partial_t A = -(1 + i\theta)A + i\partial_x^2 A + \sum_{m \geq 3} i^m d_m \partial_x^m A + iA|A|^2 + \rho \tag{7.16}$$

The even terms (with $m = 2n$, $n \in \mathbb{N}$) conserve the spatial reversibility. In contrast the odd ones ($m = 2n + 1$) break that symmetry. In the following we focus in two particular types of HOD effects, fourth order dispersion (FOD) and third order dispersion (TOD). FOD is modeled by the term $\sim d_4 \partial_x^4$, which conserve reversibility, and TOD is modeled by $\sim d_3 \partial_x^3$ which breaks it.

We will calculate the interaction potentials, and the stable and unstable separation distances, of the LL equation when each of these terms is considered, showing that the matching between the theoretically predicted separations and

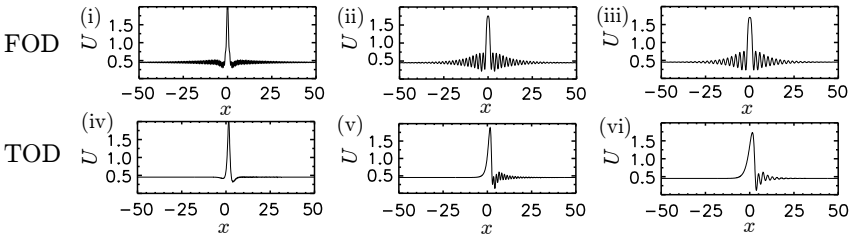

Figure 7.10: Single soliton states in the presence of FOD (i)-(iii) and TOD (iv)-(vi). Here $d_4 = 0.02, 0.1$ and 0.3 from (i) to (iii) and $d_3 = 0.1, 0.3$ and 0.6 from (iv) to (vi).

the exact ones is very accurate.

Figure 7.10 shows how FOD and TOD effects modify the shape of the single solitons, and in particular their tails.

7.5.1 Terms conserving reversibility: fourth order dispersion

The LL in the anomalous regime considering FOD terms reads

$$\partial_t A = -(1 + i\theta)A + i\partial_x^2 A + d_4 \partial_x^4 A + iA|A|^2 + \rho \tag{7.17}$$

In Figure 7.10 a single soliton state is plotted for three increasing values of d_4. These states have left/right symmetry and their oscillatory tails increase their amplitude and wavelength with d_4.

Inserting ansatz (7.6) into Eq.(7.13) the potential U_H is calculate as function of the separation z. These potentials are shown in Figures 7.11(a)-(c) for $d_4 = 0.05, 0.1$ and 0.15 respectively. Figure 7.12 shows dH/dz as function of z for the potential of Figure 7.11(c) ($d_4 = 0.15$). The intersection of the graph with zero gives the equilibrium separations z^n. Here, as before, the minimum (maximum) corresponds to stable (unstable) separation distances.

In Figure 7.13 one can see several two-soliton stationary BSs at different separation distances for $d_4 = 0.15$. Panel (i) shows the BS with the smaller distance allowed, and in panels (ii)-(iv) the two peaks of the BS are separated by one, two and four spatial oscillations (SOs) respectively. The potential prediction (see Figure 7.12) is only valid when separation between the solitons is large enough. In this way the predicted separation corresponding to states (i)-(iii), fails. However, for BSs (iv) and for (v)-(vi), where the separation is larger, the prediction is in good agreement with the real separation. A comparation between the real and the theoretical separation distances is shown in table 7.2.

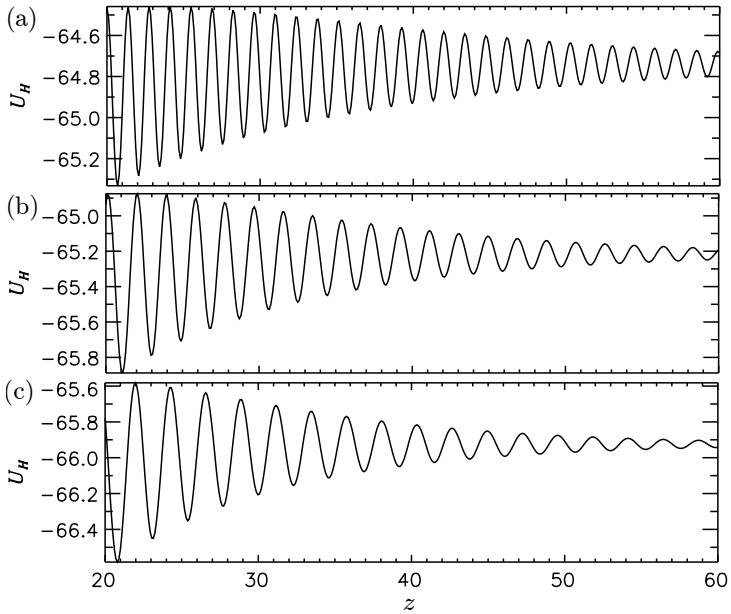

Figure 7.11: Effective interaction potential U_{H_I} for $\theta = 2.2$ and $\rho = 1.5$ for different values of d_4. In panel (a) $d_4 = 0.05$, in (b) $d_4 = 0.1$ and in (c) $d_4 = 0.15$. The minimum (maximum) corresponds to the stable (unstable) separation distances z_s^n and z_u^n respectively. Here $L = 200$.

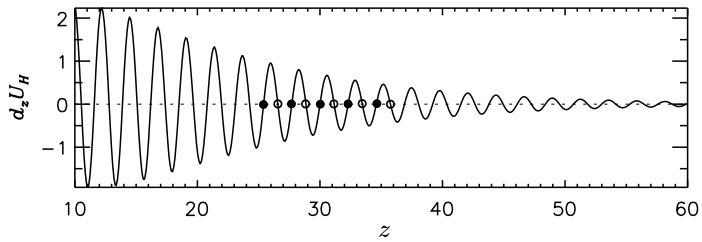

Figure 7.12: Derivative of the interaction potential U_{H_I} respect to the separation distance z corresponding to panel (c) in Figure 7.11 for $d_4 = 0.15$. The zeros of this plot correspond to the stable (signaled with •) and unstable (○).

Using the variables $y_1 = U$, $y_2 = V$, $y_3 = d_x U$, $y_4 = d_x V$, $y_5 = d_x^2 U$, $y_6 = d_x^2 V$, $y_7 = d_x^3 U$ and $y_8 = d_x^3 V$ the stationary version of Eq.(7.17) is recast to the

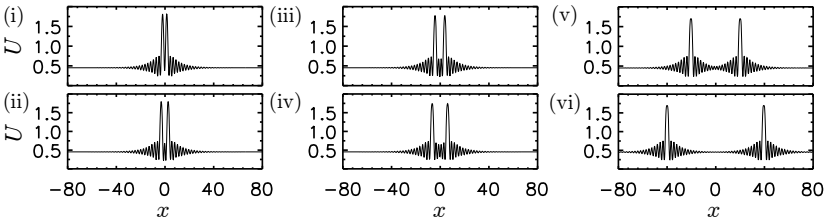

Figure 7.13: Bound states for $d_4 = 0.15$, $\theta = 2.2$ and $\rho = 1.5$. The separations correspond to $z_s^0 = 3.2117$ in (i), $z_s^1 = 5.5808774$ in (ii),$z_s^2 = 7.948731$ in (iii),$z_s^4 = 12.643589$ in (iv), $z_s^{16} = 40.41223$ in (v),$z_s^{33} = 79.503312$ in (vi). Here $L = 200$.

$d_4 = 0.15$	z_4^s	z_9^s	z_{16}^s	z_{25}^s	z_{25}^s
U_{H_I}	12.797605	24.265611	40.35027	61.032138	79.413032
Exact	12.643589	24.251682	40.41223	61.119042	79.503312

Table 7.2: In this table several stable separations z_n^s for $d_4 = 0.15$ calculated with the interaction potential and the exact ones are shown. The first row corresponds to the stable distances calculating using the potential of interaction. The second row represents the exact numerical values.

dynamical system:

$$\begin{aligned} d_x y_i &= y_{i+2}, \qquad i = 1, ..., 6 \\ d_x y_7 &= d_4^{-1}\left[y_2 + \theta y_1 - y_5 - y_1(y_1^2 + y_2^2)\right] \\ d_x y_8 &= d_4^{-1}\left[-y_1 + \theta y_2 - y_6 - y_2(y_1^2 + y_2^2)\right]. \end{aligned} \tag{7.18}$$

The eigenspectrum of the Jacobian of (7.18) evaluated at A_0 is obtained via solution of the characteristic polynomial

$$d_4^2\lambda^8 + 2d_4\lambda^6 + (1 - 2d_4\theta + 4d_4 I_0)\lambda^4 + (4I_0 - 2\theta)\lambda^2 + 3I_0^2 - 4_0 + \theta^2 + 1 = 0, \tag{7.19}$$

and consists of two sets of eigenvalues $\lambda_{1,2,3,4} = \pm q_0 \pm i k_0$ and $\lambda_{5,6,7,8} = \pm q_1 \pm i k_1$, as those shown in Figure 7.14 for $d_4 = 0.02$ (panel (a)) and $d_4 = 0.15$ (panel (b)). Due to the spatial reversibility the eigenspectrum is symmetric respect to the axes $\mathrm{Im}[\lambda] = 0$ and $\mathrm{Re}[\lambda] = 0$. Figures 7.11 from panel (a) to panel (c) show how the wavelength of the potentials increases with d_4. This dependence is shown in Figure 7.15, and it has been calculated using the potential (black diamonds) and $2\pi/k_1$ (red crosses), where k_1 is the imaginary part of the spatial eigenvalue with smallest negative real part in absolute value. As one can see the agreement is very good.

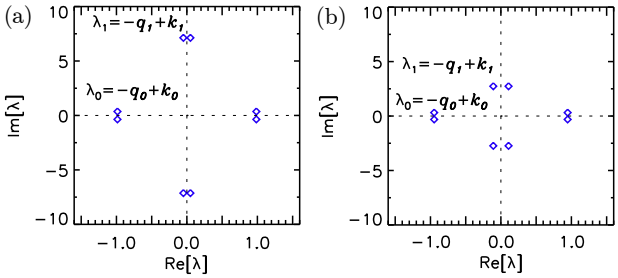

Figure 7.14: Spatial eigenvalues satisfying the characteristic polynomial (7.19) for $\theta = 2.2$, $\rho = 1.5$ and $d_4 = 0.02$ in panel (a), and $d_4 = 0.15$ in panel (b)

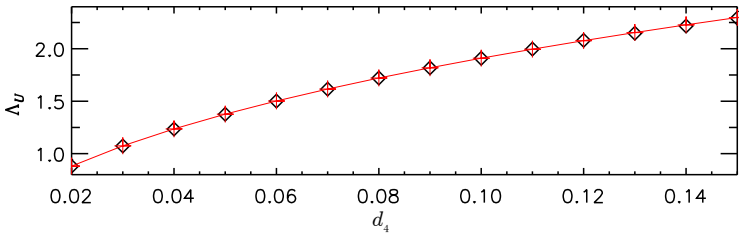

Figure 7.15: Periodicity of the potential Λ_U as function of the FOD coefficient d_4 for $\theta = 2.2$ and $\rho = 1.5$. Black diamonds are calculated directly from the potential. Red crosses stand for $2\pi/k_1$.

7.5.2 Terms breaking reversibility: third order dispersion

The effects of TOD on solitons was widely studied in Chapter 6 in both the anomalous and normal GVD regimes. With this term the LL model reads

$$\partial_t A = -(1 + i\theta)A + i\partial_x^2 A + d_3\partial_x^3 A + iA|A|^2 + \rho. \tag{7.20}$$

Equation (7.20) is not invariant under the transformation $x \to -x$ and therefore the solution of this equation is no longer left/right symmetric (see Figure 7.10(iv)-(vi)). Due to this asymmetry, a LS drifts with constant velocity c which can be determined numerically.

With TOD the shape of the oscillatory tails is well predicted by the spatial eigenvalues (Chapter 6). Here, despite of the asymmetry of the solitons, we show that BSs are also formed by the locking between the tail of each soliton and its mate's core, and that the allowed separation distances can be predicted by the spatial eigenvalues.

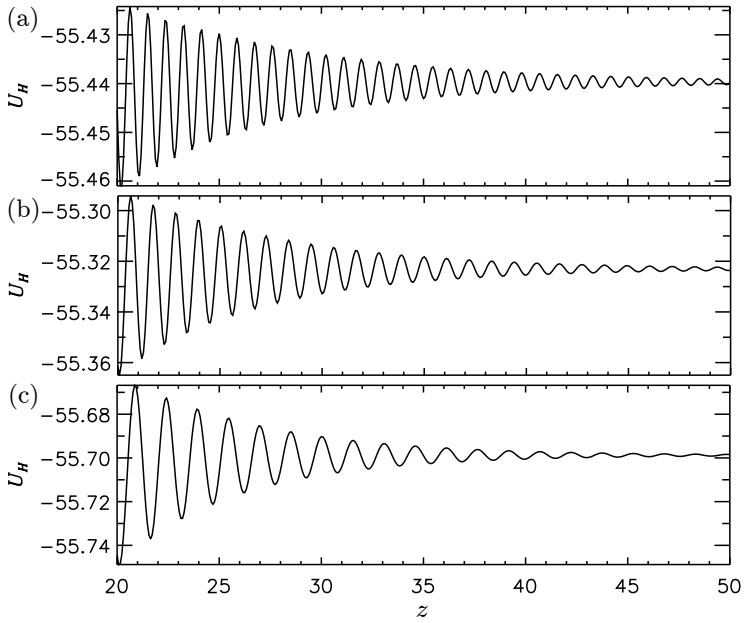

Figure 7.16: Effective potential obtained from the interaction Hamiltonian H_I for $\theta = 2.2$, $\rho = 1.5$, and different values of d_3: (a) $d_3 = 0.1$, (b) $d_3 = 0.2$ and (c) $d_3 = 0.3$.

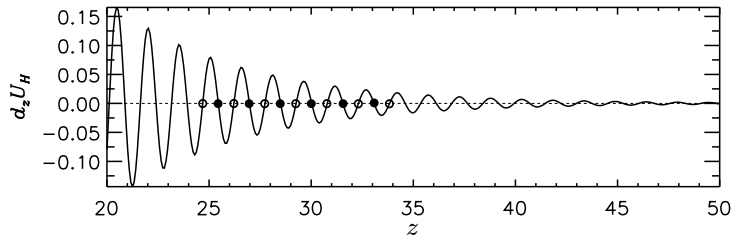

Figure 7.17: In (a) Effective potential obtained from the interaction Hamiltonian H_I for $\theta = 2.2$, $\rho = 1.5$ and $d_3 = 0.3$. In panel (b) we show dU_{H_I}/dz. The intersection of this last function with vertical axes at 0 give the stable separation distances. In this case $\Lambda_H = 1.3201666$.

In Figure 7.16 the interaction potential for three different values of d_3 is shown. As also happens with FOD, TOD modifies the shape of the potential going from a monotonic potential (see Figure 7.9) to the oscillatory potentials shown in panels (a)-(c) for $d_3 = 0.1$, 0.2 and 0.3 respectively. Here, in contrast with the LL equation, and the LL equation with FOD effects, the maximum (minimum)

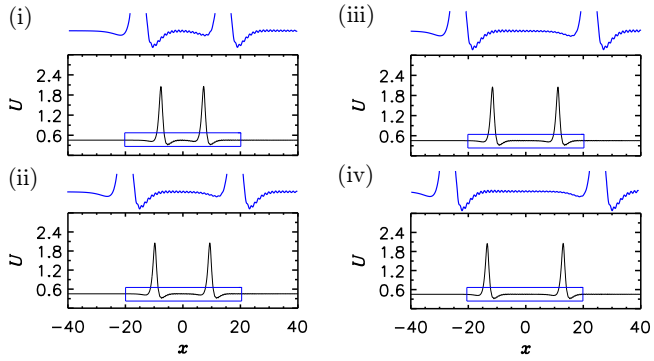

Figure 7.18: Two-pulses BSs for $d_3 = 0.1$ and different stable distances. In (a) $z_0^s = 14.8621$, in (b) $z_7^s = 19.1223$, in (c) $z_{13}^s = 22.7739$ and in (d) $z_{19}^s = 26.4255$. Here as well $L = 160$.

$d_3 = 0.1$	z_0^s	z_7^s	z_{13}^s	z_{19}^s
U_{H_I}	15.010894	19.269321	22.921311	26.572410
Exact	14.862133	19.122334	22.773986	26.425529

$d_3 = 0.3$	z_0^s	z_3^s	z_7^s	z_{13}^s
U_{H_I}	14.788130	19.357768	25.453909	34.600589
Exact	14.966661	19.517315	25.601455	34.742282

Table 7.3: Several stable separations z_n^s for $d_3 = 1$ and $d_3 = 0.3$ calculated with the interaction potential and the exact ones. The first row corresponds to the stable distances calculating using the potential of interaction. The second row represents the exact numerical values.

correspond to stable (unstable) separation distances as it was also predicted in Ref. [3]. This can be observed in Figure 7.17 for $d_3 = 0.3$.

Figure 7.18 shows four examples of BSs at stable equilibrium distances (a) $z_0^s = 14.8621$, (b) $z_7^s = 19.1223$, (c) $z_{13}^s = 22.7739$ and (d) $z_{19}^s = 26.4255$, for $d_3 = 0.1$. The separations calculated using the potential (first row) and simulations/Newton-Raphson algorithm (second row) can be compared in table 7.3 for $d_3 = 0.1$ and 0.3.

Figure 7.19 shows $\Lambda_U = z_{n+1}^s - z_n^s$ first calculated directly from the potential and calculated from the the spatial eigenvalues frequency $\mathrm{Im}[\lambda^-]$ (we plot $2\pi/\mathrm{Im}[\lambda^-]$ in Figure 7.19). For comparison, we have also added the analytical

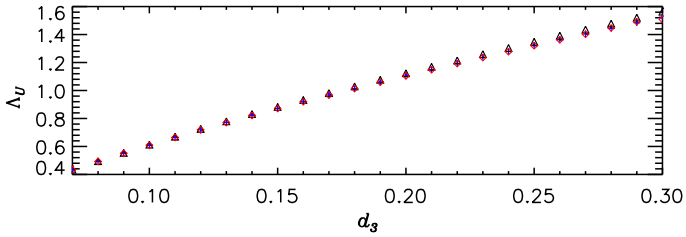

Figure 7.19: Here it is shown how the wavelength Λ_U of the potential changes in function of d_3, for a domain size $L = 160$. With blue crosses the wavelength obtained through the spatial eigenvalue λ^- obtained solving the characteristic polynomial (6.19) is shown. The black triangles represent the same quantity calculated with the analytical expresion (7.21), and the red diamonds represent the same quantity obtained directly from the potential.

approximation that we obtained in Section 6.3,

$$\lambda^- = \pm i \frac{\sqrt{1 + 2cd_3}}{d_3}. \tag{7.21}$$

As we can observe Λ_U increases with the strength of the TOD. Due to this, for the same fixed domain size, the larger the TOD strength, the smaller the number of two-soliton. To summarize, we have shown that BSs arise in the presence of HOD effects for values of (θ, ρ) where in their absence BSs are not allowed.

7.6 Effects of noise on the bound states

We have seen that BSs of solitons can be formed due to the locking, at fixed distances, of single-peak solitons, and that this locking is induced by the existence of oscillatory tails on the solitons' profiles. In this Section we study how these BSs and their stability are modified when the background is noisy. Here we focus on the effect of noise when only FOD and TOD terms are considered. The noise is incorporated to the system through a fluctuating pump intensity of the form

$$\rho = \rho_0 + \sqrt{D}\xi(x,t) \tag{7.22}$$

where $\xi(x,t)$ is a Guassian white noise of zero mean and correlation

$$\langle \xi(x,t)\xi(x',t')\rangle = \delta(t-t')\delta(x-x') \tag{7.23}$$

7.6.1 When fourth-order dispersion is considered

Figure 7.20 shows the time evolution of an initially stable BS with separation $z_0 = 40.0266$ for a FOD strength $d_4 = 0.02$ for different realizations of the noise.

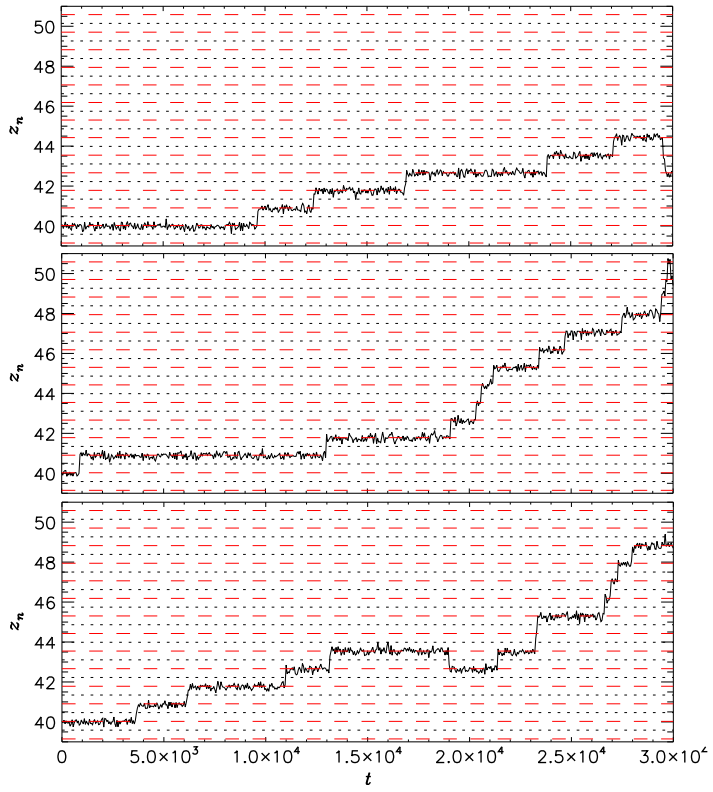

Figure 7.20: Effect of white noise $\xi(x)$ on a BS for parameter values, $\theta = 2.2$, $\rho = 1.5$ in the presence of FOD $d_4 = 0.02$. Red dashed lines represent the stable separation distances z_n^s and black dashed lines the unstable ones z_n^u, both calculated using the interaction potential. Here is $\sqrt{D} = 1.5$ and $L = 300$.

Due to the effect of noise, the positions of the two peaks of a BSs fluctuate, showing sudden jumps between neighboring equilibrium positions, increasing or decreasing the separation between peaks. The difference between the stable (red dashed lines) and unstable (black dashed lines) separations is given by $\Lambda_U/2 = z_n^s - z_n^u = 0.43987$. As time passes, in average, the two-soliton BS tends to increase its separation instead of decreasing it, not matter which initial seed is used to generate the noise. Here one can identify that the dynamics exhibits two different time scales, one fast and the other slow. The fast scale describes the evolution of the system from a given separation to the closest largest one

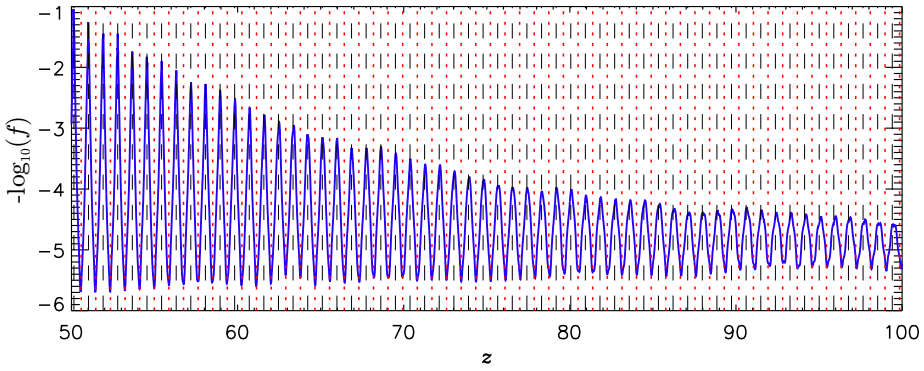

Figure 7.21: Probability of being in a given separation distance for $\theta = 2.2$, $\rho = 1.5$ in the presence of FOD $d_4 = 0.02$. Red pointed lines represent the stable separation distances z_n^s and black dashed lines the unstable ones z_n^u. Here $L = 230$ and $\sqrt{D} = 0.5$ and we have considered 70 different realizations of the noise.

(corresponding to the closest minimum into the right if one looks to Figure 7.11). The slow scale describes how, for an infinite time, the system evolves toward larger separations until reaching the minimum of the envelope of the potential. In an infinite system the separation will increase infinitely. However, our system is periodic, and therefore the larger separation allowed is $z = L/2$. Moreover, there is a direction which is facilitated by the evolution of the system, the one that increases the separation distance, as according to the asymmetric potential shown in Figure 7.11. In a symmetric potential the system would jump from a given separation to the closest one, no matters if it is larger or shorter than the former one. This occurs because the symmetry in the potential facilitates equally any direction. However, if the potential is asymmetric, the system, in the presence of noise, will evolve to the minimum of the envelope of the interaction potential, which in a periodic domain corresponds to $z = L/2$.

In order to characterize better this phenomenon we have calculated the frequency density distribution f [1] (see Figure 7.21) describing the jumping between different stable separations when noise is added. To do that we have run simulations starting from different stable BSs with separations within the range $z \in [50, 100]$, for the same amount of time, and for 70 different realizations of the noise. The election of $-\log_{10}$ in Figure 7.21 is arbitrary. The logarithmic function allows to see in detail the structure of the histogram, not clear otherwise. In this way $\log_{10}(f)$ represents the probability of reaching a given stable separation distance.

[1] The number of events that we have at each separation distance.

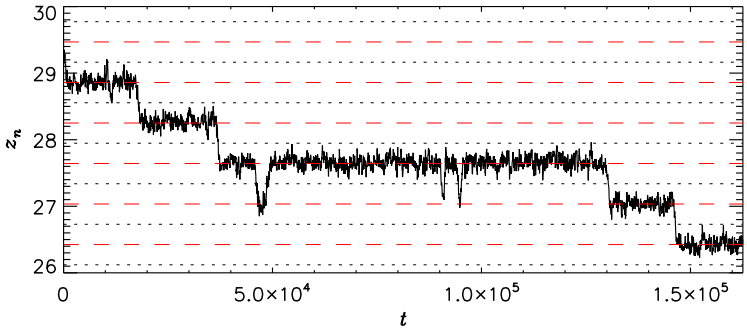

Figure 7.22: Effect of white noise $\xi(x)$ on a BS for parameter values, $\theta = 2.2$, $\rho = 1.5$ in the presence of TOD strength $d_3 = 0.1$. Red dashed lines represent the stable separation distances z_n^s and black dashed lines the unstable ones z_n^u. Here $\sqrt{D} = 1.5$ and $L = 200$.

Thus, the maxima correspond to the most probable separations and the minima to the less probable ones. The use of $-\log_{10}$ allows us to establish a correspondence with the interaction potential shown in Figure 7.11, whose minima correspond to the minima of Figure 7.21 and therefore to the basins of attraction of the system, i.e. stable separation distances (shown in red dashed lines). Thus, in a fast time scale, Figure 7.21 shows where the system spends most of its time during the temporal evolution, and one can interpret the probability as the escape time from a certain basin of attraction.

The barriers of the interaction potential, (see Figure 7.11) decrease for increasing separation distances, and consequently the barriers of $-\log_{10}(f)$ shown in Figure 7.21. Therefore, the amplitude of noise that it is necessary to apply to the system in order to make it escape from a given basin of attraction must be larger for small separations, and smaller for the larger ones. For a fixed value of noise, a BS needs more time to escape from a basin of attraction characterized by a short separation, and then with a larger barrier, than from one with a shorter separation where the barrier is smaller. Moreover, it is possible to show that the escape time dependent on the size of the barrier [14].

7.6.2 When third-order dispersion is considered

Figure 7.22 shows the evolution of BSs in the presence of only TOD effects. Here $d_3 = 0.1$, $\sqrt{D} = 1.5$, $z_0 = 26.425529$ and $\Lambda_U/2 = 0.304253$. In this case the noise generates a similar behavior i.e. the position of both peaks fluctuate until the jumping between neighboring positions occurs. Nevertheless, in contrast to the

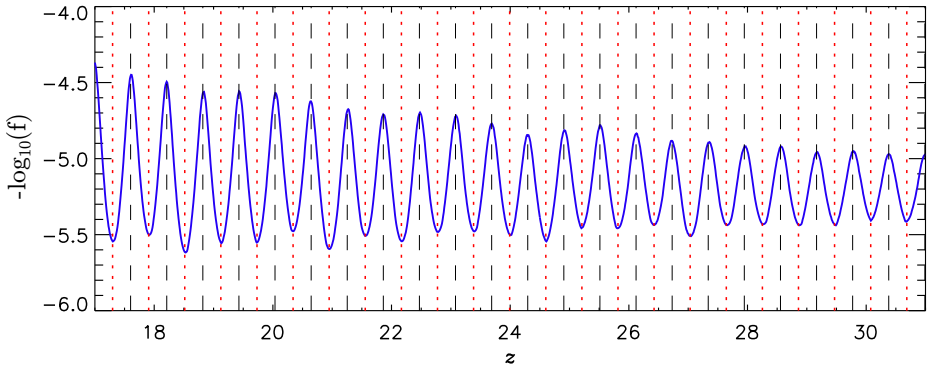

Figure 7.23: Probability of being in a given separation distance for $\theta = 2.2$, $\rho = 1.5$ in the presence of TOD $d_3 = 0.1$. Red pointed lines represent the stable separation distances z_n^s and black dashed lines the unstable ones z_n^u. Here $L = 200$ and $\sqrt{D} = 1.5$ and we have considered 54 different realizations of the noise.

FOD situation, the separation between peaks decreases in time according to the potential shown in Figure 7.16 until reaching the maximum value of its envelope. Proceeding in the same way that in the case with FOD, we have calculated the frequency histogram shown in Figure 7.23 for the BSs in the presence of noise. As before the minima of this quantity confirm the stable separation distances obtained by the interaction Hamiltonian. However, now the system evolves to minima separation.

We can summarize saying that with FOD the separation between peaks tends to increase and with TOD tends to decrease. This phenomenon can be understood by looking to the interaction potentials in both cases. While with only the GVD and FOD effects the stable separations correspond to the minimum of the potential, in the TOD case they are given by the maximum. In this context, the stochastic dynamics of a two-soliton BSs tends to the minimum of the potential envelope for the reversible cases (only GVD and FOD) and therefore to the largest separation, and to the maximum of that envelope, and consequently to the shortest separation, for the non-reversible cases (with TOD).

7.7 Conclusions

In this work we have applied the variational principle to study the interaction and the formation of BSs in the LL equation. We have derived an effective potential depending on the separation distance between solitons. The extrema of this

potential determine the stable or unstable separation distances and they are related with the overlapping of the solitons' tails of one soliton with its mates' core, and therefore can be understood by analyzing the spatial eigenvalues of Eq.(3.1). Moreover, the periodicity of the potential is determined by the spatial eigenvalues of A_0. After studying these potentials we have calculated some of the bifurcation diagrams which arise for the different BSs. Regarding the two-soliton BS, if the separation is $L/2$ or similar, solitons behave as independent ones and the resulting bifurcation diagram is of snaking type [13]. In contrast, when the separation is smaller, BSs are organized in a stack of isolas that are not connected with the pattern. If we consider arrays of more than two solitons, the bifurcation structures obtained are normally isolas.

These results can be extended for the LL when high order effects are considered. Here we have focused in the fourth order dispersion and third order dispersion effects. For both cases, spatial oscillations appears on the solitons' tails, due to the modification of the spatial eigenvalues of A_0. While in the FOD case the oscillations in the tails are symmetrical, for TOD they are asymmetric respect the symmetry plane $x = 0$.

We have shown that for parameters for which finding BSs in the LL model is difficult, a wide variety of BSs arise due to tail interaction when considering the extra dispersion terms. In both cases we calculate the equilibrium distances from the potential itself and from the spatial eigenspectrum. This is an important quantity because just knowing the separation of a single BS it is possible to predict any other stable separation.

Finally in Section 7.6 we have studied the effects of adding white Gaussian noise on the BSs for both the TOD and FOD. From the different realizations of this noise we have calculated the probability of being in a given position and we have found that the basins of attraction obtained with this method correspond exactly to the stable possition predicted by the potential.

Recently, BSs of solitons has been studied experimentally in the context of passive driven nonlinear resonators where several new binding mechanism involving Gordon/Kelly sidebands, birefringence, and dispersive waves have been identified [15], so we expect that our results are relevant for this community.

References

[1] B. A. Malomed, *Bound solitons in the nonlinear Schrodinger-Ginzburg-Landau equation,* Phys. Rev. A **44** 10 6954-6957 (1991).

[2] P. Colet, M. A. Matías, L. Gelens, and D. Gomila, *Formation of localized structures in*

bistable systems through nonlocalspatial coupling. I. General framework, Phys. Rev. E **89**, 012914 (2014).

[3] B. A. Malomed, *Bound states of envelope solitons,* Phys. Rev. E **47** 4 2874-2880 (1993).

[4] D. Cai, A. R. Bishop, N. Gronbech-Jensen, and B. A. Malomed, *Bound solitons in the ac-driven, damped nonlinear Schrodinger equation,* Phys. Rev. E **49** 2 1677-1679 (1994).

[5] I. V. Barashenkov, Yu. S. Smirnov, and N. V. Alexeeva, *Bifurcation to multisoliton complexes in the ac-driven, damped nonlinear Schrodinger equation,* Phys. Rev. E **57** 2 (1998).

[6] F. M. Mitschke and L. F. Mollenauer, *Experimental observation of interaction forces between solitons in optical fibers,* Opt. Lett. 12, 355 (1987).

[7] D. J. Kaup, *Perturbation theory for solitons in optical fibers,* Phys. Rev. A **42**, 5689 (1990).

[8] M. Tlidi, A. G. Vladimirov, and P. Mandel, Jour. of Quantum Electronics, *Interaction and stability of periodic and localized structures in optical bistable systems,* **39**, 2 (2003).

[9] M. Tlidi, P. Mandel, and R. Lefever, *Localized structures and localized patterns in optical bistability,* Phys. Rev. Lett. **73**, 640, 1994.

[10] D. Gomila, P. Colet, G-L. Oppo, and M. San Miguel, *Stable droplets and growth laws close to the modulational instability of a domain wall,* Phys. Rev. Lett. **87**, 194101 (1-4) (2001).

[11] D. Gomila, P. Colet, M. San Miguel, A. Scroggie, G-L. Oppo, *Stable Droplets and Dark Ring Cavity Solitons in Nonlinear Optical Devices* IEEE Journal of Quantum Electronics **39**, 238-244 (2003).

[12] W.J. Firth and A. Lord, *Two dimensional solitons in a Kerr cavity,* J. Mod. Opt. **43**, 1071 (1996).

[13] J. Burke, E. Enobloch, *Multipulse states in the Swift-Hohenberg equation*, Discrete and continuous dynamical systems-Suppl. September, 109-117 (2009).

[14] P. Colet, F. De Pasquale, and M. San Miguel, *Relaxation in the subcreitical pitchfork bifurcation: From critical to Gaussian scaling*, Phys. Rev. A, **43**, 10 (1991).

[15] Y. Wang, F. Leo, J. Fatome, K. Luo, J. K. Jang, M. J. Erkintalo, S. G. Murdoch, and S. Coen, *Real time observations of soliton bound states, with multiple binding mechanism, in passive nonlinear cavities,* CLEO:QELS Fundamental Science, FF2A. 6 (2016).

Chapter 8

Effects of defects and drift on the dynamics of solitons in the Lugiato-Lefever model

8.1 Introduction

In previous chapters we have analyzed the dynamics of localized structures (LSs) in the context Lugiato-Lefever equation describing one-dimensional driven optical cavities, in both the normal and anomalous regimes. There we have shown that while in the anomalous regime typical dissipative solitons (DSs) are bright, in the normal regime the DSs are dark. Although these states have a different origin, bright solitons are formed as a pattern element, and dark ones are the result of the locking of two fronts with different polarities, both of them can undergo instabilities leading to a wide variety of temporal dynamics, such as periodic oscillations [1–4] and chaos [4–6].

An interesting question is to know how the dynamics of these DSs are modified when defects and drift are present in an optical cavity. Inhomogeneities, or defects, are unavoidable in any experimental setup, and drift is also often present in many optical, fluid and chemical systems. In optical systems this can be caused by misalignments of the mirrors [7, 8], nonlinear crystal birefringence [9], or parameter gradients [10] , while in fluid and chemical systems drift is due to fluid flow [11, 12]. In synchronously pumped fiber cavities it has been shown that a mismatch in the synchronization induces drift [13], and in both, fiber

cavities and microresonators, drift can also be induced by odd high-orders on chromatic dispersion. The competition between these two ingredients can lead to a very rich DS dynamics. In particular, a special type of transient dynamics, known as excitability, can be generated [16, 17].

In this chapter we analyze the effects of these two elements on the dynamics of DSs in the Lugiato-Lefever equation, considering both periodic boundary conditions and absorbing ones. Microcavities or fiber cavities are by nature periodic. On the contrary spatial cavities filled with a nonlinear medium [18], can be modeled using absorbing boundary conditions.

Without loss of generality, we consider one-dimensional LL equation in the anomalous dispersion regime. This equation is formally identical to the LL describing a Fabry-Perot spatial cavity when one of the transverse dimensions is shorter than the critical wavelength. Hence, within this chapter we will think on a spatial cavity that is very long and narrow. The defect or spatial inhomogeneity can be induced in the system by injecting a Gaussian beam on top of the homogeneous pump. To consider this effect on the model we add the term

$$\tilde{\rho}(x) = \rho + b(x) = \rho + h\exp\left(-\left(\frac{x - x_0}{\sigma}\right)^2\right), \tag{8.1}$$

where h is the amplitude of the Gaussian beam centered at $x = x_0$, and σ its half width at half maximum. The drift, can arise easily if, for example, the mirrors of the cavity are not perfectly aligned. If these two conditions occur simultaneously, then the electric field inside the cavity is described by the equation

$$\partial_t A = -(1 + i\theta)A + i|A|^2 A + i\partial_x^2 A - c\partial_x A + \tilde{\rho}(x), \tag{8.2}$$

where we have modeled the drift by adding the general gradient term $-c\partial_x A$, being c its strength.

This chapter is organized as follows, in Section 8.2, we discuss the bifurcation scenario in the presence those two elements leading to oscillatory and excitable dynamics. We show that, with absorbing boundary conditions, the dynamics and bifurcation structure are equivalent to those found in Refs. [16, 17]. In contrast, with periodic boundary conditions, the dynamics of DSs, periodically generated at the inhomogeneity, are altered by the periodicity of the boundary conditions. Such boundary conditions allow those same DSs to interact with the defect again after having traveled one full round trip in the cavity (see Section 8.3). Later in Section 8.4 we also briefly show that the DSs dynamics can be much more complex at higher values of the cavity detuning due to the bistability of the HSSs

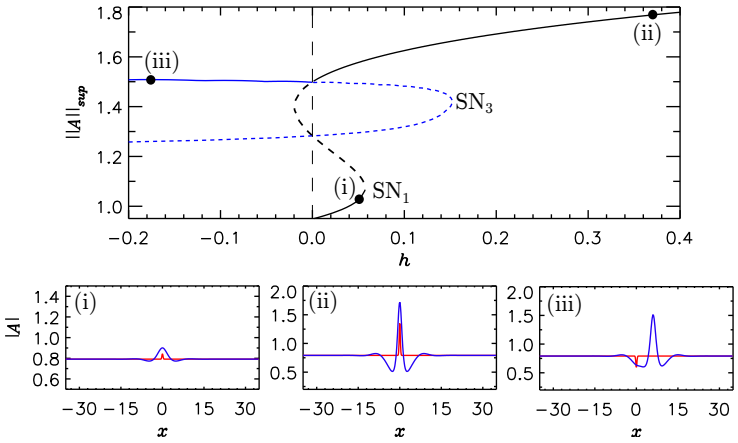

Figure 8.1: Bifurcation diagrams of the different steady-state state solutions in function of h with $c = 0$. The solid (dashed) lines represent the energy of the stable (unstable) states. The subpanels (i)-(iii) depict the absolute value of the field A inside the cavity (blue) and the corresponding profile of the defect (red pointed line). In (i), $h = 0.052$, (ii) $h = 0.556$, and (iii) $h = -0.196$.

and the proximity of the different oscillatory and chaotic instabilities. Finally, in Section 8.5, we end with a short discussion.

8.2 Dynamics and bifurcation structure for low values of detuning

In this Section, unless mentioned otherwise, we fix the values $L = 70$, $\theta = 1.56$ and $\rho = 1.137$ within the low values of the frequency detuning in the range $41/30 < \theta < 2$, and such that single DSs exist in the LL equation without drift and inhomogeneity. We also choose $\sigma = 0.2727$ around half the width of the DS at half maximum and $x_0 = L/2$, such that the inhomogeneity is centered in the $x-$domain. Similar behavior can be found for other values of θ and ρ within this region. In what follows, we analyze first the effect of the spatial inhomogeneity on the single solitons dynamics and after that we study how these dynamics change when including also the drift.

8.2.1 Dynamics induced by the spatial inhomogeneity

Figure 8.1 shows the bifurcation diagram of the steady-state solutions in the presence of a defect ($h \neq 0$), but without a drift term ($c = 0$) in more detail. The maximum absolute value of the field A is plotted as a function of h. Depending on the amplitude h of the inhomogeneity, several pinned steady states appear. The fundamental state of the system corresponds to branch (i) and is a small bump solution induced by the inhomogeneity rather than a perfect homogeneous solution as we can see in Figure 8.1(i). When increasing the value of h the system reaches a high amplitude DS (branch (ii)) pinned at its center (see Figure 8.1(ii)). Finally, for negative values of h, DSs in branch (iii) are pinned at the first oscillation of its tail as we can observe in Figure 8.1(iii). This branch is actually degenerated and there is another state corresponding to a DS pined at the other side of the defect.

8.2.2 Dynamics induced by the spatial inhomogeneity and drift

When the drift term is taken into account ($c \neq 0$), the pinned states shown in Figure 8.1 experience a force trying to detach them from the inhomogeneity. This competition between the inhomogeneity that pins the states to a fixed position and the drift force trying to pull them out, leads to the appearance of a rich variety of dynamics, namely small and large amplitude oscillations (train of solitons) and soliton excitability[1]. Figure 8.2 shows how the bifurcation scenario in Figure 8.1 changes with increasing values of the drift strength c. For low values of c two extra saddle-node bifurcations, namely SN_2 and SN_4 appear involving unstable steady state solutions (see Figure 8.2(a)). These SNs arise from the transcritical bifurcation at $h = 0$ for $c = 0$, when it becomes imperfect for $c \neq 0$. Increasing c, the SN_4 becomes soon a SNIC (saddle-node on the invariant circle) creating a limit cycle. This oscillatory solution corresponds to a periodic generation and emission of DSs from the inhomogeneity resulting in a sequence of drifting solitons called train of solitons or soliton tap [20]. This type of oscillations were also observed in the context of the Swift-Hohenberg (SH) equation with absorption in the boundaries [16, 17]. In the present case, an example of such a train of solitons (for a higher value of c) is shown in Figure 8.3(i) and Figure 8.4(i) for absorbing and periodic boundary conditions respectively. Due to the periodic boundary conditions, the train of solitons is instead reinjected on the other side of the domain, filling up the whole cavity. At

[1] This type of excitability is an emergent property of the DSs and one says that a system is said to be excitable if perturbations below a threshold decay exponentially, while perturbations above this threshold induce a large response before going back to the resting state.

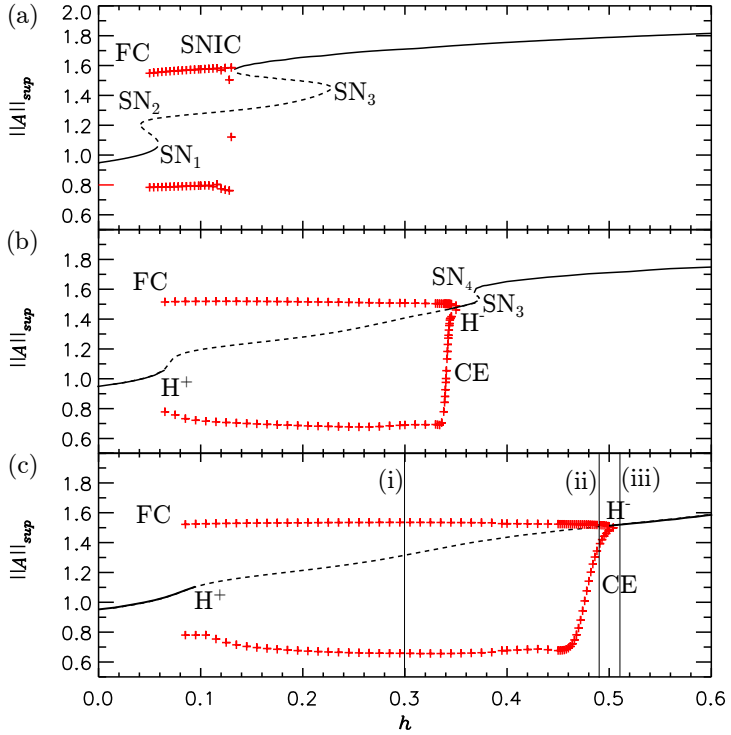

Figure 8.2: Bifurcation diagrams of the different steady-state solutions in function of h for different values of the the drift strength c: $c = 0.025$ in (a), $c = 0.06$ in (b) and $c = 0.1$ in (c). The solid (dashed) lines represent the energy of the stable (unstable) states. The + markers correspond to the extrema of oscillatory solutions, and the vertical dashed line shows the location of the Fold of Cycles (FC). Other parameters are as in Figure 9.3. The labels (i)-(iii) correspond to Figures 8.3 and 8.4.

the SNIC the period of emission of DSs diverges, and it decreases as one moves away from the SNIC bifurcation point [21].

For higher values of c (see Figure 8.2(b) for $c = 0.06$), SN_1 and SN_2 collide in a cusp bifurcation, a subcritical Hopf bifurcation H^+ appears, the SNIC disappears in favor of another saddle-node bifurcation SN_4, and a supercritical Hopf bifurcation H^- is created. Finally, increasing the value of c further (see Figure 8.2(c)), all saddle-node bifurcations have disappeared and a single branch remains with a supercritical H^- and subcritical H^+ Hopf bifurcation.

In Chapter 9 we will see that the bifurcation structure in the SH equation is

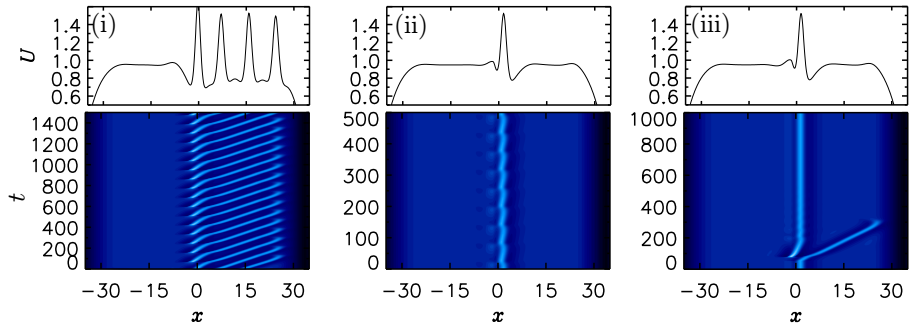

Figure 8.3: Different soliton regimes for $c = 0.1$ when considering absorbing boundary conditions. The panels (i)-(iii) depict the evolution and final profile of the absolute value of the field A inside the cavity. In panel (i), a periodic train of solitons is created at the inhomogeneity ($h = 0.3$). In panel (ii), a soliton is pinned at the inhomogeneity and locally oscillates with small amplitude ($h = 0.49$). In panel (iii) ($h = 0.51$), the system is excited by transiently ($\Delta t = 30$) changing the parameter values by $h \to h + \Delta h$, with $\Delta h = -0.3$.

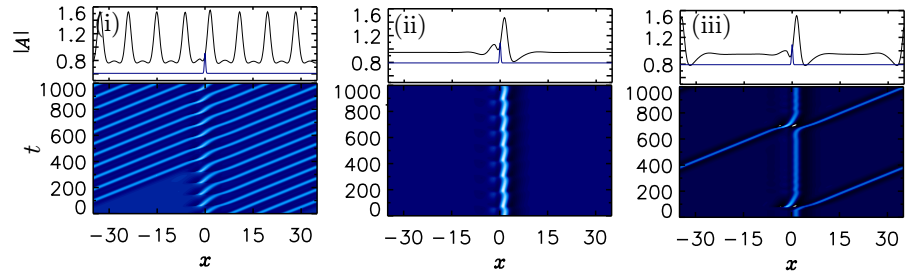

Figure 8.4: Different soliton regimes for the same parameter values than in Figure 8.3 when considering periodic boundary conditions. The regimes considered here are the same that those in Figure 8.3 for absorbing boundary conditions. In panel (i), a periodic train of solitons is created at the inhomogeneity. In panel (ii), a soliton is pinned at the inhomogeneity and locally oscillates with small amplitude. In panel (iii), the parametric excitation leads to the emission of a DSs form the defect location that continues to circulate in the cavity.

qualitatively equivalent to the one found here, showing the generality of this mechanism. In H^-, a stable limit cycle is created. This limit cycle initially corresponds to oscillations of small amplitude which remain localized at the defect position in the cavity (see Figure 8.3(ii) and Figure 8.4(ii)). When decreasing the strength of the inhomogeneity, these oscillations rapidly increase in amplitude in a so-called Canard explosion (CE) [22] and lead to the detachment of solitons from the defect. Those solitons then drift away and lead to a train of

solitons. These large-amplitude oscillations persist until a Fold of Cycles (FC) bifurcation where the stable limit cycle collides with an unstable limit cycle originating at H^+. At values of the defect strength h beyond the supercritical H^- bifurcation, the pinned DS is stable. However, the system can be excited to emit a DS from the defect location through direct perturbation of the DS profile or by transiently changing the parameter to the nearby oscillatory regime as shown in Figure 8.3(iii) for absorbing and Figure 8.4(iii) for periodic boundary conditions.

The periodic boundary conditions also have an important effect in the excitable regime encountered beyond H^-, shown in Figure 8.4(c). The excitation leads to one DS that remains pinned in the defect and another DS that drifts away from the defect. Due to the periodic boundary conditions of the system, this drifting DS eventually collides with the pinned DS from behind. This collision frees the pinned DS from the defect such that it drifts away, while the DS that was previously drifting now takes its place and remains pinned at the location of the defect. This type of dynamics reminds of the classic Newton's cradle.

8.3 Periodic versus absorbing boundary conditions

Comparing Figures 8.3 and 8.4, we see that although locally the dynamics is the same, the global system behavior with periodic boundary conditions differs from the case with absorbing boundaries.

To generate absorption in the boundaries we modify the pump normalized amplitude by $\rho \to \rho(x)$ with

$$\rho(x) = \rho \exp\left(-\frac{x - x_0}{\Lambda}\right)^{20}, \tag{8.3}$$

in such a way that, on the plateau $\rho(x) = \rho$, and at the boundaries $\rho(x)$ takes a value outside of the region of existence of DSs, and therefore DSs disappear. With these boundaries the dynamics are the same that those found in the context of the SH equation (see Chapter 9).

In contrast with the absorbing case, periodic boundary conditions lead to the recirculation of DSs in the domain and to interaction with the defect at the center of the domain and with the new DS emitted there. In particular, Figure 8.5 demonstrates that the large-amplitude oscillations ($h = 0.3$ and $c = 0.1$) are modified through this interaction. The temporal evolution of the field A at the defect position is plotted for both absorbing (black line) and periodic (red line) boundary conditions. In the case of absorbing boundary conditions, the period of the oscillations T_0 is essentially given by the Hopf frequency. The

spatial wavelength of the emitted train of solitons is therefore $\lambda_0 \simeq cT_0$. In Figure 8.5(a) one can see that the shape of the oscillations is slightly adjusted as soon as the first emitted DS reaches the defect after one roundtrip. In this case the period of the oscillations does not change considerably because the train of DSs (consisting of n peaks) emitted by the defect with a natural period T_0 has a wavelength λ_0 that is an almost exact submultiple of the cavity length $L_0 \approx n\lambda_0$. In general this will not be the case for arbitrary cavities. If the length of the cavity is $L \neq L_0$, and the same amount of peaks ($n = 9$) are emitted, then $L = n\lambda$, where now $\lambda = cT$ and therefore the period of emission of DSs from the defect is constrained by the length of the doamin i.e. $L \sim T$. This dependence can be observed in Figure 8.5(b), which compares the temporal evolution with absorbing and periodic boundary conditions for a domain size of $L \approx 85$ and with the same amount of peaks ($n = 9$) emitted. In this case, since a multiple of the natural wavelength no longer fits exactly within the cavity length, the period of the oscillations changes more considerably. Therefore, in the presence of periodic boundary conditions, and for the same number of peaks n, the period of oscillations T changes when varying the cavity length L and satisfies, together with the natural period $T_0 \sim L_0$, the relation

$$\frac{L}{L_0} \sim \frac{T}{T_0}. \tag{8.4}$$

From here one gets that if $L > L_0$ ($L < L_0$) then $T > T_0$ ($T < T_0$), so if the doamin size of the system increases (decreases) then the period T as well in order to accommodate the same amount of peaks in the modified domain. This analysis can be seen in Figure 8.6. The top panel shows the oscillation period T of the various solutions of train of solitons (A - H), while the natural period T_0 is indicated with a red solid line as reference. The bottom panel shows the amount of DSs within the train of solitons corresponding to the branches shown in the top panel. As the cavity becomes larger more solution branches coexist and the system allows for soliton trains with different amounts of DSs.

8.4 Dynamics and bifurcation structure for detunings $\theta > 2$

For high values of detuning the dynamics of DSs in the presence of spatial inhomogeneity and drift become much more complicate basically due to bistability between the bottom A_0^b and top A_0^t branches of the HSS, and due to the proximity to the instabilities leading to oscillatory and chaotic dynamics. On one hand, due to the bistability of the HSSs, convective instabilities involving these two states when $c \neq 0$ modify the scenario when considering the defect. On the other hand, for a value of ρ close to the Hopf threshold, the term $\tilde{\rho}$ defined

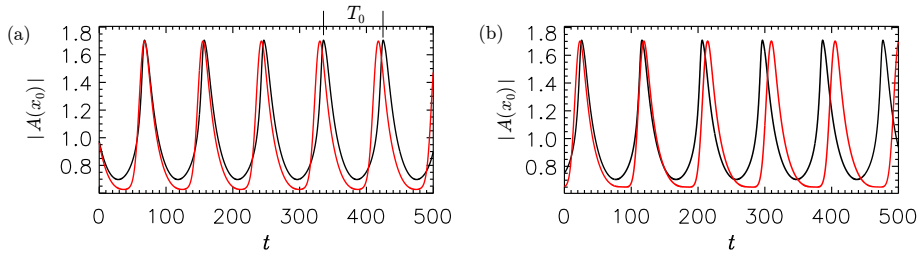

Figure 8.5: Temporal evolution of the field A at the defect position x_0 for two different boundary conditions: 1) absorbing boundary conditions (black solid line), 2) periodic boundary conditions (red dashed line). The train of solitons generated in the cavity corresponds to 9 peaks that circulate (branch H in Figure 8.6). In panel (a) the domain width $L = 78$, while in panel (b) $L = 84.8$. Here $h = 0.3$ and $c = 0.1$.

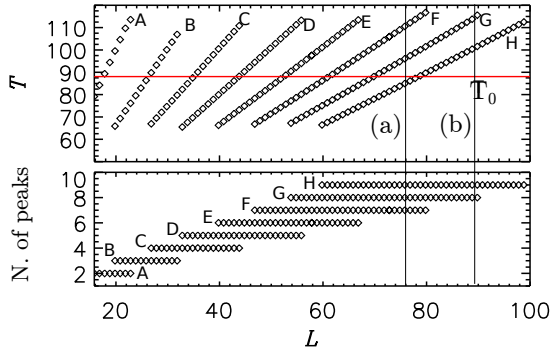

Figure 8.6: The top panel shows the oscillation period T of the various solutions of train of solitons (A - H) in the system with periodic boundary conditions. The natural period T_0 in the system with absorbing boundary conditions is plotted in dashed lines as reference. The bottom panel shows the amount of DSs within the train of solitons corresponding to the branches shown in the top panel. The labels (a)-(b) correspond to Figure 8.5(a)-(b).

by Eq.(8.1) modifies locally the value of ρ and therefore it is possible to induce locally i.e. in the neighborhood of x_0 localized oscillatory and chaotic dynamics.

Figure 8.7 illustrates how the dynamics can be altered for higher values of the frequency detuning. Here, we choose ($\theta = 3.8$, $\rho = 2.6$), values close to a Hopf instability of DSs in the LL equation without drift and defect. At such high values of θ the LL model (4.1), without defect and drift, has been shown to exhibit a wide range of oscillatory dynamics [4, 6, 23]. Trains of solitons still

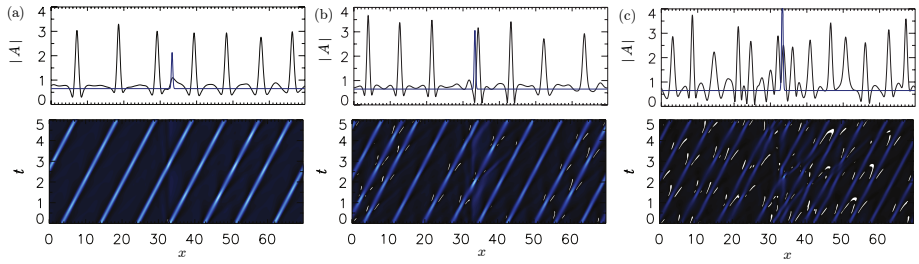

Figure 8.7: Evolution of a train of solitons for $h = 1.482$ in (a), $h = 2.682$ in (b) and $h = 5.682$ in (c). The panels depict the evolution (bottom) and final profile (top) of the absolute value of the field A inside the cavity. Other parameters are $\theta = 3.8$, $\rho = 2.6$, $c = 3$, $\sigma = 0.2727$ and $x_0 = L/2$.

exist and can originate from an oscillatory instability at the defect location that emits one DS at a time. Similar as in Figure 8.4(i), the DSs eventually fill up the whole domain and continue to circulate in the cavity. However, in contrast to the trains of stable solitons in the low detuning region (Figure 8.4(i), these solutions can now undergo a wide range of instabilities. In Figure 8.7(a) each DS within the train of solitons oscillates, but not necessarily with the same frequency. For higher values of the defect strength h, the trains of solitons start behaving more chaotically, see Figure 8.7(b)-(c). A detailed analysis of the origin and organization of these various instabilities at higher values of θ is beyond the scope of this work and will be investigated elsewhere.

8.5 Conclusions

In this chapter we have analyzed the effects that inhomogeneities or defects, and drift can have on DSs in the context of one-dimensional nonlinear optical cavities. We show how the competition between these two elements can lead to oscillations and excitability of solitons. This mechanism was first analyzed in Refs. [16, 17] using the Swift-Hohenberg equation and later in the LL model [24]. In both models it was found that a similar bifurcation scenario leads to the periodic emission of cavity solitons from locations in the cavity containing defects or imperfections.

Inhomogeneities and drift in optical cavities are unavoidable due to imperfections in the fabrication process, material properties and higher order chromatic light dispersion. Therefore, we believe that the type of dynamics studied in this work could be of considerable importance for all applications based on DS in nonlinear

optical cavities.

In Chapter 9 we will study this mechanism in detail in the prototypical Swift-Hohenberg equation. We will show that the bifurcation structure and and dynamics of solitons, in the presence of inhomogeneities and drift, are equivalent to those found here. This will confirm the generic nature of this dynamics and argue that the main ingredients for the generation of trains of solitons are a) inhomogeneities that can exert a pinning force on the soliton, b) a drift that gives rise to a pulling force on the soliton.

References

[1] P. B. Umbanhowar, F. Melo, and H. L. Swinney, *Localized excitations in a vertically vibrated granular layer,* Nature **382**, 793 (1996).

[2] W. J. Firth, A. Lord, and A. J. Scroggie, *Optical bullet holes,* Phys. Scr. T67, **12** (1996); W. J. Firth, G. K. Harkness, A. Lord, J. McSloy, D. Gomila, and P. Colet, *Dynamical properties of two-dimensional Kerr cavity solitons,* J. Opt. Soc. Am. B **19**, 747 (2002).

[3] V. K. Vanag and I. R. Epstein, *Localized patterns in reaction-diffusion systems,* Chaos **17**, 037110 (2007).

[4] F. Leo, L. Gelens, P. Emplit, M. Haelterman, and S. Coen, *Dynamics of one-dimensional Kerr cavity solitons*, Opt. Express **21**, 9180 (2013).

[5] D. Michaelis, U. Peschel, C. Etrich, and F. Lederer,*Quadratic cavity solitons the up-conversion case,* IEEE J. Quantum Electron. **39**, 255 (2003).

[6] P. Parra-Rivas, D. Gomila, M. A. Matias, S. Coen, and L. Gelens, *Dissipative soliton excitability induced by spatial inhomogeneities and drift,* Phys. Rev. A **89**, 043813 (2014).

[7] M. Santagiustina, P. Colet, M. S. Miguel, and D. Walgraef, *Walk-off and pattern selection in optical parametric oscillators,* Phys. Rev. Lett. **79**, 3633 (1997).

[8] E. Louvergneaux, C. Szwaj, G. Agez, P. Glorieux, and M. Taki, *Experimental evidence of absolute and convective instabilities in optics,* Phys. Rev. Lett. **92**, 043901 (2004).

[9] H. Ward, M. N. Ouarzazi, M. Taki, and P. Glorieux, *Transverse dynamics of optical parametric oscillators in presence of walk-off,* Eur. Phys. J. D **3**, 275 (1998)

[10] B. Schapers, T. Ackemann, and W. Lange, *Properties of feedback solitons in a single-mirror experiment,* IEEE J. Quantum Electron. **39**, 227 (2003).

[11] K. L. Babcock, G. Ahlers, and D. S. Cannell, *Noise-sustained Structure in Taylor-Couette Flow with Through-Flow,* Phys. Rev. Lett. **67**, 3388 (1991).

[12] B. von Haeften and G. Izús, *Noise-sustained structures in differential-flow reactors with autocatalytic kinetics,* Phys. Rev. E **67**, 056207 (2003).

[13] S. Coen, M. Tlidi, Ph. Emplit, and M. Haelterman, *Convection versus Dispersion in Optical Bistability,* Phys. Rev. Lett. **83** 12 (1999).

[14] M. Haelterman, S. Trillo, and S. Wabnitz, *Dissipative modulation instability in a nonlinear dispersive ring cavity*, Optics Communications **91**, 401-407 (1992).

[15] P. Parra-Rivas, D. Gomila, F. Leo, S. Coen and L. Gelens, *Third-order chromatic disper-*

sion stabilizes Kerr frequency combs, Opt. Lett. **39**, 2971-2974 (2014).

[16] P. Parra-Rivas, D. Gomila, M. A. Matías and P. Colet, *Dissipative soliton excitability induced by spatial inhomogeneities and drift,* Phys. Rev. Lett. **110**, 064103 (2013).

[17] P. Parra-Rivas, D. Gomila, M. A. Matías, P. Colet, and L. Gelens, *Competition between drift and spatial defects leads to oscillatory and excitable dynamics of dissipative solitons,* Phys. Rev. E. **93**, 012211 (2016).

[18] L. A. Lugiato and R. Lefever, *Spatial dissipative structures in passive optical systems,* Phys. Rev. Lett. **58,** 2209–2211 (1987).

[19] D. Gomila, A. J. Scroggie, and W. J. Firth, *Bifurcation structure of dissipative solitons,* Physica D 227, **70** (2007).

[20] E. Caboche, F. Pedaci, P. Genevet, S. Barland, M. Giudici, J. Tredicce, G. Tissoni, and L. A. Lugiato, *Microresonator defects as sources of drifting cavity solitons,* Phys. Rev. Lett. **102**, 163901 (2009); E. Caboche, S. Barland, M. Giudici, J. Tredicce, G. Tissoni, and L. A. Lugiato, *Cavity-soliton motion in the presence of device defects,* Phys. Rev. A **80**, 053814 (2009)

[21] A. Jacobo, D. Gomila, M.A. Matías, and P. Colet, *Effects of a localized beam on the dynamics of excitable cavity solitons,* Phys.Rev. A **78**, 053821 (2008)

[22] K. Bold, C. Edwards, J. Guckenheimer, S. Guharay, K. Hoffman, J. Hubbard, R. Oliva, and W. Weckesser, *The Forced van der Pol Equation II: Canards in the Reduced System* SIAM J. Appl. Dyn. Syst. **2**, 570 (2003).

[23] I.V. Barashenkov and Y. S. Smirnov, *Existence and stability chart for the ac-driven, damped nonlinear Schrodinger solitons,* Phys. Rev. E **54**, 5707 (1996).

[24] P. Parra-Rivas, D. Gomila, M. A. Matías, P. Colet, and L. Gelens, *Effects of inhomogeneities and drift on the dynamics of temporal solitons in fiber cavities and microresonators*, Optics Express **22**, 30943-30954 (2014).

Chapter 9

Dissipative soliton excitability induced by drift and defects

9.1 Introduction

In general, defects, or spatial inhomogeneities, are unavoidable in any experimental setup, and drift is also often present in many optical, fluid and chemical systems. In Chapter 8 we have analyzed the influence of these two elements on the dynamics of DSs in drinven nonlinear optical cavities described by the LL equation. There we have shown that the competition between both elements can lead to the generation of a very rich DS dynamics, going from oscillatory to excitable dynamics [1].

The effects of drift and defects on the DS dynamics in optical cavities was firstly studied experimentaly and numerically for the case of an injected broad area semiconductor laser (VCSEL) [2, 3]. In that type of system the defect was modeled in the cavity detuning parameter, accounting for spatial inhomogeneities introduced during the growth process of the device. Despite of the theoretical work, a complete description in terms of bifurcations was absent.

In this chapter we provaid a detailed description based on a bifurcation analysis of the dynamics of DSs induced by the presence of defects and drift in the real one-dimensional Swift-Hohenberg (SH) equation showing the generality of this mechanism [6, 7]. Contrary to the SH equation for a complex field which shows a rich variety of dynamical behaviors as shown in [8, 9], the SH equation for a real field can be considered as a prototypical system that does not exhibit any time-

oscillatory dynamics. As we will see, the competition between the two previous ingredients introduces an oscillatory instability, which can lead to a regime in which DSs are pulled one by one from the defect (referred to as a train of DSs), and to an excitable regime in which the DSs stay pinned in the defect but can be pulled out by a transient perturbation to the system. Here, as in Ref. [4], excitability is an emergent property of the DSs that has its origins in the spatial coupling. Hence, this type of excitability is different to the one arising as a local property, such as in neural models [5].

The chapter is organized as follows. In Section 9.2, we will first introduce the SH equation for a real field, a generic amplitude equation describing pattern formation in a large variety of systems [10, 11]. We then introduce additional terms in the SH equation such that it accounts for both drift and spatial inhomogeneities. Next, we proceed to analyze the individual and combined effects of drift and defects by exploring bifurcation diagrams as function of the strength of the drift and the size of the defect (Section 9.3). This analysis will reveal various regions of dynamical behavior, where we will highlight the distinctive properties of oscillatory (Section 9.4) and excitable (Section 9.5) DS dynamics. These dynamics are then shown to unfold from two Takens-Bogdanov (TB) [12–15] co-dimension two bifurcation points in Section 9.6. In Section 9.7, we discuss the generality of this drift-defect mechanism, (i) by considering a different parameter region of the SH equation and (ii) by assuming the spatial inhomogeneity is in the gain of the SH equation. Finally, we end by discussing the general aspects of the work and its particular relevance in optics (Section 9.9).

9.2 The Swift-Hohenberg equation

The SH equation for a real field u in one spatial dimension x can be written as follows,

$$\partial_t u = -\left(\partial_x^2 + k_0^2\right)^2 u + ru + au^2 - gu^3 \ , \tag{9.1}$$

with $g > 0$ to avoid divergences. Of particular interest for our purposes is that the SH equation is variational (for periodic boundary conditions), or in other words the dynamics follows a gradient [16]. This implies that the rhs of Eq.(9.1) can be written as the (functional) derivative of a certain functional, namely

$$\frac{\partial u}{\partial t} = \frac{\delta \mathcal{F}}{\delta u}, \tag{9.2}$$

with

$$\mathcal{F} = \int_0^L dx \left(-\frac{1}{2} r u^2 + \frac{1}{2} \left(\left(\partial_x^2 + k_0^2\right) u \right)^2 - \frac{1}{3} a u^3 + \frac{1}{4} g u^4 \right). \tag{9.3}$$

The dynamics in the SH equation are such that $\mathcal{F}$ decreases in time until it reaches a local minimum, i.e. a steady state that minimizes $\mathcal{F}$. As a consequence, the SH equation cannot exhibit dynamical regimes different from stationary states (i.e. this excludes oscillations and chaos). The simplicity and lack of any oscillatory dynamics will allow us to clearly identify how drift and defect terms adjust the dynamical behavior of DSs.

9.2.1 Linear stability analysis of the homogeneous steady state

The HSS solutions of the SH equation are,

$$u_s = 0, \tag{9.4}$$

$$u_s = \frac{1}{2g}\left(a \pm \sqrt{a^2 + 4g(r - k_0^4)}\right). \tag{9.5}$$

The linear stability of the HSSs in response to finite wavelength perturbations,

$$u(x,t) = u_s + \epsilon \exp(\Omega t + ikx) \ , \tag{9.6}$$

is determined by the dispersion relation

$$\Omega(k) = r + 2au_s - 3gu_s^2 - (k_0^2 - k^2)^2 \ . \tag{9.7}$$

The HSSs undergo a generalized Turing (or modulational) instability [10, 11] as a function of r if $\Omega(k)|_{k=k_c} = \frac{d\Omega}{dk}|_{k=k_c} = 0$ for a given critical value $k = k_c$. In other words, the HSS is Turing unstable when $\Omega(k)$ develops a maximum for some $k = k_c$ and this maximum is exactly zero. The trivial solution $u = 0$ becomes Turing unstable first at $r = 0$ for perturbations with critical wavenumber $k_c = \pm k_0$. At $r = k_0^4$ this trivial state is also unstable to uniform perturbations (perturbations with critical wavenumber $k_c = 0$). When $a > \sqrt{27/38}g$ (see Ref.[17]) a spatially periodic solution emerges subcritically from the Turing instability at $r = 0$. Unless mentioned otherwise, we will consider $g = 1$, $a = 1.2$ and $k_0^2 = 0.5$ throughout this work, ensuring the presence of a subcritical pattern.

9.2.2 Localized dissipative structures

Together with pattern solutions, different types of localized dissipative structures (LSs) can also arise in this system. Any stationary state of the system is solution of the stationary SH equation

$$-\left(\frac{d^2}{dx^2} + k_0^2\right)^2 u + ru + au^2 - gu^3 = 0, \tag{9.8}$$

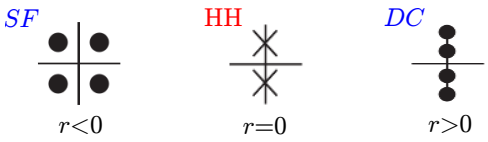

Figure 9.1: Configuration of the spatial eigenvalues (9.11). For $r < 0$, $u_s = 0$ is a SF, at $r = 0$, $u_s = 0$ undergoes a HH bifurcation, and for $r > 0$, $u_s = 0$ is a DC resonance.

that can be written using the variables $u_0 = u$, $u_1 = d_x u$, $u_2 = d_x^2 u$ and $u_3 = d_x^3 u$, as a four order reversible system

$$\begin{aligned} d_x u_0 &= u_1 \\ d_x u_1 &= u_2 \\ d_x u_2 &= u_3 \\ d_x u_3 &= (r - k_0^4) + a u_0^2 - g u_0^3 - 2k_0^2 u_2 \end{aligned} \tag{9.9}$$

In Chapter 2 we showed that LSs are in this framework, homoclinic orbits to the HSSs. In particular here we will focus on the LSs that are biasymptotic to the $u = 0$. As shown in Chapter 2, the origin and existence of these homoclinic orbits can be determined by the spatial eigenvalues of the Jacobian of system (9.9) i.e. the solutions of the characteristic polynomial

$$\lambda^2 + 2k_0^2\lambda^2 + r - k_0^4 = 0. \tag{9.10}$$

It is easy to check that the spatial eigenvalues are given by,

$$\lambda = \begin{cases} \pm ik_0 \pm \sqrt{-r}/2k_0 + \mathcal{O}(r) & \text{if } r < 0 \\ \pm ik_0 + \mathcal{O}(r) & \text{if } r = 0 \\ \pm ik_0 \pm i\sqrt{r}/2k_0 + \mathcal{O}(r) & \text{if } r > 0. \end{cases} \tag{9.11}$$

Figure 9.1 shows the different configuations of these eigenvalues as a function of r. For $r < 0$, the eigenvalues form a complex quartet and $u_s = 0$ has two stable and two unstable manifolds and therefore, homoclinic orbits to the HSS can exist. In contrast, for $r > 0$, all the eigenvalues lie on the imaginary axis and as a result no exponentially LSs can exist. At $r = 0$, the system has a HH or a Hopf bifurcation in a reversible system with 1:1 resonance, i.e. there is a pair of imaginary eigenvalues with double multiplicity, from where LSs unfold. In Ref.[17] the authors calculate using weakly nonlinear analysis a first order approximation for the pattern and LSs unfolding from the HH point at $r = 0$. With this analysis they found that, in the neigbourhood of the HH bifurcation,

the pattern can be described by

$$u(x) = 2\sqrt{\frac{-r}{\gamma_3}}\cos(k_c x + \varphi) + \mathcal{O}(r) \tag{9.12}$$

and LSs by

$$u(x) = 2\sqrt{\frac{-r}{\gamma_3}}\operatorname{sech}\left(\frac{x\sqrt{-r}}{2k_c}\right)\cos(k_c x + \varphi) + \mathcal{O}(r), \tag{9.13}$$

where $\gamma_3 = \frac{38a^2}{9k_c^4} - 3g$. Although φ at first order is arbitrary, there are only two values preserving the reversibility, namely $\varphi = 0$ and $\varphi = \pi$. These two values define two sets of LSs, one with an even number of peaks and one with an odd number of peaks. Using continuation techniques it is possible to continue these states to parameter values far from HH. In this way it is possible to calculate for each of the LSs given by (9.13) their homoclinic snaking bifurcation diagrams Refs.[17–20]. For the parameter values chosen here the homoclinic snaking corresponding to LSs with an odd number of peaks is shown in Figure 9.2. The solutions are plotted in the L_2-norm,

$$||u||^2 \equiv \int_0^L u(x)^2 dx \tag{9.14}$$

The different branches corresponding to LS solutions oscillate back and forth around the Maxwell point (the location where the Lyapunov functional $\mathcal{F}$ is equal for the subcritical pattern and the trivial solution), explaining the term *snaking structure*. The solid lines represent the stable solutions and the dashed lines the unstable ones. After crossing each saddle-node bifurcation at the right hand side of the diagram the LSs add a pair of peaks symmetrically at both sides of the existing peaks. Some examples of such LS solutions are shown in the insets. In the next Sections, we will simplify our analysis by fixing the value of the control parameter r to -0.2 and by focusing on the dynamical properties of a LS consisting of a single peak.

9.3 Overview of the drift-defect induced dynamics in the Swift-Hohenberg equation

In this paper a drift is modeled in the SH equation by introducing a gradient term

$$c\partial_x u, \tag{9.15}$$

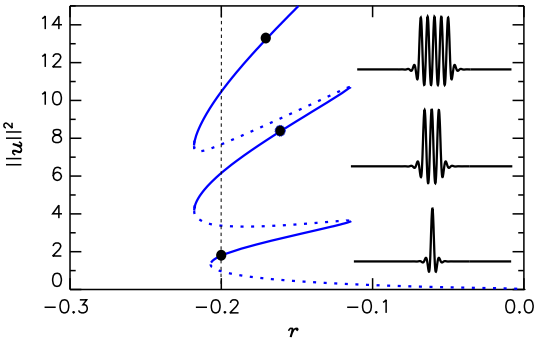

Figure 9.2: Homoclinic snaking for $k_0^2 = 0.5$, $a = 1.2$ and $g = 1$. The solid (dashed) lines represent stable (unstable) LSs. The vertical dashed line shows the value of r chosen in the analysis in Section III. The insets show the spatial profile of the LSs with an odd number of peaks, corresponding to the solid black circle on each stable branch.

with c the group velocity. The spatial defect is defined by a single Gaussian profile $b(x)$ of height h and half-width σ that is located in the center x_0 of a system with domain width L ($x_0 = L/2$):

$$b(x) = h \exp\left(-\left(\frac{x - x_0}{\sigma}\right)^2\right). \tag{9.16}$$

In the context of optical cavities this defect can be seen as a injected beam into the cavity as already described in Ref. [21].

The SH equation modified to include drift and defect thus reads:

$$\partial_t u = \tilde{r}(x)u + au^2 - gu^3 - \left(\partial_x^2 + k_0^2\right)^2 u - c\partial_x u + b(x). \tag{9.17}$$

To avoid drifting DSs from re-entering the domain on the opposite side, we use a super-Gaussian gain profile $r(x)$,

$$\tilde{r}(x) = r - 1 + \exp\left(-\left(\frac{x - x_0}{\Lambda}\right)^{18}\right). \tag{9.18}$$

in such a way that, on top of the plateau $\tilde{r}(x) = r$, and at the boundaries $\tilde{r}(x)$ takes a value outside of the prinning region, where LSs do not exist. In this way the system has an effective width 2Λ, and all drifting DSs disappear at the boundaries. Unless mentioned otherwise, we choose $\sigma = 2.045$ (roughly half the width of a DS), $\Lambda = 94.0842$ and $r = -0.2$.

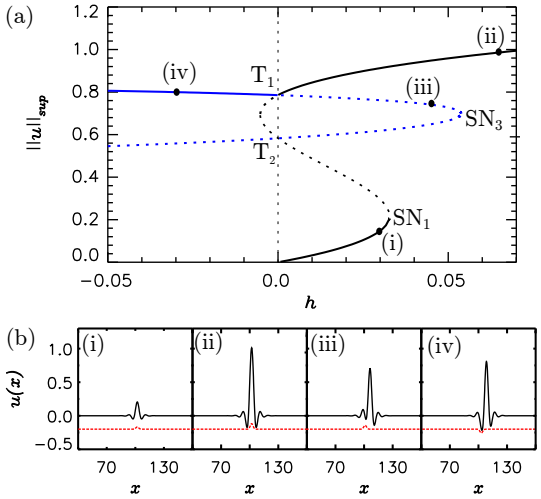

Figure 9.3: (a) Bifurcation diagram (maximum $||u||_{sup}$) as a function of the strength of the spatial defect h for $c = 0$. (b) Examples of the steady state solutions (black solid lines) corresponding to the labeled branches, together with the profiles of the spatial defect (red dashed lines displaced for clarity to negative values). SN_1 and SN_3 represent saddle-node bifurcations and T_1 and T_2 transcritical bifurcations.

9.3.1 Dissipative solitons in the presence of drift

For periodic boundary conditions, in the presence of drift, but without defects ($h = 0, c \neq 0$), spatial reversibility under the transformation $(u, x, t) \to (u, -x, t)$ is broken and the system can display convective instabilities. The solutions of Eq. (9.17) are steadily drifting states [22]. By introducing a change of variables $(x, t) \to (x - ct, t)$ this drift can be removed and the system can be studied in a reference frame moving at velocity c. In that frame the solutions can be only stationary and the system dynamics is still variational.

9.3.2 Dissipative solitons in the presence of a defect

In the presence of defects, but without drift ($c = 0$, $h \neq 0$), Eq.(9.17) is still variational with a Lyapunov functional given by,

$$\mathcal{F}_h = \mathcal{F} + \int_0^L b(x)u(x)dx, \tag{9.19}$$

and, as before, only steady state solutions of Eq. (9.17) exist.

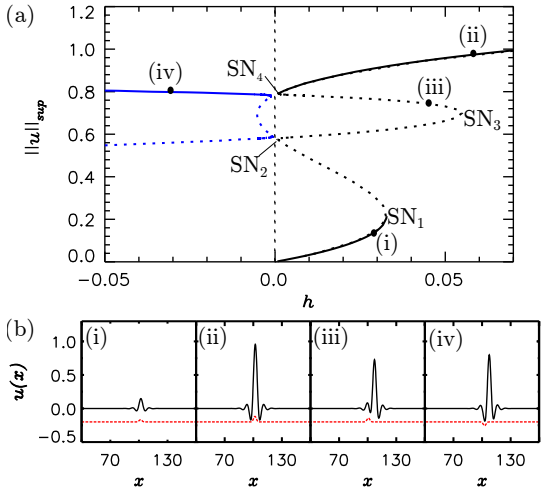

Figure 9.4: (a) Bifurcation diagram (maximum $||u||_{sup}$) as a function of the strength of the spatial defect h for $c = 0.0015$. (b) Examples of the steady state solutions (black solid lines) corresponding to the labeled branches, together with the profiles of the spatial defect (red dashed lines displaced for clarity to negative values).

One of the main consequences of the defect term is the breaking the invariance of Eq. (9.1) under the translational transformation $x \mapsto x + a$, with $a \in \mathbb{R}$. The steady state solutions are now pinned at the location of the spatial defect. We can gain a better understanding of the effects of such spatial inhomogeneities by looking at the bifurcation diagram showed in Figure 9.3, generated for periodic boundary conditions. In this diagram we plot $||u||_{sup} := max\,(u(x))$ as a function of the control parameter h. $||u||_{sup}$ is chosen here instead of the L_2-norm because it allows all different branches to be more clearly visible in this case. Each branch corresponds to a different type of solution. Examples of each type of solution are shown in the bottom panels.

The stability of the LSs $u_s(x)$ is determined by solving the eigenvalue problem

$$L[u_s(x)]\psi \equiv \left(r - (\partial_x^2 + k_0^2)^2 - c\partial_x + 2au_s - 3gu_s^2\right)\psi = \lambda\psi, \tag{9.20}$$

for the eigenvalues λ and the corresponding eigenmodes ψ, as discussed in Section 1.6. The stable steady state solutions (i), (ii) and (iv) are the main attractors of the system. Solution (i) corresponds to the fundamental solution, a small deformation of the trivial solution. Solutions (ii) and (iv) correspond to a large amplitude DS pinned at its center or at the first oscillation of its tail,

respectively. Finally, solution (iii) also represents a large amplitude DS pinned at the first minimum of its oscillatory tail, but this position is unstable.

Due to the breaking of the translational symmetry, a transcritical bifurcations T_1 and T_2 [16] take places at $h = 0$. At T_1 branch (ii) becomes unstable, while branch (iii)-(iv) is stabilized. Physically, at $h = 0$ the defect goes from being a bump to a hole. DSs tend to sit at the maximum of any inhomogeneity, such that DSs centered at the hole become unstable and shift their position until the hole coincides with the first minimum of its tail. Branch (iii) corresponds to pinned DSs whose maximum is at the right of the defect.

Here we must point out that although Eq. 9.17 with $c = 0$ is reversible in x, asymmetric solutions like (iii) and (iv) arise together with two other states with the maximum at the left side of the defect, which are degenerate in $||u||_{sup}$. One of these states is pinned at the first maximum on the right, while the other at the first minima. As it will be discussed in the next section, this degeneracy is broken by the drift. In the following, we will just focus on the DSs whose maxima are located downstream of the defect, since this branch will reconnect to branch (ii) in the presence of drift.

9.3.3 Dynamics and bifurcation structure in the presence of drift and defect

When considering the joint effect of drift and defect, it is no longer possible to describe the system in a moving reference frame and the system no longer follows gradient dynamics minimizing a functional. As a result, steady state solutions can undergo instabilities leading to time oscillatory dynamics. As previously mentioned, in the presence of only drift ($h = 0$, $c \neq 0$), solutions move with a constant velocity. By also introducing a spatial inhomogeneity ($h \neq 0$, $c \neq 0$), the drift can be compensated for if the pinning force due to the defect is stronger than the drift force trying to pull it out. As we will show below, this competition between pinning (defect) and depinning (drift) can give rise to a wide range of dynamical instabilities.

In Figure 9.4(a) we show how the bifurcation diagram of Figure 9.3 is modified when introducing a small drift ($c = 0.0015$). Even a small drift is enough to break the spatial symmetry and leads to the appearance of a pair of imperfect transcritical bifurcations that split the solution branches at $h = 0$. A saddle-node bifurcation SN_4 now connects branch (ii) (stable large amplitude DS) to branch (iii) (unstable large amplitude DSs pinned at the first tail oscillation). Likewise, the branch (iv) (stable large amplitude DSs pinned at the first tail

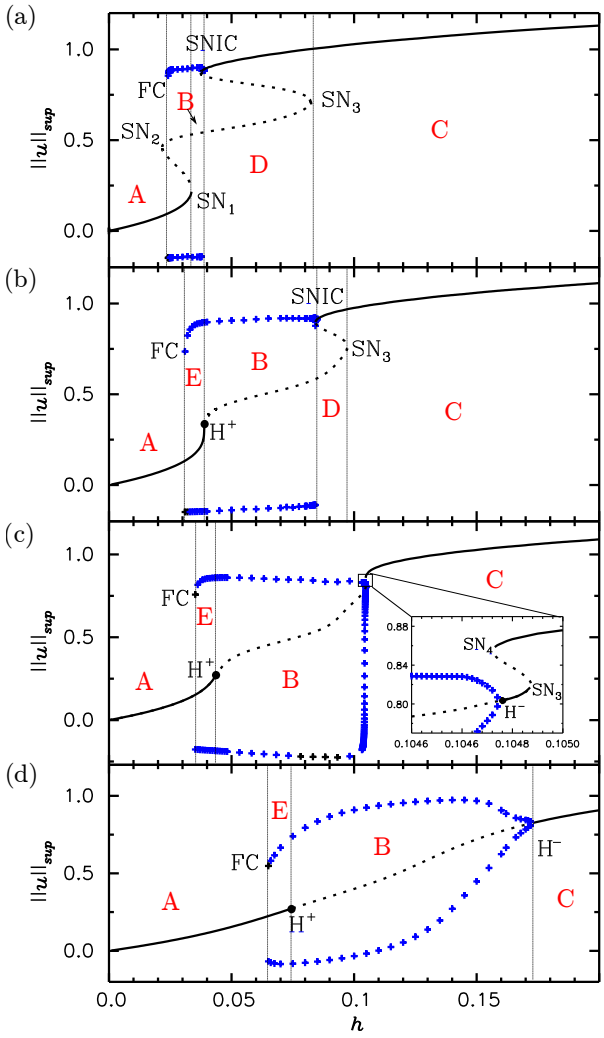

Figure 9.5: Bifurcation diagram (maximum $||u||_{sup}$) as a function of the strength of the spatial defect h for (a) $c = 0.05$, (b) $c = 0.12$, (c) $c = 0.162$, and (d) $c = 0.4$. Crosses indicate the extrema (maxima and minima) of the DS oscillatory amplitude. The main dynamical regions A - E are labeled in red.

oscillation) connects to the unstable middle branch DS, which previously (for $c = 0$) connected branch (i) and (ii). A new saddle-node bifurcation SN_2 arises

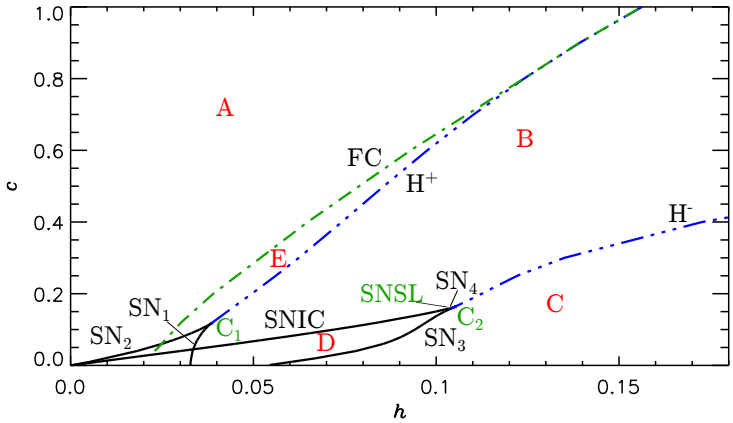

Figure 9.6: Two-parameter (c vs. h) phase diagram of the system for $a = 1.2$ and $r = -0.2$. The bifurcation lines and regions A-E are explained in the main text.

from the middle branch, while the saddle-node bifurcations SN_1 and SN_3 were already present for $c = 0$. Examples of the different profiles in the presence of a defect and small drift are shown in Figure 9.4(b). In what follows, we will focus on the region in parameter space where $h > 0$.

Figure 9.5 shows how this bifurcation structure (for $h > 0$) is modified as the drift speed c is gradually increased. Figure 9.5(a) shows the single snake-like branch for a weak breaking of the reflection symmetry ($c = 0.05$). The crosses indicate the extrema of oscillations in the amplitude of the DS at the central defect location. These oscillations originate at the saddle-node on the invariant circle (SNIC) and terminate at a fold of cycles (FC) bifurcation, which will be discussed in more detailed later. As one can observe in the two parameter (c,h) phase diagram shown in Figure 9.6 the SNIC bifurcation emanates from a codimension-two point together with the FC and the SN_4 found for lower values of c (see Figure 9.3). For increasing values of c the branches stretch (Figure 9.5(b)) and SN_1 coalesces with SN_2 in a codimension-two point known as a hysteresis or cusp bifurcation that we denote as C_1, which takes place at $(c_{C_1}, h_{C_1}) = (0.11772, 0.038529)$. For values of c just below c_{C_1}, a Hopf bifurcation appears subcritically (Figure 9.5(b)) . We denote this subcritical bifurcation as H^+, where the label + points to the subcriticallity of the bifurcation.

As c is increased further, the SNIC turns into a saddle-node bifurcation SN_4 through another codimension-two point, referred to as a saddle-node separatrix-loop (SNSL) bifurcation [14, 15]. At $(c_{C_2}, h_{C_2}) = (0.1642, 0.105467)$, SN_4 and

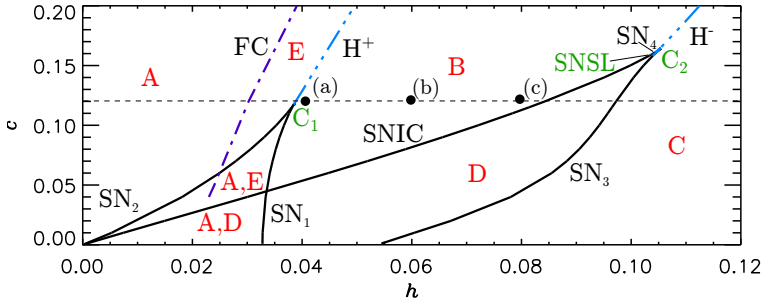

Figure 9.7: Zoom of the two-parameter phase diagram shown in Figure 9.6, such that the overlap between regions A and D, as well as A and E is visible. Labels (a)-(c) correspond to the spatio-temporal evolutions shown in Figure 9.8. Here $a = 1.2$ and $r = -0.2$.

SN_3 coalesce in another cusp bifurcation that now we label as C_2, see Figure 9.6. In Figure 9.5(c) we show the bifurcation structure changing h or c just below c_{C_2}. In the inset one can see that another Hopf bifurcation H^- has also appeared. In this case, the Hopf is supercritical (hence the symbol $-$).

Finally, for larger values of c, there is a single monotonic branch of steady state solutions (Figure 9.5(d)). From the supercritical Hopf H^- a stable limit cycle appears, which persists until FC, where it folds back to end at H^+.

Overall the phase diagram shown in Figure 9.6 has five main dynamical regions, which are labeled A - E in Figs. 9.5 - 9.7:

- Region A: The fundamental solution is stable. The system can display Type II excitability for parameters close to the FC line (see more details in Section 9.5).
- Region B: DSs oscillate periodically in time (see more details in Section 9.4).
- Region C: Stable large amplitude DSs pinned at the defect exist, while Type II excitability occurs for parameters close to the H^- line (see more details in Section 9.5).
- Region D: Stable large amplitude DSs pinned at the defect exist, while the system can also admit Type I excitability (see more details in Section 9.5).
- Region E: The fundamental solution and oscillatory DSs coexist.

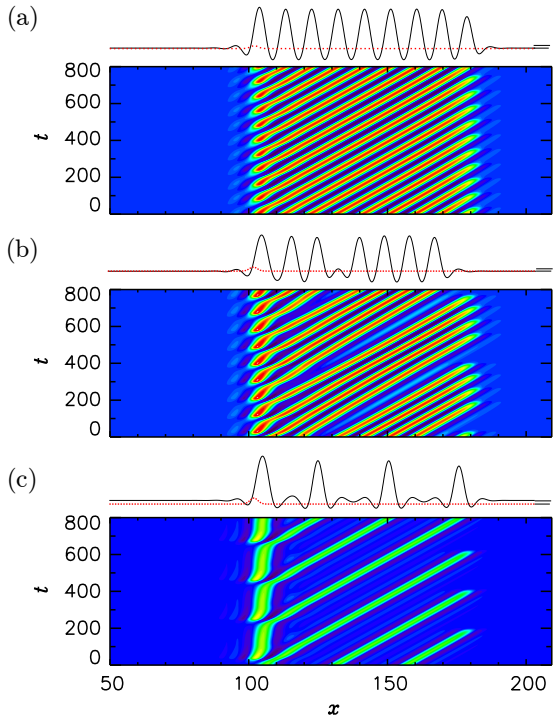

Figure 9.8: Contour plots of $u(x,t)$ showing the spatio-temporal evolution of a train of DSs for $h = 0.04$ (a), $h = 0.06$ (b), and $h = 0.08$ (c), for $c = 0.12$ and $L = 209$. Above the contour plots the spatial profile $u(x, t = 800)$ is plotted.

Figure 9.7 shows a zoom of the two-parameter phase diagram shown in Figure 9.6. The zoom allows to better observe the overlap that exists between regions A and D (bounded by the SNIC and SN_1), and between regions A and E (bounded by SN_1 and SN_2). In the next Sections, we will discuss in more detail the properties of the oscillatory (Section 9.4) and excitable (Section 9.5) dynamical regions, and we will show how the different bifurcations unfold from two Takens-Bogdanov co-dimension-two points (Section 9.6).

9.4 Oscillatory dynamics

In region B static solutions are unstable. This instability leads to DSs that remain pinned at the defect, but whose amplitude oscillates periodically in time.

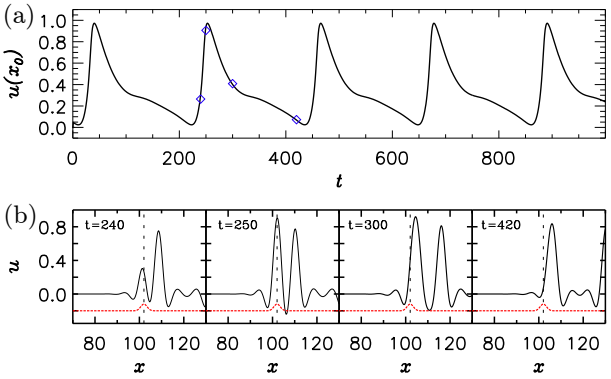

Figure 9.9: (a) Time evolution of the magnitude $u(x_0)$ at the center of the domain ($x_0 = L/2$) for a train of DSs. $h = 0.08$, $c = 0.12$, and $L = 209$. (b) Snapshots of the spatial profile $u(x,t)$ at different times (as indicated in individual panels and corresponding to the blue diamonds in panel (a)), illustrating the growth and depinning of a DS from the spatial defect. The defect is shown in a red dashed line displaced for clarity to negative values.

In Figure 9.5, crosses indicate the maximum and minimum amplitude of the oscillatory DS at the defect position. In Figure 9.5(b), where $c = 0.12$, stable oscillations originate from the SNIC and disappear at the FC. For $c = 0.12$ and $h = 0.04$, Figure 9.8(a) shows how the time-periodic oscillations of the pinned DS affect the spatial dynamics in the whole domain. The oscillations correspond to the periodic creation of a DS at the defect that then drifts away, thus generating a train of DSs originating from the defect. These drifting DSs disappear at the boundary of the domain due to the absorbing boundary conditions that are used, i.e. the super-Gaussian gain coefficient $r(x)$ given by (9.18). For all numerical simulations involving drifting structures we have used such absorbing boundary conditions, while periodic boundary conditions have been used to determine the bifurcation diagrams. Since the absorbing boundaries are located far away, close to the pinning defect the profile of the localized solutions is very similar for both boundary conditions. Furthermore, the instabilities of these localized solutions are associated to modes whose spatial profiles are also localized, and are thus practically independent of the boundary conditions. As a consequence the observed instabilities are the same for both kinds of boundary conditions.

When increasing h further ($h = 0.06$), the oscillations start showing a second time scale (Figure 9.8(b)), which becomes more pronounced for even large $h = 0.08$ (Figure 9.8(c)). Such oscillations with two time scales are characteristic of systems displaying relaxation oscillations, as for instance described by the Van

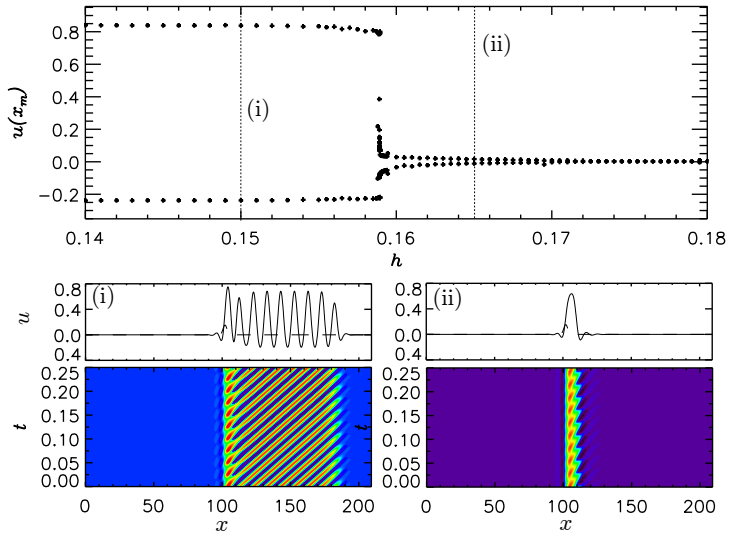

Figure 9.10: Canard explosion illustrated by plotting the maxima and minima of an oscillating DS, evaluated at $u(x = x_m)$ as function of h, for $x_m \approx 123$ and $c = 0.4$. Contour plots of $u(x, t)$ showing the spatio-temporal evolution of a train of DSs for $h = 0.136$ (i), and a small amplitude oscillation for $h = 0.164$ (ii). $c = 0.12$ and $L = 209$. Above the contour plots the spatial profile $u(x, t = 0.25)$ is plotted.

der Pol equation [14]. Figure 9.9(a) shows in more detail the time evolution of the amplitude of the DS in the center of the domain $x_0 = L/2$, confirming the presence of a fast and slow time scale. The fast time scale corresponds to the nucleation process in which a DS is created at the inhomogeneity, while the slow one is the time it takes to detach a DS once it is formed due to the drift. The time to nucleate a DS is basically independent of the drift strength, while the escape time strongly depends on it. Figure 9.9(b) shows snapshots of the full spatial profile during one period of such an oscillation.

For larger values of c, two types of oscillations are observed (see Figure 9.5(d) for $c = 0.4$). First, for $h < 0.158$, the regular train of solitons is found as shown in Figure 9.10(i). Second, for larger values of h, close to the supercritical Hopf bifurcation H^-, the strength of the defect is large enough to prevent the advection of the DS, but nevertheless the competition between drift and pinning at the defect induces small amplitude oscillations of the DS (see Figure 9.10(ii)). The transition between both types of oscillatory regimes occurs very suddenly through what it is called a canard explosion. One refers to a canard explosion

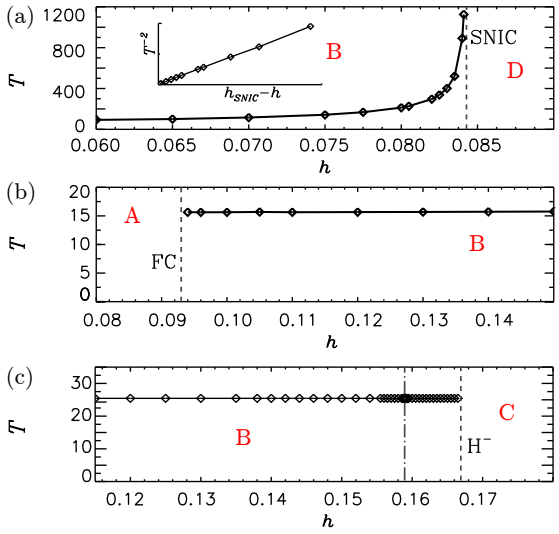

Figure 9.11: Scaling of the oscillation period T in function of h for type I (a), and Type II (b,c) excitability. (a) $c = 0.12$, (b) $c = 0.6$, (c) $c = 0.4$.

whenever varying a parameter (here h) leads to a very fast transition from small amplitude limit cycles to large amplitude relaxation oscillation cycles. This very fast transition happens within a small range of the control parameter. In Figure 9.10 the extrema of $u(x_m)$ are plotted, where $x_m \approx 123$ was chosen to be in the tail of the DS such that one can clearly differentiate between the small oscillations of the DS and the train of DSs. The canard explosion occurs for $h \approx 0.158$ close to H^-. This limit cycle corresponding to the train of DSs originating at the canard location remains stable all the way to a fold of cycle (FC) bifurcation, where it becomes unstable and disappears in H^+.

In the next Section, we will show that close to these oscillatory regions, there also exist different types of excitability of DSs.

9.5 Dissipative soliton excitability

A system is said to be excitable if perturbations below a certain threshold decay exponentially, while perturbations above this threshold induce a large response before going back to the resting state. Having a threshold is thus one of the basic ingredients in order to have excitability. A second ingredient is a reinjection

mechanism in the phase space that forces the system to go back to the resting state. Here, that reinjection mechanism corresponds to the combination of drift and absorbing boundary conditions such that any DS is eventually removed from the domain. The time scale separation present in the relaxation oscillations (train of DSs) is a strong indication of excitability: the fast time scale is related with the triggering of the perturbation, and the slow time scale is related with the time required for the system to go back to the resting state (see Figure 9.10).

In the literature it is common to find a classification for excitability that is based on whether or not there is a divergence of the period of the limit cycle involved in the dynamics [5]. Excitability is defined to be of Type I if the period diverges close to the bifurcations involved in the creation or destruction of the limit cycle, while it is of Type II if the period does not diverge and remains almost constant when approaching the bifurcation. Before discussing our system in more detail, we will briefly discuss these two types of excitability.

Type I excitability is related with two specific bifurcations, a saddle-loop (SL) bifurcation (also referred to as a homoclinic bifurcation) [16], or a SNIC bifurcation. In both bifurcations, the stable manifold of a saddle point plays the role of a separatrix in phase space, so that only perturbations bringing the system beyond this threshold trigger an excitable excursion [23]. A clear signature of this excitability is the divergence of the period of the oscillations that appear or disappear with each bifurcation. As we mentioned before, in a SNIC, a saddle-node bifurcation occurs inside a limit cycle. Before the SNIC, stable manifolds of the saddle and node states transverse to the center manifold are organized by an unstable focus inside a limit cycle. At one side of the bifurcation the system exhibits oscillatory behavior, while at the other side the dynamics of the system is excitable. Although this bifurcation is local in (one dimensional) flows on the circle, it has global characteristics in higher dimensional dynamical systems, so it is also termed as a local-global bifurcation. The best way of characterizing the presence of that bifurcation is analyzing how the period of the cycle behaves close to it. For the SNIC it is know that the period of the cycle diverges as one approaches the bifurcation (see Figure 9.11(a)), following the power law

$$T \propto (h - h_{\mathrm{SNIC}})^{-1/2}. \tag{9.21}$$

Another kind of Type I excitability is mediated by a SL bifurcation [4] in which a stable limit cycle collides with a saddle and disappears. Here, the unstable manifold of the saddle plays the role of sepatatrix in phase space. In this case the period diverges logarithmically when approaching the bifurcation,

$$T \propto \ln(h - h_{\mathrm{SL}}). \tag{9.22}$$

One of the main differences between those two mechanisms of Type I excitability is that the SNIC, due to the square-root scaling law, occurs over a broader parameter range.

Type II excitability is related with the presence of a subcritical Hopf bifurcation H^+ or a supercritical Hopf H^- bifurcation with a canard explosion. In this case there is no saddle involved, and, as a consequence, there is no separatrix in phase space. For this reason the threshold is not very well defined and one refers to a quasithreshold [5]. In Type II excitability the period of the oscillations remains practically constant as one approaches the point where such oscillations are created or destroyed (see Figure 9.11(b)-(c)).

In this work, excitability can be found in regions A, C, and D in Figure 9.6. In order to induce an excitable excursion, we use a suitable transient parameter change instead of perturbing the state of the system [23]. The transient parameter change should bring the system into the oscillatory region B. It should be long enough so that the system starts to oscillate following the periodic limit cycle, but shorter than the period of the limit cycle. Proceeding in this way a pulse can be excited before returning to the resting state. Here, we will use perturbations in h modifying the defect strength for a short time. We redefine the profile $b(x,t)$ as follows to incorporate this transient perturbation:

$$b(x,t) = (h + \Delta h H(t,t_0,t_1))\exp\left(-\left(\frac{x-x_0}{\sigma}\right)^2\right), \tag{9.23}$$

with the step function $H(t,t_0,t_1)$ defined as,

$$H(t,t_0,t_1) = \begin{cases} 0, & \text{if } t < t_0 \\ 1, & \text{if } t_0 < t < t_1 \\ 0, & \text{if } t > t_1 \end{cases} \tag{9.24}$$

Here, without loss of generality, we have chosen t_0 as the time at which the perturbation starts and $\Delta t = t_1 - t_0$ (with $t_1 > t_0$) as the duration of the perturbation.

9.5.1 Type I excitability (SNIC): region D

In our system, Type I excitability mediated by the SNIC bifurcation can be found in region D, close to the SNIC line separating regions B and D. For steady states with parameters in region D, a perturbation that brings the system beyond the excitability threshold triggers the unpinning of a DS leading to an excitability

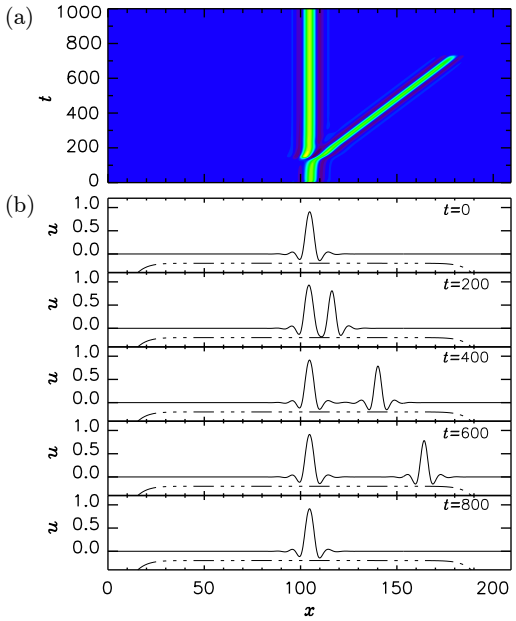

Figure 9.12: Type I excitability (SNIC): region D. An excitable excursion of the DS is shown close to the SNIC for $c = 0.12, h = 0.085$ and $\Delta h = -0.035$, $\Delta t = 10$. Panel (a) shows the contour plot of the real field u, while several spatial profiles $u(x)$ for fixed values of t are shown in (b).

excursion. This excursion is shown in Figure 9.12. The initial state corresponds to the parameters $c = 0.12$ and $h = 0.085$. By applying a perturbation $\Delta h = -0.035$ in h for a time period $\Delta t = 10$, the system is brought into region B for a time that is insufficient to complete a full limit cycle. The perturbation is long enough, however, to allow a DS to be pulled out of the defect and drift out of the finite size domain, bringing the system back to its initial state. The divergence of the period of oscillations in region B close to the SNIC can be seen in Figure 9.11(a), confirming the presence of Type I excitability.

9.5.2 Type II excitability (H^+ and H^-): regions A and C

Type II excitability is found in region A, close to region B and E, and it is mediated by the subcritical Hopf bifurcation H^+. An example of a typical excursion is shown in Figure 9.13. The initial and final resting state is not a high amplitude DS but a low bump solution, the fundamental solution. A perturbation of

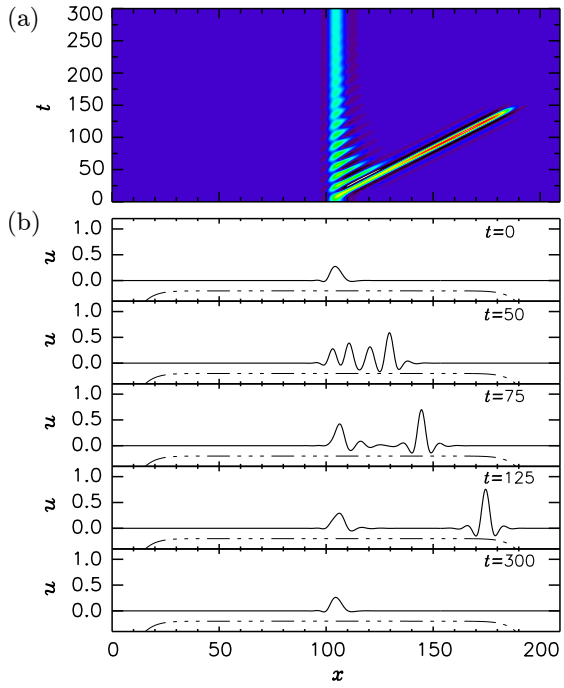

Figure 9.13: Type II excitability (H^+): region A. An excitable excursion of the DS is shown close to the FC for $c = 0.6, h = 0.092$ and $\Delta h = 0.035$ $\Delta t = 10$. Panel (a) shows the contour plot of the real field u, while several spatial profiles $u(x)$ for fixed values of t are shown in (b).

this fundamental solution in region A beyond the excitability threshold (bringing the system into region B) allows the system to generate a DS, which then drifts away, resetting the system to its resting state. If one applies a perturbation such that the system crosses FC, but not H^+, the system will find itself in region E which is bistable. The best way to trigger an excitable excursion is to perturb the system in the region where FC and H^+ are almost tangent. This way the perturbation required to excite an excursions will be smaller. Actually, the system is excitable even for $h = 0$, although in this case, very large perturbations are required to induce an excursion.

The second region of Type II excitability is found in region C, again close to region B, but this time it is mediated by the supercritical Hopf bifurcation H^-. Figure 9.14 shows an example of an excursion in region C, close to H^-. Here, the resting state is a large-amplitude DS, in contrast to the fundamental solution

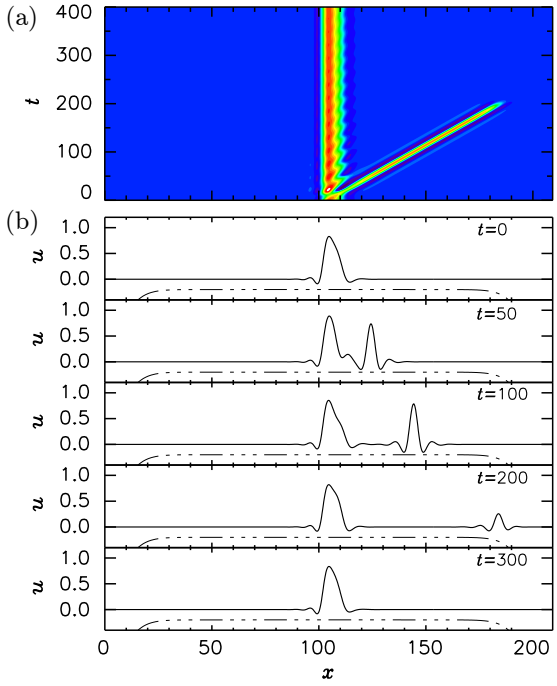

Figure 9.14: Type II excitability (H^-): region C. An excitable excursion of the DS is shown close to the H^- for $c = 0.4, h = 0.175$ and $\Delta h = -0.045$, $\Delta t = 10$. Panel (a) shows the contour plot of the real field u, while several spatial profiles $u(x)$ for fixed values of t are shown in (b).

in region A. Close to H^- in region B, DSs exhibit small amplitude oscillations, but moving a further away from H^-, a train of DSs is formed through a canard explosion, as explained in the previous section. The excitability threshold is defined by this canard explosion as the transient parameters need to be chosen such that the defect can serve as a source of DSs ($\sim$train of DSs).

9.6 Organization of the dynamics by codimension-two bifurcation points

In this Section, we will show that the various bifurcations involved in the creation of oscillations and excitability, i.e. the Hopf bifurcations (H^+, H^-) and the SNIC, are organized by codimension-two bifurcation points. Bifurcation points of codimension-two require two parameters to be varied for a bifurcation to

occur. The various bifurcations unfold from three such codimension-two points: two Takens-Bogdanov (TB) points, and one saddle-node separatrix-loop (SNSL) point.

9.6.1 Takens-Bogdanov bifurcations

A Takens-Bogdanov (or double-zero) bifurcation takes place for parameter values ($c_{\rm TB}$,$h_{\rm TB}$) if at fixed point $u_s^{\rm TB}$, the linear operator (9.20) has a zero eigenvalue with algebraic multiplicity two $\lambda_{1,2} = 0$ [12, 13]. According to the center manifold theorem, there exists a family of smooth two-dimensional invariant manifolds $W^C_{c,h}$ around the steady state $u_s^{\rm TB}$. At that point, $W^C_{c,h}$ is tangent to the linear eigenspace spanned by the eigenmodes ψ_1 and ψ_2 associated with $\lambda_{1,2} = 0$. The projection of our infinite dimensional dynamical system on the center manifold $W^C_{c,h}$ is topologically equivalent to the normal form [15]:

$$\begin{aligned} \frac{dA_1}{dt} &= A_2 \\ \frac{dA_2}{dt} &= \beta_1 + \beta_2 A_1 + A_1^2 + sA_1A_2, \end{aligned} \tag{9.25}$$

where $A_{1,2}$ represent the amplitudes of the modes $\psi_{1,2}$, and $\beta_{1,2}$ are coefficient which can be determined perturbatively, and the parameter s takes the values ± 1. In both cases the TB bifurcation involves a saddle-node bifurcation, Hopf bifurcation, and a SL bifurcation. The SL bifurcation is a global bifurcation and cannot be detected using a local analysis. Therefore, the SL bifurcation has been determined numerically. In a similar notation as we used for Hopf bifurcations, we will denote a SN bifurcation curve as $\rm SN^-$ if the transverse eigenmode is stable after crossing the center manifold. Likewise, we write $\rm SN^+$ when the mode is unstable after crossing the center manifold. For $s = +1$, a subcritical Hopf bifurcation $\rm H^+$ unfolds from the TB point, tangent to a saddle-node bifurcation $\rm SN^+$. Furthermore, a $\rm SL^+$, where an unstable cycle is destroyed, is created tangent to the Hopf bifurcation $\rm H^+$. For $s = -1$, a supercritical Hopf bifurcation $\rm H^-$ unfolds from the TB point, tangent to a saddle-node bifurcation $\rm SN^-$; and a $\rm SL^-$, where a stable cycle is destroyed, also unfolds tangent to $\rm H^-$.

Figure 9.15 and Figure 9.16 show that both types of TB bifurcations occur in the SH equation with drift and defect. In Figure 9.15 the TB point corresponds to the normal form case with $s = +1$, which we will call $\rm TB_1$. The unfolding of $\rm TB_1$ is further illustrated in Figure 9.17, where the top panels show how the bifurcation diagrams change when increasing c and as such crossing $\rm TB_1$. The bottom panels plot the real part of the largest eigenvalues associated with each

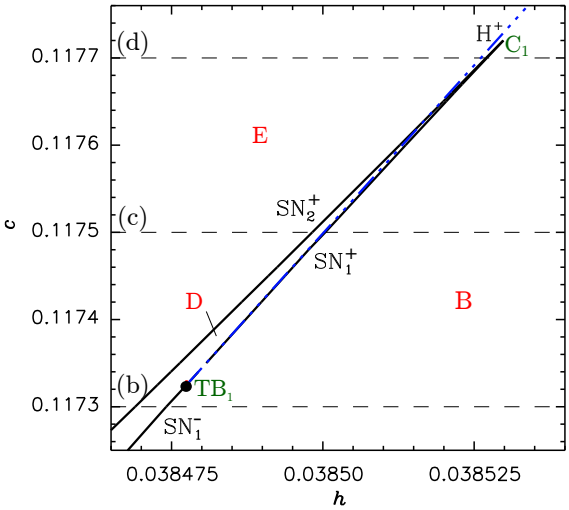

Figure 9.15: Unfolding of the Takens-Bodganov TB_1 bifurcation, completing the phase diagram in Figure 9.6 for $a = 1.2$ and $r = -0.2$. The black dashed lines refer to Figure 9.17 where the corresponding bifurcation diagrams and eigenvalues are shown. The dot-dashed blue line corresponds to H^+.

solution branch. For $c = 0.1171$, in Figure 9.17(a), the eigenmode transverse to the center manifold is stable, such that we label the saddle-node bifurcation as SN_1^-. Close to the TB_1 point ($c = 0.1173$), there exist two modes with zero eigenvalue $\mathrm{Re}[\lambda_{1,2}] = 0$ (Figure 9.17(b)). At TB_1 the transverse mode to the center manifold of the SN_1 switches from being stable to being unstable, such that we now label the saddle-node SN_1^+. At the same time, two other bifurcation lines, a subcritical Hopf bifurcation (H^+) and a saddle-loop bifurcation SL^+ (not shown in Figure 9.15) unfold. Figure 9.17(c)-(d) illustrates the situation when further increasing c ($c = 0.1175$ and $c = 0.1177$). The Hopf bifurcation H^+ moves to the left, destabilizing the branch of fundamental (low bump) solutions (labeled i) in Figure 9.3). H^+ eventually moves beyond SN_2^+, and SN_2^+ in its turn approaches SN_1^+. Increasing c further leads to the coalescence of both unstable SN curves in a cusp bifurcation C_1.

In Figures 9.16 and 9.18, we show the unfolding of the second TB point (TB_2), corresponding to the normal form case with $s = -1$. Figure 9.18(a) corresponds to the situation before crossing TB_2. Two saddle-node bifurcations can be observed: SN_4^- leading to a stable structure on the invariant circle, and SN_3^+ giving rise to unstable solution. At TB_2 (not shown in Figure 9.18), the trans-

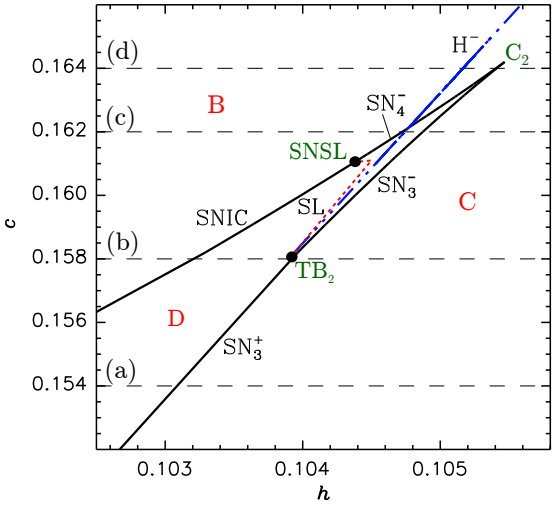

Figure 9.16: Unfolding of the Takens-Bodganov TB_2 bifurcation, completing the phase diagram in Figure 9.6 for $a = 1.2$ and $r = -0.2$. The black dashed lines refer to Figure 9.18 where the corresponding bifurcation diagrams and eigenvalues are shown. The dot-dashed blue line corresponds to H^- and the red dashed line to a SL bifurcation.

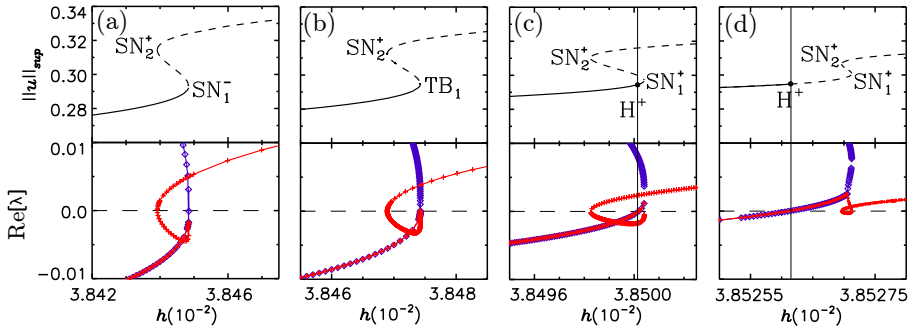

Figure 9.17: Bifurcation diagrams as a function of h (top), and the real part of the leading eigenvalues (bottom) for fixed increasing values of c crossing the TB_1 point: (a) $c = 0.1171$, (b) $c = 0.1173$, (c) $c = 0.1175$, (d) $c = 0.1177$. These values of c are also indicated as horizontal dashed lines in Figure 9.15.

verse eigenmode to the center manifold of SN_3 crosses the manifold, switching from being unstable to being stable. Therefore, after crossing TB_2, SN_3^+ becomes SN_3^-. This situation is shown in Figure 9.18(b) for $c = 0.158$. In this case

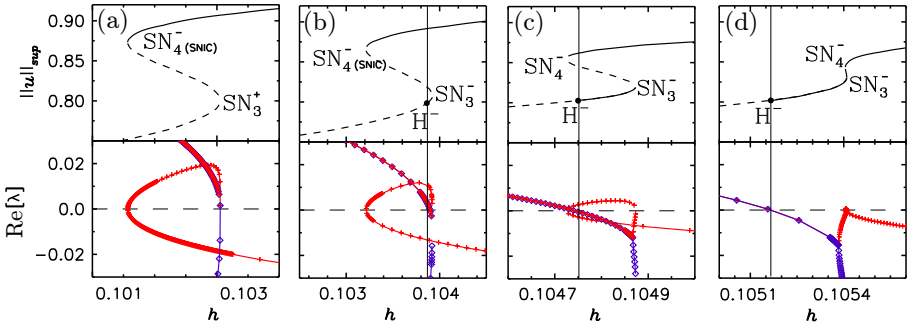

Figure 9.18: Bifurcation diagrams as a function of h (top), and the real part of the leading eigenvalues (bottom) for fixed increasing values of c crossing the TB_2 point: (a) $c = 0.154$, (b)$c = 0.158$,(c) $c = 0.162$ and (d) $c = 0.164$. These values of c are also indicated as horizontal dashed lines in Figure 9.16.

the Hopf bifurcation curve is supercritical (H^-) and creates a stable cycle which is destroyed in a SL^- bifurcation. As we mentioned before, such SL bifurcations are global bifurcations and cannot be detected locally. We used the scaling law (9.22) to extrapolate the location in parameter space of SL^-, see Figure 9.16. Close to the SL^- line, SL-mediated Type I excitability can be found in a very narrow region (not shown here). At $c = 0.162$, in Figure 9.16(c), the SN_4^- already occurs out of the cycle and H^- has moved to the left until almost crossing the SN_4^-. Finally, for $c = 0.164$, SN_3 and SN_4, both stable, are located very close and they will coalesce in the cusp bifurcation C_2.

9.6.2 Saddle-node separatrix-loop bifurcation

The destruction of the SL bifurcation is related with another codimension-2 point know as saddle-node separatrix-loop (SNSL) [5, 24]. A SNSL is a local-global codimension-2 point in which a saddle-node bifurcation takes place simultaneously with a saddle loop bifurcation. Figure 9.16 shows the unfolding of this SNSL point for the case involving the SL^-. One can see that there is a line of saddle-node bifurcations that at one side of the SNSL corresponds to a saddle-node bifurcation out of the limit circle (SN_4). At the other side, however, it corresponds to a SNIC bifurcation, where the saddle node occurs inside the limit cycle. Similarly as in TB_2, the SL^- curve also unfolds tangentially to SN_4 from the SNSL.

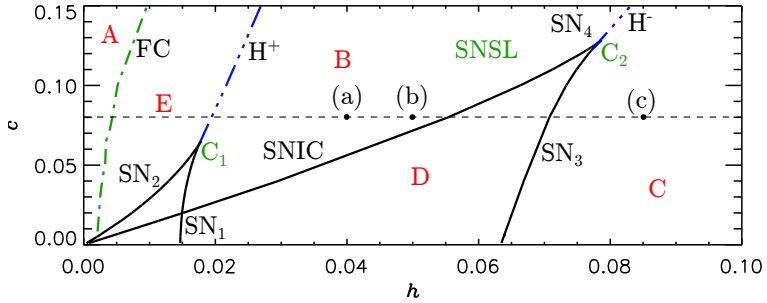

Figure 9.19: Two-parameter (c vs. h) phase diagram of the system for $a = 1$ and $r = -0.09$. The bifurcation curves and the labels of the regions corresponds to the ones in Figure 9.6. The points labeled with (a), (b) and (c) correspond to the solutions shown in Figure 9.20 for $c = 0.08$.

9.7 Robustness of the scenario with respect to parameter variations

In the previous sections, we demonstrated that the interaction between drift and a spatial defect can lead to oscillatory and excitable dynamics of a DS. We explored these phenomena by focusing on the SH equation using one parameter set (i.e. $a = 1.2$ and $r_0 = -0.2$). For this set of parameters we analyzed all bifurcations, both those of codimension-one and the codimension-two Takens-Bogdanov points serving as organizing centers of the dynamics. In this section, we show that these dynamical regimes are a general feature when including drift and defect in a broad parameter range. In order to check the consistency of the scenario in the SH equation, we studied the location of the previously characterized bifurcations for an alternative parameter set: $a = 1$ and $r = -0.09$. In Figure 9.19 we plot the phase diagram corresponding to those values. The same bifurcation curves and dynamical regions are found as in Figure 9.6. Therefore, it is not too surprising that the dynamics is largely similar as previously reported. Figure 9.20 shows the temporal evolution of several trains of solitons corresponding to different values of h for $c = 0.08$. Figure 9.20(a) shows a train of solitons for $h = 0.04$, found right in the middle of oscillatory region B in Figure 9.19. Similar as in Figure 9.10, the period of oscillations of the DS at the defect increases as one approaches the SNIC bifurcation, and a fast and slow time scale can be observed (Figure 9.20(b)). Moreover, an additional DS is regularly emitted slightly to the right of the defect. There are thus two competing oscillations: one is related with the emission of a DS at the spatial defect (and

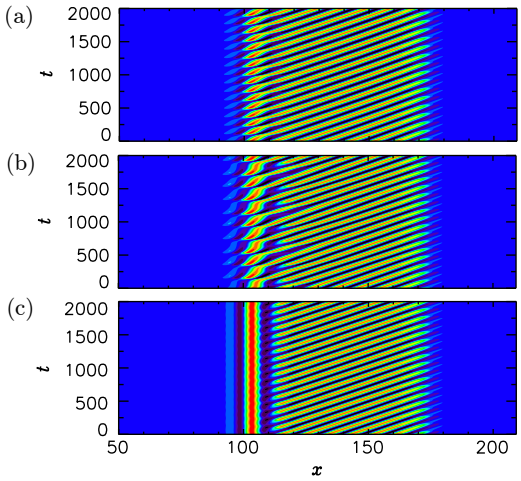

Figure 9.20: Contour plots of $u(x,t)$ showing the spatio-temporal evolution of oscillatory solutions for $c = 0.08$ (see dashed line in Figure 9.19). The defect strength is varied: $h = 0.04$ (a), 0.05 (b), 0.085 (c).

its period diverges when approaching the SNIC), and the other is related with the emission of a DS at the first oscillation of the tail of the pinned DS. This second oscillation has a period which increases when decreasing h within region B, potentially because there exists a secondary SNIC or SL bifurcation.

So far, the dynamics are similar to those reported in Figure 9.10 and Figure 9.6 for $a = 1.2$ and $r = -0.2$. However, when increasing h beyond the SNIC bifurcation, some differences can be observed. For $a = 1.2$ and $r = -0.2$, the only attractor of the system in region C was a single peak DS centered at the spatial defect (Figure 9.6). This solution exists in region C for $a = 1$ and $r = -0.09$ as well (Figure 9.19), but here, the system shows bistability between this single pinned DS and the oscillatory solution shown in Figure 9.20(c). This new limit cycle is composed of a small amplitude oscillation of the DS centered at the spatial defect and a train of solitons emitted from the first spatial oscillation of its tail (this oscillation was already present in Figure 9.20(b)). This added layer of complexity could be due to the fact that for these parameters, the pinning range of DSs and the Turing instability of the background $u = 0$ state are very close in parameter space. Therefore, DSs can be triggered not only at the spatial defect, but also from the tails of the DS.

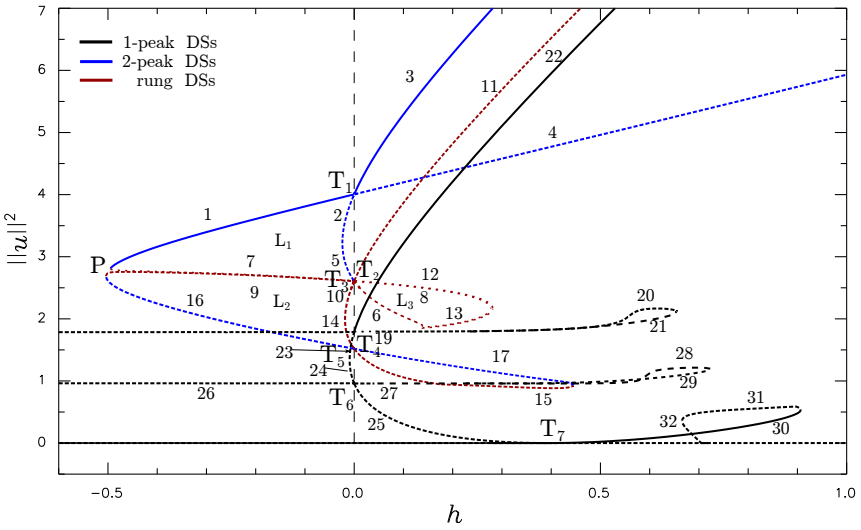

Figure 9.21: Bifurcation diagram for Eq.(9.26) with the defect in the gain term at $c = 0.0001$. Branches corresponding to DSs with two-peaks are shown in blue, DS with a single peak in black, and the asymmetric rung states in red. Solid and dashed lines represent stable and unstable states, respectively.

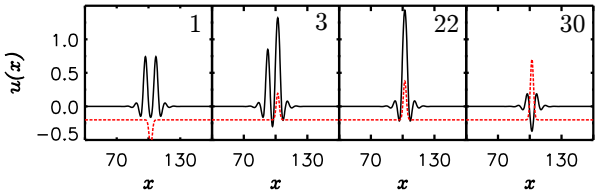

Figure 9.22: Spatial profiles $u(x)$ of the main attractors of the system for $c = 0$. The red dashed line shows the defect profile.

9.8 Spatial defect in the gain term

In this section we consider the SH equation with drift and defect, where the drift is introduced in the same way as before in Eq.(9.17), but the spatial defect is now added to the linear gain term. The resulting SH equation is given by:

$$\partial_t u = (r(x) + b(x))\, u + au^2 - gu^3 - \left(\partial_x^2 + k_0^2\right)^2 u - c\partial_x u, \tag{9.26}$$

where the spatial inhomogeneity is no longer an independent driving term in the equation (as in Eq.(9.17)), but it is part of the gain parameter that now

reads $\tilde{r}(x) = r(x) + b(x)$. In other words, the effective gain parameter $\tilde{r}$ changes around the center x_0 due to the effect of the defect and close to the borders due to the absorbing boundary conditions. We will show that in this situation the bifurcation scenario is richer and more involved. However, despite the added complexity, the competition between drift and defect still introduces similar oscillatory and excitable dynamics as before, confirming the generality of the concepts presented in this Chapter. As in Section 9.3.3, we will consider $g = 1$, $a = 1.2$ and $k_0^2 = 0.5$. In the present case, both LSs consisting of a single peak and multiple peaks are involved in the bifurcation diagram, in particular two-peak states and asymmetric rung states [25]. The rung states connect the single peak with the two-peak DSs. The existence of a pinning defect implies that these solutions can be pinned at different locations of the DS profile. For $c = 0$, DSs pinned outside the center of its profile are degenerate with a branch of solutions corresponding to DS pinned at the left of the center and another branch corresponding to DS pinned at the right. Figure 9.21 represents the bifurcation diagram for a value $c = 0.0001$. In order to make the diagram easier to understand, we plot the two-peaks DSs branches in blue, the single DSs branches in black, and the asymmetric rung states branches in red. For $c = 0$, six transcritical bifurcations (T_1...T_6) take place at $h = 0$ where the solution branches involved exchange their stability. Considering a finite value for c (as in Figure 9.21) leads to three effects. First, the transcritical bifurcations at $h = 0$ become imperfect and branches at positive and negative values of h detach in a similar way as in Section 9.3.3. Second, the branches of solutions pinned at the left or at the right of the center are no longer degenerate. Third, the pitchfork bifurcation P at negative values of h where rung states are born from two peaks DS becomes imperfect (for a more detailed picture see Figure 9.29(a) in the Appendix). Furthermore, the imperfect bifurcations arising at finite c lead to the reconnection of different branches forming isolas (loops) as described in the Appendix.

Now the fundamental solution of Eq.(9.26) is the trivial one $u = 0$ without any deformation. This fundamental solution undergoes a transcritical bifurcation at $h > 0$, labeled T_7 in Figure 9.21, where it exchanges stability with branches 25 and 31 corresponding to small bump states with one and two peaks, respectively. The other main attractors are those corresponding to the branches 1, 3, 22 and 31 and can be seen in Figure 9.22. They consist in a two-peak DS pinned at its center minimum, a two-peak DS pinned at the right peak (and another one pinned on the left peak), a single DS pinned at its center, and a small amplitude two-peak DS pinned at its central minimum.

A complete analysis of the states and reconnection of branches related with this

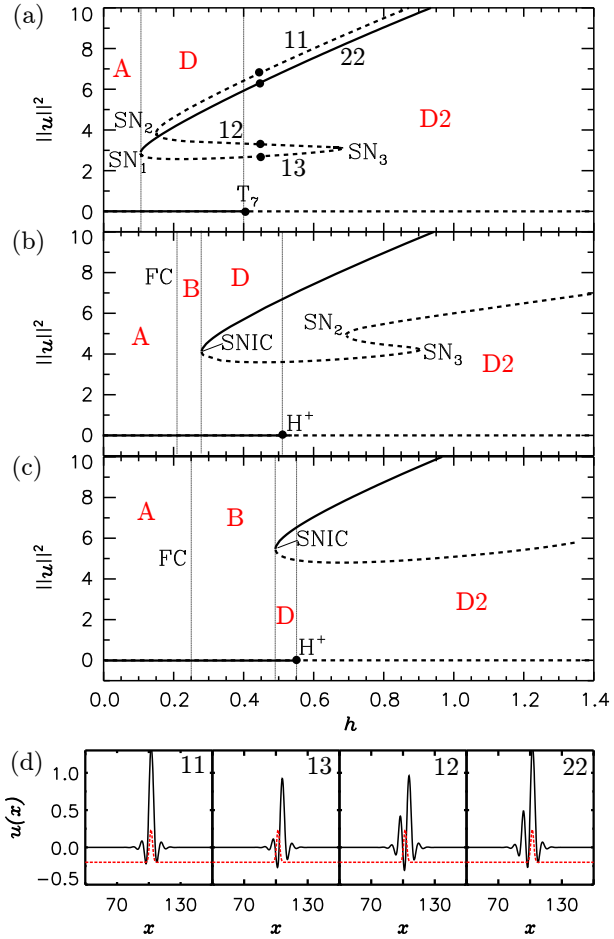

Figure 9.23: Bifurcation diagrams for Eq.(9.26) with the defect in the gain term for increasing values of the drift c: $c = 0.05$ (a), $c = 0.15$ (b), and $c = 0.3$ (c). Only the branches for $h > 0$ are shown. The main dynamical regimes are indicated in red and explained in the main text. Panel (d) shows the spatial profiles of the main attractors for $c \neq 0$.

scenario is presented in the Appendix. Here, for simplicity, we skip the unnecessary details and we focus on the study of branches 11, 12, 13 and 22, related with the one-peak DS, which are the ones necessary to explain the oscillatory and excitable dynamics in the system.

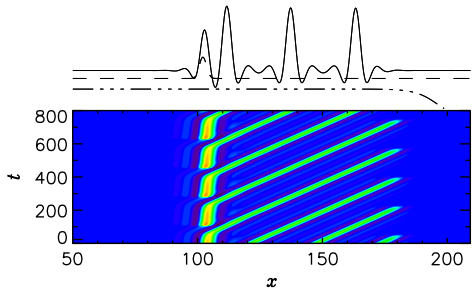

Figure 9.24: Contour plots of $u(x,t)$ showing the spatio-temporal evolution of oscillatory solutions of the high amplitude DS (train of solitons) for Eq.(9.26) with the defect in the gain term for $c = 0.15$ and $h = 0.268$. Above the contour plots the spatial profile $u(x, t = 800)$ is plotted.

For very small values of the drift c, branches 11, 12 and 13 are disconnected from branch 22, as shown in Figure 9.21. However, as c increases, branch 19, which is connected to branch 22, approaches branch 13 and reconnects with it for $c = 0.0003$ (see Appendix). As a consequence for $c > 0.0003$ branch 22 is connected to branch 11 via branches 13 and 12 as shown in Figure 9.23(a) for $c = 0.05$. The spatial profiles of the DSs corresponding to these branches are shown in Fig 9.23(d).

As the drift strength c is further increased branch 11 moves to the left of branch 12 and SN_1 becomes a SNIC bifurcation (Figure 9.23(b)). Similar as in Eq.(9.17), this SNIC bifurcation leads to oscillations of the high amplitude DS (region B). An example of these oscillations, corresponding to a train of solitons, is shown in Figure 9.24. Close to the SNIC the period of the oscillations is very large and one observes the typical time-scale separation. The period decreases for decreasing values of h moving away from the SNIC. Decreasing h even further, the oscillations disappear in a fold of cycles (FC). The stable limit cycle (train of solitons) collides with an unstable limit cycle created at the subcritical Hopf H^+ of the trivial solution. Increasing c further ($c = 0.3$), SN_2 and SN_3 coalesce in a cusp bifurcation C, while the SNIC bifurcation remains present up to higher values of c shown in Figure 9.23(c).

In the case of Eq.(9.17), we demonstrated in Section 9.5 that both Type I and Type II excitability originated close to the SNIC bifurcation, Hopf bifurcations, and the fold of cycles. Similar bifurcations occur here when the spatial defect is present in the gain term, such that one can expect to again find excitability of the high-amplitude DS solution. Figure 9.25 shows that this is indeed the case.

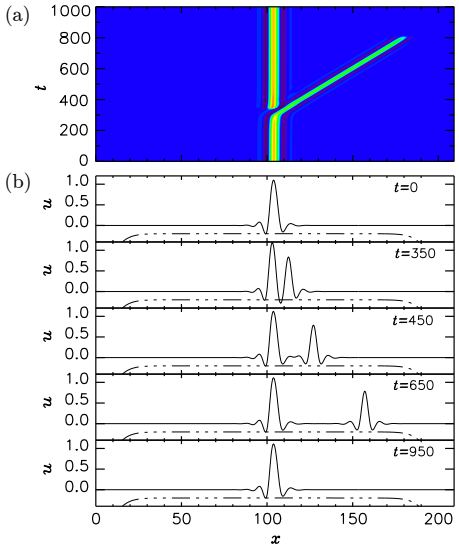

Figure 9.25: Excitable excursion of a DS for Eq.(9.26) with the defect in the gain term. The parameters are $c = 0.15$, $h = 0.281$, $\Delta h = -0.03$ and $\Delta t = 10$. Panel (a) shows the contour plot of $u(x,t)$ illustrating the spatio-temporal evolution of the excited DS. In (b) several snapshots of spatial profiles are shown for fixed values of t.

Close to the SNIC bifurcation, Type I excitability is observed by transiently perturbing the parameter set. This way, the system transiently finds itself in the oscillatory region and at the defect location a new DS is emitted and pulled towards the boundary, where it is removed from the domain.

Finally, Figure 9.26 shows the phase diagram with the organization of the various bifurcations in the parameter space (h,c). The black lines show instabilities associated to the large amplitude DS while blue lines show instabilities of the trivial solution $u = 0$. The subcritical Hopf bifurcation H^+ is shown again to unfold from a Takens-Bogdanov point (TB). Therefore, the trivial solution that become unstable at the transcritical bifurcation T_7 for values of c below TB, will become unstable at H^+ for values of c above TB. Four dynamical regions, labeled A to D are denoted in the phase diagram. These regions allow to identify where stable solutions can be found, and where they show oscillatory or excitable dynamics:

- Region A: The trivial solution is stable. This region is similar to Region A

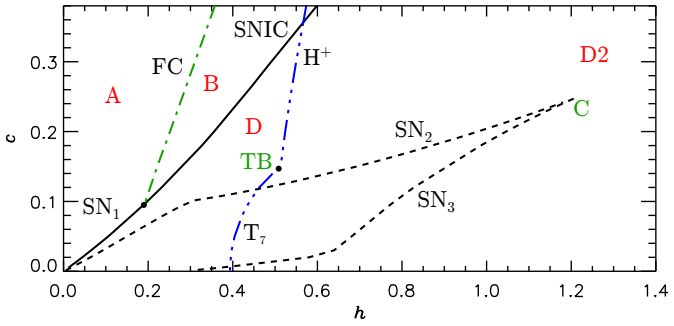

Figure 9.26: Two-parameter (c vs. h) phase diagram for Eq.(9.26) with the defect in the gain term. The bifurcations and regions A-D are explained in the main text.

in Figure 9.6. For parameters close to the FC line the system can display Type II excitability.

- Region B: The system displays DSs which oscillate periodically in time, similar as in Region B of Figure 9.6.
- Region D: The system admits stable large amplitude pinned DSs coexisting with the trivial solution $u = 0$. Within this region, the system can display Type I excitability.
- Region D2: This region is similar to Region D, but the trivial solution is now unstable. For $c > 0.35$, region D2 borders region B. As a consequence, for parameter values within region D2 close to the SNIC line, the system can display Type I excitability.

9.9 Conclusions

In this chapter, using the Swift-Hohenberg equation for a real field, we have presented a mechanism to induce dynamical instabilities of otherwise static DSs, preserving the structure of the DS. The mechanism relies on the interplay between spatial inhomogeneities and drift, together with absorbing boundary conditions, and therefore can be implemented under very general conditions. The presence of a defect and drift introduces two competing effects. On the one hand, a defect pins a DS at a fixed position, while on the other hand, the drift tries to pull it out. If the drift overcomes the pinning force, DSs are released from the inhomogeneity. Depending on the strength of the spatial defect and

the strength of the drift, we found three main dynamical regimes: i) stationary (pinned) DS solutions, ii) oscillatory regimes, where the pinned DS serves as continuous source of drifting DSs, and iii) excitability, where a perturbation may trigger a single DS that drifts away from the defect location. The excitability regime requires the presence of absorbing boundary conditions, which removes the drifting DS. For systems with periodic boundary conditions the drifting DS are reinjected and a train of solitons is typically observed instead [1]. We first reported on these results in Ref. [6]. Here, we presented a detailed bifurcation analysis, we linked these bifurcations to the presence of oscillatory and Type I and Type II excitable dynamics of DSs, and we have analyzed how these dynamics are intimately linked to the presence of various codimension-two points such as Takens-Bogdanov bifurcations and saddle-node separatrix loops. Next, we set out to show that this mechanism generating oscillations and excitability is generic, such that our analysis sheds light on the influence of defects and drift in any physical system. We have addressed this question of generality in two ways: i) we showed that the dynamics persisted for different parameter sets in the SH equation, ii) we changed the SH equation by introducing the defect in the gain term rather than including it as an independent driving term, and we demonstrated that oscillations and excitability were generated in a similar way. Furthermore, we have also shown that in different non-variational equations, such as the Lugiato-Lefever equation for a nonlinear Kerr optical cavity, the interaction of drift and defect can generate similar oscillatory dynamics [1]. Therefore the scenario described here leading to spatio-temporal dynamics of DSs does not depend on the details of the system. The results concerning the LL model were presented, in Chapter 1 for systems described by the LL equation with both absorving and periodic boundary conditions. We believe that our work provides a solid theoretical framework to explain the dynamics of DSs in systems with drift and defect. Our analysis could be especially useful in the field of optics. There, the drift can be produced by misalignments of mirrors [26, 27], nonlinear crystal birefringence [28, 29], parameter gradients [30] or by higher order effects chromatic light dispersion [31]. Inhomogeneities can originate from mirror or waveguide imperfections in an optical cavity and from the presence of fiber impurities, leading to variations in absorption coefficient or refractive index [32–34]. Synchronously pumped fiber cavities have also been shown to be modeled by a Lugiato-Lefever equation with a well-defined inhomogeneity in the pump [35, 36]. The drift-defect mechanism can explain experimental observations in semiconductor microresonators [2, 37], and could be applicable to a wide variety of other optical systems. We finally remark that the mechanism for excitability reported here is generic and therefore it can take place in a variety of systems beyond optics provided that there are spatial inhomogeneities and

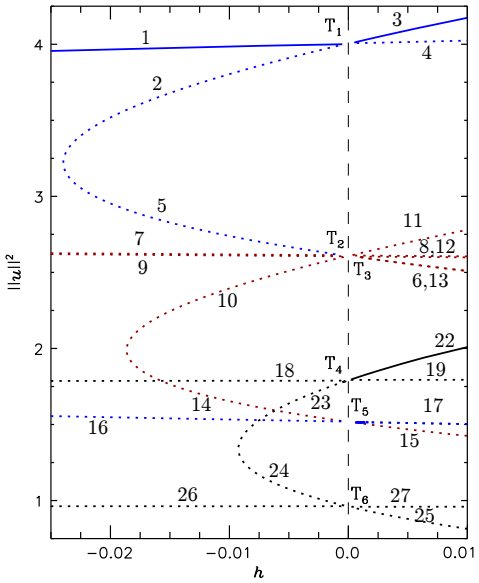

Figure 9.27: Detail of the diagram in Figure 9.21 showing the imperfect transcritical bifurcations around $h = 0$. Branches corresponding to DSs with two-peaks are shown in blue, DS with a single peak in black, and the asymmetric rung states in red. Solid and dashed lines represent stable and unstable states, respectively. T_1,...,T_6 represent transcritical bifurcations.

drift.

In Chapter 10 we will sudy a different mechanics leading to excitability of DSs, based on front interaction and anhilation.

Appendix: Reconnection of the solution branches shown in Figure 9.21

In this Appendix we analyze in detail the scenario in Section 9.8, in particular the transition that takes place when drift is considered.

As we said in the main text, at $h = 0$ the transcritical bifurcations become imperfect and branches for $h > 0$ and $h < 0$ detach. In Figure 9.27 a zoom of the diagram displayed in Figure 9.21 for $c = 0.0001$ shows the imperfect transcritical bifurcations around $h = 0$. The imperfect transcritical bifurcation labeled as T_1 involves only two-peaks states, T_4 and T_6 involve single peak DS and T_2, T_3 and

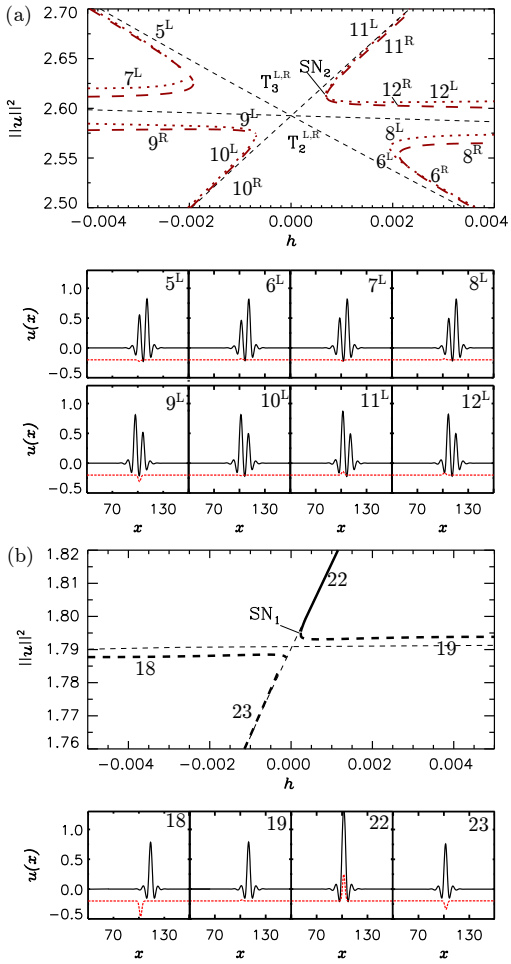

Figure 9.28: In (a) transcritical bifurcations T_2 and T_3 and their imperfections corresponding to Figure 9.27 are shown, together with examples of the spatial profiles of the L-states.The two red (dotted and dashed) lines correspond to the bifurcation for $c \neq 0$, while the black dashed lines correspond to the overlapping solution branches for c=0. In (b) Bifurcation diagram showing the transcritical bifurcation T_4 and its imperfection for $c = 0.0001$. In the bottom panel the profiles of the states corresponding to those branches are shown. The thin dashed lines represent the solution branches at $c = 0$.

T_4 a combination of rung states and two-peaks states. In the following we show in detail the unfolding of the transcritical bifurcations T_2, T_3 and T_4 due to the

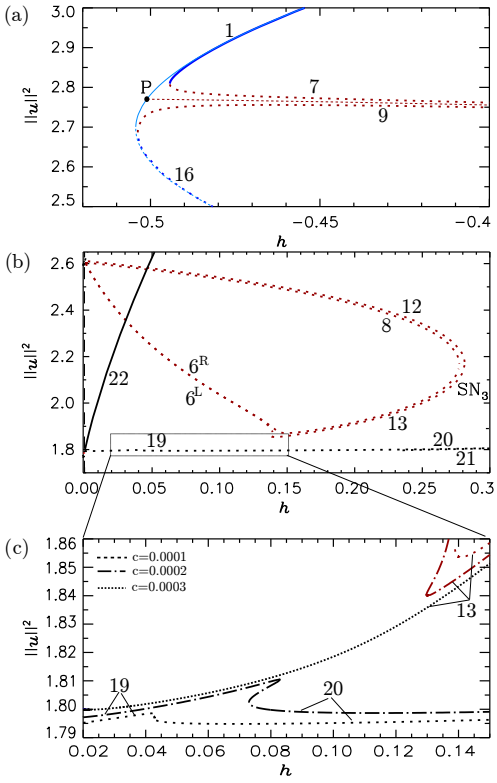

Figure 9.29: In (a) Pitchfork bifurcation (P) for $c = 0$ and its imperfection for $c = 0.0001$ are shown. In (b) and (c) we show the reconnection of solution branches 13 and 19. In (b) we plot a zoom of the diagram in Figure 9.21, showing branches 13 and 19 for $c = 0.0001$. In panel (c) a zoom of panel (b) illustrates how branches 13 and 19 approach for increasing c until they reconnect for $c = 0.0003$.

drift. Branches 5, 6, 7 and 8 are those related with T_2, and 9, 10, 11 and 12 are related with T_3. Analyzing these bifurcations in more detail (see Figure 9.28 (a)), we find that there is a doublet of transcritical bifurcations, one related with the rung states pinned at the right (labeled $T^R_{2,3}$), and one related to the solutions pinned on the left (labeled $T^L_{2,3}$), which for $c = 0$ are degenerate in norm. When the drift is included, the diagram in Figure 9.28(a) shows that those bifurcations become distinguishable and therefore, we can differentiate between rung states pinned on the left, L-states (plotted with pointed lines) and rung states pinned on the right R-states (plotted in dashed lines). The bottom panel in Figure 9.28

(a) shows the profiles corresponding to the L-states. In black dashed lines we show how the branches are connected through T_2 and T_3 for $c = 0$.

The diagram shown in Figure 9.28(b) represents the transcritical bifurcation T_4 and its imperfection corresponding to the diagram in Figure 9.27. In this bifurcation only branches 18, 19, 22 and 23, corresponding to the single-peak solitons shown in the bottom panel, are involved. In this case we only show the branches corresponding to the L-states, although as before, R-states would be also present. As a result of the imperfection of T_4 and SN_1 are created.

It is known that the rung states are asymmetric solutions connecting the solution branches with an even number of peaks with those with an odd number of peaks in the homoclinic snaking [25]. The connection of those rung states branches with the snaking occurs through a Pitchfork bifurcation. Due to the breaking of $x-$reversibility (for instance by including a drift term in the system) that pitchfork bifurcation becomes imperfect and results in the formation of isolas [22]. In our case, we are locally modifying the strength of the gain parameter r, and therefore there is the possibility of reaching the previous pitchfork bifurcation. This is what happens for $h < 0$, as shown in Figure 9.21. In the diagram of Figure 9.29(a) the pitchfork bifurcation P is plotted in more detail, and becomes imperfect when $c \neq 0$. For $c = 0$, branches 7 and 9 corresponding to the rung states are degenerate in norm, but when P becomes imperfect the degeneration disappears and the solution branches become distinguishable. This imperfect pitchfork and the imperfect transcritical bifurcations T_1, T_2, T_3 and T_5 are responsible for the formation of isolas L_1 (composed by branches 1, 2, 5 and 7) and L_2 (composed by 9, 10, 14 and 16) in Figure 9.21. When the strength of the drift further increases, the isolas shrink until eventually they disappear [22, 31].

Finally, in order to understand the transition between the diagrams in Figure 9.21 and Figure 9.23(a), we need to see how branches 11, 12, 13 and 22 reconnect. In Figure 9.29(b) we show a zoom of Figure 9.21 (c=0.0001) that includes the isola L_3, composed by branches 8 and 6^R, branches 12, 13 and 6^L, and the branches 19, 20, 21 and 22. The zoom of Figure 9.29(b) can be seen in Figure 9.29(c) for several values of the drift strength. For $c = 0.0001$, branches 19 and 20 are disconnected from 13. Increasing c those sets of branches approach as shown for $c = 0.0002$, and at some point they touch resulting in the reconnection of 19 with 13 for $c = 0.0003$.

References

[1] P. Parra-Rivas, D. Gomila, M. A. Matias, P. Colet, and L. Gelens, *Effects of inhomogeneities and drift on the dynamics of temporal solitons in fiber cavities and microresonators*, Opt. Express **22**, 3486-3493 (2014).

[2] E. Caboche, F. Pedaci, P. Genevet, S. Barland, M. Giudici, J. Tredicce, G. Tissoni, and L. A. Lugiato, *Microresonator defects as sources of drifting cavity solitons,* Phys. Rev. Lett. **102**, 163901 (2009).

[3] E. Caboche, S. Barland, M. Giudici, J. Tredicce, G. Tissoni, and L. A. Lugiato, *Cavity-soliton motion in the presence of device defects,* Phys. Rev. A **80**, 053814 (2009).

[4] D. Gomila, M. A. Matias, and P. Colet, *Excitability mediated by localized structures in a dissipative nonlinear optical cavity,* Phys. Rev. Lett.**94**, 063905 (2005); D. Gomila, A. Jacobo, M. A. Matias, and P. Colet, *Phase-space structure of two-dimensional excitable localized structures,* Phys. Rev. E **75**, 026217 (2007).

[5] E. M. Izhikevich, *Dynamical Systems in Neuroscience: The Geometry of Excitability and Bursting* (MIT Press, Cambridge (MA), 2007).

[6] P. Parra-Rivas, D. Gomila, M. A. Matías and P. Colet, *Dissipative soliton excitability induced by spatial inhomogeneities and drift,* Phys. Rev. Lett. **110**, 064103 (2013).

[7] P. Parra-Rivas, D. Gomila, M. A. Matías, P. Colet, and L. Gelens, *Competition between drift and spatial defects leads to oscillatory and excitable dynamics of dissipative solitons,* Phys. Rev. E. **93**, 012211 (2016).

[8] J. M. Soto-Crespo, and N. Akhmediev, *Interrelation between various branches of stable solitons in dissipative systems conjecture for stability criterion,* Phys. Rev. E **66**, 066610 (2002).

[9] L. Gelens, and E. Knobloch, *Traveling waves and defects in the complex Swift-Hohenberg equation,* Phys. Rev. E **84**, 056203 (2011).

[10] M. Cross and P. Hohenberg, *Pattern-formation outside of equilibrium,* Rev. Mod. Phys. **65**, 851 (1993).

[11] D. Walgraef, *Spatio-temporal Pattern Formation,* (Springer-Verlag, New York, 1997).

[12] F. Takens, *Singularities of vector fields,* Publ. Math. Inst. Hautes Etud. Sci. **43**, 47 (1974).

[13] R. I. Bodganov, *: Versal deformations of a singular point on the plane in the case of zero eigenvalues,* Funct. Anal. Appl. **9**, 144 (1975).

[14] J. Guckenheimer and P. Holmes, *Nonlinear Oscillations, Dynamical Systems, and Bifurcations of Vector Fields*, (Springer, New York, 1983).

[15] Y. A. Kuznetsov, *Elements fo Applied Bifurcation Theory*, 3rd ed. (Springer, New York, 2004).

[16] S.H. Strogatz *Nonlinear dynamics and chaos*, Westview Press, Second Edition (2014).

[17] J. Burke and E. Knobloch, *Localized states in the generalized Swift-Hohenberg equation,* Phys. Rev. E **73**, 056211 (2006).

[18] P.D. Woods, A.R. Champneys, *Heteroclinic tangles and homoclinic snaking in the unfolding of a degenerate reversible Hamiltonian-Hopf bifurcation,* Physica D **129**, 147 (1999).

[19] P. Coullet, C. Riera, C. Tresser, *Stable static localized structures in one dimension,* Phys. Rev. Lett. 84 (2000) 3069.

[20] J.M. Soto-Crespo, N. Ackmediev, G. Town, *Interrelation between various branches of stable solitons in dissipative systems-conjecture for stability criterion,* Optics Commun. **199**, 283 (2001).

[21] A. Jacobo, D. Gomila, M. A. MatÃŋas, P. Colet, Phys. Rev. A **78**, 053821 (1-9) (2008).

[22] J. Burke, S. Houghton, and E. Knobloch, *Swift-Hohenberg equation with broken reflection symmetry,* Phys. Rev. E **80**, 036202 (2009).

[23] A. Jacobo, D. Gomila, M. A. Matias, and P. Colet, *Effects of noise on excitable dissipative solitons,* New J. Physics **14**, 013040 (2012).

[24] S. Schecter, *The saddle-node separatrix-loop bifurcation,* SIAM J. Math. Anal. **18**, 1142 (1987).

[25] J. Burke, and E. Knobloch, *Snakes and Ladders: Localized states in the Swift-Hohenberg equation,* Phys. Lett. A **360**, 681-688 (2007).

[26] M. Santagiustina, P. Colet, M. S. Miguel, and D. Walgraef, *Noise-sustained convective structures in nonlinear optics,* Phys. Rev. Lett. **79**, 3633 (1997).

[27] E. Louvergneaux, C. Szwaj, G. Agez, P. Glorieux, and M. Taki, *Experimental Evidence of Absolute and Convective Instabilities in Optics,*

[28] H. Ward, M. N. Ouarzazi, M. Taki, and P. Glorieux, *Transverse dynamics of optical parametric oscillators in presence of walk-off,* Eur. Phys. J. D **3**, 275 (1998);

[29] M. Santagiustina, P. Colet, M. S. Miguel, and D. Walgraef, *Walk-Off and Pattern Selection in Optical Parametric Oscillators,* Opt. Lett. **23**, 1167 (1998).

[30] B. Schapers, T. Ackemann, and W. Lange, *Properties of feedback solitons in a single-mirror experiment,* IEEE J. Quantum Electron. **39**, 227 (2003).

[31] P. Parra-Rivas, D. Gomila, F. Leo, S. Coen and L. Gelens, *Third-order chromatic dispersion stabilizes Kerr frequency combs,* Opt. Lett. **39**, 2971-2974 (2014).

[32] P. Kramper, M. Kafesaki, C.M. Soukoulis, A. Birner, F. Müller, U. Güsele, R.B. Wehrspohn, J. Mlynek, and V. Sandoghdar, *Near-field visualization of light confinement in a photonic crystal microresonator,* Opt Lett. **29**, 174 (2004).

[33] F. Pedaci, G. Tissoni, S. Barland, M. Giudici and J. Tredicce, *Mapping local defects of extended media using localized structures,* Appl. Phys. Lett. **93**, 111104 (2008).

[34] G. Kozyreff and L. Gelens, *Cavity solitons and localized patterns in a finite-size optical cavity,* Phys. Rev. A **84**, 023819 (1-5) (2011).

[35] M. Haelterman, S. Trillo, and S. Wabnitz, *Dynamics of one-dimensional Kerr cavity solitons,* Optics Communications **91**, 401-407 (1992).

[36] M. J. Schmidberger, D. Novoa, F. Biancalana, P. St. J. Russell, and N. Y. Joly, *Multistability and spontaneous breaking in pulse-shape symmetry in fiber ring cavities,* Opt. Express **22**, 3045-3053 (2014).

[37] F. Pedaci, S. Barland, E. Caboche, P. Genevet, M. Giudici, J. R. Tredicce, T. Ackemann, A. Scroggie, W. Firth, G. L. Oppo, G. Tissoni, and R. Jaeger, *All-optical delay line using semiconductor cavity solitons,* Appl. Phys. Lett. **92**, 011101 (2008).

Chapter 10

Excitability induced by front interaction

10.1 Introduction

In spatiotemporal dynamics, excitability can appear in several kinds of extended systems. In the most straightforward case, systems which are individually excitable are coupled in space. These excitable media typically exhibit characteristic excitable waves or pulses [1–3]. Besides, extended systems can display excitable behavior in a more subtle way through the emergent dynamics of coherent structures, which does not require local excitable dynamics [4]. The excitable excursion follows the remnants of a limit cycle corresponding to an oscillatory localized structure and can be described in terms of an effective reduced phase space [4, 5].

In Chapters 8 and 9 we have also seen that DSs excitability can arise in extended systems where spatial inhomogeneities (or defects) and drift are present [6, 7]. In both chapters this phenomenon occurs through the excitation of an unstable structure, created through the destruction of an oscillatory localized structure, via Hopf, SNIC or SL bifurcations [8, 9].

The scenario presented in this Chapter, allows the possibility of having excitable behavior in a system that contain just two ingredients: 1) (local) bistable behavior, and 2) spatial coupling allowing the formation of fronts that connect the two homogeneous states. In other words, we will show that it is possible to obtain transient spatiotemporal spots having neither locally excitable dynamics (as in

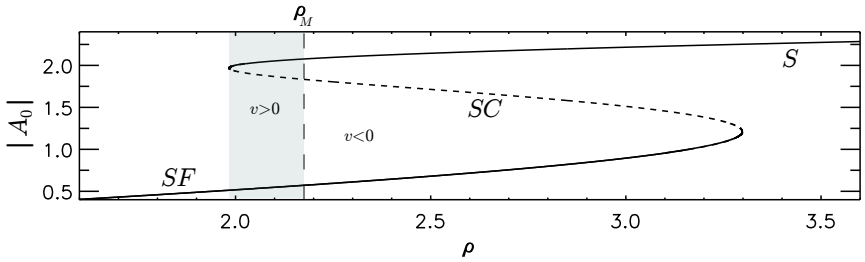

Figure 10.1: Bifurcation diagram for the HSSs A_0, where we plot $|A_0|$ in function of ρ for $\theta = 4$. The vertical dashed line represent the Maxwell point of t the system, here occurring at $\rho_M = 2.1753$, where the velocity of the fronts connecting A_0^b with A_0^t is zero. The gray region represent the range of value of ρ for which the HSSs A_0^b is excitable due to front movement and interaction.

[10]), nor oscillatory LS solution disappearing when changing a parameter (as in [4]), as bistable dynamics and spatial coupling suffice. In this sense, this could explain experimental observations of transient localized spots in a more general setting, that does not assume local excitability or the presence of LSs. Systems with bistable homogeneous states in which this mechanism could be observed include, for instance, chemical reactions [11], optical systems [12, 13], and biology. In particular in the context of cellular biology, transient localized excitations, also called patches, have been observed in early stages of cell migration. One of the most studied examples is the cellular slime mold, *Dyctiostellium discoideum*. In this system, the uniform application of the chemoattractant cAMP leads to the spontaneous emergence of localized regions of high protein concentration, patches, that after some time dismantle and appear elsewhere [14]. In [10] an explanation was suggested in terms of a two-component FitzHugh-Nagumo excitable model. However, as pointed out in [15], despite the extensive use of reaction-diffusion models, direct evidence for excitability is lacking.

To start let us first illustrate this behavior in the LL model in normal GVD regime where the system is bistable. The bistability is appreciated in the bifurcation diagram shown in Figure 10.1 for $\theta = 4$. As we have seen in previous Chapters, a front or switching wave (SW) between stable states, A_0^b and A_0^t, and vize versa can be formed. We call these fronts F_u and F_d respectively. States A_0^b and A_0^t are not equivalent, and therefore, fronts move with a constant veolcity v into the left or right depending on their orientation and the value of ρ. Then we say that the veolcity v is positive if a front F_u (resp. F_d) moves from left to right (resp. from right to left) and negative in the other case. The vertical dashed

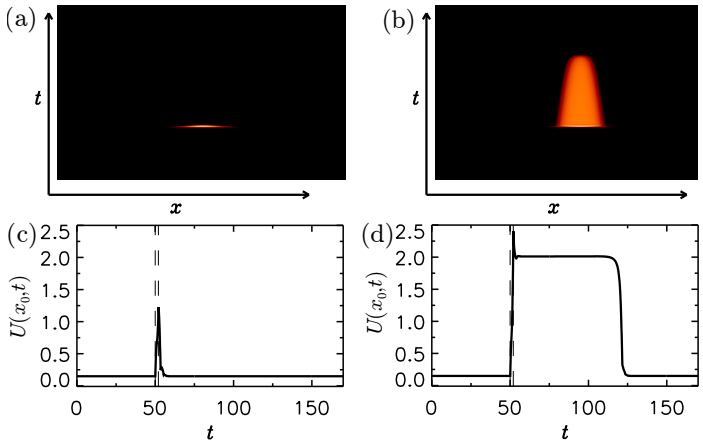

Figure 10.2: Evolution of $U(x,t) \equiv \mathrm{Re}[A]$ after a perturbation on A_0^b with $\Gamma = 15.6$, $t_0 = 50$ and $\Delta t = 2$. In (a) a sub-threshold perturbation with $G = 1.3$ is shown and in (c) the temporal evolution of the maximum of $U(x_0,t)$ is plotted. Panels (b) and (d) correspond to a super-threshold perturbation with $G = 1.5$. The vertical dashed lines in panels (c) and (d) indicate the switching on and off of the perturbation. In panels (a) and (b) the range of x is $[-20,20]$ and the range of t is $[0,200]$. Here $\theta = 4$ and $\rho = 2.16 < \rho_M$.

line shown in Figure 10.1 reprsents the Maxwell point of the system where the velocity of fronts is zero. This occurs for $\rho = \rho_M \approx 2.1753$.

For $\rho > \rho_M$, $v < 0$, and two fronts F_u and F_d, move appart such that the upper solution overruns the lower one. On the contrary, for $\rho < \rho_M$, $v > 0$, and the two fronts move closer until they annihilate. This annihilation takes place because these fronts approach and leave the top HSSs branch A_0^t in a monotonic way i.e. A_0^t is a saddle (S) point, and therefore there is no pinning. The gray region represents the interval of ρ where the system is bistable and where $v > 0$. In this situation, excitability for the A_0^b HSSs can be induced by front movement and interaction. The excitable behavior it is shown in Figure 10.2 for two time evolutions of different perturbations of the bottom HSSs. These perturbations can be generated by for example an injected Gaussian beam

$$g(x) = G \exp\left[-\left(\frac{\ln 2 (x - x_0)}{\Gamma} \right)^2 \right], \tag{10.1}$$

during a time Δt, as done in Section 9.3. Here G and x_0 are the height and center of the Gaussian and Γ is the half width at half maximum.

Small localized perturbation to the stable homogeneous state A_0^b, lead to a *fast* relaxation and smoothing due to diffusion/diffraction/dispersion. back to the stable state (see Figure 10.2(a) and (c)). Instead, if the perturbation exceeds locally the separatrix A_0^m, like it is the case in Figure 10.2(b) and (d), it may happen that A_0^b is able to connect with the other stable state A_0^t, and attracting state, by becoming two fronts connected through their head. For this to happen, the approach to the other (attracting) stable state must able to overcome the smoothening effect of diffusion/diffraction/dispersion. If the resulting two-front state is relatively broad, it will be relatively long-lived, although, ultimately, the two fronts will annihilate and the system will return to the stable homogeneous state.

Our aim in this chapter is to present a study of these finite-lifetime localized structures. First we show this in a system where fronts are formed between equivalent states. For that we will use the probably simplest example (and thus prototypical): the one-dimensional real cubic (GL) equation. Later on we will generalize the mechanism to different models where the HSSs are not equivalent, like the quintic GL equation. The structure of the chapter is as follow. In Section 10.2 we show the results in the cubic GL equation. In Section 10.3 we present how these excitability can be sustained by noise. Later, in Section 10.4 we show that this new type of excitability is also present when considering interaction between two non-equivalent fronts, as it is the case in the quintic GL equation. Moreover, we consider a variation of this mechanism considering convective instabilities in the last model, and finally in Section 10.5 we end with the Conclusions of the Chapter.

10.2 Excitability mediated by equivalent fronts

In this Section we show our results regarding front induced excitability when the two fronts are formed between equivalent stable HSSs solutions, that is the most elementary situation. For that we consider the real cubic GL equation in one extended dimension, namely

$$\partial_t u = \mu u - u^3 + \partial_x^2 u. \tag{10.2}$$

We first introduce the model and later present the main block of this study where we show that the front interaction and annihilation generates excitability.

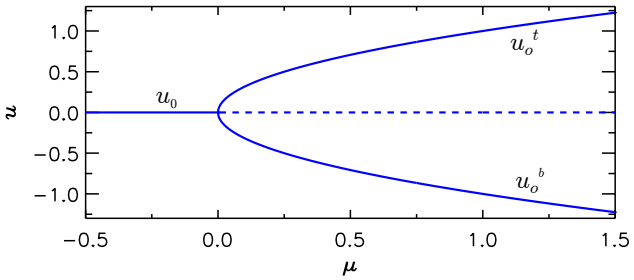

Figure 10.3: Homogeneous steady state for the cubic GL equation. The stable trivial HSSs suffers a pitchfork bifurcation at $\mu = 0$, where it becomes unstable and unfold two stable HSSs, namely u_0^t and u_0^t, with the same potential energy.

10.2.1 A general model: the real Ginzburg-Landau with cubic nonlinearity

This equation probably is the simplest partial differential equation containing the two above mentioned ingredients needed to implement front excitability, i.e. bistability and spatial coupling. The two equivalent (stable) HSSs, u_0^t and u_0^b, are given respectively by $u = \pm\sqrt{\mu}$ that are found for $\mu > 0$ (see Figure 10.3). They appear in a pitchfork bifurcation at $\mu = 0$ where $u = 0$ also becomes unstable. This unstable state acts as separatrix for the two HSSs.

The two possible front solutions, known as kink and anti-kink, have opposite polarity and connect the two equivalent states u_0^b and u_0^t of Eq. (10.2). They are given by [16],

$$u_\pm(x) = \pm\sqrt{\mu}\tanh\left(\frac{\sqrt{\mu}x}{2}\right) \tag{10.3}$$

Several examples of such fronts are shown in Figure 10.4. These fronts can be seen in a spatial dynamics context, as heteroclinic connection between u_0^b and u_0^t, whose stable and unstable manifolds approach these states monotonically. To prove that the stationary equation $\partial_t u = 0$ can be recast to the equivalent spatial dynamical system

$$\begin{aligned} d_x u_1 &= u_2 \\ d_x u_2 &= u_1^3 - \mu u_1, \end{aligned} \tag{10.4}$$

with $u_1 = u$ and $u_2 = d_x u_1$. The Jacobian of this system around any of the bifurcation states $u_0^{b,t}$ has the eigenvalues $\lambda = \pm\sqrt{2\mu}$. This shows that the stable and unstable manifolds of both states $u_0^{b,t}$, approach and leave monotonically, fact that is reflected on the shape of the fronts $u_\pm$. Due to the monotonic nature

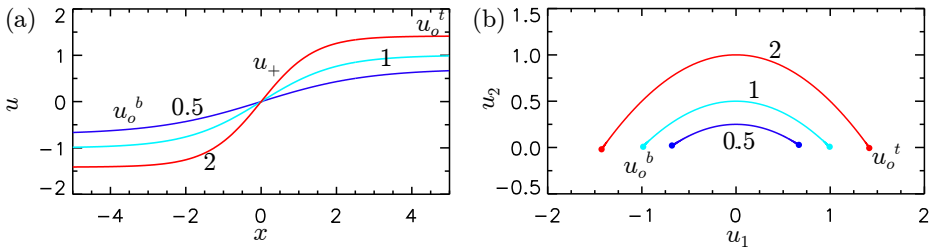

Figure 10.4: In panel (a) we plot a kink front u_+ for $\mu = 0.5, 1.0$ and 2. In (b) we show the heteroclinic connection obtained after projecting the front into the phase space (u_1, u_2).

of the fronts, they do not exhibit pinning, ultimately annihilating in a behavior known as coarsening [17].

Due to the fact that the front occurs between equivalent states i.e. both HSSs have the same potential energy $V = V_3[u] = -\mu u^2/2 + u^4/4$, the front is stationary and therefore the dynamics of the system does not favor any of the two bifurcating flat solutions. This can be shown as follows. Let us consider that, if the front moves, it does with a velocity v that depends on the control parameter μ. This velocity is the solution of the nonlinear eigenvalue problem:

$$-v(\mu)u'(x) = -\partial_u V[u] + u''(x) \tag{10.5}$$

with the boundary conditions, $u(-\infty) = u_0^b$ and $u(+\infty) = u_0^t$ and $'$ standing for derivative respect to x. Integrating Eq.(10.5) along the heteroclinic orbit we obtain the explicit equation for the front velocity given by:

$$v(\mu) = \frac{V[u_0^t] - V[u_0^b]}{\int \sqrt{u'(x)}dx}, \tag{10.6}$$

that is zero because $V[u_0^t] = V[u_0^b]$. So the front does not move.

10.2.2 Front annihilation and excitability

Previously we have seen that in the cubic GL equation (10.2) a single front between equivalent HSSs u_0^b and u_0^t does not move. In contrast this is not the case when considering two fronts with opposite polarity i.e. a kink and anti-kink states. In this situation these two fronts attract with an exponentially decaying interaction, until they annihilate each other [16]. This transient behavior knowns as coarsening is one of the basic ingredients of this mechanism of excitability. For large separation distances $d(t) = x_2(t) - x_1(t)$, between the positions $x_1(t)$

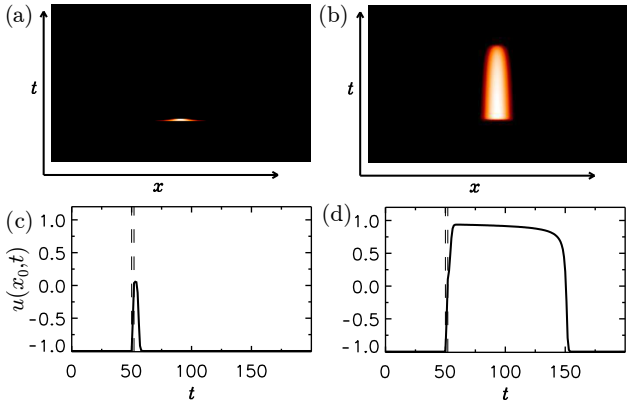

Figure 10.5: Evolution of $u(x,t)$ after a perturbation on u_0^b with $\Gamma = 15$, $t_0 = 50$ and $\Delta t = 2$. In (a) a sub-threshold perturbation with $G = 0.79$ is shown and in (c) the temporal evolution of the maximum of $u(x_0,t)$ is plotted. Panels (b) and (d) correspond to a super-threshold perturbation with $G = 81$. The vertical dashed lines in panels (c) and (d) indicate the switching on and off of the perturbation. In panels (a) and (b) the range of x is $[-22, 22]$ and the range of t is $[0, 200]$. Here $\mu = 1$.

and $x_2(t)$ for the kink and anti-kink's cores it is possible to obtain a perturbative approximation at first order for the velocity at which the fronts are attracting each other [16]. This velocity is given by,

$$\dot{d} = c \exp(-\gamma d) \tag{10.7}$$

where $c = -24\sqrt{2\mu}$ and $\gamma = \sqrt{2\mu}$. The absent of roots of this equation shows, what it was already confirmed by the spatial eigenvalues, that there is not pinning of fronts, and therefore no localized structures are present in this system.

In this framework the excitability mechanism is as follows. While the system is sitting at a stable HSS, small localized perturbations decay exponentially. Instead, for perturbations exceeding $u(x) = 0$ in a wide enough spatial region, part of the system will initially evolve to the other (attracting) HSS leading to the formation of a pair of kink-anti-kink fronts. At a second stage the two fronts interact, slowly approaching each other. If the resulting kink-anti-kink structure is relatively broad this second stage will be long-lived. Finally, at a third stage, kink and anti-kink annihilate each-other and the system returns to the initial HSSs. These structures can be viewed as excitable excursions and, following [14], we will refer to them as *patches*.

The excitable behavior is illustrated in Figure 10.5 showing the spatiotemporal

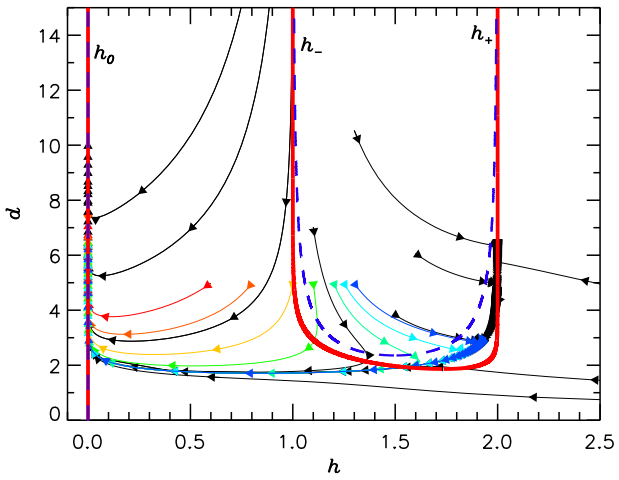

Figure 10.6: Projection of the dynamics into the (h, d) phase space. Lines with arrows show trajectories obtained integrating Eq. (10.2) starting from an initial condition (10.8) with different d_0 and H_0 . The arrows correspond to the velocity field, allowing to identify fast and slow time scales. Trajectories in color correspond to $d_0 = 4.98$ and different H_0 , whose temporal evolution is plotted in Figure 10.8. Red lines correspond to the analytical $h-$nullclines (10.11), and in blue dashed lines, those given by (10.14).

dynamics after a perturbation of u_0^b generated by adding to Eq.(10.2) during a time Δt the Gaussian spatial profile given by Eq.(10.1).

Figure 10.5(a)-(c) shows the behavior observed for low enough values of h, case in which the patch decays quite rapidly. In this context, decaying means that the two fronts that constitute the patch coarsen and annihilate. In contrast, Figure 10.5(b)-(d) shows the behavior of a patch with a slightly larger h, showing a much larger decay time. This observation points at the existence of a threshold separating two clearly different decaying ways, pointing out to excitability.

In the following, and without loss of generality, we take $\mu = 1$, being $u_0^{b,t} = \pm 1$. In *classical* Type II excitable systems with a two-dimensional phase space (e.g. the FitzHugh-Nagumo model), the excitable behavior under perturbations to a stable fixed point can be understood [18] by analyzing the shape of the nullclines in phase space [1]. Here the phase space is infinite-dimensional, however, we find a very similar scenario by considering the two-dimensional phase space (h, d)

[1] Nullclines are defined as the geometric place in which the time derivative of one of the system variables is zero, being found the fixed points at the intersection of these nullclines.

where $h(t) \equiv u(x_0, t) - u_0^b$ is the height of the patch at its center x_0, and $d(t)$ its half width at half maximum. Figure 10.6 displays the projection of the evolution obtained from numerical integration of Eq.(10.2) for a set of different initial condition of the type

$$u(x,0) = u_0^b + H_0 \exp\left[-\left(\frac{\ln 2(x-x_0)}{d_0}\right)^2\right]. \tag{10.8}$$

For d larger than the front width, we can approximate the shape of the patch by two tanh fronts back to back

$$u(x,t) = u_0^b + h(t)\left[\eta(x, x_0 - d(t)) - \eta(x, x_0 + d(t))\right] \tag{10.9}$$

where $\eta(x,a) \equiv \tanh((x-a)/\sqrt{2})$. Introducing (10.9) in Eq.(10.2) and evaluating it at $x = x_0$, one gets

$$\dot{h} = h\left[6h\tanh\left(\frac{d}{\sqrt{2}}\right) + (1-4h^2)\tanh^2\left(\frac{d}{\sqrt{2}}\right) - 3\right], \tag{10.10}$$

where we have consider that the evolution of $d(t)$ is much slower than that of $h(t)$. The $h-$nullcline is

$$h_\pm = \frac{3}{4}\coth(d/\sqrt{2}) \pm \frac{1}{4}\sqrt{4 - 3\coth^2(d/\sqrt{2})}, \quad h_0 = 0, \tag{10.11}$$

and it is plotted in Figure 10.6 using a red solid line. This $h-$nullcline is therefore composed by three pieces as shown in Figure 10.6. h_+ which is attracting and has a vertical asymptote at $h = 2$, h_- repelling with a vertical asymptote at $h = 1$ and h_0 also stable. h_+ and h_- are connected at $h = \sqrt{3}/2$, $d = \ln(7+4\sqrt{3})/\sqrt{2} \approx 1.86$.

When d is small the shape of a patch can be approximate by using a Gaussian profile, namely

$$u(x,t) = u_0^b + h(t)\exp\left[-\left(\frac{\ln 2(x-x_0)}{d(t)}\right)^2\right]. \tag{10.12}$$

Inserting (10.12) in Eq.(10.2) and evaluating at $x = x_0$, one obtains the equation

$$\dot{h} = -2\left(1 + \frac{\ln 2}{d(t)^2}\right)h + 3h^2 - h^3. \tag{10.13}$$

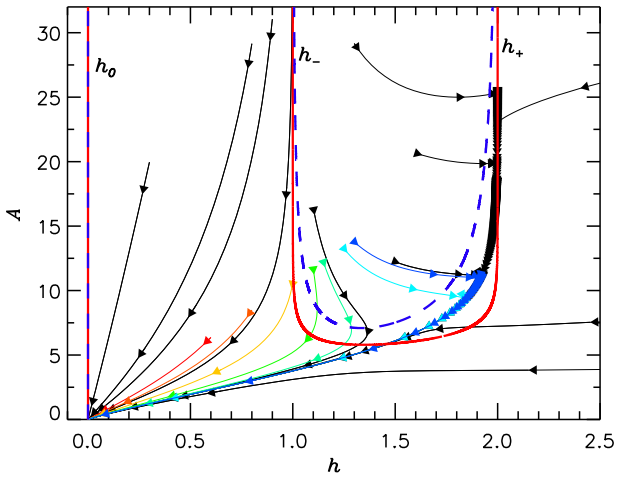

Figure 10.7: Phase space projected in variables A and h. In this variables the fixed point (resting state) is located at $(h, A) = (-1, 0)$.

With this approximation, the $h-$nullcline is given by

$$h_{\pm} = \frac{1}{2}\left(3 \pm \sqrt{1 - \frac{8\ln 2}{d^2}}\right), \quad h_0 = 0. \tag{10.14}$$

In this case we plot it with blue dashed lines. The evolution of the different initial conditions (10.8) in the phase space (h, d) is then organized by the $h-$nullclines as follows. For $h > 0$, $\dot{h} < 0$, except inside the U-shaped region delimited by h_- and h_+ where $\dot{h} > 0$. For initial conditions located at the right of h_- the trajectory evolves rapidly towards the nullcline h_+. This corresponds to the first stage of the excitable excursion. The center of the patch is very flat and evolves towards u_0^t at time scale is of order $\mathcal{O}(\mu)$ making h the fast variable of the dynamics, while d changes at a much smaller rate. The outcome of this stage is the formation of a kink-antikink pair connecting u_0^b with u_0^t and back to u_0^b. In the reduced phase space this means that the nullcline h_+ has been reached. After reaching the nullcline, the patch evolves slowly along h_+. This corresponds to the second stage of the excitable excursion in which kink and antikink slowly approach each other decreasing d following Eq.(10.7).

Finally the third stage in which kink and antikink annihilate each other corresponds to the fast jump to nullcline h_0. This reinjection mechanism is not following the remnants of a limit cycle in phase space since the system Eq.(10.2)

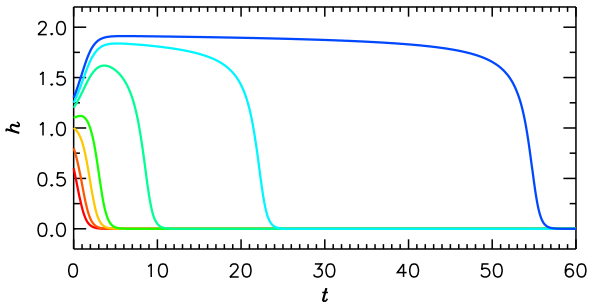

Figure 10.8: Projection of the trajectories on the h coordinate. Each color corresponds to a trajectory in Figure 10.6 and Figure 10.7. For all the trajectories $d_0 = 4.98$, and from bottom to top, $H_0 = 0.6, 0.8, 1.0, 1.1, 1.2, 1.25, 1.3$.

does not have periodic solutions. For initial conditions located at the left of h_- or below the connection of h_- with h_+, the system evolves quickly to h_0. This corresponds to sub-threshold perturbations which decay exponentially. A drawback of the (h, d) description is that the width of the patch is not well defined for $h = 0$. As a consequence it is not apparent in Figure 10.6 that all the trajectories evolve finally to u_0^b. A convenient way to avoid this is to use the area of the patch A instead of d as shown in Figure 10.7.

In this new phase space the theoretical prediction for the nullclines that we have used is

$$A = 4hd[1 - 2\exp(-L/2)] \tag{10.15}$$

for the $h-$nucline defined by Eq.(10.11), being L the size of the system and,

$$A = \sqrt{\frac{\pi}{\ln 2}}hd \tag{10.16}$$

for the nullcline defined by Eq.(10.14). In this representation all trajectories ultimately converge to the fixed point $(h, A) = (0, 0)$ which corresponds to u_0^b.

Altogether, it is evident that the $h-$nullclines organize very well the dynamics of the system. The approximate nullclines given by (10.11) agree very well with numerical simulations for large values of d (and A). For smaller values of d ($d < 3.5$) where the ansatz (10.9) is not expected to be good, the numerical simulations indicate that the nullcline h_+ is located slightly above the prediction (10.11). For this regime we have also considered the Gaussian ansatz (10.12). With nullclines predicted with this last ansatz we find, on the contrary, that the real nullcline is situated slightly bellow.

The time evolution of trajectories generated with an injected signal with different amplitude can be observed in Figure 10.8. Colors correspond to the trajectories shown in in Figure 10.6 and Figure 10.7. For $H_0 \gtrsim 1.1$ trajectories first grow while for $H_0 \lesssim 1.1$ they decay exponentially. In fact, the shape of the trajectories changes gradually and $H_0 \approx 1.1$ is a pseudo-threshold, as typical in Type II excitability.

To summarize, in this Section we have shown that annihilation of equivalent fronts with different polarities can lead to excitability without the presence of limit cycle in the dynamics. In the next Section we will study briefly how the presence of noise can trigger excitable excursions which is an interesting result due to the fact that in experimental setups fluctuations are normally present.

10.3 Effect of noise

Many studies have been devoted to the interplay between excitability and noise [19]. In particular the presence of noise can trigger excitable excursions even for subtreshold perturbations. We illustrate this effect in our system by injecting signals of the form (10.1) with a fluctuating amplitude

$$G = G^0 + \sqrt{D}\xi(t) \tag{10.17}$$

where $\xi(t)$ is a Gaussian white noise of zero mean and correlation

$$\langle \xi(t), \xi(t') \rangle = \delta(t - t'). \tag{10.18}$$

Figure 10.9 shows the effect of adding a signal of half-width $\Gamma = 15$ and duration $\Delta t = 2$ every $T = 200$. In this way it is possible to plot several events in the same figure. Those signals have $G^0 = 0.79$, just below the pseudo-threshold, and are subject to noise with $D = 0.3$. Without noise all the perturbations relax fast to u_0^b and there are no excitable patches. In contrast, when the noise is present, patches are triggered randomly.

10.4 Excitability mediated by non-equivalent fronts

So far we have focused in systems with bistability between two equivalent HSS i.e. two states with the same potential energy. Nevertheless excitable behavior can appear even when two HSSs are not equivalent, like for example in the normal GVD regime in the LL equation. In this Section we see that the mechanism previously presented generates excitability in these type of systems. To do that

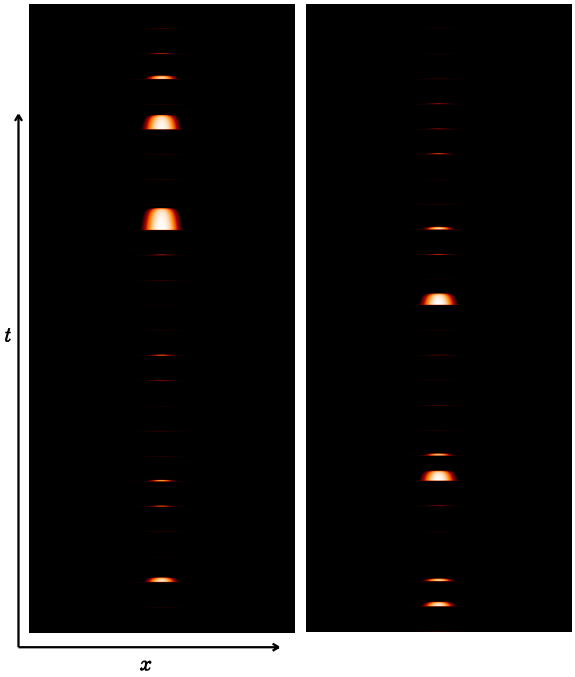

Figure 10.9: Simulation showing the dynamics generated by the repetitive addition of Gaussian signals (10.1) with a noisy amplitude (10.17). The range of x plotted is $[-22, 22]$ and the range of t is $[0, 5000]$ (left panel) and $[5000, 10000]$ (right panel). The values of the parameter are shown in the text.

we use one of the simplest models where fronts between non equivalent HSSs may occur, the one-dimensional real quintic GL equation:

$$\partial_t u = \mu u + u^3 - u^5 + \partial_x^2 u. \tag{10.19}$$

When the control parameter is set to be at the Maxwell point of the system, both the trivial and the up (down) HSSs have the same energy and a stationary front can be formed, just like in the previous case. On the contrary, when the system is not in the Maxwell point, the difference of energy between the HSSs makes that one state dominates on the other invading, in this way, all the domain.

It is known that two fronts of different polarity will move apart or closer depending on the energy balance between the forming HSSs. Here we show that in the region of parameters where the two fronts move closer, excitability can be also

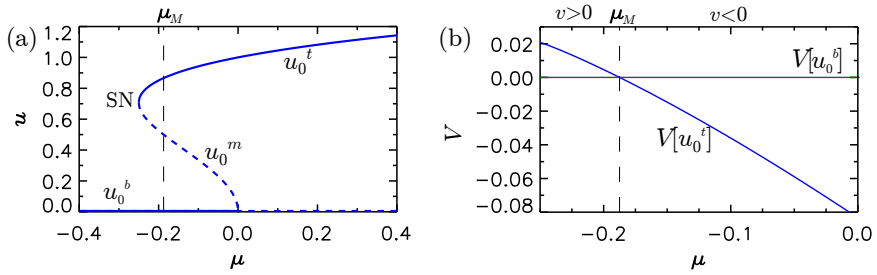

Figure 10.10: In panel (a) the subcritical pitchfork bifurcation scenario for the HHSs solutions is shown. In (b) we show the potential V of u_0^t and u_0^b in function of μ. The vertical dashed line represents the Maxwell point of the system, where $V[u_0^b] = V[u_0^t]$.

induced. To start, we first introduce some results regarding the real quintic GL equation and after that we analyze the excitability induced by these fronts.

10.4.1 The real Ginzburg-Landau with quintic non-linearity

For Eq.(10.19), the HSSs are given by the trivial solution $u_0^b = 0$ and the bifurcating states

$$u_0^m = \pm\sqrt{\frac{1}{2} - \sqrt{\mu + \frac{1}{4}}} \tag{10.20}$$

and

$$u_0^t = \pm\sqrt{\frac{1}{2} + \sqrt{\mu + \frac{1}{4}}} \tag{10.21}$$

Because Eq.(10.19) has $u \to -u$ symmetry, only positive values of amplitude u will be consider, unless stated otherwise. At $\mu = 0$, the trivial HSSs has a subcritical pitchfork bifurcation, where u_0^m unfolds unstable. Decreasing μ, the later state undergoes a SN bifurcation at $\mu = \mu_{\rm SN} \equiv -\frac{1}{4}$ from where u_0^t appears

This bifurcation scenario can be seen in Figure 10.10(a). Here in contrast to previous sections, two different types of fronts can be considered. First class are those formed between two equivalent HSSs as can be those connecting $-u_0^t$ with u_0^t. This case is equivalent to the one shown in the cubic GL equation in Section 10.2, due to its equal potential energy $V = V_5[u]$, these fronts are stationary. The second class are those fronts which occurr between u_0^b and u_0^t. At $\mu = \mu_M \equiv -\frac{3}{16}$, $V[u_0^b] = V[u_0^t]$, as seen in Figure 10.10(b), and therefore the fronts do not move. On the contrary, when $\mu \neq \mu_M$, $V[u_0^b] \neq V[u_0^t]$ and

the front is not stationary but it moves from left to right or from right to left depending on the balance between $V[u_0^b]$ and $V[u_0^t]$, that is the system evolves to the minimum potential energy configuration. As shown in Section 10.2, front velocity is given by,

$$v(\mu) = \frac{V[u_0^t] - V[u_0^b]}{\int \sqrt{u'(x)}dx}. \tag{10.22}$$

The potential of both states can be seen in Figure 10.10(b) as function of μ. When $V[u_0^t] > V[u_0^b]$, for $\mu < \mu_M$, front velocity is defined positive. The front moves from left to right and therefore u_0^b invade all the system. On the contrary, when $V[u_0^t] < V[u_0^b]$, for $\mu > \mu_M$, front velocity is defined negative and the top state will expand invading all the system.

In Ref.[23], front velocity was calculated explicitly. It was found to be,

$$v = \begin{cases} \frac{1}{\sqrt{3}}\left(2\sqrt{1+4\mu}-1\right) & \text{if} \quad \frac{-1}{4} < \mu < \frac{3}{4} \\ 2\sqrt{\mu} \quad \text{if} \quad \mu > \frac{3}{4}. \end{cases} \tag{10.23}$$

As done in the previous section, we study the spatial dynamics associated with this model. Defining the variables $u_1 = u$ and $u_2 = d_x u_1$ we can derive the system:

$$\begin{aligned} d_x u_1 &= u_2 \\ d_x u_2 &= u_1^5 - u_1^3 - \mu u_1 \end{aligned} \tag{10.24}$$

Around $u_0^b = 0$ and for $\mu < 0$, the eigenvalues of Jacobian of (10.24) satisfy $\lambda = \pm\sqrt{-\mu}$, and therefore trajectories approaching or leaving these states do it monotonically. Around u_0^t, the eigenvalues satisfy $\lambda = \pm\sqrt{4\mu + 2\sqrt{\mu + \frac{1}{4}} - 1}$, for $\mu_{\text{SN}} < \mu < 0$ and, as before, no spatial oscillations occurs around this state, which implies that no locking between fronts with different polarizations may occur. Due to this, no localized structures arise and fronts with opposite polarities move apart, or closer until they collide and annihilate each other.

10.4.2 Excitable dynamics

As we said before, at $\mu = \mu_M$, u_0^b and u_0^t have the same potential energy, and the dynamics of a patch formed between a kink and antikink fronts will be similar to the dynamics of the patches considered in Section 10.2, and therefore excitability may occurs in the same fashion than in the real cubic GL equation.

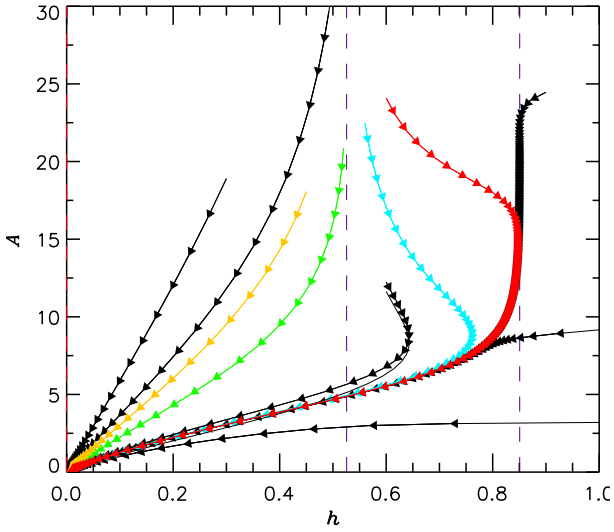

Figure 10.11: Projection of the time evolution of the patches into the 2-dimensional phase space defined by (A, h). This picture is equivalent that the one shown in Figure 10.7 in the context of the real cubic GL equation. Here $\mu = -0.2$

Here we focus on the excitability induced by the interaction of non-equivalent fronts connecting u_0^b and u_0^t, where we consider that the resting state is u_0^b, and then the excited state is a portion (patch) of states u_0^t embedded on u_0^b. With this configuration, front induced excitability can be found in regions of parameters where u_0^b is boost energetically, i.e. for $\mu < \mu_M$. In this context, the role of threshold is played by the unstable middle branch u_0^m.

For values of μ such that, $\mu > \mu_M$, u_0^t is boost energetically and any patches sitting on u_0^b do not shrink but expand until that u_0^t invades all the space. Due to this, excitability does not occur for the resting state u_0^b. At the end of this Section we will see that excitability behavior can be achieved in this regime due to the occurrence of convective instabilities.

As done in Section 10.2 the time evolution of the patches defined by Eq.(10.8) is projected on the particular space defined by (h, d) or (h, A). The $(h, A)-$projection space is show in Figure 10.11. Although quantitatively different, the scenario is qualitatively equivalent to the one shown in Figure 10.7 of Section 10.2. As we can observe, u_0^m acts as pseudo threshold, in such a way that perturbations

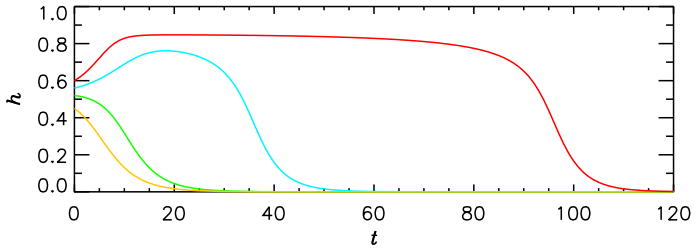

Figure 10.12: Projection of the time evolution of patches in h. The different colors refers to Figure 10.11 for $d_0 = 19.15$. From bottom to top, $H_0 = 0.45, 0.52, 0.56$ and 0.6.

bellow u_0^m will decay rapidly to u_0^b and perturbations above u_0^m will experience a large response before returning to the resting state.

Figure 10.12 shows the time evolution of initial patches with different H_0 and the same half width $d_0 = 19.15$. As done in Section 10.2. Colors correspond to the trajectories shown in Figure 10.11. For $H_0 \gtrsim 0.52$ trajectories first grow while for $H_0 \lesssim 0.52$ they decay exponentially. Here the shape of the trajectories changes gradually and $H_0 \approx 0.52$ is a pseudo-threshold, as typical in Type II excitability.

10.4.3 The non-linear convective regime

For values of μ such that, $\mu > \mu_M$, u_0^t is boost energetically and any patches sitting on u_0^b do not shrink but they expand until that u_0^t invades all the domain. Due to this, excitability does not occur for the resting state u_0^b. To avoid this situation one can induce drift instabilities by adding a convective or drift term $\sim c\partial_x u$ in Eq.(10.19), namely

$$\partial_t u = \mu u + u^3 - u^5 + \partial_x^2 u - c\partial_x u. \tag{10.25}$$

These instabilities are classified in two types, absolute and convective instabilities [20, 21]. In Chapter 6 we reviewed these instabilites in the context of LL equation when bistability occurred between an HSSs and a modulated one [22]. In our context the stable states involved in these instabilites are u_0^b and u_0^t. We say that the state u_0^b is connectively unstable, if localized perturbations are driven by the mean flow in such a way that they grow in the moving reference frame, but decay at any fixed location. On the contrary, in the absolute instability regime, localized perturbations grow at any fixed location, and the system finally reach completely the attractor u_0^t.

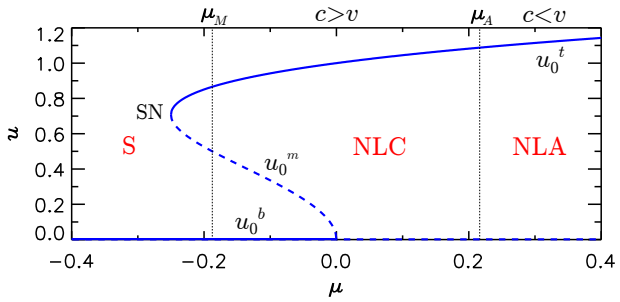

Figure 10.13: Homogeneous steady state of the quintic real GL equation. We show the absolute and convective non-linear instability regimes that arise when drift is considered.

In Ref.[20] it was shown that for $c \neq 0$, in the unstable domain ($\mu > -3/16$), the instability is nonlinear convective (NLC) when $v < c$, since, in this case, although expanding, a patch connecting u_0^b and u_0^t is finally advected out of the system. On the contrary when $v > c$, the instability is absolute (NLA) and the patch finally invades the system. Therefore the transition between NLC and NLA instabilities occurs at the value μ_A at which $v = c$, namely:

$$\mu_A = \begin{cases} \dfrac{3}{16}\left(c^2 - 1 + \dfrac{2c}{\sqrt{3}}\right) & \text{if} \quad c < \sqrt{3} \\ \dfrac{c^2}{4} & \text{if} \quad c > \sqrt{3} \end{cases} \tag{10.26}$$

The different instability regions for the HSSs of Eq.(10.25) are shown in Figure 10.13 In the NLC regime (for $\mu_M < \mu < \mu_A$), an excitable excursion can be trigger from the resting state u_0^b. In order to trigger this transient behavior we consider a the Gaussian perturbation (10.1) of finite duration and extension. To model a finite domain, we define the parameter μ to be space dependent with the shape of the super-Gaussian profile,

$$\tilde{\mu}(x) = (1+\mu)\exp\left(-\left(\frac{x - x_0}{\Lambda}\right)^{20}\right) - 1. \tag{10.27}$$

This is the same procedure that it was already used in Section 9.3. The profile (10.27) has a plateau on top of which $\tilde{\mu}(x) = \mu$ and outside $\tilde{\mu}(x) = -1$. In this way, outside the plateau the only attractor of the system is $u = u_0^b$ and therefore fronts disappear.

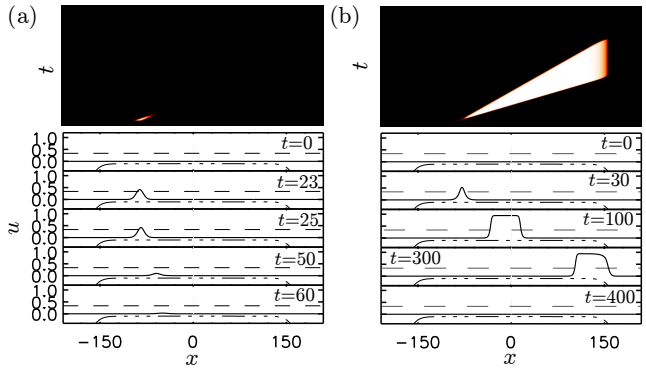

Figure 10.14: Spatiotemporal evolution of a Gaussian perturbation (10.1) with $\Gamma = 6.8$, switching on at $t = 20$ with a duration $\Delta t = 2$. In (a) $G = 0.22$, that is an under-threshold perturbation and in (b) the perturbation is over-threshold with $G = 0.23$ and we have excitable excursion in the convective regime. Here $\mu = -0.1$, $c = 1$, $\Lambda = 163.6$, $x_0 = 122.7$ and $L = 419$.

The spatiotemporal evolution of two different perturbations of the HSSs u_0^b are shown in Figure 10.14 when using the Gaussian (10.1), with $\Gamma = 6.8$ centered at $x_0 = 122.7$. Both perturbations have been switched on at $t = 20$ during a time $\Delta t = 2$. In (a), $G = 0.22$, and the height of the perturbation is not enough to generate a kink-anti-kink structure, and therefore it decays rapidly to u_0^b. This is in an under-threshold perturbation. The top panel (a) correspond to a contour plot of the evolution and the bottom one shows some snapshots of this evolution at fixed values of time. The pointed-dashed line represents the $\tilde{\mu}(x)$ and the dashed line stands for the unstable HSS solution u_0^m. In contrast, in panel (b) $G = 0.23$, in such a way that the perturbation, crosses u_0^m (the threshold in this context) and, while advected away, grows until reaching u_0^t where a kink and antikink states form a patch of height $h = u_0^t$. In this regime of parameters, the two fronts moves apart or closer at a velocity $v < c$.

Therefore the patch is advected faster than it grows, reaching the border of the plateau where both fronts annihilate each other and the system returns to the resting state $u = u_0^b$. Here, as in previous cases, we should talk about a pseudo-threshold because the transition between having excitability or not is smooth, not existing in this way a well defined separatrix.

10.5 Conclusions

To summarize, in the present Chapter we have presented and discussed evidence for a novel mechanism leading to the appearance of transient localized spatiotemporal structures, that we call patches. We have shown that these patches can be understood as excitable excursions. The mechanism presented here only requires the coexistence of two stable homogeneous solutions and a spatial coupling such that the fronts connecting the homogeneous solutions are monotonic. We have shown the existence of a pseudo-threshold such that, while sitting at one of the homogeneous states, sub-threshold perturbations decay exponentially. In contrast super-threshold perturbations induce a long excursion. The excursion is characterized by the fast emergence of a structure formed by two back to back fronts connecting the two homogeneous states followed by a slow approximation of the fronts until they eventually annihilate each-other. These two well separated time scales, which do not appear explicitly in the models used here, are an emerging property of the dynamics and allow for a clear observation of the patches. These patches resemble the excitable localized structures of [4], obtained when a stable oscillatory localized structure disappears through a limit-cycle instability, and also resemble the transient localized structures reported for a locally excitable medium [10]. From an observational point of view, while transient localized structures normally have a characteristic spatial size independent of the spatial extension of the perturbation, the size of the patches generated here is determined by that of the perturbation. From a fundamental perspective, the mechanism introduced here does not requires local excitability nor that the system supports localized structures. Furthermore, it neither requires the existence of a nearby oscillatory regime in parameter space. Thus, this mechanism could explain experimental observations of transient localized spots in more general setting. Systems with bistable homogeneous states in which this mechanism could be observed include, for instance, optical systems [12, 13] or chemical reactions [11].

This mechanism is described in the real cubic and quintic GL equations to cover both cases when the HSSs are equivalent and when they are not. We also have shows how these type of transient dynamics can be sustained with noise even for values of G bellow threshold. Finally we also have seen how convective instabilities offer a possible scenario for excitability.

References

[1] J. D. Murray, *Mathematical Biology,* 3rd ed. (Springer, New York, 2002).

[2] A. S. Mikhailov, *Foundations of Synergetics I,* (Springer, Berlin, 1994).

[3] E. Meron, *Pattern formation in excitable media,* Meron, Phys. Rep. **218**, 1 (1992).

[4] D. Gomila, M. A. Matías, and P. Colet, *Excitability mediated by localized structures in a dissipative nonlinear optical cavity,* Phys. Rev. Lett. **94**, 063905 (2005).

[5] D. Gomila, A. Jacobo, M. A. Matías, and P. Colet, *Phase-space structure of two-dimensional excitable localized structures,* Phys. Rev. E **75**, 026217 (2007); *Effects of a localized beam on the dynamics of excitable cavity solitons,* Phys. Rev. A 75, 053821 (2008).

[6] P. Parra-Rivas, D. Gomila, M. A. Matías and P. Colet, *Dissipative soliton excitability induced by spatial inhomogeneities and drift,* Phys. Rev. Lett. **110**, 064103 (2013).

[7] P. Parra-Rivas, D. Gomila, M. A. Matías, P. Colet, and L. Gelens, *Competition between drift and spatial defects leads to oscillatory and excitable dynamics of dissipative solitons,* Phys. Rev. E. **93**, 012211 (2016).

[8] J. Guckenheimer and P. Holmes, *Nonlinear Oscillations, Dynamical Systems, and Bifurcations of Vector Fields*, (Springer, New York, 1983).

[9] Y. A. Kuznetsov, *Elements fo Applied Bifurcation Theory*, 3rd ed. (Springer, New York, 2004).

[10] I. Hecht, D. A. Kessler, and H. Levine,*Transient Localized Patterns in Noise-Driven Reaction-Diffusion Systems*, Phys. Rev. Lett. **104**, 158301 (2010).

[11] B. Marts, K. Martinez, and A. L. Lin, *Front dynamics in an oscillatory bistable Belousov-Zhabotinsky chemical reaction*, Phys. Rev. E **70**, 056223 (2004); B. Marts, A. Hagberg, E. Meron, and A. L. Lin,*Resonant and nonresonant patterns in forced oscillators*, Chaos **16**, 037113 (2006); E. Meron, M. Bar, A. Hagberg, and U. Thiele, *Front dynamics in catalytic surface reactions*, Catalysis Today **70**, 331 (2001).

[12] F. Marino, G. Giacomelli, and S.Barland, *Front pinning and localized states analogues in long-delayed bistable systems,* Phys. Rev. Lett. **112**, 103901 (2014).

[13] M. Pesch, W. Lange, D. Gomila, T. Ackemann, W. J. Firth, and G.L. Oppo, *Two-dimensional front dynamics and spatial solitons in a nonlinear optical system*, Phys. Rev. Lett. **99**, 153902 (2007).

[14] M. Postma, J. Roelofs, J. Goedhart, T. W. J. Gadella, A. J. W. G. Visser, and P. J. M. V. Haastert *,Uniform cAMP stimulation of Dictyostelium cells induces localized patches of signal transduction and pseudopodia* Mol. Biol. Cell **14**, 5019 (2003).

[15] C.H. Huang, M. Tang, C. Shi, P. A. Iglesias, and P. N. Devreotes, *An excitable signal integrator couples to an idling cytoskeletal oscillator to drive cell migration*, Nat. Cell Biol. **15**, 1307 (2013).

[16] P. Coullet, C. Elphick, and D. Repaux, *Nature of spatial chaos*, Phys. Rev. Lett. **58**, 431 (1987).

[17] J. W. Cahn and J. E. Hilliard, *Free energy of a nonuniform system. I. Interfacial free energy*, J. Chem. Phys. **28**, 258 (1958).

[18] W. Gerstner and W. Kistler, *Spiking neuron models. Single neurons, populations, plasticity*, (Cambridge U.P., Cambridge (UK), 2002).

[19] B. Lindner, J. García-Ojalvo, A. Neiman, and L. Schimansky-Geier,*Effects of noise in excitable systems*, Phys. Rep. **392**, 321 (2004).

[20] J. M. Chomaz, *Absolute and convective instabilities in nonlinear systems*, Phys. Rev.

Lett. **69**, 13, (1992).

[21] A. Couairon, J. M. Chomaz, *Absolute and convective instabilities, front velocities and global modes in nonlinear systems* , Physica D **108**, 236-276 (1997).

[22] A. Mussot, E. Louvergneaux, N. Akhmediev, F. Reynaud, L. Delage, and M. Taki, *Optical fiber systems are convectively unstable*, Phys. Rev. Lett. **101**, 113904 (2008).

[23] P. Colet, M. San Miguel, D. Walgraef, *Convective and Absolute Instabilities in the Sub-critical Ginzburg-Landau Equation*, Europ. Phys, J. B **11**, 517-524, (1999).

Chapter 11

Conclusions and Outlook

11.1 Summary of results

In this thesis we have studied emergent structures in spatially extended systems, that are *dissipative*. Thermodynamically speaking such type of systems are open systems interchanging energy and matter with the medium, and therefore far from the thermodynamical equilibrium. In this context, emergent structures are known as *dissipative structures*. These structures arise in a wide number of natural systems such as fluid dynamics, plasma physics, chemistry, plant ecology, nonlinear optics and biology [1–3]. An important subgroup of the dissipative structures is the one composed of *localized states* (LSs) or *dissipative solitons* (DSs), which can be seen as spots of a one state embedded in a different one [4].

A system that is internally damped and externally driven is a relevant example of a dissipative system. In this thesis we have focused on the field of nonlinear optics where we have studied a particular type of those systems: a driven nonlinear optical cavity with losses. Here, due to the double balance between spatial coupling and nonlinearity on the one hand and gain and losses on the other, a wide variety of LSs arises.

When the material inside the cavity or the cavity has a Kerr-type nonlinearity, the dynamics of a pulse of light propagating inside the cavity is described by the Lugiato-Lefever (LL) model [5]. This model is a type of forced complex Ginzburg-Landau (FCGL) equation at $1:1$ resonance, although it can also be seen as a driven and damped nonlinear Schrodinger (NLS) equation. This equation has been widely studied since it was proposed in 1987 to describe a ring-cavity partially filled with a nonlinear medium. In the last few years it has

become widely studied by the scientific communities working on frequency comb (FC) generation in microresonators [6, 7].

Here we have investigated one particular type of driven nonlinear optical, *temporal cavities*, that are described by the one-dimensional LL equation.

Within the previous ten Chapters, using dynamical system and bifurcation theories we have analyzed in detail the different dynamical regimes that this equation exhibits depending on the control parameters of the system. By applying asymptotic methods (weakly nonlinear analysis), numerical continuation techniques and numerical simulations we have been able to analyze the dynamics, stability and bifurcation structure for the different types of static or dynamical states arising in the system, which will be of interest for experimentalists working in the field of nonlinear optical cavities and in FC generation.

In **Chapter 2** we have studied the spatial dynamics of the LL equation. This consists on analyzing the stationary LL equation as a dynamical system of finite dimension. In this context LS solutions of the stationary LL equation, biasymptotic to the homogeneous steady state (HSS), correspond to homoclinic orbits to such points. The HSS solutions are monovaluate for $\theta < \sqrt{3}$ and trivaluate for $\theta > \sqrt{3}$, with three solution branches separated by two saddle-nodes (SNs) one on the top and one on the bottom of a $S-$shape bifurcation diagram. We have performed a linear stability analysis of the spatial system around the HSS solutions and we have identified the different bifurcations that they undergo, in both the anomalous and normal group velocity dispersion (GVD) regimes. After that, using normal form theory we have identified the possible types of LSs or patterns arising from those bifurcations. Some of these results are published in Refs. [8, 9].

Chapter 3 and **Chapter 4** are focused on the anomalous GVD regime. In **Chapter 3** we analyzed the different types of patterns solutions appearing in the system. In particular we have studied in detail the pattern with the critical wavenumber k_c arising from a modulational instability (MI) for $\theta < 2$. Applying weakly nonlinear analysis around the MI and using a numerical continuation algorithm we have calculated the branches of pattern solutions for any value of $\theta < 2$. This bifurcation skeleton has allowed us to identify that for some regimes of parameters, patterns of a given wavelength λ are connected to patterns with a wavelength $\lambda/2$ and the latter ones to others with $\lambda/4$ and so on. Doing a detailed stability analysis of the patterns we have discovered that such type of connection points consist in secondary bifurcations known as *finite wave instabilities* (FWs). Furthermore, applying the same analysis we were also able to find other secondary bifurcations of the patterns such as Eckhaus bifurcations

or wave instabilities. Together with the pattern with critical wavenumber k_c we showed that there is a wide family of patterns with different wavelengths coexisting and sharing the same type of dynamics and bifurcation structure, whose region of existence expands also to $\theta > 2$.

After that, in **Chapter 4**, we have investigated the formation of bright LSs in the anomalous GVD regime. According to the spatial eigenvalues of the HSSs found in Chapter 2 two different regimes must be considered. For $\theta < 2$ normal form theory around the MI shows that bright LSs unfold, together with the pattern, when the pattern is subcritical (for $\theta > 41/30$). In this way we have obtained an asymptotic analytical solution for the LS. Later we have built up the *homoclinic snaking* bifurcation diagram for these LSs at different values of the control parameters. For $\theta > 2$ the MI has disappeared and now the LSs unfold from one of the saddle-node (SN) bifurcations of the HSSs. We have found that these type of LSs are organized in new type of bifurcation structure known as *foliated snaking*. For high values of θ these states become unstable through supercritical Hopf bifurcations and they start to oscillate in amplitude. Using numerical simulation we have identified that these oscillatory states undergo secondary bifurcations that start a route to temporal chaos. Spatiotemporal chaos is also present in this regime. These results are partially published in Ref. [8].

Chapter 5 is dedicated to the normal GVD regime. Here the LSs are dark solitons formed due to the locking of two fronts or switching waves (SWs) of different polarities connecting the top and bottom HSSs. Applying the same asymptotic techniques as in previous Chapters we have found that they unfold from the top SN of the HSSs, as predicted by the theory. Later we have shown that these states are organized in a *collapsing snaking* bifurcation structure. For high values of the cavity detuning dark solitons also undergo oscillatory instabilities where they start to oscillate in amplitude. Secondary bifurcations of these cycles start a route to temporal chaos in the same fashion as bright LSs in the anomalous regime. We have characterized the different bifurcation regions as function of the control parameters. These results were published in Refs. [9, 10].

In **Chapter 6** we studied how third order dispersion (TOD) effects modify the dynamics, stability and bifurcation structure of LSs in both the anomalous and normal GVD regimes. This effect is modeled by a term $\sim d_3\partial_x^3 A$, that on the one hand breaks the spatial reversibility symmetry of the LL model, and therefore of its solutions, and on the other hand induces a drift instability, in such a way that now any LS moves at a constant velocity determined by

the control parameters. In both regimes, we have discovered that oscillatory and chaotic dynamics are suppressed by this effect for both bright and dark structures. Furthermore the bifurcation structures are modified in different ways depending on the parameters. Moreover, in the normal dispersion regime, TOD also stabilizes bright solitons, and therefore regions of multistability between dark and bright LSs are found. This work has been published in Refs. [11, 12].

Chapter 7 is focused on the interaction of solitons and the formation of bound states (BSs), i.e. aggregations of single-peak LSs at different separation distances. Here we have focused on the anomalous regime and therefore bright solitons, although the results are general and therefore also applicable to dark solitons. We have derived an effective interaction potential using both the complete and interaction Hamiltonian of the LL equation and we have found that the stable separation distances are discrete and determined by the minimum of this potential. This is also the case when considering any reversible generalization such as adding a fourth order dispersion (FOD) effect. The potential is determined by the overlapping of the tails of one soliton with the core of the other one, and therefore the interaction is intrinsically related with the presence or absence of oscillatory tails in the solitons' profiles. Furthermore we have determined that the periodicity of the potential corresponds to the wavelength of the oscillatory tails of the solitons involved in the interaction. This principle also applies when considering terms that break spatial reversibility such as TOD, although in this case the maxima, and not the minima of the potential, determine the stable separation distances. Moreover we have studied the bifurcation diagrams for some particular arrays of LSs and we have analyzed the effects of adding a noisy background in the stability of the different BSs.

In **Chapter 8** we have investigated how the presence of inhomogeneities, (or defects) and drift modifies the dynamics of DSs in the LL model. The effects of these two elements on a soliton is that while a defect pins the soliton to a fixed position, the drift tries to pull it out. We have shown that the competition between these two ingredients induces a very rich dynamical behavior going from oscillatory states to excitability of DSs. Using bifurcation theory we have identified the bifurcations behind the origin of the previous dynamical regimes. Moreover, we have also studied the oscillatory dynamics in the presence of periodic and absorbing boundary conditions. These results have been published in Ref. [13].

In **Chapter 9** we have shown that the dynamics induced by the presence of defects and drift on DSs are generic and not just a particularity of the LL equation. To show this generality we have used the prototypical Swift-Hohenberg

(SH) equation. We have studied in detail the different dynamical regimes arising in this system such as oscillatory states (train of solitons) and excitability, and we have found that all these dynamics unfold from two Takens-Bodganov (TB) bifurcations. Type I and II excitability have been found as usual near the bifurcations where the oscillatory states appears or disappears. Furthermore we have also studied this type of dynamics when the defect appears in the gain of the model. In this case, although the bifurcation scenario is much more complex, the same dynamical regimes have been found. This research has been published in Refs. [14, 15].

Finally in **Chapter 10** we have presented a novel mechanism leading to the appearance of transient localized spatiotemporal structures, which can be understood as excitable excursions. This mechanism only requires two ingredients: the coexistence of two HSSs and spatial coupling such that the fronts connecting the two HSSs annihilate each other. This new type of excitability does not require that the system is locally excitable, nor that an oscillatory LS disappears through a limit-cycle instability. We have found that this type of behavior exists in the LL model in the normal dispersion regime. Furthermore we have studied this mechanism in detail in two cases: when the HSSs solutions are equivalent, and when they are not. For the first analysis we have used the real cubic Ginzburg-Landau (GL) equation, and for the second one the real quintic GL equation. Moreover, we have studied how excursions can be randomly triggered when noise is considered. This work was partially published in Ref. [16].

11.2 Future directions

Despite the fact that the LL model has been analyzed for several decades, and although we have tried to perform a complete and detailed study of this equation, there still remain many open questions. Here we list several directions for future research, inspired by some of the results of this work.

Unfolding of the quadruple zero bifurcation

In Chapter 2, while studying the spatial dynamics of the LL equation, we have seen that the different bifurcations that the HSSs exhibit unfold from a codimension-two point known as Quadruple zero (QZ) bifurcation with the spatial eigenvalue $\lambda = 0$ with multiplicity four. Although the unfolding of this bifurcation was already studied in Ref. [17], a complete understanding on the dynamics of LSs around this point is still lacking. In the LL equation the QZ occurs at $\theta = 2$ for both the anomalous and normal GVD regimes. A bet-

ter comprehension of this point is crucial to understand the transition between homoclinic snaking (for $\theta < 2$) and foliated snaking ($\theta > 2$) occurring in the anomalous GVD regime. We have recently found that in a neigborhood about the QZ the LL equation can be reduced to a SH-type of equation with a quadratic nonlinearity [18]. Thus we hope that the study of this last equation can help us to understand how the dynamics of the system behaves about such point.

Furthermore, it would be also interesting to study the transitions occurring in other systems when passing through this point as for example in the modified real SH equation [19]:

$$\partial_t u = \eta + \varepsilon u - u^3 - \nu \partial_x^2 u - \partial_x^4 u. \tag{11.1}$$

Here, in contrast, a preliminary analysis has shown that a transition between homoclinic and collapsing snaking occurs when going through the QZ.

Unfolding of the Fold-Hopf bifurcation

In Chapter 4, while studying bright LSs in the anomalous GVD regime, we saw that the supercritical Hopf bifurcation is responsible for the oscillatory dynamics that unfolds from a codimension-two point known as a Gravilov-Guckenheimer (GG) or Fold-Hopf (FH) bifurcation [20, 21]. It would be interesting to study the different unfoldings of its normal form and identify which one corresponds to our particular case. This can be useful in order to understand the origin of temporal chaos appearing for high values of frequency detuning.

Conservative limit of the Lugiato-Lefever model

For high values of the detuning, the dynamics of the LL equation become more and more complex, and LSs exhibit amplitude oscillations at different frequencies, temporal chaos and spatiotemporal chaos. Although the derivation of the LL equation in optical cavities is only valid for low values of detuning, from a mathematical point of view it would be interesting to study the origin of the previous dynamics when considering $\theta \to \infty$, for both the anomalous and normal regimes.

To study this problem it is first necessary to consider the rescaling, $T = \theta t$, $X = \sqrt{\theta} x$ and $\psi = A/\sqrt{\theta}$ that reduce the LL model to the following equation:

$$\partial_T \psi = -(\alpha + i)\psi + i\partial_X^2 \psi + i|\psi|^2 \psi + \sigma \tag{11.2}$$

with

$$\sigma = \frac{\rho}{\theta^{3/2}}, \qquad \text{and} \qquad \alpha = \frac{1}{\theta}. \tag{11.3}$$

If one takes $\theta \to \infty$, then $\alpha, \sigma \to 0$, and Eq.(11.3) becomes a NLS-type of equation [22]. Therefore the study of the dynamics of the LL equation for very high values of detuning reduces to the study of Eq.(11.3) for low values of α and σ. In this way the origin of the previous dynamics will be related with the point $(\alpha, \sigma) = (0, 0)$, i.e. the *conservative limit* of the LL equation.

Effects of fourth-order dispersion and nonlocal interaction on the bifurcation structure and dynamics of LSs in the LL model

In Chapter 6 we have studied how TOD effect modifies the dynamics, stability and bifurcation structure of solitons in both the anomalous and normal GVD regimes. It is known that the presence of FOD terms in the LL equation stabilizes dark solitons in the anomalous regime [23]. In future work we expect to understand how FOD and other high order effects, modify the different scenarios presented within this thesis. Together with those dispersion effects, the analysis of Raman and thermal effects, both modeled by nonlocal terms, would be relevant for theorists and experimentalist.

Understanding dynamics in general systems driven near their natural frequency

We plan to study more general systems driven near their natural frequency. We will repeat the analysis done in the LL model in a broader class of systems, those described by the forced complex GL (FCGL) equation at 1:1 resonance, namely

$$\partial_t A = (\mu + i\theta)A + (1 + i\alpha)\partial_x^2 A - (1 + i\beta)|A|^2 A + \rho. \tag{11.4}$$

Despite its generic character and importance, surprisingly little is known about the dynamics of this equation. We will characterize to which extent results obtained in the LL model are transferable to the universal Ginzburg-Landau equation at 1:1 resonance [24].

References

[1] M. Cross and P. Hohenberg, *Pattern-formation outside of equilibrium,* Rev. Mod. Phys. **65**, 851-1112, 1993.

[2] J. Murray, *Mathematical Biology,* Springer, New York, 1989.

[3] R. Hoyle, *Pattern Formation: an introduction to methods,* Cambridge Univer- sity Press, 2006.

[4] N. Akhmediev and A. Ankiewicz (eds.), *Dissipative Solitons, Lecture Notes in Physics,* Vol. 661 (Springer, New York, 2005); *Disipative Solitons: From Optics to Biology and Medicine, Lecture Notes in Physics,* Vol. 751 (Springer, New York, 2008).

[5] L. A. Lugiato and R. Lefever, Spatial dissipative structures in passive optical systems, Phys. Rev. Lett. **58**, 2209-2211, 1987.

[6] S. Coen, H. G. Randle, T. Sylvestre, and M. Erkintalo, *Modeling of octave-spanning Kerr frequency combs using a generalized mean-field Lugiato-Lefever model,* Opt. Lett. **38**, 37 (2013).

[7] Y. K. Chembo and C. Menyuk, *Spatiotemporal Lugiato-Lefever formalism for Kerr-comb generation in whispering-gallery-mode resonators,* Phys. Rev. A **87**, 053852 (2013).

[8] P. Parra-Rivas, D. Gomila, M. A. Matías, *Dynamics of localized and patterned structures in the Lugiato-Lefever equation determine the stability and shape of optical frequency combs,* S. Coen, and L. Gelens, Phys. Rev. A **89**, 043813 (2014).

[9] P. Parra-Rivas, E. Knobloch, D. Gomila, L. Gelens, *Dark solitons in the Lugiato-Lefever equation with normal dispersion,* Physical Review A **93**, 063839 (1-17) (2016).

[10] P. Parra-Rivas, D. Gomila, E. Knobloch, S. Coen, L. Gelens, *Origin and stability of dark pulse Kerr combs in normal dispersion resonators,* Optics Letters **41**, 2402-2405 (2016).

[11] P. Parra-Rivas, D. Gomila, F. Leo, S. Coen and L. Gelens, *Third-order chromatic dispersion stabilizes Kerr frequency combs*, Opt. Lett. **39**, 2971-2974 (2014).

[12] P. Parra-Rivas, D. Gomila, and L. Gelens, *Stable dark and bright soliton Kerr combs can coexist in normal dispersion resonators,* Opt. Lett. (2016).

[13] P. Parra-Rivas, D. Gomila, M. A. Matías, P. Colet, and L. Gelens, *Effects of inhomogeneities and drift on the dynamics of temporal solitons in fiber cavities and microresonators*, Optics Express **22**, 30943-30954 (2014).

[14] P. Parra-Rivas, D. Gomila, M. A. Matías and P. Colet, *Dissipative soliton excitability induced by spatial inhomogeneities and drift,* Phys. Rev. Lett. **110**, 064103 (2013).

[15] P. Parra-Rivas, D. Gomila, M. A. Matías and P. Colet, P. Parra-Rivas, D. Gomila, M. A. Matías, P. Colet, and L. Gelens, *Competition between drift and spatial defects leads to oscillatory and excitable dynamics of dissipative solitons,* Phys. Rev. E. **93**, 012211 (2016).

[16] P. Parra-Rivas, M. A. Matías, P. Colet, L. Gelens, D. Walgraef and D. Gomila, *Front interaction induces excitable behavior*, (submitted), (2016).

[17] G. Iooss, *A codimension-2 bifurcation for reversible systems*, Field Institute communications, 4, 201-217, 1995.

[18] B. Buffoni, A. R. Champneys and J. F. Toland, *Bifurcation and coalescence of a plethora of homoclinic orbits for a Hamiltonian system,* J. Dyn. and Diff. Eq., **8**, 2, 1996.

[19] M. Tlidi, P. Mandel, and R. Lefever, *Localized structures and localized patterns in optical bistability,* Phys. Rev. Lett. **73**, 640, 1994.

[20] J. Guckenheimer and P. Holmes, *Nonlinear Oscillations, Dynamical Systems, and Bifurcations of Vector Fields*,(Springer, New York, 1983).

[21] P. Gaspard, *Local birth of homoclinic chaos*, Phys. D (Amsterdam) **62**, 94 1993.

[22] I. V. Barashenkov and Y. S. Smirnov, *Existence and stability chart for the ac-driven, damped nonlinear Schrodinger solitons*, Phys. Rev. E, **54**, 5, 1996.

[23] M. Tlidi, L Gelens *High-order dispersion stabilizes dark dissipative solitons in all-fiber cavities*, Op. Lett., **35** (3), 306-308, 2010.

[24] Y.P. Ma, J. Burke, E. Knobloch, *Defect-mediated snaking: A new growth mechanism for localized structures,* Physica D **239** (2010) 1867-1883.

Appendices

Appendix A

Dynamical systems and bifurcation theory

In this chapter, we review some general results from dynamical systems theory and bifurcation theory. These topics are covered in much more depth in Refs. [1–5].

A.1 Dynamical system theory

We consider a nonlinear *dynamical system* defined by the set of n first-order ordinary differential equations

$$\dot{x} \equiv \frac{dx}{dt} = f(x, t; \mu), \tag{A.1}$$

where $x \in \mathbb{R}^n$ is a vector describing the state of the system, $t \in \mathbb{R}$ is the independent variable that we refers as "time", and $\mu \in \mathbb{R}^p$ describes system parameters. The *vector field*

$$f : \mathbb{R}^n \times \mathbb{R}^p \longrightarrow \mathbb{R}^n,$$

has the relevant information of the physical system, and Eq.(A.1) describes the evolution of the state x as determined by f. Let us initially neglect the dependence of the field with the parameters.

By a *solution* of Eq.(A.1) we mean a map, $\bar{x}$, from some interval $I \subset \mathbb{R}$ into $\mathbb{R}^n$, namely

$$\bar{x} : I \longrightarrow \mathbb{R}^n, \qquad t \longmapsto \bar{x}(t), \tag{A.2}$$

such that $\bar{x}(t)$ satisfies Eq.(A.1) i.e.

$$\dot{\bar{x}}(t) = f(\bar{x}(t), t; \mu).$$

Geometrically we can interpret the map (A.2) as a curve in $\mathbb{R}^n$, whose tangent vector at each point is defined by the dynamical system (A.1), Therefore we also refer to (A.1) as a vector field. The space of dependent variables of (A.1) i.e. $\mathbb{R}^n$ is called *phase space*.

Two types of dynamical systems can be considered depending on the the explicit dependence with the independent variable t or not. If the dynamical system explicitly depends on t i.e. $\dot{x} = f(x, t; \mu)$ it is referred as *non-autonomous* or *time dependent* dynamical system, and if the dependence with t is not explicit i.e. $\dot{x} = f(x; \mu)$ they are referred as *autonomous* or *time independent* dynamical systems. Along this thesis we will deal with the later case.

We say that the vector field f generates a flow $\phi_t : \mathbb{R} \to \mathbb{R}$, where $\phi_t(x) = \phi(x, t)$ with $t \in I \subseteq \mathbb{R}$ and satisfying

$$\frac{d}{dt}\left(\phi(x,t)\right) = f\left(\phi(x,t); \mu\right). \tag{A.3}$$

The flow ϕ_t satisfies the group properties (i) $\phi_0 = \mathrm{Id}$, and ii) $\phi_{t+s} = \phi_t \circ \phi_s$.

With this notation, a particular solution of the dynamical system which passes through x_0 at $t = 0$ can be written as $\phi(x_0, t)$. The map $\phi(x_0, \cdot) : I \to \mathbb{R}^n$ defines the *trajectory, phase curve* or *orbit* Γ of the dynamical system A.1 based on x_0:

$$\Gamma \equiv \{y : y = \phi(x_0, t)\} \tag{A.4}$$

Between the different types of solutions of (A.1) we focus in the following:

Definition 1 (Stationary, fixed point or equilibrium solution) *Given the autonomous dynamical system $\dot{x} = f(x; \mu)$, one defines a stationary solution of that system as a point $x_s \in \mathbb{R}^n$ such that $f(x_s; \mu) = 0$. Thus a solution that does not change with t. Or in terms of the flow, $\phi(x_s, t) = x_s$.*

Definition 2 (Periodic orbit) *One says that a point is periodic of period T iff $\phi(x, t + T) = \phi(x, t)$ for all t, and $\phi(x, t + s) \neq \phi(x, t)$ for all $0 < s < T$. Then, the curve $\Gamma \equiv \{y : y = \phi(x, t), 0 \leq t < T\}$ is called a periodic orbit of the system A.1, and is a closed curve in phase space.*

Definition 3 (Invariant set) *A set $\Sigma \subset \mathbb{R}^n$ is invariant under the action of the flow ϕ_t iff for all $x \in \Sigma$, then $\phi(x,t) \in \Sigma$ for all t. Stationary points, periodic orbits and strange attractors are some examples of a invariant sets. When the set Σ has differentiable structure we call it invariant manifold.*

Definition 4 (Local stable and unstable manifolds for an invariant set) *The local stable and unstable manifolds of an invariant set are defined respectively by*

$$W^s_{\text{loc}}(\Sigma) \equiv \{x \in U \subset \mathbb{R}^n : \phi_t(x) \to \Sigma, t \to \infty\} \tag{A.5}$$

$$W^u_{\text{loc}}(\Sigma) \equiv \{x \in U \subset \mathbb{R}^n : \phi_t(x) \to \Sigma, t \to -\infty\}, \tag{A.6}$$

where U is a neighborhood of the invariant set Σ both of them are invariant under the action of ϕ_t.

These definitions can be adapted for stationary points or periodic orbits.

A.2 Stability of trajectories

The stability of solutions of differential equations can be a very difficult property to pin down. Here we will concentrate in two of the most commonly used definitions. Roughly speaking, if $\bar{x}(t)$ is a solution of the dynamical system (A.1), then we say that $\bar{x}(t)$ is *stable* if solutions starting "close" to $\bar{x}(t)$ at a given time remain close to it for all later times. Moreover, $\bar{x}(t)$ is *asymptotically stable* if nearby solutions not only stay close, but also converge to $\bar{x}(t)$ as $t \to \infty$. These two types of stability can be formalized as follows.

Definition 5 (Lyapunov stability) *The solution $\bar{x}(t)$ is said to be stable (or Lyapunov stable) if, given $\epsilon > 0$, there exist a $\delta = \delta(\epsilon) > 0$ such that, for any other solution, $y(t)$, of (A.1) satisfying $||\bar{x}(t_0) - y(t_0)|| < \delta$, then $||\bar{x}(t) - y(t)|| < \epsilon$ for $t > t_0$, $t_0 \in \mathbb{R}$. Here $||\cdot||$ stands for the norm in $\mathbb{R}^n$.*

Definition 6 (Asymptotic stability) *The solution $\bar{x}(t)$ is said to be asymptotically stable if it is Lyapunov stable and for any other solution, $y(t)$, of (A.1), there exist a constant $b > 0$ such that, if $||\bar{x}(t_0) - y(t_0)|| < b$, then*

$$\lim_{t \to \infty} ||\bar{x}(t) - y(t)|| = 0.$$

These definitions provide different types of stability, however, they do not provide us with a method for determined when a given solution is or not stable. In the following we present method based on the linearization of the system (A.1) about a solution $\bar{x}(t)$. We call this procedure *linear stability analysis*.

A.3 Linearization of the nonlinear system

A good point to start the study of a nonlinear dynamical system is by characterizing the dynamics of the system near a solution $\bar{x}$. So let us consider that

$$x(t) = \bar{x}(t) + \epsilon y(t), \tag{A.7}$$

with $\epsilon \ll 1$. Inserting (A.7) in Eq.(A.1) and Taylor expanding about $\bar{x}$ gives

$$\dot{x} = \dot{\bar{x}}(t) + \dot{y}(t) = f(\bar{x}(t)) + \mathcal{D}f(\bar{x})y + \mathcal{O}(||y||^2), \tag{A.8}$$

where $\mathcal{D}f$ is the derivative (Jacobian) of f. Eq.(A.9) reduces to

$$\dot{y}(t) = \mathcal{D}f(\bar{x})y + N(y), \tag{A.9}$$

with $N = \mathcal{O}(||y||^2)$ being the nonlinear terms.

The evolution of trajectories arbitrarily close to $\bar{x}$ is then described by the *linear system*

$$\dot{y}(t) = \mathcal{D}f(\bar{x})y. \tag{A.10}$$

The first difficulty appears when one tries to solve Eq.(A.10), since here there are no general analytical methods for finding the solutions of linear ODEs with time-dependent coefficients. However, when the solution is a fixed point $\bar{x}(t) = x_s$ or a periodic orbit, the solution can be found easily.

In most of the thesis we are working with stationary solutions so from now on we will develop the theory of dynamical systems for these type of solutions. So, if $\bar{x}(t) = x_s$, then $\mathcal{D}f(\bar{x}) = \mathcal{D}f(x_s)$ is a matrix with constant coefficients and the solution of the system (A.10) through the point $y_0 \in \mathbb{R}^n$ at $t = 0$ is given by

$$y(t) = \mathrm{e}^{\mathcal{D}f(x_s)t} y_0. \tag{A.11}$$

Here the *linear flow* $\mathrm{e}^{\mathcal{D}f(x_s)t}$ is generated by the linear vector field $\mathcal{D}f(x_s)y$.

After calculating the eigenvalues $\{\lambda_i\}_{i=1,n}$ and eigenvectors $\{e_i\}_{i=1,n}$ of $\mathcal{D}f(x_s)$, solution (A.11) can be also expressed in the form

$$y(t) = \sum_{i=1}^{n} a_i e_i \mathrm{e}^{\lambda_i t}, \tag{A.12}$$

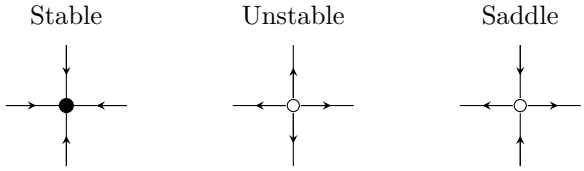

Figure A.1: Illustration of a stable, an unstable and a saddle fixed point (illustrated with straight line trajectories, for the sake of simplicity)

where a_i are constant coefficients determined by $y(t=0)$.

Then we say that $y(t)$ is asymptotically stable if all the eigenvalues of $\mathcal{D}f(x_s)$ have negative real parts. If this happens it is not difficult to prove that the equilibrium solution x_s of the nonlinear vector field (A.1) is asymptotically stable [1].

Depending on the real part of the eigenvalues we can define the stable, unstable and center subspaces for the linear system (A.10):

$$\begin{array}{l} E^s \equiv \text{span}\{e_1, \ldots, e_{n_s}\}, \\ E^u \equiv \text{span}\{e_{n_s+1}, \ldots, e_{n_s+n_u}\}, \\ E^c \equiv \text{span}\{e_{n_s+n_u+1}, \ldots, e_{n_s+n_u+n_c}\}, \end{array} \qquad n_s + n_u + n_c = n, \tag{A.13}$$

such that and where $\{e_1, \ldots, e_{n_s}\}$ are the eigenvectors of $\mathcal{D}f(x_s)$ corresponding to the eigenvalues $\{\lambda_i\}_{i=1,n_s}$ such that $\text{Re}[\lambda_i] < 0$, $\{e_{n_s+1}, \ldots, e_{n_s+n_u}\}$ those corresponding to the eigenvalues $\{\lambda_i\}_{i=n_s+1,n_s+n_u}$ with $\text{Re}[\lambda_i] > 0$ and $\{e_{n_s+n_u+1}, \ldots, e_{n_s+n_u+n_c}\}$ those corresponding to $\{\lambda_i\}_{i=n_s+n_u+1,n_s+n_u+n_c}$ such that $\text{Re}[\lambda_i] = 0$. These three subspaces are invariant under the action of the linear flow $\mathrm{e}^{\mathcal{D}f(x_s)t}$.

In this way $\mathbb{R}^n$ can be expanded as the direct sum:

$$\mathbb{R}^n = E^s \oplus E^u \oplus E^c. \tag{A.14}$$

Based on the dimensions of these subspaces one can classify the equilibrium points x_s first as *hyperbolic* if $n_c = 0$ i.e. none of the eigenvalues has a zero real part, and *non-hyperbolic* if $n_c \neq 0$. Moreover, hyperbolic equilibrium points can be:

1. *unstable* if $n_u > 0$.
2. *stable* (asymptotically stable) if $n_u = 0$.

3. a *node* if for all i, $\mathrm{Im}[\lambda_i] = 0$, and either $n_s = n$ or $n_u = n$. In the first case we say that the node is a *sink*, and in the second we call it a *source*.
4. a *saddle* if for all i, $\mathrm{Im}[\lambda_i] = 0$, with both $n_s > 0$ and $n_u > 0$.
5. a *focus* if it has a pair of complex eigenvalues $\lambda, \bar{\lambda}$.

For the non-hyperbolic points the classification is more difficult, in part because stability depends critically on nonlinear terms and they are not determined by (A.10). However, we use the term *center* to refer to a non-hyperbolic equilibrium which has a pair of imaginary eigenvalues $\lambda = \pm i\omega$.

At this point we can consider the following important question: *What can one say about the solutions of the nonlinear system (A.1) based on the knowledge obtained from the linear system (A.10)?*

Well, let us suppose that for a fixed value of parameters μ, the stationary point is hyperbolic. Then the answer to the previous question is provided by two fundamental results of dynamical systems, the Hartman-Grobman and the stable manifold theorems.

Theorem 1 (Hartman-Grobman theorem) *If $x = x_s$ is stationary hyperbolic point, then there is a continuous invertible map, h defined on some neighborhood of x_s, $U \subseteq \mathbb{R}^n$ which takes orbits of the nonlinear flow ϕ_t of* (A.1) *to those of the linear flow $\mathrm{e}^{\mathcal{D}f(x_s)t}$ of* (A.10) *i.e. they are topologically equivalents. This map can be chosen so that the parametrization of time is preserved.*

This theorem establish that the in a neighborhood of such point, the dynamics of the nonlinear system can be determined by the dynamics of the linear one. From this theorem we also know that the stability of the stationary solution $\bar{x} = x_s$ is determined by the linearization (A.10). The next theorem provides nonlinear analogues of the flat invariant E^s and E^u.

Theorem 2 (Stable manifold theorem) *If x_s is an hyperbolic point of the nonlinear system* (A.1)*, then there exist local stable and unstable manifolds $W^s_{\mathrm{loc}}(x_s)$ and $W^u_{\mathrm{loc}}(x_s)$ that are tangent to the flat invariant eigenspaces E^s and E^u at x_s and with the same dimension n_s and n_u respectively.*

These manifolds have global analogues W^s and W^u obtained by letting points in W^s_{loc} flow backwards in time and those of W^u_{loc} flow forwards:

$$\begin{aligned} W^s(x_s) &= \bigcup_{t\leq 0} \phi_t\left(W^s_{\rm loc}(x_s)\right) \\ W^u(x_s) &= \bigcup_{t\geq 0} \phi_t\left(W^u_{\rm loc}(x_s)\right) \end{aligned} \tag{A.15}$$

Two stable (or unstable) manifolds of two distinct stationary points can not intersect, nor can $W^s(x_s)$ (or $W^u(x_s)$) intersect itself. However intersections of stable and unstable manifolds of the same or distinct stationary points can occur. Moreover, these later interactions are source of much of the complex behavior found in dynamical systems. As we will see they are in the corner stone in the formation of *homoclinic orbits*.

When the equilibrium loses hyperbolicity as the control parameter μ varies, the local nonlinear dynamics will undergo a qualitative change, which is referred to as a local bifurcation. In this situation together with the stable and unstable manifolds, the a central manifold $W^c(x_s)$ can be defined tangent to E^c at x_s. As we will see in non-hyperbolic points, a different machinery based on the central manifold reduction and the normal form theory, must be applied in order to obtain some insight about the nonlinear system around the bifurcation point.

Linearization around a periodic orbit

If $\bar{x}(t) = x_P$, then $\mathcal{D}f(\bar{x}(t)) = \mathcal{D}f(x_P)$ is matrix with $T-$periodic elements. The analysis of this type of equation is covered by Floquet theory [3]. Solutions of the (A.1) take now the form

$$y(t) = A(t)y_0, \tag{A.16}$$

where $A(t)$ is the *fundamental matrix*. The stability of the periodic orbit is determined by comparing the initial perturbation y_0 with the perturbation after N periods, $y(NT)$. In this way (A.16) becomes

$$y(NT) = \sum_{i=1}^{n} b_i \Lambda_i^N \xi_i, \tag{A.17}$$

where ξ_i and Λ_i are the eigenvectors and eigenvalues of $A(T)$, and b_i are constant coefficients determined by y_0. The eigenvalues Λ_i are called Floquet multipliers and they may be complex.

Stable (unstable) perturbations are associated with Floquet multipliers $|\Lambda_i| < 1$ ($|\Lambda_i| > 1$). A periodic orbit always contains a Floquet multiplier $\Lambda = +1$ associated with perturbations $y = \dot{x}_P$ along the trajectory, which neither grow nor decay.

A.4 Reversible systems

Definition 7 (Reversible system) *We say that a dynamical system*

$$\frac{dx}{dt} = f(x(t)), \tag{A.18}$$

with $t \in \mathbb{R}^n$ and $f : \mathbb{R}^n \to \mathbb{R}^n$ a vector field that we assume to be r times differentiable is reversible if given the involution $R : \mathbb{R}^n \to \mathbb{R}^n$ satisfying

$$R \circ R = \mathrm{Id}, \tag{A.19}$$

then

$$\frac{d}{dt}\left(R(x)\right) = -f\left(R(x)\right). \tag{A.20}$$

Using the chain rule on the left of Eq.(A.20) and Eq.(A.18) the definition of reversibility for the vector field f, i.e. for the dynamical system (A.18) reduces to the relation

$$\mathcal{D}R \cdot f = -f \circ R, \tag{A.21}$$

with $\mathcal{D}R$ the Jacobian matrix of R.

All the point that are invariant under R define a subspace $\mathcal{S}$ known as *symmetric section* i.e.

$$\mathcal{S} \equiv \mathrm{fix}(R) = \{x \in \mathbb{R}^n : R(x) = x\}. \tag{A.22}$$

In particular, we say that a stationary solution x_s is a *symmetric stationary point* if $R(x_s) = x_s$ i.e. x_s is invariant under the involution R. From the linearization of the problem about a symmetric point we find that

$$\mathcal{D}R(x_s)\mathcal{D}f(x_s) = -\mathcal{D}f(x_s)\mathcal{D}R(x_s) \tag{A.23}$$

i.e. the Jacobian matrix of f anticommute with the Jacobian matrix of R, and we say that $\mathcal{D}f(x_s)$ is *infinitesimally reversible*. This $n \times n$ matrix has a characteristic polynomial $p(\lambda)$ satisfies

$$p(-\lambda) = (-1)^n p(\lambda), \qquad \lambda \in \mathbb{C}. \tag{A.24}$$

In particular if λ is an eigenvalue of $\{(x_s)$ so is $-\lambda$ and the spectrum is symmetric with respect to the real and imaginary axes.

A.5 Homoclinic and heteroclinic orbits

In dynamical systems we can understand many global phenomena in terms of stable and unstable manifolds to equilibrium, periodic orbits or other invariant sets. In this context a special orbit Γ that approaches a forward limit set Σ^+ and a backward limit set Σ^- plays a central role because it lies precisely in the intersection between the unstable manifold of Σ^- , $W^u(\Sigma^-)$ and the stable manifold of Σ^+, $W^s(\Sigma^+)$. Such an orbit is known as an *homoclinic orbit* if $\Sigma^- = \Sigma^+$, and a *heteroclinic orbit* if $\Sigma^- \neq \Sigma^+$. The codimension of an homoclinic/heteroclinic orbit can be determined by dimension counting. If $n^u = \dim(W^u(\Sigma^-))$ and $n^s = \dim(W^s(\Sigma^+))$, then the codimension of Γ n^c can be shown to be

$$n^c = n + 1 - n^s - n^u, \tag{A.25}$$

being n the dimension of the phase space. The dimensions n^u and n^s are determined by the linear theory around those limit sets.

A *heteroclinic cycle* is a homoclinic orbit which consists of two (or more) heteroclinic orbits. For example, a heteroclinic cycle between the two limit sets Σ^+ and Σ^- would involve a heteroclinic orbit from Σ^+ to Σ^- followed by a second heteroclinic orbit from Σ^- back to Σ^+. We also use the term *homoclinic cycle* to refer to a heteroclinic cycle involving limit sets which are related by symmetry.

In reversible systems, an homoclinic orbit to an stationary point $\Gamma(t) \equiv \{\bar{x}(t) : t \in \mathbb{R}\}$ is defined such that $\Gamma(t)$ is a solution to Eq.(A.18) satisfying.

$$\Gamma(t) \to x_s, t \to \pm\infty, \tag{A.26}$$

$$\Gamma(0) \in \mathcal{S}, \tag{A.27}$$

where $f(x_s) = 0, x_s \in \mathcal{S}$.

A.6 Bifurcation theory

Bifurcation theory is the study of the qualitative change in the flow $\phi(x,t)$ of (A.1) as the system parameters μ are varied. This may involve, for example, the creation or destruction of solutions, or a change in their stability. The parameter values at which such changes occur are called *bifurcation points*. The *codimension* of any particular bifurcation is the minimum number of parameters that must be independently varied for the bifurcation to occur.

In this section we overview some important results related with *local bifurcations* that have the particularity of that they can be analyzed entirely in terms of the

local behavior of solutions near a fixed point or periodic orbit. In this context, the bifurcation takes place when a hyperbolic point becomes non-hyperbolic as the control parameter μ varies. At the particular parameter value μ_c where this transition occurs $n_c \neq 0$ i.e. there is at least one $\lambda_i(\mu_c)$ such that $\mathrm{Re}[\lambda_i(\mu_c)] = 0$. The nature of this bifurcation depends on how the eigenvalue λ_i passes through the imaginary axis $\mathrm{Re}[\lambda_i] = 0$. For example, the case of a single real eigenvalue passing through $\mathrm{Re}[\lambda_i] = 0$ is known as a steady-state bifurcation, while the case of a complex conjugate pair passing through $\mathrm{Re}[\lambda_i] = \mathrm{Re}[\bar{\lambda}_i] = 0$, $\mathrm{Im}[\lambda_i] \neq 0$ is known as a Hopf bifurcation. Using the same approach that the one done with hyperbolic points, one can think about simplifying the system (A.1) as much as possible about the non-hyperbolic point, in such a way that some information can be inferred from the simplified system. There are two main techniques that can be applied in this context: first reduce the system (A.1) to the center manifold, and second simplify the vector field obtained in that manifold to a normal form of it.

Another type of bifurcations, which can not be studied locally, are the *global bifurcations*. These bifurcation are associated with changes of large portions of the phase space instead of the statbility of fixed points and therefore in the nonlocal behavior of solutions, such as the creation of a heteroclinic orbit between two fixed points.

A.6.1 Center manifold reduction

The center manifold exist just in the point where the fixed point suffers a bifurcation i.e. the point becomes non-hyperbolic when changing the value of the parameter μ. In this point one can identify two different dynamical scales, one occurring on the stable and unstable manifolds, and the one happening in the center manifold. Thus one can reduce the dynamics of the system to the last manifold. Here the two main results are the Center manifold theorem and the Shoshitaishvili theorem.

From linear algebra it is possible to find a transformation $\mathcal{M}$ such that the linear system (A.10) reads as

$$\begin{bmatrix} \dot{u} \\ \dot{v} \\ \dot{w} \end{bmatrix} = \begin{bmatrix} J_s & 0 & 0 \\ 0 & J_u & 0 \\ 0 & 0 & J_c \end{bmatrix} \begin{bmatrix} u \\ v \\ w \end{bmatrix}, \tag{A.28}$$

where $\mathcal{M}^{-1}y \equiv [u, v, w] \in \mathbb{R}^{n_s} \times \mathbb{R}^{n_u} \times \mathbb{R}^{n_c}$ and J_s, J_u and J_c are matrices having eigenvalues with negative, positive and zero real part respectively.

Applying the same transformation to the nonlinear system (A.10) one obtains

$$\begin{array}{l} \dot{u} = J_s u + N_s(u,v,w) \\ \dot{v} = J_u v + N_u(u,v,w) \\ \dot{w} = J_c w + N_c(u,v,w) \end{array} , \tag{A.29}$$

where $N_c(u,v,w)$, $N_c(u,v,w)$ and $N_c(u,v,w)$ are the first n_s, n_u and n_c components of the vector $\mathcal{M}^{-1}N(\mathcal{M}y)$. The main goal here is how to reduce the system (A.29) to a simplified decoupled system in variables u, v and w.

Theorem 3 (Central manifold theorem) *Let x_s be a stationary non-hyperbolic point of the nonlinear system* (A.1)*, possessing the flat invariant eigenspaces E^s, E^u and E^c, then there exist a C^r stable and unstable invariant manifolds W^u and W^s tangent to x_s and a C^{r-1} center manifold W^c tangent to E^c at x_c, all of them invariant for the nonlinear flow of f. The stable and unstable manifolds are unique, but W^c need not be.*

To simplify the notation let us consider that $n_u = 0$. Then the central manifold is given by

$$W^c_{\rm loc}(x_s) \equiv \{(u,w) \in \mathbb{R}^s \times \mathbb{R}^c : u = h(w), \\ ||x - x_s|| < \delta, h(x_s) = x_s, \mathcal{D}h(x_s) = 0\}. \tag{A.30}$$

To calculate the center manifold we proceed as follows:

1. The coordinates of any point on $W^c(x_s)$ must satisfy

$$u = h(w). \tag{A.31}$$

2. The coordinates $(\dot{u}, \dot{w})$ of any point on $W^c(x_s)$ must satisfy

$$\dot{u} = \mathcal{D}h(w)\dot{w}, \tag{A.32}$$

   obtained by differentiation of $u = h(w)$ with respect to time. This is the *tangency condition* between the field and the manifold, which implies that the manifold is invariant respect to the nonlinear flow.

3. Any point of $W^c(x_s)$ must obey the dynamics generated by the system (A.29), and therefore, after substituting

$$\begin{array}{l} \dot{u} = J_s h(w) + N_s(h(w),w) \\ \dot{w} = J_c w + N_c(h(w),w), \end{array} \tag{A.33}$$

into Eq.(A.32) gives

$$\mathcal{D}h(w)[J_c w + N_c(h(w), w)] = J_s h(w) + N_s(h(w), w). \tag{A.34}$$

Then in order to calculate the center manifold described by $h(w)$ one has to solve Eq.(A.34). Normally to solve this equation one use power series expansions that allow us to obtain a solution with a given degree of accuracy.

Another important result is analogues to the Hartman-Grobman theorem but for non-hyperbolic points the Shoshitaishvili theorem states that in a neighborhood of $x = x_s$, the flow of (A.29) (with $n_u = 0$) is topologically equivalent to the flow of the decoupled system

$$\begin{aligned} \dot{u} &= J_s u \\ \dot{w} &= J_c w + N_c(h(w), w). \end{aligned} \tag{A.35}$$

A.6.2 Normal form theory

Onces the nonlinear field is reduced to its central manifold, the next step in the analysis is to simplified that system as much as possible, until reducing it to inst *normal form*. The procedure is as follows. The starting point is the set of equations from (A.35) on the central manifold

$$\dot{w} = Jw + N(w), \tag{A.36}$$

where $J = J_c$ and $N(w) = N_c(h(w), w)$ the nonlinear term, which can be Taylor expanded

$$N(w) = N_2(w) + N_3(w) + \cdots + N_{r-1}(w) + \mathcal{O}(||w||^r). \tag{A.37}$$

Taking the near identity transformation

$$w = \tilde{w} + h(\tilde{w}) = \tilde{w} + \sum_{i \geq 2} h_i(\tilde{w}), \tag{A.38}$$

where $h_i \in H_i$ is an vector valued homogeneous polynomial of degree i, and inserting it on Eq.(A.36) one arrives to

$$\dot{\tilde{w}} = J\tilde{w} + \underbrace{Jh_2(\tilde{w}) - \mathcal{D}h_2(\tilde{w})J\tilde{w}}_{L_J^{(2)} h_2(\tilde{w})} + N_2(\tilde{w}) + L_J^{(3)} h_3(\tilde{w}) + N_3(\tilde{w}) + \cdots \mathcal{O}(||\tilde{w}||^r) =$$

$$J\tilde{w} + \sum_{i \geq 2}^{r-1} L_J^{(i)} h_i(\tilde{w}) + N_i(\tilde{w}) + \mathcal{O}(||\tilde{w}||^r). \tag{A.39}$$

The linear operator $L_J^{(i)} : H_i \to H_i$ defined by

$$L_J^{(i)} h_i(\tilde{w}) = J h_i(\tilde{w}) - \mathcal{D}h_i(\tilde{w}) J\tilde{w} \tag{A.40}$$

is called the *homological operator* and is the Lie derivative associated with the vector field Jy. Our main goal will be to find transformations h_i satisfying

$$L_J^{(i)} h_i(\tilde{w}) = N_i(\tilde{w}), \tag{A.41}$$

in such a way that we can simplify into normal form as many terms as we can. However, $N_i(\tilde{w})$ belongs to a polynomial space H_i which can be descomposed as

$$H_i = \mathrm{Im}(L_J^{(i)}) \oplus \mathrm{Comp}[\mathrm{Im}(L_J^{(i)})], \tag{A.42}$$

where $\mathrm{Im}(L_J^{(i)})$ is the image of the operator, and $\mathrm{Comp}[\mathrm{Im}(L_J^{(i)})]$ its complementary subspace. Thus, the nonlinear components $N_i(\tilde{w})$ can be written as $N_i(\tilde{w}) = N_i^{nr}(\tilde{w}) + N_i^{r}(\tilde{w})$, with $N_i^{nr}(\tilde{w})$ belonging to $\mathrm{Im}(L_J^{(i)})$ which can be eliminated and $N_i^{r}(\tilde{w})$, belonging to $\mathrm{Comp}[\mathrm{Im}(L_J^{(i)})]$, which do not. These last terms are then known as *resonant terms*. Hence, with these considerations the system (A.36) can be reduced to its normal form

$$\dot{\tilde{w}} = J\tilde{w} + N_2^r(\tilde{w}) + N_3^r(\tilde{w}) + \cdots + N_{r-1}^r(\tilde{w}) + \mathcal{O}(||\tilde{w}||^r). \tag{A.43}$$

The election of $\mathrm{Comp}[\mathrm{Im}(L_J^{(i)})]$ determines the *normal form style*, and there are two main approaches.

- If J can be diagonalized, then the *Poinaré normal form* can be obtained by choosing $\mathrm{Comp}[\mathrm{Im}(L_J^{(i)})] \equiv \mathrm{Ker}(L_J^{(i)})$.
- If J can not be diagonalized, then the *Elphick normal form* can be obtained by choosing $\mathrm{Comp}[\mathrm{Im}(L_J^{(i)})] \equiv \mathrm{Ker}(L_{J^\dagger}^{(i)})$, being $J^\dagger$ the adjoint matrix of J.

The resulting normal form is not necessarily unique due to the sometimes arbitrary choices involved in selecting the resonant terms. Also, the transformation in (A.38) formally preserves the dynamics of the original system but this is not necessarily true for the truncated normal form obtained by solving (A.43) up to some finite order. For the reader interested in this topic we recomend Ref. [1] and references therein.

A.6.3 Codimenison-one bifurcations

Here we review some of the main codimension-one bifurcation that appears in this thesis.

Saddle-Node bifurcation

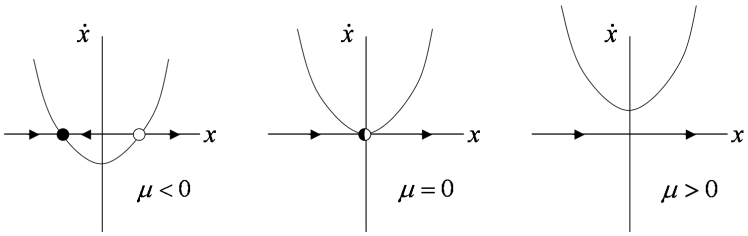

Figure A.2: Phase portrait for the saddle node bifurcation $\dot{x} = \mu + x^2$. The direction of the vector field is drawn on the horizontal axis (figure based on [4])

The first example of a bifurcation type is the saddle-node bifurcation, which is the basic mechanism by which fixed points are created and destroyed. Consider the normal (one-dimensional) form for the saddle node bifurcation

$$\dot{x} = \mu + x^2 \tag{A.44}$$

For $\mu < 0$ we have two fixed points $x_+ = \sqrt{-\mu}$ and $x_- = -\sqrt{-\mu}$, x_+ is unstable and x_- is stable, see Figure A.2). As μ increases, the fixed points move towards each other. At $\mu = 0$ (the bifurcation point) both points coincide and we end up with a half-stable fixed point. If we further increase μ, the fixed points disappear into thin air.

So in a saddle-node bifurcation two fixed points (one stable and one unstable fixed point) move towards each other, collide and mutually annihilate when a parameter is varied in a certain direction. In the other direction, two fixed points suddenly appear [4].

Transcritical bifurcation

The transcritical bifurcation is the standard mechanism for changes in stability of fixed points. It does not involve any creation or destruction of fixed points. The normal form for the transcritical bifurcation is

$$\dot{x} = \mu x - x^2 \tag{A.45}$$

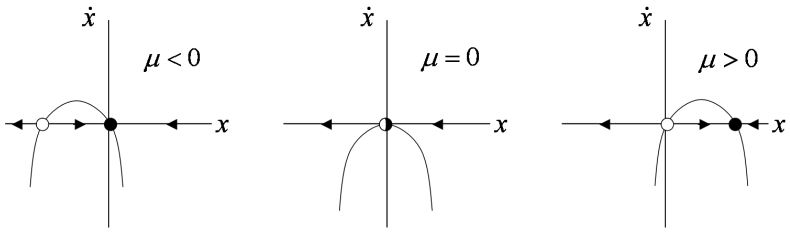

Figure A.3: Phase portrait of the transcritical bifurcation $\dot{x} = \mu x - x^2$. The direction of the vector field is drawn on the horizontal axis (figure based on [4])

For $\mu < 0$ we have an unstable fixed point at $x = \mu$ and a stable fixed point at $x = 0$ (see Figure A.3). As we increase μ, the unstable fixed point approaches the origin. At $\mu = 0$ (bifurcation point) both fixed points coincide. When $\mu > 0$ the origin has become unstable, while $x = \mu$ is now stable. You can say that the two fixed points "exchanged" their stability.

Pitchfork bifurcation

The pitchfork bifurcation is, just as the saddle-node bifurcation, a mechanism to create or destroy fixed points. It is a characteristic bifurcation for systems with inversion symmetry. Hence it often occurs in physical problems that have an intrinsic symmetry. Fixed points then tend to appear and disappear in symmetrical pairs. There are two different types of pitchfork bifurcations, the supercritical and the subcritical pitchfork bifurcation.

The normal form for the supercritical pitchfork bifurcation is

$$\dot{x} = \mu x - x^3 \tag{A.46}$$

Note that this equation is invariant under the transformation $x \to -x$. When $\mu < 0$, the origin is the only fixed point, and it is stable (see Figure A.4). When $\mu = 0$, the origin is still stable but not as stable as when $\mu < 0$. When $\mu > 0$, the origin has become unstable and two new stable fixed points appear symmetrically around the origin at $x = \pm\sqrt{\mu}$.

The normal form for the subcritical pitchfork bifurcation is

$$\dot{x} = \mu x + x^3 \tag{A.47}$$

so that the cubic term is no longer stabilizing (pulling $x(t)$ back toward $x = 0$), but destabilizing. By changing $\mu \to -\mu$, $\dot{x}$ in Eq. A.47 becomes exactly $-\dot{x}$ from

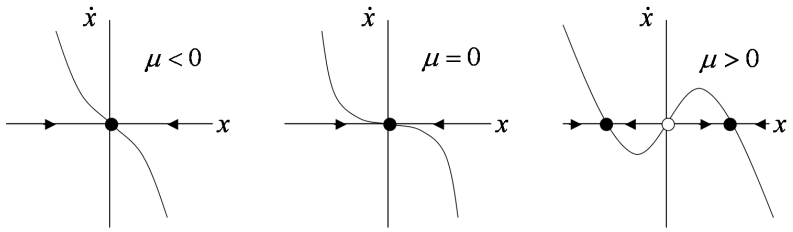

Figure A.4: Phase portrait of the pitchfork bifurcation $\dot{x} = \mu x - x^3$. The direction of the vector field is drawn on the horizontal axis (figure based on [4])

Eq. A.46. So by inverting the μ-axis and inverting the stability of every fixed point of the supercritical case, we obtain the subcritical case.

Hopf bifurcation

In all the previous bifurcations real eigenvalues passed through $\lambda = 0$, thus they were all zero-eigenvalue bifurcations. But the Hopf bifurcation is quite different. At a Hopf bifurcation two complex conjugate eigenvalues cross the imaginary axis at the same time. So at the bifurcation the eigenvalues are purely imaginary. This means that at a Hopf bifurcation, a time-periodic solution appears or disappears near a steady state [4]. The Hopf bifurcation is only possible in two or more dimensional systems. It has no one-dimensional counterpart, as opposed to the previous bifurcations which can all occur in a one-dimensional system. There are two different types: supercritical and subcritical Hopf bifurcations. At a supercritical Hopf bifurcation, the fixed point becomes unstable and gets surrounded by a stable limit cycle. The normal form (in polar coordinates) is

$$\begin{aligned} \dot{r} &= \mu r - r^3 \\ \dot{\theta} &= \omega \end{aligned} \tag{A.48}$$

where the radial equation is identical to the supercritical pitchfork Eq. A.46. The resulting phase portrait is shown in Figure A.5. At a subcritical Hopf bifurcation, a fixed point gets unstable after colliding with an unstable limit cycle. The trajectories close to the fixed point simply flow to a distant attractor after the bifurcation has occurred. The normal form is

$$\begin{aligned} \dot{r} &= \mu r + r^3 - r^5 \\ \dot{\theta} &= \omega \end{aligned} \tag{A.49}$$

where the radial equation is almost identical to the subcritical pitchfork Eq. A.47. The term $-r^5$ (stabilizing term) is added to play the role of distant attractor to

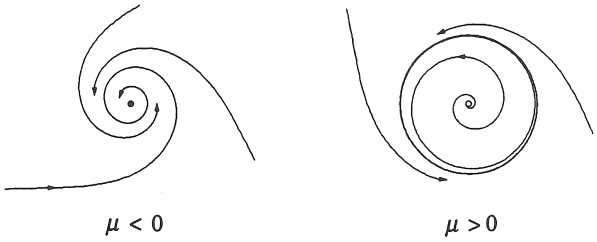

Figure A.5: Phase portrait of the normal form of the supercritical Hopf bifurcation, above and below the bifurcation point $\mu = 0$. When $\mu > 0$, the origin has become unstable and the trajectories flow outward to the new stable limit cycle with amplitude $\sqrt{\mu}$ (figure from [4]).

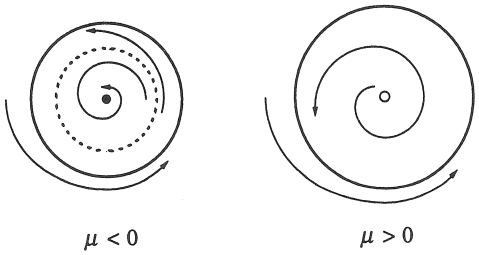

Figure A.6: Phase portrait of the normal form of the subcritical Hopf bifurcation, above and below the bifurcation point $\mu = 0$. The unstable limit cycle surrounding the origin for $\mu < 0$, shrinks continuously with increasing μ until it collides with the origin ($\mu = 0$), after which the origin becomes unstable and the trajectories flow to some distant attractor ($\mu > 0$). In this case the distant attractor is the large stable limit cycle on the outside, generated by the extra $-r^5$ term in Eq. A.49 (figure from [4]).

which the trajectories can evolve after the origin becomes unstable. The typical phase portrait of a two-dimensional subcritical Hopf bifurcation is shown in Figure A.6.

Saddle-node on the invariant circle

The s*addle-node on invariant circle* (SNIC) bifurcation, also known as *saddle-node infinite-period* (SNIPER), or as *saddle-node central homoclinic bifurcation*, is a particular case of the saddle-node in two dimensions. It appears when a stable and unstable fixed points that collide at the bifurcation point are located on a limit cycle. Therefore, the normal form can be written in one dimension

provided that the variable is the position inside the circle

$$\dot{\theta} = \omega - \mu \sin\theta \tag{A.50}$$

If $\mu = 0$ this equation reduces to a uniform oscillator. The control parameter

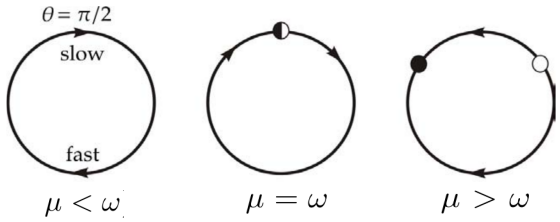

Figure A.7: Phase portrait for the saddle-node on invariant circle bifurcation.

μ introduces a non-uniformity in the flow around the cycle, the flow is faster at $\theta = -\pi/2$ and slower at $\theta = \pi/2$. Since μ increases this non-uniformity becomes more pronounced. When μ is slightly less than ω ($\mu < \omega$) the phase takes a long time to pass through the point $\theta = \pi/2$ (this is called a bottleneck), after which it completes the rest of the cycle very fast (Figure A.7). At $\mu = \omega$ the system no longer oscillates and a fixed point appears at $\theta = \pi/2$. Finally, for $\mu > \omega$ this fixed point splits in a stable and an unstable fixed points (as in the saddle-node bifurcation), the limit cycle is broken, and all the trajectories end at the stable fixed point. Since this is a special case of the saddle-node bifurcation there is also an eigenvalue that becomes 0 at the bifurcation point.

Beyond the bifurcation point the system is said to be *excitable*, while resting on the stable fixed point, if the system undergoes a small perturbation it decays back to the resting state. But, if the system is perturbed beyond the saddle, it will make a long excursion on what remains of the limit cycle. An important signature of this bifurcation is how the period of the oscillations scales as μ tends to ω. It can be shown that the period depends on μ as [4].

$$T = \frac{2\pi}{\sqrt{\omega^2 - \mu^2}} \tag{A.51}$$

Due to this dependence this bifurcation is also called infinite period bifurcation, given that the period tends to infinity at the bifurcation point.

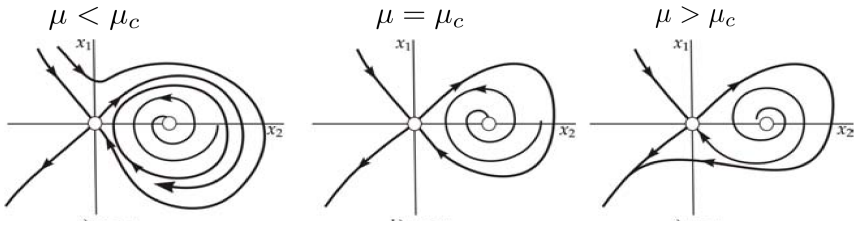

Figure A.8: Phase portrait for the SL or homoclinic bifurcation.

Saddle-Loop or Homoclinic bifurcation

In this bifurcation, an unstable fixed point collides with a limit cycle becoming a homoclinic orbit (that is why this bifurcation is also known as *homoclinic* or saddle-homoclinic bifurcation) [3, 6]. Unlike the previous bifurcations discussed, in this bifurcation there is no change of sign of the real part of an eigenvalue at the bifurcation point. This is because the bifurcation involve changes of large portions of the phase space instead of changes on the stability of fixed points. At a difference with the previous cases, this is a global bifurcation. The lowest number of dimensions in which this bifurcation can occur is two (since it requires the presence of a limit cycle). Therefore, the lower dimensional normal form that can be written for this bifurcation is

$$\begin{aligned} \dot{x}_1 &= x_2 \\ \dot{x}_2 &= \mu + x_1 + x_1^2 + x_1 x_2. \end{aligned} \tag{A.52}$$

For $\mu < \mu_c$ the system has a stable limit cycle and a unstable fixed point at the origin (Figure A.8). When μ tends to μ_c the limit cycle approaches to the saddle, and for $\mu = \mu_c$ the limit cycle and the saddle collide, creating a homoclinic orbit. Then, for $\mu > \mu_c$ the saddle connection breaks, and the loop is destroyed. In this bifurcation the period of the oscillations also tends to infinity as μ tends to μ_c , as in the SNIC bifurcation. In this case, however, the period of the oscillations scales as $\ln(\mu - \mu_c)$ [4]. If there is a fixed point close to the saddle, beyond the bifurcation the system also behaves in an excitable way as it happens with the SNIC bifurcation.

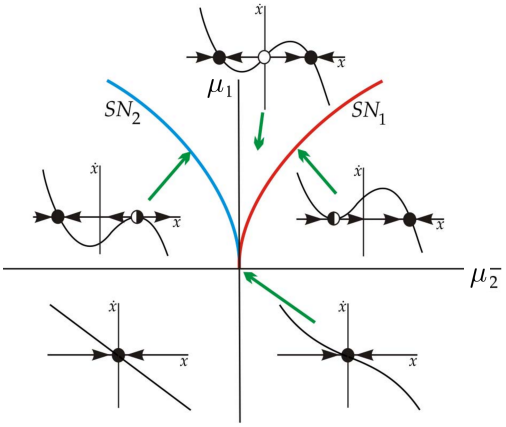

Figure A.9: Unfolding for the Cusp bifurcation

A.6.4 Codimension-two bifurcations

The hysteresis or Cusp bifurcation

A *hysteresis* or *cusp* bifurcation is the point where two branches of saddle-node bifurcation curve meet tangentially. For nearby parameter values, the system can have three fixed points which collide and disappear pairwise via the saddle-node bifurcations. Since this bifurcation involves two saddle-nodes, the lowest dimension needed for it to occur is one. Therefore, in one dimension, the normal form of this bifurcation is

$$\dot{x} = \mu_1 + \mu_2 x - x^3 \tag{A.53}$$

In Figure A.9 we plot the bifurcation diagram. The lines SN_1 and SN_2 correspond to the two saddle node bifurcations, and are given by $\mu_1 = \pm\mu_2^{3/2}/\sqrt{3}$ for $\mu_2 > 0$ (the plus sign corresponds to the SN_1 line and the minus to the SN_2). In the region between the two lines there are three fixed points, two stable and a unstable fixed point. At the bifurcation lines one of the stable fixed points collides with the unstable one and therefore outside the wedge only a stable fixed point remains.

Takens-Bodganov bifurcation

The *Takens-Bogdanov* (or *double-zero*) bifurcation occurs when a fixed point has two eigenvalues that become 0 simultaneously. Three codimension-1 bifurcations

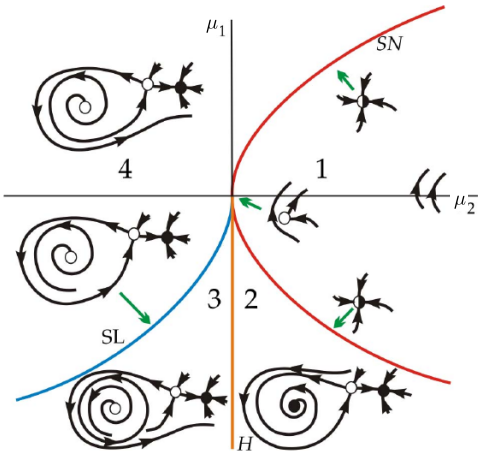

Figure A.10: Phase diagram showing the unfolding of the Takens-Bodganov bifurcation.

occur nearby the Takens-Bogdanov; a saddle-node, a Hopf and a saddle-loop bifurcation. The presence of a Takens-Bogdanov bifurcation implies the presence of a Hopf bifurcation, therefore it can occur only for systems of dimension two or more. Hence, the lowest dimensional normal form that can be written is in two dimensions, and yields

$$\begin{aligned} \dot{x}_1 &= x_2 \\ \dot{x}_2 &= \mu_1 + \mu_2 x_1 + x_1^2 + s x_1 x_2. \end{aligned} \tag{A.54}$$

We will show here the case for $s = -1$ for which the Hopf bifurcation is supercritical. The case $s = 1$ can be reduced to the case $s = -1$ by the substitution $t \to -t$, $x_2 \to -x_2$. This does not affect the bifurcation curves but the limit cycle becomes unstable. The unfolding of this bifurcation is plotted in Figure A.10. The lines SN corresponds to the saddle-node bifurcation and is given by $\mu_1 = \mu_2^2/4$. The Hopf bifurcation occurs along the line H, given by $\mu_1 = 0$ and $\mu_2, 0$. The line SL corresponds to the saddle-loop bifurcation, and is given by $\mu_1 = 6\mu_2^2/25 + \mathcal{O}(\mu_2^3)$ and $\mu_2 < 0$. The Takens-Bogdanov bifurcation occurs at the origin where there is a fixed point with two zero eigenvalues. Nearby the bifurcation the system has two fixed points, a saddle and a non-saddle stationary point. For $\mu_2 > 0$ the non-saddle is an unstable fixed point and for $\mu_2 < 0$ is a stable fixed point. The saddle and the non-saddle collide and disappear in a saddle-node bifurcation that occurs along the SN line. For $\mu_2 < 0$ the stable fixed point undergoes a Hopf bifurcation generating a limit cycle (line

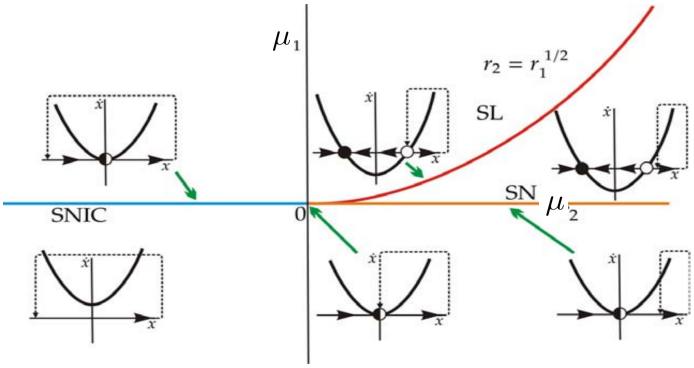

Figure A.11: Phase diagram showing the unfolding of the SNSL bifurcation

H in Figure A.10). This limit cycle then degenerates into a homoclinic orbit to the saddle, and disappears in the saddle-loop bifurcation along the SL line. This bifurcation can also be seen as the point in which a saddle-node bifurcation between a stable fixed point and a saddle (SN line for $\mu_2 < 0$) becomes a saddle-node bifurcation between a saddle and a unstable fixed point. Therefore from the unfolding of this critical point a Hopf and a saddle-loop bifurcation emerge.

Saddle-node separatrix loop bifurcation

A *saddle-node separatrix loop bifurcation* (SNSL) is the point where a saddle-node bifurcation (off limit cycle) becomes a saddle-node on invariant circle [7, 8]. It is also called called *saddle-node non-central homoclinic bifurcation* or *saddle-node homoclinic orbit bifurcation* [9]).

Three codimension-one occur nearby the SNSL point; a saddle-node, a saddle-loop and a saddle-node on invariant circle bifurcation. Hence, the presence of a SNSL bifurcation implies the nearby presence of a limit cycle, and therefore the minimum dimension in which this bifurcation can occur is two. In this case we choose to take a normal form in one dimension with a reset condition which defines a closed manifold. This normal form is

$$\dot{x} = \mu_1 + x^2, \quad \text{if} \;\; x \to \infty, \;\; \text{then} \;\; x = \mu_2. \tag{A.55}$$

The unfolding of this bifurcation is shown in Figure A.11. The line SN corresponds to the saddle-node (off limit cycle) bifurcation given by $\mu_1 = 0$ for $\mu_2 > 0$. The saddle-node on invariant circle occurs along the line SNIC, given

by $\mu_1 = 0$ for $\mu_2 < 0$. The line SL is corresponds to the saddle-loop bifurcation and is given by $\mu_2 = \mu_1^{1/2}$. The SNSL bifurcation occurs at the origin, where the three lines meet. In the plane $\mu_1 < 0$ the system behaves as if a limit cycle where present; x grows to infinity and then is reinjected to a finite value μ_2. Crossing the SNIC line, a stable and unstable fixed point appear, while x is reinjected before these two fixed points. As we have already explained for the SNIC bifurcation this creates an excitable behavior.

If we now cross the $\mu_1 = 0$ axis through the SN line, a stable and unstable fixed point also appear. For large values of μ_2 the reinjection point of x now is beyond the pair of fixed points a limit cycle is created and the system is bistable. For initial conditions above the saddle the system will end at the fixed point, and for initial conditions beyond the saddle x will grow to infinity and then be reinjected again beyond the saddle staying always in this region of the phase space. Crossing the SL line the system undergoes a saddle-loop bifurcation, in this case the reinjection point coincides with the saddle. Crossing this line coming from the bistability region (that is, decreasing μ_2) the limit cycle is destroyed, and we are back to the region of excitable behavior. Finally at the SNSL point the saddle-node bifurcation occurs at the same time as the limit cycle collides with the saddle

References

[1] S. Wiggins, *Introduction to applied nonlinear dynamical systems and chaos*, Springer, Second Edition (2003).

[2] J. Guckenheimer and P. Holmes, *Nonlinear Oscillations, Dynamical Systems, and Bifurcations of Vector Fields*,(Springer, New York, 1983).

[3] P. Glendinning, *Stability, instability and chaos: An introduction to the theory of nonlinear differential equations*, (Cambridge University Press, USA 1994)

[4] S.H. Strogatz *Nonlinear dynamics and chaos*, Westview Press, Second Edition (2014).

[5] Y. A. Kuznetsov, *Elements fo Applied Bifurcation Theory*, 3rd ed. (Springer, New York, 2004).

[6] S. Wiggins, *Global bifurcations and chaos: analytical methods*, Springer-Verlag. New-Yorks, UK (1988).

[7] S. Schecter, *The saddle-node separatrix-loop bifurcation,* SIAM J. Math. Anal., **19**, 1142-1156 (1987).

[8] E. M. Izhikevich, *Int. J. Bifurcation Chaos Appl. Sci. Eng.*, **10**, 1171-1266 (2000).

[9] E. M. Izhikevich, *Dynamical Systems in Neuroscience,* MIT Press, Cambridge (2007).

Appendix B

Analytical and numerical methods for nonlinear equations

In this appendix we briefly describe the analytical and numerical methods which have been used along this thesis. The numerical algorithm used within this thesis have been implemented in FORTRAN 77 and IDL.

B.1 Weakly non-linear analysis

Upon the analytical approximations to solve nonlinear problems we find the perturbation or asymptotic methods [1]. According to theses techniques the solution of a physical problem can be represented by the first terms of an asymptotic expansion. These expansions may be carried out in terms of a parameter (small or large) which appears naturally in the equations, or which may be artificially introduce for convenience. Such expansions are called *parameter perturbations*. Moreover if the spatio-temporal scales are well separated, we can applied a multiple scales expansion.

Let us consider that the the physical system is described by the physical field $u(x,t,\epsilon)$, which dynamics is determined by the differential equation (ODE or PDE) $\Delta[u(x,t),\nabla^k]=0$. In particular in this thesis we are going to apply this method for solving ODE in the x variable i.e. equations of the type $\Delta[u(x),\partial_x^k]=0$, then we can express the physical field u as an asymptotic series in the small parameter ϵ

$$u = u_0\epsilon^0 + u_1\epsilon^1 + u_2\epsilon^2 + \cdots , \tag{B.1}$$

with $0 < \epsilon \ll 1$, related with the parameter distance to a given nascent bifurcation, and where the coefficients u_i at each order in ϵ are functions of multiple spatial scales $x, X_1, X_2 \cdots$ [2]. For example if $u_i = u_i(x, X(x))$ with $X = \epsilon x$ any derivative of the field u_i is expressed as

$$\partial_x u_i(x, X) = \partial_x u_i(x, X) + \epsilon \partial_X u_i(x, X). \tag{B.2}$$

The requirement that the physical field u in the form of the expansion (B.1) solves the original equation $\Delta[u(x), \partial_x^k] = 0$ leads to an equation of the form

$$\Delta_0 \epsilon^0 + \Delta_1 \epsilon^1 + \Delta_2 \epsilon^2 + \cdots = 0, \tag{B.3}$$

where Δ_i denotes the terms collected at the i_{th} order in ϵ. Since these equations must hold for all values of ϵ, each coefficient Δ_i must vanish independently because sequences of ϵ are linearly independent, and then one gets the following hierarchy of conditions:

$$\begin{array}{ll} \mathcal{O}(\epsilon^0): & \Delta_0 = 0 \\ \mathcal{O}(\epsilon^1): & \Delta_1 = 0 \\ \mathcal{O}(\epsilon^2): & \Delta_2 = 0 \\ & \vdots \end{array} \tag{B.4}$$

The i_{th} condition $\Delta_i = 0$ generally takes the form

$$L u_i = f_i[u_j] \qquad j < i, \tag{B.5}$$

where L is a linear operator obtained from linearizing around the nascent instability in the original equation, and f_i is a function of $u_{j<i}$ and their space and time derivatives.

The key feature here is that the linear operator L is singular (non invertible), and therefore Eq.(B.5) does not have a non-trivial solution unless the *solvability condition* is satisfied [3, 4]. To define this condition one has first to define the adjoint operator $L^\dagger$ and its nullvector w satisfying the adjoint homogeneous equation

$$L^\dagger w = 0. \tag{B.6}$$

$L^\dagger$ is defined by the equation

$$\langle u, L^\dagger v \rangle = \langle L u, v \rangle, \tag{B.7}$$

with $\langle \cdot, \cdot \rangle$ being a suitable inner product. The boundary conditions on v are determined by requiring that the boundary term in Eq.(B.7), known as the bilinear concomitant, vanishes identically.

In this framework, the Fredholm alternative theorem states that the Eq.(B.5) has nontrivial solution if given a nullvector w of the adjoint operator $L^\dagger$, the condition

$$\langle w, f_i \rangle = 0, \tag{B.8}$$

called the solvability condition, is satisfied.

In general, the i_{th} order condition (B.5) can be solved for u_i as long as Eq.(B.8) is satisfied, and one can proceed to the next order. Otherwise, Eq.(B.8) provides a solvability condition on u_j ($j < i$) that must be satisfied in order that a solution for u_i exists.

B.2 Split-step integration method

In this Section, we describe the numerical method used to integrate PDE, like those appearing in this thesis. The PDEs that have been considered in this work can be written in the following form:

$$\partial_t u(x,t) = F[u(x,t)] \equiv a_0 u(x,t) + \sum_{j\geq 1} u_j \partial_x^j u(x,t) + \mathcal{N}(u(x,t)), \tag{B.9}$$

where $x \in \mathbb{R}^n$ (along this thesis $n = 1$), $a_j \in \mathbb{C}$ and $\mathcal{N}(u(x,t))$ is a nonlinear function of the field $u(x,t)$, that can be real or complex.
The time evolution of u subjected to periodic boundary conditions is obtained by numerically solving Eq. (B.9) in Fourier space. This method is pseudo-spectral and accurate up to second order in time. We start by computing the Fourier transform of Eq. (B.9), giving the evolution in time of each Fourier mode $\tilde{u}(q,t)$:

$$\partial_t \tilde{u}(q,t) = -\alpha_q \tilde{u}(q,t) + \tilde{\mathcal{N}}(\tilde{u}(q,t)), \tag{B.10}$$

where

$$\alpha_q = -(a_0 + \sum_{j\geq 1} (iq)^j). \tag{B.11}$$

At any time, the amplitude $\tilde{\mathcal{N}}(\tilde{u}(q,t))$ is calculated by taking the inverse Fourier transform of $\tilde{u}(q,t)$, computing the nonlinear term in real space and then calculating the Fourier transform of this term (using e.g. a standard FFT subroutine). Eq. (B.10) is integrated numerically in time with a two-step method. For reasons of convenience, we define the time step to increase by $2\delta t$ at each iteration.
In order to solve the system numerically, the field u needs to be discretized in space with a sufficiently large spatial resolution. Due to the corresponding small spatial step size, the range of values q is large such that the linear time scales

α_q can take a wide range of values. This stiffness problem is circumvented by treating the linear terms exactly by using the formal solution:

$$\partial_t \tilde{u}(t) = e^{-\alpha_q t}\left(\tilde{u}(t_0)e^{\alpha_q t_0} + \int_{t_0}^{t} \tilde{\mathcal{N}}(\tilde{u}(s))e^{\alpha_q s}ds\right), \tag{B.12}$$

where for simplicity the dependence of q on the field A has been omitted in the notation. From Eq. B.12, the following relation is found:

$$\frac{\tilde{u}(t+\delta t)}{e^{-\alpha_q \delta t}} - \frac{\tilde{u}(t-\delta t)}{e^{\alpha_q \delta t}} = e^{-\alpha_q t}\int_{t-\delta t}^{t+\delta t} \tilde{\mathcal{N}}(\tilde{u}(s))e^{\alpha_q s}ds. \tag{B.13}$$

The term on the right-hand side is then simplified using a Taylor expansion around $s = t$ assuming small values of δt:

$$\tilde{\mathcal{N}}(\tilde{u}(t))\frac{e^{\alpha_q \delta t} - e^{-\alpha_q \delta t}}{\alpha_q} + O(\delta t^3). \tag{B.14}$$

Substituting this result into the evolution equation (B.13) leads to

$$\tilde{u}(n+1) = e^{-2\alpha_q \delta t}\tilde{u}(n-1) + \frac{1 - e^{-2\alpha_q \delta t}}{\alpha_q}\tilde{\mathcal{N}}(\tilde{u}(n)) + O(\delta t^3), \tag{B.15}$$

where n is used for $n\delta t$. This expression is called the *slaved leap frog* scheme [5]. In order for this scheme to be stable, a corrective algorithm is needed. Following steps similar to the ones before, the following auxiliary expression can be found:

$$\tilde{u}(n) = e^{-\alpha_q \delta t}\tilde{u}(n-1) + \frac{1 - e^{-\alpha_q \delta t}}{\alpha_q}\tilde{\mathcal{N}}(\tilde{u}(n-1)) + O(\delta t^2). \tag{B.16}$$

Using Eqs. (B.15)-(B.16), we use the numerical method below, also referred to as the two-step method [6]:

1. Compute $\tilde{\mathcal{N}}(\tilde{u}(n-1))$ from $\tilde{u}(n-1)$ by going to real space.
2. Eq. (B.16) is used to obtain an approximation for $\tilde{u}(n)$.
3. Using this approximated $\tilde{u}(n)$, the nonlinear term $\tilde{\mathcal{N}}(\tilde{u}(n))$ is calculated.
4. $\tilde{u}(n+1)$ is obtained using Eq. (B.15).

At each iteration $\tilde{u}(n+1)$ is thus obtained from $\tilde{u}(n-1)$ as time advances by $2\delta t$. The total error is of order $O(\delta t^3)$ despite the fact that the intermediate step is accurate to $O(\delta t^2)$.

B.3 Newton-Raphson method for the stationary problem

Here we are interested in finding the stationary solutions i.e. $\partial_t u = 0$ of Eq.(B.9), and therefore solutions to

$$F[u(x,t)] \equiv a_0 u(x,t) + \sum_{j\geq 1} u_j \partial_x^j u(x,t) + \mathcal{N}(u(x,t)) = 0. \tag{B.17}$$

To solve this nonlinear equation we will use a Newton-Raphson method. If we consider that the first estimate of the solution is denoted by $u^{(0)}$, we can perform a Taylor expansion of $F[u]$ around $u^{(0)}$,

$$F[u] = F[u^{(0)}] + \mathcal{D}F[u^{(0)}](u - u^{(0)}) + \mathcal{O}(2), \tag{B.18}$$

where $\mathcal{D}F$ is the functional derivative of F.

If u is a solution of (B.17) then, using the expansion (B.18), we can write:

$$u = u^{(0)} - \mathcal{D}F[u^{(0)}]^{-1} F[u^{(0)}] + \mathcal{O}(2) \tag{B.19}$$

This approximate solution u will be a new estimate $u = u^{(1)}$ for a new iteration. So we have a sequence of estimates:

$$\begin{aligned} u^{(1)} &= u^{(0)} - \mathcal{D}F[u^{(0)}]^{-1} F[u^{(0)}] + \mathcal{O}(2) \\ u^{(2)} &= u^{(1)} - \mathcal{D}F[u^{(1)}]^{-1} F[u^{(1)}] + \mathcal{O}(2) \\ u^{(3)} &= u^{(2)} - \mathcal{D}F[u^{(2)}]^{-1} F[u^{(2)}] + \mathcal{O}(2) \\ u^{(n+1)} &= u^{(n)} - \mathcal{D}F[u^{(n)}]^{-1} F[u^{(n)}] + \mathcal{O}(2) \end{aligned} \tag{B.20}$$

We will work with the discretization of the previous type equations.In this way, the functional F will be a vector field of dimension n

$$F : \mathbb{R}^N \longrightarrow \mathbb{R}^N, \qquad [u(x_1), \cdots, u(x_N)] \longmapsto [F_1(u), \cdots, F_N(u)]. \tag{B.21}$$

and the nonlinear stationary partial differential equation, will be system o N nonlinear equations

$$\begin{aligned} F_1(u(x_1), \cdots, u(x_N)) &= 0 \\ F_2(u(x_1), \cdots, u(x_N)) &= 0 \\ &\vdots \\ F_N(u(x_1), \cdots, u(x_N)) &= 0. \end{aligned} \tag{B.22}$$

Newton method with parameters

If we take parameters μ into account we have to solve the equation $F[u,\mu]=0$, that defines a parametric curve of one dimension $\gamma(s)\in F^{-1}(0)$ in $\mathbb{R}^{n+1}$. This curve is a branch of solutions that gives the dependence of the solution on the parameter μ. To parametrize such curve $Q(u,\mu,s)=0$. to the system (B.22) that now depends on μ. Now for each value of s this system has $N+1$ equations and $N+1$ unknowns.

There are several ways to choose the parametrization of γ. Herein we will consider only two,

1. **The natural parametrization**, is the most obvious choice and uses the parameter μ as a curve parameter too, so $Q=\mu-s$. In this case problems will occur at the turning points of the curve, where we have $\frac{du}{d\mu}=\infty$. One solution to this problem consist use the norm of u as a parameter for passing through the the fold.

2. **The pseudo arclength parametrization**, use the arclength of the curve to make the parametrization. This parametrization is defined by the condition

$$||\gamma'(s)||=1, \qquad ||\frac{du}{ds}||^2+\left(\frac{d\mu}{ds}\right)^2=1. \tag{B.23}$$

B.4 Continuation techniques for stationary solutions

At this point we are prepared to introduce the bases of *continuation methods* for stationary solutions of PDEs. A continuation method is based on the obtention of the parametric curve γ, i.e. the dependence of the stationary field with the parameter μ. Here we apply a *predictor-corrector* algorithm. To illustrate the bases of this method, we will first consider the natural parametrization scheme. After that we will see how the the method is modified for considering the pseudo arclength parametrization. So from now on we choose $s=\mu$.

In the coming sections we follow closely Refs. [7–9] and therein.

B.4.1 Predictor methods

We will consider two types of predictor methods.

1. The *constant predictor* consist in that if we know the solution u_0 for the parameter μ_0 we can guess as a approximate solution in the parameter

$\mu_1 = \mu_0 + \Delta\mu$,

$$u_1^{(0)} = u_0 = u(\mu_0) \tag{B.24}$$

2. Another method consist in approximate $u^{(0)}(\mu_1)$ by its Taylor expansion about μ_0

$$u^{(0)}(\mu_1) = u(\mu_0) + \left(\frac{du}{d\mu}\right)_{\mu_0} (\mu_1 - \mu_0) + \mathcal{O}(2) \tag{B.25}$$

truncated at some order. Depending of how many terms we took in the expansion we have different, and more precise, initial approximations. In particular the *Euler predictor method* considers that $u^{(0)}(\mu_1)$ is approximated by the first order in the previous expansion

$$u_1^{(0)} = u_0 + \dot{u}_0 \Delta\mu_1, \tag{B.26}$$

with $\dot{u}_0 = \left(\frac{du}{d\mu}\right)_{\mu_0}$. To obtain the tangent vector $\dot{u}_0$ to the curve $u(\mu)$ at $u_0 = u(\mu_0)$, we have that $F[u, \mu] = 0$, and from there:

$$\frac{dF}{d\mu}|_{\mu_0} = \mathcal{D}F_{(u_0,\mu_0)} \frac{du}{d\mu}|_{\mu_0} + \frac{\partial F}{\partial \mu}|_{\mu_0} = 0.$$

Therefore, to obtain such a vector we have to solve the linear system

$$\mathcal{D}F_{(u_0,\mu_0)} \dot{u}_0 = \partial_\mu F|_{\mu_0} = 0. \tag{B.27}$$

B.4.2 Corrector method

To make corrections in the previous guess for the solution of the equation we use a correction method based in the Newton-Raphson algorithm described at the beginning of this appendix. So, in this case, given a solution u_0 at the parameter value μ_0, i.e. (u_0, μ_0) of $F[u, \mu] = 0$, our problem will be to compute the solution (u_1, μ_1) with $\mu_1 = \mu_0 + \Delta\mu_1$. Again using applying the Newton-Raphson algorithm we will have to solve the system,

$$\mathcal{D}F[u_1^{(0)}, \mu_1] \Delta u_1^{(n)} = -F[u_1^{(n)}, \mu_1] u_1^{(n+1)} = u_1(n) + \Delta u_1^{(n)}, \tag{B.28}$$

with n representing the estimate of the solution.

So for each solution (u_k, μ_k) we have to iterate enough n times. For (u_1, μ_1) we have,

$$\begin{aligned}
u_1^{(1)} &= u_1^{(0)} - \mathcal{D}F[u_1^{(0)}, \mu_1]^{-1} F[u_1^{(0)}, \mu_1] + \mathcal{O}(2) \\
u_1^{(2)} &= u_1^{(1)} - \mathcal{D}F[u_1^{(1)}, \mu_1]^{-1} F[u_1^{(1)}, \mu_1] + \mathcal{O}(2) \\
u_1^{(3)} &= u_1^{(2)} - \mathcal{D}F[u_1^{(2)}, \mu_1]^{-1} F[u_1^{(2)}, \mu_1] + \mathcal{O}(2) \\
u_1^{(n+1)} &= u_1^{(n)} - \mathcal{D}F[u_1^{(n)}, \mu_1]^{-1} F[u_1^{(n)}, \mu_1] + \mathcal{O}(2),
\end{aligned}$$

(B.29)

with $u^{(0)}(\mu_1)$ chosen using the constant or Euler predictor. In the following we will consider only the first term,so for us $u^{(0)}(\mu_1) = u(\mu_0)$.

B.4.3 Keller pseudo-arclength continuation

Here we describe the continuation method that uses the pseudo-arclength parametrization of the curve γ given by $||\gamma'(s)|| = 1$. The problem consists in given a point $(\mu_0, u_0) = (\mu(s_0), u(s_0))$ to continue it along the curve γ until reaching the point $(\mu_1, u_1) = (\mu(s_1), u(s_1))$, both of them parametrized by the pseudo-arclength s. For more details see Refs. [7–9].

The condition used here is described by the equation,

$$Q(u, \mu, s) = (u_1 - u_0)^T \dot{u}_0 + (\mu_1 - \mu_0)\dot{\mu}_0 - \Delta s = 0, \tag{B.30}$$

In this method we will use the Euler predictor given by

$$\begin{aligned} u_1^{(0)} &= u_0 + \dot{u}_0 \Delta s \\ \mu_1^{(0)} &= \mu_0 + \dot{\mu}_0 \Delta s. \end{aligned} \tag{B.31}$$

The system which we have to solve is given by

$$G[u, \mu] = \begin{bmatrix} F[u, \mu] \\ Q(u, \mu, s) \end{bmatrix} = \begin{bmatrix} 0 \\ 0 \end{bmatrix}. \tag{B.32}$$

Applying the Taylor expansion of G up to first order we get

$$\begin{bmatrix} \mathcal{D}F & \partial_\mu F \\ \delta_u Q & \partial_\mu Q \end{bmatrix}_{(u_1^{(m)}, \mu_1^{(m)})} \begin{bmatrix} \Delta u_1^{(m)} \\ \Delta \mu_1^{(m)} \end{bmatrix} = - \begin{bmatrix} F[(u_1^{(m)}, \mu_1^{(m)}] \\ Q[u_1^{(m)}, \mu_1^{(m)}, s] \end{bmatrix}. \tag{B.33}$$

Or in a more compact way:

$$\begin{aligned} \mathcal{D}G[v_1^{(m)}, \mu_1]\Delta v_1^{(m)} &= -G[v_1^{(m)}, \mu_1] \\ v_1^{(m+1)} &= v_1^{(m)} + \Delta v_1^{(m)}, \end{aligned} \tag{B.34}$$

where we have defined the vector $v_k^{(m)} = [u_k^{(m)}, \mu_k^{(m)}]$.

To build the predictor (B.31) we have to calculate first the tangent vector $\dot{v}_0 = [\dot{u}_0, \dot{\mu}_0]$ to the point (u_0, μ_0) and after that any tangent vector $\dot{v}_k = [\dot{u}_k, \dot{\mu}_k]$ to the point (u_k, μ_k). For the first case we need to solve the two next equations:

$$\begin{aligned} &\mathcal{D}F[u_0, \mu_0]\dot{u}_0 = \partial_\mu F[u_0, \mu_0] \\ &\dot{\mu}_0 = \sqrt{\xi||\dot{u}_0||^2 + 1}. \end{aligned} \tag{B.35}$$

And for any other point we solve the system [7]:

$$\left[\begin{array}{cc} \mathcal{D}F & \partial_\mu F \\ \dot{u}_k & \dot{\mu}_k \end{array} \right]_{(u_{k+1}, \mu_{k+1})} \left[\begin{array}{c} \dot{u}_{k+1} \\ \dot{\mu}_{k+1} \end{array} \right] = - \left[\begin{array}{c} 0 \\ 1 \end{array} \right] \tag{B.36}$$

So the algorithm of the Keller pseudo-arclength continuation is as follows. If given the point (u_0, μ_0) we want to obtain (u_1, μ_1):

1. We take as initial input (u_0, μ_0) and Δs, and the tangent vector $(\dot{u}_0, \dot{\mu}_0)$ that we have previously calculated using Eq.(B.35).
2. We apply the Euler predictor (B.31) as initial guess for the solution.
3. We apply the Newton-Raphson correction by solving the system (B.34), until obtaining the best approximation $v_1^{(m+1)} = v_1$ to the exact solution.
4. We calculate the tangent vector $(\dot{u}_1, \dot{\mu}_1)$ to the point (u_1, μ_1) by solving the system (B.36).
5. We go to point 2 to obtain (u_2, μ_2) and so on.

References

[1] A. Nayfeh, *Perturbation methods*, Wiley, Canada (1973).

[2] P. Glendinning, *Stability, instability and chaos: An introduction to the theory of nonlinear differential equations*, (Cambridge University Press, USA 1994)

[3] M. Cross and P. Hohenberg, *Pattern-formation outside of equilibrium,* Rev. Mod. Phys. **65**, 851-1112, 1993.

[4] I. Stakgold, *Boundary Value Problems of Mathematical Physics: Volume 1* Society for Industrial and Applied Mathematics, Philadephia, PA, (2000).

[5] U. Frisch, Z. S. She , and O. Thual, *Viscoelastic behavior of cellular solutions to the Kuramoto-Sivashinsky model,* J. Fluid. Mech. **168,** 221, (1986).

[6] R. Montagne, E. Hernández-García, A. Amengual, and M. San Miguel, *Wound-up phase turbulence in the complex Ginzburg-Landau equation,* Phys. Rev. E **56**, 151-167, (1997).

[7] E. J. Doedel, *Lecture notes of numerical analysis of nonlinear equations*

[8] H. B. Keller, *Lectures on numerical methods in bifurcation problems*, Tata Institute of Fundamental Research, Springer-Verlag, (1986).

[9] H. D. Mittelmann, A pseudo-arclength continuation method for nonlinear eigenvalue problems, SIAM J. Numer. Anal., **23**, 5, (1986).

Appendix C

Weakly nonlinear analysis near the Hamiltonian-Hopf bifurcation

C.1 Introduction

In this appendix calculate weakly nonlinear LSs using multiple scale perturbation theory near the Hamiltonian-Hopf (HH) bifurcation in the Lugiato-Lefever (LL) equation for both the anomalous and normal GVD regimes. The HH point is occurs for any value of $\theta < 2$ by the condition $I_0 = I_c = 1$, i.e,

$$\rho_c = \sqrt{1 + (\theta - 1)^2} \tag{C.1}$$

We fix the value of the detuning parameter θ and we suppose that the LSs emerging from the HH point can be described by the ansatz

$$\begin{bmatrix} U \\ V \end{bmatrix} = \begin{bmatrix} U \\ V \end{bmatrix}^* + \begin{bmatrix} u \\ v \end{bmatrix}, \tag{C.2}$$

where U^* and V^* correspond to the HSS A_0 and u and v capture the spatial dependence.

We expand both the homogeneous and the spatial dependent components of the ansatz (C.2) as:

$$\begin{bmatrix} U \\ V \end{bmatrix}^* = \begin{bmatrix} U_c \\ V_c \end{bmatrix} + \epsilon^2 \begin{bmatrix} U_2 \\ V_2 \end{bmatrix} + ... \tag{C.3}$$

$$\begin{bmatrix} u \\ u \end{bmatrix} = \epsilon \begin{bmatrix} u_1 \\ v_1 \end{bmatrix} + \epsilon^2 \begin{bmatrix} u_2 \\ v_2 \end{bmatrix} + \epsilon^3 \begin{bmatrix} u_3 \\ v_3 \end{bmatrix} + ... \tag{C.4}$$

where ϵ is the expansion parameter defined as [1]

$$\epsilon = \sqrt{\frac{\rho - \rho_c}{\delta_c}}, \tag{C.5}$$

and

$$\delta_c \equiv \frac{1}{2} \left(\frac{d^2\rho}{dI_0^2} \right)_{I_c}. \tag{C.6}$$

We consider all the variables to be functions of x and X, i.e. $u_i = u_i(x, X(x))$ and $v_i = v_i(x, X(x))$. Then the differential operator on any of those fields will be

$$\partial_x^2 u_i(x, X(x)) = \partial_x^2 u_i + 2\epsilon \partial_x \partial_X u_i + \epsilon^2 \partial_X^2 u_i. \tag{C.7}$$

Now introducing expansions (C.3) and (C.4) into the stationary LL equation (2.3) we can separate order by order in ϵ the components of the expansions (C.3) and (C.4). In following sections we solve the problem order by order in parameter ϵ.

C.2 Equations at $\mathcal{O}(\epsilon^0)$

The first order in the asymptotic series give us the HSS (Homogeneous steady state) at the HH point.

$$\mathcal{O}(\epsilon^0) : \begin{bmatrix} -1 & \theta - I_c \\ -(\theta - I_h) & -1 \end{bmatrix} \begin{bmatrix} U_c \\ V_c \end{bmatrix} + \begin{bmatrix} \rho_c \\ 0 \end{bmatrix} = \begin{bmatrix} 0 \\ 0 \end{bmatrix} \tag{C.8}$$

From Eq.(C.8) we obtain that,

$$\begin{bmatrix} U_c \\ V_c \end{bmatrix} = \begin{bmatrix} \dfrac{\rho_c}{1 + (I_c - \theta)^2} \\ \dfrac{(I_c - \theta)\rho_c}{1 + (I_c - \theta)^2} \end{bmatrix} \tag{C.9}$$

C.3 Equations at $\mathcal{O}(\epsilon^1)$

$$L \begin{bmatrix} u_1 \\ v_1 \end{bmatrix} = \begin{bmatrix} 0 \\ 0 \end{bmatrix} \tag{C.10}$$

where,

$$L = \begin{bmatrix} -(1+2U_cV_c) & \theta - I_c - 2V_c^2 - \nu\partial_x^2 \\ -(\theta - I_c - 2U_c^2 - \nu\partial_x^2) & -1 + 2U_cV_c \end{bmatrix} \tag{C.11}$$

To solve Eq.(C.10), we consider the ansatz

$$\begin{bmatrix} u_1 \\ v_1 \end{bmatrix} = \begin{bmatrix} a \\ b \end{bmatrix} \left(\phi(X)e^{ik_cx} + \bar{\phi}(X)e^{-ik_cx}\right) \tag{C.12}$$

The solvability condition for this equation with the previous ansatz gives us the value of k_c. Inserting the ansatz in the equation we have

$$\begin{bmatrix} -(1+2U_cV_c) & \theta - I_c - 2V_c^2 + \nu k_c^2 \\ -(\theta - I_c - 2U_c^2 + \nu k_c^2) & -1 + 2U_cV_c \end{bmatrix} \begin{bmatrix} a \\ b \end{bmatrix} = \begin{bmatrix} 0 \\ 0 \end{bmatrix} \tag{C.13}$$

This system has nontrvial solutions if its determinant is zero i.e. $\det[\cdot] = 0$. From there we get the characteristic polynomial

$$k_c^4 + (2\theta - 4I_c)\nu k_c^2 + 1 + \theta^2 + 3I_c^2 - 4\theta I_c = 0 \tag{C.14}$$

with the solution

$$k_c = \pm\sqrt{(2I_c - \theta)\nu \pm \sqrt{I_c^2 - 1}}. \tag{C.15}$$

The value of I_0 will be determine later on. The solution of Eq.(C.13) will be given by,

$$\begin{bmatrix} a \\ b \end{bmatrix} = \begin{bmatrix} \dfrac{\theta - 2V_c^2 - I_c + \nu k_c^2}{1 + 2U_cV_c} \\ 1 \end{bmatrix} \tag{C.16}$$

being $\mu \in \mathbb{R}$, absorved by ϕ.

Then the solution of Eq.(C.10) takes the form

$$\begin{bmatrix} u_1 \\ v_1 \end{bmatrix} = \begin{bmatrix} a \\ 1 \end{bmatrix} \left(\phi(X)e^{ik_0x} + \bar{\phi}(X)e^{-ik_cx}\right) \tag{C.17}$$

with

$$a = \frac{\theta - 2V_c^2 - I_c + \nu k_c^2}{1 + 2U_cV_c} \tag{C.18}$$

C.4 Equations at $\mathcal{O}(\epsilon^2)$

At $\mathcal{O}(\epsilon^2)$ we obtain the next system of equations:

$$\underbrace{L\begin{bmatrix} U_2 \\ V_2 \end{bmatrix} + \begin{bmatrix} \delta \\ 0 \end{bmatrix}}_{=0} + L\begin{bmatrix} u_2 \\ v_2 \end{bmatrix} + \begin{bmatrix} 0 & -2\nu\partial_x\partial_X \\ 2\nu\partial_x\partial_X & 0 \end{bmatrix}\begin{bmatrix} u_1 \\ v_1 \end{bmatrix} + \begin{bmatrix} -2u_1v_1 & -(3v_1^2+u_1^2) \\ 3u_1^2+v_1^2 & 2v_1u_1 \end{bmatrix}\begin{bmatrix} U_c \\ V_c \end{bmatrix} = \begin{bmatrix} 0 \\ 0 \end{bmatrix} \quad \text{(C.19)}$$

We separate between the spatial dependent and the homogeneous components.

HSS contribution

The HSS contribution satisfy

$$\underbrace{\begin{bmatrix} -(1+2U_cV_c) & \theta - I_c - 2V_c^2 \\ -(\theta - I_c - 2U_c^2) & -1+2U_cV_c \end{bmatrix}}_{L_0}\begin{bmatrix} U_2 \\ V_2 \end{bmatrix} + \begin{bmatrix} \delta_c \\ 0 \end{bmatrix} = \begin{bmatrix} 0 \\ 0 \end{bmatrix} \quad \text{(C.20)}$$

In this case the operator L_0 is not singular and then we can calculate its inverse and obtain the solution of Eq.(C.20) as:

$$\begin{bmatrix} U_2 \\ V_2 \end{bmatrix} = L_0^{-1}\begin{bmatrix} -\delta_c \\ 0 \end{bmatrix} \quad \text{(C.21)}$$

with the inverse operator

$$L_0^{-1} = d_0\begin{bmatrix} -1+2U_cV_c & -(\theta - I_c - 2V_c^2) \\ \theta - I_c - 2U_c^2 & -(1+2U_cV_c) \end{bmatrix} \quad \text{(C.22)}$$

and

$$d_0 = (\det L_0)^{-1} = 1 + \theta^2 + 3I_c^2 - 4\theta I_c \quad \text{(C.23)}$$

Then the solution is given by:

$$\begin{bmatrix} U_2 \\ V_2 \end{bmatrix} = \delta_c d_0\begin{bmatrix} 1-2U_cV_c \\ 2U_c^2 + I_c - \theta \end{bmatrix} = \delta_c\begin{bmatrix} \tilde{U}_2 \\ \tilde{V}_2 \end{bmatrix} \quad \text{(C.24)}$$

Space dependent contribution

This is given by

$$L\begin{bmatrix} u_2 \\ v_2 \end{bmatrix} = \begin{bmatrix} 0 & 2\nu\partial_x\partial_X \\ -2\nu\partial_x\partial_X & 0 \end{bmatrix}\begin{bmatrix} u_1 \\ v_1 \end{bmatrix} + \begin{bmatrix} 2u_1v_1 & 3v_1^2+u_1^2 \\ -(3u_1^2+v_1^2) & -2v_1u_1 \end{bmatrix}\begin{bmatrix} U_c \\ V_c \end{bmatrix} \quad \text{(C.25)}$$

To solve this we will first evaluate the rhs of Eq.(C.25). The first term in RHS of Eq.(C.25) is:

$$\begin{bmatrix} 0 & 2\nu\partial_x\partial_X \\ -2\nu\partial_x\partial_X & 0 \end{bmatrix}\begin{bmatrix} u_1 \\ v_1 \end{bmatrix} = \begin{bmatrix} 2\nu\partial_x\partial_X v_1 \\ -2\nu\partial_x\partial_X u_1 \end{bmatrix} =$$

$$2\nu\begin{bmatrix} 1 \\ -a \end{bmatrix}\partial_x\partial_X\left(\phi(X)e^{ik_cx}+c.c.\right) = \underbrace{2\nu k_c\begin{bmatrix} 1 \\ -a \end{bmatrix}}_{\begin{bmatrix} a_1 \\ b_1 \end{bmatrix}}\left(i\phi'(X)e^{ik_cx}+c.c.\right) \quad \text{(C.26)}$$

Proceeding in the same way with the second term on rhs of Eq.(C.25) we obtain the contributions of each element of the matrix. Those terms are given by:

Then the second terms is

$$\begin{bmatrix} 2u_1v_1 & 3v_1^2+u_1^2 \\ -(3u_1^2+v_1^2) & -2v_1u_1 \end{bmatrix}\begin{bmatrix} U_c \\ V_c \end{bmatrix} = \begin{bmatrix} 4a & 6+2a^2 \\ -(6a^2+2) & -4a \end{bmatrix}\begin{bmatrix} U_c \\ V_c \end{bmatrix}|\phi(X)|^2 +$$

$$\begin{bmatrix} 2a & 3+a^2 \\ -(3a^2+1) & -2a \end{bmatrix}\begin{bmatrix} U_c \\ V_c \end{bmatrix}\left(\phi^2(X)e^{2ik_cx}+\bar{\phi}^2(X)e^{-2ik_cx}\right) =$$

$$= \begin{bmatrix} a_0 \\ b_0 \end{bmatrix}|\phi(X)|^2 + \begin{bmatrix} a_2 \\ b_2 \end{bmatrix}\left(\phi^2(X)e^{2ik_cx}+\bar{\phi}^2(X)e^{-2ik_cx}\right) \quad \text{(C.27)}$$

with the coefficients

$$\begin{bmatrix} a_0 \\ b_0 \end{bmatrix} = \begin{bmatrix} 4aU_c+(6+2a^2)V_c \\ -(6a^2+2)U_c-4aV_c \end{bmatrix} \quad \text{(C.28)}$$

and

$$\begin{bmatrix} a_2 \\ b_2 \end{bmatrix} = \begin{bmatrix} 2aU_c + (3+a^2)V_c \\ -(3a^2+1)U_c - 2aV_c \end{bmatrix} \tag{C.29}$$

In this way we will have

$$L \begin{bmatrix} u_2 \\ v_2 \end{bmatrix} = \begin{bmatrix} a_0 \\ b_0 \end{bmatrix} |\phi(X)|^2 +$$

$$\begin{bmatrix} a_1 \\ b_1 \end{bmatrix} \left(i\phi'(X)e^{ik_c x} + c.c.\right) + \begin{bmatrix} a_2 \\ b_2 \end{bmatrix} \left(\phi^2(X)e^{2ik_c x} + c.c.\right) \tag{C.30}$$

To evaluate the lhs of Eq.(C.30) we have know how the operator acts on the same bases in which the rhs is written. For that we consider the ansatz:

$$\begin{bmatrix} u_2 \\ v_2 \end{bmatrix} = \begin{bmatrix} A_0 \\ B_0 \end{bmatrix} |\phi(X)|^2 +$$

$$\begin{bmatrix} A_1 \\ B_1 \end{bmatrix} \left(i\phi'(X)e^{ik_c x} + c.c.\right) + \begin{bmatrix} A_2 \\ B_2 \end{bmatrix} \left(\phi^2(X)e^{2ik_c x} + c.c.\right) + \text{h.harmonics} \tag{C.31}$$

Then, the operator maps the ansatz of Eq.(C.31) to:

$$L \begin{bmatrix} u_2 \\ v_2 \end{bmatrix} = L_0 \begin{bmatrix} A_0 \\ B_0 \end{bmatrix} |\phi(X)|^2 + L_1 \begin{bmatrix} A_1 \\ B_1 \end{bmatrix} \left(i\phi'(X)e^{ik_c x} + c.c.\right) +$$

$$L_2 \begin{bmatrix} A_2 \\ B_2 \end{bmatrix} \left(\phi^2(X)e^{2ik_c x} + c.c.\right) + \text{h.o.h} \tag{C.32}$$

with the operators

$$L_1 = \begin{bmatrix} -(1+2U_cV_c) & \theta - I_c - 2V_c^2 + \nu k_c^2 \\ -(\theta - I_c - 2U_c^2 + \nu k_c^2) & -1 + 2U_cV_c \end{bmatrix} \tag{C.33}$$

$$L_2 = \begin{bmatrix} -(1+2U_cV_c) & \theta - I_c - 2V_c^2 + 4\nu k_c^2 \\ -(\theta - I_c - 2U_c^2 + 4\nu k_c^2) & -1 + 2U_cV_c \end{bmatrix} \tag{C.34}$$

Now comparing Eq.(C.30) with Eq.(C.32) order by order in $e^{\pm nik_c x}$ we get the following set of equations.

Equation at $\mathcal{O}(e^{\pm 0 i k_0 x})$:

$$L_0 \begin{bmatrix} A_0 \\ B_0 \end{bmatrix} = \begin{bmatrix} a_0 \\ b_0 \end{bmatrix} \tag{C.35}$$

L_0 is invertible with L_0^{-1} given by Eq.(C.22). Then the solution of the previous system is:

$$\begin{bmatrix} A_0 \\ B_0 \end{bmatrix} = d_0 \begin{bmatrix} (-1+2U_cV_c)a_0 - (\theta - I_c - 2V_c^2)b_0 \\ (\theta - I_c - 2U_c^2)a_0 - (1+2U_cV_c)b_0 \end{bmatrix} \tag{C.36}$$

Equation at $\mathcal{O}(e^{\pm i k_c x})$:

$$L_1 \begin{bmatrix} A_1 \\ B_1 \end{bmatrix} = \begin{bmatrix} a_1 \\ b_1 \end{bmatrix} \tag{C.37}$$

As we saw before $\det(L_1) = 0$, and L_1 is not invertible. To obtanin the solvability condition for this equation we calculate $L_1^\dagger$ and its nullvector.

$$L_1^\dagger = \begin{bmatrix} -(1+2U_cV_c) & -(\theta - I_c - 2U_c^2 + \nu k_c^2) \\ \theta - I_c - 2V_c^2 + \nu k_c^2 & -1 + 2U_cV_c \end{bmatrix} \tag{C.38}$$

and the nullvector verifying $L_1^\dagger \mathbf{w} = 0$,

$$\mathbf{w} = \begin{bmatrix} w_1 \\ w_2 \end{bmatrix} = \zeta \begin{bmatrix} \dfrac{\theta - I_c - 2U_c^2 + \nu k_c^2}{-(1+2U_cV_c)} \\ 1 \end{bmatrix} \tag{C.39}$$

where $\zeta \in \mathbb{R}$. We can choose $\zeta = 1$.
Then the solvability condition for Eq.(C.37),

$$w_1 a_1 + w_2 b_1 = w_1 - a = 0 \tag{C.40}$$

gives

$$\boxed{w_1 = a} \tag{C.41}$$

Using the expressions derived previously for w_1 and a we arrive to the condition,

$$w_1 = a \Longrightarrow -\frac{\theta - I_c - 2U_c^2 + \nu k_c^2}{1 + 2U_cV_c} = \frac{\theta - 2V_c^2 - I_c + \nu k_c^2}{1 + 2U_cV_c}$$

$$k_c^2 = \nu(2I_c - \theta) \tag{C.42}$$

Equation (C.15) together with Eq.(C.42) give us the that the condition

$$I_c = 1 \tag{C.43}$$

Ones, conditions Eq.(C.43) and eq.(C.42) are satisfied, we can solve Eq.(C.37). For that we multiply both sides of the equation by $[1, 0]$ and we get

$$B_1 = \frac{\begin{bmatrix} 1 & 0 \end{bmatrix} \begin{bmatrix} a_1 \\ b_1 \end{bmatrix}}{\begin{bmatrix} 1 & 0 \end{bmatrix} L_1 \begin{bmatrix} A_1/B_1 \\ 1 \end{bmatrix}} = \frac{a_1}{-(1+2U_cV_c)(A_1/B_1) + (\theta - I_c - 2V_c^2 + \nu k_c^2)}$$

Without loss of generality we choose $A_1 = 0$ and then we have:

$$\boxed{B_1 = \frac{2\nu k_c}{(\theta - I_c - 2V_c^2 + \nu k_c^2)}}$$

Equation at $\mathcal{O}(e^{\pm 2ik_0x})$:

$$L_2 \begin{bmatrix} A_2 \\ B_2 \end{bmatrix} = \begin{bmatrix} a_2 \\ b_2 \end{bmatrix} \tag{C.44}$$

In this case L_2 is invertible with

$$L_2^{-1} = d_2 \begin{bmatrix} -1 + 2U_cV_c & -(\theta - I_c - 2V_c^2 + 4\nu k_c^2) \\ (\theta - I_c - 2U_c^2 + 4\nu k_{2)} & -(1 + 2U_cV_c) \end{bmatrix} \tag{C.45}$$

and

$$d_2 = \det(L_2)^{-1} = \left(1 - 2I_c(\theta - I_c) + (\theta - I_c)^2 + 8k_c^2\theta\nu - 16k_c^2 I_c\nu + 16k_c^4\right)^{-1} \tag{C.46}$$

Then the solution of Eq.(C.44) is

$$\begin{bmatrix} A_2 \\ B_2 \end{bmatrix} = d_2 \begin{bmatrix} (-1 + 2U_cV_c)a_2 - (\theta - I_c - 2V_c^2 + 4\nu k_c^2)b_2 \\ (\theta - I_c - 2U_c^2 + 4\nu k_c^2)a_2 - (1 + 2U_cV_c)b_2 \end{bmatrix} \tag{C.47}$$

C.5 Equations at $\mathcal{O}(\epsilon^3)$

$$L \begin{bmatrix} u_3 \\ v_3 \end{bmatrix} + \mathcal{M}_1 \begin{bmatrix} u_2 \\ v_2 \end{bmatrix} + \mathcal{M}_2 \begin{bmatrix} u_1 \\ v_1 \end{bmatrix} + \mathcal{M}_3 \begin{bmatrix} U_c \\ V_c \end{bmatrix} + \mathcal{M}_4 \begin{bmatrix} u_1 \\ v_1 \end{bmatrix} = \begin{bmatrix} 0 \\ 0 \end{bmatrix} \tag{C.48}$$

with

$$\mathcal{M}_1 = \begin{bmatrix} 0 & -2\nu\partial_{xX}^2 \\ 2\nu\partial_{xX}^2 & 0 \end{bmatrix}, \tag{C.49}$$

$$\mathcal{M}_2 = \begin{bmatrix} -2(U_cV_2 + V_cU_2) & -2(3V_cV_2 + U_cU_2) - \nu\partial_X^2 \\ 2(3U_cU_2 + V_cV_2) + \nu\partial_X^2 & 2(V_cU_2 + U_cV_2) \end{bmatrix}, \tag{C.50}$$

$$\mathcal{M}_3 = 2\begin{bmatrix} -(u_1v_2 + v_1u_2) & -(3v_1v_2 + u_1u_2) \\ 3u_1u_2 + v_1v_2 & v_1u_2 + u_1v_2 \end{bmatrix} \tag{C.51}$$

and

$$\mathcal{M}_4 = \begin{bmatrix} 0 & -(u_1^2 + v_1^2) \\ u_1^2 + v_1^2 & 0 \end{bmatrix} \tag{C.52}$$

L is singular so we need a solvability condition for Eq.(C.48). Using the nullvector of $L^\dagger$,

$$\mathbf{w}(x) = \zeta \begin{bmatrix} w_1 \\ 1 \end{bmatrix} \left(e^{ik_cx} + e^{-ik_cx}\right) \tag{C.53}$$

and the inner product

$$\langle f, g\rangle = \int_0^L \bar{f}(x)^T \cdot g(x)dx \tag{C.54}$$

we get the solvability condition:

$$\underbrace{\langle \mathbf{w}, \mathcal{M}_1 \begin{bmatrix} u_2 \\ v_2 \end{bmatrix}\rangle}_{\text{I}} + \underbrace{\langle \mathbf{w}, \mathcal{M}_2 \begin{bmatrix} u_1 \\ v_1 \end{bmatrix}\rangle}_{\text{II}} + \underbrace{\langle \mathbf{w}, \mathcal{M}_3 \begin{bmatrix} U_0 \\ V_0 \end{bmatrix}\rangle}_{\text{III}} + \underbrace{\langle \mathbf{w}, \mathcal{M}_4 \begin{bmatrix} u_1 \\ v_1 \end{bmatrix}\rangle}_{\text{IV}} = 0 \tag{C.55}$$

Now we calculate each term in Eq.(C.55)

Calculation of I

$$\mathcal{M}_1 \begin{bmatrix} u_2 \\ v_2 \end{bmatrix} = -2\nu k_c \begin{bmatrix} -B_1 \\ A_1 \end{bmatrix} \left(\phi''(X)e^{ik_cx} + \bar{\phi}''(X)e^{-ik_cx}\right) + 8\nu k_c \begin{bmatrix} -B_2 \\ A_2 \end{bmatrix} \left(i\phi(X)\bar{\phi}(X)e^{2ik_cx} - i\bar{\phi}(X)\bar{\phi}'(X)e^{-2ik_cx}\right) \tag{C.56}$$

and then

$$\langle \mathbf{w}, \mathcal{M}_1 \begin{bmatrix} u_2 \\ v_2 \end{bmatrix} \rangle = 4L\zeta\nu k_c(w_1 B_1 - A_1)\mathrm{Re}[\phi''(X)] \tag{C.57}$$

Calculation of II

Writing $U_2 = \delta_c \tilde{U}_2$ and $V_2 = \delta \tilde{V}_2$ we have:

$$\mathcal{M}_2 \begin{bmatrix} u_1 \\ v_1 \end{bmatrix} = 2\delta_c \begin{bmatrix} -(U_c\tilde{V}_2 + V_c\tilde{U}_2)a - (3V_c\tilde{V}_2 + U_c\tilde{U}_2) \\ (3U_c\tilde{U}_2 + V_c\tilde{V}_2)a + (V_c\tilde{U}_2 + U_c\tilde{V}_2) \end{bmatrix} \left(\phi(X)e^{ik_c x} + c.c.\right) +$$

$$\nu \begin{bmatrix} -1 \\ a \end{bmatrix} \left(\phi''(X)e^{ik_c x} + c.c.\right) \tag{C.58}$$

and then we have

$$\langle \mathbf{w}, \mathcal{M}_2 \begin{bmatrix} u_1 \\ v_1 \end{bmatrix} \rangle = 4\delta L\zeta(w_1 M_1 + M_2)\mathrm{Re}[\phi(X)] \tag{C.59}$$

where

$$\boxed{\begin{array}{c} M_1 = -(U_c\tilde{V}_2 + V_c\tilde{U}_2)a - (3V_c\tilde{V}_2 + U_c\tilde{U}_2) \\ \\ M_2 = (3U_c\tilde{U}_2 + V_c\tilde{V}_2)a + (V_c\tilde{U}_2 + U_c\tilde{V}_2) \end{array}} \tag{C.60}$$

Calculation of III

$$\mathcal{M}_3 \begin{bmatrix} U_c \\ V_c \end{bmatrix} = 2 \begin{bmatrix} -(u_1v_2 + v_1u_2)U_c - (3v_1v_2 + u_1u_2)V_c \\ (3u_1u_2 + v_1v_2)U_c + (v_1u_2 + u_1v_2)V_c \end{bmatrix} \tag{C.61}$$

Now we evaluate one by one the elements u_1v_2, v_1u_2, v_1v_2 and u_1u_2 of $\mathcal{M}_3$.

$$u_1v_2 = a(B_0 + B_2)\underbrace{\left(|\phi|^2\phi e^{ik_c x} + c.c.\right)}_{\Phi_1} +$$

$$aB_1\underbrace{\left(i\phi'\phi e^{2ik_c x} - i\bar{\phi}'\phi + c.c.\right)}_{\Phi_2} + aB_2\underbrace{\left(\phi^3 e^{3ik_c x} + c.c.\right)}_{\Phi_3} \tag{C.62}$$

$$v_1u_2 = (A_0 + A_2)\Phi_1 + A_1\Phi_2 + A_2\Phi_3 \tag{C.63}$$

$$u_1 u_2 = a(A_0 + A_2)\Phi_1 + aA_1\Phi_2 + aB_2\Phi_3 \tag{C.64}$$

$$v_1 v_2 = (B_0 + B_2)\Phi_1 + B_1\Phi_2 + B_2\Phi_3 \tag{C.65}$$

Ones we have evaluated each element we can calculate the inner product,

$$\langle \mathbf{w}, \mathcal{M}_3 \begin{bmatrix} U_c \\ V_c \end{bmatrix} \rangle = 4L\zeta(w_1 N_1 + N_2)\mathrm{Re}\left[|\phi|^2\phi\right] \tag{C.66}$$

with N_1 and N_2 are given by

$$\boxed{\begin{array}{c} N_1 = -(aU_c + 3V_c)(B_0 + B_2) - (U_c + aV_c)(A_0 + A_2) \\ \\ N_2 = (U_c + aV_c)(B_0 + B_2) + (3aU_c + V_c)(A_0 + A_2) \end{array}} \tag{C.67}$$

Calculation of IV

$$\mathcal{M}_4 \begin{bmatrix} u_1 \\ v_1 \end{bmatrix} = (u_1^2 + v_1^2) \begin{bmatrix} -v_1 \\ u_1 \end{bmatrix} =$$

$$(a^2 + 1) \begin{bmatrix} -1 \\ a \end{bmatrix} \left(3|\phi(X)|^2\phi(X)e^{ik_c x} + \phi^3(X)e^{3ik_c x} + c.c.\right) \tag{C.68}$$

and therefore,

$$\langle \mathbf{w}, \mathcal{M}_4 \begin{bmatrix} u_1 \\ v_1 \end{bmatrix} \rangle = 6L\zeta(a^2 + 1)\underbrace{(a - w_1)}_{=0}\mathrm{Re}\left[|\phi(X)|^2\phi(X)\right] = 0 \tag{C.69}$$

Amplitude equation for ϕ

Finally, after adding I, II, III and IV and equaling to zero, we get that the equation for ϕ reads:

$$\alpha_1\phi''(X) + \delta_c\alpha_2\phi(X) + \alpha_3|\phi(X)|^2\phi(X) = 0 \tag{C.70}$$

with

$$\alpha_1 = k_c\nu(aB_1 - A_1) \tag{C.71}$$

$$\alpha_2 = aM_1 + M_2 \tag{C.72}$$

$$\alpha_3 = aN_1 + N_2 \tag{C.73}$$

C.6 Solution of the amplitude equation

To solve Eq.(C.70) we take the ansatz $\phi(X) = Ae^{i\varphi}$, with $A \in \mathbb{R}^+$. With this ansatz two kind of solutions can be found depending on the fact that A depends on X or does not.

• If $A \neq A(X)$, then Eq.(C.70) becomes

$$\delta\alpha_2 A + \alpha_3 A^3 = 0$$

, with the solutions $A_0 = 0$ and $A_\pm = \pm\sqrt{-\delta\alpha_2/\alpha_3}$. Then the solution will be $\phi = \sqrt{-\dfrac{\delta\alpha_2}{\alpha_3}}e^{i\varphi}$, with φ arbitrary (due to the translational invariance).

• If $A = A(X)$, then Eq.(C.70) becomes

$$A''(X) = \beta_1 A(X) + \beta_2 A^3(X) \tag{C.74}$$

with $\beta_1 = -\delta\alpha_2/\alpha_1$ and $\beta_2 = -\alpha_3/\alpha_1$. Now we write the previous equation as a dynamical system and calculate the orbits in the phase portrait.

$$\begin{cases} \dot{x} = y \\ \dot{y} = \beta_1 x + \beta_2 x^3 \end{cases} \tag{C.75}$$

This system has three fixed points at $(x, y) = (0, 0)$ and $(x, y) = (\pm\sqrt{-\beta_1/\beta_2}, 0)$. The Jacobian matrix of the previous system evaluated at $(x, y) = (0, 0)$, has the eigenvalues $\pm\sqrt{\beta_1}$. Then $(0, 0)$ will be a saddle-point of the system if $\beta_1 > 0$.

The orbits in the phase space are given by

$$y^2 = \beta_1 x^2 + \beta_2 \frac{x^4}{2} + C_0. \tag{C.76}$$

If localized structures exist they will necessary pass by the saddle-point $(x, y) = (0, 0)$ from where we get that $C_0 = 0$. With this

$$\dot{x} = \pm\sqrt{\beta_1 x^2 + \beta_2 \frac{x^4}{2}} \tag{C.77}$$

that after making the change of variables $z^2 = \beta_1 x^2 + \beta_2 \dfrac{x^4}{2}$, can be written as:

$$\dot{z} = z^2 - \beta_1 \tag{C.78}$$

From there we arrive to the integral equation

$$\int \frac{dz}{\left(\frac{z}{\sqrt{\beta_1}}\right)^2 - 1} = \int \beta_1 dt \tag{C.79}$$

Taking the change of variables $\xi = \frac{z}{\sqrt{\beta_1}}$, $dz = \sqrt{\beta_1} d\xi$,

$$\int \frac{d\xi}{\xi^2 - 1} = \sqrt{\beta_1} \int dt \tag{C.80}$$

and after integrating we get,

$$\ln\left(\frac{1+\xi}{1-\xi}\right) = -2\sqrt{\beta_1}(t - t_0).$$

Where t_0 comes from the integration constant. In this way we can write,

$$\frac{1+\xi}{1-\xi} = e^{-2\sqrt{\beta_1}(t-t_0)}$$

and from there, using that $\tanh x = \dfrac{\mathrm{e}^{2x} - 1}{\mathrm{e}^{2x} + 1}$, we get

$$z = \sqrt{\beta_1} \frac{e^{-2\sqrt{\beta_1}(t-t_0)} - 1}{e^{-2\sqrt{\beta_1}(t-t_0)} + 1} = \sqrt{\beta_1} \tanh\left(-\sqrt{\beta_1}(t - t_0)\right).$$

recovering the x variable,

$$x = \sqrt{\frac{2\beta_1}{\beta_2}\left(\tanh^2\left(\sqrt{\beta_1}(t-t_0)\right) - 1\right)} = \sqrt{\frac{-2\beta_1}{\beta_2}} \operatorname{sech}\left(\sqrt{\beta_1}(t-t_0)\right)$$

In the original variables,

$$\phi(X) = \sqrt{\frac{-2\beta_1}{\beta_2}} \operatorname{sech}\left(\sqrt{\beta_1}(X - X_0)\right) e^{i\varphi} \tag{C.81}$$

C.7 Patterns and bright solitons

If $A \neq A(X)$ then

$$\phi_p(x) = \sqrt{-\frac{\alpha_2}{\alpha_3}(\rho - \rho_c)}e^{i\varphi} \tag{C.82}$$

and we have a pattern or modulated solution:

$$\begin{bmatrix} U \\ V \end{bmatrix} = \begin{bmatrix} U_c \\ V_c \end{bmatrix} + \begin{bmatrix} \tilde{U}_2 \\ \tilde{V}_2 \end{bmatrix} (\rho - \rho_c) + 2 \begin{bmatrix} a \\ 1 \end{bmatrix} \phi_p(x)\cos(k_c x) \tag{C.83}$$

When $\alpha_2/\alpha_3 > 0$, the pattern bifurcates subcritically toward $\rho < \rho_c$ and when $\alpha_2/\alpha_3 < 0$ it does supercriticaly towards $\rho > \rho_c$. The transition between supercritical and subcritical takes place at the value of θ where α_2/α_3 becomes zero. goes from negative to positive. This value corresponds to $\theta = 41/30 \approx 1.37$, as it was already predicted in Refs. [2, 3].

When $\alpha_2/\alpha_3 > 0$, and $A = A(X)$ we have that:

$$\phi_s(x) = \sqrt{\frac{-2\alpha_2(\rho - \rho_c)}{\alpha_3}}\operatorname{sech}\left(\sqrt{\frac{-\alpha_2(\rho - \rho_c)}{\alpha_1}}x\right)e^{i\varphi} \tag{C.84}$$

and there a localized bright soliton solution given :

$$\begin{bmatrix} U \\ V \end{bmatrix} = \begin{bmatrix} U_c \\ V_c \end{bmatrix} + \begin{bmatrix} \tilde{U}_2 \\ \tilde{V}_2 \end{bmatrix} (\rho - \rho_c) + 2 \begin{bmatrix} a \\ 1 \end{bmatrix} \phi_s(x)\cos(k_c x) \tag{C.85}$$

References

[1] J. Burke, A. Yochelis, and E. Knobloch, *Classification of spatially localized oscillations in periodically forced dissipative systems,* SIAM J. Appl. Dyn. Syst. **7**, 651 (2008).

[2] L. A. Lugiato and R. Lefever, *Spatial dissipative structures in passive optical systems,* Phys. Rev. Lett. **58**, 2209-2211, 1987.

[3] M. Tlidi, R. Lefever and P. Mandel, *Pattern selection in optical bistability,* Quantum Semiclass. Opt. 8 931 (1996).

Appendix D

Weakly nonlinear analysis near reversible Takens-Bodganov bifurcation

In this appendix calculate weakly nonlinear LSs using multiple scale perturbation theory near the reversible Takens-Bodganov (RTB) bifurcation in the Lugiato-Lefever (LL) equation for both the anomalous and normal GVD regimes. The RTB occurs at the saddle-node $\mathrm{SN}_{hom,1}$ of the HSS solution for $\theta > 2$ in the anomalous regime and for $\theta < 2$ in the normal one. On the contrary $\mathrm{SN}_{hom,2}$ is a RTB only in the normal regime when $\theta > \sqrt{3}$. These saddle-nodes occur at the points

$$I_r \equiv I_{t,b} = \frac{1}{3}(2\theta \pm \sqrt{\theta^2 - 3}). \tag{D.1}$$

Here we perform the calculations using I_r as the label correpnding to the RTB point, non matter the if it corresponds to the $\mathrm{SN}_{hom,1}$ or $\mathrm{SN}_{hom,2}$.

We fix the value of the detuning parameter θ and we suppose that the LSs emerging from the RTB point can be described by the ansatz

$$\begin{bmatrix} U \\ V \end{bmatrix} = \begin{bmatrix} U \\ V \end{bmatrix}^* + \begin{bmatrix} u \\ v \end{bmatrix}, \tag{D.2}$$

where U^* and V^* correspond to the HSS A_0 and u and v capture the spatial dependence.

The pump amplitude parameter ρ is defined in function of I_0 as

$$\rho = \sqrt{I_0^3 - 2\theta I_0^2 + (1+\theta^2) I_0} \tag{D.3}$$

and we can sonsider the Taylor expansion about the bifurcation point I_r

$$\rho(I_0) = \underbrace{\rho(I_r)}_{\rho_r} + \underbrace{\left(\frac{d\rho}{dI_0}\right)_{I_r}}_{=0} (I_0 - I_r) + \underbrace{\frac{1}{2}\left(\frac{d^2\rho}{dI_0^2}\right)_{I_r}}_{\delta_r} \underbrace{(I_0 - I_r)^2}_{\epsilon^2} + \cdots \tag{D.4}$$

$\rho = \rho(I_0)$ has an extreme at $I_0 = I_r$, a maximum if $I_r \equiv I_b$ and a minimum if $I_r \equiv I_t$, and therefore we have that

$$\left(\frac{d\rho}{dI_s}\right)_{I_0} = 0. \tag{D.5}$$

Then we can define the expansion parameter ϵ measuring the parameter distance from the RTB as

$$\epsilon = \sqrt{\frac{\rho - \rho_r}{\delta_r}} \tag{D.6}$$

If $I_r \equiv I_b$ then

$$\delta_r \equiv \delta_b = \frac{1}{2}\left(\frac{d^2\rho}{dI_0^2}\right)_{I_b} = -\frac{\sqrt{\theta^2 - 3}}{2\rho_b} < 0 \tag{D.7}$$

and if $I_r \equiv I_t$ then

$$\delta_r \equiv \delta_t = \frac{1}{2}\left(\frac{d^2\rho}{dI_0^2}\right)_{I_t} = \frac{\sqrt{\theta^2 - 3}}{2\rho_t} > 0. \tag{D.8}$$

Nos we can expand both the homogeneous and the spatial dependent components of the ansatz (D.2) in funciton of ϵ as:

$$\begin{bmatrix} U \\ V \end{bmatrix}^* = \begin{bmatrix} U_r \\ V_r \end{bmatrix} + \epsilon \begin{bmatrix} U_1 \\ V_1 \end{bmatrix} + \epsilon^2 \begin{bmatrix} U_2 \\ V_2 \end{bmatrix} + ... \tag{D.9}$$

and

$$\begin{bmatrix} u \\ v \end{bmatrix} = \epsilon \begin{bmatrix} u_1 \\ v_1 \end{bmatrix} + \epsilon^2 \begin{bmatrix} u_2 \\ v_2 \end{bmatrix} + ... \tag{D.10}$$

where we allow the fields u_i and v_i to depend on the rescaling variable $X = \sqrt{\epsilon}x$.

Now introducing expansions (D.9) and (D.10) into the stationary LL equation (2.3) we can separate order by order in ϵ the components of the expansions (D.9) and (D.10). In Section D.1 we perform the weakly nonlinear analysis for the HSSs and in Section D.2 we do it for the spatial dependent components.

D.1 Asymptotic for the homogeneous steady state solutions

For the HSSs solutions we colect the terms of the same order in ϵ and we obtain the following equations and components for the expansion.

D.1.1 Equations at $\mathcal{O}(\epsilon^0)$

$$\mathcal{O}(\epsilon^0): \begin{bmatrix} -1 & \theta - I_r \\ -(\theta - I_r) & -1 \end{bmatrix} \begin{bmatrix} U_r \\ V_r \end{bmatrix} + \begin{bmatrix} \rho_r \\ 0 \end{bmatrix} = \begin{bmatrix} 0 \\ 0 \end{bmatrix} \tag{D.11}$$

From Eq.(D.11) we obtain that,

$$\begin{bmatrix} U_r \\ V_r \end{bmatrix} = \begin{bmatrix} \dfrac{\rho_r}{1 + (I_r - \theta)^2} \\ \dfrac{(I_r - \theta)\rho_r}{1 + (I_r - \theta)^2} \end{bmatrix} \tag{D.12}$$

D.1.2 Equations at $\mathcal{O}(\epsilon^1)$

$$\begin{bmatrix} -(1 + 2U_r V_r) & \theta - I_r - 2V_r^2 \\ -(\theta - I_r - 2U_r^2) & -1 + 2U_r V_r \end{bmatrix} \begin{bmatrix} U_1 \\ V_1 \end{bmatrix} = \begin{bmatrix} 0 \\ 0 \end{bmatrix} \tag{D.13}$$

If we define the linear operator

$$L \equiv \begin{bmatrix} -(1 + 2U_r V_r) & \theta - I_r - 2V_r^2 \\ -(\theta - I_r - 2U_r^2) & -1 + 2U_r V_r \end{bmatrix} \tag{D.14}$$

we can just write Eq.(D.13) as

$$L \begin{bmatrix} U_1 \\ V_1 \end{bmatrix} = \begin{bmatrix} 0 \\ 0 \end{bmatrix} \tag{D.15}$$

After some algebra we find that two out of the four components of the operator L are zero, and therefore we have:

$$L = \begin{bmatrix} 0 & 0 \\ -(\theta - I_r - 2U_r^2) & -2 \end{bmatrix} \tag{D.16}$$

Because of this, L is not invertible and that the system given by Eq.(D.15) has infinite number of solutions that can be written as

$$\begin{bmatrix} U_1 \\ V_1 \end{bmatrix} = \mu \begin{bmatrix} 1 \\ \eta \end{bmatrix} \tag{D.17}$$

with

$$\eta = \frac{-1}{2}(\theta - I_r - 2U_r^2) \tag{D.18}$$

To determine the value of μ we need to solve the $\mathcal{O}(\epsilon^2)$ system.

D.1.3 Equations at $\mathcal{O}(\epsilon^2)$

For order ϵ^2 we have the system

$$L \begin{bmatrix} U_2 \\ V_2 \end{bmatrix} = \begin{bmatrix} 2U_1V_1 & 2V_1^2 + I_1 \\ -(2U_1^2 + I_1) & -2V_1U_1 \end{bmatrix} \begin{bmatrix} U_r \\ V_r \end{bmatrix} - \begin{bmatrix} \delta_r \\ 0 \end{bmatrix} \tag{D.19}$$

where $I_1 = U_1^2 + V_1^2$. Because L is singular Eq.(D.19) has no solution unless the solvability condition is satisfied. To obtain this condition we need first to calculate the adjoint operator of L. In our case is just $L^\dagger = L^T$ and then:

$$L^\dagger = \begin{bmatrix} 0 & -(\theta - I_r - 2U_r^2) \\ 0 & -2 \end{bmatrix} \tag{D.20}$$

The nullvector of $L^\dagger$ is given by the solution of the next system of equations:

$$L^\dagger \begin{bmatrix} w_1 \\ w_2 \end{bmatrix} = \begin{bmatrix} 0 \\ 0 \end{bmatrix}. \tag{D.21}$$

again this system has an infinite number of solutions that we can write as:

$$\begin{bmatrix} w_1 \\ w_2 \end{bmatrix} = \begin{bmatrix} \zeta \\ 0 \end{bmatrix} \tag{D.22}$$

with $\zeta \in \mathbb{R}$. In the following we will take $\zeta = 1$.

The *Fredholm alternative theorem* confirm that an equation $Lu = f$ has non-trivial solution if given the nullvector w of $L^\dagger$, i.e. $L^\dagger w = 0$, the condition $\langle w, f \rangle = 0$ (solvability condition) is satisfy, being $\langle \cdot, \cdot \rangle$ the inner product defined in our case as the vector multiplication.

For our problem this condition is given by

$$\begin{bmatrix} 1 & 0 \end{bmatrix} \begin{bmatrix} 2U_1V_1U_r + (2V_1^2 + I_1)V_r - \delta_r \\ -(2U_1^2 + I_1)U_r - 2V_1U_1V_r \end{bmatrix} = \begin{bmatrix} 0 \\ 0 \end{bmatrix} \tag{D.23}$$

or just

$$2U_1V_1U_r + (2V_1^2 + I_1)V_r - \delta_r = 0 \tag{D.24}$$

Now using that $V_1 = \mu\eta$, and $U_1 = \mu$, one finds that the value $\mu = \mu_r$ satisfying Eq.(D.24) is

$$\mu_r \equiv \mu_{t,b} = \pm\sqrt{\frac{\delta_r}{3\eta^2 V_r + 2\eta U_r + V_r}} \tag{D.25}$$

For $I_r = I_b$ the denominator inside the square root is negative for any value of θ, but $\delta_r = \delta_b < 0$ so we everything inside the square root is positive. For $I_r = I_t$ the denominator is positive as well as the $\delta_r = \delta_t$. The question now is which sign must we take in Eq.(D.25).

For a value of $\rho \approx \rho_r$, the HSS is bivaluate for both $\mathrm{SN}_{hom,1}$ and $\mathrm{SN}_{hom,2}$. In terms of the amplitude $I_0 = |A|^2$ we have the expansion:

$$I_0(\rho) = I_r + \epsilon \underbrace{(2U_rU_1 + 2V_rV_1)}_{\pm\Lambda} + \mathcal{O}(\epsilon^2) \tag{D.26}$$

If $\rho \approx \rho_b$ ($\mathrm{SN}_{hom,1}$) the value $-\Lambda$ corresponds to the A_0^b branch and $+\Lambda$ to the A_0^m branch, and if $\rho \approx \rho_t$ ($\mathrm{SN}_{hom,2}$) $-\Lambda$ corresponds to the A_0^m branch and $+\Lambda$ to the A_0^t branch. From spatial eigenvalues analysis we know that the localized structures, if any, must be biasymptotic to the stable bottom or top branch. Then we need to choose $I_0(\rho) = I_r - \epsilon\Lambda$, around $\mathrm{SN}_{hom,1}$ and $I_0(\rho) = I_r + \epsilon\Lambda$ $\mathrm{SN}_{hom,1}$, where $\pm\Lambda = 2U_rU_1 + 2V_rV_1 = 2\mu_r(U_r + V_r\eta)$ with the $\pm$ coming from μ_r.

D.2 Asymptotic for spatial dependence solutions

Considering now the complete ansatz (including the space dependent terms) for the localized structures that we want to find, we get order by order the equations:

D.2.1 Equations at $\mathcal{O}(\epsilon^1)$

We can write it in matricial form and we get,

$$L\begin{bmatrix} U_1 + u_1 \\ V_1 + v_1 \end{bmatrix} = \begin{bmatrix} 0 \\ 0 \end{bmatrix} \tag{D.27}$$

and we know that $L[U_1, V_1]^T = [0, 0]^T$ then

$$L\begin{bmatrix} u_1 \\ v_1 \end{bmatrix} = \begin{bmatrix} 0 \\ 0 \end{bmatrix}. \tag{D.28}$$

The solution for this last equation can be written as:

$$\begin{bmatrix} u_1 \\ v_1 \end{bmatrix} = \begin{bmatrix} U_1 \\ V_1 \end{bmatrix} \psi(X) \tag{D.29}$$

with $\psi(X)$ a function to be determined from the higher order equations.

D.2.2 Equations at $\mathcal{O}(\epsilon^2)$

For the next order $\mathcal{O}(\epsilon^2)$ and after some algebra we get

$$\underbrace{L \begin{bmatrix} U_2 \\ V_2 \end{bmatrix} + \begin{bmatrix} -2U_1V_1 & -(2V_1^2 + I_1) \\ 2U_1^2 + I_1 & 2V_1U_1 \end{bmatrix} \begin{bmatrix} U_r \\ V_r \end{bmatrix} + \begin{bmatrix} \delta_r \\ 0 \end{bmatrix}}_{=0} +$$

$$+ L \begin{bmatrix} u_2 \\ v_2 \end{bmatrix} + \begin{bmatrix} -(2U_rV_1 + 2U_1V_r) & -(\nu\partial_X^2 + 6V_rV_1 + 2U_rU_1) \\ \nu\partial_X^2 + 6U_rU_1 + 2V_rV_1 & 2V_rU_1 + 2U_rV_1 \end{bmatrix} \begin{bmatrix} u_1 \\ v_1 \end{bmatrix} +$$

$$+ \begin{bmatrix} -2v_1u_1 & -(3v_1^2 + u_1^2) \\ 3u_1^2 + v_1^2 & 2v_1u_1 \end{bmatrix} \begin{bmatrix} U_r \\ V_r \end{bmatrix} = \begin{bmatrix} 0 \\ 0 \end{bmatrix} \tag{D.30}$$

where $I_1 = U_1^2 + V_1^2$.

If we define the operators,

$$\mathcal{P}_1 \equiv \begin{bmatrix} -(2U_rV_1 + 2U_1V_r) & -(\nu\partial_X^2 + 6V_rV_1 + 2U_rU_1) \\ \nu\partial_X^2 + 6U_rU_1 + 2V_rV_1 & 2V_rU_1 + 2U_rV_1 \end{bmatrix} \tag{D.31}$$

and

$$\mathcal{P}_2 \equiv \begin{bmatrix} -2v_1u_1 & -(3v_1^2 + u_1^2) \\ 3u_1^2 + v_1^2 & 2v_1u_1 \end{bmatrix} \tag{D.32}$$

we can write Eq. D.33 as

$$L \begin{bmatrix} u_2 \\ v_2 \end{bmatrix} = -\mathcal{P}_1 \begin{bmatrix} u_1 \\ v_1 \end{bmatrix} - \mathcal{P}_2 \begin{bmatrix} U_r \\ V_r \end{bmatrix} \tag{D.33}$$

Due to the singularity of L, Eq.(D.33) has no solution unless another solvability condition is satisfied. As before and in order to derive that condition we multiply

both sides of Eq.(D.33) by the nullvector of $L^\dagger$ (see Eq.(D.22)), resulting: and then the solvability condition is:

$$\left[\begin{array}{cc} 1 & 0 \end{array}\right] \mathcal{P}_1 \left[\begin{array}{c} u_1 \\ v_1 \end{array}\right] + \left[\begin{array}{cc} 1 & 0 \end{array}\right] \mathcal{P}_2 \left[\begin{array}{c} U_r \\ V_r \end{array}\right] = 0 \tag{D.34}$$

The dependence of ψ with X will be determined by this condition. To continue we evaluate the first term on the left of Eq.(D.34)

$$\mathcal{P}_1 \left[\begin{array}{c} u_1 \\ v_1 \end{array}\right] =$$

$$\left[\begin{array}{c} -(2U_rV_1 + 2U_1V_r)U_1\psi(X) - \nu\psi''(X)V_1 - (6V_rV_1 + 2U_rU_1)V_1\psi(X) \\ \nu\psi''(X)U_1 + (6U_rU_1 + 2V_rV_1)U_1\psi(X) + (2V_rU_1 + 2U_rV_1)V_1\psi(X) \end{array}\right] \tag{D.35}$$

and then

$$\left[\begin{array}{cc} 1 & 0 \end{array}\right] \mathcal{P}_1 \left[\begin{array}{c} u_1 \\ v_1 \end{array}\right] = -(2U_rV_1 + 2U_1V_r)U_1\psi(X)$$

$$- \nu\psi''(X)V_1 - (6V_rV_1 + 2U_rU_1)V_1\psi(X) = \alpha_1\psi''(X) + \alpha_2\psi(X) \tag{D.36}$$

with

$$\alpha_1 = -\nu V_1 \tag{D.37}$$

and

$$\alpha_2 = -(6V_rV_1^2 + 4U_rU_1V_1 + 2V_rU_1^2) = -2(3V_rV_1^2 + 2U_rU_1V_1 + V_rU_1^2) =$$

$$= -2\mu^2(3\eta^2V_r + 2\eta U_r + V_r) = -2\delta_r \tag{D.38}$$

From the second term on the left of Eq.(D.34) we get:

$$\mathcal{P}_2 \left[\begin{array}{c} U_r \\ V_r \end{array}\right] = \left[\begin{array}{cc} -2V_1U_1\psi^2(X) & -(3V_1^2 + U_1^2)\psi^2(X) \\ (3U_1^2 + V_1^2)\psi^2(X) & 2V_1U_1\psi^2(X) \end{array}\right] \left[\begin{array}{c} U_r \\ V_r \end{array}\right] =$$

$$\left[\begin{array}{c} -2V_1U_1U_r - (3V_1^2 + U_1^2)V_r \\ (3U_1^2 + V_1^2)U_r + 2V_1U_1V_r \end{array}\right] \psi^2(X) \tag{D.39}$$

and then

$$\left[\begin{array}{cc} 1 & 0 \end{array}\right] \mathcal{P}_2 \left[\begin{array}{c} U_r \\ V_r \end{array}\right] = -(2V_1U_1U_r + 3V_1^2V_r + U_1^2V_r)\psi^2(X) = \alpha_3\psi^2(X) \quad \text{(D.40)}$$

with

$$\alpha_3 = -(3V_1^2V_r + U_1^2V_r + 2U_1U_rV_1) = \frac{\alpha_2}{2} = -\delta_r \quad \text{(D.41)}$$

The solvability condition given by Eq.(D.34) is reduced to an ODE for $\psi(X)$ given by,

$$\alpha_1\psi''(X) + \alpha_2\psi(X) + \alpha_3\psi^2(X) = 0 \quad \text{(D.42)}$$

Eq.(D.42) is the amplitude equation around the RTB bifurcation.

D.3 Solution of the amplitude equation

We can write the previous equation as a dynamical system in space. In order to not complicate the notation we rename temporary the variables, $X \mapsto t$, $\psi(X) \mapsto x(t)$ and we define $y(t) = \dot{x}(t)$. In the fashion the dynamical system is:

$$\left\{\begin{array}{l} \dot{x} = y \\ \dot{y} = ax - bx^2 \end{array}\right. \quad \text{(D.43)}$$

with $a = -\alpha_2/\alpha_1$ and $b = \alpha_3/\alpha_1$. This system has two fixed points at $(x, y) = (0, 0)$ and $(x, y) = (-\alpha_2/\alpha_3, 0)$. If analyze their linear spectrum we get:

1. The jacobian matrix of the previous system evaluated at $(x_1, y_1) = (0, 0)$, has the eigenvalues $\pm\sqrt{-\alpha_2/\alpha_1}$. In order to have an homoclinic orbit (i.e. LSs), one need, at least, one stable and one unstable directions, hence (x_1, y_1) must be a saddle. The table D.1 shows the different values that the coefficient α_{21} takes in the different configurations

$\nu = 1$	$\sqrt{3} < \theta < 2$	$\theta > 2$
$I_r = I_b$	$\alpha_{21} > 0$, (x_1, y_1) is a center	$\alpha_{21} < 0$, (x_1, y_1) is a saddle
$I_r = I_t$	$\alpha_{21} > 0$, (x_1, y_1) is a center	$\alpha_{21} > 0$, (x_1, y_1) is a center

$\nu = -1$	$\theta < 2$	$\theta > 2$
$I_r = I_b$	$\alpha_{21} < 0$, (x_1, y_1) is a saddle	$\alpha_{21} > 0$, (x_1, y_1) is a center
$I_r = I_t$	$\alpha_{21} < 0$, (x_1, y_1) is a saddle	$\alpha_{21} < 0$, (x_1, y_1) is a saddle

Table D.1: Evaluation of the coefficient α_{21} at (x_1, y_1) for different configurations.

2. The jacobian matrix of the previous system evaluated at $(x_2, y_2) = (-\alpha_2/\alpha_3, 0)$, has the eigenvalues $\pm\sqrt{\alpha_2/\alpha_1}$. Table D.2 shows the different configurations obtained.

$\nu = 1$	$\sqrt{3} < \theta < 2$	$\theta > 2$
$I_r = I_b$	$\alpha_{21} > 0$, (x_2, y_2) is a saddle	$\alpha_{21} < 0$, (x_2, y_2) is a center
$I_r = I_t$	$\alpha_{21} > 0$, (x_2, y_2) is a saddle	$\alpha_{21} > 0$, (x_2, y_2) is a saddle
$\nu = -1$	$\theta < 2$	$\theta > 2$
$I_r = I_b$	$\alpha_{21} < 0$, (x_2, y_2) is a center	$\alpha_{21} > 0$, (x_2, y_2) is a saddle
$I_r = I_t$	$\alpha_{21} < 0$, (x_2, y_2) is a center	$\alpha_{21} < 0$, (x_2, y_2) is a center

Table D.2: Evaluation of the coefficient α_{21} at (x_2, y_2) for different configurations.

Written

$$\frac{dy}{dt} = \frac{dy}{dx}\dot{x} = y\frac{dy}{dx},$$

and combining the two ODEs in Eq.(D.43), one gets

$$y\frac{dy}{dx} = ax - bx^2. \tag{D.44}$$

Integrating it we get,

$$y^2 = ax^2 - \frac{2}{3}bx^3 + C_0.$$

Because we are looking for an homoclinic orbit, such orbit must be homoclinic to the saddle point $(x, y) = (0, 0)$ (it has stable and unstable manifolds). Then the equation for the phase path have to pass by $(x, y) = (0, 0)$. From there we derive that $C_0 = 0$ and then,

$$y = \pm\sqrt{ax^2 - \frac{2}{3}bx^3} \tag{D.45}$$

Making the change of variables $z^2 = a - \frac{2}{3}bx$, we can write

$$\dot{x} = y = \pm\sqrt{ax^2 - \frac{2}{3}bx^3} = \pm x\sqrt{a - \frac{2}{3}bx} = \pm xz$$

We write everything in function of z, ($x = \frac{3}{2b}(a - z^2)$ and $\dot{x} = -\frac{3}{b}z\dot{z}$) and we get:

$$\dot{z} = \pm\frac{1}{2}(z^2 - a) \tag{D.46}$$

making some readjustment we can integrate,

$$\int \frac{-dz}{1-\left(\frac{z}{\sqrt{a}}\right)^2} = \int \frac{a}{2} dt \tag{D.47}$$

taking the change of variables $\xi = \frac{z}{\sqrt{a}}$, $dz = \sqrt{a} d\xi$,

$$\int \frac{d\xi}{\xi^2 - 1} = \pm \frac{\sqrt{a}}{2} \int dt \tag{D.48}$$

we obtain

$$-\frac{1}{2} \ln\left(\frac{1+\xi}{1-\xi}\right) = \pm \frac{\sqrt{a}}{2} t + C_1.$$

We can absorbe the constant C_1 defining $C_1 = -\sqrt{a} t_0/2$, and from there

$$\frac{1+\xi}{1-\xi} = e^{\pm\sqrt{a}(t-t_0)}$$

and from there, using that $\tanh x = \frac{1-\mathrm{e}^{-2x}}{1+\mathrm{e}^{-2x}}$, we get

$$z = \sqrt{a} \frac{1 - e^{\pm\sqrt{a}(t-t_0)}}{1 + e^{\pm a(t-t_0)}} = \sqrt{a} \tanh\left(\frac{\pm\sqrt{a}(t-t_0)}{2}\right).$$

recovering the x variable,

$$x = \frac{3a}{2b}\left(1 - \tanh^2\left(\frac{\pm\sqrt{a}(t-t_0)}{2}\right)\right) = \frac{3a}{2b} \mathrm{sech}^2\left(\frac{\pm\sqrt{a}(t-t_0)}{2}\right) = -\frac{3\alpha_2}{2\alpha_3} \mathrm{sech}^2\left(\frac{1}{2}\sqrt{-\frac{\alpha_2}{\alpha_1}}(t-t_0)\right).$$

In the original variables,

$$\psi(X) = -3\mathrm{sech}^2\left(\frac{1}{2}\sqrt{-\frac{\alpha_2}{\alpha_1}}(X - X_0)\right) \tag{D.49}$$

This solution will exist when the coefficient $\alpha_{21} = \alpha_2/\alpha_1$ is negative.

D.4 Localized structures: Bright and dark solitons

After considering the changes $X = \sqrt{\epsilon}x$ and $\epsilon = \sqrt{\dfrac{\rho - \rho_r}{\delta_r}}$, Eq. (D.49) reads

$$\psi(x) = -3\mathrm{sech}^2\left(\frac{1}{2}\sqrt{-\frac{\alpha_2}{\alpha_1}}\left(\frac{\rho-\rho_r}{\delta_r}\right)^{1/4} x\right) \tag{D.50}$$

and due to the translational invariance of the system one can choose $x_0 = 0$. Therefore, the localized structure is the pulse,

$$\begin{bmatrix} U \\ V \end{bmatrix} = \begin{bmatrix} U_r \\ V_r \end{bmatrix} + \mu_r\sqrt{\frac{\rho-\rho_r}{\delta_r}}\begin{bmatrix} 1 \\ \eta \end{bmatrix}[1+\psi(x)]\,. \tag{D.51}$$

Where we have considered for HSS just contributions ϵ^0 and ϵ^1 and for the spatial one ϵ^1. The LS (D.51) is a bright pulse when $\mu_r = \mu_b$, and dark one when $\mu_r = \mu_t$.

List of publications

International peer-reviewed journals

1. P. Parra-Rivas, D. Gomila, M. A. Matías, and P. Colet, *Dissipative soliton excitability induced by spatial inhomogeneities and drift,* Physical Review Letters **110**, 064103 (1-5) (2013).

2. P. Parra-Rivas, D. Gomila, M. A. Matías, S. Coen, and L. Gelens, *Dynamics of localized and patterned structures in the Lugiato-Lefever equation determine the stability and shape of optical frequency combs,* Physical Review A **89**, 043813 (1-12) (2014).

3. P. Parra-Rivas, D. Gomila, F. Leo, S. Coen, and L. Gelens, *Third-order chromatic dispersion stabilizes Kerr frequency combs,* Optics Letters **39**, 2971-2974 (2014).

4. P. Parra-Rivas, D. Gomila, M. A. Matías, P. Colet, and L. Gelens, *Effects of inhomogeneities and drift on the dynamics of temporal solitons in fiber cavities and microresonators,* Optics Express **22**, 30943-30954 (2014).

5. P. Parra-Rivas, D. Gomila, M. A. Matías, P. Colet, and L. Gelens, *Competition between drift and spatial defects leads to oscillatory and excitable dynamics of dissipative solitons,* Physical Review E **93**, 012211 (1-17) (2016).

6. P. Parra-Rivas, D. Gomila, E. Knobloch, S. Coen, and L. Gelens, *Origin and stability of dark pulse Kerr combs in normal dispersion resonators,* Optics Letters **41**, 2402-2405 (2016).

7. P. Parra-Rivas, D. Gomila, E. Knobloch, and L. Gelens, *Dark solitons in the Lugiato-Lefever equation with normal dispersion,* Physical Review A **93**, 063839 (1-17) (2016).

8. P. Parra-Rivas, D. Gomila, and L. Gelens, *Stable dark and bright soliton Kerr combs can coexist in normal dispersion resonators* (submitted to Optics Letters).

9. P. Parra-Rivas, M. A. Matías, P. Colet, L. Gelens, D. Walgraef and D. Gomila, *Front interaction induces excitable behavior* (submitted to Physical Review Letters).

Book chapters

1. P. Parra-Rivas, D. Gomila, L. Gelens, M. A. Matías, and P. Colet, *Dynamics of Dissipative Solitons in Presence of Inhomogeneities and Drift* in *Nonlinear Optical Cavity Dynamics: From Microresonators to Fiber Lasers* (Ph. Grelu, ed.), Wiley, 107-128 (2015).

International conference papers

1. P. Parra-Rivas, D. Gomila, E. Knobloch, L. Gelens and S. Coen, *Origin and stability of dark pulse Kerr frequency combs in normal dispersion microresonators* Nonlinear Photonics 2016: Photonics and Fiber Technology 2016. Sydney, Australia: Optical Society of America, NM5A.5.

2. P. Parra-Rivas, D. Gomila, E. Knobloch, L. Gelens, S. Coen, *Stability Analysis of Dark Pulse Kerr Frequency Combs in Normal Dispersion Optical Microresonators* , CLEO: QELS Fundamental Science, FM2A. 5.

3. P. Parra-Rivas, D. Gomila, L. Gelens, *Characterizing the dynamics of cavity solitons and frequency combs in the Lugiato-Lefever equation,* SPIE Photonics Europe, 989403-989403-10.

4. P. Parra-Rivas, D. Gomila, F. Leo, S. Coen, L. Gelens, *Stabilization of frequency combs using third order dispersion* Optical Sensors, JM5A. 48.

5. P. Parra-Rivas, D. Gomila, M. A. Matias, F. Leo, S. Coen, and L. Gelens, *Modeling Kerr frequency combs using the Lugiato-Lefever equation: a characterization of the multistable landscape* SPIE Photonics Europe, 91361V-91361V-9.

6. L. Gelens, P. Parra-Rivas, F. Leo, D. Gomila, M. A. Matias, S. Coen, *Spatio-temporal stability of 1D Kerr cavity solitons* SPIE Photonics Europe, 91360J-91360J-10.